Long-time Correlations in Nonequilibrium Dispersion Forces

Dissertation

zur Erlangung des akademischen Grades

doctor rerum naturalium

(Dr. rer. nat.)

im Fach Physik

Spezialisierung: Theoretische Physik

eingereicht an der

Mathematisch-Naturwissenschaftlichen Fakultät

der Humboldt-Universität zu Berlin

von

M.Sc. Daniel Reiche

Präsidentin der Humboldt-Universität zu Berlin

Prof. Dr. Sabine Kunst

Dekan der Mathematisch-Naturwissenschaftlichen Fakultät

Prof. Dr. Elmar Kulke

Gutachter:

1. Prof. Kurt Busch
2. Prof. Jean-Jacques Greffet
3. Prof. Gert-Ludwig Ingold

Tag der mündlichen Prüfung: 13. Januar 2021

Ich erkläre, dass ich die Dissertation selbständig und nur unter Verwendung der von mir gemäß §7 Abs. 3 der Promotionsordnung der Mathematisch-Naturwissenschaftlichen Fakultät, veröffentlicht im Amtlichen Mitteilungsblatt der Humboldt-Universität zu Berlin Nr. 42/2018 am 11.07.2018, angegebenen Hilfsmittel angefertigt habe.

Ich habe mich nicht anderwärts um einen Doktorgrad in dem Promotionsfach beworben und besitze keinen entsprechenden Doktorgrad.

Berlin, den 8. September 2020

Humboldt-Universität zu Berlin
Mathematisch-Naturwissenschaftliche Fakultät
Institut für Physik

Long-time Correlations in Nonequilibrium Dispersion Forces

Daniel Reiche

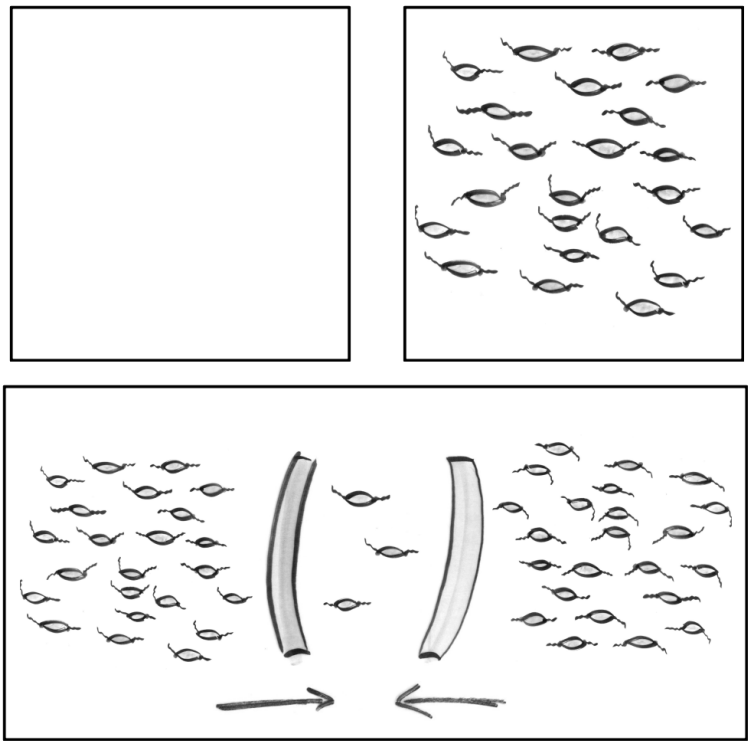

Prof. Kurt Busch | Dr. Francesco Intravaia

Für Sie, und für Ihn.

Abstract

We explore the dynamics of open quantum systems in both equilibrium and nonequilibrium situations. Our focus lies on the quantum-optical dispersion interaction between a microscopic particle and a complex electromagnetic environment. We argue that long-time correlations in the system can be essential for understanding the dynamics of the particle.

We define long-time correlations as those contributions to the autocorrelation function of quantum operators which scale as an inverse power law in the time delay. Incorporating long-time correlations into our theoretical model safeguards the self-consistency of our description and allows us to consider the full back-action of the environment on the particle. Moreover, it leads us to the prediction of previously overlooked effects and mechanisms determining dispersion forces in equilibrium and nonequilibrium. Our examples range from the interaction entropy of the magnetic Casimir-Polder effect, over the impact of material properties and geometric considerations for experimental setups, all the way down to the thermodynamics of quantum friction. We further provide the reader with a guideline when and how to include long-time correlations into theoretical models and what effects can be expected to emerge in the context of quantum-optical dispersion forces.

Zusammenfassung

Wir untersuchen die Dynamik von offenen Quantensystemen sowohl im Gleichgewicht als auch im Nichtgleichgewicht. Unser Fokus liegt dabei auf der quantenoptischen Dispersionswechselwirkung zwischen einem mikroskopischen Teilchen und einer komplexen elektromagnetischen Umgebung. Wir sind der Meinung, dass Langzeitkorrelationen in dem System essenziell zum Verständnis der Dynamik des Teilchens beitragen können.

Unter Langzeitkorrelationen verstehen wir die Beiträge zur Autokorrelationsfunktion von Quantenoperatoren, die als ein inverses Potenzgesetz in der Verzögerungszeit skalieren. Das Einbeziehen von Langzeitkorrelationen in unser theoretisches Modell sichert die Selbstkonsistenz unserer Beschreibung und ermöglicht es uns, die Rückkopplung der Umgebung auf das Teilchen vollständig zu berücksichtigen. Darüber hinaus erlaubt es uns die Vorhersage von bisher übersehenen Effekten und Mechanismen, die das Verhalten von Dispersionskräften im Gleichgewicht und Nichtgleichgewicht bestimmen. Unsere Beispiele reichen von der Wechselwirkungsentropie des magnetischen Casimir-Polder-Effekts, über den Einfluss von Materialeigenschaften und geometrischen Überlegungen auf experimentelle Aufbauten, bis hin zur Thermodynamik von Quantenreibung. Wir geben den Leser_innen außerdem eine Orientierungshilfe, wann und wie Langzeitkorrelationen in theoretische Modellbildungen einbezogen werden müssten und welche Auswirkungen im Zusammenhang mit quantenoptischen Dispersionskräften zu erwarten sind.

Popular Abstract - Research on Nothing

The following essay is based on a talk I gave to a nonexpert audience with diverse professional backgrounds. It aims to provide an intuitive and popular introduction to the field of quantum fluctuation-induced phenomena as well as the main outcomes of the present thesis for nonscientists.

Try to picture the vacuum.

The naive concept of nothing is rather simple: Take a confined volume and remove everything, all the particles and all the radiation. Whatever left is supposed to be vacuum. It is dark, cold, quiet, taste- and odorless. Perfect vacua are equivalent to each other and by definition the most simple system we can think of.

Intriguingly, however, real effects arise from what appears to be nothing. We call these effects *vacuum forces*. They explain why some bugs or beetles walk walls and certain chemical elements bond. Vacuum forces are setting fundamental constraints to the miniaturization of technical devices.

Presently, we witness exciting times for the physics of vacuum forces. Their existence is undoubtedly proven and they provide a powerful instrument in our toolbox for the design of future technologies. However, to this day, we are not yet certain about their exact properties and discover unprecedented insights and features with each passing decade. This is especially true in nonequilibrium situations, for instance when there is movement or a temperature gradient. Here, our understanding of these peculiar vacuum forces is still limited and contributing to closing the gap is the aim of the present thesis.

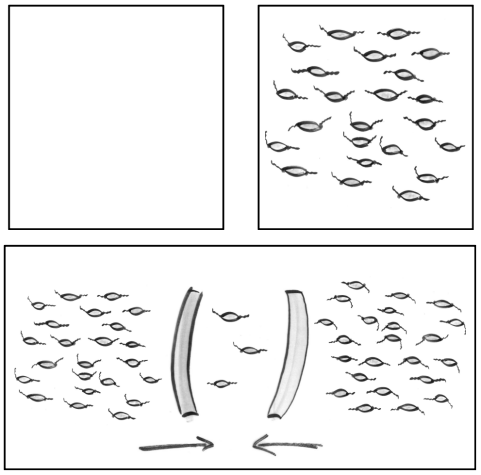

Figure 1: Visualization of the concept of vacuum from the perspective of modern physics. (*top left*) Classically, vacuum describes the absence of everything. (*top right*) Physics predicts virtual particles that exist even in vacuum. (*bottom*) The vacuum is modified by the presence of bodies and can lead to macroscopic forces.

To understand what vacuum forces are, we need to extend our vocabulary to the unintuitive. Suppose, for the moment, that there is something left in vacuum. For a lack of better words, say the vacuum is filled with *virtual particles*. They are neither a particle nor radiation and impossible to see directly. The question then is, whether we are able to tell the difference to the naive notion, to which there is no such thing as virtual particles.

A reliable answer to that question needs to be found via experiment: Consider a vacuum and this time we additionally introduce two plates forming a cavity. Being the observing experimentalist, we want to know whether the plates move. The naive notion of vacuum

prompts a trivial answer: No, there is nothing to cause any motion. Virtual particles, on the other hand, yield more interesting results. The two objects divide the vacuum in two areas: The cavity and the rest. Some of the virtual particles will fit in the cavity, but many more will have to remain outside. Those outside, disturbed by the boundary, exert a pressure on the plates. Those inside, likewise, push in opposite direction aiming for more space. But, since there are much fewer virtual particles inside, they cannot oppose the external force. Eventually the plates move towards each other; physicists call the cause of this motion *vacuum force*. Fascinatingly, such a mechanism can indeed be observed in experiments. Any objects in close proximity attract each other. Not because of gravity or electrostatics, but due to the mere existence of the vacuum between the bodies.

In the naive picture, there is no way to tell one vacuum from another; they are all equally simple. In the picture of virtual particles, however, the term vacuum is more ambiguous. In some situations, we will never notice the action of virtual particles at all. In other situations, the vacuum represents the dominating source of interaction. As a rule of thumb, whenever objects get as close as one millionth of a meter, or about hundred times thinner than the average human hair, we need to think about vacuum forces. That was our starting point in the endeavor of addressing the blank spaces on the map of knowledge on vacuum forces. We constructed a scenario where these forces are most striking, that is for instance when something very small (atom) is moving in the close vicinity to something comparably large (solids).

In particular, we were able to develop a comprehensive theoretical formalism revealing fascinating features: Vacuum forces in mechanical nonequilibrium are highly non-additive. Twice the amount of interacting bodies does not account for twice the vacuum force. The resulting force can be much stronger. We also found that the presence of a material can instigate rotations on moving atoms with counterintuitive direction. It is very much like the situation of a ball rolling down the hill, but only, in the case of atoms, the ball is rotating with opposite sense than what we are used to. From a fundamental perspective, we were able to advance state-of-the-art theories to a more general (thermodynamic) foundation by carefully scrutinizing the work exerted by the vacuum forces. Previous models would have predicted a slowly moving atom to heat up indefinitely over time. Luckily, this seems not to be the case, which we could show using a careful "bookkeeping" of any infused or lost energy in the system. Although apparently abstract, our configuration is actually quite close to modern experimental setups. It is not uncommon to shoot atoms through microscopic structures and measure the impact of the interaction. In order to confirm our theoretical predictions experimentally in the near future, we intensively studied the impact of the chosen geometry and materials and developed suitable conditions as well as concrete instructions for potential realizations in the laboratory.

If we wish to classify vacuum forces within the physics research of the last century, their exploration is not born in the attempt to find ever smaller and smaller building blocks of our world. It is not reliant on rapidly advancing experimental mega-projects in order to push existing theories to the most extreme regimes. And it is certainly not aiming for making singular statements in idealized conditions. Instead, the proper treatment of vacuum forces inevitably requires to explore the interplay between different theories, parameter regimes and scientific disciplines. What is taken for granted in one situation might completely fail in combination with another situation. In the present thesis, we intend to shine a light on the complexities and the richness of this very interdisciplinary and comprehensive field of research.

Preface and Outline

We introduce the field of quantum-optical fluctuation-induced effects, outline the scope of the thesis and provide an overview of its structure. In contrast to the previous Chapter which is supposed to be an introduction to the general public, the following considerations are addressed to physicists and represent the beginning of the main body of the thesis.

It is one of the most intriguing insights of modern physics that macroscopic forces can arise from what appears to be nothing. According to quantum electrodynamics, there is no free space in the classical sense of an empty vacuum [1]. Even at zero temperature, as a consequence of the Heisenberg uncertainty principle, the quantum vacuum is full of fluctuating fields and is by no means unique – as its name might suggest – but strongly dependent on the surrounding structures and on the motion of the observer. By implication, the physical system under investigation shows "signs" of quantum and thermal fluctuations, which nowadays go under a large class of effects called *fluctuation-induced phenomena*: Examples are measurable forces emerging from nonvanishing correlations in the system, although all physical (quantum) observables might vanish in the mean [2]. In the classical regime, where the main source of "noise" in the system often is of thermal nature, the probably most prominent example of such a system is the collision-driven, apparently random motion of tiny particles in a liquid, the so-called Brownian motion. Its theoretical study gathered pace at the dawn of the last century [3] and finds recent application in, e.g., the mimicking of biological systems in the form of directed "microswimmers" [4] or explaining the biological adhesion processes [5]. Going down in size, the impact of quantum features becomes inevitable. This, of course, enriches the variety as well as complexity of fluctuation-induced phenomena and it is probably no surprise that fluctuation-induced interactions became an important aspect in both engineering and fundamental research. To name only a few examples, fluctuation-induced interactions gained recent attention [6] for explaining the structure formation of the early universe [7–9], they play a significant role in the design of experiments detecting gravitational waves [10], or understanding the transition from quantum to classical [11, 12] and even impact asperity friction in micro-machines [13] as well as aeolian sand formation [14].

In the case of quantum fluctuations, the origin of fluctuations can be traced back to the uncertainty principle in the context of field quantization [1, 15]. In free space, this can lead to deviations from Maxwell's classical theory, but not until very high field intensities are involved [16]. An experimental confirmation of this regime hence remains to be practically challenging [17, 18]. In the presence of materials, however, the consequences of a fluctuating vacuum show quite naturally at low energy scales, where measurable forces occur between objects. Among the most famous, we find the van der Waals [2] and Casimir(-Polder) interactions [19, 20], which describe primarily attractive forces between neutral atoms and/or bodies due to quantum and thermal fluctuations of their respective polarization [21]. Their existence was confirmed by pioneering experiments [22, 23] and the accuracy of the measurements as well as the range of available setups has vastly improved since [24–30] framing fluctuation-induced forces in *equilibrium* as a well-understood tool in the manipulation of nano- and microscale devices.

Equilibrium can only be considered as an approximation to the physical reality and the extension of fluctuation-induced phenomena to *nonequilibrium* situations seems natural. Nonequilibrium phenomena are mostly closer to actual experiments and can come in many forms. For instance, different parts of the total system are held at different temperatures leading to heat transfer. Or parts of the system, say, an atom, are in relative motion with respect to other parts, where quantum friction forces can arise [31]. To this day, theoretical investigations exploring nonequilibrium phenomena heavily rely on equilibrium techniques severely simplifying the statistical properties of the interaction. One powerful principle which has been invoked for the understanding of such systems is the fluctuation-dissipation-relation (FDR): It establishes a detailed balance between incoming and outgoing power of an open quantum system in *equilibrium* and ensures that the system is in a state of maximal entropy for given average internal energy [32]. The FDR is commonly applied also to systems in *nonequilibrium*, under the assumption that Thermal Equilibrium might hold Locally (LTE) [33]. This assumption significantly reduces the mathematical complexity of the problem and was, e.g., recently applied to the situation of temperature gradients between macroscopic bodies [34–41], atom-surface forces in thermal [42, 43] as well as mechanical [43–45] nonequilibrium or under the influence of external driving fields [46], chains of rotating particles [47] and for computing the radiation of a relativistic electron close to an interface [48].

Experimentally, the LTE approximation is sometimes quite useful for modeling fluctuation-induced phenomena, prompting some authors to justify its application retroactively (see e.g. Ref. [49] for a recent realization of near-field radiative heat transfer). However, the theoretical basis for LTE and the conditions in which it fails to apply are usually not well justified or explained. For one, detailed balance in the sense of the equilibrium FDR is broken under nonequilibrium conditions and the LTE is known to often disregard back-action of the environment [50–52]. Further, in quantitative terms, it was proven to be insufficient in the context of atom-surface quantum friction, e.g., underestimating the force by roughly half [53] or misrepresenting other important mechanisms completely [M1, M2]. Equilibrium is a strong condition to assume, locally or globally. One has to be particularly careful and provide justification before making such an assumption.

Other methods describing nonequilibrium atom-surface interactions have their own strengths and drawbacks. For instance, the Born-Markov approximation (BM) [54, 55] or a time-dependent first-order perturbative treatment (TDPT) of the atomic level shift [56] do not rely on the assumption of equilibrium [57]. However, with respect to back-action and memory effects, these methods can only partially capture the impact of material properties. The reason is that, by construction, the BM and the TDPT formalism are limited to a perturbative approach in orders of the coupling between the respective subsystems which is then assumed to be weak in order to truncate the expansion. In the case of quantum friction, such approximations can have severe consequences. It has been shown that the constraint of weak coupling between system and bath can lead to an incorrect velocity scaling [57, 58] or the erroneous prediction of exponentially vanishing forces [43, 58].

All these techniques, the LTE, BM and TDPT approaches, although sometimes sufficient to predict certain quantities, have one “flaw” in common: They all underestimate the importance of long-time correlations one way or the other. The Born-Markov approximation, e.g., neglects the temporal memory of the system completely. This is somewhat related to perturbative

approaches, where the interaction is approximated near the resonance and the long-time backaction of the environment on the system is underrepresented. The LTE approach, on the other hand, manages to take off-resonant interactions into account, but fails to resolve the correlation between spatially separated subsystems; something that – as we will see – can be crucial for the dynamics of open systems.

In the present manuscript, we put a special emphasize on long-time/low-frequency correlations between the constituents of a coupled open quantum system in both equilibrium and nonequilibrium. To this end, we consider a microscopic point-like particle coupled to a macroscopic geometry made from realistic (dispersive and dissipative) materials and highlight the impact of long-time correlations on the quantum fluctuation-induced interaction based on a spectral analysis of the desired (non)equilibrium observables. Further, in the situation of mechanical nonequilibrium, we intend to explain and overcome some of the drawbacks of applying equilibrium-based approaches. Including the full range of relevant timescales using an exactly solvable formalism, we extensively discuss the effects of long-time correlations that are commonly ignored in the state-of-the-art literature. We will illustrate our findings using many different examples of particle-surface dispersion forces and, eventually, complete our discussion by putting the main theoretical advancements of the present manuscript on a general thermodynamic foundation. We thereby quantify the error of previous approximate or perturbative approaches. It is, after all, the self-consistent treatment including the full (long-time) backaction of the environment on the system of interest that allows to make reliable predictions and completely grasp the underlying physics of the system.

Outline

The main body of the thesis consists of five Chapters. Every Chapter is prefaced with a brief summary and, following the main body of the Chapter, separately concluded. The logical frame of the present thesis is given by Chapters 1 and 4: In Chapter 1, we introduce the concept of material-modified vacuum fluctuations as well as the material models used throughout the remaining Chapters. We put a special emphasis on analyzing the long-time fluctuations, given by the low-frequency behavior of the fluctuation's spectral decomposition. In this way, Chapter 1 serves a two-fold purpose by (i) introducing the main theoretical concepts used in the present thesis and (ii) already applying them to low-frequency field fluctuations in (non)equilibrium situations. Chapter 4, on the other hand, stands at the end of the thesis and revisits the concepts introduced in Chapter 1 from a thermodynamic point of view. We discuss the steady-state thermodynamics of mechanical nonequilbrium (power flux and energy) and find an intuitive and fundamental reason for the importance of correctly capturing long-time correlations in certain situations by connecting our formalism to the so-called nonequilibrium fluctuation-dissipation inequality. Further, we discuss in detail the realms of applicability of commonly applied assumptions (TDPT, LTE, BM) based on our more accurate description.

The two Chapters inside the frame of the Chapters 1 and 4 are concerned with explicit applications and discuss examples of quantum fluctuation-induced effects in equilibrium (Chapter 2) and mechanical nonequilibrium (Chapter 3), respectively. Concretely, in Chap. 2 we review the description of Casimir-Polder forces in equilibrium based on macroscopic electrodynamics and summarize some previous results. We discuss the impact of long-time correlations in the

context of the Casimir-Polder effect with (i) spatial nonlocality induced by the material or the geometry as well as (ii) a finite temperature in the system, and (iii) the behavior of the entropy in the limit of vanishing temperatures and a temperature-dependent dissipation rate. In Chapter 3, we deal with the situation of mechanical nonequilibrium, i.e. the particle in relative motion with respect to the surrounding material. We discuss the motion-induced modifications of the Casimir-Polder force as well as quantum friction, which is a pure nonequilibrium effect. To this end, we manage to describe the interaction between particle and material-modified vacuum for both effects (Casimir-Polder and quantum friction) including the back-action of the environment on the dynamics of the particle in a fully self-consistent way. A schematic of the thesis' outline can be found in Fig. 1.

In combination, Chapters 3 and 4 describe the main findings of the present thesis. Even though Chapters 1 and 2 consist, to a large extent, of original work with respect to the particular choice of material, geometry or perspective on the considered effect, it is the results of Chapters 3 and 4 that represent the major theoretical advancement to the field.

We conclude our work in Chapter 5, where we provide an extensive discussion of the fundamental and experimental implications of the present thesis thereby placing it in the context of related research. Further, we lay out additional details in the attached appendices.

The thesis contains material by the author that has been published or is about to be published elsewhere. In particular, the Chapters 1, 2, 3 and 4 are partially based on Refs. [M3, P1], Ref. [M3], Refs. [M1, M2, M4, M5, P2, P3] and Refs. [M2, M6], respectively.

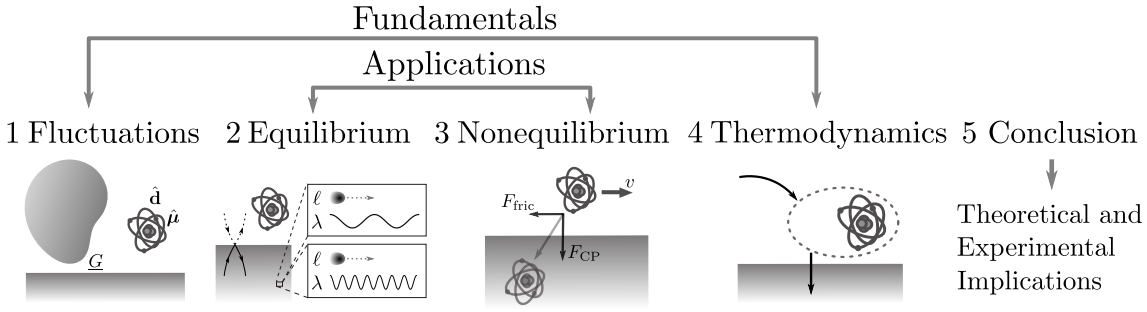

Figure 1: Logical organization of the thesis. Chapters 1 and 4 contain the fundamental results of the work framing the concrete applications to physical setups which are described in Chapters 2 and 3. We conclude in Chapter 5 by discussing the theoretical and experimental implications of our work. For illustration, we assigned a sketch to every part of the thesis' main body that will be discussed in full detail in the corresponding Chapter.

Contents

CHAPTER 1

Fluctuations of the Electromagnetic Field

We provide a brief introduction to atom-surface interactions, specify the physical system and introduce the main quantities of interest. Based on the formalism of macroscopic electrodynamics, we discuss the *second order correlations* (second moment) of the electromagnetic field which we will also call *fluctuations* using both terms interchangeably. Reviewing the most important material models for our purposes and touching the type of nonequilibrium considered in the thesis, we put special focus on the fluctuation's low-frequency/long-time behavior. The present chapter contains work by the author that has been published in Ref. [M3] or is about to be published [P1].

Studying fluctuation-induced phenomena in quantum optical systems combines a wide range of physical disciplines ranging from nonequilibrium quantum field theory via the thermodynamics of open (quantum) systems to the description of collective excitations in solid state physics. Roughly speaking, by *fluctuations* (or noise), we refer to quantities that are zero in the mean, but have non-vanishing higher order correlations. In physics, fluctuation-induced interactions have a rich history. Starting from the first theoretical descriptions of classical Brownian motion by Einstein [3], Smoluchowski [59] and Langevin [60] at the dawn of the last century, fluctuation-induced phenomena have entered the realm of optics with the discovery of the most fundamental quantum uncertainty [1, 61–65] and the description of molecular attraction by London just a few years later [2]. It is, in fact, this very last effect we are interested in: The interaction between a number of microscopic and macroscopic bodies mediated by the material-modified fluctuations of the vacuum. As we will explain in detail below, neutral bodies and/or particles separated by vacuum attract each other due to the mere presence of quantum and thermal fluctuations and the corresponding effects have instigated their own area of research usually referred to as *Casimir physics* [66]. First explored in a quantum field theoretical description by Casimir and Polder in 1948 [19, 20], various related phenomena in both equilibrium [67] and nonequilibrium [43] have been investigated with an ever growing interest to this day (see e.g. [68–70]). Due to its physical richness and importance for further technical advancements (see also preface and Chapter 5), Casimir physics has grown into a broad field and hence we abstain here from giving a comprehensive literature overview. Instead, we refer the reader to some excellent recent volumes [66, 67, 71–77] and focus on atom-surface interactions in the following.

The present thesis is concerned with the interaction between a single particle and its macroscopic electromagnetic environment. In the next paragraphs, following Ref. [66], we briefly review the experimental developments addressing fluctuation-induced atom-surface interactions. With respect to its closely related counterpart, the Casimir effect describing the interaction of *macroscopic* bodies [19], the equilibrium interaction between *microscopic particles and macroscopic bodies* is usually referred to as the *Casimir-Polder* effect [20]. Since a unifying theoretical framework was developed by Lifshitz [78] and later by Dzyaloshinskii, Lifshitz and Pitaevskii

[79], many related effects have been shown to be based on the very same underlying physical principles. We lay out that very principles in detail in the following Chapter. The distinction between, say, different distance regimes or experimental setups, is hence a matter of nomenclature. In our case, in order to simplify the terminology, this means that the term "Casimir-Polder interaction" is supposed to cover all distance scales. To be precise, this includes separations between particle and a material-vacuum interface that are small (historically London/van der Waals regime) and large (historically the Casimir-Polder regime) with respect to the dominant atomic transition frequency; as well as any intermediate regime. Moreover, we will extent the understanding of the word to nonequilibrium scenarios later in Chapter 3.

Since its first theoretical prediction for equilibrium systems by Casimir and Polder in 1948 [20], the fluctuation-induced quantum interaction between an atom and the material-modified (quantized) electromagnetic field registers an unhindered surge of interest that, to some extend, is connected to advancing experimental techniques as we depict in Fig. 1.1. One of the first comprehensive studies on molecular attraction, that considered the field theoretical predictions of Casimir and Polder, was conducted by Derjaguin and collaborators in 1956 [22]. Among other observations, they could identify the non-additive behavior of such forces. Non-additivity, in this context, means that the interaction with multiple bodies does not yield the force computed by adding all the interactions between pairs of bodies separately. We will turn to this topic in more detail in Chapter 3. Later, qualitative studies were conducted first indirectly by studying the thickness of Helium films on surfaces in 1972 [80] and later directly by measuring the deflection of an atomic beam due to the interaction with a cylinder in 1975 [81]. They could confirm an inverse cubed dependence of the Casimir-Polder interaction on the distance z_a between atoms and macroscopic surfaces in the regime of small separations (historically referred to as van der Waals regime). It took almost two more decades to obtain the first high-precision quantitative measurements in both the sub-micron regime by Sandoghdar *et al.* in 1992 [82] (historically referred to as van der Waals regime) and one year later the micron-range by Sukenik *et al.* [23] (historically referred to as Casimir-Polder regime). Both experiments detected the intensity of a sodium beam transmitted through a planar cavity of variable width and especially the latter confirmed the expected change of the force in its power law dependence on the atom-surface separation z_a from z_a^{-3} to z_a^{-4} [20]. So far, the experiments were measuring the Casimir-Polder force without explicitly studying the impact of temperatures on the interaction. This was not changed until 2007, where the temperature-dependence of the force was measured by Obrecht *et al.* in the micron range by observing the dipole oscillations of a Bose-Einstein condensate of ^{87}Rb atoms trapped magnetically in the vicinity of a flat surface and heated to some hundreds of Kelvin [83]. The intermediate range between the limiting scenarios of large or small atom-surface separations was first studied in 2010 using the reflection of ground-state rubidium atoms from an evanescent wave barrier created at the surface of a glass prism by Bender *et al.* [25].

In summary, it took roughly six decades to acquire a more or less comprehensive experimental probe of the Casimir-Polder effect with respect to the variations of distance and temperature. This is related in part to the complex methods needed in order to predictably control the dynamics of atoms which have been mainly developed since the mid nineteen eighties [84, 85] (see also Chap 5). Here, precision measurements and experimental advancements have posed a number of additional challenges and possibilities.

For instance, quantum fluctuation-induced phenomena are quite sensitive to a large number of parameters, one of them being the proper characterization of materials composing the macroscopic bodies. For instance, the choice of the material model might lead to very different predictions especially for low-frequency contributions to the spectrum of the fluctuations. Comparing the experimental results with the theoretical predictions has lead to a so far unresolved dispute on the correct material description at low-frequencies (i.e. much smaller than any surface excitation), the so-called Plasma-Drude controversy [86–88]. We will address this topic and in particular its relation to low-frequency/long-time correlations in Chapter 2.

Similarly, with the dawn of technologies allowing for a precise control of nano-particles [89–91] and, in particular, atoms [24, 92–99], Casimir-Polder forces became accessible in various other contexts. To name only a few examples, atom-surface forces were studied using atomic mirrors where the addition of the near-field van der Waals potential and an evanescent laser field created a repulsive potential near the surface [100]. Or, in the context of quantum reflection, researchers exploited the wave character of the particle in combination with the attractive surface potential in order to study specular reflection of slow atoms from a solid [101]. Further, the interaction between particle and surface can become important in atom-interferometric setups, where the de Broglie wave of the atoms was used to implement interferometry experiments [102, 103], and played a role in the design of so-called atom chips [27]. Developing a reliable theoretical framework in these situations is still a matter of debate and plays the key role in benefiting from atom-surface interactions in future experimental designs.

Lastly, we would like to mention that most of the previously discussed works relate to quantum fluctuations in equilibrium. Nonequilibrium, in contrast, is much closer to most realistic situations and, at least since the development of the full Master equation for quantum Brownian motion with nonlocal dissipation and colored noise by Hu, Paz and Zhang in 1992 [50] and the discovery of the nonequilibrium equality by Jarzynski in 1996 [104], the study of nonequilibrium systems has become one of the main branches of current research (see e.g. Refs. [43, 105–108]). For the case of atom-surface interactions, we want to mention three different types of nonequilibrium: (i) Excited atoms under the influence of external fields, (ii) thermal gradients in the system and (iii) mechanical nonequilibrium due to the relative motion of subsystems. In the first case (i), the atom is prepared in an excited state and in combination with the atomic dressing that originates from the interaction with the environment [109], the spontaneous decay rate of the atom is altered (usually enhanced) [110]. Experimentally, this effect was first described by Purcell in 1946 [111] for dissipation-less cavities and later extended to dispersive and dissipative bodies using for example a Green's function formalism [56, 110, 112] or a Master equation approach [113, 114]. Spontaneous emission has hence become an integral part of experiments with excited atoms [66, 113, 115] and a frequently used tool in photonics and plasmonics (see e.g. Ref. [29, 116–119]). In the second case (ii), some parts of the system are held at temperatures different from the rest of the system which leads to heat currents between the subsystems [33] and a thermal contribution to, e.g., Casimir-Polder forces [120]. Such a situation for macroscopic objects was studied experimentally measuring the thermal conductance between a sphere and a plate[1] for separations between tens of nanometers to microns [122], more recently by measuring the radiative heat flux between two parallel plates with gap sizes

[1] Choosing the sphere-plate geometry allows for an easier alignment of the objects and hence a better distance control in comparison to the two-plate setup [121].

between hundreds and thousands of nanometers [49], or by addressing the heat flux by coupling the phonons of the respective bodies [123] (see also Ref. [124] for an efficient control of the directionality, strength and even coherence of thermal light sources). In the case of atoms in thermal nonequilibrium fields, the modified Casimir-Polder force was measured first in Ref. [83] and can feature strong long-range behaviors [34] and intriguing temperature-scalings [125–127]. In the last case, mechanical nonequilibrium (iii), where the particle is in relative motion with respect to the macroscopic body, we can expect velocity-dependent corrections to the Casimir-Polder force [54]. Further[2], current theory predicts a decelerating force acting on the atom, the so-called quantum friction [31, 43, 105]. So far, quantum friction as well as velocity-corrections to the Casimir-Polder force have, to the best of our knowledge, completely eluded from any experimental confirmation. One of the first concrete experimental proposals appeared just recently[3]: Farías *et al.* propose to measure the geometric phase accumulated by an NV-center in diamond (representing the atomic degrees of freedom) attached to a cantilever's tip which is brought in close proximity to a rotating gold surface [30]. We will discuss experimental approaches to detect the traces of atomic motion in more detail in Chapter 5. Without going too much into detail here, by inspecting Fig. 1.1, we might conclude that nonequilibrium situations are possibly one of the next milestones in probing atom-surface dispersion forces.

Coming back to the theoretical perspective, the aim of the following Sections is to establish the formalism of electromagnetic fluctuations (Sec. 1.1), relating them to the low-frequency behavior of the interaction between particle and field. We further introduce the chosen material models in Sec. 1.2 and set the main theme of the thesis explaining on qualitative grounds why an extension of the state-of-the-art theory might be necessary (Sec. 1.3). We conclude with a brief summary in Sec. 1.4.

[2]Usually, quantum friction is considered at constant velocity for simplicity. For accelerated atoms, the non-uniform motion can lead to photon generation from the vacuum, referred to as *dynamical Casimir effect* [128, 129]. For moving (oscillating) atoms, such an behavior was, e.g., investigated by Ref. [130] and can be shown to be related to the Fulling-Davis-Unruh effect [131, 132].

[3]We note that another attempt was made earlier by Volokitin in 2016 who proposed to emulate the atomic motion by means of an electric current [133].

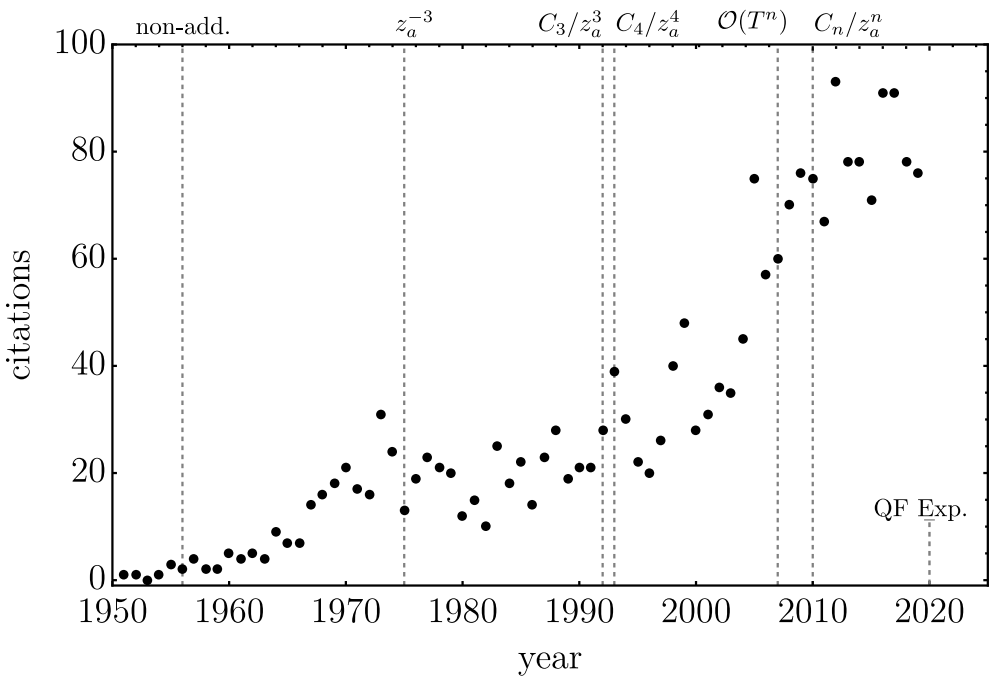

Figure 1.1: Citations per year of Casimir and Polder's original work [20] (following [67, 68]). The data is acquired using the "Dimensions" software [134]. We highlight the important experimental milestones confirming parts of the effect by dashed vertical lines. From left to right: Non-additivity was explored by Derjaguin et al. [22], the dependence on the atom-surface separation in the near-field (z_a^{-3}) was studied qualitatively by Shih et al [81], the quantitative estimate was obtained in the near-field (C_3/z_a^3) by Sandoghdar et al. [82] and in the far-field (C_4/z_a^4) by Sukenik et al. [23], temperature corrections ($\mathcal{O}(T^n)$) were studied by Obrecht et al. [83] and the intermediate distance regime (C_n/z_a^n) by Bender et al. [25]. Here, the constants C_3, C_4, C_n indicate that a quantitative analysis was performed in the reference. We further mark one of the first proposals for a potential method to measure quantum friction ("QF Exp.") by Farías et al. [30].

1.1 Quantum electrodynamics of material-modified vacuum fluctuations

We focus on electromagnetic fluctuation-induced phenomena. To be more precise, we are concerned with a neutral microscopic object interacting with one or more macroscopic bodies. The difference in size is to be understood in the way that the particle (i) cannot encounter any significant geometrical changes of its surrounding during the time of observation and (ii) the distance between any well-separated subsystems (atom, bulk, etc.) is much larger than typical inter-atomic distances of solid states (usually in the range of angstrom). Particle and bulk constitute an open quantum system, where the macroscopic body and the electromagnetic fields effectively act as a statistical bath.

1.1.1 Fluctuation-induced coupling and Maxwell's equations

We can combine the electromagnetic field in vacuum and matter using the framework of macroscopic quantum electrodynamics. In absence of external driving fields, the particle effectively interacts with what we will from now on call the *material-modified vacuum field*: The electromagnetic vacuum field influenced by the geometrical and dielectric properties of the surrounding material distribution.

Throughout the thesis, we are interested in non-magnetic and homogeneous bulk materials for simplicity. The particle can, in principle, possess both electric and magnetic polarizable features. However, since the interaction originating from magnetic properties is much weaker than the electric interaction in many situations [see discussion below Eq. (1.1)], we predominantly consider electric dipoles in most parts of the thesis and discuss the magnetic interaction in Sec. 2.2. Most importantly, since we are interested in fluctuation-induced interactions, all the objects in the system are electrically neutral and there are no free charges or currents in our system. We have sketched the general outline of our system in Fig. 1.2

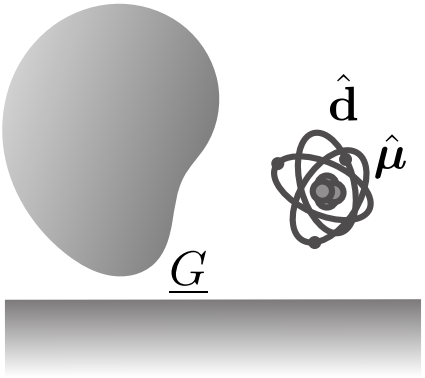

Figure 1.2: Sketch of the system we consider: A microscopic particle with electric (magnetic) dipole moment $\hat{\mathbf{d}}$ ($\hat{\boldsymbol{\mu}}$) interacts with a macroscopic material distribution described by the Green tensor $\underline{G}$.

Ignoring, for the time being, the interaction between the particle and any potential external driving fields, the prevalent state of the field+matter mixture is its respective ground state at zero temperature, or the thermal state if we include an extra heat bath of temperature T. Coupling particle and field perturbs the system and establishes a new common ground state with coupling-dependent energy [135, 136]; the dynamics of particle and electromagnetic environment are inseparably intertwined, even at zero temperature. At leading order, the corresponding coupling scale depends on the particles electric dipole moment $\mathbf{d}$, and the strength of the involved electric field $\mathbf{E}$. The electric dipole moment derives from intrinsic material parameters which we can relate to the elementary charge e and the Bohr radius a_0

such that $|\mathbf{d}| \propto ea_0$ in first approximation[4]. Even though dispersion forces – as their name suggests – depend on a wide range of frequencies, the presence of material interfaces will favor some wavelengths. As a rough estimate, the wavelengths λ dominating the interaction are at the order of the separation z between particle and the closest surface of the surrounding bodies $\lambda \sim z$. Note that we neglect possible surface resonances for simplicity. The fluctuating electric field, on the other hand, can be assumed[5] to scale with the inverse-cubed distance as it is the case e.g. for the atom-plate van der Waals force [138], $|\mathbf{E}| \propto z^{-3}$. On interaction time-scales of the order $t \sim z/c$ with c the speed of light, we obtain for the coupling scale (coupling rate $\times$ interaction time $\sim |\mathbf{dE}|t/\hbar$) of the interaction in the limiting case of very small separations[6] ($z = 1$ nm)

$$\frac{(ea_0)^2}{\hbar\epsilon_0}\frac{1}{z^3}\frac{z}{c} \approx 3 \times 10^{-4} \ll 1, \tag{1.1}$$

where we inserted Planck's reduced constant $\hbar$ and the vacuum permittivity ϵ_0 to get the correct units. The square of the dipole moment ($e^2a_0^2$) occurs because we are interested in the fluctuation-induced interactions where the observable vanishes in the mean. Accordingly, the corresponding coupling rate $g \equiv (ea_0)^2/\hbar\epsilon_0 z_a^3 \approx 0.05$ eV lies way below the main excitation energies for typical atoms and materials which are usually in the order of some electronvolts for atoms of the alkali metal group and conducting bulk materials [139–142]. In addition to the electric interaction, there will always be a magnetic component. Note, however, that the magnetic interaction will give only sub-leading contributions since the ratio between electric and magnetic dipole interaction scales as $(ea_0)^2/([\mu_\mathrm{B} g_\mathrm{s}]^2\epsilon_0\mu_0) \sim \alpha_\mathrm{fs}^{-2} \ll 1$, where $\alpha_\mathrm{fs} \approx 1/137$ is Sommerfeld's fein-structure constant and the magnetic dipole moment is determined by Bohr's magneton μ_B and the electron's Landé factor g_s [143]. This rough estimate has two main consequences for the general framework of our theory.

First, in terms of interaction strength and within the realm of our assumptions, we can grasp the most relevant part of the physics focusing on the dipole interaction only. Note, however, that multipole corrections can modify the interaction at very small distances between particle and surface [144]. Also, they can be relevant for a direction-dependent coupling with material interfaces as it is the case, e.g., for complex or chiral particles [145]. Multipole corrections also increase the prediction's accuracy [146], or can influence rotational degrees of freedom (see Sec. 3.2). In the remaining course of the thesis, however, it will be sufficient to consider the dominant dipole response of the particle; leaving higher-order multipole corrections unattended (see e.g. Refs. [147, 148] for a general treatment of the multipole expansion).

Second, due to its weakness [Eq. (1.1)], we conclude that the fluctuation-induced interaction between the material-modified vacuum field and a microscopic particle can be considered linear to a very good approximation.

[4] In principle, the response of the particle is also self-consistently modified by the interaction with its surrounding such that the dipole moment will hence also depend on field parameters. We will see in the remainder of the thesis that this will constitute a higher order correction for most cases we are interested in.

[5] Another, more systematic way to deduce the inverse cubed dependence is by means of the local density of states of the electric quantum vacuum field ρ_e. In the vicinity of a planar interface, it scales as $\rho_\mathrm{e} \propto z_a^{-3}$ [137].

[6] For even smaller separations, we enter the realm of inter-atomic distances and the formalism of macroscopic quantum electrodynamics might not hold anymore.

For linear systems, the quantum equations of motion coincide in their structure with the famous Maxwell equations [74], but the classical fields are promoted to quantum operators[7] for the electric field $\hat{\mathbf{E}}$, the electric displacement $\hat{\mathbf{D}}$, the magnetic induction $\hat{\mathbf{B}}$ and the magnetic field $\hat{\mathbf{H}}$. In our case, the lack of excess electric charges symmetrizes the source equations and leads to a vanishing geometrical flux for the electric displacement field operator as well as the magnetic induction[8],

$$\boldsymbol{\nabla}_{\mathbf{r}} \cdot \hat{\mathbf{D}}(\mathbf{r}, t) = 0, \qquad \boldsymbol{\nabla}_{\mathbf{r}} \cdot \hat{\mathbf{B}}(\mathbf{r}, t) = 0, \tag{1.2}$$

where $\mathbf{r}$ is the position, t the time and $\boldsymbol{\nabla}_{\mathbf{r}}$ the nabla operator with respect to spatial coordinates. Further, since we have no free currents, the curl equations similarly symmetrize

$$\boldsymbol{\nabla}_{\mathbf{r}} \times \hat{\mathbf{E}}(\mathbf{r}, t) + \partial_t \hat{\mathbf{B}}(\mathbf{r}, t) = 0, \qquad \boldsymbol{\nabla}_{\mathbf{r}} \times \hat{\mathbf{H}}(\mathbf{r}, t) - \partial_t \hat{\mathbf{D}}(\mathbf{r}, t) = 0, \tag{1.3}$$

where ∂_t is the partial derivative with respect to time. Note that charge conservation by means of the continuity equation is ensured automatically by Eqs. (1.2) and (1.3). In general, the electric field and displacement operators as well as the magnetic field and induction operators are related by

$$\hat{\mathbf{D}} = \epsilon_0 \hat{\mathbf{E}} + \hat{\mathbf{P}}, \qquad \epsilon_0 c^2 \hat{\mathbf{B}} = \hat{\mathbf{H}} + \hat{\mathbf{M}}, \tag{1.4}$$

which take the considered geometry and material properties into account. In the previous lines, ϵ_0 is the vacuum permittivity and c the speed of light. For the most parts of the discussion, we are interested in the situation of a vacuum with vanishing external fields. Hence, if not stated otherwise, we can write that[9]

$$\langle \hat{\mathbf{E}} \rangle = \langle \hat{\mathbf{D}} \rangle = \langle \hat{\mathbf{B}} \rangle = \langle \hat{\mathbf{H}} \rangle = 0. \tag{1.5}$$

Here, the quantum average $\langle \cdot \rangle$ is taken over the system's density matrix. Although they seem quite familiar, there are major differences between Eqs. (1.2), and (1.3) and their classical counterparts. Since the dynamical quantities are operators, their equations of motion now allow for both classical and quantum phenomena [153]. Further, Eqs. (1.2) and (1.3) meet the needs of the system's quantum character and include both classical as well as the field's and material's quantum zero-point fluctuations. Whenever necessary, we will assume the former to originate from an external macroscopic bath keeping the field+matter system at finite temperature T. However, even at zero temperature and in spite of Eqs. (1.5), there will always be non-vanishing correlations, e.g. $\langle \hat{\mathbf{E}}^2 \rangle \neq 0$, contrasting the classical theory.

To be more precise, we follow the approach of Rytov [154] and interpret Maxwell's equations as stochastic differential equations [155], where the vacuum field as well as the material in the

[7] "That it is abstract is unfortunate, but necessary" [149].

[8] We choose the Heisenberg-picture, where the Maxwell equations take over the role of the Schrödinger equation explicitly showing their relativistic invariance [150]. Further, throughout the thesis, we employ the canonical quantization scheme. We remark that this might not be the most fundamentally viable choice and refer the interested reader to a recent review [151] on triviality arguments in interacting quantum field theories such as Haag's theorem [152].

[9] For static fields, this could formally also be done by redefining every operator as $\hat{O} \to \hat{O} - \langle \hat{O} \rangle$.

system, although electrically neutral, act as a source of noise at temperature T.

For simplicity, we assumed the particle to be approximately point-like at its center-of-mass position $\mathbf{r}_a$. For the microscopic particle, in particular, this means that its electric $\hat{\mathbf{d}}$ and/or magnetic $\hat{\boldsymbol{\mu}}$ dipole moments give rise to a polarization $\hat{\mathbf{P}}_\mathrm{p} = \hat{\mathbf{d}}(t)\delta(\mathbf{r}-\mathbf{r}_a)$ and magnetization $\hat{\mathbf{M}}_\mathrm{p} = \hat{\boldsymbol{\mu}}(t)\delta(\mathbf{r}-\mathbf{r}_a)$ that interact with the field+matter composite, where we defined the three-dimensional Dirac delta $\delta(\mathbf{r}-\mathbf{r}')$. Note that the assumption of a point-like particle can become problematic in some situations. For instance, when we are concerned with the so-called radiation reaction for classical charged particles or the spontaneous vacuum decay of quantum oscillators. In both cases the equations of motion feature runaway solutions violating causality. This problem has been discussed thoroughly in the literature and can, e.g., be solved by lifting the point-like restriction by introducing a form factor for the particle and taking proper care of the field's back-action on the dynamics of the particle. We will encounter similar situations in this thesis and for now refer the reader to Refs. [156–161].

The vacuum field and the macroscopic bulk material, on the other hand, instigate their own polarization field

$$\hat{\mathbf{P}}_\mathrm{B} = \hat{\mathbf{P}}_\mathrm{N} + \hat{\mathbf{P}}_\mathrm{E} \tag{1.6}$$

decomposing into the polarization $\hat{\mathbf{P}}_\mathrm{N}$ related to intrinsic quantum and thermal fluctuations of the material degrees of freedom [162] and (self-consistently) the field-induced polarization $\mathbf{P}_\mathrm{E}$. Again, the field operators are supposed to be zero in their quantum average, i.e. $\langle\hat{\mathbf{d}}\rangle = \langle\hat{\boldsymbol{\mu}}\rangle = \langle\hat{\mathbf{P}}_\mathrm{N}\rangle = \langle\hat{\mathbf{P}}_\mathrm{E}\rangle = \mathbf{0}$. The specifics of the material are encoded in its response to external perturbations in terms of the susceptibility tensor $\underline{\chi}$ [147]. The susceptibility enables us to relate polarization and perturbation. Defining the permittivity tensor amplitude in frequency space[10]

$$\underline{\epsilon}(\mathbf{r},\mathbf{r}',\omega') = \delta(\mathbf{r}-\mathbf{r}')\mathbb{1} + \underline{\chi}(\mathbf{r},\mathbf{r}',\omega') \tag{1.7}$$

with $\mathbb{1}$ the three-dimensional unit matrix, we can write, e.g., for the polarization amplitude resulting from an external electric field

$$\hat{\mathbf{P}}_\mathrm{E}(\mathbf{r},\mathbf{r}',\omega) = \epsilon_0 \int \mathrm{d}^3\mathbf{r}' \ \Big[\underline{\epsilon}(\mathbf{r},\mathbf{r}',\omega) - \delta(\mathbf{r}-\mathbf{r}')\Big]\cdot\hat{\mathbf{E}}(\mathbf{r}',\omega). \tag{1.8}$$

Note that the permittivity can describe both vacuum and material such that we chose the integral domain to be the full space. For a given polarization noise $\hat{\mathbf{P}}_\mathrm{N}$ and permittivity $\underline{\epsilon}(\mathbf{r},\mathbf{r}',\omega)$, we have collected the necessary set of equations to solve the problem formally. Upon applying a Fourier transform in time (see Eq. (A.1) for our particular definition and choice of prefactors) and the curl to the Eqs. (1.3) as well as combining them with Eqs. (1.4), (1.6) and (1.8), we obtain

$$\boldsymbol{\nabla}_\mathbf{r}\times\boldsymbol{\nabla}_\mathbf{r}\times\begin{Bmatrix}\hat{\mathbf{E}}(\mathbf{r},\omega)\\ \hat{\mathbf{B}}(\mathbf{r},\omega)\end{Bmatrix} - \frac{\omega^2}{c^2}\int \mathrm{d}^2\mathbf{r}' \ \underline{\epsilon}(\mathbf{r},\mathbf{r}',\omega)\begin{Bmatrix}\hat{\mathbf{E}}(\mathbf{r}',\omega)\\ \hat{\mathbf{B}}(\mathbf{r}',\omega)\end{Bmatrix} = \frac{\omega^2}{\epsilon_0 c^2}\begin{Bmatrix}\hat{\mathbf{F}}_\mathrm{E}(\mathbf{r},\omega)\\ \hat{\mathbf{F}}_\mathrm{B}(\mathbf{r},\omega)\end{Bmatrix}, \tag{1.9}$$

[10] We only distinguish between a function and its Fourier transform via its arguments; i.e. $t \leftrightarrow \omega$ for time and frequency and similarly for position and wavevector.

where the condensed notation is to be understood row-wise in order to highlight the similarity of the wave equations for the electric and magnetic field operator. Therein, we have further defined

$$\hat{\mathbf{F}}_{\mathrm{E}}(\mathbf{r},\omega) := \left[\boldsymbol{\nabla}_{\mathbf{r}} \times \hat{\boldsymbol{\mu}}(\omega)/(-\mathrm{i}\omega) + \hat{\mathbf{d}}(\omega)\right] \delta(\mathbf{r}-\mathbf{r}_a) + \hat{\mathbf{P}}_{\mathrm{N}}(\mathbf{r},\omega), \tag{1.10a}$$

$$\omega^2 \hat{\mathbf{F}}_{\mathrm{B}}(\mathbf{r},\omega) := \left[\boldsymbol{\nabla}_{\mathbf{r}} \times \boldsymbol{\nabla}_{\mathbf{r}} \times \hat{\boldsymbol{\mu}}(\omega) - \mathrm{i}\omega\hat{\mathbf{d}}(\omega)\right] \delta(\mathbf{r}-\mathbf{r}_a) - \mathrm{i}\omega\hat{\mathbf{P}}_{\mathrm{N}}(\mathbf{r},\omega). \tag{1.10b}$$

The right hand sides (r.h.s.) of Eq. (1.9) can be interpreted as (stochastic) driving terms for the integro-differential equations. Recalling that we have no external fields, the only electromagnetic excitation other than vacuum fluctuations themselves can arise from (i) the particle by means of its (fluctuating) electric and magnetic dipole moments and (ii) the material distribution. This will be a reoccurring theme throughout the thesis: In our case, fluctuation-induced phenomena are dependent on a limited number of essential parameters; the only ingredients are the properties of the microscopic particle, the macroscopic material distribution, temperature of the system and the motion of an observer (see e.g. Chap. 3). For comparison, even though external drives and additional interactions might be necessary for an experimental investigation of setup, fluctuation-induced phenomena even exist in the theoretical limit of equilibrium and zero temperature.

We can solve the wave equations exactly using the Green tensor $\underline{G}_{\mathrm{E}}$ for the electric and $\underline{G}_{\mathrm{B}}$ for the magnetic fields, respectively. In the context of electrodynamics, the Green tensor solves for the field distribution at position $\mathbf{r}$ of a point charge at position $\mathbf{r}'$ in a, in principle, arbitrary geometry and material distribution. In our case, the Green tensor solves the equation

$$\boldsymbol{\nabla}_{\mathbf{r}} \times \boldsymbol{\nabla}_{\mathbf{r}} \times \underline{G}_{\mathrm{E/B}}(\mathbf{r},\mathbf{r}',\omega) - \frac{\omega^2}{c^2} \int \mathrm{d}^3\bar{\mathbf{r}}\, \underline{\epsilon}(\mathbf{r},\bar{\mathbf{r}},\omega) \cdot \underline{G}_{\mathrm{E/B}}(\bar{\mathbf{r}},\mathbf{r}',\omega) = \frac{\omega^2}{\epsilon_0 c^2}\delta(\mathbf{r}-\mathbf{r}') \tag{1.11}$$

which is formally identical in the electric ($\hat{\mathbf{E}}$) and the magnetic ($\hat{\mathbf{B}}$) case, but subject to different boundary conditions [147]. Since the Green tensor is physically a susceptibility, as e.g. also is the permittivity, it must be real in the time domain and we further assume the system to be reciprocal[11]. From that follows [58]

$$\underline{G}(\mathbf{r},\mathbf{r}',\omega) = \underline{G}^*(\mathbf{r},\mathbf{r}',-\omega), \qquad \underline{G}(\mathbf{r},\mathbf{r}',\omega) = \underline{G}^{\mathrm{T}}(\mathbf{r}',\mathbf{r},\omega), \tag{1.12}$$

where the star denotes the complex conjugate and T the transpose of a matrix. An extensive list and discussion of the Green tensors used in this thesis can be found in Appendix A. One particular solution of the original equations (1.9) is then found by splitting the full source distribution into infinitely many infinitely dense point sources and integrating over the relevant volume of the perturbation [147]. Since we include vacuum fluctuations in our consideration, the relevant volume is given by full space.

[11] Reciprocity is broken, e.g., when chiral materials are considered that differentiate in their response between different polarizations of light. We refer to Refs. [163–165] for generalizations to non-reciprocal media in the context of fluctuation-induced interactions.

For t_i being the initial time of the experiment, we can write the fields in time domain as

$$\begin{Bmatrix} \hat{\mathbf{E}}(\mathbf{r},t) \\ \hat{\mathbf{B}}(\mathbf{r},t) \end{Bmatrix} = \int_0^{t-t_i} \mathrm{d}\tau \int \mathrm{d}^3\mathbf{r}' \begin{Bmatrix} \underline{G}_{\mathrm{E}}(\mathbf{r},\mathbf{r}',\tau) \\ \underline{G}_{\mathrm{B}}(\mathbf{r},\mathbf{r}',\tau) \end{Bmatrix} \cdot \begin{Bmatrix} \hat{\mathbf{F}}_{\mathrm{E}}(\mathbf{r}',t-\tau) \\ \hat{\mathbf{F}}_{\mathrm{B}}(\mathbf{r}',t-\tau) \end{Bmatrix}. \tag{1.13}$$

In order to ensure causality, the wave equation will always posses odd orders of time derivatives or, equivalently, an imaginary part in the frequency domain [51]. This means that the system's dynamics is not time-reversal invariant and contains an overall attenuation of the excitation's amplitude; the evolution is damped. Hence, at sufficiently large times, e.g. when the system reaches a steady state or even equilibrium, the homogeneous solution of Eq. (1.9) (describing the transition regime to the steady-state) is suppressed. In this case, Eq. (1.13), representing the particular (driven) solution, gives the *full* solution of our system. It prevails in the long term limit since the vacuum and thermal fluctuations always guarantee a minimum supply of energy determined by the system's dissipative properties as we will discuss in the next Section. We have emphasized already that Eq. (1.9) describes a set of *stochastic* differential equations, but this fact has not been used yet. It is the aim of the next Section to discuss this feature in more detail.

1.1.2 The equilibrium fluctuation-dissipation relation

Material-modified vacuum fluctuations and the interaction with the microscopic particle induce electromagnetic field excitations (see Eqs. (1.9) and e.g. Refs. [67, 156]), albeit only with small probability due to the small energy scales involved (see Sec. 1.1.1). In other words, the system is perturbed, where the exact underlying distribution depends on the properties of the system, most notably its electromagnetic density of states (emDOS) [M3, 137, 166]. Due to the fundamental nature of material-modified vacuum fluctuations, the "driving" will prevail formally even at infinitely long observation times and zero temperature; they are an inevitable feature of every physical system.

Simultaneously, energy can be lost to the environment via different dissipation channels[12]. To name a few examples, the most intuitive loss channel is probably the dissipation in the macroscopic bulk material, which leads to phonon excitation within the lattice and in consequence the transformation of energy into heat. There are also coherent interaction phenomena between electromagnetic waves and the quasi-particle excitations of the conduction electrons in the material which can cause the electromagnetic excitations to loose energy, e.g. so-called Landau damping [167], some of which we will discuss in the following Section 1.2. Note, however, that even in the absence of macroscopic materials, the vacuum itself acts as a thermodynamic bath and shows dissipative properties as, for instance, leading to the spontaneous decay of excited particles [112]. After a sufficiently long time, when all the transient dynamics that depend on the initial dynamics abated, gains and losses balance and the system can reach a steady state [44, 168]. Under certain additional restrictions, the system can also approach equilibrium at temperature T [169]. Equilibrium, in particular, is installed when the system reaches its state of maximal entropy and its density matrix can be written in an exponential Gibbs form

[12] Sometimes this is referred to as *open system paradigm*; a fundamental physical framework ensuring causality in the interaction [113].

[170–172]. We will turn our full attention to that matter in Chap. 4 with a particular focus on nonequilibrium situations where no equilibrium, but steady-states can be achieved. For now, let us simply assume that the system reaches an equilibrium state with constant *mean* energy. Hence, whatever energy enters the systems needs to be dissipated in equal measure and vice versa.

The rather intuitive balance between "in" and "out" in the equilibrium state[13] finds its formal materialization in the so-called *fluctuation-dissipation-relation* (FDR) [32]. Theoretically, this powerful principle establishes a detailed balance between incoming and outgoing energy per unit time of an open quantum system in *equilibrium* and ensures that the system is in a state of maximal entropy. Pioneered by Nyquist [175] and extended to the quantum world by Callen and Welton [176], the mathematical formulation of this balance became an instructive concept for understanding fluctuation-induced forces on neutral microscopic particles placed near macroscopic objects in various contexts; ranging from fundamental questions of the applicability of thermodynamic laws [M3, M6, 135, 177, 178] to sophisticated applications such as the trapping of cold atoms near ultrathin optical fibers [24, 179]. Further examples are extensively discussed in the remainder of the thesis. As its name suggests, the FDR establishes a connection between the fluctuations of a physical observable and the dissipative losses. The latter is represented by the imaginary part of the corresponding linear susceptibility describing the response of the observable with respect to perturbations [180]. In our case, for the system introduced in the previous Section (Sec. 1.1.1), the FDR connects the noise polarization $\hat{\mathbf{P}}_\mathrm{N}$ with the linear susceptibility of the material distribution, i.e. its permittivity tensor $\underline{\epsilon}$. Following Ref. [162], we obtain [32]

$$\left\langle \hat{\mathbf{P}}_\mathrm{N}(\mathbf{r},\omega)\hat{\mathbf{P}}_\mathrm{N}(\mathbf{r}',\omega') \right\rangle = 4\pi\hbar \left[n(\omega,T)+1 \right] \mathrm{Im}\left[\underline{\epsilon}(\mathbf{r},\mathbf{r}',\omega) \right] \delta(\omega+\omega'), \tag{1.14}$$

where we define the mean bosonic occupation number $n(\omega,T) = (\exp[\hbar\omega/(k_\mathrm{B}T)]-1)^{-1}$ for the field excitation with k_B denoting the Boltzmann constant. Equation (1.14) is valid in the full space including the vacuum. Naively, this seems to evoke a contradiction to the fact that the permittivity of the pure vacuum is real and constant resulting in $\mathrm{Im}\underline{\epsilon}(\mathbf{r},\mathbf{r}',\omega) \to 0$ for the permittivity amplitude at $\mathbf{r},\mathbf{r}' \notin V$ with V the volume of the macroscopic bodies. In accordance with the FDR, we have that no dissipation would automatically mean vanishing fluctuations which cannot be true due to the unavoidable zero-point fluctuations. This apparent mismatch was resolved by Lifshitz who proposed to treat $\mathrm{Im}\underline{\epsilon}$ as finite even for vacuum and perform the limit $\mathrm{Im}\underline{\epsilon} \to 0$ at the end of the calculation [78]. Following Lifshitz, according to Eq. (1.13) the polarization noise induces an electric field at late times ($t - t_i$ much larger than the memory time of the setup) that reads

$$\hat{\mathbf{E}}_\mathrm{N}(\mathbf{r},\omega) = \int \mathrm{d}^3\mathbf{r}'\, \underline{G}(\mathbf{r},\mathbf{r}',\omega)\cdot\hat{\mathbf{P}}_\mathrm{N}(\mathbf{r}',\omega) \tag{1.15}$$

in Fourier space, where $\underline{G}$ is the electric Green tensor defined in Eq. (1.11) For the sake of clarity and brevity, we will focus on the electric part of the interaction from now on and we refer

[13] We note that the balance in equilibrium and at zero temperature is merely of formal nature since no actual work is being performed [173, 174]. We address this issue in more detail in Chapter 4 [see below Eq. (4.8)].

the reader to Ref. [74, 143, 147, 180] for an explicit evaluation of the magnetic field operator. Note that, to shorten notation, we omit the index of the Green tensor indicating its electric or magnetic character. In the following, we will always refer to the electric Green tensor, except for Sec. 2.2. The corresponding expression for the magnetic part follows analogously. Upon employing the FDR of second kind [181]

$$\mathrm{Im}\underline{G}(\mathbf{r},\mathbf{r}',\omega) = \int \mathrm{d}^3\mathbf{r}_1 \int \mathrm{d}^3\mathbf{r}_2\, \underline{G}(\mathbf{r},\mathbf{r}_1,\omega)\cdot \mathrm{Im}\left[\underline{\epsilon}(\mathbf{r}_1,\mathbf{r}_2,\omega)\right]\cdot \underline{G}^*(\mathbf{r}_2,\mathbf{r}',\omega) \tag{1.16}$$

and the fact that the Green tensor fulfills the crossing relation [see Eq. (1.12)], we obtain the fluctuation-dissipation relation for the electric field in absence of the microscopic particle,

$$\left\langle \hat{\mathbf{E}}_\mathrm{N}(\mathbf{r},\omega)\hat{\mathbf{E}}_\mathrm{N}(\mathbf{r}',\omega')\right\rangle = 4\pi\hbar\left[n(\omega,T)+1\right]\mathrm{Im}\left[\underline{G}(\mathbf{r},\mathbf{r}',\omega)\right]\delta(\omega+\omega'). \tag{1.17}$$

A few comments on the FDRs in Eqs. (1.14) and (1.17) are in order. First, the appearance of the delta function is related to the fact that the system is stationary. It is the mathematical consequence of exploiting causality for the Green tensor and sending $t-t_i\to\infty$, where the infinite is to be understood in the way that the time difference is much larger than the system's memory time [32]. Second, we note that the field fluctuation in equilibrium for given positions $\mathbf{r},\mathbf{r}'$ and frequency ω, or , in other words, the auto-correlation of $\hat{\mathbf{E}}_\mathrm{N}$, is completely determined by the temperature, the geometry and the dissipative properties of the system. The latter two are encoded in the Green tensor's imaginary part. Third, the dependence of the Green tensor on both positions $\mathbf{r}$ and $\mathbf{r}'$ technically allows to include spatial dispersion in the material description. As we will see later, spatial dispersion sensitively modifies the long-time correlations of the interaction and we will discuss models including such features in Sec. 1.2 and their impact on dispersion forces in Secs. 2.1 and 3.4. For spatially local materials, however, the functional dependence boils down to a simple Dirac delta in the expression of the permittivity (see below). Fourth, the magnitude of the material-modified vacuum fluctuations grows with the temperature. This can be seen directly from the boson occupation number ($\omega>0$)

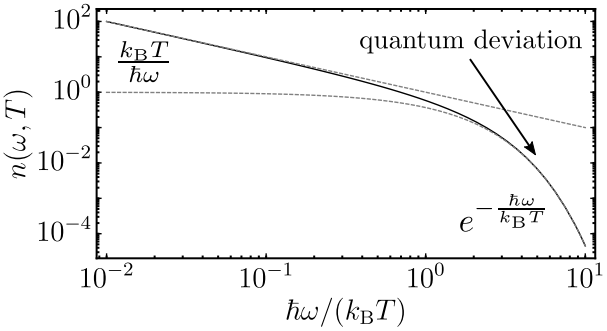

Figure 1.3: Bosonic occupation number as a function of the ratio between photon and thermal energy. We depict the asymptotes of Eq. (1.18) in gray and dashed.

$$n(\omega,T) = \frac{1}{e^{\frac{\hbar\omega}{k_\mathrm{B}T}}-1} \sim \begin{cases} e^{-\frac{\hbar\omega}{k_\mathrm{B}T}} & ,k_\mathrm{B}T\ll\hbar\omega \\ \frac{k_\mathrm{B}T}{\hbar\omega} & ,k_\mathrm{B}T\gg\hbar\omega \end{cases}. \tag{1.18}$$

For temperatures much larger than the corresponding frequencies dominating the interaction, we restore the classical Nyquist relation for thermal fluctuations which can be related with the classical statistical concept of the equipartition of energy, i.e. $\langle\hat{\mathbf{E}}_\mathrm{N}(\mathbf{r},\omega)\hat{\mathbf{E}}_\mathrm{N}(\mathbf{r}',\omega')\rangle\propto k_\mathrm{B}T$

[175]. In the opposite limit, with negligible impact of the temperature, the bosonic occupation number exponentially approaches zero for positive frequencies. However, due to the inevitable zero point fluctuations, the field correlation is still finite and we can write $n(\omega, T) + 1 \sim \theta(\omega)$ with $\theta(\omega)$ the Heaviside step function. We report the full dependence of the bosonic occupation number in Fig. 1.3.

We have established that the correlations of the electric field, or its fluctuations, can never vanish. At zero temperature, they are purely of quantum origin. For finite temperature, thermal fluctuations add up to the quantum fluctuations and effectively modify the corresponding fluctuation spectrum. It is important to note that the quantitative impact of the thermal fluctuations depends on the chosen frequency and can be relevant for frequencies [see Eq. (1.18) and Fig. 1.3]

$$\omega \lesssim \omega_T = \frac{k_\mathrm{B} T}{\hbar} \tag{1.19}$$

which, at room temperature $T = 289\,\mathrm{K}$, evaluates to roughly $\omega_T \approx 0.02$ eV. This is far below the atomic dipole transitions of typical alkali metals and the material resonances of common metals[14]. Consider, e.g., the case of rubidium ^{87}Rb whose dominant dipole transition is at the order of $\omega_\mathrm{Rb} \approx 1.3$ eV which corresponds to a temperature $T_\mathrm{Rb} \sim 1.5 \times 10^4$ K [140]. Most experiments dealing with microscopic particles occur at rather small temperatures way below room temperature in order to control the particle's motion [89, 96, 183]. We note that the important temperature scale is given by the relative difference between particle and environment and the environment can be much "hotter" than the particle even below room temperature. However, the important thing is that the coupling between particle and environment is either weak or short enough to allow the particle to equilibrate. Hence, in our case it is sufficient to study the impact of finite temperature at frequencies much smaller than the system's resonances only[15]. In order to illustrate this more clearly, let us consider the simplest case of the field fluctuations in vacuum. The only remaining dissipation channel is connected to the decay of a dipole excitation into vacuum and is encoded in the imaginary part of the vacuum Green tensor $\underline{G}_0$ [56, 112]. Using the expression for the Green tensor in appendix A evaluated at the same position $\mathbf{r} = \mathbf{r}'$, we obtain $\mathrm{Im}[\lim_{\mathbf{r}'\to\mathbf{r}} \underline{G}_0(\mathbf{r}, \mathbf{r}')] = \omega^3/(6\pi\epsilon_0 c^3)\mathbb{1}$ with $\mathbb{1}$ the three-dimensional identity matrix[16].

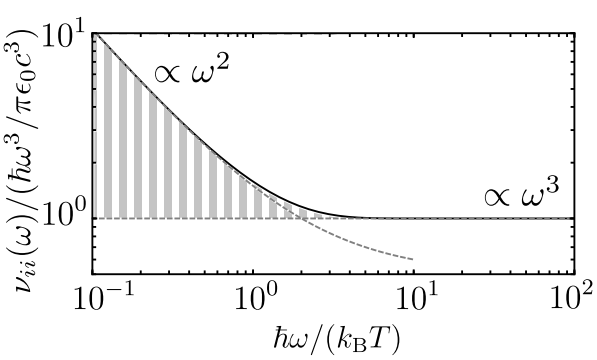

Figure 1.4: Power spectrum of the electric field fluctuations of the quantized vacuum at temperature T [see Eq. (1.20)]. We report the asymptotic expressions of Eq. (1.21) in gray dashed and highlight the finite-temperature deviation with gray stripes.

[14] For dielectrics, such as silicon nitride or glass, the relevant resonance frequency scales can be much smaller and comparable to ω_T which has been used, e.g., in the context of radiative heat transfer [122, 182].

[15] The situation can be different for magnetic interactions. The typical magnetic dipole transition lies in the range of micro-electronvolts which already corresponds to some tens of milli-kelvin [M3, 143, 184]. We will discuss this topic in more detail in Sec. 2.2.

[16] The cubed frequency dependence is typical for radiative decay into vacuum and can be connected to the third derivative with respect to time in the equations of motion describing radiation reaction and/or spontaneous decay rates; see discussion above Eq. (1.6).

We hence obtain for the field's power spectrum $\underline{\nu}$ of the pure vacuum, i.e. the electric energy stored in the field fluctuations per frequency ($\omega > 0$) [P1],

$$2\pi\delta(\omega+\omega')\underline{\nu}(\omega) \equiv \lim_{\mathbf{r}'\to\mathbf{r}} \left\langle \hat{\mathbf{E}}_{\mathrm{N}}(\mathbf{r},\omega)\hat{\mathbf{E}}_{\mathrm{N}}(\mathbf{r},\omega') \right\rangle = \frac{\hbar}{3\pi}\frac{\omega^3}{\epsilon_0 c^3}\left[n(\omega,T)+1\right]\delta(\omega+\omega')\mathbb{1} \tag{1.20}$$

effectively inheriting the temperature dependence of the bosonic occupation number weighted with the cubic vacuum decay rate.

In accordance with Eq. (1.18), the vacuum field fluctuations feature two distinct regimes, dominated by either vacuum or thermal fluctuations, which are separated by the thermal frequency ω_T. At zero temperature, the thermal regime vanishes identically. For finite temperatures, however, there always exists a regime dominated by thermal noise exceeding the zero-point fluctuations. To be precise, we consider the (coordinate-invariant) trace over the fields power spectrum $\mathrm{Tr}\underline{\nu} \equiv \nu_{ii}$ (sum over identical indices) and obtain asymptotically ($\omega > 0$)

$$\nu_{ii}(\omega) \sim \hbar\frac{\omega^3}{\pi\epsilon_0 c^3}\begin{cases}\theta(\omega), & \hbar\omega \gg k_{\mathrm{B}}T \\ \frac{k_{\mathrm{B}}T}{\hbar\omega}+\frac{1}{2}, & \hbar\omega \ll k_{\mathrm{B}}T\end{cases}. \tag{1.21}$$

To this end, we interpreted the Bose function as a functional distribution and employed the distributional expansion put forward by Estrada and Fulling [185, 186]. We refer to appendix B for the details. Note that, in the thermal regime, the field fluctuations scale quadratically in frequency in contrast to the cubic frequency scaling of the zero-point fluctuations. Further, they become independent of $\hbar$ pointing towards their classical origin. We report the full numerical evaluation in Fig. 1.4: As expected, the finite temperatures adds further to the field's power spectrum and their impact becomes most eminent for sufficiently low frequencies.

The fluctuation-dissipation-relations in Eqs. (1.17) and (1.20) prescribe a precise relation between the electric field fluctuations and the dissipation in the system at given frequency and temperature. While the equilibrium temperature is usually set by external (experimental) parameters, the relevant frequency scale is ultimately set by the quantity of interest, i.e. the physical observable, and can be experimentally accessed by the interaction with a test particle. As a first example, consider the case of an atom with one dominant electric dipole transition of frequency ω_a in its respective ground state placed in free space. In equilibrium at zero temperature, the atom will remain in the ground state (coupled system+bath) and cannot be excited macroscopically. At non-zero temperature, however, there is a finite probability of exciting the atom. The corresponding excitation rate Υ can be expected to scale with the energy stored in the electromagnetic field fluctuations, $\Upsilon \propto \langle\hat{\mathbf{E}}^2\rangle$, and the coupling between atom and field given by the atom's dipole elements[17] $\mathbf{d}$, $\Upsilon \propto |\mathbf{d}|^2$, where the modulus takes care of the fact that there is no distinct direction in vacuum. The relevant frequency scale is then set by the atomic transition ω_a and by means of a more careful derivation using Fermi's golden rule [56, 112], we obtain

$$\Upsilon(T) = \frac{|\mathbf{d}|^2}{\hbar}\frac{\omega_a^3}{3\pi\epsilon_0 c^3}n(\omega_a,T), \tag{1.22}$$

[17] Note that we do not consider the dipole operator here, but instead its absolute spatial components only.

where we recognize the cubic scaling with the atomic frequency from the free space Green tensor. As expected, the excitation rate vanishes at zero temperature as can bee seen immediately from Eq. (1.18). For finite temperature, the excitation rate is monotonously growing and for temperatures $T \gg \hbar\omega_a/k_\mathrm{B}$, we enter the linear regime, $\Upsilon \propto k_\mathrm{B}T$. Defining the vacuum polarizability[18] of the atom $\alpha_0 = 2|\mathbf{d}|^2/(3\hbar\omega_a)$ and taking, again, a ^{87}Rb atom ($\alpha_0 = 5.26 \times 10^{-39}$ Fm^2) at room temperature (289 K) with an electric transition frequency of $\omega_a = 1.3$ eV, the excitation rate evaluates to $\Upsilon \approx 2 \times 10^{-4}\mathrm{s}^{-1}$. This means that every $\Upsilon^{-1} \approx 1.1$ hours, one atom gets excited just by room temperature radiation. In order to excite one atom per second on average, we would need a temperature of around $T \approx 424$ K (around 151 °C). Hence, when the time scale of observation in experiments is much smaller than Υ^{-1}, noise induced excitations can safely be neglected. In the above example, this is mainly due to the high atomic transition frequency ω_a. For magnetic interactions, however, the transition frequencies are usually much smaller; in the range of some hundred MHz. Fluctuation-induced transitions from one magnetic spin state to another are therefore much more likely to happen, even at room temperature. This has severe consequences for recent experiments concerning the trapping and manipulating atoms in so-called *atom chips* [27]. Here, atoms are trapped in the vicinity of a surface due to the combination of the magnetic field of a conducting wire and a constant magnetic field perpendicular to the wire. At a given distance from the wire, the interaction potential corresponding to the field distribution shows a minimum. Atoms with specific spin states are attracted by this minimum whilst others, with spin of opposite sign, are repelled. Hence, spontaneous *spin-flips* lead to losses of atoms in the trap and impose a major constraint in the design of these devices. Note that the interaction with the surface of the chip (encoded in the Green tensor) will also alter the interaction and can increase the rate of spin-flips (see e.g. Ref. [187] and the following Section). In general, the latter effect is related to the Purcell effect [111].

Even though the power spectrum of the electromagnetic field can feature a quite rich structure of effects, it completely depends on the specifics of the setup and the observable of interest when it comes to the time and energy scales involved in the actual interaction. For instance, while the electric excitation rate is mostly unaffected by the long-time correlations introduced in the system due to room temperature (for typical atoms the relevant frequency is much larger than the thermal regime reported in Fig. 1.4), this can be vastly different for magnetic properties of the atom. In any case, for atomic excitation rates, the interaction leading to the spontaneous excitation of atoms is highly confined to a small frequency interval around the relevant transition due to the constructive interference of the interaction at the transition energy associated with Fermi's golden rule [1, 56, 112]. In the course of the present thesis, we will discuss many different situations covering a broad range of frequencies (as e.g. in Chap. 2 or Section 3.3) or particularly low frequency effects (as e.g. in Sec. 3.4). Prior to that, we generalize the previous discussion to a more realistic context involving dissipative and dispersive macroscopic materials. It turns out that not only temperature, but also the dissipative properties of a bulk material, via the FDR, contribute to the power spectrum of the field fluctuations and particularly impact the small frequency regime, where "small", again, is to be understood as frequencies smaller than any resonances of the system.

[18] Using that $[\alpha_0/\epsilon_0] = \mathrm{m}^3$, we conclude that $[\Upsilon] = \mathrm{s}^{-1}$, as expected.

1.2 Material properties and the influence of long-time correlations

In the previous Section, we focused on the rather unrealistic case of pure vacuum containing maximally one atom. Much closer to reality and most experiments is the situation including macroscopic materials. In particular, this means that we need to specify the geometry and the material properties. To this end, we will adopt a rather general approach that connects the chosen geometry with the specifics of the material using certain interface properties. Our approach comes with the advantage that the material properties itself, given by their respective permittivity $\underline{\epsilon}$, can be calculated for the setup of an infinitely extended bulk which is technically comparably easy since we do not need to take boundary conditions into account. We then still have to find the appropriate connection to the finite-volume geometry, especially in the vicinity of the boundaries.

Throughout the thesis, we will consider different geometries for the material distribution, e.g. planar, cylindrical and spherical. For clarity, we focus on *planar* structures in the present Section. Further, we assume that the material extends over an infinite half-space, even though most of the following results can be generalized and applied directly to more complicated scenarios as, for instance, a thin sheet or a planar cavity (see Secs. 2.1 and 3.4).

We are then interested in the correlations of the electric field in the vacuum modified by the presence of the surface. At fixed altitude from the surface z, the system is translation-invariant with respect to directions parallel to the interface. Using the symmetries of our system, we can employ a spatial Fourier transform such that Eq. (1.17) reduces to [58]

$$\left\langle \hat{\mathbf{E}}_{\mathrm{N}}(\mathbf{p},z,\omega)\hat{\mathbf{E}}_{\mathrm{N}}(\mathbf{p}',z,\omega')\right\rangle = 2\hbar(2\pi)^3\left[n(\omega,T)+1\right]\underline{G}_{\Im}(\mathbf{p},z,\omega)\delta(\omega+\omega')\delta(\mathbf{p}+\mathbf{p}') \tag{1.23}$$

where $\mathbf{p}$ is the parallel (to the surface) component of the wavevector $\mathbf{k} = \mathbf{p} + q\mathbf{z}$ with $\mathbf{z}$ the unit vector in direction perpendicular to the surface and q the corresponding component of the wavevector. We further defined $\underline{G}_{\Im} = (\underline{G} - \underline{G}^{\dagger})/(2\mathrm{i})$ with the dagger denoting the Hermitian transpose, replacing the simple imaginary part in real-space expressions [Eq. (1.17)]; thereby highlighting also non-symmetric parts of the Green tensor. Upon performing a Fourier transform in the wavevectors, we obtain for the electric field's power spectrum [see Eq. (1.20)]

$$\underline{\nu}(\omega) = 2\hbar\int\frac{\mathrm{d}^2\mathbf{p}}{(2\pi)^2}\left[n(\omega,T)+1\right]\underline{G}_{\Im}(\mathbf{p},z,\omega) \tag{1.24}$$

which is valid in equilibrium of the complete system at temperature T. For linear systems, the Green tensor decomposes into a sum of the vacuum contribution $\underline{G}_0$ in absence of any materials and a *scattered* contribution $\underline{g}$ taking the boundary conditions of the material into account [188]. Since we discussed the vacuum contribution in the last Sec. 1.1.2, the scattered contribution is the main object of interest in the following.

In our case, the scattered Green tensor in Fourier space at a position $z > 0$ with $z = 0$ being the position of the interface reads (see Ref. [189] and appendix A)

$$\underline{g}(\mathbf{p}, z, \omega) = \frac{\kappa}{2\epsilon_0} \left(r^p(\omega, p) \tilde{\mathbf{P}}_+ \tilde{\mathbf{P}}_- + \frac{\omega^2}{\kappa^2 c^2} r^s(\omega, p) \tilde{\mathbf{S}} \tilde{\mathbf{S}} \right) e^{-2\kappa z}, \tag{1.25}$$

where $\tilde{\mathbf{P}}_\pm = \frac{p}{\kappa}\mathbf{z} \mp \mathrm{i}\frac{\mathbf{p}}{p}$ and $\tilde{\mathbf{S}} = \frac{\mathbf{p}}{p} \times \mathbf{z}$ are the norm of the "p" (TM) and "s" (TE) polarization vectors and we defined $\kappa = \sqrt{p^2 - \omega^2/c^2}$ ($\mathrm{Re}\kappa > 0$, $\mathrm{Im}\kappa < 0$ and $|\mathbf{p}| = p$). Note from the exponential that for fixed position above the surface z, the Green tensor features both evanescent and propagating waves depending on the value of κ being real or imaginary, respectively. Remarkably, the complete information on the interaction with the material interface properties is encoded in the transverse magnetic (r^p) and the transverse electric (r^s) reflection coefficients that couple to the two respective polarizations in a planar setup [147]. For simplicity, we have assumed the bulk material to be isotropic, hence the dependence of the reflection coefficients on the wavevector's modulus. However, we allowed for an, in principle, fully nonlocal response of the material to field perturbations in both temporal and spatial dimensions. In this way, the fluctuations of the field connected to a scattering at the vacuum-material interface are not only dependent on temperature and frequency, but also on the distance from the surface as well as the length scales of the chosen material (model). We note, however, that the calculation of the reflection coefficients is non-trivial as we will discuss briefly in the following. Consequently, the material properties are imprinted in the power spectrum $\underline{\nu}$. In other words, by changing the material properties or the geometric outline of the setup, we modify the emDOS in the vicinity of the surface. Since the latter can be related to the Green tensor's imaginary part [190], material and geometry likewise determine qualitatively as well and quantitatively the fluctuations of the electromagnetic fields. Eventually, the chosen material and the exact properties of the used theoretical model will decide on the features of dispersion forces.

1.2.1 Interface model and spatial nonlocality of conductors

The material models we use in the present thesis have been discussed intensively elsewhere (see e.g. the textbooks [191–196]). In the present Section, we mainly state the results closely following Refs. [M4, M5, 180]. For planar interfaces, we have established that the material response is given by the transverse electric and magnetic reflection coefficients, r^s and r^p, respectively. For a single infinitely extended bulk in the lower half-space, the corresponding expressions have been found by many authors before and, especially for nonlocal materials, have been investigated in various contexts [197–210]. One possible approach is to express them using the transverse electric and magnetic surface impedances, Z^s and Z^p, as [147, 211]

$$r^s = \frac{Z^s/Z_0^s - 1}{Z^s/Z_0^s + 1}, \qquad r^p = \frac{1 - Z^p/Z_0^p}{1 + Z^p/Z_0^p}, \tag{1.26}$$

where $Z_0^{s/p}$ denote the corresponding expressions for the impedance in vacuum. Note that the reflection coefficients allow for both temporal and spatial nonlocality. A derivation of the surface impedances *ab initio* is non-trivial and, especially in order to include possible spatially

nonlocal features, we need to rely on further assumptions on the behavior of the material in close vicinity of the planar boundary. We focus, for now, on *conductors* such as simple metals or doped semi-conductors. Dielectrics are discussed in Sec. 1.2.3 in the spatially local case. For metals, specifying the surface properties amounts to finding the behavior of the source current density close to the interface [210]. Generally, in order to properly match the field modes inside and outside of the medium, we need to employ appropriate boundary conditions. The "natural" choice are Maxwell boundary conditions [147, 209]. Assuming non-magnetic materials and no free charges such that we have vanishing surface currents [147, 212], the boundary conditions yield for the tangential components

$$\mathbf{n} \times \hat{\mathbf{E}}_2 = \mathbf{n} \times \hat{\mathbf{E}}_1, \qquad \mathbf{n} \times \hat{\mathbf{B}}_2 = \mathbf{n} \times \hat{\mathbf{B}}_1 \tag{1.27}$$

and similarly for the normal components, where $\mathbf{n}$ is a unit vector normal to the surface and the indices "1" and "2" denote the different sides of the interface. For spatially local materials on both sides of the interface, the previous conditions are sufficient to describe reflection and transmission at the surface. However, for spatially nonlocal materials on at least one side of the interface, the situations is much more delicate. In contrast to the electromagnetic field in local dielectrics (e.g. vacuum), we now have an additional set of equations, namely rather involved material equations, which need to be solved alongside with Maxwell's equations. Hence, we also need additional boundary conditions in order to uniquely define the physical setup. The more comprehensive the material description, the more complex the mode structure of the equations of motion. For instance, spatially dispersive materials feature additional longitudinal modes. The usual Maxwell boundary conditions are then insufficient to describe the behavior of the additional modes. This observation lead to the development of the concept of *additional boundary conditions* (ABC) in order to account for the mismatch [200, 203, 211]. This has been, for instance, quite successful for describing nonlocal effects such as the anomalous skin effect [200, 213–216].

We emphasize, however, that assuming ABCs requires some additional assumptions and some degree of additional physical modeling on the setup. For one, we will work in the so-called *dielectric approximation*, where the length scale connected to spatial dispersion (e.g. the bulk electron's mean free path) is small in comparison to the geometric dimensions of the body [209, 211]. Further, the ABCs need to specify the current density as well as the charge density at the interface. For simplicity, we neglect spill-out effects [217] which amounts to a vanishing charge density at the surface. For the current density, one can, e.g., distinguish between "slip" and "no-slip" boundary conditions, where the former assumes the normal component of the current density and the latter assumes the complete current density to vanish at the surface, respectively [212]. For an alternative approach, we refer the reader to Refs. [209, 210], where it was shown that, for reciprocal materials under the dielectric approximation, the assumption of ABCs can be circumvented by means of Huygen's principle and the extinction theorem.

In the present thesis, we are interested in the main qualitative impact of spatial dispersion on the quantum fluctuations of the electromagnetic field. For our purposes it will hence be sufficient to employ one of the most commonly used models, i.e. the semi-classical infinite barrier model, that does assume extra boundary conditions.

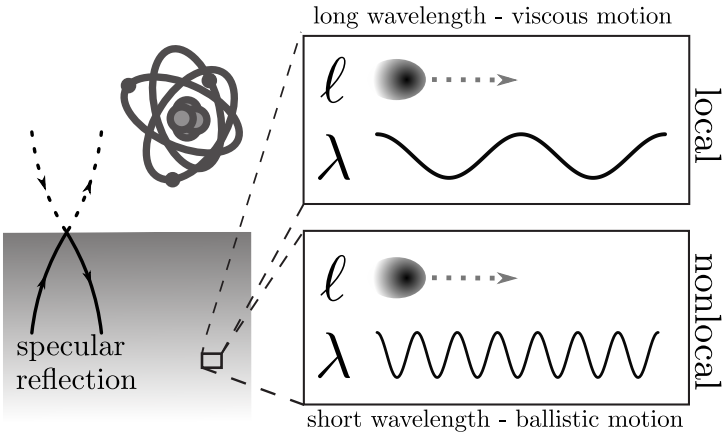

Figure 1.5: Details of the material description we use. For the planar interface, we assume specular reflection of electrons at the material-vacuum interface. Further, depending on the ratio between the wavelength λ of the radiation dominating the interaction and the bulk electron's mean free path ℓ, the material response is either local or spatially nonlocal (see main text).

One of the most successful and simple models for the study of a nonlocal response is the so-called semi-classical infinite barrier model (SCIB) [211]. It assumes that the electron's dynamics remains unchanged from the inside of the bulk up to a position infinitesimally close to the surface which then can be treated as a sharp boundary. At the boundary itself, bulk electrons are assumed to be reflected specularly at the metal/vacuum interface which is implemented by means of additional boundary conditions for the normal component of the current density which is supposed to vanish (slip boundary condition [212]) [202, 211, 218, 219]. Specular reflection is a reasonable assumption as long as the root-mean-square roughness of the surface is much smaller than the electron's mean free path [211]. In the opposite case, where we deal with comparably large roughness or polycrystalline metals, the assumption might break down and we would need to consider diffusive scattering at the interface [216, 220, 221]. Further, we note that for distances of the particle very close to the surface, the SCIB model is also a matter of discussion [222, 223]. However, for the distance regimes we are interested in, the boundary of the bulk can effectively be considered as planar. The dynamics of the Maxwell equations can then be solved exactly and the surface impedances read [200, 211]

$$Z^p(\omega,p)=\frac{2\mathrm{i}c}{\pi\omega}\int_0^\infty\frac{\mathrm{d}q}{k^2}\left[\frac{q^2}{\epsilon_t(\omega,k)-\frac{c^2k^2}{\omega^2}}+\frac{p^2}{\epsilon_l(\omega,k)}\right],\quad Z^s(\omega,p)=\frac{2\mathrm{i}c}{\pi\omega}\int_0^\infty\mathrm{d}q\;\frac{1}{\epsilon_t(\omega,k)-\frac{c^2k^2}{\omega^2}},\tag{1.28}$$

where $k=|\mathbf{k}|$. Further, $\epsilon_l(\omega,k)$ and $\epsilon_t(\omega,k)$ are the longitudinal and transverse bulk permittivities which, in general, depend on the frequency ω and the modulus of the wavevector k of the incoming radiation. They are related to the permittivity tensor $\underline{\epsilon}$ introduced earlier by first assuming homogeneity inside the bulk [$\underline{\epsilon}(\mathbf{r},\mathbf{r}',\omega)=\underline{\epsilon}(\mathbf{r}-\mathbf{r}',\omega)$], performing a Fourier transform in spatial coordinates and then diagonalizing the respective tensor leaving the two scalar functions $\epsilon_{t/l}$ [180, 211]. The surface impedances and the permittivities describe the response of the conductor to external perturbations [193] which can be divided in two limiting regimes: If the electron's mean-free path ℓ cannot be neglected with respect to the wavelength λ of the electromagnetic field, the wave can resolve the ballistic motion of the electrons and spatial nonlocality is significant. In the opposite case, the wave averages over a multi-scattering scenario and can only perceive an effective picture of the electrons in the bulk. In this limit, correlations between

separated point are not resolved and the material response is local in good approximation, i.e. we can discard the k dependence of the permittivity such that $\epsilon_l(\omega, k) = \epsilon_t(\omega, k) \equiv \epsilon(\omega)$. From that we recover the usual Fresnel reflection coefficients [147] with the surface impedances

$$\frac{Z^p(\omega,p)}{Z_0^p(\omega,p)} = \frac{\sqrt{\frac{\omega^2}{c^2}\epsilon(\omega) - p^2}}{\epsilon(\omega)\sqrt{\frac{\omega^2}{c^2} - p^2}}, \qquad \frac{Z^s(\omega,p)}{Z_0^s(\omega,p)} = \frac{\sqrt{\frac{\omega^2}{c^2} - p^2}}{\sqrt{\epsilon(\omega)\frac{\omega^2}{c^2} - p^2}} \tag{1.29}$$

which are also valid for dielectrics (see Sec. 1.2.3). Further the roots in Eq. (1.29) are to be taken with positive imaginary part. We depict the assumption of specular reflection within the SCIB model and the different limiting scenarios leading to local or nonlocal behavior in Fig. 1.5.

Equations (1.28) enable us to completely characterize the electromagnetic response of the conductor in terms of the bulk permittivity. Keeping the limitations (planar surface, specular reflections, ABCs) in mind, such a formulation drastically simplifies the modeling process since we now can consider an infinitely extended medium with higher symmetry than the interface-case to calculating the response. In the following two Sections, we briefly introduce some descriptions for the most common classes of materials, conductors and dielectrics, and focus on their different characteristics for low frequencies.

1.2.2 Metals and the bulk permittivity of the electron liquid

The most simple notion of a conductor, or metal, is in terms of the so-called *Drude model*. The Drude model is based on a partially filled conduction band which effectively leads to unbound electrons that can move "freely" inside the material [194]. If we consider these electrons to be non-interacting, but take a phenomenological dissipation time Γ motivated by collisions between the electrons and the other constituents of the lattice (ions, impurities, electrons) into account, the metal can be considered as a damped *gas* of free electrons interacting with an ionic background [191, 212]. Such an approach receives unbroken attention to this day and has been stunningly successful (see e.g. Refs. [140, 224, 225] for some recent examples), considering its long history that can be traced back to P. Drude in 1900 [226]. To be precise, neglecting magnetic properties, we can relate the (classical) motion of currents $\mathbf{j}$ to the electric field $\mathbf{E}$ at position $\mathbf{r}$ in the spatially homogeneous case by [147]

$$\left(\partial_t + \Gamma\right)\mathbf{j}(\mathbf{r},t) = \frac{\epsilon_0 c^2}{\lambda\!\!\!^{-2}_{\mathrm{p}}}\mathbf{E}(\mathbf{r},t) \tag{1.30}$$

with $\lambda\!\!\!^{-}_{\mathrm{p}} = c/\omega_{\mathrm{p}}$ the reduced wavelength related to the characteristic collective plasma excitation frequency ω_{p} of the metal (roughly 9 eV for gold [140]). For the corresponding permittivity, we combine Eq. (1.8) for local materials with Eq. (1.30) and use that $\partial_t \mathbf{P}(\mathbf{r},t) = \mathbf{j}(\mathbf{r},t)$, which yields

$$\epsilon_{\mathrm{Dr}}(\omega) = 1 - \frac{\omega_{\mathrm{p}}^2}{\omega(\omega + \mathrm{i}\Gamma)}. \tag{1.31}$$

The Drude model is local by construction and in combination with the surface properties, i.e. by inserting into Eqs. (1.29), it leads to distinct surface resonances propagating along the direction of the surface, but evanescently decaying in direction perpendicular to the interface[19]. The dispersion relation $\omega_{\rm sp} = \omega_{\rm sp}(p)$ of these so-called surface plasmon-polaritons (SPP) is given by

$$cp = \pm\frac{\sqrt{\epsilon_{\rm Dr}(\omega_{\rm sp})}}{\sqrt{\epsilon_{\rm Dr}(\omega_{\rm sp})+1}}\omega_{\rm sp} \Rightarrow \omega_{\rm sp} \sim -{\rm i}\frac{\Gamma}{2} \pm \frac{1}{2}\sqrt{\omega_{\rm p}^2 - \left(\frac{\Gamma}{2}\right)^2} \approx \frac{\omega_{\rm p}}{\sqrt{2}} - {\rm i}0^+, \tag{1.32}$$

where we considered the non-retarded limit[20] in the second step and weak dissipation $\Gamma \ll \omega_{\rm p}$ in the third. For a particle interacting with the surface, the SPP will constitute the main surface-induced mode coupling to the atomic degrees of freedom and will be re-occuring throughout the thesis (see Chaps. 2, 3 and 4). To the best of our knowledge, the first works directly aimed to study the electromagnetic surface response date back to Garnett explaining the color of glasses [228, 229] and later also contained in works on the scattering properties of dielectric spheres by Gustav Mie [230], the modern formalism was pioneered by Ritchie [231, 232]. In their non-dissipative version ($\Gamma = 0$), the SPP excitations have gained large interest in the field of *plasmonics* [190, 233–235]. We report the dispersion relation in the inset of Fig. 1.6.

However, for our purposes it is not the resonance itself that we are interested in. As we discussed in the previous Section and will extend to nonequilibrium situations in the following Section, the typical energy scales of the fluctuation-induced interactions we are interest in, lie way below the actual SPP resonance, but rather coincide with their broad-band tail in the low-frequency regime. In other words, the SPP resonance will always feature a finite width due to dissipation (and eventually causality in the open system paradigm) such that correctly capturing the dissipative part of the surface resonance is of eminent importance for the description of fluctuation-induced interactions in nonequilibrium situations. Part of the Drude model's success can be accounted

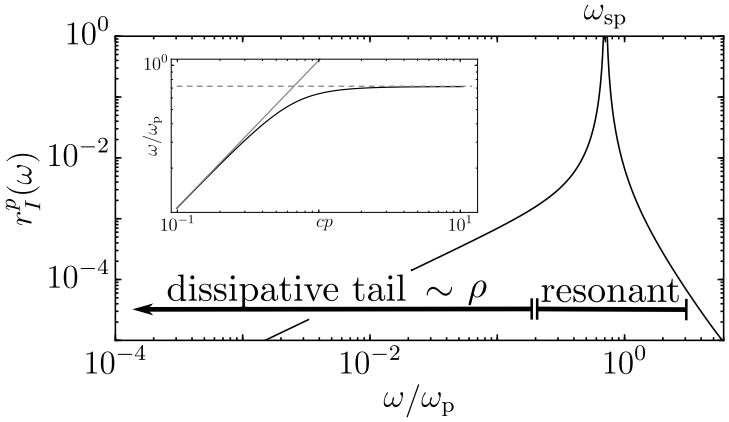

Figure 1.6: Imaginary part of r^p using the Drude model and parameters for gold [140]. **Inset:** Dispersion relation of Eq. (1.32) (black, solid) with the light line (gray, solid) and the non-retarded limit (gray, dashed).

[19] We note that a planar interface separating vacuum from a semi-infinite Drude metal features further resonances such as bulk plasmons [180, 227].

[20] Excluding retardation physically ignores the effects originating from a finite speed of light c. In frequency domain, this quantitatively alters the dispersion relation in vacuum $\omega = cp$ and pronounces the impact of comparably large wavelengths since $\lambda^{-1} \sim \omega/c$ becomes much smaller than the relevant length scales of the system; here the wavelength of the SPP. Formally, as a conscious short-cut, the corresponding results can be obtained from sending $c \to \infty$.

for by the sufficiently good description of the frequency regime around the electron plasma resonance as well as the relatively simple inclusion of dissipation. In the low-frequency regime, which is particularly important for us, there is however still some room for more accurate predictions. For instance, we will show in the present thesis that the Drude model is insufficient to describe the low-temperature behavior of the magnetic Casimir-Polder entropy (see Chap. 2 and Ref. [M3]) or the quantum frictional force at atom-surface separations smaller than the bulk electron's mean free path (see Chap. 3 and Refs. [M4, M5]). Due to its simplicity, in spite of the limited physical processes it can capture, the Drude model still serves as the main figure of merit in terms of material models in most of our considerations. Since the distinction between the SPP resonance itself and its dissipative low-frequency tail is of major importance for understanding the results of the present thesis, we would like to quantify this by the example of the transverse magnetic reflection coefficient r^p using the Drude model. For the transverse electric reflection coefficient, similar relations can be derived (see Sec. 2.2 and Ref. [M3]). At frequencies $\omega \sim \omega_{\rm sp}$, r^p is resonant in the sense of Eq. (1.32). The SPP can be resonantly excited as can be seen from the imaginary part of the reflection coefficient which gives the losses of electromagnetic energy to the material excitations. In the near-field where retardation is negligible, we obtain a delta-shaped absorption of the electromagnetic energy at the SPP resonance frequency for vanishing dissipation.

$$r_I^p(\omega) \sim \frac{\Gamma\omega\omega_{\rm sp}^2}{(\Gamma\omega)^2 + \left(\omega_{\rm sp}^2 - \omega^2\right)^2} \sim \omega_{\rm sp}^2\delta(\omega^2 - \omega_{\rm sp}^2), \qquad \Gamma \ll \omega_{\rm sp}, \tag{1.33}$$

where the index I gives the imaginary part of an expression and quantifies the strength of the dissipation. For finite dissipation, the delta-peak is broadened to become a Lorentzian with finite width $\sim \Gamma/2$.

For frequencies $\omega \ll \omega_{\rm p}$, r_I^p vanishes for $\omega \to 0$ and for the Drude model, we obtain

$$r_I^p(\omega) \sim 2\epsilon_0\rho\omega, \tag{1.34}$$

where we defined $\rho = \Gamma/(\epsilon_0\omega_{\rm p}^2)$ which, in the case of metals, can be related to their resistivity. In the simple Drude model, we obtain a spatially local resistivity $\rho = $ const. and r_I^p scales linearly in frequency. The latter behavior is sometimes referred to as *Ohmic* and a quite typical behavior for most (even spatially nonlocal, see below) materials (see e.g. Ref. [236] for examples of non-Ohmic behavior). Comparing to Eq. (1.33), we observe that, changing the dissipative properties of the metal will predominantly impact the low-frequency behavior of the material's response, while the resonant regime $\sim \omega_{\rm sp}$ is only weakly affected. Indeed, for the most common materials, it is usually reasonable to assume that $\Gamma \ll \omega_{\rm sp}$ (for instance, in the case of gold, we have $\Gamma/\omega_{\rm sp} \approx 5 \times 10^{-2}$ [140]). More generally, dissipation defines the low-frequency tail of the reflection coefficient and ρ can in principle be spatially dispersive. From Eqs. (1.26) and (1.28), we obtain for Ohmic materials [M4]

$$\rho(p) = \frac{2}{\pi\epsilon_0}\left[1 + \frac{2}{\pi}\int_0^\infty {\rm d}q\ \frac{p}{k^2\epsilon_l(0,k)}\right]^{-2} \int_0^\infty {\rm d}q\ \frac{p}{k^2}{\rm Im}\left\{\frac{\partial_\omega\epsilon_l(\omega,k)_{|\omega=0}}{[\epsilon_l(0,k)]^2}\right\} \tag{1.35}$$

which reduces to ρ when the local Drude permittivity is inserted. Again, similar relations can be defined for the transverse electric reflection coefficient [M3]. In the limit of no dissipation (which is always artificial), $\rho(p) \to 0$, but the SPP resonance will remain [M3]. In most of the parts of the present thesis, we consider the resonances of the system in order to understand its electromagnetic structure ($\sim \omega_\mathrm{p}$). However, most of the times, we are actually concerned with their dissipative low-frequency tail of the spectrum ($\sim \rho$). We depict a numerical evaluation of r^p in Fig. 1.6 sketching the distinction between resonance and its low-frequency tail.

At this point, we would like to remark that this is only part of the picture. In fact, the dissipative low-frequency behavior of the semi-infinite bulk can be connected to diffusive bulk modes that arise in conducting materials under the influence of slowly varying magnetic fields, the so-called *eddy modes* [147, 237–239]. They contribute to the mode density of the particle-field interaction as purely imaginary (overdamped) modes and can be describes by the distance-dependent diffusion rate $\sim \Gamma \lambda\!\!\!^{-2}_\mathrm{p}/z^2$ for the local Drude model. The impact of the eddy modes is usually strongly reduced in the transverse magnetic reflection coefficient such that they are essentially transverse electric polarized [M3]. Interestingly, they play a fundamental role in understanding the low-temperature entropy of the magnetic Casimir-Polder interaction and we turn our full attention to this problem in Sec. 2.2. For the time being, however, we focus on the reflection of transverse magnetic polarized waves and stick with the heuristic picture of SPP resonances and their dissipative tails displayed in Fig. 1.6 for the sake of clarity of the drawn arguments.

Describing the electrons of a conducting material as a non-interacting gas is obviously limited. For one, due to their charge and quantum nature, the interaction between the electrons is influenced by the Coulomb force and the Fermi-Dirac statistics determining the rules for occupying energy levels, respectively. At least, the multi-body interaction effectively introduces a spatial correlation in the electronic system. The probably obvious approach is to extend the non-interacting gas model and consider the electrons of the material as a compressible fluid [191]. This approach was pioneered by Landau [167, 240, 241] who considered a non-interacting gas of electrons, gradually turned on the interaction and thereby performed the "transition from the gas to the liquid" [240]. The fictional particles of the gas are called *quasi-particles* and by slowly introducing the interaction in the system, we allow for labeling the new, interacting quantum states using the non-interacting quantum numbers. Hence, we can reduce the discussion to finding a single distribution function $f(\mathbf{\Pi})$ with $\mathbf{\Pi}$ the wave momentum of the quasi-particles, thereby establishing a statistical picture rather than an exact single-particle description [192]. Note that we need to exercise some care with the speed the interaction is turned on. In fact, the process needs to proceed slow enough that our energy resolution is smaller than the energies of interest (roughly given by the temperature). On the other hand, we cannot employ a completely adiabatic process since the interaction must be turned on faster than the typical decay rate of an excitation so that the notion of quasi-particles does not loose its meaning since they would always be overdamped. Keeping both principles in mind gives a range of validity of the Fermi liquid theory which is usually well-justified for excitation strength (or temperatures) small compared to the energy at the Fermi surface [192]. Mathematically, we employ fluid dynamical equations to describe the electromagnetic response, where the actual electrons are describes as quasi-particle excitations of the electron fluid [191]. Following Eqs. (1.28) it is sufficient to provide expressions for the functions $\epsilon_{l,t}(\omega, k)$ in order to fully characterize the

electromagnetic scattering at the vacuum-material interface.

Whether the inclusion of spatial nonlocality is actually necessary depends on the wavelength of the radiation dominating the interaction. For our case, the relevant wavelength is roughly given by the separation between particle and surface, $\lambda \sim z_a$ [see Eq. (1.25)]. For distances larger than the electron's mean free path $\ell = v_\mathrm{F}/\Gamma (\approx 50$ nm for gold) with $v_\mathrm{F} \sim \alpha_\mathrm{fs} c$ the Fermi velocity of the electrons and $\alpha_\mathrm{fs} \approx 1/137$ the fein-structure constant, the correlations between spatially separated positions come unnoticed due to the limited capacity of the wavelength to resolve the microscopic dynamics. We effectively probe relatively large portions of the material at once. Below such separations, the opposite is true and spatial dispersion becomes important (see Fig. 1.5). The wave can resolve the ballistic motion and coherently interact with the quasi-particles of the electron liquid. For separations as close as the Thomas-Fermi wavelength, $\lambda_\mathrm{TF} = v_\mathrm{F}/\sqrt{3}\omega_\mathrm{p}$, corrections due to the quantum nature of the material become dominant and we need to include inter-atomic interactions into the description. The Thomas-Fermi wavelength characterizes the electrostatic screening of charges in the Fermi fluid and can be considered the analog of the Debye length at zero-temperature [242]. In the presence of an interface, it can be related to the spatial distribution of the electron density near the surface [243]. Note, however, that for typical materials, λ_TF is at the order of angstrom which lies beyond the applicability of our macroscopic quantum electrodynamic approach. We display a sketch of the different regimes in Fig. 1.7.

In the following, we review three rather common approaches that lie on both ends of the spectrum of analytical complexity, the so-called hydrodynamic model being the most simple and the so-called Boltzmann-Mermin model the most involved one. We further discuss an intermediate description, the extended hydrodynamic model, that covers some features of the Boltzmann-Mermin model, but is slightly more complicated than the hydrodynamic description.

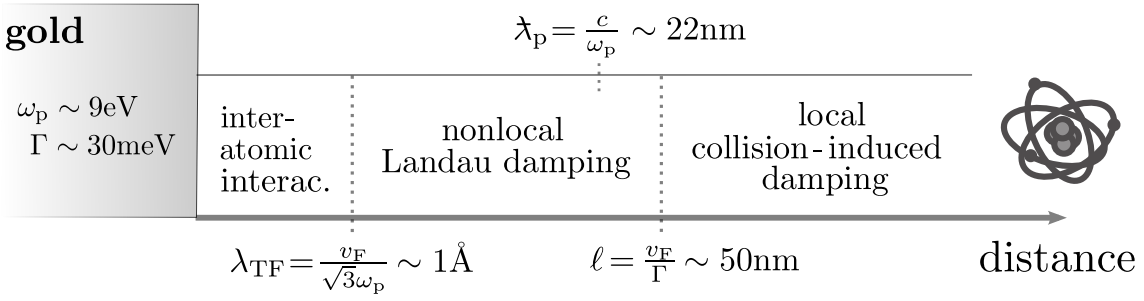

Figure 1.7: Distances between particle and surface and the necessary material features of conductors that need to be taken into account. We use parameters for gold [140]. Since the wavelength dominating the interaction scales with the separation, $\lambda \sim z$, spatial dispersion becomes important for separations at the order of the electron's mean free path ℓ. Below the Thomas-Fermi wavelength λ_TF, we would need to consider inter-atomic interactions with the lattice of the bulk which lays beyond the applicability of our theory.

Hydrodynamic model

Starting with the simplest of the mentioned models, the hydrodynamic description demands the quasi-particles of the electron liquid, i.e. the Fermi liquid, to obey both charge conservation by means of the continuity equation and momentum conservation by means of the Euler equation [191]. The latter presumes that the Fermi liquid, under the influence of an external Lorentz force, includes collision-induced damping of the electrons as well as attenuation of the field due to the Fermi pressure (originating from the Pauli-exclusion principle) [191, 212, 244]. Linearizing the resulting equations of motion yields the rather simple permittivities [245]

$$\epsilon_l(\omega,k) = 1 - \frac{\omega_\mathrm{p}^2}{\omega(\omega+\mathrm{i}\Gamma)-\beta^2k^2}, \qquad \epsilon_t(\omega,k) = 1 - \frac{\omega_\mathrm{p}^2}{\omega(\omega+\mathrm{i}\Gamma)} = \epsilon_\mathrm{Dr}(\omega). \tag{1.36}$$

We note that only the longitudinal permittivity is affected by the nonlocality which means that only the transverse magnetic reflection coefficient is modified [Eq. (1.28)]. The essential parameter quantifying the nonlocality in the hydrodynamic model is the compressibility β of the electron fluid which, in the present case, is connected to the Fermi pressure [246]. For $\beta \to 0$, we recover the spatially local Drude model. Depending on the implicit assumptions leading to the hydrodynamic equations (see e.g. [245–247]), different values have been reported in the literature ranging from $\beta^2 = v_\mathrm{F}^2/3$ in the low-frequency Thomas-Fermi description [194] to the high-frequency approximation $\beta^2 = 3v_\mathrm{F}^2/5$ [M5, 233], respectively. Due to the simple structure of Eqs. (1.36), the integrals in Eq. (1.28) can be solved exactly and we can find closed expressions for the reflection coefficients (see appendix D and e.g. Refs. [204, 205, 248]). The features of the surface plasmon-polaritons resemble the simple Drude model in the quasi-static limit modified by the appearance of the compressibility. Choosing β to be constant, we obtain in the dissipation-less limit ($\Gamma = 0$) [233]

$$\omega_\mathrm{sp}^2 = \frac{1}{2}\left[\omega_\mathrm{p}^2 + \beta^2k^2 + \beta k\sqrt{2\omega_\mathrm{p}^2+\beta^2k^2}\right]. \tag{1.37}$$

For long wavelengths $\beta k \ll \omega_\mathrm{p}$, we obtain the correction due to weak-nonlocality as [249]

$$\omega_\mathrm{sp} \sim \frac{\omega_\mathrm{p}}{\sqrt{2}} + \frac{\beta k}{2}. \tag{1.38}$$

For comparison, the impact of the nonlocal correction becomes comparable to the Drude SPP energy for wavelengths $\lambda = 2\pi/k \sim \pi\beta/\omega_\mathrm{sp} (\approx 0.6\,\mathrm{nm}$ for gold [140]). In turn, this means that the corresponding atom-surface separations where nonlocality within the hydrodynamic description becomes important should be less than one nanometer for gold; thereby already lying outside the range of applicability of our theory for typical metals and the planar interface[21]. Again, for our purposes, we are more interested in the dissipative properties of the material response. Although the fluid's compressibility β introduces a dependence on the radiation's wavevector in the material response, specifically a resonant energy transfer occurring at $\omega/k = \beta$ (assuming $\Gamma = 0$), there are no additional damping mechanisms above the

[21] This changes, for example, for different geometries where strong-field enhancement and nonlocal effects due to curvatures in the geometry can be expected; see e.g. Refs. [208, 250–252] for recent examples.

Thomas-Fermi wavelength λ_{TF} (see Fig. 1.8) other than the collision-induced damping Γ. By implication, the low-frequency behavior of the reflection coefficients is not changed with respect to the material's resistivity and in fact is equivalent to the simple Drude model [Eq. (1.34)]. Hence, from the perspective of fluctuations of the material-modified vacuum, the standard hydrodynamic model only weakly impacts the low-frequency/long-time regime.

Boltzmann-Mermin model

For metals, several more involved models have been developed (see for example [202]). Following Refs. [184, 197, 211, 218, 253, 254], we model the electron plasma[22] in terms of the statistical distribution function $f = f(\mathbf{r}, \mathbf{\Pi}, t)$ as a function of their position $\mathbf{r}$, time t and momentum which, in first approximation, can be written as $\mathbf{\Pi} = m_e \mathbf{v}_e$, where m_e denotes the electron mass and $\mathbf{v}_e$ is the velocity. In such an (effective) description, the individual particle nature of the electron becomes less meaningful, but instead we can again speak of *quasi-particle excitations* of the plasma distribution in phase space [191]. In equilibrium, we assume that the motion of the electrons is isotropic and their distribution to depend on the modulus of the speed only, i.e. $f_0(\mathbf{r}, \mathbf{\Pi}, t) = f_0(v_e)$ with $v_e = |\mathbf{v}_e|$. Further, we take the quantum nature of the particles into account by considering fermionic statistics at temperature T much smaller than the Fermi temperature $T \ll T_{\mathrm{F}}$ ($T_{\mathrm{F}} \approx 10^5$ K for metals) such that we can write f_0 in terms of the zero-temperature Fermi-Dirac distribution,

$$f_0(v_e) = \frac{3}{4\pi} \frac{n_0}{v_{\mathrm{F}}^3} \theta(v_{\mathrm{F}} - v_e), \tag{1.39}$$

where n_0 is the equilibrium density of electrons [242]. Under external perturbations, however, we consider small deviations of f from the equilibrium density f_0 and employ the Boltzmann equation for the dynamics in phase space, i.e.

$$\partial_t f + \mathbf{v} \cdot \boldsymbol{\nabla}_{\mathbf{r}} f + \partial_t \mathbf{\Pi} \cdot \boldsymbol{\nabla}_{\mathbf{\Pi}} f = -(f - f_0)\Gamma. \tag{1.40}$$

On the r.h.s. of Eq. (1.40) we have written the collision term in the relaxation time approximation by introducing the phenomenological parameter Γ [255] coinciding with the corresponding parameter in the Drude model in certain limits (see below).

Consequently, we recover the expressions used in Refs. [211, 218] for the longitudinal and transverse permittivity, respectively,

$$\epsilon_l(\omega, k) = 1 + \frac{\omega_{\mathrm{p}}^2}{\omega + \mathrm{i}\Gamma} \frac{3u^2 g_l(u)}{\omega + \mathrm{i}\Gamma g_l(u)}, \qquad \epsilon_t(\omega, k) = 1 - \frac{\omega_{\mathrm{p}}^2}{\omega(\omega + \mathrm{i}\Gamma)} g_t(u), \tag{1.41}$$

where ω_{p} is the plasma frequency of the metal and

$$g_l(u) = 1 - u \,\mathrm{arccoth}\,(u)\,, \qquad g_t(u) = \frac{3}{2}\left[u^2 - (u^2 - 1) u \,\mathrm{arccoth}\,(u)\right] \tag{1.42}$$

[22] We use the term *plasma* since this approach shows several similarities with the description of a non-relativistic plasma [242].

are dimensionless functions of $u = (\omega + \mathrm{i}\Gamma)/(v_\mathrm{F} k)$. We stress that, although Eq. (1.40) is derived from classical considerations[23], we have included quantum features of the electron gas using the Fermi-Dirac distribution for f_0. The dynamics of the plasma is effectively modified through the addition of a pressure term behaving at low frequency as the Thomas-Fermi pressure. It can be shown that Eqs. (1.41) coincide with the semi-classical limit of the Lindhard-Mermin dielectric functions [191, 195, 197, 211, 253], which incorporate quantum corrections[24] when the wavevectors become comparable to or larger than the Fermi wavevector $k_\mathrm{F} = m_e v_\mathrm{F}/\hbar$. Hence we call the previous description *Boltzmann-Mermin* model. As long as the wavelength of the radiation is much larger than the de Broglie wavelength of the electron at the Fermi surface, our semiclassical descriptions holds and quantum corrections would become important for separations between particle and surface of $z \lesssim 1/k_\mathrm{F} \approx 0.5\text{Å}$ (beyond the range of applicability of our theory) [M3]. As for the hydrodynamic description, it can be shown that for typical parameters, the considerably more complicated Boltzmann-Mermin model only deviates slightly from the local Drude result in the resonant regime, $\omega \sim \omega_\mathrm{sp}$ (see Fig. D.1 in appendix D for a numerical evaluation). In the dissipative low-frequency regime, however, the Boltzmann-Mermin model can diverge strongly from both the local Drude model and the usual hydrodynamic description depending on the chosen wavevector. By means of Eq. (1.35), we obtain for the (transverse magnetic) dissipation [M4]

$$\rho(p) \sim \frac{\frac{1}{\epsilon_0 \omega_\mathrm{p}} Q\left(p\lambda_\mathrm{TF}, \frac{\pi^2-4}{2\pi p \ell}\right)}{p\lambda_\mathrm{TF}\left(\sqrt{1+p^2\lambda_\mathrm{TF}^2} + p\lambda_\mathrm{TF}\right)^2}, \quad Q(a,b) = \frac{a^2\left(a^2+1\right)}{\sqrt{3}} \int_0^1 dx \frac{1+bx}{\sqrt{1-x^2}} \frac{x^3}{\left(a^2+x^2\right)^2}. \tag{1.43}$$

Again, for the sake of a lucid argument, we ignore the transverse electric coefficient for which related expressions can be found [M3]. The function $Q(a,b)$ is real and finite for $b = 0$ which corresponds to the physical limit of a non-interacting gas with infinite mean free path ($\ell \to \infty$) and zero collision-induced dissipation ($\Gamma \to 0$). Moreover, since the dissipation linear in frequency [Eq. (1.43)] is finite shows that the Boltzmann-Mermin model features an Ohmic behavior. Further, the function $\rho(p)$ shows a maximum at $p \sim 1/(5\lambda_\mathrm{TF})$ which can exceed the local Drude resistivity $\rho = \Gamma/(\epsilon_0 \omega_\mathrm{p}^2)$ by more than one order of magnitude (see Fig. 1.8 and Ref. [M4]). We emphasize that the Boltzmann-Mermin model includes another damping mechanism in addition to collision-induced damping that remains finite even in the limit of $\Gamma \to 0$. This can be seen best from the permittivities of Eq. (1.41) which feature two limiting regimes. For values $|u| \to \infty$, related to $v_\mathrm{F} \ll \omega/k$ and/or $k\ell \ll 1$, the dielectric functions in Eqs. (1.43) recover the usual local Drude description of the metal [147], i.e. $\epsilon_l(\omega,k) = \epsilon_t(\omega,k) \to \epsilon_\mathrm{Dr}(\omega)$. In the opposite limit, $|u| \to 0$, related to $v_\mathrm{F} \gg \omega/k$ and/or $k\ell \gg 1$ [M4], the permittivities read

$$\epsilon_l\left(\omega,k\right) \sim 1 + \frac{3}{k^2\lambda_\mathrm{TF}^2} + \mathrm{i}\frac{\omega\Gamma_l^\mathrm{L}(k)}{\omega_\mathrm{p}^2}, \qquad \epsilon_t\left(\omega,k\right) \sim 1 - \frac{3}{k^2\lambda_\mathrm{TF}^2} + \mathrm{i}\frac{\omega_\mathrm{p}^2}{\omega\Gamma_t^\mathrm{L}(k)}, \tag{1.44}$$

[23] The Boltzmann equation can also be obtained from quantum methods in certain limiting cases [244, 256].

[24] Including dissipation in the Lindhard model requires some attention, because merely replacing $\omega \to \omega + \mathrm{i}\Gamma$ in Lindhard's quantum dielectric function does not conserve the local electron number [211, 253, 257].

where $\Gamma_l^{\mathrm{L}}(k) = 3\pi\omega_{\mathrm{p}}^4/(2v_{\mathrm{F}}^3k^3)$ and $\Gamma_t^{\mathrm{L}}(k) = 4v_{\mathrm{F}}k/(3\pi)$ are the semiclassical damping rates for longitudinal and transverse fields propagating in a fermionic plasma [167, 258]. Since the collision-damping completely dropped from Eqs. (1.44), the additional damping mechanism prevails as the main source of attenuation of the field in the nonlocal limit ($|u| \to 0$). The physical mechanism behind the finite dissipation even for vanishing Γ is the *Landau damping* [167, 258]. Landau damping is related to the quasi-particle's distribution in phase space since it occurs when the average phase velocity of the electromagnetic wave is equal or smaller than the electron's average speed which in our case is given by the Fermi velocity, i.e. $\omega/k \leq v_{\mathrm{F}}$. Since the common velocity distributions of quasi-particles in the conductor are decreasing with increasing velocity, e.g. the classical Boltzmann distribution or the quantum Fermi-Dirac distribution, the effect is featured by both classical and quantum systems. This means that the specific (semi-classical) damping rates $\Gamma_l^{\mathrm{L}}(k)$ and $\Gamma_t^{\mathrm{L}}(k)$ for longitudinal and transverse fields propagating in the fermionic plasma, respectively, are rooted in our choice for the equilibrium distribution f_0. The corresponding relation for the fully classical Boltzmann-distribution at finite temperature can be found in Ref. [259]. Lastly, we note that the nonlocal properties and the Landau damping are carried through the surface impedances to the electromagnetic response of the material/vacuum interface which explains the involved shape of the low-frequency dissipation in Eq. (1.43).

Extended hydrodynamic model

Comparing the low-frequency behavior of the standard hydrodynamic description [Eq. (1.34)] with the more involved Boltzmann-Mermin model [Eq. (1.43)], it becomes clear that properly including Landau damping into the material description comes with a considerable amount of complexity. In the limit of weak nonlocality (measured by large values of $|u|$), we can connect the hydrodynamic and the Boltzmann-Mermin model. The approach was first put forward by Halevi [246] and, based on the hydrodynamic permittivities of Eqs. (1.36), modifies the compressibility factor β in order to avoid the full complexity of the Boltzmann-Mermin model. Still, it manages to incorporate Landau damping in a qualitative way. We note that recently Mortensen et al. [198] have suggested a similar extension of the standard hydrodynamic model via a complex compressibility coefficient in order to capture the physics of nano-gap structures in numerics.

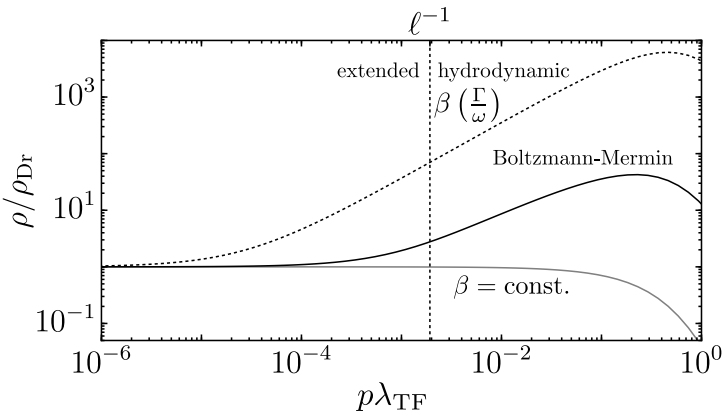

Figure 1.8: Low-frequency dissipation $\rho(p)$ [Eq. (1.35)] normalized by the local Drude value $\rho_{\mathrm{Dr}} = \Gamma/(\epsilon_0\omega_{\mathrm{p}}^2)$ for the hydrodynamic model with constant compressibility factor (gray), the Boltzmann-Mermin model (black) and the extended hydrodynamic model (black, dashed). We use parameters for gold [M4, 140] and the Fermi velocity $v_{\mathrm{F}} = \alpha_{\mathrm{fs}}c$. Adapted from [M5].

Following Halevi's approach, however, by equating the two longitudinal permittivities in (1.41) and (1.36), we obtain

$$\frac{\beta^2}{v_F^2} = \frac{\omega\left[u^2 + \frac{1}{3g_l(u)}\right] + \mathrm{i}\frac{\Gamma}{3}}{\omega + \mathrm{i}\Gamma}. \tag{1.45}$$

Note that the transverse permittivity remains unchanged in the hydrodynamic description. An expansion in $1/|u|$ gives at the leading order the complex and frequency-dependent compressibility factor,

$$\beta^2 \sim \frac{\frac{3}{5} + \frac{\mathrm{i}}{3}\frac{\Gamma}{\omega}}{1 + \mathrm{i}\frac{\Gamma}{\omega}} v_\mathrm{F}^2. \tag{1.46}$$

The compressibility factor, being constant and real in the standard hydrodynamic model, becomes a complex function of frequency that reproduces the previously mentioned limiting values of $\beta \sim v_\mathrm{F}/\sqrt{3}$ and $\beta \sim v_\mathrm{F}\sqrt{3/5}$ for the low and high frequency limit, respectively. In the limit of sufficiently large collision damping, Eq. (1.46) introduces an additional phase between the fermion plasma and the electromagnetic wave preserving some features of Landau damping since it allows for phase velocities smaller than the electron's Fermi velocity, i.e. $(1/|u| \ll 1)$

$$\sqrt{v_\mathrm{F}^2 - \frac{\Gamma^2}{k^2}} \ll \frac{\omega}{k} \leq v_\mathrm{F}. \tag{1.47}$$

The previous relation also serves as a lower bound to the validity of the approximation in terms of the phase velocity of the electromagnetic field and leads to a simple additive behavior for the different damping mechanisms (collision-induced and Landau damping) for low frequencies. Indeed, expanding the transverse magnetic reflection coefficient accordingly, we obtain

$$\rho(p) \sim \rho_\mathrm{H}(p) + \rho_\mathrm{La}(p), \tag{1.48}$$

where $\rho_\mathrm{H}(p)$ is the expression of the standard hydrodynamic description [see discussion below Eqs. (1.36)] and ρ_La is the correction related to Landau damping. The exact expressions can be found in appendix D and we report a numerical evaluation as a function of the wavevector in Fig. 1.8. In full similarity to the Boltzmann-Mermin model, the dissipation of the *extended hydrodynamic model* (as we call it from now on) shows a distinct maximum, this time at $p \sim 1/(2\lambda_\mathrm{TF})$, but tends to overestimate the impact of Landau damping in comparison to the Boltzmann-Mermin model. Nevertheless, the extended hydrodynamic description can serve as a first qualitative estimate of the impact of Landau damping on the physical system (Sec. 3.4.1).

1.2.3 Dielectrics

In addition to a conducting part, which is well-described by the models introduced in the previous Section, many materials feature a dielectric response due to bound charges in the lattice structure or a completely filled valence band allowing for interband transitions depending on the external frequency driving the material [194]. The simplest approach to describe the dielectric features is in terms of a Lorentz oscillator [147, 236]

$$\epsilon_{\mathrm{Lo}}(\omega) = \epsilon_\infty - \frac{(\epsilon_0^{\mathrm{qs}} - \epsilon_\infty)\omega_0^2}{\omega^2 - \omega_0^2 + \mathrm{i}\tilde{\Gamma}\omega} \tag{1.49}$$

with ϵ_∞ the background permittivity, ϵ_0^{qs} the quasi-static permittivity constant, ω_0 the resonance frequency of the dielectric excitation and $\tilde{\Gamma}$ another phenomenological dissipation rate mostly connected to phononic coupling. In combination with the Drude model describing the conducting background of the material, we already found one of the easiest approaches to characterize the electromagnetic response of semi-conductors [260]

$$\epsilon(\omega) = \epsilon_\infty - \frac{\omega_{\mathrm{p}}^2}{\omega(\omega + \mathrm{i}\Gamma)} - \sum_j \frac{\Omega_j^2}{\omega^2 - \omega_j^2 + \mathrm{i}\omega\tilde{\Gamma}_j}, \tag{1.50}$$

where the sum over j takes the existence of multiple resonances ω_j with coupling strength Ω_j and dissipation $\tilde{\Gamma}_j$ into account. The exact parameters depend on the chosen material (see e.g. Ref. [261] for a discussion of doped silicon in the context of Casimir forces). Note that Eq. (1.50) is local per construction and there are many more advanced models available depending on the precise context. For instance, inter-band transitions can be taken more carefully into account by means of a Tauc-Lorentz model, where $\mathrm{Im}\epsilon(\omega) \propto \theta(\hbar\omega - E_g)$ with E_g the Tauc optical gap, which is sometimes used for describing so-called transparent conducting oxides such as indium-tin-oxide [260, 262, 263]. Further, one can realize extra-ordinary dispersion relations of the electromagnetic response for more exotic materials such as the linear dispersion occurring in graphene near the Dirac-point [P2, 264–266] or similarly in photonic meta-materials [267]. Lastly, we want to mention high precision calculations determining the electronic band-structure of a wide range of dielectrics and semi-conductors employing density functional theory [268, 269].

However, we are especially interested in any form of dissipation that the considered material can feature. We aim to identify the general mechanisms connected to a (generic) low-frequency response first and to come back to the exact material model when discussing actual experimental realizations later (see Chap. 5). Indeed, upon inserting Eq. (1.49) into Eq. (1.35), we can define the Ohmic dissipation of a Lorentz dielectric $\rho_{\mathrm{Lo}} = (\epsilon_0^{\mathrm{qs}} - \epsilon_\infty)\tilde{\Gamma}/(\epsilon_0\omega_0^2[1 + \epsilon_0^{\mathrm{qs}}]^2)$ in full resemblance to the case of a local Drude oscillator [Eq. (1.34)]. In other words, we will concentrate on conducting materials in most parts of the present thesis in order to be close to already existing experimental realizations (see Chap. 5) as well as to ensure a better comparability between the discussed effects by keeping the impact of the material model unchanged. Qualitatively, the discussed effects do not depend on the particularities of the considered material, but rather on the general properties such as the existence, magnitude and functional dependence of the imaginary part of the bulk material's electromagnetic response in the low-frequency regime.

1.2.4 Impact of materials on field fluctuations

Having introduced the material models, it is interesting to explore their impact on the fluctuations of the field [see Eqs. (1.25) and (1.24)]. Focusing on conductors, we have seen that different descriptions can vary in their low-frequency behavior. The corresponding specifics are inherited by the Green tensor of the setup from the reflection coefficient. In the planar case, focusing on the scattered contribution and the limit of small separations from the surface, where retardation effects can usually be neglected, Eq. (1.24) reduces to

$$\underline{g}(\mathbf{p}, z, \omega) \sim \frac{p}{2\epsilon_0} r^p_{\mathrm{NF}}(\omega, p) e^{-2pz} \left(\mathbf{z} - \mathrm{i}\frac{\mathbf{p}}{p}\right)\left(\mathbf{z} + \mathrm{i}\frac{\mathbf{p}}{p}\right), \tag{1.51}$$

where the subscript "NF" denotes the near-field expression of the transverse magnetic reflection coefficient. Note that for the electric interaction the impact of the transverse electric reflection coefficient can be neglected in the near-field regime [270]. Inserting Eq. (1.51) into (1.24) yields for the fluctuation spectrum of the electric field operator

$$\nu_{ii}(\omega) \sim \frac{2\hbar}{\pi}\theta(\omega) \int_0^\infty \mathrm{d}p\; p^2 \rho(p) e^{-2pz} \overset{\rho(p)=\rho}{\to} \nu_{\mathrm{Dr}} \equiv \frac{4\hbar}{\pi}\frac{\rho}{(2z)^3}\theta(\omega) \tag{1.52}$$

at small frequencies $\omega \ll \omega_{\mathrm{sp}}$, Ohmic materials and at zero temperature, where we used the local Drude limit in the second step and $\rho(p)$ is defined by Eq. (1.35). Indeed, at low frequencies, the local electromagnetic density of states which is closely related to the field fluctuations [190], sensitively depends on the dissipative properties of the bulk ρ. For local material models, twice the amount of dissipation ($\rho \to 2\rho$) adds up linearly and means that the fluctuations are twice as strong ($\nu_{\mathrm{Dr}} \to 2\nu_{\mathrm{Dr}}$). Further, due to the lack of spatial dispersion in the local description, the dissipative properties ρ decouple from the geometric integral which can then be perform exactly [Eq. (1.52)].

In the nonlocal case, however, where $\rho = \rho(p)$, the fluctuations always derive from a combination of geometry and material properties: The integral over wavevectors in Eq. (1.52) selects the parallel component of the wavevectors participating in the dissipative process as a function of distance [M4]. Such a non-trivial combination of the system's properties can lead to a non-additive increase of low-frequency fluctuations which, e.g. for the Boltzmann-Mermin model, differs about one order of magnitude from the local Drude model. We depict a numerical evaluation in Fig. 1.9.

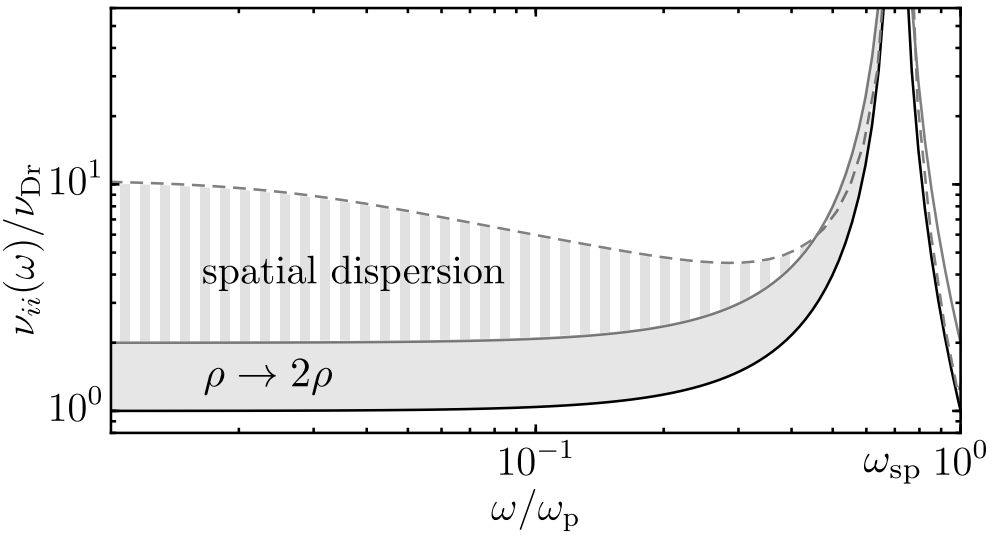

Figure 1.9: Fluctuations of the electric field at distance $z = 10$ nm in front of an infinitely extended planar half-space made from conductor normalized by its respective low-frequency limit value, evaluated using the local Drude model [second step in Eq. (1.52)]. Parameters are taken from [140] and we use $v_{\mathrm{F}} = \alpha_{\mathrm{fs}} c$. We depict the values for the Drude model with resistivity ρ (black, solid), the Drude model with twice the resistivity $\rho \to 2\rho$ (gray, solid) and the Boltzmann-Mermin description (gray, dashed).

1.3 Nonequilibrium configurations

1.3.1 The importance of long-time correlations

Taking the ground state fluctuations of the quantum vacuum as a reference, we have seen in the previous Sections that the fluctuations quantitatively increase if either the system is set to a finite temperature $T > 0$ or if we introduce macroscopic materials putting some constraints on the boundaries of the vacuum. For one, the presence of materials introduces further length scales in the system and the fluctuations of the material-modified vacuum show a peak resonance at the excitation frequencies of the material. We found that both the finite temperature and the material via its dissipative properties modified in particular the low frequency regime $\hbar\omega \ll \hbar\omega_r, k_\mathrm{B}T$ with ω_r being the resonance frequency of the chosen material (model). While the resonance itself turned out to be rather robust against changes in the parameters or even the considered models, we found the low-frequency regime to be very sensitive to such changes (see Sec. 1.2). In every case, we restricted our discussion to the situation that the field+matter(+particle) system is in global equilibrium at temperature T.

In the present Section, we generalize the discussion to nonequilibrium situations. We start by discussing the situation of thermal nonequilibrium, where spatially separated subsystems are held at different temperatures. Since such systems, in the context of atom-surface dispersion forces, already achieved some coverage in the literature (see below), we mostly comment on the relation between low-frequency correlations in the system and corrections due to temperature gradients and quickly move on to one of the main topics of the present thesis: Mechanical nonequilibrium, where spatially separated subsystems are in constant motion relative to each other (see Chap. 3). For most experimentally realistic situations, it turns out that putting the system out of equilibrium impacts the field's power spectrum especially for low frequencies. The long-time correlations depend delicately on the interplay between temperature, geometry, material and nonequilibrium statistics.

Suppose we consider the electric interaction between a particle with dominating dipole resonance ω_a and the material-modified vacuum with material resonances ω_r. Let us assume that it is possible to define different temperatures in the system, say, T_s for the material and T_f for the vacuum field. For simplicity, we assume that both T_s and T_f are small enough that the probability of exciting the atom is vanishingly small (see discussion below Eq. (1.19) and Sec. 1.2). For the material-modified vacuum field, in leading order, the change in the emDOS is proportional to the difference in the respective thermal occupation numbers. For well-behaved functional dependencies of the material properties in the sense of a test function [185], we can employ the distribution expansion put forward by Estrada *et. al.* [185, 186] and obtain for the difference in the thermal occupation numbers ($T_s > T_f$)

$$n(\omega,T_s) - n(\omega,T_f) \sim \frac{\pi^2}{3}\frac{k_\mathrm{B}^2}{\hbar^2}\mathrm{sgn}(\omega)\left[\delta^{(1)}(\omega)\left(T_f^2 - T_s^2\right) + \frac{\pi^2}{15}\frac{k_\mathrm{B}^2}{\hbar^2}\delta^{(3)}(\omega)\left(T_f^4 - T_s^4\right)\right], \quad (1.53)$$

where $\delta^{(n)}(\omega)$ denotes the n-th derivative of the Dirac delta. Clearly, the impact of the temperature gradient is accentuated at $\omega \to 0$. For comparison, in recent experiments dealing with blackbody radiation [127] or near-field heat transfer [49, 122, 123] one reaches temperatures

$\Delta T \equiv T_s - T_f$ in the range of some tens to some hundred Kelvin. Choosing metals as well as $T_s = 450\text{K}$ and $T_f = 296\text{K}$ [127], the corresponding energy scale

$$\hbar\omega_{\Delta T} \equiv k_\text{B}\sqrt{(T_s^2 - T_f^2)} \approx 0.03\text{eV} \ll \omega_r, \omega_a \tag{1.54}$$

is clearly situated in the range of low-frequency interactions between alkali atoms and conductors. Due to the imbalance in (local) temperatures, there occurs a heat flow from the hotter to the colder reservoir. Especially for small separations, the corresponding exchange of energy can be dominated by the evanescent coupling of the near-field radiation (gap smaller than the peak-wavelength of the blackbody spectrum, usually several hundreds of nanometers) and exceeds the black-body limit by several orders of magnitude [33, 181]. Due to the fundamental nature of the interaction, studying the near-field heat transfer allows for acquiring information about the body's properties [271] and was theoretically first described by Polder and van Hove [33, 272]. Driven by the surge in experimental possibilities, the theory has been further developed to cover many situations ranging from many bodies with multiple temperatures [35, 36] (see also Refs. [273, 274] for an application to cylindrical objects), the study of the system's dynamical approach towards a steady-state as well as the impact of a finite plate-thickness [275], to non-reciprocal bodies [276–278] violating detailed balance in certain cases [279] and their relation to the photon thermal hall effect [280], all the way down to phonon-assisted heat transfer [123, 281, 282]. In addition to heat currents between separated subsystems held at different temperatures, also the Casimir-Polder forces acquires nonequilibrium contributions [125] that can lead to intriguing long-range behaviors in the atom-plate scenario which have been explored theoretically by Antezza *et al.* [34, 283] and were confirmed experimentally just a little later [83]. The theory based on fluctuation electrodynamics (see Sec. 1.1 and Refs. [124, 125, 284, 285]) has been generalized using a QED treatment in order to compute atomic level shifts [286] and more complicated setups with multiple particles and/or multilayered plates [38, 287]. It is important to note, however, that the approach of Ref. [34, 125], which is based on Rytov's fluctuational electrodynamics [154] and includes dissipation of the atom in a rather heuristic way, makes explicit use of the so-called Local Thermal Equilibrium (LTE) approximation (see Sec. 1.3) which has been shown to potentially cause thermodynamic inconsistencies if not applied carefully [288, 289] (see also Chap. 4). Independently, the situation of an atom interacting with a thermal field of a hot sphere[25] was considered by Sonnleitner *et al.* [126]. Based on a calculation of atomic level shifts, not regarding dissipation, they explained long-range forces experienced by the atom using the ac-Stark shift due to the thermal field of the sphere. Such forces seem to scale in fourth order of temperature pointing towards a connection to black body radiation [126, 293]. A recent experimental study of the interaction between atoms and spatially-dependent temperature distributions (in the particular case realized using a hollow cylinder), which uses atom-interferometry and confirms the predictions of Ref. [126], was done by Haslinger *et al.* [127]. In any case, it is the low-frequency fluctuations in the sense of Eq. (1.53) that determines the temperature corrections and hence the theoretical prediction is highly sensitive to the chosen material model and, in particular, the dissipation in the material. Since this is not a prerogative of thermal gradients, but thermal corrections in general [see

[25] The corresponding Casimir-Polder force was, e.g., considered in Refs. [290–292].

discussion around Eq. (1.19)], we will restrict our considerations in that regard to equilibrium and discuss the interaction of an atom with a finite-temperature sphere in Sec. 2.1.

The case for mechanical nonequilibrium is slightly more involved, but equally instructive. Suppose that now the particle and the macroscopic body are in relative motion with respect to each other. For simplicity, we assume that the relative motion takes place at constant velocity v in x-direction. We discuss these assumptions more carefully in Chap. 4. Due to the relative motion, the radiation relevant for the interaction will be perceived by the particle as Doppler-shifted (non-relativistic). From the perspective of the laboratory, the frequency mediating the interaction is hence given by

$$\omega \to \omega_{\mathbf{p}}^{+} \equiv \omega + p_x v \tag{1.55}$$

with p_x being either positive or negative depending on the direction of the wave. Consequently, this means that we need to evaluate the field's power spectrum at the same Doppler-shifted frequencies in order to study its fluctuations, i.e.

$$\underline{\nu}(\omega, v) = 2\hbar \int \frac{\mathrm{d}^2\mathbf{p}}{(2\pi)^2} \left[n(\omega_{\mathbf{p}}^{+}, T) + 1 \right] \underline{G}_{\Im}(\mathbf{p}, z, \omega_{\mathbf{p}}^{+}) \tag{1.56}$$

with $n(\omega, T) + 1 \sim \theta(\omega)$ at zero temperature [P1]. Indeed, in Chaps. 3 and 4, we will derive the previous relation more carefully and see that it holds quite generally. Let us consider, again, the case of an atom moving with respect to a thermal field at temperature T. In contrast to the equilibrium case of a static system [see Eq. (1.20)] the finite velocity introduces another length scale into the system, in addition to temperature T and frequency ω. Ignoring, for the time being, the presence of materials (compare to Sec. 1.2), the only relevant reference scale is the speed of light such that we can expect correction as a function of $\propto |v|/c$, where the modulus, in accordance with the symmetries of the system, takes account of the fact that a change of direction cannot influence the result. In fact, due to the simple form of the imaginary part of the vacuum Green tensor, it is straight forward to show that the leading order corrections to the electric field fluctuations due to a finite velocity are at the order of $\mathcal{O}(v^2/c^2)$. For non-relativistic velocities $v \ll c$, we obtain by a more careful computation (see appendix B) that ($\omega > 0$)

$$\nu_{ii}(\omega, v) \sim \hbar \frac{\omega^3}{\pi \epsilon_0 c^3} \begin{cases} \theta(\omega) \left(1 + \frac{10}{3} \frac{v^2}{c^2} \right), & \hbar\omega \gg k_{\mathrm{B}} T, \\ \frac{k_{\mathrm{B}} T}{\hbar\omega} \left(1 + 2\frac{v^2}{c^2} \right) + \frac{1}{2} \left(1 + \frac{10}{3} \frac{v^2}{c^2} \right), & \hbar\omega \ll k_{\mathrm{B}} T. \end{cases} \tag{1.57}$$

The previous result needs to be handled with extra care. The quantities in gray are a mere consequence of our non-relativistic treatment considering the electric field only at the moment. Very fundamentally, for constant velocities and zero temperatures, the system is Lorentz invariant and the apparent velocity-corrections need to vanish (in gray). The presence of an additional body or a finite temperature breaks Lorentz invariance and its strong constraints do not apply. In any case, relativistic corrections, as in the previous equation, are at the order of v/c which is, in our case, irrelevant with respect to the corresponding velocity scale [$\sim v/(z\omega)$] we will encounter in the presence of macroscopic bodies [see Eq. (1.58)]. For instance, choosing

v to be the speed of sound, we would obtain a correction at the order of $v^2/c^2 \approx 1.3 \times 10^{-12}$. In the present Section, we will still state those erroneously appearing relativistic corrections, because they will help us to motivate the mathematical structure of low-frequency quantum fluctuations and in particular their qualitative connection to classical fluctuations. When computing real observables, however, we will always be sure to treat the vacuum contributions properly and enforce Lorentz invariance explicitly [see e.g. Eq. (4.2.1)]. Keeping this in mind, we observe, as in the equilibrium case, two different regimes, one dominated by quantum the other by thermal fluctuations. In addition to the overall increase of the fluctuations due to the motion, we observe that also the thermal regime, where Lorentz invariance does not apply, is modified quantitatively by adding a term $\propto 2v^2/c^2$. As already mentioned, since we are working in the non-relativistic regime, corrections at orders v/c, at this point, need to be treated with some skepticism. Still, it is worth noting that the Lorentz-invariant (vacuum) part of the fluctuations react differently to the motion of an observer than the parts of the fluctuations that are not Lorentz invariant (thermal). We report a numerical evaluation of the nonequilibirum field fluctuations in Fig. 1.10.

In the presence of macroscopic bodies, the situation can change considerably since the material parameters introduce further length scales into the system (see Sec. 1.2 for details). In addition to the velocity, we saw that the wavevectors dominating the interaction scale roughly with the inverse distance from the surface. Let z be the distance to the closest body, the energy of the fluctuations due to the mechanical nonequilibrium scales as

$$\omega \sim \omega_v \equiv \frac{v}{z} \approx 2 \times 10^{-5} \text{ eV}, \tag{1.58}$$

where we have chosen the speed of sound for the velocity and a separation of ten nanometer in order to obtain a roughly representative estimate. This is much smaller than most (electric) material resonances of metals and lies in a regime where most realistic materials respond ohmically ($r_I^p \propto \omega$). Hence, the relative motion affects mostly what we consider to be small frequencies. In full resemblance of the thermal frequency ω_T [see Eq. (1.19) and Fig. 1.4], the appearance of a new frequency scale, in this case v/z, modifies the frequency scaling of the field fluctuations. To see this more clearly, we consider again the simple case of an infinite half space described by the spatially local Drude model introducing the plasma frequency ω_p and the phenomenological resistivity ρ. We have already seen that the dissipation ($\propto \rho$) determines the behavior of the field fluctuations at low frequencies $\omega \ll \omega_\mathrm{p}$, while higher frequencies are dominated by the excitation of surface resonances (surface plasmon-polaritons) at roughly $\omega_\mathrm{sp} = \omega_\mathrm{p}/\sqrt{2}$. For example, if the metallic bulk is made of gold, the plasma frequency is in the range of some electronvolts [140] exceeding ω_v by far. In accordance with the previous discussion, the mechanical energy scale ω_v is hence operating in the dissipative regime $\omega_v \lesssim \epsilon_0 \omega_\mathrm{p}^2 \rho$ and related to long-time correlations in the field. Note that, due to the dimensions of our system, the thermal wavelength is much larger than the wavelengths dominating the interaction for typical parameters, i.e. $\lambda_T = \hbar c/(k_\mathrm{B} T) \gg p^{-1} \sim z$, such that the corresponding thermal excitation can be considered to be quasi-static [147]. Indeed, the thermal wavelength is of the order of micrometers for $T \approx 2 \times 10^3$ K and needs to be even larger for smaller separations. Hence, for most situations, *high temperature* thermal radiation contributes little to the power

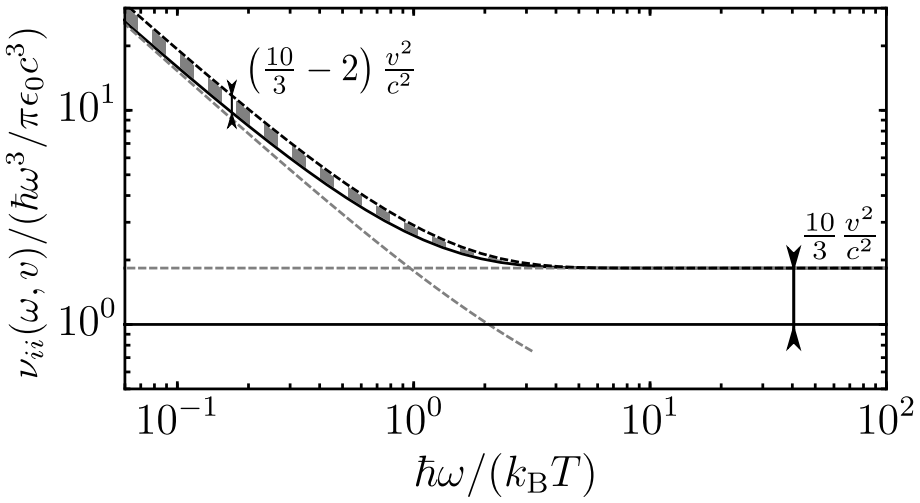

Figure 1.10: Nonequilibrium power spectrum of the (non-relativistic) electric field fluctuations of the vacuum at temperature T and a moving observer at velocity v (black, solid). We report the asymptotic expressions of Eq. (1.57) (gray, dashed). For a better visibility, we chose $v/c = 0.5$. In more realistic situations the correction due to a finite velocity is indistinguishable from the base line [see discussion above Eq. (1.58)]. Even though the velocity correction is somewhat artificial since we do not consider Lorentz invariance explicitly (see main text), it is interesting to note that thermal (not Lorentz invariant) and quantum fluctuations of the vacuum (Lorentz invariant) respond differently in quantitative terms. For comparison, we further report the result assuming LTE [see Eq. (1.69], black dashed) which cannot resolve this difference (emphasized in gray stripes).

spectrum. It is hence more interesting to consider the limit of vanishingly small temperatures[26]. More precisely, upon combining Eqs. (1.56) and (1.25), we obtain at zero temperature and for frequencies $\omega \ll \omega_\mathrm{p}$ that

$$\nu_{ii}(\omega \to 0, v) \sim \frac{\hbar\rho}{2\pi}\frac{\omega}{z^3}\begin{cases}1, & \hbar\omega \gg \hbar\frac{v}{z},\\ \frac{3}{2\pi}\frac{v}{z}\frac{1}{\omega}+\frac{1}{2}, & \hbar\omega \ll \hbar\frac{v}{z}.\end{cases} \tag{1.59}$$

The field fluctuations again feature a change in frequency scaling by one magnitude and we explicitly point at the strong formal resemblance with the discussion on zero velocities, but finite temperatures [see Eq. (1.21)]. In the remainder of the present thesis we will elaborate further on the latter analogy. Similar to the situation of studying different materials, the impact of the nonequilibrium situation on the field's fluctuations is relatively small in the frequency region of the system's resonances (see Fig. 1.9). Below those resonances, more precisely for frequencies $\omega \sim v/z$, the impact of the finite velocity becomes quite evident due to the change in frequency scaling we observe in Eq. (1.59). We report the numerical results in Fig. 1.11 and find that for sufficiently small frequencies, the fluctuations related to the motion are not only adding up

[26] We refer the reader to the discussion around Eq. (1.53) and in particular Chap. 2 for a discussion of higher order temperature corrections.

to the zero-point fluctuations, but become the dominant source of fluctuations in the system. Coming back to our main interest, a particle interacting with the material-modified vacuum, this means that at the energy scale $\hbar\omega_v$, the long-time correlations between the field degrees of freedom ($\propto \langle\hat{\mathbf{E}}^2\rangle$), mediated by the interaction with the particle at position ($\mathbf{r}, \mathbf{r}' \to \mathbf{r}_a$ in the Green tensor), can represent the main source of interaction in the dynamical case. Capturing those long-time correlations correctly in the theoretical description is hence crucial to understand and predict related physical phenomena. We will discuss this in full detail in Chap. 3. In the next Section, we highlight that commonly applied assumptions and approximation to nonequilibrium situations either neglect the low-frequency regimes (shaded area in Fig. 1.9) completely (e.g. first-order perturbation theory, quantum regression hypothesis) or only partially capture them (e.g. Local Thermal Equilibrium). Quantitatively, the error depends on the quantity of interest and the specifics of both the material distribution and the particle.

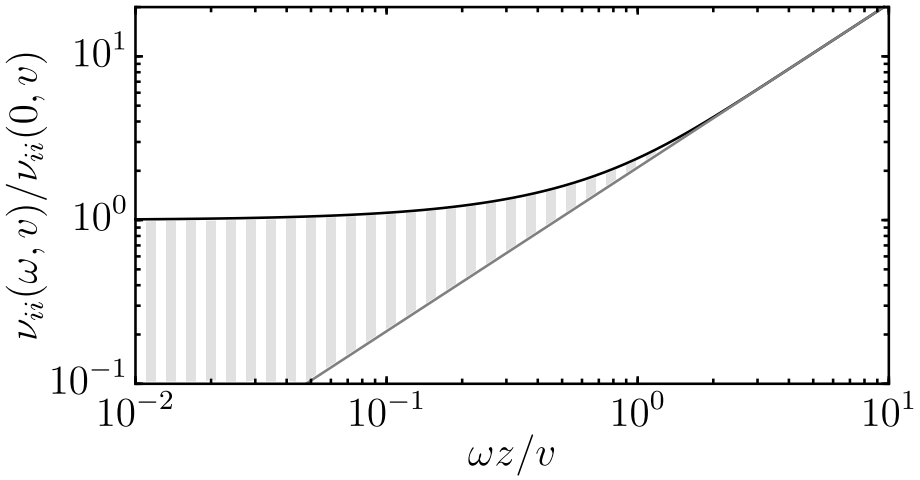

Figure 1.11: Power spectrum (black, solid) of the material-modified vacuum fluctuations in mechanical nonequilibrium [Eq. ((1.56))] in the presence of a conductor (gold described by the Drude model in Eq. 1.31 with parameters from Ref. [140]) extending over an infinite half space [Eq. (1.25)]. We normalize to the zero frequency limit of Eq. (1.59) and show the limit of large frequencies $\omega \gg \omega_v$ (gray, solid). The enclosed area (gray, shaded) gives the correction to the fluctuations due to the nonequilibrium scenario (black, solid) which is incidentally the error of the LTE assumption (gray, solid) (see Sec. 1.3.2 and Chap. 4).

1.3.2 The statistics of fields in mechanical nonequilibrium

We conclude this Chapter by relating our discussion to some fundamental statistical properties and certain commonly applied approaches to quantum-optical nonequilibrium systems. For simplicity, we focus on the case of mechanical nonequilibrium (finite velocity relative motion between particle and material-modified field) and zero temperatures since this is the case where we can present our result in the most lucid form. This Section serves a two-fold purpose: First, we introduce important statistical concepts we refer to in the remainder of the thesis and, second, we clearly delineate the approach we take by distinguishing it from related concepts, most of them being less powerful in the context of dispersion forces and not capable of reproducing some of the results in this thesis.

To begin with, we recall the relation for the field fluctuations in mechanical nonequilibrium stated in Eq. (1.56) for zero temperature,

$$\underline{\nu}(\omega, v) = 2\hbar \int \frac{\mathrm{d}^2\mathbf{p}}{(2\pi)^2} \theta(\omega_{\mathbf{p}}^+) \underline{G}_{\Im}(\mathbf{p}, z, \omega_{\mathbf{p}}^+). \tag{1.60}$$

We explicitly show in Chap. 3 and 4 that this is indeed the correct (self-consistent) result within the realm of our assumptions. However, for now, we consider it as a reference in order to demonstrate the impact of different assumptions and approximations on the underlying statistics. From the perspective of the system's properties, i.e. the experimental outline, $\underline{\nu}$ is determined by (i) the resonances of the system and (ii) long-time correlations. The former is related to peaks in the scattering spectra [294], the latter to the corresponding tails or, in physical terms, the back-action of the environment on a certain point that evoked the initial perturbation [50, 136]. Note that, when long-time correlations are important for the interaction, this already points towards the necessity of using a fully self-consistent description.

To explore the difference of resonances and long-time correlations more clearly, lets consider first the case of equilibrium, i.e. $\omega_{\mathbf{p}}^+ \to \omega$ ($v = 0$). From the appearance of the delta function in Eq. (1.17), we can see that the correlation tensor in equilibrium is stationary with respect to time delays $\tau = t - t'$. Further, the Green tensor, physically being a susceptibility, must respect causality, which, for our definition of the Fourier transform, means that the Green tensor is a holomorphic function in the upper complex frequency plane including the real axis. Upon tracing, performing a Fourier transform and employing the crossing relation ($\underline{G}(\mathbf{p}, z, \omega) = \underline{G}^*(\mathbf{p}, z, -\omega^*)$ [147]), we can write (see also Ref. [58] for a similar decomposition for the power spectrum of a particle interaction with its electromagnetic environment)

$$\nu_{ii}(\tau, 0) = \frac{\hbar}{\pi} \lim_{\mathbf{r}' \to \mathbf{r}} \left(-\pi \sum_{\mu} c_\mu e^{-\mathrm{i}\Omega_\mu \tau} + \mathrm{Tr} \int_0^\infty \mathrm{d}\xi \; \underline{G}_I(\mathbf{r}, \mathbf{r}', -\mathrm{i}\xi) e^{-\xi\tau} \right), \tag{1.61}$$

where Ω_μ are the complex resonances of the Green tensor in the fourth quadrant of the complex frequency plane, the constants $c_\mu = \mathrm{Res}\left[G_{ii}(\mathbf{r}, \mathbf{r}', \omega), \Omega_\mu\right]$ are given by the corresponding residues (Res[·]), we understand the integral to be performed approaching the imaginary frequency axis from the right $\omega \to -\mathrm{i}\xi + 0^+$ and we assumed for simplicity that the Green tensor

features simple poles only[27]. Note that the Green tensor might also feature branch cuts, e.g. propagating modes in direction perpendicular to the material interface $k_z \sim \sqrt{p^2 - \omega^2/c^2}$ or so-called eddy modes along the negative imaginary axis (see Sec. 2.2). Equation (1.61) then needs to be modified integrating over these branch cuts [295]. However, already from the more simple situation, we can deduce two separate time regimes from Eq. (1.61). The first term vanishes exponentially for times longer than the shortest decay rate of the mode, $\tau \gg \mathrm{Im}[\Omega_\mu]^{-1}$. The second term, on the other hand, captures the behavior at low frequencies and usually yields an inverse power law dependence $\propto \tau^{-2(m+1)}$, where $m = 0, 1, 2, ...$ We further used that the Green tensor's imaginary part is odd in frequency [58]. To be more specific, we again consider the case of an infinite metallic half space described by the Drude model. For simplicity, we take the scattered part of the Green tensor only and restrict our discussion to the close vicinity of the material interface (near-field limit) so that the main interaction stems from evanescent waves and we can ignore the impact of freely propagating modes in order to avoid the troubles coming with the existence of branch cuts in the complex frequency plane. The system then features one distinct resonance involving surface plasmon-polaritons at frequncy ω_sp and the corresponding field fluctuations in time domain read ($\tau > 0$)

$$\nu_{ii}(\tau, 0) \sim \frac{\hbar}{\epsilon_0} \frac{\omega_\mathrm{sp}}{16\pi z^3} \left[e^{-\mathrm{i}\omega_\mathrm{sp}\tau} e^{-\frac{\tau_\mathrm{M}}{\tau}} + \frac{2}{\pi} \frac{\Gamma}{\omega_\mathrm{sp}} \frac{1}{\tau^2 \omega_\mathrm{sp}^2} \right], \tag{1.63}$$

where z, again, is the distance from the surface. For the details on the calculation we refer to appendix B. If we were to ignore the power law contribution, the exponential decay would cause the interaction at time intervals $\tau \gg \tau_\mathrm{M}$ to be practically uncorrelated with itself. In other words, the memory on previous events is more or less irrelevant for the present event. In the particular case of a infinite half space made from gold, the dissipation rate of a surface plasmon polariton in the local Drude description leads to roughly [140]

$$\tau_\mathrm{M} \equiv \frac{2}{\Gamma^\mathrm{Au}} \approx 0.04 \text{ ps}. \tag{1.64}$$

For much larger times, the memory can be safely neglected, a situation that sometimes is referred to as *Markovianity*. Note, however, that a truly Markovian system needs to be perfectly uncorrelated in time, i.e. $\underline{\nu}(\tau, 0) \propto \delta(\tau)$. The finite, but exponentially small correlation time, introduced by the residues of the Green tensor [first term in Eq. (1.63)] can be related to the fluctuations of the dissipative bath. For sufficiently large times $\tau \gg \tau_\mathrm{M}$, the dynamics can be effectively considered as Markovian. In accordance with the Mittag-Leffler theorem [118], we

[27] We can generalize the discussion in the context of the so-called *resonant state expansion* [295], sometimes also referred to as *residue decomposition* [118]. Here, it is used that the Green tensor can be written as

$$\underline{G}(\mathbf{r}, \mathbf{r}', \omega) = \frac{c^2}{2\omega} \sum_\mu \frac{\mathbf{f}_\mu(\mathbf{r}) \mathbf{f}_\mu(\mathbf{r}')}{\omega_\mu - \omega}, \tag{1.62}$$

where the sum is taken over the system's resonances ω_μ and $\mathbf{f}_\mu(\mathbf{r})$ is the corresponding complex field distribution. Including dissipation, the resonances ω_μ feature a finite complex part depending on the particular properties of the system. This builds the basis for the theory of *quasi-normal modes* which is successfully applied to the analysis of complex photonic structures [118, 162, 294–296].

can connect the exponential to a Lorentzian in frequency space

$$\tilde{\nu}_{ii}(\omega, 0) \sim \frac{\hbar}{\epsilon_0} \frac{1}{16\pi z^3} \frac{\Gamma\omega_{\mathrm{sp}}}{(\omega - \omega_{\mathrm{sp}})^2 + \left(\frac{\Gamma}{2}\right)^2}, \tag{1.65}$$

where the tilde denotes the approximation neglecting the second term in Eq. (1.63). For $\omega \to 0$, the approximation of Eq. (1.65) approaches a constant, while the full result, including the second non-Markovian term in Eq. (1.63) goes to zero since

$$\nu_{ii}(\omega) \propto \omega. \tag{1.66}$$

This means that the quasi-Markovian approximation of the field's power spectrum effectively models the resonances as a Lorentzian with finite width. Such an approximation holds better, the closer one works to the real part of the actual resonance. It fails, however, to accurately describe the tails of the power spectrum as it fails to capture the correct long-time behavior of the system which can sustain over a comparably large period of time. Indeed, equating the two terms in the brackets of Eq. (1.63), we find that the power law dependence on τ already dominates the dynamics at time-scales

$$\tau \gg \tau_c \lesssim \tau_{\mathrm{M}}. \tag{1.67}$$

In the case of the metallic interface, for instance, we obtain by equating the terms in Eq. (1.63) that $\tau_c \approx 0.002$ ps. For systems in nonequilibrium, this can become highly problematic. Depending on the situation, we have already seen that the corresponding energy scales for thermal as well as mechanical nonequilibrium are much smaller than common electric resonances. Hence, the Markovian approach can be insufficient for describing nonequilibrium dispersion forces in the mentioned situations. We report a numerical evaluation of the scenario in both time and frequency domain in Fig. 1.12.

Finally, we want to mention that there are certain situations, though, where the Markovian approach works quite well. This has to do with the importance of dissipation for the existence of long-time correlations in the system. Investigate, again, Eq. (1.63): The impact of the power law dependence on the time delay τ is closely related to dissipation in the system. The smaller the ratio $\Gamma/\omega_{\mathrm{sp}}$, the smaller the corresponding contribution of long-time correlations[28]. In the limit of vanishing dissipation, we achieve a perfectly coherent oscillation with the frequency ω_{sp}. This limit finds broad application in the context of cavity quantum electrodynamics (QED) or the related fields of cavity optomechanics [297–299] and molecular polaritonics [300], where the setup is designed in a way to "make the field of one photon large" [113]. Concretely, cavity quantum electrodynamics assumes that there is a finite number of modes that strongly interact with the system of interest. Such a situation is mostly achieved by means of a strong and coherent Laser field inside an ideally loss-less cavity [113]. We note, however, that there is no explicit

[28] One related and rather convenient quantity in the context of cavity QED is the cooperativity parameter, $C = \frac{g^2}{\gamma\kappa}$, where $g^2 = \omega|\mathbf{d}|^2/(2\hbar\epsilon_0 V)$ is the dipole coupling with $\mathbf{d}$ the dipole moment and V the volume of the cavity, γ the particle's linewidth and κ the cavity linewidth. Note that the coupling rate is a function of frequency ω. For the coherent interactions of cavity QED, one has to meet the so-called Laser threshold $2C \gtrsim 1$. Further, the saturation photon number $n_s = \gamma^2/(8g^2)$ needs to be large. For more details see [113].

need for a driving field in order to promote the interaction with certain modes only [301]. The important thing is that we find a situation where the large continuous range of potentially relevant interaction frequencies is truncated to only a few important ones, which usually excludes the dissipative low-frequency spectrum (for details we refer, e.g., to Ref. [113]). In many cases, this justifies approximations on the statistics of the interaction between a particle and the electromagnetic environment such as the Markov approximation, a statistical decoupling of certain subsystems (Born-Oppenheimer approximation [113] or Born-Markov approximation for the bath degrees of freedom [54, 55]), or the rotating wave approximation [52, 302]. Dissipation is then usually included in terms of a (Markovian) Lindblad equation [303, 304]. Technically, one can then reduce the interaction to a small number of discrete modes described by a Lorentzian spectrum similar to Eq. (1.65) (see, e.g., Refs. [305–307]); a procedure that is conventionally applied in the context of time-dependent perturbation theory [56, 57]. For fluctuation-induced interactions, in comparison, we have almost exactly the opposite situation: Weak to no driving fields or in general a weak coupling cannot single out a dominant interaction resonance and we need to consider the full power spectrum of the interaction with an *infinite* number of *infinitely dense* modes. In the following, we will argue that one should consider the full spectrum of modes rather than single resonances. As we will see in the remainder of the thesis, this includes most importantly the long-term correlations in the system, where common

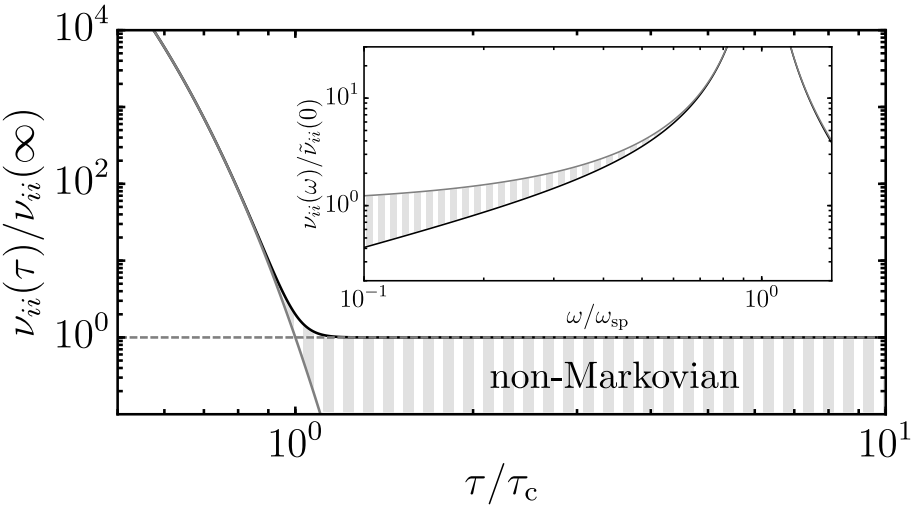

Figure 1.12: Field correlations [Eq. (1.61)] as function of the time delay $\tau = t - t'$ and the corresponding asymptotics in gray [Eq. (1.63)]. For better visibility, we ignore the oscillating factor $e^{-i\omega_{sp}\tau}$ and normalize by the large-τ result, i.e. $\nu_{ii}(\infty) \propto \tau^{-2}$. **Inset:** The corresponding relation in frequency space and we normalize by the zero-frequency quasi-Markovian result [Eq. (1.65)]. Everything is evaluated using the Drude model with parameters for gold from Ref. [140]. The shaded area gives the non-Markovian correction which is positive in time domain and negative in frequency domain. As expected, the Markovian calculation works perfectly close to resonance, but fails to describe the tails of the correlation.

approximations employed in cavity QED are not well-justified for certain systems.

In summary, the Markovian assumption is inappropriate for the type of nonequilibrium interaction we are interested in.

A more accurate approach that has been used quite successfully is the assumption that Thermal Equilibrium might hold Locally (LTE) [33] (see Chap. , 3 and 4). The LTE approach amounts to assuming the field at position $\mathbf{r}$ to be in equilibrium with its immediate environment, not regarding the dynamics of the global system. The idea is that a global system can be divided into a finite number of subsystems: In each subsystem, the net flow of energy or particles vanishes and we might define a common temperature and chemical potential for this subsystem [43, 308, 309]. We refer to Chapters 3, 4 and Fig. 3.5 for a concrete systematization and quantification of this concept in the context of atom-surface interactions. In technical terms, the LTE translates to using the equilibrium occupation number for the field correlations at frequency ω in Eq. (1.56), i.e.

$$n(\omega_{\mathbf{p}}^{+},T)+1 \to n(\omega,T)+1. \tag{1.68}$$

Such a small change can have a profound impact on the low-frequency regime of the field fluctuations. More explicitly, we review the situation of pure vacuum (no material) at finite temperature, and obtain for the field's power spectrum with adjusted occupation number (see appendix B)

$$\begin{aligned}\nu_{ii}^{\mathrm{LTE}}(\omega,v) &= 2\hbar\left[n(\omega,T)+1\right]\mathrm{Tr}\int\frac{\mathrm{d}^2\mathbf{p}}{(2\pi)^2}\underline{G}_{\Im}(\mathbf{p},z,\omega_{\mathbf{p}}^{+}) \\ &\sim \mathrm{sgn}(\omega)\left(1+\frac{10}{3}\frac{v^2}{c^2}\right)\begin{cases}\theta(\omega)\frac{\hbar\omega^3}{\pi\epsilon_0 c^3}, & \hbar\omega \gg k_{\mathrm{B}}T\\ \left[\frac{k_{\mathrm{B}}T}{\hbar\omega}+\frac{1}{2}\right]\frac{\hbar\omega^3}{\pi\epsilon_0 c^3}, & \hbar\omega \ll k_{\mathrm{B}}T\end{cases}.\end{aligned} \tag{1.69}$$

Again, we want to highlight that the appearance of the velocity-correction is a consequence of our non-relativistic approach to a, at zero-temperature, Lorentz invariant system [see discussion below Eq. (1.57)]. Comparing Eq. (1.69) to the corresponding full nonequilibrium calculation in Eq. (1.57), we observe that the LTE approach does reproduce the overall scaling, but cannot capture the quantitative difference between quantum and thermal fluctuations that we observed in the full calculation. It treats the thermal and the quantum fluctuations equally even though they relate to different frequency regimes and thereby misinterprets the low-frequency fluctuations in this particular situation. We graphically represent the difference between Eqs. (1.57) and (1.69) in Fig. 1.10 (black, dashed). It turns out that this is quite typical for the LTE approach. For instance, as we discuss in Chap. 3, in the case of quantum friction, which is dominantly derived from such long-time correlations between particle and bath, the low-frequency behavior with respect to temperature is replaced by the low-frequency behavior of the respective material model. Here, the LTE *underestimates* the emDOS and gives an incorrect prefactor. We stress that the LTE approach is not only a quantitative issue. Changing the perspective from field-only to incorporating the interaction of the field with a particle into our description (as we do in the remainder of the thesis), it turns out that the LTE approach is equivalent to ignoring the long-time correlations between the two subsystems; local thermal equilibrium means little information on events that are remote in time or space. Its validity

hence also depends on the properties of the particle and the coupling strength to the material-modified vacuum. In some cases, the assumption of local thermal equilibrium might be well-justified. For instance, when the particle possesses a macroscopic number of internal degrees of freedom that couple only weakly to the environment, the subsystem might indeed establish a local equilibrium in good approximation. In other cases, however, local thermal equilibrium is rather unlikely to accommodate. For instance, when the interacting particle is an atom with no intrinsic degrees of freedom, the LTE approach can be unreliable (see Chap. 3 and Ref. [M1]). Even worse, in Chap. 4, we show that the LTE approach can be very problematic from the conceptual point of view. In fact, incorrectly describing or neglecting the memory of the interaction or the long-time correlations between system and environment – as the Markovian, the LTE and related approximations do – can lead to non-existent thermodynamic instabilities, such as, in the case of quantum friction, an over-time increase to infinity of the internal energy of the atom [M6]. At this point, that might be naively understood by noting that thermodynamics requires a complete and self-consistent description of the system's states [310]. Neglecting some of them disturbs the balance.

1.4 Summary

In the present Chapter, we introduced the concept of dispersion forces which we theoretically model in the context of macroscopic quantum electrodynamics. We are interested in the interaction between microscopic particles interacting with the material-modified vacuum in certain equilibrium and nonequilibrium situations. To this end, we introduced the most relevant material models at the center of the following analysis, described the Green tensor formalism which we use to describe the macroscopic geometry and established the relevant length scales in the system. The latter are given by the temperature, the separation between particle and the closest material interface, the particular properties and resonances of the particle, the chosen material distribution and lastly the degree of nonequilibrium in the system.

We put a special emphasize on the electromagnetic field fluctuations in terms of the second-order auto-correlation tensor (power spectrum) for the electric field operator $\hat{\mathbf{E}}$, so far in absence of any coupling to an atom $\hat{\mathbf{E}} \to \hat{\mathbf{E}}_{\mathrm{N}}$, i.e.

$$2\pi\delta(\omega+\omega')\underline{\nu}(\omega) \equiv \lim_{\mathbf{r}'\to\mathbf{r}} \left\langle \hat{\mathbf{E}}_{\mathrm{N}}(\mathbf{r},\omega)\hat{\mathbf{E}}_{\mathrm{N}}(\mathbf{r}',\omega') \right\rangle \tag{1.70}$$

and the corresponding relation for the magnetic field operator. Since we are interested in fluctuation-induced phenomena, $\underline{\nu}$ is the main quantity for our purposes. In general, it can be shown that the power spectrum features two distinct regimes: (i) A resonant regime for frequencies in the vicinity of one of the system's modes which features exponentially decaying correlation times and (ii) a broad-band regime for small frequencies which features a correlation time that decays as a power law. We depict a generic nonequilibrium power spectrum in Fig. 1.13. While the first regime (i) is sufficiently well described by an underlying quasi-Markovian statistics (practically no memory), the second regime (ii) needs more care: In equilibrium, the non-Markovian behavior of the low-frequency regime is captured by the fluctuation-dissipation relation (FDR) that is very sensitive to changes in the dissipative properties of the material. We discuss this aspect in particular in Chap. 2. For nonequilibrium situations, on the other hand, another length scale related to the degree and type of nonequilibrium is introduced in the regime of low-frequency correlations. In certain situations, it is possible to promote the equilibrium FDR to the nonequilibrium description by assuming local thermal equilibrium (LTE) for spatially separated subsystems. However, the LTE captures the low-frequency fluctuations of nonequilibrium situations only partially. For more accurate descriptions, we need to consider a fully self-consistent nonequilibrium (NEq) calculation which, in general, is arbitrarily complicated. In Chap. 3, we manage to find an exact description for the case of mechanical nonequilibrium in the steady-state and use it to explore the impact of different statistical assumptions on the underlying physics of quantum optical nonequilibrium situations from the thermodynamic perspective in Chap. 4. It turns out that in all these situations, the impact of low-frequency correlations, i.e. long-time correlations in the system or between subsystems, can be of highest importance in order to correctly grasp the physics and make reliable predictions. To the best of our knowledge, investigating the impact of such long-time correlations explicitly is a position that has rarely been taken on in the relevant literature. We aim to show in the following Chapters that new and intriguing physics can emerge from what is quite often understood as negligible.

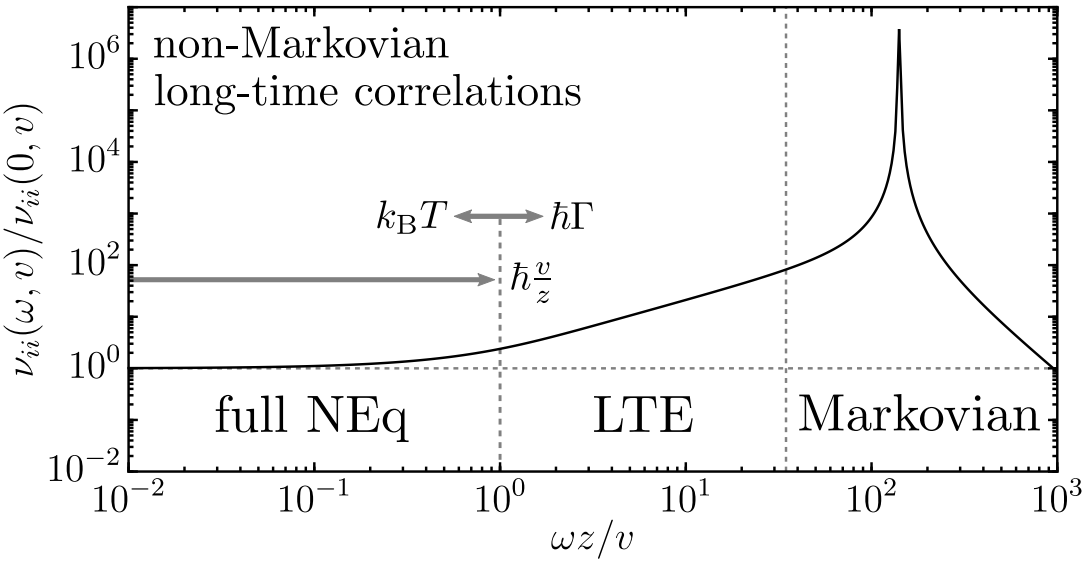

Figure 1.13: Typical power spectrum describing the field fluctuations of the material-modified vacuum in the situation of mechanical nonequilibrium with constant velocity v [Eq. (1.60)]. We focus on the near-field limit of the scattered Green tensor for an infinitely extended conducting half-space. In order to create a clearly visible data set, we chose $z = 10^{-9}\,\mathrm{m}$ and $v/z \approx 0.045\,\mathrm{eV}$. The energy scales are given by $k_\mathrm{B}T \approx 0.025\,\mathrm{eV}$ for room temperature $T = 289\,\mathrm{K}$ and dissipation $\hbar\Gamma \approx 0.03\,\mathrm{eV}$ for gold [140]. Usually, we work with much smaller velocities and temperatures, such that the thermal energy scale is much smaller and the dissipative energy scale much larger than the velocity scale; even though this is slightly different for the parameters chosen here. Note that all the phenomena we are interested in are mostly related to the low-frequency region, where the Makovian approximation fails and we need to employ either the Local Thermal Equilibrium approach (LTE) or preferrably a full nonequilibrium (NEq) calculation.

CHAPTER 2

Equilibrium Casimir-Polder Interaction

We discuss the Casimir-Polder interaction between an electrically and magnetically polarizable particle and the material-modified vacuum in equilibrium. We put special emphasis on two distinct situations where the impact of long-time correlations in the system is most eminent: The finite-temperature corrections to the electric Casimir-Polder free energy and the low-temperature behavior of the magnetic Casimir-Polder entropy. We thereby address some recent issues connected to the use of the appropriate material descriptions at low frequencies. The present chapter contains work by the author that has been published in Ref. [M3].

After extensively studying the fluctuations of the material-modified vacuum field in various situations, we now turn our attention to the perspective of the microscopic particle and explore the implications of the interaction with the field. Remarkably, the interaction between an atom and the surrounding vacuum is a problem in theoretical physics with a rich history [1, 311, 312] that still does not fail to produce new insights and intriguing applications [313–315]. Modern experiments are able to operate at the micro- and nanoscale [27, 316, 317] and the influence of quantum fluctuations is not an exotic curiosity anymore. The corresponding dispersion forces have become a rather commonly used tool in the design and manipulation of such experiments [28, 29, 75, 318], which are largely expedited by comprehensive theoretical models.

As a first concrete example for fluctuation-induced interactions, it is instructive to study the force experienced by an atom coupled to the vacuum field in the presence of macroscopic bodies. In equilibrium, the dominating (electric) contribution to the Casimir-Polder potential is given by the free energy [138]

$$\mathcal{F} = -\frac{1}{2}\langle \hat{\mathbf{d}}(t) \cdot \hat{\mathbf{E}}(\mathbf{r}_a, t)\rangle \tag{2.1}$$

of an electrically polarizable particle at position $\mathbf{r}_a$ with dipole moment $\hat{\mathbf{d}}$ introduced into the material-modified electric field $\hat{\mathbf{E}}$. The quantum average is taken over an initially factorized state and we work in the Heisenberg picture, i.e. all operators are time-dependent. Note that the prefactor of $1/2$ hints to the fact that we have a polarizable particle with fluctuating dipole moment rather than a static dipole [147]. Indeed, the average in Eq. (2.1) does not factorize for finite times, since the quantum operators are supposed to vanish in the mean; the interaction is *fluctuation-induced*. The corresponding force acting on the particle is equivalent to the spatial derivative of the free energy in the direction perpendicular to a surface. In our convention, a negative sign corresponds to an attractive force towards a surface, a positive sign means repulsion. Upon invoking quantum linear response theory and demanding causality, the free

energy can be written as [138, 180]

$$\mathcal{F} = -\hbar \operatorname{Im} \int_0^\infty \frac{\mathrm{d}\omega}{2\pi} \coth\left[\frac{\hbar\omega}{2k_\mathrm{B}T}\right] \operatorname{Tr}\left[\underline{\alpha}^T(\omega)\cdot\underline{G}^T(\mathbf{r}_a,\mathbf{r}_a,\omega)\right], \tag{2.2}$$

where $\underline{\alpha}^T(\omega)$ is the polarizability of the atom and $\underline{G}^T(\mathbf{r}_a,\mathbf{r}_a,\omega)$ the electric Green tensor of the setup evaluated at temperature T. The Green tensor is defined in Eq. (1.11) and its temperature dependence, in general, comes from the fact that the behavior of materials can vary with the temperature (see Sec. 2.2). For the atom, the temperature dependence can be related to a thermal occupation of the available levels and we will derive a specific model in Sec. 2.1.1. After the pioneering work of Casimir and Polder [20], the theoretical framework has been developed most notably by Dzyaloshinskii, Lifshitz and Pitaevskii [79]. The form of Eq. (2.2) for the Casimir-Polder force has been used and re-derived by many authors since [56, 138] and was applied to various contexts [66, 74]. For instance, equation (2.2) can be understood as the leading order term expanding Ford, Lewis, and O'Connel's *remarkable* formula [162, 319] for values $|\mathrm{Tr}[\underline{\alpha}^T(\omega)\cdot\underline{G}^T(\mathbf{r}_a,\mathbf{r}_a,\omega)]| \ll 1$ [162]. Hence, for the time being, we refrain from providing a detailed derivation of the previous equations and refer instead to Chapter 3, where we solve for a more general case and Eq. (2.2) appears as a special case.

The fluctuation-induced population of the electromagnetic field mode at temperature T,

$$\frac{1}{2}\coth\frac{\hbar\omega}{2k_\mathrm{B}T} = \frac{1}{2} + n(\omega,T) \tag{2.3}$$

with the Bose distribution $n(\omega,T)$ [Eq. (1.18)], can be separated in a vacuum (first term) and a thermal contribution (second term). Similarly, the Casimir(-Polder) force in equilibrium arises from a zero-temperature vacuum contribution and a thermal component. At zero temperature, the interaction is mediated by the zero-point fluctuations of the quantum vacuum only and we can write

$$\mathcal{F} = -\hbar \operatorname{Tr} \int_0^\infty \frac{\mathrm{d}\xi}{2\pi}\, \underline{\alpha}(\mathrm{i}\xi)\cdot\underline{G}(\mathbf{r}_a,\mathbf{r}_a,\mathrm{i}\xi), \tag{2.4}$$

where we used that the susceptibilities ($\underline{\alpha}^{T=0} \equiv \underline{\alpha}$, $\underline{G}^{T=0} \equiv \underline{G}$) are analytic in the upper frequency half-plane in order to perform a Wick rotation $\omega \to \mathrm{i}\xi$ [32]. To gain some quantitative insight, let us consider the case of an atom in front of a spatially local semi-infinite half-space described by the Green tensor in Eq. (1.25). In order to keep it simple, for the time being, we model the particle's polarizability as isotropic, i.e. $\underline{\alpha}(\omega) \to \alpha(\omega)\mathbb{1}$. We refer to Sec. 2.1.1 for a more accurate model. Upon inserting into Eq. (2.4), we obtain for spatially local materials in the notation defined below Eq. (1.25) that

$$\mathcal{F}(z_a) = -\hbar \int_0^\infty \frac{\mathrm{d}\xi}{2\pi}\, \frac{\alpha(\mathrm{i}\xi)}{4\pi\epsilon_0} \int_0^\infty \mathrm{d}p\; p\kappa e^{-2\kappa z_a} \left[\left(1+\frac{p^2}{\kappa^2}\right) r^p(\mathrm{i}\xi) - \frac{\xi^2}{c^2\kappa^2} r^s(\mathrm{i}\xi)\right], \tag{2.5}$$

where $\kappa = \sqrt{p^2+\xi^2/c^2}$. Here, as in all following cases, we have considered the scattered part of the Green tensor only (see Chap. 1) since we are interested in the interaction with the surface

[74]. The vacuum part, e.g., gives rise to the Lamb shift [320] and has been discussed elsewhere [67]. The integration domain in Eq. (2.5) is constrained by the exponential to $\kappa \sim 1/2z_a$ and the polarizability further constraints the range of frequencies to $\xi \lesssim \omega_a$ with ω_a the dominant dipole transition. If the distances are such that $\xi \sim c/(2z_a) \lesssim \omega_a$, the polarizability may be considered as static, i.e. $\alpha(\mathrm{i}\xi) \to \alpha_0$. For the reflection coefficients we then have that $r^p(\mathrm{i}\xi) = -r^s(\mathrm{i}\xi) \sim (\sqrt{\epsilon}-1)/(\sqrt{\epsilon}+1)$ with ϵ the permittivity of the material, such that the free energy reads

$$\mathcal{F}(z_a) \sim -\hbar\, \frac{\alpha_0 c}{8\pi\epsilon_0 z_a^4} \int_0^\infty \frac{\mathrm{d}x}{2\pi}\, e^{-2x} \frac{\sqrt{\epsilon(\mathrm{i}xc/z_a)}-1}{\sqrt{\epsilon(\mathrm{i}xc/z_a)}+1} \left(1+2x+2x^2\right), \qquad z_a \gg \lambda_{\mathrm{sp}}, \lambda_a, \tag{2.6}$$

for distances larger than the corresponding wavelength of the surface plasmon polariton resonances $\lambda_{\mathrm{sp}} = 2\pi c/\omega_{\mathrm{sp}}$. We note that, focusing on alkali metal atoms and metal surfaces, we usually have $\omega_a < \omega_{\mathrm{sp}}$ such that $\lambda_{\mathrm{sp}} < \lambda_a = 2\pi c/\omega_a$. For instance, using parameters for gold [140] and rubidium [142], Eq. (2.6) is valid for distances larger than micrometers. If we further assume the material to be made from a perfect conductor with vanishing resistivity and no plasma oscillations, $(\sqrt{\epsilon}-1)/(\sqrt{\epsilon}+1) \to 1$ and we recover the Casimir-Polder asymptote for long distances [20, 138], i.e. $\mathcal{F}(z_a) \sim -(3\hbar c\alpha_0)/(32\pi^2\epsilon_0 z_a^4)$. Instead, at shorter distances, we need to invoke the frequency cut-off from the atom's polarizability $\xi \lesssim \omega_a < \omega_{\mathrm{sp}}$ such that the wavelengths mediating the interaction are comparably small $\lambda \sim 1/p \ll \lambda_a$. We can then employ the near-field approximation of the Green tensor [Eq. (1.51)] and obtain for small separations, where retardation can be neglected, that

$$\mathcal{F}(z_a) \sim -\frac{\hbar}{16\pi^2\epsilon_0 z_a^3} \int_0^\infty \mathrm{d}\xi\; \alpha(\mathrm{i}\xi) \frac{\epsilon(\mathrm{i}\xi)-1}{\epsilon(\mathrm{i}\xi)+1}, \qquad z_a \ll \lambda_{\mathrm{sp}}, \lambda_a. \tag{2.7}$$

Considering additionally perfect conductors, we recover the van der Waals limit [159]. Combining Eqs. (2.6) and (2.7), we recover the transition from the near-field to the far-field regime of the interaction, i.e. $\mathcal{F} \propto z_a^{-3} \to z_a^{-4}$ with z_a the distance between atom and surface, at roughly the atomic transition wavelength λ_a, that we discussed in Chapter 1 (see Fig. 1.1) [20].

It is important to note that the Casimir-Polder force remains finite for vanishing dissipation inside the material. This means that, even when dissipation is included in the material description, the dominant contribution under the integral stems from frequencies around the surface resonance [321]. For example, if we employ the Drude model (Sec. 1.2.2) incorporating low-frequency dissipation into Eq. (2.7) and write the isotropic polarizability of the atom in linear approximation as $\alpha(\omega) \sim \alpha_0\omega_a^2/(\omega_a^2-\omega^2)$ (see Ref. [138] and Sec. 2.1.1 for details), the Casimir-Polder free energy is given by

$$\mathcal{F}(z_a) \sim -\hbar\omega_a \frac{\alpha_0}{32\pi\epsilon_0 z_a^3} \frac{\omega_{\mathrm{sp}}}{\omega_a+\omega_{\mathrm{sp}}} - \mathcal{O}\left(\frac{\Gamma}{\omega_{\mathrm{sp}}}, \frac{\Gamma}{\omega_a}\right) \tag{2.8}$$

with Γ the damping rate of the Drude model. The inclusion of dissipation reduces the free energy, but for common metals such as gold the reduction is marginal since $\Gamma/\omega_{\mathrm{sp}} \approx 0.005$ [140]. In this simple situation, the impact of long-time correlations is subdominant and a variation in the low-frequency behavior of the field fluctuations can only be of quantitative interest.

As a second example, let us explore the impact of spatial dispersion on the setup and use the extended hydrodynamic description instead of the Drude model (see Sec. 1.2.2 and appendix D.1). The impact of spatial dispersion is most eminent in close proximity to the surface, namely when the interaction can resolve the ballistic motion of the bulk electrons. The relevant length scale is here given by the bulk electron's mean free path ℓ and for typical metals we are safe to use the near-field expansion of the free energy since $\ell \lesssim \lambda_{\rm sp}$. Further, in addition to the collision-induced Drude damping, spatial dispersion introduces another length scale into the system, i.e. $\lambda_{\rm nl}(\omega) = \sqrt{3}\lambda_{\rm TF}\beta(\omega)/v_{\rm F}$ with $\lambda_{\rm TF}$ the Thomas-Fermi wavelength, $v_{\rm F}$ the Fermi velocity and $\beta(\omega)$ the nonlocal compressibility factor [Eq. (1.46)]. It is connected to Landau damping and the compressibility of the Fermi fluid. For vanishing dissipation, $\Gamma \to 0$, on the other hand, $\beta(\omega) \to \sqrt{3/5}v_{\rm F}$ such that $\lambda_{\rm nl}(\omega) \to \sqrt{9/5}\lambda_{\rm TF}$ becomes constant and the effect of Landau damping is effectively switched off in the model. Still, using that the transverse magnetic reflection coefficient in the near-field can be written as $r^p_{\rm NF}(\mathrm{i}\xi, p) \sim [\xi(\xi+\Gamma)/\omega_{\rm sp}^2 + 1 + 6v_{\rm F}^2p^2/5\omega_{\rm sp}^2]^{-1}$ for $p\lambda_{\rm nl} \gg 1$ [Eq. (D.14)], the expression for the van der Waals free energy of Eq. (2.7) is modified and changes its distance dependence to

$$\mathcal{F}(z_a) \sim -\hbar\omega_a \frac{5\alpha_0\omega_{\rm sp}^2}{96\epsilon_0 v_{\rm F}^2 z_a}, \qquad z_a \ll \sqrt{\frac{9}{5}}\lambda_{\rm TF}, \tag{2.9}$$

where we used that $\omega_a, \Gamma \ll \omega_{\rm sp}$ for good conductors and typical atoms [140, 142]. Even though the change in distance scaling due to spatial nonlocality is intriguing, for most common materials, the Thomas-Fermi wavelength is at the order of angstroms, such that the previous result can rather be seen as a theoretical peculiarity for the simple setup of a planar interface. Further, for our purposes, we note that the low-frequency characteristics of the model plays a minor role in obtaining the previous result. Since we are interested in the impact of long-time correlations, one might be tempted to think that the Casimir-Polder effect is an inconvenient example. However, the situation turns around when thermal corrections to the zero temperature force are considered, where the low-frequency dissipative dynamics actually dominates the physics leading to the correction terms. This will be our main focus in Sec. 2.1.2.

Depending on the length scales of the system and the temperature defining the thermal wavelength $\lambda_T = \hbar c/(k_{\rm B}T)$, either of the two contributions, zero-temperature and finite temperature [Eq. (2.3)], can be dominating. For instance, for an atom separated from a plate by the distance $z_a \lesssim 1\mu$m, the vacuum contribution to the force will dominate for temperatures $T \lesssim 300\,$K since $\lambda_T \gtrsim z_a$. The interaction is effectively dominated by zero temperature fluctuations as we discussed in the previous paragraph. In general, however, finite temperature effects have to be taken into account. To this end, we can exploit the pole structure of the coth-function in the complex plane in order to integrate Eq. (2.2) which yields [138]

$$\mathcal{F} = \pi k_{\rm B}T \sum_{n=0}^{\infty}{}' \varpi^T(\mathbf{r}_a, \mathrm{i}n\nu), \tag{2.10}$$

where the prime indicates that the term $n = 0$ counts with an extra prefactor $1/2$, we have defined the first Matsubara frequency $\nu = 2\pi k_{\rm B}T/\hbar$ [79, 170] and the temperature-dependent function $\varpi^T(\mathbf{r}_a, \omega) = -\mathrm{Tr}[\underline{\alpha}^T(\omega) \cdot \underline{G}^T(\mathbf{r}_a, \mathbf{r}_a, \omega)]/\pi$ [M3]. Note that for temperatures much

smaller than the temperatures corresponding to the smallest resonance in the system, i.e. $k_\mathrm{B}T \ll \hbar\omega_r, \omega_a$ and $\lambda_T \gg z_a$, the Matsubara frequencies become sufficiently dense such that we can approximate the sum by an integral and immediately arrive at Eq. (2.4). For most electric transitions and realistic temperatures, this is almost always given [see below Eq. (1.19)], but can become very different for magnetic transitions (see Sec. 2.2). In the limit of high temperatures, however, the thermal contribution to the force will prevail over the quantum noise, $\mathcal{F} \propto k_\mathrm{B}T$ [322]. This can immediately be seen from the high-temperature expansion of the Bose function [Eq. (1.18)]. In the example of a planar interface, this behavior is reached for $\lambda_T \ll z_a$ and it can be shown that only the first Matsubara term contributes in this case [138].

In order to shift this exemplary discussion of high and low temperature limits to a more concrete level, it is interesting to consider the Casimir-Polder entropy

$$\mathcal{S} = -\frac{\mathrm{d}}{\mathrm{d}T}\mathcal{F} = -\frac{\mathrm{d}}{\mathrm{d}T}\pi k_\mathrm{B}T \sum_{n=0}^{\infty\prime} \varpi^T(\mathbf{r}_a, \mathrm{i}n\nu). \tag{2.11}$$

In general, the function $\varpi^T(\mathbf{r}_a, \omega) = [\varpi^T(\mathbf{r}_a, -\omega^*)]^*$ fulfills the crossing relation [155, 323] and is analytic in the upper complex frequency plane. It allows for an intrinsic temperature dependence that originates from the material properties of the involved bodies and particles. Further, $\varpi^T(\mathbf{r}_a, \mathrm{i}\xi)$ is real-valued along the positive axis $\xi > 0$. Following Ref. [M3], we stress that the entropy in Eq. (2.11) and the free energy in Eq. (2.2) as well as any other quantities describing the Casimir-Polder interaction are *differential* quantities[1]: They describe the observable in the interacting system relative to the same observable in the noninteracting system. For example, we calculate the energy for finite separation minus the same energy at infinite distances between particle and macroscopic environment. In this sense, the function ϖ^T is related to the difference in the number of modes in the frequency interval $[\omega, \omega + \mathrm{d}\omega]$ between the interacting and the noninteracting configuration, i.e. the system's differential mode density[2] [M3]

$$\varkappa^T(\mathbf{r}_a, \omega) = -\partial_\omega \mathrm{Im}\varpi^T(\mathbf{r}_a, \omega). \tag{2.12}$$

At sufficiently high frequencies, any material becomes transparent (ultraviolet transparency) such that also any scattering processes vanish [19, M3]. Mathematically, this physical condition implies that $\varpi^T \to 0$ for $|\omega| \to \infty$ and in combination with the crossing relation, we find $\mathrm{Im}\varpi^T \to 0$ for $\omega \to 0$. Hence, the integral $\int_0^\infty \mathrm{d}\omega\ \varkappa^T = 0$ which indicates that the total number of modes is equal in both the interacting and the noninteracting situation. Note, however, the total number can be infinite and the spectral distribution can be very different in the two scenarios. Similarly, in the limit of large temperatures with respect to the system's resonances, the function $\lim_{T\to\infty} \varpi^T(\mathbf{r}_a, \mathrm{i}n\nu) = 0$ if $n \neq 0$ and we find that the sum reduces to

[1] This is already visible in Casimir's original publication [19]. A sketch of an oversimplified version of his considerations can be found in the popular abstract at the very beginning of the present thesis.

[2] One intuitive way to see the connection is to integrate Eq. (2.2) by parts and define the free energy per mode $f(\omega) = \hbar\omega/2 + k_\mathrm{B}T\ln(1 - \exp[\hbar\omega/k_\mathrm{B}T])$ in order to write the free energy of a generic system as $\mathcal{F} = \int_0^\infty \mathrm{d}\omega\ f(\omega)\varkappa^T(\mathbf{r}_a, \omega)$ [310, 324].

the first term

$$\mathcal{S} \sim -\frac{\pi k_\mathrm{B}}{2}\left(\varpi^T(\mathbf{r}_a,0)+T\partial_T\varpi^T(\mathbf{r}_a,0)\right), \qquad T\to\infty. \tag{2.13}$$

At the leading order, the entropy is finite. In the opposite limit, assuming that ϖ^T is well-behaved at $\omega\sim 0$ in the sense of a proper test function (infinitely differentiable [185, 186]), we can employ the cotangent expansion of Estrada and Fulling [186] in combination with Eq. (2.2) and find

$$\mathcal{S} \sim \frac{\pi^2}{3}\frac{k_\mathrm{B}^2}{\hbar}\varkappa^0(\mathbf{r}_a,0)T, \qquad T\to 0. \tag{2.14}$$

The entropy vanishes linearly with temperature. In the general case, where no such assumption can be made on the function ϖ^T, the situation is considerably more complicated. Depending on the properties of the function ϖ^T, it might happen that the limits of small temperatures and small frequencies do not commute [M3, 143, 324–326],

$$\lim_{T\to 0}\varpi^T(\mathbf{r}_a,\alpha T) \neq \lim_{T\to 0}\lim_{\omega\to 0}\varpi^T(\mathbf{r}_a,\omega), \qquad \forall\alpha\neq 0. \tag{2.15}$$

In such a situation, we can find the low-temperature expression from Eq. (2.11) using an advanced summation method developed in Ref. [326] and further refined in Ref. [M3]. By reinterpreting the sum in terms of the residue theorem, we can solve the resulting expression approximately using contour integration and obtain (see Refs. [M3, 326] for details)

$$\mathcal{S} \sim -\frac{\pi k_\mathrm{B}}{2}\left[\varpi^T(\mathbf{r}_a,0)-\varpi^T(\mathbf{r}_a,\mathrm{i}\nu)\right]-\frac{2}{3}\frac{\pi^2 k_\mathrm{B}^2}{\hbar}\partial_\nu\varpi^T(\mathbf{r}_a,\mathrm{i}\nu)T-\frac{\hbar}{2}\int_0^\infty \mathrm{d}\xi\ \partial_T\varpi^T(\mathbf{r}_a,\mathrm{i}\xi), \quad T\to 0. \tag{2.16}$$

At zero temperature, Eq. (2.16) leads to a finite value $\mathcal{S}_0$.

Equations (2.13)-(2.16) connect the behavior of the Casimir-Polder entropy at high and low temperatures to the behavior of the function ϖ^T at low frequencies $\omega\to 0$ in the complex frequency plane. In fact, as we will see in Sec. 2.2, even the integral in Eq. (2.16) is negligible most of the times [M3]. On a related thought, we can compare our results for the Casimir-Polder free energy and entropy and relate the behavior at high and low temperatures to the sign of the force at small and large separations (see e.g. [327]): If the interaction is attractive at large separations, the corresponding entropy is positive at large temperatures and vice versa. At small temperatures, the situation is more complicated and closely related to the behavior of $\varkappa^T$. For instance, it can be shown that $\varkappa^T$ is positive for an interaction that is repulsive at large separations [327, 328]. This implies that the Casimir entropy can change sign for at least one intermediate temperature and can hence behave non-monotonically [328]. For the possible constant value $\mathcal{S}_0$, we once again have a positive sign for repulsive forces and a negative sign for attractive forces. We note that, in principle, a negative entropy does not pose a problem due to the differential character of the quantity. It is the finite value $|\mathcal{S}_0|>0$ that will require more work to understand.

Since low frequencies are closely intertwined with dissipation in the system (see Chap. 1), it is indeed the long-time correlations in the system that determine the entropy in the limiting cases with respect to temperature. In the recent decades, the complicated behavior and the connection to the interaction at small frequencies prescribed by Eq. (2.16) has lead to some debates in the community which go under the name of *Plasma-Drude controversy*, where the experimental data in many regimes seems to be better described by the so-called plasma model which is the dissipation-less ($\Gamma = 0$) version of the Drude description [M3, 86–88, 224, 239, 322, 329–331], and the seeming *violation of Nernst theorem* by Eq. (2.16) [M3, 177, 178, 325, 332–335]. We will cover these problems in more detail in Sec. 2.2, where we highlight the distinct role of low-frequency fluctuations for understanding the peculiar behavior.

2.1 Casimir-Polder force at finite temperatures

We have introduced the general properties of the electric Casimir-Polder interaction and found that the force at zero temperature [Eq. (2.4)] dominantly derives from frequencies at the order of the system's resonances, while the dissipative low-frequency behavior yields sub-leading contributions only. In realistic scenarios, one can never completely exclude the influence of a finite temperature. For temperatures much larger than the corresponding energy of the system resonances, i.e. $k_{\mathrm{B}}T \gg \hbar\omega_r$, where the thermal nature of vacuum fluctuations dominates, we have shown on general grounds that the Casimir-Polder force scales linearly in T [Eq. (2.13)]. From a practical point of view, however, this regime is less important in most experimental situations since for commonly used atoms, such as rubidium, the corresponding temperatures lie in the range of some tens of thousands of Kelvin [see discussion below Eq. (1.19)]. For smaller temperatures, both quantum and thermal fluctuations contribute to the force and it is interesting to consider the first correction to the zero-temperature result in orders of $k_{\mathrm{B}}T/\hbar\omega_a$ with ω_a the dominating atomic resonance. This will be our main focus in subsections 2.1.2 and 2.1.3. Before we can get there, it is important to quantify our estimates on the atomic response by deriving an explicit model in the following subsection 2.1.1.

2.1.1 Linear atomic model

The characteristics of models used to the describe the internal degrees of freedom of an atom vary widely with the considered interaction strength [313, 336], the impact of nonlinear effects such as saturation and the internal structure [337, 338], the particular application [96, 300] and the properties of the surrounding electromagnetic field leading to dressing [109, 116]. For our purposes, since we are interested in fluctuation-induced interactions, which are comparably weak [Eq. (1.1)], and further focus on temperatures that are much smaller than the particle's resonances diminishing the probability of exciting the atom thermally, we can safely neglect nonlinear effects. We instead consider the atom's polarizability in the linear regime. Further, for simplicity, we focus on a single dominant dipole transition.

In first order of the atom-field coupling and at zero temperature, the atom's polarizability follows from standard quantum mechanical linear response theory. Demanding causality and stationarity, we obtain by straight-forward algebra the ground-state polarizability [138]

$$\underline{\alpha}(\omega) \sim \frac{\mathrm{i}}{\hbar}\int \mathrm{d}\tau\ \theta(\tau)e^{\mathrm{i}\omega\tau}\langle 0|[\hat{\mathbf{d}}(\tau),\hat{\mathbf{d}}(0)]|0\rangle = \frac{\alpha_0\omega_a^2}{\omega_a^2-(\omega+\mathrm{i}\varepsilon)^2}\mathbb{1}, \qquad \varepsilon\to 0^+, \tag{2.17}$$

where $|0\rangle$ denotes the zero-temperature atomic ground state without any materials present and we assumed the dipole moments to be isotropic such that we can write $\alpha_0 \equiv 2\sum_j d_j d_j^*/(3\hbar\omega_a)$ with d_j the matrix element between the ground and the transition state. Further, we introduced $\varepsilon \to 0$ to account for the Heaviside theta encoding causality in Fourier space. Strictly speaking, equation (2.17) gives the linear response of a two-level system (or an oscillator) to small electric field perturbations in vacuum. Due to the vanishingly small imaginary part, the atom's polarizability does not feel the impact of its surroundings: The perturbative approach has removed the complex frequency shift induced by the environment, the so-called dressing, and what is left is the vanishing ε. The only change in electromagnetic field energy occurs from

an exact absorption of a photon since $\mathrm{Im}\underline{\alpha}(\omega) \sim \delta(\omega \pm \omega_a)$. We note that the polarizability of the atom is modified by finite temperatures since the probabilities for certain levels in the atom to be excited varies. For the simple case of a single two-level transition, the thermal dependence reduces to a prefactor gauging the thermal energy against the transition energy [M3, 138],

$$\underline{\alpha}^T(\omega) = \tanh\left[\frac{\hbar\omega_a}{2k_\mathrm{B}T}\right]\underline{\alpha}(\omega), \tag{2.18}$$

which restores the zero-temperature polarizability for $k_\mathrm{B}T \ll \hbar\omega_a$.

As any susceptibility, equation (2.17) fulfills the crossing relation, i.e. $\underline{\alpha}(\omega) = \underline{\alpha}^*(-\omega)$. This is particularly noteworthy in comparison to nonlinear models of an atom using a two-level system interacting with resonant (laser-)radiation [85, 115, 339, 340]. The nonlinear dynamics can lead to collective phenomena [336] and includes saturation effects, as it is typical in the description using the optical Bloch equations [85]. In terms of possible applications, the optical Bloch equations are thereby more flexible than our description. However, due to the approximations involved, the corresponding limit of small fields or large detuning with the driving field yields a polarizability that is much simpler than Eq. (2.17), i.e. $\underline{\alpha}(\omega) \sim \alpha_0\omega_a/2(\omega_a - \omega)$. For one, it violates the crossing relation or in other words the reality of the response function in the time domain [147]. Such a model is hence inappropriate for our system, where we need to be particularly careful with the low-frequency, off-resonant behavior of the fluctuations in the system.

Conserving the fundamental principle of the crossing relation [147] and providing a well-approximated description for the atomic response near its dominant dipole resonance, Eq. (2.17) is hence our preferred choice and was already successfully employed in (broad-band) Casimir-Polder forces [43, 77], (near-)resonant light-scattering by a cloud of strongly interacting atoms [341, 342] or even many-body van der Waals interactions in chemistry [343, 344]. However, in Section 1.3 we argued that, in nonequilibrium situations, long time-correlations might become particularly important. Such correlations are connected to the dissipative part of the interaction. For the atomic model in Eq. (2.17), this means that we need to exercise greater caution when computing the resonance's imaginary part $\gamma = \gamma(\omega) > 0$ which can be a function of frequency and is positive to ensure causality[3]. Finding the functional form of γ amounts in our case to incorporating the coupling of the atom's internal degrees of freedom to the material-modified vacuum (dressing due to the environment). To this end, we note that even though the simple model in Eq. (2.17) is derived from fully quantum mechanical principles, the first-order perturbation result shows strong resemblance with a standard oscillator model for the atomic dipole moment in terms of a quantum Langevin equation [M2, 58, 155, 157]. This is due to the fact that we want to remain in the linear regime [138] and provides the key for solving the dipole's dynamics self-consistently. In general, solving the dynamics would require us to diagonalize the system's (very large) Hamiltonian which encodes the coupling between oscillator modes and the environment [155, 345, 346]. Instead, we rather focus on the dipole's equation of motion and combine it with linear response theory for the electric field [171]. In

[3]One of the first approaches considering a finite (constant) dissipation $\gamma > 0$ in the context of spontaneous emission was developed by Wigner and Weisskopf [312].

the linear regime, such an approach is exact and fully (non-perturbatively) incorporates the coupling and flow of information between system and environment. Specifically, we write in the harmonic limit

$$\frac{\ddot{\hat{\mathbf{d}}}(t)+\omega_a^2\hat{\mathbf{d}}(t)}{\alpha_0\omega_a^2}=\hat{\mathbf{E}}(\mathbf{r}_a,t). \tag{2.19}$$

Indeed, if the electric field operator is replaced by the material-modified vacuum field only, $\hat{\mathbf{E}}\to\hat{\mathbf{E}}_\mathrm{N}$, which is equivalent to neglecting the impact of the presence of the atom on the field configuration, we immediately recover Eq. (2.17) by taking the resolvent of Eq. (2.19) in the frequency domain. However, the electric field in presence of the atom, even in the linear regime, contains a contribution to the field induced by the atom [Eq. (1.13)] which effectively modifies the dipole dynamics in a self-consistent way. Upon inserting the full expression $\hat{\mathbf{E}}=\hat{\mathbf{E}}_\mathrm{N}+\hat{\mathbf{E}}_\mathrm{in}$ (see Chapter 1) into Eq. (2.19) and recalling our assumption that the temperatures are small enough to not macroscopically excite the atom, Eq. (2.19) can be written in the steady state as $\hat{\mathbf{d}}(\omega)=\underline{\alpha}_\mathrm{dr}(\omega)\hat{\mathbf{E}}_\mathrm{N}(\mathrm{r}_a,\omega)$, where we defined the dressed polarizability

$$\underline{\alpha}_\mathrm{dr}(\omega)=\frac{\alpha(\omega)}{1-\alpha(\omega)\underline{G}(\mathbf{r}_a,\mathbf{r}_a,\omega)} \tag{2.20}$$

with $\alpha(\omega)=\alpha_0\omega_a^2/(\omega_a^2-\omega^2)$ the bare polarizability of Eq. (2.17). Since the Green tensor decomposes into a vacuum part and a scattered contribution (see Chapter 1), our model for the dressed polarizability physically contains spontaneous emission [132] as well as dispersion and dissipation due to the presence of the material [M4, M6]. Further, since $\underline{G}(\mathbf{r}_a,\mathbf{r}_a,\omega)$ is a symmetric tensor, the dressed polarizability is also symmetric. Similar expressions have been, for example, considered in Refs. [156, 161, 347] and we will use this approach as a basis for self-consistently describing systems in mechanical nonequilibrium in Chapters 3 and 4. Most importantly, in comparison to the bare polarizability, the dressed atomic polarizability includes the exact re-summation of multiple round-trips of the radiation between particle and surface as can be seen directly from expanding Eq. (2.20) in orders of α_0 [58]. We refer to Ref. [162] for a systematic approach to re-summing Casimir(-Polder) interactions to all orders of coupling.

In summary, even though our approach is restricted by the assumption that the atom can not be macroscopically excited by thermal energy, we do go beyond first order perturbation theory in the atom-field coupling. Such an approach accounts for the fact that system and bath are inseparably intertwined in open quantum systems. Neglecting the environment's non-Markovian behavior as well as a finite coupling leading to back-action from the environment onto the particle is appropriate in only a limited number of cases (mostly cavity QED setups [303]). In fact, both of the latter assumptions (sometimes called Born-Markov approximation [58, 303]) are usually combined in the so-called quantum regression hypothesis [303, 348] (QRH) that is motivated by Onsager's regression conjecture [349, 350] which yields the same equations of motion for the correlation of an observable as for its mean value [348]. However, for quantum systems, the QRH has been shown to fail in the case of quantum fluctuation-induced phenomena [351] and an accurate treatment requires the proper inclusion of dissipation in the system [M6, 135, 351, 352]. In other words, comparing to textbooks of statistical physics [169, 310], where the notion of thermodynamics is usually understood with an infinitely weak coupling between

system and environment, the statistics and dynamics of fluctuating open quantum systems, in principle, needs to include higher orders of coupling [50, 66, 136, 353]. To be precise, from Eq. (2.20), we can write the denominator as $\omega_a^2 - \underline{\Delta}(\omega) - \omega^2 - \mathrm{i}\alpha_0\omega_a^2\gamma(\omega)\omega$ with $\underline{\Delta}(\omega) \in \mathbb{R}$ the resonance shift [M6, 67, 320] and the dissipative part of the complex resonance reads [53, 138]

$$\underline{\gamma}(\omega) = \frac{\mathrm{Im}\underline{G}(\mathbf{r}_a, \mathbf{r}_a, \omega)}{\omega}, \tag{2.21}$$

where the tensorial structure takes possible anisotropies due to the geometry into account. Upon employing the fluctuation-dissipation relation of second kind [138], the imaginary part of the complex polarizability can be written as

$$\mathrm{Im}\underline{\alpha}_{\mathrm{dr}}(\omega) = \underline{\alpha}_{\mathrm{dr}}(\omega) \cdot \mathrm{Im}\left[\underline{G}(\mathbf{r}_a, \mathbf{r}_a, \omega)\right] \cdot \underline{\alpha}_{\mathrm{dr}}^{\dagger}(\omega) \tag{2.22}$$

and we restore the fluctuation-dissipation relation for the atomic dipole: In the language of Chapter 1, the atom's linear susceptibility as well as the fluctuations of its dynamics in the steady-state depend on the field fluctuations [Eq. (1.24)],

$$\left\langle \hat{\mathbf{d}}(\omega)\hat{\mathbf{d}}(\omega') \right\rangle = 2\pi\delta(\omega + \omega')\ \underline{\alpha}_{\mathrm{dr}}(\omega) \cdot \underline{\nu}(\omega) \cdot \underline{\alpha}_{\mathrm{dr}}^{\dagger}(\omega). \tag{2.23}$$

Combining the previous two equations with the results of Chapter 1, the imaginary part of the polarizability scales for small frequencies, e.g., as $\mathrm{Im}\underline{\alpha}_{\mathrm{dr}}(\omega \to 0) \propto \alpha_0^2\omega^3$ for an atom in vacuum or $\mathrm{Im}\underline{\alpha}_{\mathrm{dr}}(\omega \to 0) \propto \alpha_0^2\omega$ for an atom in the near-field of a planar interface modeled by the spatially local Drude model. For comparison, the leading order contribution in α_0 is given by the bare polarizability and vanishes for small frequencies[4], i.e. $\mathrm{Im}\underline{\alpha}(\omega \to 0) \sim \mathcal{O}(\alpha_0) \to 0$ [34, 125]. This emphasizes that, in processes that are of higher order in α_0, the coupling to the environment induces low-frequency/long-time fluctuations in the interaction.

2.1.2 Low-temperature corrections

The integral in Eq. (2.2), in principle, expands over the full range of frequencies and hence the dominant contributions can be expected to originate from frequencies at the order of the system's resonances. The Bose-factor, however, truncates the domain of frequencies contributing to the integral and the chosen temperature controls whether the dominating contribution to the terms connected to $T \neq 0$ cover the system's resonances or not. In order to set the temperature scale we hence need to specify the resonances of the atom and the geometry.

In addition to the atomic resonance, the material composing the macroscopic body can feature a number of resonances ω_n $(n = 1, 2, ...)$ corresponding to collective excitations of the material's degrees of freedom. For instance, a perfectly planar interface between vacuum and a metallic bulk can feature surface plasmon-polaritons [231, 232] whose characteristic frequency is at the order of electronvolts, i.e. $\omega_{\mathrm{sp}}^{\mathrm{Au}} \sim 6\ \mathrm{eV} \equiv 74 \cdot 10^3\ \mathrm{K}$ for gold [140]. Similarly, the lowest resonances of a dielectric sphere can be in a similar energy range; see e.g. Refs. [139, 141] for a theoretical analysis based on Mie resonances for silicon and hybrid materials, respectively.

[4] To this end, we employ the relation $\lim_{\gamma\to 0}(x \pm \mathrm{i}\gamma)^{-1} = \mathrm{P.V.}x^{-1} \mp \mathrm{i}\pi\delta(x)$ with P.V. the Cauchy principal value.

For details, we refer to Chapter 1. The relevant temperature scales we are interested in are considerably low and we can expand the thermal contributions to the CP force in orders of

$$k_{\mathrm{B}}T \ll \hbar\omega_a, \hbar\omega_n. \tag{2.24}$$

Using Eq. (2.3), we can separate the zero-temperature contribution in Eq. (2.4) from the thermal contribution to the Casimir-Polder free energy $\mathcal{F}^{\mathrm{th}} = \int_0^\infty \frac{\mathrm{d}\omega}{2\pi} n(\omega,T) f(\omega)$ with $f(\omega) = -2\hbar \mathrm{Im}\mathrm{Tr}[\underline{\alpha}\cdot\underline{G}]$. For $\mathcal{F}^{\mathrm{th}}$, in the limit of Eq. (2.24), the Bose factor selects the low-frequency contributions and we can approximate

$$\mathcal{F}^{\mathrm{th}} = \int_0^\infty \frac{\mathrm{d}\omega}{2\pi}\, n(\omega,T) f(\omega) \sim a_j \int_0^\infty \frac{\mathrm{d}\omega}{2\pi}\, n(\omega,T)\omega^j = \frac{a_j}{2\pi}\Gamma_{\mathrm{R}}(j+1)\zeta(j+1)\left(\frac{k_{\mathrm{B}}T}{\hbar}\right)^{j+1}, \tag{2.25}$$

where, $\Gamma_{\mathrm{R}}(x)$ and $\zeta(x)$ are the gamma function and the Riemann zeta-function, respectively, and $f(\omega) \sim a_j\omega^j$ with $j > 0$ is the low-frequency behavior of the function $f(\omega)$. The specific temperature scaling hence depends on the specifics of the material and geometry encoded in the Green tensor.

When the integral kernel of Eq. (2.2) is well-behaved for small frequencies in the sense of a test function [186] the exponent in Eq. (2.25) will be integer-valued, i.e. $j \in \mathbb{Z}$, and we expect even powers in the temperature expansion of the Casimir-Polder force. This simplifies the computation of the low-temperature result as we can employ the asymptotic moment expansion put forward by Refs. [185, 186]. To this end, the test function [Eq. (2.2)] needs to be infinitely differentiable at $\omega = 0$ which sensitively depends on the specifics of the geometry and the chosen material (model). In general, however, more sophisticated designs for geometry and material might produce more exotic frequency scalings (see e.g. Ref. [236] for a recent example discussing meta-materials in the context of mechanical nonequilibrium). Even in the case of a half-space made from a Drude model, an irregular behavior of the integral kernel at $\omega \sim 0$ can occur when temperature gradients are present in the system [125]. For instance, when the material half-space is held at a different temperature than the vacuum field, other scaling than even integers for the powers of temperature can occur ($T^2 \to T^{3/2}$) [34]. Further, similar situations can appear in the limit of vanishing dissipation in the material [M3] as we will discuss in full detail in the following Section. Any of these situations would mean that the following considerations are not applicable and we need to utilize Eq. (2.25) instead.

For the present Section, we will always be dealing with functions that *are* proper test functions. Using that $2n(\omega,T) = \mathrm{sgn}(\omega)\coth[\hbar\omega/(2k_{\mathrm{B}}T)] - 1$ and regarding the expression $\coth\left[\hbar\omega/(2k_{\mathrm{B}}T)\right]$ as a distribution, we have for $\tau = \hbar/(2k_{\mathrm{B}}T) \to \infty$ that [185, 186]

$$\coth\left[\tau\omega\right] \sim \mathrm{sgn}[\omega] - \frac{\pi^2}{6}\frac{\delta^{(1)}(\omega)}{\tau^2} - \frac{\pi^4}{360}\frac{\delta^{(3)}(\omega)}{\tau^4}, \tag{2.26}$$

where $\delta^{(n)}$ is the n-th derivative of the Dirac delta distribution. Using the relations $\delta^{(n)}(\omega) = (-1)^n\delta(\omega)\partial_\omega^n$ and $\int_0^\infty \mathrm{d}\omega\ \delta(\omega)f(\omega) = f(0)/2$, we obtain for the thermal correction to the equi-

librium Casimir-Polder force

$$\mathcal{F}^{\mathrm{th}} \sim -\frac{\pi}{3}\frac{k_{\mathrm{B}}^2 T^2}{\hbar}\mathrm{Im}\lim_{\omega\to 0}\left[\partial_\omega + \frac{\pi^2}{15}\left(\frac{k_{\mathrm{B}}T}{\hbar}\right)^2\partial_\omega^3\right]\mathrm{Tr}\left[\underline{\alpha}_{\mathrm{dr}}(\omega)\cdot\underline{G}(\mathbf{r}_a,\mathbf{r}_a,\omega)\right], \tag{2.27}$$

where we used the dressed polarizability. We would have obtained the same expressions from Eq. (2.25) for odd positive integers of j. Further, the previous result is quite instructive for our purposes since it explicitly displays the importance of the low-frequency behavior of the system's Green tensor and the atomic polarizability and thereby the focus is set on the dissipative properties of the system. In particular, this means that including the dressing of the atomic polarizability, which is mostly concerned with low-frequency dissipation and the coupling to the material-modified vacuum, is substantially important for calculating higher order corrections in α_0 to the Casimir-Polder force. Even though we will focus on the first order terms in α_0 in the following for simplicity, our generalized and re-summed version including back-action and dressing of the atom allows for readily computing higher-order corrections to the force. Our approach can hence be used for providing high-precision predictions which is, at the moment, left to future work.

In first order of the atomic polarizability, we can replace $\underline{\alpha}_{\mathrm{dr}} \sim \alpha_0$ and obtain

$$\mathcal{F}^{\mathrm{th}} \sim -\alpha_0\frac{\pi}{3}\frac{k_{\mathrm{B}}^2}{\hbar}T^2\lim_{\omega\to 0}\partial_\omega\mathrm{Tr}\left[\underline{G}_I(\mathbf{r}_a,\mathbf{r}_a,\omega)\right] + \mathcal{O}(T^4), \tag{2.28}$$

where we used that $\partial_\omega\underline{\alpha}_I(\omega\to 0)\to 0$ in leading order α_0 and the subscript I denotes the imaginary part. Physically, this means that we work in the regime where the dominant contribution to the force stems from the dissipative properties of the material-modified electromagnetic environment (encoded in the imaginary part of the Green tensor) and we neglect the dissipation channels of the atom. As a first example, we consider again the semi-infinite half space made from a local Drude model. Upon inserting the Green tensor in Eq. (1.25), we find in the near-field of the interface and in leading order temperature that

$$\mathcal{F}^{\mathrm{th}} \sim -\hbar\Gamma\frac{\alpha_0}{12\epsilon_0 z_a^3}\frac{T^2 k_{\mathrm{B}}^2}{\hbar^2\omega_{\mathrm{p}}^2}. \tag{2.29}$$

Remarkably, the previous result completely depends on the dissipative behavior of the Drude metal and vanishes in the limit of a perfect conductor. Comparing with Eq. (2.8) and choosing parameters for a rubidium atom [142] and gold [140], we indeed find that the thermal contribution becomes relevant for temperatures ($\omega_a < \omega_{\mathrm{sp}}$)

$$k_{\mathrm{B}}T \gtrsim \hbar\omega_{\mathrm{sp}}\sqrt{\frac{3\omega_a\omega_{\mathrm{sp}}}{4\pi\Gamma(\omega_a+\omega_{\mathrm{sp}})}} \sim \hbar\omega_{\mathrm{sp}} \tag{2.30}$$

which lies outside our range of our assumptions. We note that the previous relation can be very different when other materials are chosen. For instance, choosing germanium instead of gold, the resistivity increases by roughly 6 orders of magnitude [354, 355], reducing the temperature in Eq. (2.30) by three orders of magnitude. Further, since the thermal correction is very

sensitive to the low-frequency behavior of the material and the chosen geometry, it can serve as a bench-mark for probing the various cases in the experiment. To illustrate this more clearly, we compute the thermal corrections to the Casimir-Polder force experienced by an atom in front of a sphere in the next Section. This allows us to additionally explore the impact of curved geometries. For a similar treatment in planar geometries we refer the reader to Refs. [34, 83, 125, 143, 293, 332, 356] as well as Sec. 2.2.

2.1.3 Atom in the vicinity of a sphere

In order to explicitly evaluate Eq. (2.28) for an atom in front of a sphere of radius R, we require an expression for the electric Green tensor of the geometry. We owe it to the high symmetry of our system that such a task becomes analytically tractable by means of a partial wave analysis (sometimes called eigenfunction expansion) [188, 230, 357]. The (dispersive) surface properties of the sphere's finite boundaries are taken into account in terms of Mie's famous coefficients [230, 358]. Physically, the Mie coefficients depend on the material properties via the permittivity function and encode the extinction, i.e. the attenuation of an impinging field due to both scattering and absorption [358]. The spherical interface is thereby modeled as sharp boundaries. For metallic spheres, the Mie resonances can be related to a discrete, but infinite number of surface plasmon-polariton excitations of frequency $\omega_n^2 \sim \omega_\mathrm{p}^2 n/(2n+1)$ with ω_p the bulk plasma frequency and $n \in \mathbb{Z}^+$ [359]. In this way, the Mie coefficients describe the complex reflection and absorption processes for waves interacting with the sphere and fully characterize the scattering and extinction properties of the interaction [360]. Similar to the planar geometry, the light scattering by small spherical particles and in particular probing their surface plasmon-polaritons has experienced an unabated interest in the last century due to its wide range of technological applications ranging from fundamental physics to bio-medicine (see Ref. [359] for a recent review). In parallel, the theoretical description and in particular the numerical techniques describing the systems are ever advancing (see Refs. [212, 234, 235, 361, 362] to name only a few). For instance, the local material description in combination with the hard-wall interface boundary conditions used originally by Mie [230] is continuously refined to include spatial nonlocality [198, 363] as well as an extension to smeared-out interfaces (see, e.g. most recently, Ref. [364]) leading to so-called *spill-out* of the electron density at the material-vacuum interface [217]. Finding the proper description for the surface properties of the geometry is a non-trivial and highly debated problem (see, e.g., Refs. [222, 223, 365] for a debate on planar interfaces and also Sec. 1.2 for our discussion of spatially dispersive material models). In the present Section, however, the main objective is to qualitatively discuss the impact of the surface's curvature on Casimir-Polder forces. Hence, we turn our attention to the simplest case of a sphere de-

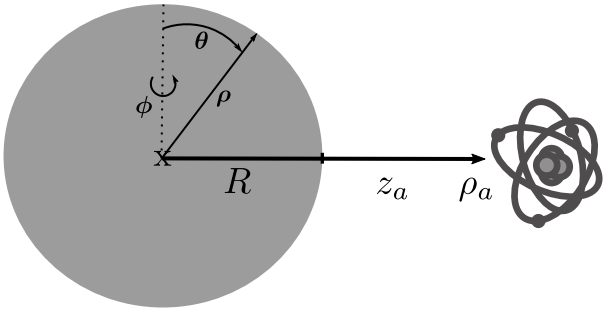

Figure 2.1: An atom interacting with a dielectric sphere of radius R at distance z_a and position $\rho_a = R + z_a$ in spherical coordinates given by the unit vectors $(\boldsymbol{\rho}, \boldsymbol{\theta}, \boldsymbol{\phi})$.

scribed by a spatially local material with permittivity $\epsilon(\omega)$ and follow the approach of Refs. [188, 357] for finding the electric Green tensor. Upon solving the electromagnetic problem with spherical boundary conditions, the electric Green tensor can be written in a closed form in terms of a discrete sum over the resonances of the sphere (due to the finite angular dimensions of the object) and becomes a function of the complex scattering coefficients $r_n^{s/p}$, which now carry the index $n \in \mathbb{Z}^+$ related to the corresponding resonance and the superscript denotes the respective polarization. For instance, placing the source outside of the sphere and measuring the scattered field at some other position in vacuum, the coefficients $r_n^{s/p}$ are closely related to the Mie coefficients of the scattering problem originally considered in [230] (see also [358]). We report the explicit form of $\underline{G}$ in appendix A. Further, in order to highlight the effect of the curvature, we focus on the behavior at long distances $z_a \gtrsim R$, where z_a is the distance from the surface measured along the radial direction in spherical coordinates with origin in the center of the sphere (see Fig. 2.1). An extensive discussion of the equilibrium contribution to the atom-sphere Casimir-Polder force at *zero temperature* can be found in Ref. [292]. For completeness, we report here the main asymptotic results. Subsequently, we set the main focus on the generalization of the atom-sphere Casimir-Polder force to finite temperatures.

Focusing on the impact of the geometry, we ignore the vacuum part of the Green tensor and insert its scattered contribution only (see Sec. 1.2 and appendix A). At zero temperature, we recover[5] the result of Ref. [292],

$$\mathcal{F}^0 \sim -\frac{\mathrm{i}\hbar}{(4\pi)^2\epsilon_0 c}\sum_{n=1}^{\infty}(2n+1)\int_0^\infty \frac{\mathrm{d}\xi}{2\pi}\,\alpha(\mathrm{i}\xi)\frac{\xi}{\rho_a^2} \times \lim_{\omega\to\mathrm{i}\xi}\left\{k_\mathrm{v}^2\rho_a^2\left[h_n(k_\mathrm{v}\rho_a)\right]^2 r_n^s + \left[n(n+1)\left[h_n(k_\mathrm{v}\rho_a)\right]^2 + \left(\frac{\mathrm{d}[\rho_a h_n(k_\mathrm{v}\rho_a)]}{\mathrm{d}\rho_a}\right)^2\right] r_n^p\right\}, \tag{2.31}$$

where $k_\mathrm{v} = \omega/c$, $r_n^s = r_n^s(\omega, R)$ ($r_n^p = r_n^p(\omega, R)$) is the n-th order scattering coefficient of s (p) polarization, $\rho_a = R + z_a$ the radial position of the atom with respect to the center of the sphere and $h_n(x)$ the n-th order spherical Hankel function of first kind [366]. We note that the result does not depend on the atom's angular position due to the symmetries of our system. In order to compute the limiting behavior of the previous expression with respect to the atom-surface separation, we follow Ref. [292] and first note the series expansion of the spherical Hankel function can be written as[6] [366]

$$h_n(x) = e^{\mathrm{i}x}\sum_{m=0}^{n}\mathrm{i}^{m-n-1}\frac{a_m^n}{x^{m+1}} \tag{2.32}$$

with expansion constants a_m^n. Computing the integral at complex frequencies $\omega = \mathrm{i}\xi$, the Hankel functions need to be evaluated at purely complex arguments and we find that the function in Eq.

[5]The different prefactor of $\mathrm{i}/4\pi$ with respect to Ref. [292] arises from a slightly different definition of the Mie coefficients in Eq. (A.19) and the fact that we use SI-units instead of Gaussian units.

[6]For example, we have that $h_1(x) = -\left(\frac{1}{x} + \frac{\mathrm{i}}{x^2}\right)e^{\mathrm{i}x}$ or $h_2(x) = \mathrm{i}\left(\frac{1}{x} + 3\mathrm{i}\frac{1}{x^2} - 3\frac{1}{x^3}\right)e^{\mathrm{i}x}$.

(2.31) is exponentially decreasing with increasing distance, i.e. $h_n(\mathrm{i}x) \propto e^{-x}$. This constrains the range of frequencies contributing to the integral to $\xi \lesssim \frac{c}{\rho_a} < \frac{c}{R}$. Consequently, we have that [292]

$$|k_\mathrm{v} R| \sim \frac{\xi R}{c} \lesssim \frac{R}{\rho_a}. \tag{2.33}$$

Further, we note that the scattering coefficients can be written using a regular Taylor series in their argument, i.e. $r_n^p \propto (k_\mathrm{v} R)^{2n+1}$ and $r_n^s \propto (k_\mathrm{v} R)^{2n+3}$. In combination with the previous relations, this means that the number of contributing Mie resonances depends on the ratio between radius of the sphere and the distance of the atom, i.e. R/ρ_a. For large separations $\rho_a \gg R$, the dominating contribution to the force stems from the term $n = 1$, while for very small atom-surface separations, we need an increasing number of Mie resonances as $R/\rho_a \sim 1$. The physical interpretation is clear: We have chosen a spherical coordinate system to describe the interaction. At large separations, the atom perceives the full sphere in the lowest order of the multi-pole expansion. However, the closer the atom gets to the surface, the less can the atom record the actual curvature of the sphere and we need an increasing number of spherical multipoles in order to resolve the interface that is perceived as being almost planar. Indeed, in the limiting case, one can show that we recover the Casimir-Polder interaction of an atom with a perfectly planar interface [292]. For large separations, on the other hand, the dominating contribution stems from the scattering coefficient r_1^p. For small arguments $|k_\mathrm{v} R| \ll 1$, we can employ the Padé approximation [367] and obtain (see also Refs. [368, 369] for a recent discussion on the Padé approximation in the context of the sphere's Mie resonances)

$$r_1^p \sim -\frac{\alpha_\mathrm{sph}(\omega)}{6\pi R^3} \frac{(k_\mathrm{v} R)^3}{1 - \frac{3}{5}\frac{\epsilon-2}{\epsilon+2}(k_\mathrm{v} R)^2 - \mathrm{i}\frac{\alpha_\mathrm{sph}(\omega)}{6\pi R^3}(k_\mathrm{v} R)^3}, \tag{2.34}$$

where we have identified the standard polarizability of a spherical dielectric [147]

$$\alpha_\mathrm{sph}(\mathrm{i}\xi) = 4\pi\epsilon_0 R^3 \frac{\epsilon(\mathrm{i}\xi) - 1}{\epsilon(\mathrm{i}\xi) + 2} \tag{2.35}$$

which describes the far-field response of a dielectric sphere and is nothing but the Clausius-Mossotti relation[7] [147]. Inspecting Eq. (2.34), we observe that r_1^p has a finite imaginary part even if the permittivity ϵ of the material is purely real, namely when the extinction is given by the scattering of radiation at the sphere only and there are no internal loss channels [358]. For comparison, the standard polarizability of the sphere α_sph can feature extinction only for true absorption, i.e. when the permittivity has a finite imaginary part. This means that the electromagnetic response of the spherical particle contains two distinct loss mechanisms, (i) intrinsic damping due to a macroscopic number of particle degrees of freedom and (ii) radiative damping due to the losses of energy to the environment [370]. Intrinsic damping is encoded in

[7] Perhaps better known for its corresponding formula in terms of the material's refractive index, the Lorentz-Lorenz relation, the Clausius-Mossotti relation provides a connection between the polarizability for a number density $N = n/V$ of n molecules in the volume V to the permittivity of the material. For $n = 1$ and a sphere of volume $V = 4\pi R^3/3$, this yields exactly Eq. (2.35) [147, 358].

the imaginary part of the material's permittivity $\epsilon(\omega)$. For example, for a local Drude model, the intrinsic damping leads to a linear dependence on frequency in the particle's polarizability for $\omega \to 0$, i.e. $\alpha_{\mathrm{sph}} \propto \omega$. Radiative damping, on the other hand, is given by the imaginary part of the denominator in Eq. (2.34) and – for constant ϵ – shows the typical ω^3-dependence that is a characteristic of the radiation reaction of small particles [159]. For completeness, we note that the real part of the denominator in Eq. (2.34) shifts the particle's resonance frequency and the second term, in particular, is referred to as dynamical depolarization [371]. The impact of dissipation on fluctuation-induced forces is usually most prevalent in the low-frequency regime of the interaction (see Refs. [43, M4, M5], Sec. 1.2 and also below). This means that we can expect the intrinsic dissipation mechanism, which is likely to decrease more slowly with decreasing frequency (e.g. linear in comparison to cubic behavior), to prevail in most situations and we can safely employ Eq. (2.35). However, in the case of a perfect dielectric (or e.g. atoms [M2]) with no intrinsic dissipation channels ($\epsilon_I = 0$), the cubic frequency scaling of the radiation-induced damping needs to be considered and we need to use the more involved expression of Eq. (2.34) instead.

To be concrete, let us consider the case of finite intrinsic dissipation of the particle, $\epsilon_I \neq 0$. In the non-trivial case of large separations ($R/\rho_a \ll 1$), we already found that the important part of the interaction stems from the first Mie coefficient $n = 1$ and we can write

$$r_1^p \sim -\frac{\alpha_{\mathrm{sph}}(\omega)}{6\pi R^3}(k_{\mathrm{v}}R)^3. \tag{2.36}$$

Combining Eqs. (A.26) and (2.32), the Green tensor can be written as

$$\underline{G}(\mathbf{r}_a, \mathbf{r}_a, \mathrm{i}\xi) \sim \frac{\alpha_{\mathrm{sph}}(\mathrm{i}\xi)}{(4\pi)^3\epsilon_0^2}\frac{e^{-2\frac{\xi\rho_a}{c}}}{\rho_a^6}\left\{4\left(1+\frac{\xi\rho_a}{c}\right)^2\boldsymbol{\rho\rho} + \left[\boldsymbol{\theta\theta}+\boldsymbol{\phi\phi}\right]\left[1+\frac{\xi\rho_a}{c}+\left(\frac{\xi\rho_a}{c}\right)^2\right]^2\right\}, \tag{2.37}$$

where the vector dyadics denote the tensorial structure in terms of the unit vectors in spherical coordinates $(\boldsymbol{\rho}, \boldsymbol{\theta}, \boldsymbol{\phi})$. Inserting into Eq. (2.31) and substituting $x = \xi\rho_a/c$ for the frequency integral, we can see that the corresponding force scales as $\mathcal{F}^0 \propto -\rho_a^{-7}$ [292] which shows an inverse distance dependence that is three powers larger than the corresponding interaction between an atom and a planar interface [Eq. (2.6)]. Physically, it corresponds to the retarded interaction between the atom's and the sphere's dipole moments since $\mathcal{F}^0 \propto \alpha(\omega)\alpha_{\mathrm{sph}}(\omega)$.

The finite-temperature correction to the vacuum fluctuation-induced equilibrium interaction is given by the low-frequency scaling of the Green tensor's imaginary part [see Eq. (2.28)]. For frequencies smaller than any of the system's resonances ($\omega \to 0$), we again have that $|k_{\mathrm{v}}R| \ll 1$ and the expansion for large separations of the Green tensor in Eq. (2.37) still holds[8]. In order to derive an explicit expression, we need to specify the material of the sphere first. In the local regime, many dielectric materials are sufficiently well-described by a mixture of a Drude and a Lorentz model [147, 226] (see Sec. 1.2), where the Drude model, i.e. $\epsilon_{\mathrm{Dr}}(\omega) = 1 - \omega_{\mathrm{p}}^2/(\omega^2 + \mathrm{i}\Gamma\omega)$ with ω_{p} the plasma frequency and Γ a phenomenological dissipation rate,

[8] As we mentioned earlier, the low-frequency and large-distance behavior can also be connected to the limit of high temperatures which is quite typical for Casimir-Polder forces; see e.g. Refs. [M3, 327].

describes the conducting features of the material and the Lorentz model encodes dielectric oscillations, i.e. $\epsilon_{\mathrm{Lo}}(\omega) = \epsilon_\infty - (\epsilon_0^{\mathrm{qs}} - \epsilon_\infty)\omega_0^2/(\omega^2 - \omega_0^2 + \mathrm{i}\tilde{\Gamma}\omega)$ with ϵ_∞ the background permittivity, ϵ_0^{qs} the quasi-static permittivity constant, ω_0 the resonance frequency of the dielectric excitation and $\tilde{\Gamma}$ another phenomenological dissipation rate mostly connected to phonon coupling[9].

Considering an intrinsic semi-conductor with no conducting features, we can write $\epsilon = \epsilon_{\mathrm{Lo}}$ which yields a linear term in the dissipation rate $\tilde{\Gamma}$ in the expression for the Green tensor:

$$\mathrm{Tr}\ \underline{G}_I(\mathbf{r}_a, \mathbf{r}_a, \omega) \sim \frac{9}{8\pi^2}\frac{R^3}{\rho_a^6}\frac{\epsilon_0^{\mathrm{qs}} - \epsilon_\infty}{\epsilon_0(2+\epsilon_0^{\mathrm{qs}})^2}\frac{\tilde{\Gamma}\omega}{\omega_0^2}. \tag{2.38}$$

For comparison, if the conducting part cannot be neglected in the dielectric response, it will usually dominate the first temperature correction,

$$\mathrm{Tr}\ \underline{G}_I(\mathbf{r}_a, \mathbf{r}_a, \omega) \sim \frac{9}{8\pi^2}\frac{R^3}{\rho_a^6}\frac{\Gamma\omega}{\epsilon_0\omega_0^2}, \tag{2.39}$$

and the impact of the Lorentz term only contributes in higher orders of frequency. In both cases, the Green tensor is Ohmic in frequency and hence the leading temperature correction is in second order,

$$\mathcal{F}^{\mathrm{th}} \sim -\frac{3}{32\pi^2}\frac{\alpha_0\alpha_{\mathrm{sph}}(0)}{\epsilon_0^2\rho_a^6}\begin{cases}\frac{\epsilon_0^{\mathrm{qs}}-\epsilon_\infty}{(2+\epsilon_0^{\mathrm{qs}})^2}\frac{k_{\mathrm{B}}^2T^2}{\hbar^2\omega_0^2}\ \hbar\tilde{\Gamma}, & \epsilon = \epsilon_{\mathrm{Lo}},\\ \frac{k_{\mathrm{B}}^2T^2}{\hbar^2\omega_{\mathrm{p}}^2}\ \hbar\Gamma, & \epsilon = \epsilon_{\mathrm{Lo}} + \epsilon_{\mathrm{Dr}},\end{cases} \tag{2.40}$$

where we used that $\underline{\alpha}_I^{(\prime)}(\omega \to 0) \to 0$ in our simple model of Eq. (2.28).

The case is considerably more complicated for vanishing intrinsic dissipation $\tilde{\Gamma} = \Gamma \to 0$. Radiation-induced damping becomes important and we need to respect the full expression for the first order scattering coefficient given in Eq. (2.34). Interestingly, the Green tensor's imaginary part now scales in third order frequency, which is typical for the scattering of electromagnetic waves from spherical particles to their environment (see Chap. 1), i.e.

$$\mathrm{Tr}\ \underline{G}_I(\mathbf{r}_a, \mathbf{r}_a, \omega) \sim \frac{1}{\pi}\frac{\alpha_{\mathrm{sph}}^2(0)}{(4\pi\epsilon_0)^3}\frac{\omega^3}{c^3\rho_a^6} + \frac{11}{15\pi}\frac{\alpha_{\mathrm{sph}}(0)}{(4\pi\epsilon_0)^2}\frac{\omega^5}{c^5\rho_a}, \tag{2.41}$$

where the cubic regime becomes relevant for frequencies (or distances)

$$\omega_{\mathrm{t}} \gtrsim \sqrt{\frac{11}{15}\frac{\alpha_{\mathrm{sph}}(0)}{4\pi\epsilon_0}\frac{c^2}{\rho_a^5}}. \tag{2.42}$$

The relevant frequency scales can be expected to be much smaller than the electric surface resonances. For instance, for a separation of $z_a = 1\mu\mathrm{m}$, the transition frequency ω_{t} is much smaller than a percent of the dominant dipole transition frequency of $^{87}\mathrm{Rb}$ [142] for a radius

[9] The exact parameters depend on the chosen material. For instance, see Ref. [261] for a discussion of doped silicon in the context of Casimir forces or Ref. [260] for the modeling of so-called transparent conducting oxides such as indium-tin-oxide.

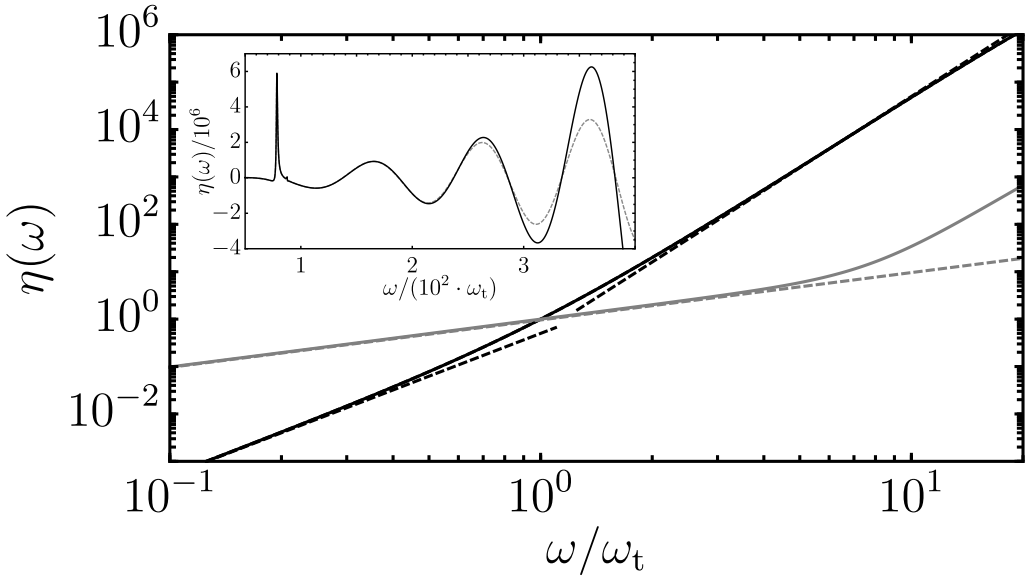

Figure 2.2: Normalized imaginary part of the scattered Green tensor of a sphere [Eq. (A.26)], $\eta(\omega) \equiv \mathrm{Tr}\,\underline{G}_I(\mathbf{r}_a, \mathbf{r}_a, \omega)/\mathrm{Tr}\,\underline{G}_I(\mathbf{r}_a, \mathbf{r}_a, \omega_\mathrm{t})$, as a function of frequency measured in multiples of ω_t [see Eq. (2.42)]. We depict the low-frequency result using the local Drude model (gray, solid line) and the dissipation-less ($\tilde{\Gamma} = 0$) Lorentz model (black, solid line). As an example of the Drude model we choose parameters for gold ($\omega_\mathrm{p} = 9\,\mathrm{eV}$ and $\Gamma = 30 \times 10^{-3}\,\mathrm{eV}$ [140]) and for the dissipation-less Lorentz model we choose the parameters for intrinsic silicon ($\epsilon_0^\mathrm{qs} = 11.87$, $\epsilon_\infty = 1.035$ and $\omega_0 = 4.34\,\mathrm{eV}$ [372]). Further, we use $R = 10\,\mathrm{nm}$ for the sphere's radius and an atom-surface distance of $z_a = 9R$. The corresponding asymptotic expansions of Eqs. (2.39) and (2.41), respectively, are given in dashed lines. For the dissipation-less model, we can clearly identify the ω^3 and the ω^5 regimes separated at ω_t. **Inset:** We display $\eta(\omega)$ for a larger range of frequencies (black, solid) using the Drude model with parameters for gold and compare to the Padé approximant [Eq. (2.34)] (gray, dashed). The Padé approximant works better, the smaller the ratio R/ρ_a and becomes exact for $\omega \ll \omega_t$. The oscillatory behavior stems from the spherical Hankel functions in Eq. (A.26).

of the sphere in the range from some tens of nanometers (e.g. $\sim 71.5\,\mathrm{nm}$ [89]) even to the millimeter-scale (e.g. Ref. [127]). We display a numerical evaluation of the previous behavior in Fig. (2.2).

For the temperature correction to the equilibrium Casimir-Polder force, the dissipation-less Lorentz model (e.g. intrinsic silicon) yields at least fourth order in T and we find

$$\mathcal{F}^\mathrm{th} \sim -\frac{\pi^2}{45}\frac{c\hbar}{\rho_a}\frac{\alpha_0\alpha_\mathrm{sph}^2(0)}{(4\pi\epsilon_0)^3\rho_a^9}\left(\frac{k_\mathrm{B}T}{\hbar c/\rho_a}\right)^4. \tag{2.43}$$

In conclusion, we note that the temperature correction originates from the low-frequency behavior of the interaction and is hence highly sensitive to the chosen material (model) for the

sphere in terms of its dissipative properties. For finite dissipation at low frequencies, $\mathcal{F}^{\mathrm{th}}$ scales quadratic in T. For vanishing material dissipation, the Casimir-Polder free energy at large distances acquires leading order contributions in the fourth power of temperature and the material length scales are replaced by retardation effects, i.e. $\hbar\Gamma \to c\hbar/\rho_a$. Also, the leading order temperature correction is less sensitive to the atom-surface distance: We obtain a ρ_a^{-6} dependence instead of ρ_a^{-7} for the zero-temperature component which is in accordance with previous results on similar systems (see e.g. Ref. [M3] and the following Section for first order temperature corrections to the magnetic Casimir-Polder interaction). Comparing, formally, to the zero-temperature result in the large distance regime $\mathcal{F}^0$ for metallic spheres given by Eq. (67) of Ref. [292], this means that the thermal contribution $\mathcal{F}^{\mathrm{th}}$ becomes comparable to $\mathcal{F}^0$ at distances

$$R + z_a \gtrsim \frac{23}{6\pi}\frac{c}{\Gamma}\left(\frac{\hbar\omega_{\mathrm{p}}}{k_{\mathrm{B}}T}\right)^2 = \frac{23}{6\pi}\frac{\omega_{\mathrm{p}}^2}{c\Gamma}\lambda_T^2 \gg \lambda_T \tag{2.44}$$

in accordance with our initial assumptions allowing for the perturbative expansion. For most common materials, this already lies in the regime where the linear temperature dependence becomes effective and our result of Eq. (2.40) should rather be seen as a quantitative correction to the zero-temperature result for distances $R + z_a \ll \lambda_T$. For completeness, we refer the reader to Refs. [34, 83] for the situation of thermal nonequilibrium for a planar interface, where the temperature "corrections" can actually become dominating. Generalizing their results to the spherical geometry is left for future work.

The Casimir-Polder interaction between an atom and a macroscopic body derives from a complex interplay between material parameters, geometry, coupling strength, separation and the atomic properties. At finite temperatures, the low-frequency behavior of the macroscopic bodies encoded in their material properties as well as their geometric structure, is of particular importance for computing the leading-order corrections. As we have seen above, using different models can have a profound impact on the theoretical predictions. A similarly sensitive dependence of the prediction on the material parameters can be observed when calculating the differential entropy of the interaction at low temperatures; which is the focus of the next Section.

2.2 Low-temperature entropy of atom-surface interactions

Motivated by our findings that long-time correlations determine the thermal contributions to the Casimir-Polder force at large atom-surface separations, we recall that there is an intrinsic connection of that very to regime to the behavior of the entropy at small temperatures (see discussion below Eq. (2.16)). Indeed, exploring the Casimir-Polder interaction in different setups has spiked an interesting controversy about the physical consistency of the low-frequency characteristics of certain material models [178, 222, 223, 239, 333, 373–375] and a number of works studying on how to distinguish them experimentally [40, 224, 330, 376, 377]. This can be traced back to room temperature experiments designed to measure the Casimir force between a gold-coated sphere and a plane which appear to favor the dissipation-less plasma model with permittivity $\epsilon = 1 - \omega_{\mathrm{p}}^2/\omega^2$ over its dissipative counterpart, the Drude model. In a range of distances $\lesssim 1\,\mu$m the measurements seem to show an agreement with the Lifshitz formula [78], i.e. the corresponding relation of the fluctuation-induced force between macroscopic bodies [162], in combination with the plasma model, but discard the Drude description [86–88, 329, 331]. In contrast, using the Drude model seems to agree better with experiments performed in the $1...7\,\mu$m range [322]. In the latter case, the authors have been particularly careful in removing a residual background electrostatic component to the force. As a matter of fact, experiments designed to measure the impact of material models on Casimir(-Polder) forces are constrained by probing the dielectric function at low frequencies. Results can differ between samples [259] and especially for low frequencies, which correspond to long iteration times, one is always obliged to use extrapolation techniques for $\omega \to 0$ [225].

From the theoretical perspective, as we will illustrate in the following, the experimental discrepancy between the Drude and the plasma description of the material continues to the thermodynamic level, where one can observe a finite entropy at zero temperature [325, 335] which seems to contradict Nernst theorem [194, 378, 379]. In its simplest formulation, Nernst theorem states that the entropy of a system should vanish at $T \to 0$ [380]. In the statistical interpretation, this means that the ground state of the system is unique and hence well-ordered. Nernst himself applied his theorem to finite-sized systems and demands that the equilibrium entropy at zero temperature is independent of external parameters such as volume, pressure or temperature [381]. However, for infinite systems, some investigations hint towards relating the low-temperature behavior of the entropy to the statistical features of low-energy excitations [382–385]. The proper value of the entropy then needs to be defined in the thermodynamic limit, where the free energy is divided by the system's extensive parameters [383, 385]. Along these line, the notion of a bulk entropy per particle [386] becomes meaningful and we can establish a more general connection to the possible degeneracy of the ground state [379, 385]. Interestingly, even though the electric contribution to the Casimir-Polder interaction is usually much stronger [143], it is the *magnetic* contribution to the low-temperature entropy that becomes problematic. This is due to the peculiar features of the transverse electric reflection coefficient which is pronounced in the magnetic interaction [M3], while the impact of transverse magnetic waves is screened from the divergence of the dielectric function for $\omega \to 0$ [M3, 326].

In the context of the Casimir-Polder interaction, there is yet, to the best of our knowledge, no rigorous and sufficient solution of neither the plasma-Drude controversy nor the seeming violation of Nernst theorem. Even though the inclusion of spatial nonlocality can resolve

some of the issues connected to the entropy problem [M3, 387] (as we will see below), it fails to shine light on the mismatch between theoretical predictions and experiments since in the corresponding distance regime, the nonlocal model deviates only marginally from the local Drude description (see Sec. 1.2.1). In the following, we refrain from directly addressing the Nernst theorem, but rather investigate the underlying physical processes. To this end, we relate the zero-temperature entropy of the magnetic Casimir-Polder interaction to the statistical behavior of low-frequency eddy modes in the respective models and thereby provide the basis for an informed interpretation of different situations [M3, 180].

2.2.1 Magnetic Casimir-Polder free energy and residual entropy

The interaction between a polarizable planar interface and the magnetic dipole moment $\hat{\boldsymbol{\mu}}$ is formally very similar to the electric interaction introduced earlier, but the typical energy scales can be very different. For instance, the dominating magnetic transition frequency ω_a is at the order of a few hundred MHz or a few GHz which corresponds to temperatures $T_a \approx 10^{-2}\,\mathrm{K}$. Consequently, when interacting with a metallic Drude material, the penetration depth of the electromagnetic radiation into the material corresponding to the magnetic resonance (skin depth), i.e. $\delta_a = \sqrt{2D/\omega_a}$ with $D = \Gamma\lambda_\mathrm{p}^2$ the diffusion constant (see Sec. 1.2.2), can be at the order of micrometers already [140, 143]. Formally, however, we can readily write down the *magnetic* polarizability of the atom in the thermal mixture

$$\underline{\beta}^T(\omega) = \tanh\left[\frac{\hbar\omega_a}{2k_\mathrm{B}T}\right]\underline{\beta}(\omega). \tag{2.45}$$

Here, $\underline{\beta}(\omega)$ is the zero-temperature polarizability of Eq. (2.17) replacing $\alpha_0\mathbb{1} \to 2\boldsymbol{\mu}\boldsymbol{\mu}/(\hbar\omega_a)$, where we allow for anisotropy in the magnetic response of the particle and $(\boldsymbol{\mu})_j \equiv \mu_j$ are the transition matrix elements. The magnetic Green tensor $\underline{G}_\mathrm{B}$, on the other hand, obeys the same equation of motion as its electric counterpart [Eq. (1.11)] and varies in the applied boundary conditions only. For the simple case of a planar interface, this amounts to interchanging the reflection coefficients $r^p \leftrightarrow r^s$ [66, 143, 147, 180]. The magnetic Casimir-Polder free energy is hence given by Eq. (2.10) with

$$\varpi^T(\mathbf{r}_a,\omega) = -\frac{1}{\pi}\mathrm{Tr}\left[\underline{\beta}^T(\omega)\cdot\underline{G}_\mathrm{B}(\mathbf{r}_a,\mathbf{r}_a,\omega)\right]. \tag{2.46}$$

Since the entropy problem is eventually concerned with the material description, we start with exploring the impact of spatial nonlocality on the magnetic Casimir-Polder free energy $\mathcal{F}_\mathrm{B}$, given by the Boltzmann-Mermin model for the electric permittivity introduced in Sec. 1.2.1, and compare it to its local counterpart, the Drude model. Since the effects of spatial nonlocality become important for comparably large wavevectors and for the planar interface we have $p \sim z_a^{-1}$, we focus on the near-field regime. We find that, for large distances $\ell \ll \delta_a \ll z_a$, the Drude and the Boltzmann-Mermin model behave alike. The free energy scales as $\mathcal{F}_\mathrm{B}(z_a) \propto z_a^{-3}$ [143] very much resembling the electrical counterpart (see Eq. (2.7)), except for the different

sign. The magnetic Casimir-Polder interaction is repulsive[10]. At separations $z_a \ll \delta_a$, however, the distance dependence changes in both the local and the nonlocal description. For the local Drude material model, we use that the magnetic polarizability restricts the involved frequencies to $\omega \ll \omega_a$. Similarly, the material permittivity is different from its vacuum value only for frequencies $\omega \lesssim \omega_\mathrm{p}$. Using further that $p \sim z_a^{-1}$ and $z_a \ll \delta_a$, we find for $\omega/(cp) \ll 1$ that

$$r^s \sim \frac{\epsilon(\omega)-1}{4}\frac{\omega^2}{c^2p^2}. \tag{2.47}$$

The transverse magnetic contribution is strongly damped due to the additional prefactor $\omega^2/(c^2p^2)$ in the expression for the Green tensor (Eq. (1.25) with interchanged reflection coefficients). This enables us to obtain the expression for the magnetic free energy using the Drude model in the sub-skindepth regime by straight-forward integration[11], i.e.

$$\mathcal{F}_\mathrm{B}^\mathrm{lc}(z_a) \sim \pi k_\mathrm{B}T {\sum_{n=0}^{\infty}}' \frac{n^2\nu^2}{c^2 z_a}\left[\epsilon(\mathrm{i}n\nu)-1\right]\Phi^T(\mathrm{i}n\nu) \sim \frac{\pi k_\mathrm{B}T}{\lambda\!\!\!^{-2}_\mathrm{p} z_a}{\sum_{n=0}^{\infty}}' \frac{n}{n+\frac{\Gamma}{\nu}}\Phi^T(\mathrm{i}n\nu), \tag{2.48}$$

where we defined the function $\Phi^T(\omega) = \mu_0(\mathrm{Tr}[\underline{\beta}^T(\omega)] + \beta^T_{zz}(\omega))/(8\pi)^2$ with μ_0 the vacuum permeability and the subscript denotes the zz component of the matrix. As soon as we reach distances at the order of the bulk electron's mean free path $\ell \sim z_a$, the magnetic Casimir-Polder free energy behaves as [M3]

$$\mathcal{F}_\mathrm{B}(z_a) \sim \frac{\pi k_\mathrm{B}T}{\lambda\!\!\!^{-2}_\mathrm{p}}\ln\left[\frac{\tilde{\gamma}_\mathrm{E}\ell}{2z_a}\right]{\sum_{n=0}^{\mathrm{Int}[\Gamma/\nu]}}' \frac{4n\nu}{v_\mathrm{F}}\Phi^T(\mathrm{i}n\nu), \tag{2.49}$$

where $\mathrm{Int}[x]$ gives the largest integer smaller than x and $\tilde{\gamma}_\mathrm{E} = e^{-\gamma_\mathrm{E}}$ with γ_E the Euler-Mascheroni constant. We report the details of the derivation in appendix C.1. Spatial dispersion leads to a non-algebraic change in the distance scaling of the free energy and reduces the strength of the interaction with respect to its local counterpart [204]. We report numerical results of the magnetic free energy evaluated over the full range of distances within the near-field regime using the Boltzmann-Mermin model in Fig. 2.3. We observe that spatial dispersion attenuates the interaction by more than 10% as soon as the atom-surface separation becomes comparable to the mean free path ℓ. This is especially remarkable in contrast to other models including spatial nonlocality. For instance, if we were to choose the (extended) hydrodynamic description instead of the Boltzmann-Mermin model (see Sec. 1.2.1), we would not record any deviation from the local Drude result, since the transverse electric reflection coefficients remains unchanged in these descriptions.

[10] We refer the reader to Ref. [21] discussing that repulsion is indeed a characteristic of the magnetic interaction and to Refs. [388–397] for some examples of attractive Casimir interactions.

[11] Our result slightly deviates from the asymptotic expression found in Ref. [143, 398]. The difference is quite subtle and by a careful application of the considered limits, we can show the two results to be indeed related: In comparison to our result, the asymptote reported in Ref. [143, 398] features an additional assumption on the dissipation rate in the material which limits the applicable regime. We report the calculation in appendix C.1.

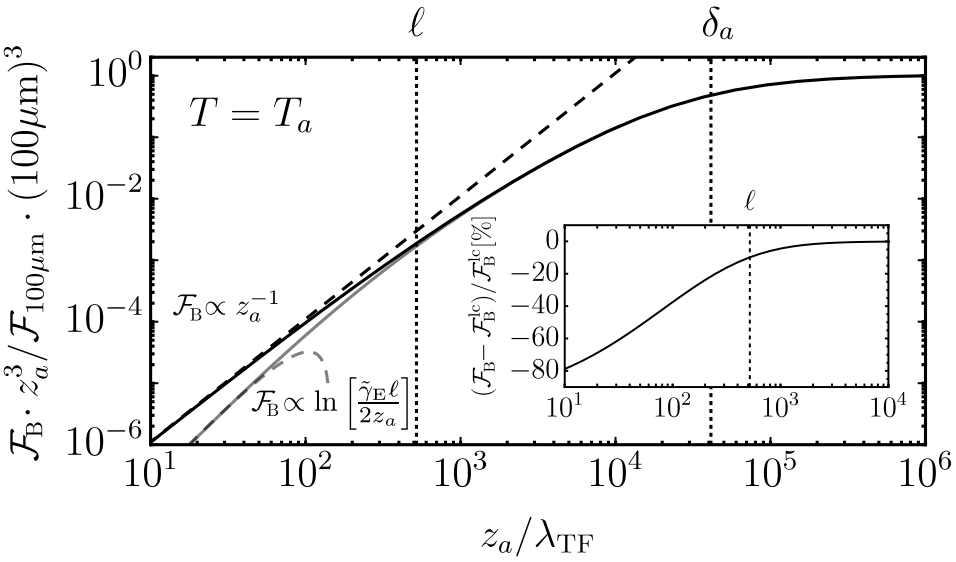

Figure 2.3: Magnetic Casimir-Polder free energy $\mathcal{F}_\mathrm{B}$ of a magnetically polarizable atom in front of a semi-infinite half-space at temperature $T = T_a$ as a function of separation z_a with λ_TF the Thomas-Fermi wavelength. We normalize to the force using the Drude model at $z_a = 100\,\mu$m and multiply by z_a^3. For separations smaller than the skin depth at the atomic transition frequency δ_a, the curve starts to deviate from the cubic distance scaling and for z_a smaller than the bulk-electron's mean free path, the impact of spatial dispersion in the material becomes important (Boltzmann-Mermin, gray). The black line denotes the respective behavior using the local Drude model. We display the respective asymptotes of Eqs. (2.48) and (2.49) in dashed. **Inset:** Relative deviation of the nonlocal [$\mathcal{F}_\mathrm{B}$] from the local [$\mathcal{F}_\mathrm{B}^\mathrm{lc}$] description in percent. For simplicity, we assume the magnetic dipole to be directed parallel to the surface [$\beta_{xx}^T = \beta_{yy}^T$, $\beta_{zz}^T = 0$], choose parameters for gold [140] and set $v_\mathrm{F} = \alpha_\mathrm{fs} c$ (α_fs fein-structure constant) and $\omega_a = 2\,\mu$eV. Adapted from [M3].

For the entropy, as we have noted earlier, the case can become more subtle. Following Eqs. (2.14) and (2.16), the result depends on the behavior of the system's differential mode density $\varkappa^T(\mathrm{r}_a, \omega)$ at $\omega \sim 0$. For instance, if we employ the local Drude model, we obtain $\varkappa^T(\mathbf{r}_a, 0) \sim \Phi^T(0)/(Dz_a) > 0$ with $D = \Gamma\lambda_\mathrm{p}^2$ the diffusion coefficient [180]. For separations $z_a \gg \ell$ this is identically the result one would obtain using the nonlocal Boltzmann-Mermin description. At the order of the bulk electron's mean free path, however, spatial dispersion leads to deviations from the local result and we can write $\varkappa^T(\mathbf{r}_a, 0) \sim 4\Phi^T(0)\ln[\ell/(2z_a)]/(v_\mathrm{F}\lambda\!\!\!^{-2}_\mathrm{p}) > 0$ in the limiting case for $z_a \ll \ell$ (see appendix C.2) [180]. In accordance with our observation from the free energy, the differential mode density of the nonlocal model is reduced with respect to the local scenario. More importantly, upon inserting into Eq. (2.14), we obtain a linearly vanishing, positive entropy $\mathcal{S} \propto T$ as $T \to 0$. To this end, we (artificially) assumed that any system parameters describing the materials, such as Γ or ℓ, are constant with respect to changes in the temperature and can be seen as independent variables in performing the limit.

While assuming an independence from temperature is well-justified for the general (Fermi-Dirac) statistics of the electrons in the fluid for a wide range of temperatures $0 \leq T \ll T_\mathrm{F}$ with T_F the Fermi temperature, this is not necessarily true for the parameter values of the respective material model. For one, it is clear that the phenomenological dissipation rate Γ in the conductor is different at either a few tens or a few hundreds of Kelvin. Since $\Gamma = \Gamma(T)$ is related to collisions between the electronic quasi-particle excitations of the Fermi fluid and other particles such as phonons or impurities in the material, it is reasonable to assume that the collision-induced dissipation decreases with lower temperature leading to an increase in the mean free path ℓ. If we further assume the semi-infinite bulk material to be made of a *perfect crystal*, where all lattice atoms are perfectly periodically aligned and we can ignore the impact of possible defects, Γ can be connected to the collisions between elementary particles in the system only. Its functional dependence is then described by the Bloch-Grüneisen formula [399, 400] which, at low temperature, yields $\Gamma(T) \propto T^m$ with $m \geq 2$ (e.g. $m = 2$ for electron-electron scattering and $m = 5$ for electron-phonon scattering) [M3, 399, 401, 402]. In such a situation, the Green tensor of the setup becomes implicitly temperature-dependent $\underline{G} \to \underline{G}^T$. Moreover, from the power law prescribed by the Bloch-Grüneisen formula, we have that $\Gamma(T)/T \to 0$ for $T \to 0$ such that the limits of zero temperature and zero frequency do not necessarily commute anymore[12]. From Eq. (2.15) we conclude that a non-zero entropy defect can occur due to the vanishing diffusion coefficient $D = D(T) = \Gamma(T)\lambda\!\!\!^{-2}_\mathrm{p}$. Indeed, upon using Eq. (2.16) in combination with the local Drude model featuring a temperature-dependent dissipation rate $\Gamma = \Gamma(T)$, we obtain [M3, 180]

$$\mathcal{S}_0 = 4\pi k_\mathrm{B} \frac{\Phi^0(0)}{z_a^3} F\left(\frac{z_a}{\lambda\!\!\!^{-}_\mathrm{p}}\right), \tag{2.50}$$

where we define the positive, monotonically increasing function $F(x) = -\int_0^\infty \mathrm{d}y\ y^2 e^{-2y}(y - \sqrt{y^2+x^2})/(y+\sqrt{y^2+x^2})$ and we restore the result of Ref. [143] in the limit $z_a \ll \lambda\!\!\!^{-}_\mathrm{p}$ with $F \to 1/4$. Interestingly, if we use the nonlocal Boltzmann-Mermin model instead, we can use that $\lim_{T\to 0} \varpi^T(\mathbf{r}_a, 0) = 0$ and the results of appendix C.2 obtaining a vanishing entropy even if $\Gamma(T)/T \to 0$, i.e.

$$\mathcal{S} \sim -\frac{2\pi}{9} k_\mathrm{B} \nu \frac{\Phi^T(0)}{v_\mathrm{F} \lambda\!\!\!^{-2}_\mathrm{p}} \ln\left[\left(\frac{2}{\tilde{\gamma}_\mathrm{E}}\right)^3 \frac{\nu}{\nu^\mathrm{nl}}\right] \propto T \ln\left[\frac{T^\mathrm{nl}}{T}\right], \tag{2.51}$$

where we defined the frequency scale $\nu^\mathrm{nl} = 4v_\mathrm{F}\lambda\!\!\!^{-2}_\mathrm{p}/(3\pi z_a^3) = \lambda\!\!\!^{-2}_\mathrm{p}\Gamma^\mathrm{L}_t(1/z_a)$ with Γ^L_t defined below Eq. (1.44) and T^nl gives the temperature corresponding to ν^nl. We note that the entropy at small temperatures, where small refers to the respective temperature of the atomic transition frequency, features a non-algebraic behavior in the nonlocal case. We report a numerical evaluation of the different scenarios in Fig. 2.4.

The residual entropy in Eq. (2.50) represents the apparent violation of Nernst theorem

[12] However, it is important to note that in realistic metallic systems, we will certainly never obtain the idealistic situation of a perfect crystal. Imperfections in the periodicity such as impurities or other static defects will always cause the system to have a residual resistivity Γ_0 at $T = 0$ such that $\Gamma(T) \sim \Gamma_0 + \Gamma(T)$ [402].

mentioned earlier. Due to the general structure of Eq. (2.15), it might come to no surprise that similar results have been obtained in various other setups such as the Casimir configuration [325, 332, 403]. Even though it is possible to construct physical situations that unambiguously violate Nerst theorem [404], it still appears to be enigmatic how this can happen in the simple setup of one atom and a macroscopic bulk, arguably one of the simplest setups possible. Admittedly, the Drude model is an oversimplification of the complex processes known to solid state physics. It artificially enforces local behavior and neglects spatial correlations that are bound to become important for a diverging mean free path $\ell = \ell(T) \propto T^{-m}$. The inclusion of spatial nonlocality, on the other hand, seems to resolve the issue and has also been previously reported for the Casimir interaction between macroscopic bodies [180, 259, 387]. The appearance of Γ_t^{L} in Eq. (2.51) clearly hints towards the importance of Landau damping in preventing the residual entropy. However, different nonlocal models, such as the extended hydrodynamic description, would behave very similar to the local Drude model since the transverse electric reflection coefficient, which determines the entropy at low temperatures, remains unchanged [see Eq. (1.36)]. This poses the question on where to draw the line. In the following we get to the bottom of the apparent conceptual contradiction by analyzing the overdamped modes in the material. It is in fact the exact quantum thermodynamical properties of that very modes that dominate the long-time correlations in the system and hence the behavior of the entropy.

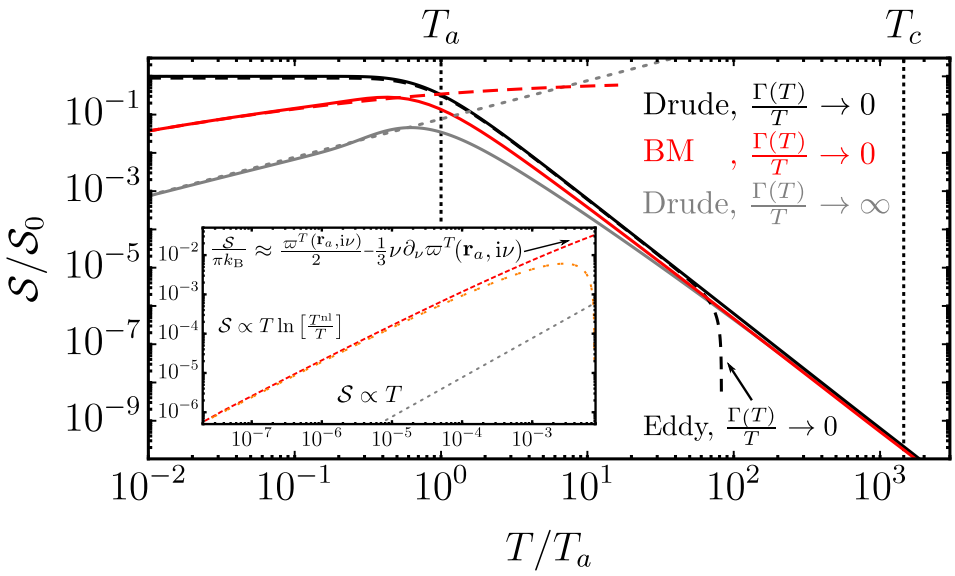

Figure 2.4: Magnetic Casimir-Polder entropy normalized to $\mathcal{S}_0$ [Eq. (2.50)] as a function of temperature with $T_a = \hbar\omega_a/k_{\mathrm{B}}$. We choose $z_a = 1\,\mu$m and parameters as in Fig. 2.3. We depict the cases of a Drude model with constant dissipation rate (gray) and both the Boltzmann-Mermin model (red) and the Drude model (black) with temperature dependent dissipation $\Gamma(T) = \Gamma(T/T_c)^5$ as well as the corresponding asymptotes given by Eq. (2.16) in dashed lines. For temperatures $T \gg T_c = \hbar v_{\mathrm{F}}/(k_{\mathrm{B}} z_a)$, spatial dispersion becomes negligible. We further display the entropy solely connected to the eddy modes in the Drude model (black, dashed). **Inset:** Zoom to the behavior at $T \ll T_a$ and the asymptotics of the nonlocal Boltzmann-Mermin model [Eq. (2.51)] (orange). Adapted from [M3].

2.2.2 Quantum thermodynamics of overdamped modes

The low-temperature entropy is determined by the behavior of the mode density $\varkappa^T(\mathbf{r}_a,\omega)$ at small frequencies. In order to identify the responsible physical mechanism, we to analyze the resonance structure of the transverse electric surface impedance since it plays the central role in the evaluation of $\varkappa^T$. Starting from Eq. (1.28), we can substitute $x = p/k$ and write the impedance as an integral over the nonlocal transverse permittivity ϵ_t,

$$\frac{Z^s(\omega,p)}{Z_0^s(\omega,p)} = -\frac{2}{\pi}\int_0^1 \mathrm{d}x \frac{1}{\sqrt{1-x^2}} \frac{p\sqrt{p^2-\frac{\omega^2}{c^2}}}{\epsilon_t\left(\omega,\frac{p}{x}\right)\frac{\omega^2x^2}{c^2}-p^2} \sim \frac{\sqrt{\frac{\omega^2}{c^2}-p^2}}{\sqrt{\epsilon_t(\omega,p)\frac{\omega^2}{c^2}-p^2}}, \tag{2.52}$$

where we used that the inverse root $1/\sqrt{1-x^2}$ diverges for $x \to 1$. Mathematically, we can now determine the structure of $\varkappa^T$ in the complex plane from the zeros of $\epsilon_t(\omega,p)\frac{\omega^2}{c^2} - p^2$. In the region $|\omega| \sim 0$, we find a logarithmic branch cut parallel to the $\mathrm{Re}[\omega]$-axis from the expression of ϵ_t between the points $\omega_\pm^{\mathrm{L}} = \pm v_{\mathrm{F}}p - \mathrm{i}\Gamma$, where the negative imaginary part is related to causality in time domain. Physically, this branch cut corresponds to an infinite number of infinitely dense modes connected to Landau damping in the material when the phase velocity of the wave matches the Fermi velocity of the quasi-particle excitations in the Fermi liquid, $\omega/p \lesssim v_{\mathrm{F}}$. We note that the branch cut persists even in the limit of $\Gamma \to 0$, where the corresponding modes are sometimes called *van Kampen modes* after one of their first descriptions [258, 405]. Additionally, from the crossing relation, we note that $\epsilon_t(\omega,p)\frac{\omega^2}{c^2} - p^2$ can have purely imaginary roots in the lower half of the complex frequency plane. The corresponding modes are referred to as *overdamped* [M3, 406]. Substituting $\omega = -\mathrm{i}\xi = -\mathrm{i}\Gamma(1-s)$, we find

$$s^3\frac{\lambda\!\!\!^{-2}_{\mathrm{p}}}{\ell^2} + \frac{\Gamma^2}{\omega_{\mathrm{p}}^2}s(1-s)^2y^2 - (1-s)g_t(y)y^2 \stackrel{!}{=} 0, \tag{2.53}$$

where the function g_t is defined in Eq. (1.42), we defined $y = s/(p\ell) > 0$ and we have that $s < 1$ due to causality and $s > 0$ from the branch cut connected to Landau damping. For most metals, we can neglect the term $\propto \Gamma^2/\omega_{\mathrm{p}}^2$ and can solve the resulting cubic equation by considering s and y as independent variables and find the (real) solution

$$s(y) \sim 2y\frac{\ell}{\lambda\!\!\!^{-}_{\mathrm{p}}}\sqrt{\frac{g_t(y)}{3}}\sinh\left(\frac{1}{3}\mathrm{arcsinh}\left[\frac{3}{2x}\frac{\lambda\!\!\!^{-}_{\mathrm{p}}}{\ell}\sqrt{\frac{3}{g_t(y)}}\right]\right). \tag{2.54}$$

Hence, we obtain another branch cut along the negative imaginary axis between the points $\omega = -\mathrm{i}\xi_0^{\mathrm{nl}}$ and $\omega = -\mathrm{i}\Gamma$ prescribed by the parametric solution

$$\xi_0^{\mathrm{nl}}(p) \sim \begin{cases} \Gamma(1-s(x)) \\ p = \frac{s(y)}{y\ell} \end{cases}, \qquad p \leq \frac{1}{\lambda\!\!\!^{-}_{\mathrm{e}}(\ell)} \equiv \frac{1}{\ell}\left[\frac{3\pi}{4}\frac{\ell^2}{\lambda\!\!\!^{-2}_{\mathrm{p}}}\right]^{\frac{1}{3}}. \tag{2.55}$$

We emphasize that the branch point $0 \leq \xi_0^{\mathrm{nl}} \leq \Gamma$ prescribes a finite branch cut only for wavevectors $p \leq 1/\lambda\!\!\!^{-}_{\mathrm{e}}(\ell)$ which we find by setting $\xi_0^{\mathrm{nl}} = \Gamma$. Together, the two branch cuts form an upside-down T-shaped structure (see Fig. 2.5).

To obtain some physical insight, lets consider the local Drude limit of the previous equations. Mathematically, this amounts to neglecting the spatial dispersion in the material's transverse electric permittivity or, equivalently, setting $g_t \to 1$ in Eq. (2.53). In the limit of good conductors ($\Gamma \ll \omega_{\mathrm{p}}$), we then obtain

$$s \sim \frac{1}{1+p^2\lambda\!\!\!^{-2}_{\mathrm{p}}} \to \xi_0^{\mathrm{lc}} \sim \Gamma \frac{p^2\lambda\!\!\!^{-2}_{\mathrm{p}}}{1+p^2\lambda\!\!\!^{-2}_{\mathrm{p}}}. \tag{2.56}$$

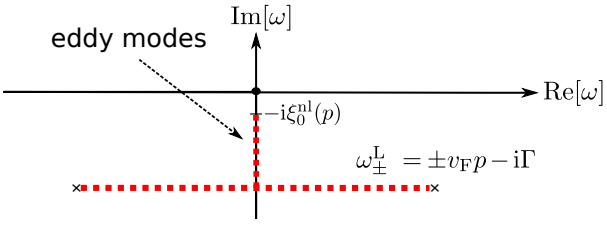

Figure 2.5: Pole structure of the surface impedance [Eq. (2.52)] in the complex frequency plane around $|\omega| \sim 0$. We find two branch cuts related to eddy modes (ξ_0^{nl}) and (dissipative) van Kampen modes ($\omega_{\pm}^{\mathrm{L}}$). Adapted from [M3].

Accordingly, in the local limit, the branch cut related to Landau damping disappears and we obtain an isolated branch cut along the negative imaginary axis between the points $\xi_0^{\mathrm{lc}} \leq \xi \leq \Gamma$. Equation (2.56) formally describes the purely complex solution in Fourier domain to an eigenvalue problem of the form $(\partial_t - \lambda\!\!\!^{-2}_{\mathrm{p}}[\partial_t - \Gamma]\nabla^2)\mathbf{V}(\mathbf{r},t) = 0$ for any vector valued function $\mathbf{V}$. In order to extract the physical meaning of the function $\mathbf{V}$, we recall that the local Drude model leads to Eq. (1.30) for the relation between current and electric field in the bulk material. Since one can show that inside the metal the fields are predominantly magnetic in nature [147, 238], we can combine Eq. (1.30) with Maxwell's equations and find for the magnetic field $\mathbf{B}$ inside a Drude metal the relation

$$\partial_t \mathbf{B}(\mathbf{r},t) = (\lambda\!\!\!^{-2}_{\mathrm{p}}\partial_t + D)\nabla^2\mathbf{B}(\mathbf{r},t) \tag{2.57}$$

with $D = \Gamma\lambda\!\!\!^{-2}_{\mathrm{p}}$ the diffusion coefficient. Indeed, the modes in Eq. (2.56) describe the local dynamics of diffusive magnetic fields. If we further consider the Ohmic limit at low frequencies (late times), we can neglect the partial derivative on the right hand side of Eq. (2.57) and obtain a true diffusion equation $\partial_t \mathbf{B}(\mathbf{r},t) = D\nabla^2\mathbf{B}(\mathbf{r},t)$ for the quasi-static dynamics of the magnetic field in conducting materials. The eigenmodes of such an equation are purely imaginary and hence overdamped. Physically, the corresponding modes $\xi_0^{\mathrm{lc}} \sim Dp^2$ represent the so-called *eddy modes* [147, 237–239]. Eddy modes, or currents, appear in conductors under the influence of slowly varying magnetic fields and have been found to be responsible for the residual entropy in the plane-plane Casimir configuration at zero temperature using the perfect crystal description [227, 324] (see also Refs. [407–409]). In fact, we can show that very same behavior also for the magnetic Casimir-Polder setup [M3, 180]. To this end, we expand the poles of the Green tensor by means of the Mittag-Leffler theorem [162] which associates a Lorentzian spectrum centered at zero frequency to every overdamped mode $\omega = -\mathrm{i}\xi$. Such an expansion enables us to isolate the contribution to the differential mode density $\varkappa^T$ stemming solely from eddy modes [M3]

$$\varkappa^T_{\mathrm{eddy}}(\mathbf{r}_a,\omega) = \partial_\omega \int_0^\Gamma \frac{\mathrm{d}\xi}{\pi} \frac{\omega}{\omega^2+\xi^2} \mathrm{Im}\varpi^T(\mathbf{r}_a, -\mathrm{i}\xi + 0^+). \tag{2.58}$$

Interestingly, upon inserting the expressions for the Green tensor and the permittivity of the Drude model with temperature-dependent dissipation rate $\Gamma = \Gamma(T)$, we have shown in earlier work [180] that the mode density of the complete system is solely determined by the eddy modes, i.e. $\varkappa^T(\mathbf{r},\omega) \sim \varkappa^T_{\mathrm{eddy}}(\mathbf{r}_a,\omega)$ in the limit $\omega \to 0$. As one could now expect, upon replacing $\varkappa^T \to \varkappa^T_{\mathrm{eddy}}$ in Eq. (2.16), the low-temperature entropy is given by the corresponding entropy associated with the eddy currents $\mathcal{S}_{\mathrm{eddy}}$ which identifies the eddy modes as being responsible for the residual entropy. We report a numerical evaluation of $\mathcal{S}_{\mathrm{eddy}}$ in Fig. 2.4 and refer to Refs. [M3, 180] for the mathematical details. For our purposes, we note that the eddy mode's mode density at zero frequency $\varkappa^T_{\mathrm{eddy}}(\mathbf{r}_a,0) \sim \Phi^T(0)/(Dz_a)$ diverges in the limit $\Gamma \to 0$. Focusing on the thermodynamic implications of a non-vanishing entropy, we can interpret Eq. (2.56) as an energy scale needed for exciting the dispersive eddy modes

$$E^{\mathrm{lc}} \equiv \hbar\nu^{\mathrm{lc}} \sim \frac{D}{z_a^2}, \tag{2.59}$$

where we used the relation $p \sim z_a^{-1}$ and approximated $z_a \gg \lambda\!\!\!^{-}_{\mathrm{p}}$. Comparing to the thermal energy $k_{\mathrm{B}}T \gg E^{\mathrm{lc}}$, we find that the eddy modes are *always thermally excited* in the limit $T \to 0$ if $\Gamma(T)/T \to 0$ [227, 324]. To some extend the system behaves classically even at zero temperature which can be seen from estimating the free energy associated with eddy modes

$$\begin{aligned}\mathcal{F}_{\mathrm{eddy}} &= k_{\mathrm{B}}T \int_0^\infty \mathrm{d}\omega\ \ln 2\sinh\left[\frac{\hbar\omega}{2k_{\mathrm{B}}T}\right] \varkappa^T_{\mathrm{eddy}}(\mathbf{r}_a,\omega) \\ &\sim -k_{\mathrm{B}}T \int_0^{\nu^{\mathrm{lc}}} \frac{\mathrm{d}\omega}{\omega} \int_0^\omega \mathrm{d}\tilde{\omega}\ \varkappa^T_{\mathrm{eddy}}(\mathrm{r}_a,\tilde{\omega}) \overset{T\to 0}{\to} -k_{\mathrm{B}}TN^{\mathrm{lc}}.\end{aligned} \tag{2.60}$$

When we consider the perfect crystal model in combination with the local Drude description, the free energy of the setup behaves as a classical gas of $N^{\mathrm{lc}} = \varkappa^T_{\mathrm{eddy}}(\mathbf{r}_a,0)\nu^{\mathrm{lc}}$ particles (classical oscillators) in the limit of vanishing temperature [410, 411]. The corresponding entropy hence remains constant and is given by the number of modes N^{lc} participating in the interaction. The residual entropy effectively decouples from the interaction with the field and is completely described by the eddy modes inside the bulk material. Even at zero temperature, the number of (differential) modes N^{lc} remains finite which, mathematically, can be related to a finite-sized branch cut of the differential mode density for all values of ξ/Γ (see right panel of Fig. 2.6). In summary, the peculiar behavior of the entropy can be explained with the finite-temperature disorder of eddy modes in the material that is frozen down onto the ground state of the system[13].

Now, since the relation for the local eddy modes was obtained by enforcing the local limit on Eq. (2.53), the flaw leading to the residual entropy is apparent. Assuming a local response for low temperatures is artificial and we instead need to consider the nonlocal limit of Eq. (2.53). Using that the function $g_t(y) \sim 3\pi|y|/4$ for $y \ll 1$, we obtain in the good conductor limit ($\lambda\!\!\!^{-}_{\mathrm{p}} \ll \ell$) of the spatially nonlocal material ($v_{\mathrm{F}}/c \gg \Gamma/\omega_{\mathrm{p}}$)

$$\xi_0^{\mathrm{nl}}(p) \sim \Gamma_t^{\mathrm{L}}(p)p^2\lambda\!\!\!^{-2}_{\mathrm{p}}, \qquad\qquad p \leq \frac{1}{\lambda\!\!\!^{-}_{\mathrm{e}}(\ell)}. \tag{2.61}$$

[13] Such a behavior is reminiscent of glassy systems [227, 324].

Remarkable, Landau damping takes over the role of collision-induced damping and we can, in similarity to the local consideration using that $p \sim z_a^{-1}$, define the energy scale

$$E^{\mathrm{nl}} \equiv \hbar\nu^{\mathrm{nl}} \sim \hbar\lambda\!\!\!^{-}_{\mathrm{p}}^2 \Gamma_t^{\mathrm{L}}(z_a^{-1}) = \frac{4}{3\pi}\frac{\hbar v_{\mathrm{F}} \lambda\!\!\!^{-}_{\mathrm{p}}^2}{z_a^3}, \qquad z_a > \lambda\!\!\!^{-}_e. \tag{2.62}$$

In contrast to Eq. (2.59), the energy associated to eddy currents in the nonlocal description assumes a temperature-independent value such that one can achieve the case $k_{\mathrm{B}}T \ll E^{\mathrm{nl}}$. Repeating our analysis of the free energy, we can still connect $\mathcal{F}_{\mathrm{eddy}} \sim -k_{\mathrm{B}}TN^{\mathrm{nl}}$ to a number of $N^{\mathrm{nl}} = \varkappa^T_{\mathrm{eddy}}(\mathbf{r}_a, 0)\nu^{\mathrm{nl}}$ classical oscillators. However, in the nonlocal description, their number is suppressed with decreasing temperature by the condition $p \lesssim \lambda\!\!\!^{-}_{\mathrm{e}}^{-1} \propto \ell^{1/3}(T)$. Mathematically, this leads to a shrinking branch cut at the negative imaginary axis connected to eddy modes in the nonlocal description that eventually disappears in the limit $T \to 0$ (see right panel of Fig. 2.6). Physically, the eddy modes are frozen out or disappear due to the Fermi-Dirac distribution dictating the underlying distribution of the Fermi-liquid. Even though the Landau dissipation rate appears in Eq. (2.62), it is eventually the concrete statistics of the quasi-particles in the bulk that determines the ultimate functional behavior. In our case, Nernst theorem is fulfilled in the nonlocal description not by the inclusion of Landau damping per se, but the fundamental quantum nature of the Fermi-Dirac statistics. Of course, the latter is represented in the former.

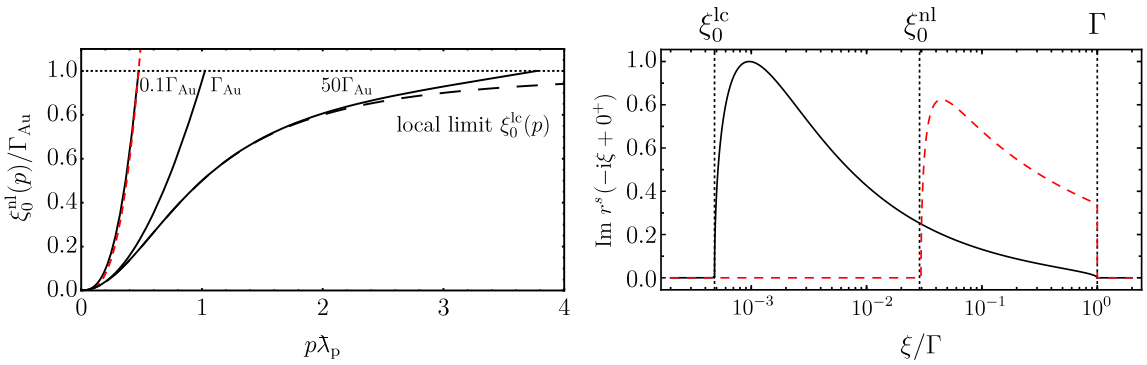

Figure 2.6: Left: Parametric solution for the nonlocal eddy modes ξ_0^{nl} [Eq. (2.55)] normalized to the dissipation rate of gold Γ_{Au} as a function of the wavevector p. We use parameters as in Fig. 2.3 and display the results for different values of collision-induced damping (solid, black), the local Drude limit (dashed, black) and the nonlocal asymptote of Eq. (2.61) (dashed, red). **Right:** Imaginary part of the transverse electric reflection coefficient at imaginary frequencies $\omega = \mathrm{i}\xi + 0^+$. We report the behavior close to the branch cut (see Fig. 2.5) using the local Drude model (solid, black) and the nonlocal Boltzmann-Mermin model (dashed, red). We report the values of the branch points of Eqs. (2.56) and (2.61). We set $\Gamma = 10^{-5}\,\mathrm{eV}$ and $p = 1/\mu\mathrm{m}$ ($\lambda\!\!\!^{-}_{\mathrm{e}}^{-1} \approx 3/\mu\mathrm{m}$) in order to resolve the difference between the local and the nonlocal regime: For decreasing dissipation rate Γ, the branch cut associated to the nonlocal model disappears, while the local version always remains finite in size (see main text). Adapted from [M3].

Statistics of a single overdamped mode

The previous results are extraordinary in the sense that the behavior of the magnetic Casimir-Polder interaction, which can be considered as a wide-range frequency phenomenon, can be explained in the limit of small temperatures solely by means of overdamped modes. To see this more clearly, we consider finally the thermodynamics of a single overdamped mode ξ. For constant ξ, the free energy $\mathcal{F}_\xi$ can usually be separated by means of Eq. (2.3) into a sum of the vacuum $\mathcal{E}_\xi$ and thermal contribution $\Delta\mathcal{F}_\xi$. As in the case of an harmonic oscillator [410–412], the expression

$$\mathcal{E}_\xi = \frac{1}{\pi}\int_0^{\Lambda\to\infty} \mathrm{d}\omega\ \frac{\hbar\omega}{2}\frac{\xi}{\xi^2+\omega^2} \sim \hbar\xi \ln\frac{\Lambda}{\xi} \tag{2.63}$$

diverges and needs regularization using the cut-off frequency Λ. The thermal contribution, on the other hand, reads

$$\Delta\mathcal{F}_\xi = \frac{k_\mathrm{B}T}{\pi}\int_0^\infty \mathrm{d}\omega\ \ln\left[1-e^{-\frac{\hbar\omega}{k_\mathrm{B}T}}\right]\frac{\xi}{\xi^2+\omega^2} \to -\frac{\pi k_\mathrm{B}^2T^2}{6\hbar\xi}, \qquad T\to 0. \tag{2.64}$$

Given the free energy, we obtain the partition function in equilibrium from $Z=\exp[-\mathcal{F}_\xi/(k_\mathrm{B}T)]$ which allows us access to the energy density of states $\rho_\mathrm{dos}(E)$ via the Laplace transform $Z=\int_0^\infty \mathrm{d}E\rho_\mathrm{dos}(E)\exp[-E/(k_\mathrm{B}T)]$ [169]. Following Ref. [166], we find that the system has a unique ground state at $E=\mathcal{E}_\xi$ that is followed by a continuous spectrum of states,

$$\rho_\mathrm{dos}(E) = \delta(E-\mathcal{E}_\xi) + \Delta\rho(E-\mathcal{E}_\xi)\theta(E-\mathcal{E}_\xi), \tag{2.65}$$

where the function $\Delta\rho(x)\to\pi/(6\hbar\xi)$ for $x\to 0$. Consequently, the entropy vanishes at $T=0$.

The situation considerably changes if we consider the overdamped mode to be depending on temperature $\xi=\xi(T)$ in a way that $\xi/T\to 0$ for $T\to 0$. We now have

$$\Delta\mathcal{F}_\xi \to -\frac{k_\mathrm{B}T}{2}\ln\left[\frac{k_\mathrm{B}T}{\hbar\xi}\right], \qquad T\to 0. \tag{2.66}$$

Moreover, both $\mathcal{E}_\xi$ and $\Delta\mathcal{F}_\xi$ become temperature dependent and the distinction of Eqs. (2.63) and (2.64) becomes meaningless. Instead, for vanishing temperatures, we have $\Delta\mathcal{F}_\xi \gg \mathcal{E}_\xi$ and the partition function takes the form $Z\sim\sqrt{k_\mathrm{B}T/(\hbar\xi)}$, rather resembling the behavior of a free particle trapped in a box [410, 411]. In the limit $T\to 0$, the partition function $Z\sim L/\lambda_\mathrm{dB}\to\infty$ diverges as the "size" $L\propto\sqrt{\hbar/\xi}$ of the oscillator is much larger than the thermal de Broglie wavelength $\lambda_\mathrm{dB}\propto\sqrt{\hbar^2/(k_\mathrm{B}T)}$. From the theoretical perspective, quantum corrections need to be included in such a regime, which is exactly what the Drude model (resembling the classical oscillator) missed in contrast to the Boltzmann-Mermin model in our considerations of the Casimir-Polder entropy.

If we specify to the case of eddy modes inside the metal, $\xi = x\Gamma(T)$, and perform a common shift for the energy of all modes by the factor $(\hbar\Gamma/[k_\mathrm{B}T])^{1/2}$, the relevant partition function and the corresponding energy density of states can be written, respectively, as

$$\tilde{Z} \sim \left[\frac{1}{x}\right]^{\frac{1}{2}}, \qquad \tilde{\rho}_\mathrm{dos}(E) \sim \left[\frac{1}{x}\right]^{\frac{1}{2}} \delta(E). \tag{2.67}$$

Noteworthy, we obtain a ground state with degeneracy $x^{-1/2}$. In other words, the Drude model in combination with the perfect crystal description induces a situation that resembles a degenerate ground state for the differential Casimir-Polder entropy. The particular degeneracy varies from mode to mode as a function of ξ and the particular contribution to the magnetic Casimir-Polder entropy derives from a sum over all available modes. The inclusion of spatial nonlocality in terms of the Fermi-Dirac statistics, in contrast, manages to effectively reduce the number of available states with shrinking temperature leading to a unique ground state. Lastly, we note that the value of the differential degeneracy $\exp[-\mathcal{S}_0/k_\mathrm{B}]$ turns out to be distance-dependent, because the spectral mode density differs between the interacting and the noninteracting situation [M3]. We depict the situation in Fig. 2.7.

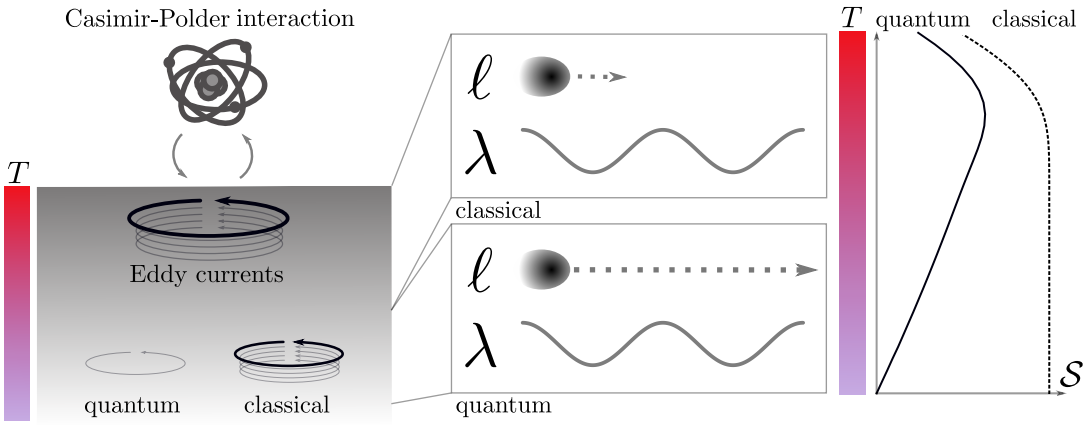

Figure 2.7: Schematic visualization of the magnetic Casimir-Polder entropy in the limit of vanishing temperatures T. For decreasing temperatures, the mean free path ℓ of the bulk electrons becomes comparable to the wavelength λ dominating the interaction. In this limit, quantum effects connected to nonlocality reduce the number of eddy modes, which dominate the behavior of the entropy causing it to vanish. Artificially forcing the system to remain in the local regime, however, leaves a macroscopic number of classically behaving eddy modes even in the ground state which yields a finite entropy at $T = 0$.

2.3 Summary

In the present Chapter, we discussed the equilibrium Casimir-Polder interaction between a neutral atom and the material-modified vacuum originating from an interface at distance z_a. Considering the example of a semi-infinite half space made from a conducting material, we recovered the van der Waals limit ($\propto z_a^{-3}$) and the Casimir-Polder limit (z_a^{-4}) for local material models and at zero temperature. We further introduced a linear atomic model and discussed the impact of spatial dispersion. We found the electric zero-temperature force experienced by the atom to be dominated by large ($\sim$ resonance) frequencies in the mode density. For this simple setup, the low-frequency fluctuations are only of minor quantitative importance. However, this is turned around when temperature corrections or the limiting behavior of thermodynamic quantities such as the entropy is considered.

We discussed the first temperature correction to the electric Casimir-Polder force between an atom and a sphere of radius R. For temperatures much smaller than the temperature corresponding to the dominant atomic dipole transition, the first correction to the zero-temperature result is very sensitive to the specifics of the sphere's material and the origin of dissipation in the interaction. When the sphere is made from an Ohmic dissipative material, we find that the leading order correction scales quadratic in the temperature T and linear in the respective dissipation ρ. In contrast, when the sphere is made from a non-dissipative dielectric, such as an intrinsic semiconductor, the only possible mechanism of dissipation is connected to scattering of electromagnetic waves at the surface of the sphere and the simple asymptotes known from dissipative materials fail. For this situation, we developed a refined technique based on a Padé expansion of the sphere's (Mie) scattering coefficients and obtained that the temperature correction to the free energy scales in fourth order of T while replacing $\rho \to c\hbar/z_a$. There lies some potential in not only tayloring these forces, but high precision measurements could also be used to distinguish between more and less suitable material models.

From the fundamental side, we considered the behavior of the *magnetic* Casimir-Polder entropy in the limit of vanishing temperatures and addressed an issue connected to Nernst theorem (entropy vanishes at zero temperature) that was discussed in the literature recently. Depending on the chosen material model and the characteristics of the assumptions on the bulk lattice (perfect crystal), one can observe a residual finite entropy at $T = 0$ contradicting Nernst theorem when the material response is enforced to behave spatially local (Drude model). However, if we choose a particular nonlocal model that respects the quantum characteristics of the Fermi-Dirac statistics of bulk electrons at low temperatures, the entropy shows a more regular behavior and does indeed vanish. Relating these observations with overdamped low-frequency excitations in the metal, the so-called eddy modes, we performed a quantum statistical analysis of their behavior in the respective models. We find that the (differential) entropy of the system at finite temperature is determined by a number of eddy modes behaving in their statistics as classical particles. In the limit of vanishing temperatures, the proper quantum description of the material reduces the number of modes participating in the interaction leading to a non-degenerate ground state and a vanishing entropy. The local model, on the other hand, fails to do so and the high-temperature disorder is "frozen down" onto the now degenerate ground state. In this way, we provide the underlying physical basis for interpreting a number of related observations. For instance, in Ref. [413], it was found that the local Drude and its dissipation-

less counterpart, the plasma model, yield different results in the limit of a diverging plasma frequency, where actually the unique limit of a perfect conductor should be recovered. This apparent mismatch is very likely to be understood by the tools we developed. Moreover, we could show that the complex dynamics of the magnetic Casimir-Polder entropy, which shows many different degrees of freedom and distinct resonances, can be explained by a careful scrutiny of the long-time correlations between system and environment.

CHAPTER 3

Mechanical Nonequilibrium

We generalize our discussion of equilibrium fluctuation-induced phenomena to a particle in motion with respect to a macroscopic ensemble of objects. Moving along the direction of translational invariance of the environment, the system can reach a nonequilibrium steady-state. We find a statistically self-consistent description for the dynamics of the particle's internal degrees of freedom in the nonequilibrium steady-state. The resulting polarizability of the particle is dressed by both the electromagnetic field *and* the internal degrees of freedom. Based on that model, we study the velocity corrections to the Casimir-Polder force and the quantum frictional force emerging from nonequilibrium. The latter turns out to be highly sensitive to long-time correlations in the system. The present chapter contains work by the author that has been published in Ref. [M1, M2, M4, M5] or is about to be published [P2, P3].

In the present Chapter we aim to advance the previous discussions of atom-field interactions to the situation of mechanical nonequilibrium, where the particle is moving with respect to the rest frame of the material-modified vacuum. In contrast to the equilibrium case, where the textbook formalism of statistical mechanics applies and we can rely on the powerful fluctuation-dissipation-relation [32, 66, 169, 176], the treatment of fluctuations in nonequilibrium quantum systems is highly non-trivial [106, 108] and an active field of research with ever growing interest [414–417]. One strong branch of this research works in the direction of so-called fluctuation theorems. Originally derived for classical systems by, e.g., Jarzynski [104], Crooks [418] or Hatano and Sasa [419], they were quickly extended to the quantum realm [420–425]. In short, fluctuation theorems relate the probability of observing a certain amount of work, heat or particle number to the same experiment performed in the opposite time-direction; thereby measuring the violation of time-reversal symmetry [417]. By construction, such theorems can be valid for systems driven arbitrarily far from equilibrium, but need a well-defined initial as well as final state of the system. Similar relations have been studied for nonequilibrium steady states, where the initial state plays a subordinate role and the final state of the full system is not in equilibrium, first for the classical case [419, 426, 427] and later for the (Markovian [428]) quantum case [429]. The fluctuation theorems cover a wide range of systems and provide a deep insight into the general statistical properties of nonequilibrium quantum systems. In the particular case of a concrete physical system, however, it might also be insightful to determine the statistical distribution, i.e. the Wigner function [430], or solve the proper equations of motion in order to obtain knowledge about forces, currents or the dynamics of the system. For the former, we refer to Ref. [50] for the Hu-Paz-Zhang master equation[1] describing linear oscillator systems including dissipation, dispersion and non-Markovianity.

[1] A formal solution of the can be found in Refs. [431, 432] and, e.g, Ref. [433] gives a recent application.

A commonly used approach to model the equations of motion for a stochastically driven quantum system employs the formalism of Langevin equations [155] and will be the method of choice for our purposes. Modeling fluctuation-induced interactions using a stochastically driven (Langevin) equation has been quite successful in physics and chemistry, see e.g. Refs. [135, 157–159, 162, 307, 351, 411] and Refs. [343, 344], respectively. The corresponding equations of motion find their rigorous justification in Hamiltonian dynamics [155, 162, 434] or, equivalently, the influence functional formalism [106, 346, 353, 435] by applying consecutive coarse-graining procedures [42, 436, 437]. Discussing the equation of motion for a concrete system allows us to avoid many technicalities that come with more general approaches. In this way, our approach circumvents the construction of fluctuation theorems by a less general but more flexible approach[2]: We construct the equations of motion for the moving particle's internal degrees of freedom and solve them exactly for long times, i.e. when the system reaches a steady-state. Throughout we exploit the weakness of fluctuation-induced interactions such that we can concentrate on the linear regime (see Chapter 1). The obtained solutions for the particle's internal degrees of freedom are then used to construct the correlation matrices explicitly.

In the following, we generalize the linear quantum stochastic differential equation in equilibrium [Eq. (2.19)] to the nonequilibrium situation in Sec. 3.1. To the best of our knowledge, such an approach has been first employed by Intravaia *et al.* in 2016 for the interaction of an atom with the material-modified vacuum [53] and was recently extended to the possibility of including also internal degrees of freedom for the particle by the author, Busch and Intravaia in 2020 [M2]. We develop our model and comment on the tensorial structure of the particle's power spectrum in Sec. 3.2. After that, we discuss in detail the resulting velocity-corrections to the Casimir-Polder interaction (Section 3.3) as well as the quantum frictional force emerging from the nonequilibrium situation (Section 3.4); always putting the main focus on the long-time correlations between separated subsystems. We conclude with a summary in Sec. 3.5.

[2] In this way, the present Chapter serves as an extensive exemplary playground for studying the situation of nonequilibrium. In the next Chapter 4 we put our findings on a thermodynamic basis and briefly touch the theory of fluctuations in nonequilibrium by means of the fluctuation-dissipation inequality [422].

3.1 Open system dynamics of a polarizable particle

We consider an atom moving with non-relativistic velocity v in the direction along the translational symmetry axis of an ensemble of macroscopic objects. Without loss of generality, we further assume it to coincide with the x-axis. The remaining axes of the coordinate system are chosen accordingly, see Fig. 3.1. Later in this Chapter, we will specify the general geometry to a planar interface, a planar cavity and a cylindrical cavity. The bodies surrounding the atom are supposed to be comprised of a linear, spatially homogeneous and non-magnetic material (see Chapter 1). We focus on the *electric* fluctuation-induced interaction between the atomic dipole moment $\hat{\mathbf{d}}$ and the material-modified electric field $\hat{\mathbf{E}}$. Further, we are interested in atom-surface separations in the nano- to micrometer regime where the formalism of macroscopic quantum electrodynamics applies and demand that the atom's center of mass approximately obeys a classical trajectory. This implicitly includes the existence of an external *agent* driving the atom in such a way as to maintain uniform motion. To this end, we assume that the back-action of our total system, composed of the particle and the material-modified vacuum field, on the agent is sufficiently small compared to the force that the agent exerts on the system to keep the atom moving at uniform velocity. Thus, we can safely consider the inflow of energy to the moving particle from the agent and the outflow of energy from the particle to the field modified by the material. The back-action of the material-modified vacuum field on the particle, appearing as dynamical corrections to the Casimir-Polder force (see Section 3.3) as well as a nonequilibrium drag force counteracting the motion, so-called quantum friction (see Section 3.4), is of course included. It will be the main focus of our investigation. Due to dissipation, the system possesses a typical memory time τ_{c} characterizing the maximum duration at which temporal correlations are still relevant. At times much larger than τ_{c}, we assume that the particle's center of mass obeys the trajectory

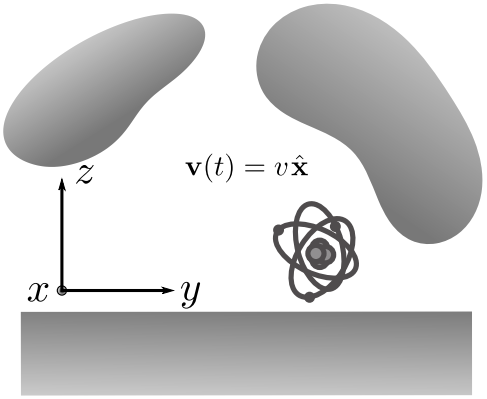

Figure 3.1: A microscopic particle, say, an atom, moves with velocity v along the direction of invariance of an ensemble of macroscopic bodies.

$$\mathbf{r}_{\mathrm{a}}(t) = \mathbf{R}_{\mathrm{a}} + x_a(t)\mathbf{x} \sim \mathbf{R}_{\mathrm{a}} + (x_a + vt)\mathbf{x}, \qquad t \gg \tau_{\mathrm{c}}, \tag{3.1}$$

where $\mathbf{R}_{\mathrm{a}}$ is the transversal position of the particle with respect to the closest surface, x_a some constant position along the x-axis and $\mathbf{x}$ the unit vector in x direction (see Fig. 3.1). We briefly comment on that the range of validity of this assumption at the end of the Chapter (see Sec. 3.5). Finally, we assume zero temperature and that the initial states of the atom and the bulk were factorized in the distant past at time t_i, i.e.

$$\hat{\rho}(t_i) = \hat{\rho}_{\mathrm{f+m}}(t_i) \otimes \hat{\rho}_{\mathrm{a}}(t_i), \tag{3.2}$$

where $\hat{\rho}_{\mathrm{f+m}}$ is the density matrix of the field+matter mixture and $\hat{\rho}_{\mathrm{a}}$ the density matrix of the particle. Even though this means that the global system is not in equilibrium at the initial

time of the experiment, the respective subsystems are: At zero temperature, both the particle and the material-modified vacuum field are in their respective ground states. The factorization of the system's initial state is a mere technical simplification an can be extended to entangled states. We refer the reader, e.g., to Ref. [353] for a discussion on non-factorizing initial states. For our purposes, however, since we are interested in the late-time dynamics of a dispersive open quantum system, the exact choice of the initial conditions is of technical nature only, as long as the system can reach a nonequilibrium steady-state. Similarly, the exact acceleration protocol leading to the uniform motion of the atom represents a transient not affecting the steady-state properties [44].
Based on the fundamental solutions of Maxwell's equations presented in Chapter 1, we can write the electric field operator in linear response for a time-dependent particle trajectory and passive systems as [53, 58, P3]

$$\begin{aligned}\hat{\mathbf{E}}(\mathbf{r}_a(t),t) &= \hat{\mathbf{E}}_{\mathrm{N}}(\mathbf{r}_a(t),t) + \hat{\mathbf{E}}_{\mathrm{in}}(\mathbf{r}_a(t),t) \\ &= \hat{\mathbf{E}}_{\mathrm{N}}(\mathbf{r}_a(t),t) + \int_{t_i}^{t} \mathrm{d}t'\; \underline{G}(\mathbf{r}_a(t),\mathbf{r}_a(t'),t-t')\hat{\mathbf{d}}(t') \\ &= \hat{\mathbf{E}}_{\mathrm{N}}(\mathbf{r}_a(t),t) + 2\mathrm{i}\int_0^{t-t_i} \mathrm{d}\tau \int \frac{\mathrm{d}\omega}{2\pi}\int \frac{\mathrm{d}h}{2\pi}\; \underline{G}_{\Im}(h,\mathbf{R}_a,\omega)\hat{\mathbf{d}}(t-\tau)e^{\mathrm{i}[x_a(t)-x_a(t-\tau)]h-\mathrm{i}\omega\tau},\end{aligned} \tag{3.3}$$

where we used the homogeneity of the vacuum to write $\underline{G}(\mathbf{r},\mathbf{r}',t) = \underline{G}(\mathbf{r}-\mathbf{r}',t)$, employed Eq. (A2) of the appendix in Ref. [58], defined $\underline{G}_{\Im} = (\underline{G}-\underline{G}^{\dagger})/(2\mathrm{i})$ and performed a spatial Fourier transform in direction of motion with h the parallel wavevector along the x axis. Here, assuming that the Fourier transform exists [see discussion below Eq. (3.11)], we use the conventions

$$\underline{G}(\mathbf{r}_a(t),\mathbf{r}_a(t'),t) = \int \frac{\mathrm{d}\omega}{2\pi}\int \frac{\mathrm{d}h}{2\pi}\; \underline{G}(h,\mathbf{R}_a,\omega)e^{\mathrm{i}([x_a(t)-x_a(t')]h-\omega t)}, \tag{3.4a}$$

$$\hat{\mathbf{E}}_{\mathrm{N}}(\mathbf{r}_a(t),t) = \int_0^{\infty} \frac{\mathrm{d}\omega}{2\pi}\int \frac{\mathrm{d}h}{2\pi}\hat{\mathbf{E}}_{\mathrm{N}}(h,\mathbf{R}_a,\omega)e^{\mathrm{i}(x_a(t)h-\omega t)} + H.c. \tag{3.4b}$$

with $H.c.$ the Hermitian conjugate. It is important to notice that the complete time-dependence of the particle's trajectory is moved to the complex exponential. Hence, under the integral, the operators formally coincide with their equilibrium counterparts for given frequency and wavevector. The impact of nonequilibrium enters the equations by an involved convolution describing the exact time-evolution. As we will see in the present and the following Chapter, this will be a major prerequisite for the existence of the nonequilibrium steady-state and allows us to solve the system exactly at late times. Eventually, we can even derive a detailed balance for the power flow in and out of the atomic subsystem in the steady-state based on that previous relations (see Chapter 4). The decomposition of Eqs. (3.3) and (3.4) hence represents one important pillar of our formalism. We provide a summary of the underlying assumptions on our model for the particle's intrinsic degrees of freedom in Fig. 3.2.

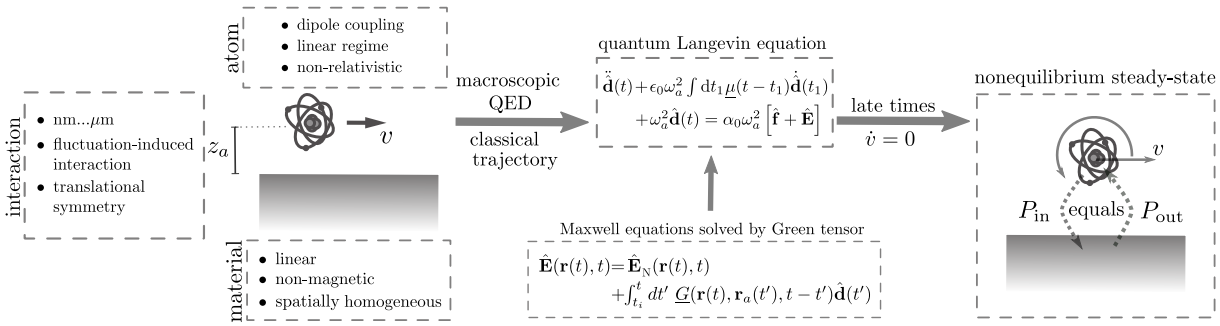

Figure 3.2: Overview of the different approximations and assumptions we make in order to describe an atom moving along the direction of invariance of macroscopic material bodies. In the nonequilibrium steady-state, we record a balance between the incoming P_{in} and the outgoing power P_{out} in the atomic subsystem (see Chap. 4).

From the perspective of the moving particle, we can distinguish two different physical damping mechanisms: *Intrinsic* dissipation, arising from a large number of degrees of freedom inside the particle itself, and *radiation-induced* damping which originates from the interaction with the (quantized) electromagnetic field. For instance, in the case of a dielectric sphere, we have already seen this subdivision in Eq. (2.34) of Section 2.1.3. In contrast to previous approaches modeling the particle dynamics (see e.g. Refs. [43, 105]), we aim to describe the different fluctuation and dissipation mechanisms on the same footing and model the particle's internal structure in terms of an isotropic three-dimensional Drude-Lorentz oscillator. In this way, the particle's electric dipole moment interacts with both the electromagnetic field *and* with a bath accounting for internal losses. As explained earlier, instead of diagonalizing a (very) large Hamiltonian, we focus on the equation of motion for the particle's dipole moment in the Heisenberg picture [74] in combination with linear response theory [32]. The dipole operator then obeys the evolution [M2]

$$\ddot{\hat{\mathbf{d}}}(t)+\epsilon_0\omega_a^2\int \mathrm{d}t_1\;\underline{\mu}(t-t_1)\dot{\hat{\mathbf{d}}}(t_1)+\omega_a^2\hat{\mathbf{d}}(t)=\alpha_0\omega_a^2\left[\hat{\mathbf{f}}(t)+\hat{\mathbf{E}}(\mathbf{r}_a(t),t)\right], \tag{3.5}$$

where $\mathbf{r}_a(t)$ is the particle's trajectory, ω_a its internal electronic transition frequency and α_0 its static polarizability. If we, for the time being, disregard the electric field $\hat{\mathbf{E}}$, Eq. (3.5) represents the three-dimensional generalization of the quantum Langevin equation that previously appeared in the literature [155, 345]. $\hat{\mathbf{f}}(t)$ is the bath's Langevin force operator connected to the internal dissipation and describes the free evolution of the particle's internal dissipative degrees of freedom. The response kernel $\underline{\mu}$, on the other hand, is stationary and in linear response given by (see Chap. 1) [171]

$$\underline{\mu}(\tau)=\frac{\mathrm{i}}{\hbar}\theta(\tau)\left\langle\left[\hat{\mathbf{f}}(\tau),\hat{\mathbf{f}}(0)\right]\right\rangle, \tag{3.6}$$

where the quantum average is taken over the state in Eq. (3.2). In solid state theory, the previous expression becomes exact if the particle's dissipative degrees of freedom are modeled as a superposition of bosonic operators such as coupled harmonic oscillators, a relatively common

approach to dissipation in the linear regime [155, 438]. Note that the functional form of the memory kernel ensures causality and the proper boundaries for the integral in Eq. (3.5). Both quantities, the memory kernel and the internal Langevin force, are related via the fluctuation-dissipation theorem in Fourier domain, i.e. [32, 176]

$$\langle \hat{\mathbf{f}}(\omega)\hat{\mathbf{f}}(\omega')\rangle = 4\pi\hbar\,\theta(\omega)\,\alpha_0^{-1}\epsilon_0\omega\,\underline{\mu}_{\Re}(\omega)\delta(\omega+\omega') \tag{3.7}$$

with $\underline{\mu}_{\Re} = [\underline{\mu} + \underline{\mu}^{\dagger}]/2$ and, as a reminder, $\theta(\omega)$ the Heaviside step function. Technically, $\underline{\mu}$ is a response function [195] and can be rather involved depending on the energy spectrum of the parameters governing the particle's dissipative internal dynamics. However, its form is strictly constrained by thermodynamics considerations [155] demanding that $\underline{\mu}_{\Re}$ is positive semi-definite, $\mathrm{Det}[\underline{\mu}(\omega)]$ must have poles in lower part of the complex-frequency plane and, for an Ohmic internal dissipation mechanism, must tend to a symmetric real tensor in the limit $\omega \to 0$. This last characteristic is different in case of sub- or super-Ohmic dissipation, which can arise in case the frequency spectrum of the internal degrees of freedom is not sufficiently flat; see for example Ref. [439] for an application of such concepts. We note that, despite the oscillator has a scalar (isotropic) coupling α_0, we allow for an anisotropic internal dissipation through the tensorial form of $\underline{\mu}$. We will employ this property explicitly in Section 3.4.3. Also, the three-dimensional structure of Eq. (3.5) allows the particle – or to be precise, the dipole orientation connected to the modulus of the vector components of the dipole operator in position space – to rotate and, therefore, to absorb or emit angular momentum [45, M1, 440]. We will discuss this in more detail in Section 3.2. The total electric field $\hat{\mathbf{E}}$ in Eq. (3.5) results from the sum of the fluctuating field in absence of the particle ($\hat{\mathbf{E}}_{\mathrm{N}}$) and of an induced field that is generated by the dipole operator and back-scattered from the surfaces ($\hat{\mathbf{E}}_{\mathrm{in}}$); see Chapter 1. It is further reasonable to assume the statistical independence of the dissipative mechanisms and require that $\langle \hat{\mathbf{E}}_{\mathrm{N}}(\mathbf{r},t)\hat{\mathbf{f}}(t)\rangle = 0$. Such an assumption describes a wide range of systems including, to the best of our knowledge, most of the previous works on fluctuation-induced phenomena in mechanical nonequilibrium. However, in some circumstances, for instance when the internal degrees of freedom carry some charge, the statistical independence of noise terms might be violated [M2].

Before proceeding, some comments on the range of applicability of our model are in order. Our model is based on the powerful tool of linear response theory. Focusing on the particle's internal degrees of freedom first, the relevant information about the system's specifics is here encoded in the memory kernel and, in general, we are taking non-Markovianity, anisotropy as well as spatial and temporal nonlocality into account. The particles response in terms of the memory kernel can feature a complex resonance structure determined by its thermalization and dissipation properties, as long as the general properties of causality, passivity and reality in time domain are respected [see discussion below Eq. (3.6)]. Given the possibility of including both external and internal degrees of freedom in the dynamics of the particle, our model allows to describe microscopic systems such as molecules [441], NV centers in nanodiamonds [30, 442, 443], and nanoparticles [444], where the impact of internal degrees of freedom on their quantum dynamics can be significant in regard of their dissipative characteristics. For instance, we are thinking about vibrations or deformations within matrix-embedding defects (e.g. NV centers) or the interaction with other impurities in the system [445], or electron-electron or electron-

phonon scattering mechanisms in metallic nanoparticles [402, 446], or ro-vibrational modes and electronic interactions with other states in molecules which broaden relevant electron level transitions [307].

The second source of dissipation is radiation-induced damping, which originates from the interaction of the system with the quantized electromagnetic field. Light and matter degrees of freedom mix (dressing) and give rise to hybrid polaritonic states. The dressing is responsible for frequency shifts and line-broadening in the particle's spectrum[3]. We model the coupling of the moving particle to the electromagnetic field through its electric dipole moment by means of a linear oscillator relation (Drude-Lorentz model [147]). Here, the spring force is related to the binding energy of the particle's electrons and the frequency ω_a corresponds to the dominant resonant transition of the particle. In principle, the potential energy binding the electrons can be nonlinear as long as restoring force remains to be linear [448]. Here, the external perturbation, given by the material-modified vacuum field in mechanical nonequilibrium, must correspond to an energy which is smaller than the characteristic energy for internal interactions of the particle . For fluctuation-induced phenomena in quantum electrodynamics, this is usually true for distances between separate subsystems that are larger than a few angstroms [M1, M4, 162, 347]. Also, we emphasize that our model avoids the rotating-wave approximation (RWA) which is often applied to near-resonant atom-field interactions [113]. The RWA is based on the estimate that rapidly oscillating terms in a Hamiltonian can be neglected [303]. For dissipative open quantum systems, this has been shown to be very problematic in some cases [52, 449–452].

As noted earlier, our model does not allow for saturation effects. Saturation can occur in two-level and nonlinear systems when the particle's excited states are fully occupied (in some cases, such as lasing systems, this is referred to as population inversion [303]) and cannot store any further energy at the moment. For multiple atoms, the saturation can further lead to collective phenomena, such as super-radiance [336], which, in turn, can have an affect on the fluctuation-induced interactions between particles when they are prepared in excited states [119, 453–455]. Such a situation usually negligible for the energy scales of systems we are interested in. Further, the nonlinear description usually needs to rely on sensitive assumptions on the system+bath coupling such as the Born-Markov assumption [119, 453], the rotating wave approximation [455] or time-dependent perturbation theory [454] which, as we extensively argue in Chapters 1, 3 and 4, are questionable for our main focus of studying long-time correlations.

In order to solve Eq. (3.5), we note that the response kernels in Eq. (3.5) ($\propto \underline{\mu}_{\Re}$ and $\propto \underline{G}_{\Im}$) are positive semi-definite for positive frequencies in equilibrium ensuring causality and hence the existance of the Fourier transform [155] (see also appendix F). At late times $-t_i, t \gg \tau_c$ and zero velocity $v = 0$, it can be shown that our dynamical system equilibrates thermally [136] and we recover the equilibrium model used in Sec. 2.1.1. For finite atomic velocities $v \neq 0$, however, the state of the system deviates from the *global* equilibrium situation [421]. Also, for finite coupling strength, system and environment are inseparably intertwined and the assumption that equilibrium ensues *locally* is not given automatically. Yet, the two dissipation channels explained above lead to finite correlation times between system and environment establishing irreversibility in the interaction. When the different irreversible processes balance, the dynamics of the system becomes time-independent for $t \gg t_c$ and it reaches a nonequilibrium steady-

[3]For instance, we refer to recent investigations of related phenomena in the field of molecular polaritonics [300, 447].

state (NESS) [168]. Such a state is characterized by a non-vanishing current of energy in the complete system due to the external drive [428]. In our case, this means that the external agent constantly needs to infuse energy into the system in order to balance frictional losses to the bath [M1, M6]. For now, it ensures that our system is not lasing and implicitly constraints the range of valid velocities as follows: We employ a Fourier transform of Eq. (3.5) and obtain

$$\underline{\alpha}_\mu^{-1}(\omega)\hat{\mathbf{d}}(\omega) \sim \underline{\Delta}(\omega, v)\hat{\mathbf{d}}(\omega) + \int \frac{\mathrm{d}h}{2\pi}\hat{\mathbf{E}}_\mathrm{N}(h, \mathbf{R}_a, \omega + vh)e^{\mathrm{i}x_a h} + \hat{\mathbf{f}}(\omega), \tag{3.8}$$

where we defined the (complex) resonance frequency renormalization which encodes dissipation and dispersion due to the interaction with the electromagnetic environment, i.e.

$$\underline{\Delta}(\omega, v) = \int \frac{\mathrm{d}h}{2\pi}\, \underline{G}(h, \mathbf{R}_a, \omega + vh) \tag{3.9}$$

and the intrinsically damped polarizability $\underline{\alpha}_\mu = \alpha_0[1 - \omega^2/\omega_a^2 - \mathrm{i}\epsilon_0\omega\underline{\mu}(\omega)]^{-1}$. To this end, we employed Eq. (3.1) for the asymptotic particle trajectory and used that the Green tensor fulfills the Kramers-Kronig relations in position space [147] such that we can write

$$\begin{aligned}\mathrm{i}\int \mathrm{d}t\; e^{\mathrm{i}\omega t}\int_0^\infty \mathrm{d}\tau \int \frac{\mathrm{d}\omega'}{2\pi}\int \frac{\mathrm{d}h}{2\pi}\, \underline{G}_\Im(h, \mathbf{R}_a, \omega')\hat{\mathbf{d}}(t-\tau)e^{\mathrm{i}[x_a(t)-x_a(t-\tau)]h - \mathrm{i}\omega'\tau} \\ = \frac{1}{2}\lim_{\chi\to-\infty}\int \mathrm{d}t\; e^{\mathrm{i}\omega t}\int_\chi^\infty \mathrm{d}\tau\; \int \frac{\mathrm{d}h}{2\pi}\, \underline{G}(h, \mathbf{R}_a, \tau)\hat{\mathbf{d}}(t-\tau)e^{\mathrm{i}[x_a(t)-x_a(t-\tau)]h}.\end{aligned} \tag{3.10}$$

Note that we could extend the τ integral to $-\infty$ since the Green tensor is zero for negative time-differences τ due to causality. Solving the integrals on both side of the Fourier transform in the previous equation, we find the identity

$$\frac{1}{2}\int \frac{\mathrm{d}h}{2\pi}\; \left[\lim_{\delta\to0}\int \frac{\mathrm{d}\omega'}{\pi}\frac{\underline{G}_\Im(h, \mathbf{R}_a, \omega')}{\omega' - (\omega + vh) + \mathrm{i}\delta} - \underline{G}(h, \mathbf{R}_a, \omega + vh)\right]\hat{\mathbf{d}}(\omega) = 0 \tag{3.11}$$

which is valid in the nonequilibrium steady-state. Using that $\lim_{\delta\to0}(x \pm \mathrm{i}\delta)^{-1} = \mathcal{P}x^{-1} \mp \mathrm{i}\pi\delta(x)$ with $\mathcal{P}$ the Cauchy principal value, the previous equation can be interpreted as a generalized Kramers-Kronig relation for the driven system. Indeed, at zero velocity, we can decompose $\underline{G}_\Im = \underline{G}_I^\mathrm{s} - \mathrm{i}\underline{G}_R^\mathrm{as}$ with s (as) the symmetric (anti-symmetric) part of the tensor and I (R) the imaginary (real) part of an expression. Eq. (3.11) then reduces to the regular Kramers-Kronig relations for the electric Green tensor [147]. One crucial requirement for the (generalized) Kramers-Kronig relations to hold is that the Green tensor is analytic in the upper frequency half-plane. Equivalently, this means that the complex poles of the Green tensor and similarly of the polarizability solving the dipole's linear equation of motion are located at the lower complex frequency plane. However, since we evaluate the polarizability at Doppler-shifted frequencies, for sufficiently high velocities (at the order of the system's electric resonances) and depending on the geometry and the material properties, the velocity-dependent poles can move to the upper frequency plane. The motion then effectively acts as an additional gain in the system. The Fourier transform then can become meaningless due to an exponential increase of the susceptibilities for large arguments and the above relations need not to be valid anymore.

For instance, a similar behavior was observed in Ref. [347] for the equations of motion of a moving (linear) atom when the corresponding frequency $v/z_a \sim \omega_{\mathrm{sp}}$ is at the order of the surface excitation ω_{sp} of a lossless metal. In such a situation, the NESS does not necessarily exist within the present description. Instead, we would need to solve the exact dynamics of the system including initial conditions and/or take the (physical) saturation effects of the particle into account by means of using, e.g., a nonlinear system for modeling the particle's internal dynamics (see e.g. Ref. [456] for a study of the behavior of the complex poles of a driven nonlinear system). In the remainder of the thesis, we will see that relation (3.11) holds certainly true at least for the experimentally relevant velocities much smaller than the typical system resonances for alkali atoms and conducting bodies (see e.g. Eq. (1.58) and the subsequent discussion). From now on, when we demand the system to be causal or well-behaving, we mean it in the sense of Eq. (3.11). This particularly affects the present and the following Chapter.

In the steady-state, we can solve Eq. (3.5) self-consistently by means of Eq. (3.8),

$$\hat{\mathbf{d}}(\omega) = \underline{\alpha}(\omega, v) \cdot \left[\int \frac{\mathrm{d}h}{2\pi} \hat{\mathbf{E}}_{\mathrm{N}}(h, \mathbf{R}_a, \omega + vh) e^{\mathrm{i}x_a h} + \hat{\mathbf{f}}(\omega), \right] \tag{3.12}$$

as a function of the velocity-dependent polarizability tensor

$$\underline{\alpha}(\omega, v) = \underline{\alpha}_{\mu}(\omega) \cdot \left[1 - \underline{\Delta}(\omega, v) \underline{\alpha}_{\mu}(\omega) \right]^{-1}. \tag{3.13}$$

In contrast to the bare polarizability obtained in time-dependent quantum linear response theory (see Sec. 2.1.1), the velocity-dependent and dressed polarizability $\underline{\alpha}(\omega, v)$ shows an involved structure due to the self-consistent inclusion of (i) the internal degrees of freedom, (ii) the dressing due to the material-modified vacuum and (iii) the velocity-dependence. This interplay of different physical mechanisms has a profound impact on the tensorial structure of the polarizability which we discuss in the following Section 3.2. Combining Eqs. (3.4) and (1.23), it is possible to show that the material-modified vacuum field fluctuations obey the fluctuation-dissipation relation we anticipated earlier [see Eq. (1.56)],

$$\underline{\nu}(\omega, v) = 2\hbar \lim_{T \to 0} \int \frac{\mathrm{d}h}{2\pi} \left[n(\omega + vh, T) + 1 \right] \underline{G}_{\Im}(h, \mathbf{R}_a, \omega + vh), \tag{3.14}$$

where we assumed zero temperature in accordance with our initial assumptions. Equation (3.14) can be expressed in planar coordinates by replacing the general invariance along the direction of motion with its planar representation, i.e. $\mathrm{d}h/(2\pi) \to \mathrm{d}^2\mathbf{p}/(2\pi)^2$ with $\mathbf{p}$ the component of the three-dimensional wavevector parallel to the interface which then exactly yields Eq. (1.56). Note that the field does not depend on the particle's internal degrees of freedom ($\sim \underline{\mu}$) since we assumed vacuum field and intrinsic (Langevin) noise of the particle to be uncorrelated. In contrast, for the power spectrum of the dipole fluctuations $\langle \hat{\mathbf{d}}(\omega) \hat{\mathbf{d}}(\omega') \rangle = 4\pi^2 \underline{S}(\omega, v) \delta(\omega + \omega')$, we obtain [M2]

$$\underline{S}(\omega, v) = \frac{\hbar}{\pi} \underline{\alpha}(\omega, v) \cdot \underline{\mathcal{D}}(\omega, v) \cdot \underline{\alpha}^{\dagger}(\omega, v), \tag{3.15}$$

where the dissipation kernel $\underline{\mathcal{D}}(\omega, v)$ results from the two-time correlator of the (quantum) noise terms associated with the different dissipation mechanisms, i.e.

$$\underline{\mathcal{D}}(\omega, v) = \frac{\omega\epsilon_0\theta(\omega)}{\alpha_0}\underline{\mu}_{\Re}(\omega) + \underline{\nu}(\omega, v). \tag{3.16}$$

Again, since we assumed the external and the intrinsic degrees of freedom of the particle to be uncorrelated, the intrinsic dissipation is not affected by the relative motion. Further, both channels add linearly in $\underline{\mathcal{D}}$. However, from Eq. (3.15) we find that intrinsic and induced dissipation in general interlace in the dipole dynamics, even though their statistical origins were assumed to be uncorrelated. We emphasize that Eq. (3.15) already displays the self-consistency of our approach: Fluctuations in the material-modified vacuum field drive the particle and vary the dynamics of its respective dipole fluctuations. That very dipole fluctuations, in turn, determine the dynamics of the field by means of Eq. (3.3). In this way, Eqs. (3.14) and (3.15) are the nonequilibrium fluctuation-dissipation relations that self-consistently describe the statistics of the interaction. We will put our main focus on the physical implications of the self-consistency in Chapter 4.

3.2 Rotational degrees of freedom

We now focus on the tensorial structure of the particle's polarizability [Eq. (3.13)]. This will give us some insight into different forms of anisotropies in the time-evolution of the dipole moment with respect to the spatial direction. Interestingly, such anisotropies can either occur due to the characteristics of the particle and the surface (molecules or bifringent dielectrics) or from the pure interaction with the material-modified vacuum field in mechanical nonequilibrium. The latter, as we will see in the following, can cause the atom to "rotate". We want to emphasize that, when speaking about the *direction* of the dipole, we refer to its spatial degrees of freedom encoded in the average magnitude of the dipole operator's vector components; which is not to be confused with its quantum degrees of freedom. For instance, in the simplest case of an (externally) fixed dipole moment, where the direction $\mathbf{d}$ of the dipole is given by $\hat{\mathbf{d}} \to \mathbf{d}\hat{q}(t)$ and $\hat{q}(t)$ describes the quantum operator evolving in time [58, 434]. As a consequence, the particle's power spectrum will become symmetric and we exclude rotations of the dipole that are induced by the interaction with the material-modified vacuum per construction. In the following, we discuss the more general case, the atomic dipole operator consists of three distinct spatial quantum degrees of freedom.

In leading order of the atomic vacuum polarizability α_0 coupling particle and field, we can neglect the dressing of the particle's response ($\underline{\Delta} \to 0$) such that the corresponding polarizability becomes velocity-independent,

$$\underline{\alpha}(\omega, v) \sim \underline{\alpha}_\mu(\omega). \tag{3.17}$$

This is equivalent to the situation of a single dipole coupled to macroscopic number of intrinsic linear dissipative degrees of freedom and could, e.g, represent a metallic nano-particle. The tensor structure is hence given by $\underline{\mu}$. Allowing for anisotropy, it is still possible to define a preferred coordinate system (from the perspective of the particle) by means of the principal axis theorem in which $\underline{\mu}$ becomes diagonal. Hence, $\underline{\alpha}_\mu$ can also be diagonalized. Note that, depending on the exact form of $\underline{\mu}$, the diagonal elements of the polarizability can vary in their magnitude. Such a situation becomes relevant, e.g., for larger molecules with macroscopic spatial extension [457, 458] or if the molecules are intrinsically chiral [459].

Keeping higher orders of α_0 and neglecting, for the time being, the internal degrees of freedom ($\underline{\mu} \to 0$), our particle model is dominated by the interaction with the electric field and suitable to describe, e.g., neutral atoms. The polarizability can then be written as

$$\underline{\alpha}(\omega, v) \sim \alpha(\omega) \left[1 - \alpha(\omega)\underline{\Delta}(\omega, v)\right]^{-1}, \tag{3.18}$$

where $\alpha(\omega)$ is the bare (undressed) polarizability we defined below Eq. (2.20). Note that, in contrast to the leading order in α_0 [Eq. (3.17)], the tensorial structure of the polarizability is now determined by the tensor $\underline{\Delta}$. At zero velocity and simple geometries, we can still diagonalize $\underline{\alpha}$, but anisotropies may emerge from the interaction with the environment. In the situation of the particle interacting with a planar surface, this simply means that it will make a difference if the dipole is oriented parallel or perpendicular to the surface. Indeed, taking the expression for the Green tensor in appendix A.1, we have that $\underline{\Delta}(\omega, 0) \propto \mathrm{diag}[1, 1, 2]$ such that the polarizability $\underline{\alpha}(\omega, 0)$ is not isotropic with respect to the direction perpendicular to the

surface. More interestingly, for finite velocities, the polarizability is in general *not* diagonal[4]. Instead, due to the structure of $\underline{\Delta}$ [Eq. (3.9)], the polarizability is connected to both the Green tensor's diagonal and off-diagonal elements which can be rather involved. Still, some general remarks useful for our analysis are possible. As any matrix, the Green tensor can be decomposed into a symmetric (s) and a skew-symmetric (as) part, $\underline{G} = \underline{G}^{\mathrm{s}} + \underline{G}^{\mathrm{as}}$. Inserting into Eq. (3.18) and computing the inverse matrix, it is possible to obtain the atomic polarizability which also contains skew-symmetric components, i.e.

$$\underline{\alpha}(\omega, v) = \underline{\alpha}^{\mathrm{s}}(\omega, v) + \underline{\alpha}^{\mathrm{as}}(\omega, v). \tag{3.19}$$

Moreover, it can be shown[5] that the skew-symmetric part of the Green tensor is related in a Cartesian basis to the three dimensional generator $\underline{L}_i$ of rotations around the i-axis with ϵ_{ijk} the Levi-Civita symbol [M1, M2, P2, 461]. We can then show by applying some algebra that $\underline{\alpha}^{\mathrm{as}}_{jk} \propto [\underline{L}_i]_{jk} = -\mathrm{i}\epsilon_{ijk}$. The skew-symmetric part of the polarizability is hence, in general, not zero but rather proportional to the Hermitian generators of the rotation group. Such a decomposition can be related to a spin-dependent part of the electromagnetic density of states [303, 461, 462], including the so-called spin-momentum locking of light [463, 464] due to the properties of the macroscopic materials encoded in the Green tensor (see Refs. [465–467] for recent experiments). We refer to Secs. 3.4.2 and 3.4.3 for explicit examples in the context of quantum friction using different geometries. Without going too much into detail at this point, the intuitive interpretation is the following: In contrast to the intrinsic dissipation mechanisms, where the appropriate coordinate system depends on the form of the particle and the material only, the external coupling to the material-modified vacuum field, and hence the tensorial structure of the particle's polarizability, is determined by the macroscopic geometry of the system. Diagonalization might not only be impossible, but moreover the specifics of the surroundings (or the external drive) can induce anisotropies in the response of the particle with respect to the spin and/or momentum of the (virtual) photons that are absorbed or emitted by the particle [M1, 461].

It is important to notice that the symmetric and the skew-symmetric part of the particle's polarizability enter the description in different orders of coupling ($\propto \alpha_0$): In lowest order α_0, we obtain ($\underline{\mu} = 0$)

$$\underline{\alpha}(\omega, v) = \alpha(\omega)\left[1 + \alpha(\omega)\underline{\Delta}(\omega, v)\right] + \mathcal{O}(\alpha_0^3). \tag{3.20}$$

Comparing Eq. (3.19) with Eq. (3.20) yields

$$\underline{\alpha}^{\mathrm{s}}(\omega, v) \sim \alpha(\omega)\left[1 + \alpha(\omega)\ \underline{\Delta}^{\mathrm{s}}(\omega, v)\right], \qquad \underline{\alpha}^{\mathrm{as}}(\omega, v) \sim \alpha^2(\omega)\ \underline{\Delta}^{\mathrm{as}}(\omega, v). \tag{3.21}$$

The complex resonance shift $\underline{\Delta}$ becomes sub-leading and the non-isotropic behavior of the

[4] A similar situation can occur, e.g., when the particle itself is isotropic and at fixed position ($v = 0$), but the interacting surface is made from a bi-refringent dielectric material. Here, the polarizability obtains off-diagonal elements that are related to a polarization-dependent response to the electromagnetic field [28, 388, 460].

[5] To this end, we (i) note that the (unitary) three-dimensional correlation matrix of the electric field operator is related to the Green tensor by the fluctuation-dissipation theorem, (ii) decompose the result using the fundamental generators of unitary matrices (the so-called Gell-Mann matrices) and (iii) apply orthogonal transformations in order to obtain the irreducible tensor operators [461].

atomic response enters in second order of the static polarizability α_0. This highlights the effects of incorporating the back-action from the environment on the particle, which is encoded in higher orders of perturbations in α_0. Restricting the description to the first order in α_0, one would be neglecting the quantitative aspects of the dressing due to the interaction between particle and environment. One would additionally loose qualitative aspects of the interaction, in this case the skew-symmetric parts of the particle's polarizability. We stress that the appearance of skew-symmetric parts in the polarizability tensor is a signature of the nonequilibrium situation at $v \neq 0$ since at zero valocity, they would vanish identically as

$$\underline{\Delta}^{\mathrm{as}}(\omega, 0) = \int \frac{\mathrm{d}h}{2\pi}\, \underline{G}^{\mathrm{as}}(h, \mathbf{R}_a, \omega) \to 0, \tag{3.22}$$

where we used that $\underline{G}^{\mathrm{as}}(-h, \mathbf{R}_a, \omega) = -\underline{G}^{\mathrm{as}}(h, \mathbf{R}_a, \omega)$ [58, 189].
To see this more clearly, we consider the example of an atom ($\underline{\mu} = 0$) moving parallel with respect to a planar interface along the x-direction (see Fig. 3.4). The electric Green tensor for such a situation, i.e. an infinitely extended half-space, can be found in appendix A. Integrating over the wavevector along the direction of motion at Doppler-shifted frequencies, the complex resonance shift $\underline{\Delta}$ yields a structure of the polarizability of the form

$$\underline{\alpha}(\omega, v) = \underline{\alpha}_D(\omega, v) - \alpha_R(\omega, v)\underline{L}_y = \underline{\alpha}^{\dagger}(-\omega, -v), \tag{3.23}$$

where $\underline{\alpha}_D(-\omega, -v) = \underline{\alpha}_D^*(\omega, v) \sim \mathcal{O}(\alpha_0)$ is a diagonal matrix, $\alpha_R(-\omega, -v) = -\alpha_R^*(\omega, v) \sim \mathcal{O}(\alpha_0^2)$ a complex function and the only remaining generator for rotations is $\underline{L}_y$ in accordance with the symmetries of our system. We note that, even though $\underline{\alpha}_D$ is diagonal, its elements are not identical due to the asymmetry of our system. This would only be true in lowest order α_0, where $\underline{\alpha}_D \sim \alpha(\omega)$ and the dressing is neglected. We have seen earlier [Eq. (3.15)] that the quantum stochastic motion of the atomic dipole operator leads to a non-vanishing average fluctuation in the magnitude of the dipole moment $\propto \langle \hat{\mathbf{d}}^2 \rangle$. Noting that Eq. (3.5) describes three distinct oscillator degrees of freedom $\hat{d}_i$ with $i = 1, 2, 3$, it is interesting to ask whether there is a relative relation between the different spatial directions $\propto \hat{d}_i \hat{d}_j$. To this end, we define the angular momentum vector [M1, 461, 468]

$$\boldsymbol{\mathcal{L}} = \frac{1}{\alpha_0 \omega_a^2} \left\langle \hat{\mathbf{d}}(t) \times \dot{\hat{\mathbf{d}}}(t) \right\rangle, \tag{3.24}$$

where the cross product acts on the spatial components of the operators. Due to the symmetries of our system, the only non-vanishing part is the y-component which becomes a constant in the nonequilibrium steady-state given by

$$\mathcal{L}_y(v) = \int \mathrm{d}\omega\ \omega\ \mathrm{Tr}\left[\underline{\alpha}(\omega, v) \cdot \underline{\nu}(\omega, v) \cdot \underline{\alpha}^{\dagger}(\omega, v) \cdot \underline{L}_y\right]. \tag{3.25}$$

Similarly, we can define the dipole vector's moment of inertia as a measure of asymmetry in

the quantitative difference between the elements of the atom's power spectrum, i.e.

$$\underline{M}_{ij} = \frac{1}{\alpha_0 \omega_a^2} \left\langle \hat{\mathbf{d}}(t)^2 \delta_{ij} - \hat{d}_i(t)\hat{d}_j(t) \right\rangle \overset{t\to\infty}{\to} \frac{1}{\alpha_0 \omega_a^2} \int \mathrm{d}\omega \, \left(\mathrm{Tr}\left[\underline{S}(\omega, v)\right] \delta_{ij} - \underline{S}_{ij}(\omega, v) \right), \quad (3.26)$$

where the second step indicated by the arrow describes the limit of late times (NESS). Again, due to the symmetries of the motion along the x-axis, only the yy-component of the moment of inertia,

$$\underline{M}_{yy}(v) = \int \mathrm{d}\omega \, \mathrm{Tr}\left[\underline{\alpha}(\omega, v) \cdot \underline{\nu}(\omega, v) \cdot \underline{\alpha}^\dagger(\omega, v) \cdot \underline{L}_y^2 \right], \quad (3.27)$$

remains finite. Along these lines, performing the quantum average, we can define an average sense of rotation for the stochastic motion of the three-dimensional dipole vector $\mathbf{d}$ [468], where the rotation vector $\boldsymbol{\Omega}$ is given by

$$\underline{M} \cdot \boldsymbol{\Omega} = \boldsymbol{\mathcal{L}} \quad (3.28)$$

and reduces to $\boldsymbol{\Omega} = (0, \Omega, 0)^T$ in our particular situation. Combining the previous results, the rotation frequency is given by [M1]

$$\Omega = \Omega(v) = \frac{\int \mathrm{d}\omega \; \omega \; \mathrm{Tr}\left[\underline{S}(\omega, v) \cdot \underline{L}_y \right]}{\int \mathrm{d}\omega \; \mathrm{Tr}\left[\underline{S}(\omega, v) \cdot \underline{L}_y^2 \right]}, \quad (3.29)$$

where the matrix $\underline{L}_y^{(2)}$ selects the skew-symmetric (symmetric) part of the atom's power spectrum in the numerator (denominator). Again, some comments are in order.

First, we note that in accordance with the stationarity of the system, $\dot{\boldsymbol{\mathcal{L}}} = 0$ such that all torques acting on the system balance on average [M1].

Second, since the skew-symmetric parts vanish at zero velocity such that $\underline{S}^{\mathrm{T}}(\omega, 0) = \underline{S}(\omega, 0)$ is symmetric [Eq. (3.22)], the rotation frequency $\Omega \to 0$ at zero velocity as expected.

Third, at non-zero velocities, $\Omega(v)$ can be finite. In leading order of the vacuum polarizability, we can neglect the material-induced anisotropy of the particle's response and approximate the power spectrum by $\underline{S}(\omega, v) \sim \frac{\hbar}{\pi} |\alpha(\omega)|^2 \underline{\nu}(\omega, v)$. Note, however, that the anisotropy, to some extent, is still encoded in the field fluctuations $\underline{\nu}$. Further, since the integral expands over the full range of frequencies, we can write for $\alpha_0 \ll \epsilon_0 z_a^3$ that $\alpha_0 \omega |\alpha(\omega)|^2 \sim (\pi/2\omega_a)[\delta(\omega - \omega_a) - \delta(\omega + \omega_a)]$ which yields a linear dependence of the average rotation frequency on the velocity, i.e.

$$\Omega(v) \sim -v \frac{2\omega_a \int \mathrm{d}h \; h \; \underline{G}^{\mathrm{as}\prime}_{R,xz}(h, \mathbf{R}_a, \omega_a)}{\int \mathrm{d}h \; \left(\underline{G}^{\mathrm{s}}_{I,xx}(h, \mathbf{R}_a, \omega_a) + \underline{G}^{\mathrm{s}}_{I,zz}(h, \mathbf{R}_a, \omega_a) \right)}, \quad (3.30)$$

where the prime indicates a derivative with respect to frequency, the subscripts denote the components of the tensor, we assumed that ω_a is within the Ohmic range of the bulk material and expanded for small velocities $v \ll \omega_a z_a$ using that $h \sim 1/z_a$ for our setup. In order to gain a quantitative insight, we consider the near-field regime of a planar interface made from a local material model with transverse magnetic reflection coefficient r^p. The system has two

directions of invariance such that we can replace the infinitesimal wavevector element with $\mathrm{d}h/(2\pi) \to \mathrm{d}^2\mathbf{p}/(2\pi)^2$. Upon employing (1.51), we obtain

$$\Omega(v) \sim -v/z_a. \tag{3.31}$$

The previous result is to be understood as a rough estimate since we neglected the explicit anisotropies appearing in the tensor structure of the particle's polarizability[6]. Still, we can already deduce the important qualitative properties: The magnitude of the average rotation frequency is determined by the velocity and the properties of the surface, i.e. in leading order only the atom-surface distance. The closer the atom is to the surface or the higher the velocity, the bigger the effect. As expected, changing the direction of motion reverses the sense of rotation. More interesting is the sign of the rotation. In our convention this means that the particle is rotating in the opposite direction to what one would expect intuitively from the classical picture. Projecting the direction of motion on a plane, the average rotation of the atom is *counterclockwise* around the y-axis pointing into the plane (see Fig. 3.4), exactly the opposite of what one might expect from the classical intuition. For comparison, a clasically rolling wheel on a surface will rotate clockwise and experience a classical rolling friction similarly decelerating the motion. This result is quite remarkable and means that, on average, the direction of the fluctuation-induced atomic dipole vector is rotating. We want to emphasize that, since Eq. (3.5) describes in fact three distinct (spatial) oscillator degrees of freedom, the "rotation" is meant in terms of the average relation in magnitude of fluctuations in different spatial directions. Also, it is worth pointing out that Eq. (3.29) leaves the flexibility for defining an average spectral rotation given by the respective integral kernel. At different frequencies, the results can vary in both magnitude and sign; all of them adding up under the integral giving our particular choice of defining the "average rotation". Hence, the overall sign is not uniquely fixed, but rather given by the specifics of the system and the complex interplay of the material-dependent interaction at given frequencies.

Physically, the rotation of the atom can be understood by relating the skew-symmetric parts of the Green tensor and its related quantities to the average of the quantum spin[7] angular

[6] In fact, a more careful derivation that includes the anisotropy of the polarizability yields a similar qualitative behavior, but shows a quantitative correction as [M1, 236]

$$\Omega(v) \sim -\frac{v}{z_a}\left(1+\left[r_R^p(\omega_a)/3r_I^p(\omega_a)\right]^2\right)^{-1}. \tag{3.32}$$

Due to the Casimir-Polder interaction with the surface, the oscillator is not isotropic with respect to the direction perpendicular to the surface [Eq. (3.19)]. However, this is already the case when the skew-symmetric parts of the Green tensor are ignored. Since the main physical mechanism leading to the rotation stems mathematically from the skew-symmetric part of the field fluctuations $\underline{\nu}$, the correction is not necessary for our qualitative discussion. For typical metals, this number will be smaller than the one reported in the main text and for rubidium [142] above a gold surface [140] with the dynamical parameters obtained in Ref. [30] evaluates to roughly some tens to hundreds of MHz.

[7] We remark that light carries both orbital and spin angular momentum. Separating both contributions and assigning physical meaning to them is non-trivial and we refer the reader to Ref. [469] for further details. In our case, "spin" is supposed to be understood as defined in Eq. (3.33).

momentum operator density $\hat{\mathbf{s}}$ for the non-interacting field [469–471]

$$\mathbf{s}(\mathbf{r},t) = \langle \hat{\mathbf{s}}(\mathbf{r},t)\rangle = \frac{\epsilon_0}{2}\langle \hat{\mathbf{E}}_\mathrm{N}(\mathbf{r}(t),t)\times\hat{\mathbf{A}}_\mathrm{N}(\mathbf{r}(t),t)\rangle + H.c., \tag{3.33}$$

where $\hat{\mathbf{A}}_\mathrm{N}$ is the vector potential operator of the non-interacting material-modified vacuum field. In principle, the electric field can contain both transverse (connected to the vector potential) and longitudinal (connected to the scalar potential) components. However, in the Weyl representation of the fields and Green tensors for planar geometries [189], the longitudinal parts are absorbed in the p-polarized field [472] such that we can write without loss of generality (analogous to the minimal coupling scheme [434]) that $\hat{\mathbf{E}}_\mathrm{N} = -\partial_t\hat{\mathbf{A}}_\mathrm{N}$. The vector $\mathbf{s}$ is independent from the properties of the particle and provides the spin density of states of the electric field at position $\mathbf{r}$. Upon employing the field decomposition of Eq. (3.4a) and combining with Eq. (3.14), we obtain the stationary solution

$$\mathbf{s}(\mathbf{r}, t\gg\tau_\mathrm{c}) \sim \hbar\int_0^\infty \frac{\mathrm{d}\omega}{2\pi}\int\frac{\mathrm{d}h}{2\pi}\,\boldsymbol{\rho}_\mathrm{s}(h,\mathbf{R}_a,\omega). \tag{3.34}$$

In analogy to the commonly used concept of the local density of states ρ_e (LDOS) [190], we defined the *spin* local density of states

$$\boldsymbol{\rho}_\mathrm{s}(h,\mathbf{R}_a,\omega) = -2\mathrm{i}\epsilon_0\frac{\mathrm{Tr}\left[\underline{\mathbf{L}}\cdot\underline{G}_R^\mathrm{as}(h,\mathbf{R}_a,\omega)\right]}{\omega} \tag{3.35}$$

as the intergral kernel of the average spin angular momentum vector. Further, we used the identity $(\mathbf{a}\times\mathbf{b})_i = -\mathrm{i}\underline{L}_{i,kj}a_jb_k$ for any vectors $\mathbf{a}$ and $\mathbf{b}$ [462]. We note that, in contrast to the usual LDOS, where the trace of the Green tensor's imaginary part is computed and hence only symmetric components can contribute, i.e. $\rho_\mathrm{e}\propto\mathrm{Tr}\underline{G}_I^\mathrm{s}$ [190], its spin-analog measures the skew-symmetric part of the Green tensor for given frequency and wavevector. Since it carries information about the spin degrees of freedom of the electric field, it additionally becomes vector-valued. We note that in vacuum, where spin and momentum of light have the same direction, only two values (±1) for the spin can be allowed and spin zero is forbidden since the (massless) photon can never be at rest. However, in the near field of a surface, where the spin is orthogonal to the direction of the propagation and longitudinal fields are allowed, the situation can be different [M1, 464]. In this way, $\underline{G}_\Im = \underline{G}_I^\mathrm{s} - \mathrm{i}\underline{G}_R^\mathrm{as}$ encodes the properties of both the LDOS and the spin LDOS for the material-modified electric field without the coupling to the atom. Interestingly, in our self-consistent description, the properties of the field are inherently connected to the fluctuation dynamics of the particle since $\underline{S}\propto\underline{G}_\Im$ and determine the probability that the atom emits (absorbs) photons for frequencies $\omega>0$ ($\omega<0$) [125]. The spin (polarization) state of the radiation is then reflected in the symmetry properties of $\underline{G}_\Im$: The symmetric part, $\underline{G}_I^\mathrm{s}$ being even with respect to h, is independent of the direction of the wavevector and hence related to spin zero (linear polarization). The skew-symmetric part, $\underline{G}_R^\mathrm{as}$ being odd in h, is sensitive to the sign of the wavevector and associated with polaritons having nonzero spin along the y-axis. In order to determine the correct relation between the wavevector and the spin of the photon, we focus on the scattered part of the Green tensor and recall that (see Chap. 1), especially in the near-field regime, the main excitations mediating the interaction

are evanescent surface waves, the surface plasmon-polaritons (SPP) for metals. The SPPs are *confined* in z-direction due to the presence of the interface. In general, any confinement of light leads to longitudinal field components [464, 473] which, from Eq. (3.33), induce a transverse spin-component that flips sign when the direction of propagation is reversed; spin and momentum are *locked* [464]. In other words, the direction of the wavevector unambiguously sets the spin of the SPP. Using an interpretation for positive h along the x-axis, the spin is negative (right-hand rule, rotating counter-clockwise) and vice versa [M1]; see Fig. 3.3.

In equilibrium, at position $\mathbf{r}_a$ above the surface, the probability of detecting (virtual) radiation with wavevector of opposite sign is equally high. Mathematically, the odd components of the spin LDOS $\boldsymbol{\rho}_\mathrm{s}$ contribute equally to the integral and hence the corresponding average spin density of the electric field vanishes, i.e. $\mathbf{s} \to 0$.

From the perspective of the moving atom, however, the situation is substantially different, because the probability of emitting and absorbing photons with non-zero spin is effectively tilted due to the Doppler-shift. To be precise, we rewrite the average rotation frequency in leading order α_0 as[8]

$$\Omega(v) \sim \frac{\hbar}{\epsilon_0 M_{yy}(v)} \int \mathrm{d}\omega \int \frac{\mathrm{d}h}{2\pi} \theta(\omega + hv) \times \omega(\omega + hv)\ |\alpha(\omega)|^2 \boldsymbol{\rho}_{\mathrm{s},y}(h, \mathbf{R}_a, \omega + hv), \tag{3.36}$$

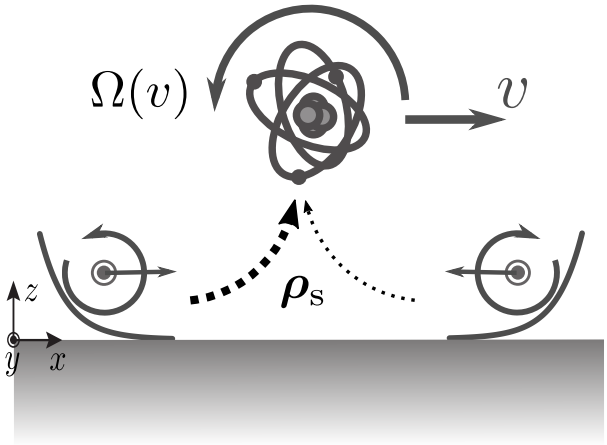

Figure 3.3: An atom moving in x-direction with constant velocity v undergoes a rotation of frequency $\Omega(v)$ around the y-axis (pointing into the plane) in counter-intuitive direction due to an imbalance in the interaction with spin-momentum-locked surface waves modifying the spin LDOS $\boldsymbol{\rho}_\mathrm{s}$ (see main text).

where the extra subscript gives the y-component of the spin LDOS. At zero velocity, the probability of emitting or absorbing photons with non-zero spin is equally high and the average rotation of the particle vanishes. At finite velocity, however, the Doppler shift favors the absorption of photons traveling in positive x-direction. In the near-field, due to the spin-momentum locking, these photons carry a negative spin such that the atom absorbs negative angular momentum and starts to rotate counter-clockwise contrary to the classical intuition; see Fig. 3.3. The spin-dependent exchange of photons has consequences for the forces experienced by the atom. In the context of quantum friction, we will discuss this topic further in Sec. 3.4.2.

It is opportune to highlight that our result is a mere consequence of the nonequilibrium statistics of the fluctuation-induced atom-surface interaction. Only the system's dynamics induces the rotation. Recently, there has been a considerable amount of interest in rotating microscopic systems and we emphasize that our result contrasts seemingly related works: To name a few examples, similar studies on neutral particles throughout assumed the rotation to

[8] Again, including the asymmetries in the atom's polarizability, or higher orders in α_0, would lead to a number of extra frequency- and wavevector-dependent prefactors.

be enforced on the particle by external measures and studied the resulting dispersion forces [45, 47, 440, 474], partially drawing the connection to spin-momentum locking of light in the vicinity of a surface [45]. We emphasize that enforcing the rotation enabled the previous authors the use of approximate techniques such as the approach of Local Thermal Equilibrium (LTE). Further, general quantum mechanical rotations disconnected from the interaction with a surface have been studied for microscopic rotors such as extended molecules interacting with thermal gases by means of a Markovian Master equation [468, 475]. For even larger particles, there has been a surge of interest in the rotational motion of levitated nano-particles such as the rotation of a nanoscopic sphere made from a birefringent material (equivalent to asymmetries in $\underline{G}^{\mathrm{as}}$) induced by a polarized Laser beam [476]. The torsional vibration of an optically levitated non-spherical particle in vacuum (equivalent to modifications in $\underline{\mu}$) was examined by studying the deviations in the polarization of an interacting Laser [477]. Later, the rotation of such a non-spherical particle, in this case a nano-rod rotating at MHz frequencies, was shown to be substantially stabilized by the interaction with a periodic driving [478].

In any of those cases, however, the rotation was instigated by asymmetries in the interaction due to either (i) external forces exerting torques, (ii) an asymmetric shape of the particle and as a result an asymmetric polarizability in vacuum or (iii) a birefringent material interface breaking the invariance with respect to spatial directions. Instead, linking the quantum stochastic fluctuations of the atom to the Doppler effect and spin-momentum locking, the average rotation we observe reveals an *intrinsic* asymmetric feature of atom-surface interactions that does not depend on any other artificially imposed external parameters other than than the relative motion of the system's constituents.

Further, we mention that it was eventually the proper treatment of long-time correlations (small frequencies) between atom and material-modified field that allowed us to obtain the non-vanishing average rotational dynamics of the particle. This remains true even though the broad range of frequencies considered by the integral in Eq. (3.29) can give the impression that near-resonant frequencies $\omega \sim \omega_a$ are accentuated in the determination of the rotation frequency. For comparison, we revisit the previous calculation using some of the commonly used approximations (see Chap. 1). For instance, the LTE misrepresents low-frequency fluctuations. Mathematically, the LTE amounts to neglecting the θ-function under the integral in the field fluctuations $\underline{\nu}$ or, more concretely, in Eq. (3.36) [53]. Also, most approaches are also restricted to a second order perturbation in the atomic dipole moment [43] which would additionally ignore the dressing of the atom and instead use $\underline{\alpha}(\omega, v) \to \alpha(\omega)$. This would remove the off-diagonal elements from the evaluation of the spin LDOS and hence simply "overlook" the average rotation. In other words, without incorporating the long-time correlations between the respective subsystems, capturing the relevant physics instigating the average rotation would have been impossible [M1].

Lastly, we highlight that the skew-symmetric parts of the Green tensor and the related quantities are a fundamental geometric property independent of the particular observable and the interaction between field and particle. Still, we can identify those terms to be responsible for the spin-dependent coupling of the material-modified vacuum field and the particle. In this way, in order to design our notation as intuitively as possible, we want to address effects originating from the skew-symmetric terms of the Green tensor and the polarizability as *rotational degrees of freedom* in the sense of Eq. (3.29) from now on.

3.3 Dynamical Casimir-Polder interaction

We proceed by studying the fluctuation-induced forces acting on the moving microscopic particle (see Fig. 3.4). In the present Section, after deriving the general formalism, we focus on the component perpendicular to the surface, the Casimir-Polder (CP) force and its velocity-dependent nonequilibrium corrections. As a broadband phenomenon, the Casimir-Polder force entails an equilibrium contribution that is quantitatively dominant in comparison to the corrections stemming from mechanical nonequilibrium. It will turn out in the following that for most times, the CP force is quantitatively well-covered by the application of LTE for most simple situations [43]. Not covered by the LTE, however, is the rich physics emerging form nonequilibrium interactions. Our approach (Sec. 3.1) allows for including nonequilibrium contributions and thereby a coupling of the field fluctuations to the atom's translational as well as rotational degrees of freedom (Sec. 3.2) exactly. In this way, we manage to advance existing estimates for the CP force: In addition to the well-known results reported in the literature [19, 79, 479–481], we observe a term that is connected to motion-induced rotations of the atom which increases the attraction towards the surface. Analyzing the statistics of the system's fluctuations, we provide an intuitive physical understanding of this extra term. Motion-induced nonequilibrium includes additional low-frequency fluctuations which, although quantum in their origin, resemble the behavior of classical (thermal) fluctuations.

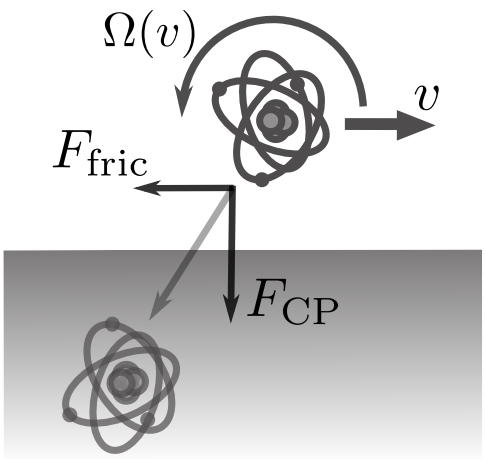

Figure 3.4: An atom moving with respect to a planar interface interacts with its induced image in the material. Due to the motion, the atom experiences the velocity-dependent Casimir-Polder force F_{CP}, is decelerated by the quantum friction force F_{fric} and undergoes a rotation with average frequency $\Omega(v)$ in counterintuitive direction (see Sec. 3.2).

3.3.1 Non-perturbative treatment in the nonequilibrium steady-state

Neglecting magnetic effects, the Lorentz force experienced by the particle (here described in terms of its electric dipole $\hat{\mathbf{d}}$) at time t reads [138]

$$\mathbf{F}(t) = \lim_{\mathbf{r}\to\mathbf{r}_a} \sum_j \left\langle \hat{d}_j(t) \nabla \hat{E}_j(\mathbf{r}(t), t) \right\rangle , \tag{3.37}$$

where the nabla operator ∇ indicates the gradient with respect to spatial coordinates and the index $j = x, y, z$ denotes the vector components of an expression (in Cartesian coordinates). The electric field operator $\hat{\mathbf{E}}$ is evaluated at the position of the particle $\mathbf{r}(t) = \mathbf{r}_a(t)$ and the ensemble average is performed over the initially factorized state [Eq. (3.2)]. Without loss of generality, we assume the relative motion of the particle to be in vacuum following the classical trajectory of Eq. (3.1) along the $\mathbf{x}$-direction. Splitting the nabla operator $\nabla = \nabla_{\parallel} + \nabla_{\perp}$ into

contributions parallel ($\parallel$) and perpendicular ($\perp$) to the surface, the force decomposes into

$$\mathbf{F}(\mathbf{R}_a, t) = F_{\mathrm{fric}}(t)\mathbf{x} + F_{\mathrm{CP}}(t)\mathbf{R}_a \tag{3.38}$$

with $\mathbf{R}_a$ again the position of the particle perpendicular to the surface. We recall that, even though we keep the geometry of the macroscopic environment as general as possible, we still assume that it has a translational symmetry with respect to the axis of motion such that the CP force will always be perpendicular to the direction of motion. For planar geometries, e.g., $\mathbf{R}_a = \mathbf{z}_a$ coincides with the height of the particle along the z axis. In general, however, we have $|\mathbf{R}_a| = z_a$. At zero temperature, the first term of Eq. (3.38) is referred to as *quantum friction* [31]. The second part, F_{CP}, is known as the (dynamic) *Casimir-Polder force* [19] and the main object of interest in the following.

For linear materials and sufficiently small field intensities, we can expand the electric field operator $\hat{\mathbf{E}}$ using the wavevectors h parallel to the direction of motion by means of Eq. (3.4). The decomposition in Fourier space enables us to obtain the nonequilibrium field operator as a functional of its usual (zero-velocity) equilibrium creation and annihilation operators $\hat{\mathbf{E}}_{\mathrm{N}}(h, \mathbf{R}_a, \omega)$. Choosing normal ordering of operators and splitting the field into the creation and annihilation operators in the rest frame of the surface, the explicit vacuum contribution $\hat{\mathbf{E}}_{\mathrm{N}}$ formally vanishes from the evaluation of Eq. (3.37) since the field is forced onto its ground state at zero temperature and we assumed a factorization of the density matrix at the initial time of the interaction. This does not mean that the vacuum field $\hat{\mathbf{E}}_{\mathrm{N}}$ is irrelevant for the derivation of the force. Its properties are rather hidden in the dynamics of the time-dependent dipole operator and they become explicitly visible again when we consider correlations functions, i.e. the tensor $\underline{\Delta}(\omega, v)$ in the particle's polarizability [Eq. (3.18)]. In other situations, e.g. when symmetric ordering is chosen [43] or when we work at finite temperatures [P1], $\hat{\mathbf{E}}_{\mathrm{N}}$ must be considered in all steps of the calculation. The final result is independent of the chosen ordering and this is a mere act of convenience to simplify the derivation. A detailed discussion of the chosen ordering and the expansion of operators can be found in Ref. [58] which we follow closely for this part. The induced contribution $\hat{\mathbf{E}}_{\mathrm{in}}$, on the other hand, derives from the geometry's linear response to a perturbation of the particle's dipole moment and is given by Eq. (3.3). Performing a Fourier transform of Eq. (3.3), reinserting into Eq. (3.37) and executing the limit of late times, where the system reaches the NESS, a lengthy but straight-forward calculation yields

$$F_{\mathrm{CP}} = F_{\mathrm{CP}}(v) = \frac{1}{\pi}\int_0^\infty \mathrm{d}\omega \int \frac{\mathrm{d}h}{2\pi} \int \mathrm{d}\nu\, \mathcal{P}\left(\frac{\mathrm{Tr}\left[\underline{S}(\nu, v)\cdot \partial_{z_a} \underline{G}_{\Im}^{\mathrm{T}}(h, \mathbf{R}_a, \omega)\right]}{\nu + \omega - hv} \right). \tag{3.39}$$

Here, we define the dipole's steady-state power spectrum $\underline{S}(\nu, v)$ [see above Eq. (3.15)], $\mathcal{P}$ is the Cauchy principal value, the superscript "T" denotes the transpose of a matrix and $\mathrm{Tr}\,[\cdot]$ gives the trace of an expression with respect to its spatial components. Further, we used $z_a = |\mathbf{R}_a|$ as the distance of the particle from the closest surface, employed the symmetries of our system in order to replace $\lim_{z\to z_a} \partial_z \underline{G}(\mathbf{r}_a, \mathbf{r}, \omega) \to \frac{\partial_{z_a}}{2} \lim_{z\to z_a} \underline{G}(\mathbf{r}_a, \mathbf{r}, \omega)$ and skipped the redundant argument of the Green tensor after performing the limit $z \to z_a$ [189].

Equation (3.39) closely follows the arguments put down for its frictional counterpart in Ref. [58] and can be seen as the nonequilibrium generalization of the equilibrium Casimir-Polder force (see Chapter 2 or Refs. [58, 162]). It shows that the Casimir-Polder interaction is a broad-band phenomenon (wide range of frequencies and wavevectors contribute). The force is determined by the system's geometry and materials, encoded in the Green tensor $\underline{G}$, and the statistics of the fluctuations, encoded in the particle's power spectrum $\underline{S}$. The Green tensor, characterized by the chosen materials, is in many cases known either analytically [188] or accessible using advanced numerical techniques, see e.g. [146, 224, 235, 482, 483]. The power spectrum, however, is strongly dependent on the underlying model describing the dynamics of the particle's dipole such as the one we outlined in Sec. 3.1. In the following, the power spectrum will hence serve as the working point for including nonequilibrium contributions into the interaction. Before we apply our specific model to the equation (3.39), some general arguments can be laid out.

A first insight can be obtained by noting that the power spectrum is self-adjoint per construction: It decomposes into a real (R), symmetric (s) and a purely imaginary (I), skew-symmetric (as) contribution

$$\underline{S} = \underline{S}_R^{\mathrm{s}} + \mathrm{i}\underline{S}_I^{\mathrm{as}}. \tag{3.40}$$

Note that the first term can be connected to translational degrees of freedom of the particle and the second term encodes its rotational dynamics [M1, 461] as introduced in the previous Section. In Eq. (3.39), due to the properties of the trace evaluating the product of a symmetric and a skew-symmetric matrix identically to zero, $\underline{S}_R^{\mathrm{s}}$ and $\underline{S}_I^{\mathrm{as}}$ couple to the symmetric and skew-symmetric part of the Green tensor independently. As a result, we can unambiguously distinguish between forces deriving from the different types of the particle's dynamics. In order to further simplify Eq. (3.39), we need to solve the principal value. To this end, we recall that the Green tensor fulfills the generalized Kramers-Kronig relations of Eq. (3.10). We can exploit these analytic properties to integrate parts of Eq. (3.39) and obtain

$$\begin{aligned} F_{\mathrm{CP}} = &\int \frac{\mathrm{d}h}{2\pi} \int_{-\infty}^{hv} \mathrm{d}\omega \ \mathrm{Tr}\left[\underline{S}(hv-\omega,v)\cdot\partial_{z_a}\underline{G}_{\Re}^{\mathrm{T}}(h,\mathbf{R}_a,\omega)\right] \\ &+ \frac{1}{\pi}\mathcal{P}\int_0^{\infty}\mathrm{d}\omega \int \frac{\mathrm{d}h}{2\pi}\int_0^{\infty}\mathrm{d}\nu \ \frac{\mathrm{Tr}\left[\underline{S}_-^{\mathrm{s}}(\nu,v)\cdot\partial_{z_a}\underline{G}_I^{\mathrm{s}}(h,\mathbf{R}_a,\omega)+\mathrm{i}\underline{S}_+^{\mathrm{as}}(\nu,v)\cdot\partial_{z_a}\underline{G}_R^{\mathrm{as}}(h,\mathbf{R}_a,\omega)\right]}{\nu-(\omega-hv)}, \end{aligned} \tag{3.41}$$

where $\underline{G}_{\Re} = (\underline{G}+\underline{G}^{\dagger})/2 = \underline{G}_R^{\mathrm{s}} + \mathrm{i}\underline{G}_I^{\mathrm{as}}$ and we define the even (+) and odd (−) part of the particle's power spectrum with respect to its frequency argument

$$\underline{S}_{\pm}(\nu,v) = \underline{S}(\nu,v) \pm \underline{S}(-\nu,v). \tag{3.42}$$

Although Eq. (3.41) displays a fairly lengthy structure, it reveals that, in order to fully integrate the principal value, it will be sufficient to provide information about the even (odd) part of the power spectrum only for the coupling to the particle's translational (rotational) degrees of freedom. It is reasonable to assume that the response of the particle to external perturbations

is approximately linear [66]. This enables us to write the particle's dipole operator as

$$\hat{\mathbf{d}}(\omega) \sim \underline{\alpha}(\omega, v)\hat{\mathbf{g}}(\mathbf{r}_a, \omega), \tag{3.43}$$

where we introduce the velocity-dependent atomic polarizability tensor $\underline{\alpha}$ and $\hat{\mathbf{g}}$ denotes any fluctuating electric field that is, in general, evaluated in nonequilibrium at the position of the particle $\mathbf{r}_a$ for given frequency ω. In the previous Section, we already discussed an explicit model leading to the previous relation [Eq. (3.12)] which will later serve as our main example (for other examples, see Refs. [43, 162, 484, 485]). However, the consideration is slightly more general since we do not rely on a specific model for the particle's polarizability. The point is that the main criterion we exploit in order to derive the expression for the Casimir-Polder force is the linearity of the system and the information on the microscopic origin of the fluctuating field, may it be either from intrinsic dissipative degrees of freedom of the particle or the open quantum system surrounding the particle, is secondary. For the time being, this is why we chose to change notation here and we will resume with our concrete model from Eq. (3.12) in Sec. 3.3.2. Concretely, we only need that $\underline{\alpha}$ does not depend on $\hat{\mathbf{g}}$ anymore. Also, the polarizability is considered to be real and causal in time domain. It hence fulfills the crossing relation, i.e. $\underline{\alpha}^*(\omega, v) = \underline{\alpha}(-\omega, v)$, for all $v \ll c$, where c is the speed of light.

In the static situation, at $v = 0$, we require that the system can equilibrate tending towards a Gibbs state [171, 172]. Fluctuations are then in exact balance with dissipation and we can compute the power spectrum $4\pi^2\underline{S}(\omega, 0)\delta(\omega + \omega') = \langle\hat{\mathbf{d}}(\omega)\hat{\mathbf{d}}(\omega')\rangle_{v=0}$ by means of the zero-temperature fluctuation-dissipation theorem $\langle\hat{\mathbf{g}}(\mathbf{r}_a, \omega)\hat{\mathbf{g}}(\mathbf{r}_a, \omega')\rangle_{v=0} = 4\pi\hbar\theta(\omega)\underline{G}_{\Im}(\mathbf{r}_a, \omega)\delta(\omega + \omega')$ [32], where $\underline{G}$ is the Green tensor solving the equations of motion connected to $\hat{\mathbf{g}}$ for $v = 0$ and $\theta(\omega)$ denotes the Heaviside function. Upon using the fluctuation-dissipation-relation (FDR) of second kind, i.e. $\underline{\alpha}_{\Im}(\omega) = \underline{\alpha}(\omega)\underline{G}_{\Im}(\mathbf{r}_a, \omega)\underline{\alpha}^\dagger(\omega)$, we obtain $\underline{S}(\omega, 0) = \frac{\hbar}{\pi}\theta(\omega)\underline{\alpha}_{\Im}(\omega)$ with $\underline{\alpha}(\omega, 0) \equiv \underline{\alpha}(\omega)$. Inserting the latter into Eq. (3.39), using Kramers-Kronig relations and performing a Wick rotation (see Chap. 2), we restore the usual expression for the equilibrium Casimir-Polder force

$$F_{\mathrm{CP}} = \frac{\hbar}{2\pi}\int\frac{\mathrm{d}h}{2\pi}\int_0^\infty \mathrm{d}\xi\ \mathrm{Tr}\left[\underline{\alpha}(\mathrm{i}\xi)\cdot\partial_{z_a}\underline{G}(h, \mathbf{R}_a, \mathrm{i}\xi)\right] \tag{3.44}$$

that is widely treated in the literature [56, M3, 74, 112, 138, 143, 486].

In the nonequilibrium case, at $v \neq 0$, the above considerations can only be seen as a limiting scenario. For nonzero velocities, the field $\hat{\mathbf{g}}$ is given in a nonequilibrium state and we cannot directly apply the FDR. However, the assumption that the particle can reach a steady-state in motion of constant velocity in combination with the linear relation of Eq. (3.43) is already a strong enough constraint to the system that the nonequlibrium field can be expressed as a function of equilibrium fields in Fourier space. In accordance with the expansion of the electric vacuum field in Eq. (3.4), we have that

$$\hat{\mathbf{g}}(\mathbf{r}(t), t) = \int\frac{\mathrm{d}\omega}{2\pi}e^{-\mathrm{i}\omega t}\int\frac{\mathrm{d}h}{2\pi}\hat{\mathbf{g}}(h, \mathbf{R}_a, \omega)e^{\mathrm{i}hx_a(t)}. \tag{3.45}$$

Notably, all the information about the dynamics of the system is now encoded in the exponential. The dipole moment of Eq. (3.43) reads $\hat{\mathbf{d}}(\omega) = \underline{\alpha}(\omega, v)\int\frac{\mathrm{d}h}{2\pi}e^{\mathrm{i}hx_a(t)}\hat{\mathbf{g}}(h, \mathbf{R}_a, \omega + hv)$,

where $\hat{\mathbf{g}}$ becomes, in general, wavevector dependent and fulfills the equilibrium FDR in Fourier space, i.e. $\langle\hat{\mathbf{g}}(h,\mathbf{R}_a,\nu)\hat{\mathbf{g}}(h',\mathbf{R}_a,\nu')\rangle = 2\hbar(2\pi)^2\theta(\nu)\underline{G}_{\Im}(h,\mathbf{R}_a,\nu)\delta(\nu+\nu')\delta(h+h')$. Again, $\underline{G}$ is the, now wavevector dependent, linear susceptibility solving the equations of motion connected to $\hat{\mathbf{g}}$. Further, $\underline{G}$ obeys the crossing relation $\underline{G}(h,\mathbf{R}_a,\omega) = \underline{G}^*(-h,\mathbf{R}_a,-\omega)$. In this case, the power spectrum in dynamic nonequilibrium reads $\underline{S}(\omega,v) = \frac{\hbar}{\pi}\int\frac{\mathrm{d}h}{2\pi}\theta(\omega+hv)\underline{\alpha}(\omega,v)\cdot\underline{G}_{\Im}(h,\mathbf{R}_a,\omega+hv)\cdot\underline{\alpha}^\dagger(\omega,v)$. Upon employing the FDR of second kind, $\underline{\alpha}_{\Im}(\omega,v) = \int\frac{\mathrm{d}h}{2\pi}\underline{\alpha}(\omega,v)\cdot\underline{G}_{\Im}(h,\mathbf{R}_a,\omega+hv)\cdot\underline{\alpha}^\dagger(\omega,v)$, we can write the full atomic power spectrum as [53]

$$\underline{S}(\omega,v) = \frac{\hbar}{\pi}\theta(\omega)\underline{\alpha}_{\Im}(\omega,v) + \underline{J}(\omega,v), \tag{3.46}$$

where vanishing motion of the particle restores the equilibrium FDR and we explicitly separate the nonequilibrium (non-LTE) contribution [487]

$$\underline{J}(\omega,v) = \underline{J}^\dagger(\omega,v) \to 0, \qquad \text{if } v\to 0. \tag{3.47}$$

We depict a sketch of the separation in LTE and non-LTE terms in the fluctuation-dissipation relation of Eq. (3.46) in Fig. 3.5. Interestingly, we can also show that the nonequilibrium contributions fulfill the crossing relation

$$\underline{J}(\omega,v) = \underline{J}^*(-\omega,v) \tag{3.48}$$

which, in our case, is a direct consequence of the nonequilibrium steady-state and the linear behavior of the particle's polarizability with respect to perturbations. Since we are working in the linear regime, Eq. (3.46) resembles classical nonequilibrium fluctuation-dissipation relations as, e.g., reported in Refs. [428, 488, 489]. Recall that the separation of translational and rotational degrees of freedom (connected to the symmetric/skew-symmetric part of $\underline{G}$) translates in the Casimir-Polder force to the odd/even part of the power spectrum [see Eq. (3.41)]. Using the nonequilibrium fluctuation-dissipation relation of Eq. (3.46), the latter reduce to

$$\underline{S}^{\mathrm{s}}_{-}(\omega,v) = \frac{\hbar}{\pi}\left[\underline{\alpha}^{\mathrm{s}}_I(\omega,v) + \underline{J}^{\mathrm{s}}_R(\omega,v) - \underline{J}^{\mathrm{s}}_R(-\omega,v)\right] = \frac{\hbar}{\pi}\underline{\alpha}^{\mathrm{s}}_I(\omega,v), \tag{3.49a}$$

$$\underline{S}^{\mathrm{as}}_{+}(\omega,v) = -\mathrm{i}\frac{\hbar}{\pi}\left[\underline{\alpha}^{\mathrm{as}}_R(\omega,v) - \underline{J}^{\mathrm{as}}_I(\omega,v) - \underline{J}^{\mathrm{as}}_I(-\omega,v)\right] = -\mathrm{i}\frac{\hbar}{\pi}\underline{\alpha}^{\mathrm{as}}_R(\omega,v), \tag{3.49b}$$

where the non-LTE contributions cancel due to Eq. (3.48). Upon inserting into Eq. (3.41), we can evaluate the Cauchy principal value by means of the (generalized) Kramers-Kronig relations [Eq. (3.10)] and obtain for the dynamic Casimir-Polder force

$$\begin{aligned} F_{\mathrm{CP}} = \frac{\hbar}{2\pi}\int\frac{\mathrm{d}h}{2\pi}\Bigg(&\mathrm{Im}\int_0^\infty \mathrm{d}\omega\ \mathrm{Tr}\left[\underline{\alpha}(\omega-hv,v)\cdot\partial_{z_a}\underline{G}^{\mathrm{T}}(h,\mathbf{R}_a,\omega)\right] \\ &-\mathrm{Re}\int_0^{hv}\mathrm{d}\omega\ \mathrm{Tr}\left[\underline{\alpha}_{\Im}(\omega-hv,v)\cdot\partial_{z_a}\underline{G}_{\Re}(h,\mathbf{R}_a,\omega)\right] \\ &+2\mathrm{Re}\int_{-\infty}^{hv}\mathrm{d}\omega\ \mathrm{Tr}\left[\underline{J}(hv-\omega,v)\cdot\partial_{z_a}\underline{G}^{\mathrm{T}}_{\Re}(h,\mathbf{R}_a,\omega)\right]\Bigg). \end{aligned} \tag{3.50}$$

In its closed form, Eq. (3.50) has, to the best of our knowledge, not been reported in the literature yet. In combination with the different representations we will deduce in the following, Eq. (3.50) represents the main result of the present Section. While the first two terms of Eq. (3.50) would have also emerged within the LTE approximation ($\underline{S} \propto \underline{\alpha}_{\Im}$), the last term takes full account of dynamical nonequlibrium effects ($\underline{S} \propto \underline{J}$). Furthermore, Eq. (3.50) allows for rotations of the particle that occur due to the interaction with the vacuum field [M1] (see previous Section). Within the assumptions of the formalism, Eq. (3.50) is obtained non-perturbatively and can considered to be exact. It includes the full renormalization of the bare atomic resonances due to the interaction with the environment and is valid in arbitrary order of the atom-surface coupling ($\propto \alpha_0$). In particular, in contrast to equilibrium-based approaches that scale in first order $F_{\mathrm{CP}} \sim \mathcal{O}(\alpha_0)$ [43], our result reveals that proper non-LTE (nonequilibrium) effects contribute in second order $F_{\mathrm{CP}} \sim \mathcal{O}(\alpha_0^2)$ since $\underline{J} \sim \mathcal{O}(\alpha_0^2)$.

In order to assess the concurrence with related results in the literature, we can simplify Eq. (3.50) by imposing additional constraints. Consider first a *symmetric* two-time correlation tensor $C_{ij}(\tau, v) = \langle \hat{d}_i(\tau)\hat{d}_j(0)\rangle = C_{ji}(\tau, v)$ selecting only the real, symmetric part of the particle's power spectrum $\underline{S} = \underline{S}^{\mathrm{s}}_R$. This corresponds to neglecting the atom's rotational degrees of freedom [58]: We reduce the three-dimensional structure of the dipole operator $\hat{\mathbf{d}}$ to a single quantum degree of freedom $\hat{\mathbf{d}} \to \mathbf{d}\hat{q}$ which forces the dipole to be static in space (see discussion at the beginning of Sec. 3.2). In the symmetric situation, the Casimir-Polder force reads

$$\begin{aligned} F_{\mathrm{CP}} = \frac{\hbar}{2\pi}\int \frac{\mathrm{d}h}{2\pi}\Bigg(&\mathrm{Im}\int_0^\infty \mathrm{d}\omega\ \mathrm{Tr}\left[\underline{\alpha}^{\mathrm{s}}(\omega - hv, v)\cdot\partial_{z_a}\underline{G}^{\mathrm{s}}(h, \mathbf{R}_a, \omega)\right] \\ &- 2\theta(h)\int_0^{hv}\mathrm{d}\omega\ \mathrm{Tr}\left[\underline{\alpha}^{\mathrm{s}}_I(\omega - hv, v)\cdot\partial_{z_a}\underline{G}^{\mathrm{s}}_R(h, \mathbf{R}_a, \omega)\right] \\ &+ 2\theta(h)\int \mathrm{d}\omega\ \mathrm{Tr}\left[\underline{J}^{\mathrm{s}}_R(hv - \omega, v)\cdot\partial_{z_a}\underline{G}^{\mathrm{s}}_R(h, \mathbf{R}_a, \omega)\right]\Bigg). \end{aligned} \tag{3.51}$$

If we additionally neglect the term $\underline{J}^{\mathrm{s}}_R \to 0$, consider the polarizability in lowest order α_0, ignore the tensor structure of the polarizability as well as its velocity-dependence ($\underline{\alpha}(\omega, v) \sim \alpha(\omega)$) and focus on planar geometries $\mathrm{d}h/2\pi \to \mathrm{d}^2\mathbf{p}/(2\pi)^2$, Eq. (3.51) contains the result obtained by Kyasov and Dedkov as a special case [43, 479–481].

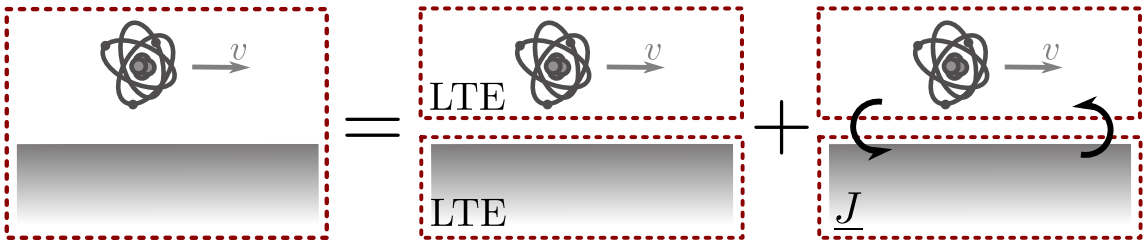

Figure 3.5: The statistics of a open quantum system in nonequilibrium is inseparably intertwined with the environment. For linear systems, this can be decomposed into a contribution that assumes Local Thermal Equilibrium (LTE) and a non-LTE contribution ($\underline{J}$) [Eq. (3.46)]. The commonly used assumptions of LTE considers the first term only.

3.3.2 Low-velocity correction for atoms

We now specify the general result of Eq. (3.50) to our particular model for the particle's dynamics introduced in Sec. 3.1. Further, we consider the experimentally relevant limit of an atom at low velocities and discuss the case of an atom in front of a semi-infinite half-space made from a spatially local, conducting material. To this end, we ignore possible internal dissipative degrees of freedom of the particle ($\underline{\mu} = 0$), replace the generic fluctuating quantum field operator $\hat{\mathbf{g}} \to \int \frac{\mathrm{d}h}{2\pi} \hat{\mathbf{E}}_{\mathrm{N}}(h, \mathbf{R}_a, \omega) \exp[\mathrm{i}x_a h]$, identify the Green tensor $\underline{G}$ with the electric Green tensor introduced in Chapter 1 and employ the relation for the atom's polarizability of Eq. (3.18). Inserting the atomic model into Eq. (3.50), the Casimir-Polder force $F_{\mathrm{CP}} = F^{\mathrm{e}}_{\mathrm{CP}} + F^{\mathrm{ne}}_{\mathrm{CP}}$ in dynamical nonequilibrium can be written as the sum of two contributions. First, a version of the equilibrium term with Doppler-shifted atomic polarizability [see Eq. (3.44)],

$$F^{\mathrm{e}}_{\mathrm{CP}} = \frac{\hbar}{2\pi} \mathrm{Im} \int \frac{\mathrm{d}h}{2\pi} \int_0^\infty \mathrm{d}\omega \ \mathrm{Tr} \left[\underline{\alpha}(\omega - hv, v) \cdot \partial_{z_a} \underline{G}^{\mathrm{T}}(h, \mathbf{R}_a, \omega) \right]. \tag{3.52}$$

Second, a nonequilibrium correction where both the frequency domain and the integral kernel are connected to the Doppler-shift, i.e.

$$\begin{aligned} F^{\mathrm{ne}}_{\mathrm{CP}} = \frac{\hbar}{2\pi} \mathrm{Re} \int \frac{\mathrm{d}h}{2\pi} \frac{\mathrm{d}\tilde{h}}{2\pi} \int_{-\infty}^{hv} \mathrm{d}\omega \qquad & (3.53) \\ \times \left[\underline{\alpha}(\omega - hv, v) \cdot \ \underline{G}_{\Im}(\tilde{h}, \mathbf{R}_a, \omega + [\tilde{h} - h]v) \cdot \underline{\alpha}^{\dagger}(\omega - hv, v) \right]_{jk} \\ \times \partial_{z_a} \left[-\underline{G}_{\Re}(h, \mathbf{R}_a, \omega)\theta(\omega) + 2\underline{G}^{\mathrm{T}}_{\Re}(h, \mathbf{R}_a, \omega) \left\{ \theta(\omega + [\tilde{h} - h]v) - \theta(\omega - hv) \right\} \right]_{kj}. \end{aligned}$$

We sum over the matrix indices $j, k = x, y, z$ and note that the partial derivative with respect to the atom-surface separation is acting explicitly on $\underline{G}_{\Re}$ only [see discussion below Eq. (3.39)]. The first part of previous expression ($\propto -\underline{G}_{\Re}$) could have been equally obtained within the LTE approximation. The second part ($\propto 2\underline{G}^{T}_{\Re}$), however, is a pure non-LTE result connected to $\underline{J}$. In order to extract the leading-order dynamics in the atomic dipole moment (related to its vacuum polarizability α_0), we first note that we can evaluate the θ-function in Eq. (3.53) using that

$$\begin{aligned} & \int \mathrm{d}\tilde{h} \left[\theta(\omega' + \tilde{h}v) - \theta(\omega') \right] \mathrm{Tr} \left[\underline{G}_{\Im}(\tilde{h}, \mathbf{R}_a, \omega' + \tilde{h}v) \cdot \underline{G}^{\mathrm{T}}_{\Re}(h, \mathbf{R}_a, \omega) \right] \qquad (3.54) \\ & = \int \mathrm{d}\tilde{h} \ \theta(\tilde{h}v - |\omega'|) \\ & \times \left\{ \mathrm{Tr} \left[\underline{G}^{\mathrm{s}}_I(\tilde{h}, \mathbf{R}_a, \tilde{h}v - |\omega'|) \cdot \underline{G}^{\mathrm{s}}_R(h, \mathbf{R}_a, \omega) \right] + \frac{\omega'}{|\omega'|} \mathrm{Tr} \left[\underline{G}^{\mathrm{as}}_R(\tilde{h}, \mathrm{R}_a, \tilde{h}v - |\omega'|) \cdot \underline{G}^{\mathrm{as}}_I(h, \mathbf{R}_a, \omega) \right] \right\}. \end{aligned}$$

The emerging modulus can then be solved with the help of the relation

$$\int \mathrm{d}\tilde{h} \int_{-\infty}^{hv} \mathrm{d}\omega \ \theta(\tilde{h}v - |\omega - hv|) = \int \mathrm{d}\tilde{h} \int_{[h-\tilde{h}]v}^{hv} \mathrm{d}\omega \ \theta(\tilde{h}). \tag{3.55}$$

Next, we recall that the symmetric (skew-symmetric) part of the atomic polarizability scales in first (second) order of the vacuum polarizability α_0 [Eq. (3.21)]. From the same consideration, we note that the (complex) resonance shift $\underline{\Delta}$ related to the material-vacuum interface becomes sub-leading with respect to the resonance frequency ω_a and the non-isotropic behavior of the atomic response enters first in second order of the vacuum polarizability. This means that, in leading order α_0, $F_{\mathrm{CP}}^{\mathrm{e}}$ is practically unaffected by the atom's rotational degrees of freedom. Consequently, up to second order in the polarizability, we can write

$$F_{\mathrm{CP}}^{\mathrm{e}} = \frac{\hbar}{2\pi}\mathrm{Im}\int\frac{\mathrm{d}h}{2\pi}\int_0^\infty \mathrm{d}\omega\ \alpha(\omega-hv)\mathrm{Tr}\left[\left\{1+\alpha(\omega-hv)\underline{\Delta}(\omega-hv,v)\right\}\cdot\partial_{z_a}\underline{G}^{\mathrm{T}}(h,\mathbf{R}_a,\omega)\right]. \tag{3.56}$$

For $F_{\mathrm{CP}}^{\mathrm{ne}}$, on the contrary, the motion-induced asymmetry in the system allows the non-diagonal parts of the Green tensor to couple in a way that both the atom's translational and rotational degrees of freedom contribute dominantly. Indeed, in leading order, the nonequilibrium contribution to the dynamical Casimir-Polder force scales quadratically in α_0 and derives from the symmetric as well as the skew-symmetric parts of the Green tensor, i.e.

$$\begin{aligned} F_{\mathrm{CP}}^{\mathrm{ne}} &= -\frac{\hbar}{\pi}\mathrm{Tr}\int\frac{\mathrm{d}h}{2\pi}\frac{\mathrm{d}\tilde{h}}{2\pi} \\ &\times\left(\frac{1}{2}\int_0^{hv}\mathrm{d}\omega\ |\alpha(\omega-hv)|^2\left[\underline{G}_I^{\mathrm{s}}(\tilde{h},\omega+\delta_h v)\cdot\partial_{z_a}\underline{G}_R^{\mathrm{s}}(h,\omega)+\underline{G}_R^{\mathrm{as}}(\tilde{h},\omega+\delta_h v)\cdot\partial_{z_a}\underline{G}_I^{\mathrm{as}}(h,\omega)\right]\right. \\ &\left.-\int_{-\delta_h v}^{hv}\mathrm{d}\omega\ \theta(\tilde{h})|\alpha(\omega-hv)|^2\left[\underline{G}_I^{\mathrm{s}}(\tilde{h},\omega+\delta_h v)\cdot\partial_{z_a}\underline{G}_R^{\mathrm{s}}(h,\omega)-\underline{G}_R^{\mathrm{as}}(\tilde{h},\omega+\delta_h v)\cdot\partial_{z_a}\underline{G}_I^{\mathrm{as}}(h,\omega)\right]\right). \end{aligned} \tag{3.57}$$

To shorten notation, we skipped the dependence on the atom-surface separation $\mathbf{R}_a$ and defined $\delta_h = \tilde{h} - h$. It is worth emphasizing that, in contrast to $F_{\mathrm{CP}}^{\mathrm{e}}$ which derives from the full frequency range, $F_{\mathrm{CP}}^{\mathrm{ne}}$ is strictly bounded by frequencies related to the atom's velocity. Dynamical nonequilibrium introduces another (Doppler-shifted) frequency scale into the system and its impact decreases for slacking motion. By implication, the possibility of resonant energy transfer between the system and its environment occurs when the Doppler-shift becomes comparable to the resonances (either atomic or material) in the system. This usually is connected to a dramatic change in the velocity-scaling of the corresponding force [53, 236]. Since the corresponding transition velocities are rather high for typical metals ($v/c \gtrsim 10^{-3}$ [M1]), we do not consider this case in full detail here. For practical reasons, however, we are rather interested in comparably small velocities (much smaller than the corresponding resonances) since they are most likely to be achieved in experiments (see Chapter 5). In the form of Eqs. (3.52), (3.56) and (3.57), the low-velocity expansion can be performed readily. From Eq. (3.52), we obtain in leading order of the vacuum polarizability

$$F_{\mathrm{CP}}^{\mathrm{e}} \sim \frac{\hbar}{2\pi}\partial_{z_a}\mathrm{Im}\int\frac{\mathrm{d}h}{2\pi}\int_0^\infty\mathrm{d}\omega\left(\alpha(\omega)+v^2\frac{h^2}{2}\alpha''(\omega)\right)\mathrm{Tr}\left[\underline{G}(h,\mathbf{R}_a,\omega)\right]+\mathcal{O}(\alpha_0^2). \tag{3.58}$$

Here, the prime indicates a derivative with respect to frequency and we omitted terms of the order $\mathcal{O}(\alpha_0^2)$ (see Eq. (3.62) for an explicit expression). We note that expanding the force in orders of α_0, the dressing of the particle's polarizability due to the material-modified vacuum becomes subleading such that we could use the funtion $\alpha(\omega)\mathbb{1} \equiv \underline{\alpha}_{\mu=0}(\omega)$ defined below Eq. (3.9). The leading-order correction in the atom's velocity is quadratic as one could have expected from the symmetries of the system; changing the direction of motion should not influence the force perpendicular to the surface. From Eq. (3.53), on the other hand, we obtain

$$F_{\mathrm{CP}}^{\mathrm{ne}} \sim \alpha_0^2 v^2 \frac{\hbar}{2\pi} \int \frac{\mathrm{d}h}{2\pi} \frac{\mathrm{d}\tilde{h}}{2\pi} \tag{3.59}$$
$$\times \operatorname{Tr}\left[\left\{ \frac{h^2}{2} + \tilde{h}^2 \theta(\tilde{h}) \right\} \underline{G}_I^{s\prime}(\tilde{h}, \mathbf{R}_a, 0) \cdot \partial_{z_a} \underline{G}_R^{s}(h, \mathbf{R}_a, 0) - \tilde{h} h \underline{G}_R^{\mathrm{as}\prime}(\tilde{h}, \mathbf{R}_a, 0) \cdot \partial_{z_a} \underline{G}_I^{\mathrm{as}}(h, \mathbf{R}_a, 0) \right],$$

where we assumed Ohmic materials, i.e. a linear scaling of the Green tensor's imaginary part for small frequencies (true for most common materials, see Sec. 1.2). In the second line of the previous equation, the first term in the curly brackets corresponds to the LTE approximation and the second term is a consequence of the non-LTE contribution to the fluctuation-dissipation-relation [see Eq. (3.46)]. The last term of Eq. (3.59), however, is solely connected to the LTE approximation when the velocity-dependent dressing of the atom due to the material interface is included; the corresponding non-LTE term evaluates to exactly zero. This has an interesting consequence when we recall that the symmetric and the skew-symmetric part of the Green tensor couple to the translational and the rotational degrees of freedom via the atomic power spectrum, respectively. Since the last term in Eq. (3.59) is given by the skew-symmetric part of the Green tensor only and we could argue that it derives solely from the LTE contribution of the power spectrum [$\underline{S} \sim \underline{\alpha}_{\Im}$], we conclude that the rotational degrees of freedom in the evaluation of the force are unaffected by the non-LTE contributions of the power spectrum [$\underline{S} \sim \underline{J}$].

Especially for small velocities, the importance of small frequencies, or large correlation times, for the nonequilibrium Casimir-Polder force becomes evident: While $F_{\mathrm{CP}}^{\mathrm{e}}$ derives from the full spectrum of resonances in the system, F_{CP}^{ne} is related to frequencies $\omega \to 0$. Interestingly, as a consequence we have that $F_{\mathrm{CP}}^{\mathrm{e}}$ can be interpreted as originating from the direct interaction between the atom and the bulk in leading order α_0, i.e. $F_{\mathrm{CP}}^{\mathrm{e}} \propto \alpha_0 \underline{G}$. $F_{\mathrm{CP}}^{\mathrm{ne}}$, on the other hand, is in leading order α_0 already quadratic in the electric Green tensor, $F_{\mathrm{CP}}^{\mathrm{ne}} \propto \underline{G}_{I/R}^{s/\mathrm{as}\prime}(\tilde{h}, \mathbf{R}_a, 0) \cdot \underline{G}_{R/I}^{s/\mathrm{as}}(h, \mathbf{R}_a, 0)$. Since we related the quadratic scaling in the Green tensor to the environment-induced dressing of the particle's polarizability, $F_{\mathrm{CP}}^{\mathrm{ne}}$ can be interpreted as originating from a more subtle mechanism: At zero frequency, the real part of the Green tensor can physically be related to the reflective properties of the surface, while its imaginary part (at all frequencies) is connected to any form of dissipation in the electromagnetic environment [147]. Eq. (3.59) couples reflection and dissipation via the interaction with the atom to form a distance-dependent force. In other words, $F_{\mathrm{CP}}^{\mathrm{ne}}$ can be understood as the back-action of the material-modified electromagnetic field on itself mediated by the atom [M2, P3, M6]. We report a schematic visualization of the two contributions to the nonequilibrium Casimir-Polder force in Fig. 3.6.

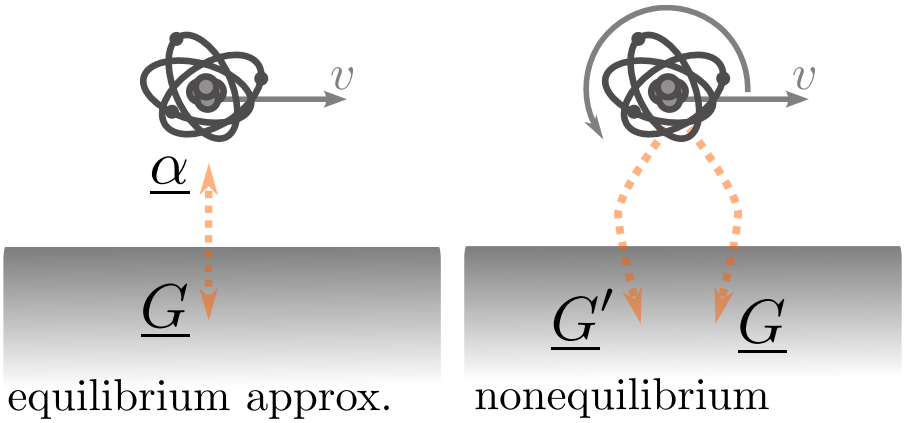

Figure 3.6: A particle ($\underline{\alpha}$) moving at velocity v in the vicinity of a macroscopic body ($\underline{G}$) [Eq. (3.50)]. We obtain two contributions to the atom-surface force given by Eqs. (3.58) and (3.59), respectively. **Left:** One contribution stems from the direct interaction between atom and surface, derives in first order of the atom's polarizability and is a broadband-phenomenon (large range of frequencies contributes). **Right:** The other contribution can be connected to an interaction of the surface with itself ($\underline{G} \leftrightarrow \underline{G}'$) mediated by the atom (see main text). It includes rotations of the atom and scales in second order of the atom's polarizability.

Semi-infinite half space

In order to gain a more quantitative insight, we consider once again the explicit expression for the Green tensor of a planar interface separating vacuum from an infinitely extended half space in the near-field regime [Eq. (1.51)]. For the scattered part of the Green tensor, we again replace our general description with the coordinates appropriate for a planar interface, $\mathrm{d}h/2\pi \to \mathrm{d}^2\mathbf{p}/(2\pi)^2$ such that the relevant symmetric and skew-symmetric part of the scattered Green tensor read [189]

$$\underline{G}^{\mathrm{s}}(\mathbf{p}, z_a, \omega) = \frac{p}{2\epsilon_0} r\, e^{-2pz_a} \mathrm{diag}\left[\frac{p_x^2}{p^2}, \frac{p_y^2}{p^2}, 1\right], \qquad \underline{G}^{\mathrm{as}}(\mathbf{p}, z_a, \omega) = -\frac{p_x}{2\epsilon_0} r\, e^{-2pz_a} \underline{L}_y, \tag{3.60}$$

where $\mathrm{diag}[\cdot,\cdot,\cdot]$ gives a diagonal matrix, $r \equiv r_{\mathrm{NF}}^{p} = (\epsilon(\omega)-1)/(\epsilon(\omega)+1)$ is the near-field approximation of the interface's transverse magnetic reflection coefficient and we use the Drude model $\epsilon(\omega) = 1 - \omega_{\mathrm{p}}^2/[\omega(\omega + \mathrm{i}\Gamma)]$ (see Chap. 1) for simplicity. Upon inserting the Green tensor into Eq. (3.58), we recover the result for the Casimir-Polder force in dynamical nonequilibrium reported by Dedkov and Kyasov [43] in leading order of the atom's polarizability

$$F_{\mathrm{CP}}^{\mathrm{e}} = -\frac{3\hbar}{16\pi^2}\frac{\alpha_0}{\epsilon_0}\frac{1}{z_a^4}\int_0^\infty \mathrm{d}\xi\, \frac{\epsilon(\mathrm{i}\xi)-1}{\epsilon(\mathrm{i}\xi)+1}\left(\frac{\omega_a^2}{\omega_a^2+\xi^2} + \frac{5}{2}\frac{v^2\omega_a^2}{z_a^2}\frac{\omega_a^2-3\xi^2}{(\omega_a^2+\xi^2)^3}\right) + \mathcal{O}(\alpha_0^2). \tag{3.61}$$

In the previous line we exploited that the involved functions are analytical in the upper complex frequency plane in order to perform a Wick rotation replacing $\omega \to \mathrm{i}\xi$ with $\xi \geq 0$ [138]. In next-to-leading order, their result is corrected by

$$\mathcal{O}(\alpha_0^2) = -\frac{9\hbar}{8\pi^3}\frac{1}{\epsilon_0^2}\frac{1}{(2z_a)^7}\int_0^\infty \mathrm{d}\xi\; r^2\alpha^2\left(1+\frac{v^2}{2z_a^2}\left[5\frac{\alpha'^2}{\alpha^2}+6\frac{r'}{r}\frac{\alpha'}{\alpha}+2\frac{r''}{r}+5\frac{\alpha''}{\alpha}\right]\right), \tag{3.62}$$

where the prime, again, denotes the derivative with respect to the real frequency ω and both the reflection coefficient and the atomic polarizability are afterwards evaluated at imaginary frequencies, i.e. $\alpha = \alpha(\omega) \to \alpha(\mathrm{i}\xi)$ and $r \to r(\mathrm{i}\xi)$. The force is attractive towards the surface [21] and scales in leading order with the atom-surface separation as $\propto z_a^{-4}$. Note that $F_{\mathrm{CP}}^{\mathrm{e}}$ expands over the full range of frequencies and considers every resonance in the system such that the Casmir-Polder force remains finite even for vanishing dissipation rate $\Gamma \to 0$, i.e.

$$\begin{aligned} F_{\mathrm{CP}}^{\mathrm{e}} = &-\frac{3\hbar}{2\pi}\frac{\alpha_0}{\epsilon_0}\frac{\omega_a}{(2z_a)^4}\frac{1}{1+\delta\omega} \\ &\times\left[\left(1+10\frac{v^2}{\omega_{\mathrm{sp}}^2(2z_a)^2}\frac{1}{(1+\delta\omega)^2}\right)+\frac{3}{16\pi}\frac{\alpha_0}{\epsilon_0(2z_a)^3}\frac{1+3\delta\omega+\delta\omega^2}{(1+\delta\omega)^2}\left(1+\frac{v^2}{\omega_{\mathrm{sp}}^2(2z_a)^2}f\right)\right] \end{aligned} \tag{3.63}$$

with $\delta\omega = \omega_a/\omega_{\mathrm{sp}}$, $\omega_{\mathrm{sp}} = \omega_{\mathrm{p}}/\sqrt{2}$ the surface plasmon-polariton frequency and the positive constant

$$f = 2\frac{8+40\delta\omega+16\delta\omega^2+5\delta\omega^3+\delta\omega^4}{(1+\delta\omega)^2(1+3\delta\omega+\delta\omega^2)}. \tag{3.64}$$

The prefactor in Eq. (3.63) is the well-known limit of the dissipation-less Casimir-Polder force in the near-field, the first term in the brackets is the finite-velocity correction obtained by assuming LTE and/or second order perturbation in the atomic dipole moment [43] and the last term in the brackets is our higher order correction in $\mathcal{O}(\alpha_0^2)$. Interestingly, every order in α_0 carries corrections in order $\mathcal{O}(v^2)$ in addition to the constant contribution $\mathcal{O}(v^0)$ with respect to velocity. Further, we note that every combination of α_0 and v comes with a different distance law. In combination with the involved dependency on $\delta\omega$ of each prefactor, it is not necessarily obvious how the corrections impact the force quantitatively whithout specifying the system. Focusing on atoms from the alkali metal group and a good conductor as the material of the interface, the corrections turn indeed out to be small at reasonably distances. Indeed, choosing a rubidium atom in front of a gold surface, we have that $\delta\omega \lesssim 1$ [140, 142] which further enables us to neglect contributions at the order of $\mathcal{O}(\delta\omega^2)$. Since, in the near-field, we consider distances $z_a \ll 2\pi c/\omega_a$ [M3] and we further have from validity arguments of our theory that $\alpha_0/(\epsilon_0 z_a^3) \ll 1$ (see Chap. 1), we can easily see that the corrections, in this particular case, are many orders of magnitude smaller than the equilibrium contribution to the Casimir-Polder interaction. We lastly note that, for a finite dissipation rate $\Gamma > 0$, the Casimir-Polder force is reduced with respect to the expression given in Eq. (3.63).

For the nonequilibrium contribution [Eq. (3.59)], only the low-frequency regime of the material's optical response is relevant. The transverse magnetic reflection coefficient below the plasmonic resonance reads $r \sim 1+2\mathrm{i}\epsilon_0\rho_{\mathrm{lc}}\omega+\mathcal{O}(\omega^2)$ with the constant local dissipation $\rho_{\mathrm{lc}} = \Gamma/(\epsilon_0\omega_{\mathrm{p}}^2)$ which, in the case of a Drude metal, can be identified with the material's resistivity. Combining with Eq. (3.59) yields

$$F_{\mathrm{CP}}^{\mathrm{ne}} = -F_{\mathrm{CP}}^{r} = -\hbar\frac{9}{\pi^3}\frac{\alpha_0^2 v^2 \rho_{\mathrm{lc}}}{\epsilon_0}\frac{1}{(2z_a)^9}, \tag{3.65}$$

where F_{CP}^{r} denotes the contribution to the force originating from the rotational degrees of freedom which are connected to the skew-symmetric part of the Green tensor. The force F_{CP}^{t} one would have obtained by ignoring the rotational degrees of freedom and regarding the translational ones only would be twice as strong as $F_{\mathrm{CP}}^{\mathrm{ne}}$ in Eq. (3.65), i.e. $|F_{\mathrm{CP}}^{t}| = 2|F_{\mathrm{CP}}^{\mathrm{r}}|$. We hence find that the particle's rotational degrees of freedom tend to reduce the strength of $F_{\mathrm{CP}}^{\mathrm{ne}}$ in simple geometries with a non-zero spin local density of states. For the planar setup, in accordance with the more general result of Eq. (3.59), the two terms connected to the LTE approximation, one related with translation and the other related to rotations of the atom, partially compensate each other. Rotational degrees of freedom play a rather subtle, but vital role in the evaluation of $F_{\mathrm{CP}}^{\mathrm{ne}}$: The rotation itself is instigated by the mere interaction of the moving particle with the material-modified quantum vacuum, such that the precise value of $F_{\mathrm{CP}}^{\mathrm{ne}}$ turns out to be quite sensitive with respect to properly including to the back-action of the environment onto the system. Hence, equation (3.65) strongly depends the motion-induced nonequilibrium correlations in the system and can only be covered in part by the application of equilibrium techniques. In this way, our results contrast related works, where particle rotations are *imposed* externally and, for example, lateral Casimir forces with respect to material interfaces can appear [45, 490].
As expected, the contribution of the Casimir-Polder force connected to nonequilibrium is a dynamic phenomenon only since $F_{\mathrm{CP}}^{\mathrm{ne}} \propto v^2$. More interestingly, it is immanently connected to dissipation in the material as $F_{\mathrm{CP}}^{\mathrm{ne}} \propto \rho_{\mathrm{lc}}$. In contrast to Eq. (3.63), it vanishes in the limit $\rho_{\mathrm{lc}} \to 0$ and *increases linearly* with growing dissipation. We further note that, since $F_{\mathrm{CP}}^{\mathrm{e}} \propto \alpha_0/z_a^4$ and $F_{\mathrm{CP}}^{\mathrm{ne}} \propto \alpha_0^2/z_a^9$, the non-LTE contribution is quantitatively sub-leading for the configuration considered here; which explains the wide success of the LTE approximation in the context of nonequilibrium Casimir-Polder forces. However, the qualitative difference in scaling with respect to dissipation in the bulk material, $F_{\mathrm{CP}}^{\mathrm{e}}$ being decreased and $F_{\mathrm{CP}}^{\mathrm{ne}}$ being increased, hints to the possible design of more sophisticated setups, where this quantitative discrepancy is weakened. For instance, we can think of putting the atom inside a planar cavity. When both sides of the cavity are made from exactly the same material, the total Casimir-Polder force will vanish at the cavity's center due to symmetry reasons. If the planes of the cavity show slightly different material properties, this exceptional point will be displaced towards the plate with smaller dissipation if connected to $F_{\mathrm{CP}}^{\mathrm{e}}$ and towards the plate with larger dissipation when connected to $F_{\mathrm{CP}}^{\mathrm{ne}}$, respectively. In this way, it is theoretically possible to present the contribution to the Casimir-Polder force of Eq. (3.65) more prominently for at least one distinguished point inside the cavity.

3.3.3 Thermal interpretation in terms of the atomic power spectrum

From a general perspective, Eq. (3.65) represents the force arising from the low-frequency interactions; that is to say the long-term correlations in the system. The assumption of LTE, on the other hand, demands sufficiently short correlation times between separated subsystems and amounts to neglecting exactly the latter contributions. Mathematically, this difference is encoded in the nonequilibrium fluctuation-dissipation relation of Eq. (3.46). For the time being, we concentrate on the planar interface described by a Drude model in the near-field regime for clarity of arguments, but the following discussion applies similarly to more general situations. At zero velocity, the power spectrum reduces to the usual FDR and vanishes for small frequencies

$$\underline{S}(\omega,0)=\frac{\hbar}{\pi}\theta(\omega)\underline{\alpha}_{\Im}(\omega)\overset{\omega\to 0}{\to}0, \qquad \underline{J}(\omega,0)=0, \tag{3.66}$$

due to the properties of the Green tensor's imaginary part [see FDR of second kind above Eq. (3.46)]. In other words, for smaller and smaller frequencies, the accessible power of (fluctuating) excitations in the systems shrinks, eventually going to zero. For finite velocities $0<v\lesssim\omega_{\mathrm{p}}z_a,\omega_{\mathrm{a}}z_a$, however, we obtain in leading order α_0 for the power spectrum

$$\underline{S}(\omega\to 0,v)\sim\frac{\hbar}{\pi}\alpha_0^2\int\frac{\mathrm{d}^2\mathbf{p}}{(2\pi)^2}\theta(p_x)\underline{G}_{\Im}(\mathbf{p},z_a,p_xv)\sim\alpha_0^2\frac{2\rho_{\mathrm{lc}}}{\pi^3}\frac{\hbar|v|}{(2z_a)^4}\begin{pmatrix}1&0&-\mathrm{i}\frac{v}{|v|}\frac{3\pi}{8}\\0&\frac{1}{2}&0\\\mathrm{i}\frac{v}{|v|}\frac{3\pi}{8}&0&\frac{3}{2}\end{pmatrix}. \tag{3.67}$$

The symmetries of the power spectrum with respect to tensorial components ($\underline{S}=\underline{S}^{\dagger}$) directly translate into the direction of motion: While its symmetric components are completely unaffected by the direction of motion ($\propto|v|$), its asymmetric components switch sign if the atom moves in opposite direction such that

$$\underline{S}(0,-v)=\underline{S}^{T}(0,v)=\underline{S}^{*}(0,v), \tag{3.68}$$

which can be seen directly from Eq. (3.67). Recalling that the asymmetric tensor components are connected to rotational degrees of freedom of the atom, it becomes evident that the atom can change its sign of rotation if its direction of motion is reversed [M1]. Neglecting $\underline{J}$ and focusing on the assumption of LTE, on the other hand, gives

$$\underline{S}^{\mathrm{LTE}}(0,v)=\lim_{\omega\to 0}\frac{\hbar}{\pi}\theta(\omega)\underline{\alpha}_{\Im}(\omega,v)=2\underline{S}^{\mathrm{as}}(\omega\to 0,v), \tag{3.69}$$

such that only the skew-symmetric parts survive at low frequencies. The impact of dynamic nonequilibrium becomes evident when we compare the previous results with Eq. (3.66). Discarding the simplifications of LTE and incorporating rotational degrees of freedom, we generalize the statistics of the interaction in two different ways: First, by including skew-symmetric components of the Green tensor, the LTE contribution of the power spectrum acquires a velocity-dependent and non-vanishing skew-symmetric part for frequencies $\omega\to 0$ [see Eq.

(3.69)]. It is this extra skew-symmetric contribution that diminishes the force with respect to a corresponding LTE calculation [see discussion below Eq. (3.65)]. Second, by including the nonequilibrium contributions exactly, we add another non-zero term $\underline{J}$ to the power spectrum that has both symmetric and skew-symmetric contributions and quantifies the impact of nonequilbrium statistics in our description [see Eq. (3.67)]. Woven in Eq. (3.57), it is the main responsible part of the interaction leading to the nonequilibrium correction of the force in Eq. (3.65).

We report a numerical evaluation of the different situations [Eqs. (3.66)-(3.69)] in Fig. 3.7. Indeed, the low-frequency behavior of the power spectrum is strongly modified due to the impact of rotations and/or velocity-corrections. For larger frequencies, near the atomic or material resonances, the different situations become indistinguishable, very much resembling our general considerations in Chapter 1. Since Casimir-Polder forces are a broad-band phenomenon explicitly including the resonant frequency regime, this explains the quantitative success of the LTE approximation [see Eq. (3.61)]. Physically, however, studying the (low-frequency) nonequilibrium contribution [Eq. (3.65)] allows insights to the fundamental statistical nature of fluctuation-induced atom-surface interactions which will become most evident in the remainder of this Chapter.

From the qualitative point of view, the motion-modified behavior of the low-frequency power spectrum described above resembles the fluctuating dynamics of thermal systems at small temperature (see also Chap. 2). The appearance of low-frequency fluctuations indicates the existence of constant (motion-induced) fluctuations [428, 489] and it is interesting to note that it occurs in a regime where usually classical (temperature-induced) fluctuations are dominant. Indeed, for quantum systems in equilibrium with their surroundings at temperature T, low frequencies usually correspond to the classical regime [32]. This can be seen from the average equilibrium energy per mode ω,

$$u(\omega,T)=\frac{\hbar\omega}{2}\coth\left[\frac{\hbar\omega}{2k_{\mathrm{B}}T}\right]\sim k_{\mathrm{B}}T, \tag{3.70}$$

which restores the classical (high-temperature) equipartition theorem for $\omega/T\to 0$. If we consider the Casimir-Polder force experienced by a static atom, the corresponding equilibrium fluctuation-dissipation theorem at finite temperature reads (see Eq. (3.9) for definition of $\underline{\Delta}$)

$$\underline{S}(\omega,T)=\frac{\hbar}{\pi}\left(n(\omega,T)+1\right)\underline{\alpha}_I^{\mathrm{Th}}(\omega)\overset{\frac{\hbar\omega}{k_{\mathrm{B}}T}\to 0}{\sim}\frac{k_{\mathrm{B}}T}{\pi\omega}\alpha_0^2\,\underline{\Delta}_I^s(\omega,0) \tag{3.71}$$

which is the famous Nyquist relation [175]. The fluctuations scale linearly in temperature, vanish at zero temperature and hence behave classically. Here, $n(\omega,T)$ gives the Bose occupation number and $\underline{\alpha}_I^{\mathrm{Th}}(\omega)$ is the equivalent of Eq. (3.13) at zero velocity and evaluated in a thermal average [M3, 138]. For small frequencies, we can evaluate Eq. (3.71) in the near-field and obtain

$$\underline{S}(0,T)\sim\alpha_0^2 k_{\mathrm{B}}T\frac{\rho_{\mathrm{lc}}}{16\pi^2 z_a^3}\mathrm{diag}[1,1,2], \tag{3.72}$$

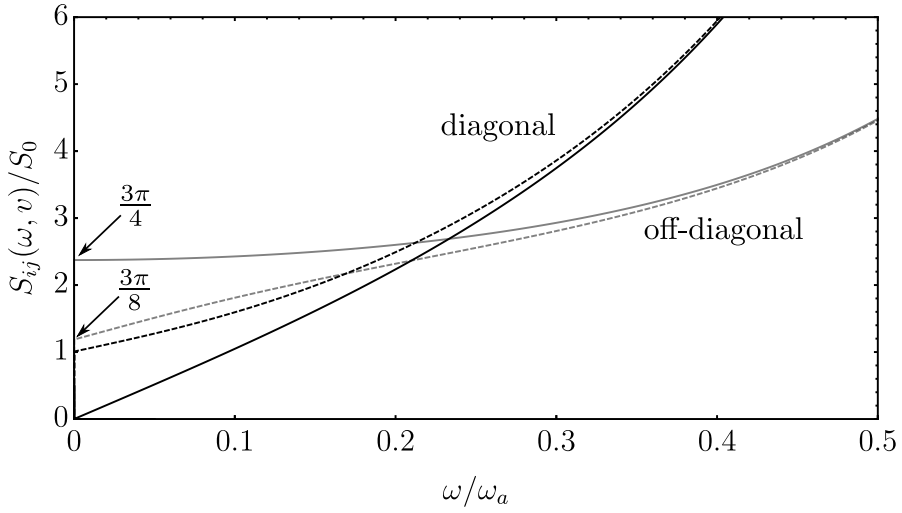

Figure 3.7: Low-frequency behavior of the diagonal (xx-component, black) and the off-diagonal (modulus of xz-component, gray) components of the atomic power spectrum S_{ij} in the LTE approximation (solid line) and the full nonequilibrium result from Eqs. (3.46) and (3.47) (dashed). We normalize to $S_0 = \alpha_0^2 \hbar \frac{2\rho_{1c}}{\pi^3} \frac{|v|}{(2z_a)^4}$ and recover the limits of Eqs. (3.67) and (3.69). We chose the velocity $|v| = 10^{-3}c$, the atom-surface separation $z_a = 1$ nm, typical parameters of gold ($\Gamma = 30$ meV and $\omega_\mathrm{p} = 9$ eV) and ^{87}Rb ($\alpha_0 = 4\pi\epsilon_0 \times 47.28$ Å^3 and $\omega_a = 1.27$ eV) [140].

where we considered the symmetric part of the Green tensor only since the skew-symmetric components do not contribute to the Casimir-Polder force in the static situation. For comparison, the temperature-corrections to the thermal Casimir-Polder force,

$$F_\mathrm{CP}^\mathrm{Th} = \mathrm{Tr} \int_0^\infty \frac{\mathrm{d}\omega}{2\pi}\, \hbar \coth\left[\frac{\hbar\omega}{2k_\mathrm{B}T}\right] \mathrm{Im}\left[\underline{\alpha}^\mathrm{Th}(\omega) \cdot \partial_{z_a} \underline{\Delta}^s(\omega, 0)\right], \tag{3.73}$$

then evaluate by means of the cotangent expansion reported in Ref. [186] to

$$F_\mathrm{CP}^\mathrm{Th} \sim F_\mathrm{CP}^0 + F_\mathrm{CP}^2 + \alpha_0^2 \frac{\pi}{6\hbar} (k_\mathrm{B}T)^2 \partial_{z_a} \mathrm{Tr}\left[\underline{\Delta}_R^s(0,0) \cdot \underline{\Delta}_I^{s\prime}(0,0)\right]. \tag{3.74}$$

Here, $F_\mathrm{CP}^0 \propto \alpha_0 T^0$ and $F_{CP}^2 \propto \alpha_0 T^2$ denote the well-known terms of lowest order in α_0 (see Chap. 2). The previous relations show some formal similarities to the power spectrum and the nonequilibrium correction to the Casimir-Polder force at zero temperature but finite velocity [see Eqs. (3.67) and (3.65)]. Indeed, if we compare the xx-contributions of both Eqs. (3.72) and (3.67), the role of temperature in equilibrium is taken over by the velocity for the atom in motion, i.e. $T \to (2/\pi)(\hbar v/k_\mathrm{B} z_a)$. This hints to the fact that the interaction between a moving atom and the material-modified field induces low-frequency fluctuations that statistically behave as if they were of thermal origin. We refer the reader to Ref. [132] for a more rigorous and detailed discussion.

Clearly, the previous analogy is a vast simplification of the underlying physics and can only serve the purpose of providing an intuitive picture of the impact of motion-induced nonequilibrium. We stress that Eq. (3.65) is purely quantum in its origin since $F_{\mathrm{CP}}^{\mathrm{ne}} \to 0$ as $\hbar \to 0$. Also, in the nonequilibrium situation, the limit of small frequencies is more subtle, since it includes wavevectors connected the direction of motion explicitly as $\omega \sim p_x v$. Especially the latter involves the complex, anisotropic interaction of the quantum electromagnetic field with both the atom's translational and rotational degrees of freedom. The similarities to systems with finite temperature, however, allow us to understand the sign of

$$F_{\mathrm{CP}}^{\mathrm{ne}} < 0 \tag{3.75}$$

pointing towards the surface. In order to keep the atom at constant velocity, we need to apply a constant driving force that balances the decelerating quantum friction. This energy is dissipated into the environment and, by implication, induces further fluctuations into the system. These fluctuations dominate for low frequencies and thereby resemble classical behavior. As a consequence, we obtain the nonequilibrium fluctuation-dissipation relation [Eq. (3.46)] that prescribes a power per frequency of the interaction that exceeds its equilibrium counterpart [Eq. (3.67)]. In other words, each source of fluctuations, either behaving classical or quantum, contributes to the energy of the interaction, modifies the interaction and adds up to the overall attractive effect [21].

Our formalism generalizes previous work and shows that mechanical nonequilibrium can induce a contribution to the Casimir-Polder force that is dominated by the low-frequency regime of the interaction. Those frequencies probe the dissipative properties of the material and are usually less associated with Casimir-Polder forces which are commonly understood as a broad-band phenomenon. This potentially adds another facet in the interpretation of sophisticated material studies (see, e.g., recent work on hyperbolic metamaterials [29] in the context of Casimir-Polder forces) and directly applies to already existing experimental setups for high precision measurements of atom-surface interactions (see, e.g., matter-wave interferometry where high velocity atoms interact with a nanometer-size grating [103]). In the following Section, we change our focus and explore the impact of low-frequency correlations in the system in the context of quantum friction.

3.4 Quantum friction

Simply put, the fluctuation-induced interaction between the particle and the macroscopic material can be intuitively understood by the particle interacting with its induced image below the surface [77, 491]. If both subsystems are set in relative motion and the particle's image travels in a medium with some degree of dissipation[9], the force attracting the particle to the surface acquires a parallel component (see Fig. 3.4), which, at zero temperature, goes under the name of quantum friction [31]. As we laid out in Chapter 1 and will see in the following, the interaction leading to quantum frictional forces are mainly given by frequencies $\omega \lesssim v/z_a$ and lie way below most (electric) resonances of quantum optical systems. Hence, quantum friction is particularly sensitive to a proper modeling of that very low-frequency fluctuations in the system.

In recent years there has been a dispute about the correct scaling of the force with respect to velocity and the separation of the particle from the surface [219] leading to a relatively wide range of predictions, see e.g. Refs. [54, 219, 492–496]. As it turns out, the friction force on atoms is very sensitive on the assumptions on the underlying statistics of the interaction. We refer the reader to Refs. [44, M6, 355] for an overview of the different approaches and the underlying statistical assumptions. Keeping the discussions presented in the previous Chapters in mind, this comes to no surprise: From the Fourier expansion of Eqs. (3.4) in the nonequilibrium steady-state, where the particle follows a uniform trajectory, one can see that the velocity and distance scaling are intimately connected to the functional behavior of the system's Green tensor with respect to frequency and wavevectors, respectively. In combination with the low energy scales ($\sim \hbar v/z_a$) that are relevant for quantum friction, this is exactly the regime where we found the strongest variation from model to model (see Chap. 1). Indeed, just recently we and others could show that a proper description of atom-surface quantum friction calls for an inclusion of long-time correlations between system and environment [53, 57, M4, M6]. In doing so, e.g., one obtains in the simplest case of an atom interacting with a planar, Ohmic and spatially local interface, that the frictional force scales as $F_{\text{fric}} \propto -v^3/z_a^{10}$. We will see in the following that this can certainly be different depending on the low-frequency behavior of the fluctuation spectrum or equivalently the (spin) local density of states in the nonequilibium situation. However, it is opportune to emphasize that, to the best of our knowledge, there is yet no convincing experimental evidence of quantum friction that could resolve the dispute once and for all.

[9] Dissipation, here, is to be understood in a very broad sense and not necessarily bound to dissipative properties of the material absorbing and transforming energy into, e.g., heat, even though it will be the dominating source of dissipation in our discussion. It could very well also arise from extinction mechanisms due to the scattering of radiation at finite-size particles [230] or from the Cherenkov condition assigned to waves traveling in media (see Ref. [132] and references therein). In general, we use *dissipation* synonymously with a non-vanishing imaginary part of the Green tensor.

Non-perturbative treatment and velocity expansion

We extensively introduced our formalism in Secs. 3.1 and 3.3. Based on the derivation we provided for the dynamic Casimir-Polder force and in accordance with the original derivation put forward in Ref. [58], it relatively simple at this point to deduce the corresponding expression for the parallel component of the force. Let h again be the wavevector along the direction of motion, the field expansions are exactly the same as in Sec. 3.1. Starting once again from Eq. (3.37), the parallel component of the Lorentz force [Eq. (3.38)] is obtained by considering the spatial derivative with respect to the coordinates parallel to the interface. Mathematically, this boils down to replacing the derivative with respect to z_a by the parallel wavevector h and the principal value in Eq. (3.39) with a delta function, i.e.

$$\frac{1}{2\pi}\partial_{z_a}\mathcal{P}\frac{1}{\nu+\omega-hv} \to -h\delta(\nu+\omega-hv). \tag{3.76}$$

It is therefore much simpler to compute the ν-integral in Eq. (3.39) and the quantum friction force readily evaluates to [58]

$$F_{\text{fric}} = F_{\text{fric}}(v) = -2\int_0^\infty \mathrm{d}\omega \int \frac{\mathrm{d}h}{2\pi}\, h\mathrm{Tr}\left[\underline{S}(hv-\omega,v)\cdot\underline{G}^{\mathrm{T}}_{\Im}(h,\mathbf{R}_a,\omega)\right]. \tag{3.77}$$

As expected, for $v=0$, the integral kernel is an odd function of the wavevector such that the frictional forces vanishes in equilibrium. For finite velocities, however, the friction derives from two physically distinct terms in the steady-state [M1]:

$$F_{\text{fric}} = F^t + F^r. \tag{3.78}$$

The first term, $F^t \propto \mathrm{Tr}[\underline{S}^{\mathrm{s}}_R\cdot\underline{G}^{\mathrm{s}}_I]$, is related to the symmetric parts of the power spectrum and the Green tensor. We will refer to it as the *translational* component of the friction force. The second term, in contrast, is related to the skew-symmetric parts of the corresponding tensors, i.e. $F^r \propto \mathrm{Tr}[\underline{S}^{\mathrm{as}}_I\cdot\underline{G}^{\mathrm{as}}_R]$. We will consequently refer to it as the *rotational* contribution to the frictional force in the sense of Section 3.2. In full resemblance to our formula for the dynamic Casimir-Polder force, Eq. (3.77) is highly general in the sense that it is (i) non-perturbative with respect to the electric atom-surface coupling ($\sim\alpha_0$), (ii) obeys the full nonequilibrium statistics of the NESS and thereby (iii) self-consistently includes the back-action of the environment on the particle and (iv) includes both translational as well as rotational degrees of freedom for the average linear motion of the particle. In certain situations, however, it can be opportune to simplify the description and fix the direction of the dipole vector transferring its quantum properties into a scalar operator, $\hat{\mathbf{d}} = \mathbf{d}\hat{q}(t)$. Describing the atom as a rigid dipole can be interesting, e.g., if the interaction is intrinsically asymmetric or one simply wants to avoid the complexities connected to rotational degrees of freedom. In this case, the two-time correlation tensor of the particle becomes symmetric in the steady-state, $\underline{C}(\tau,v) = \underline{C}^{\mathrm{T}}(\tau,v)$ and hence $\underline{S}^{\mathrm{as}}_I(\omega,v)=0$ such that the rotational component of the friction force F^r vanishes identically. In fact, as explained earlier, the rigid dipole is a commonly applied approach [43] and in the next Section we will use it to study the impact of different (nonlocal) material models, where rotational degrees of freedom are not needed to grasp the important physics.

As anticipated earlier, the velocity scaling of the friction is closely related to the frequency scaling of the susceptibilities involved in the interaction; in our case the intrinsic memory kernel of the particle ($\underline{\mu}$) and the electric Green tensor of the material-modified vacuum field ($\underline{G}$). From the expression for the power spectrum in Eq. (3.15), we recall that we assumed that the distinct dissipation mechanisms for the particle – intrinsic ("int", related to $\underline{\mu}$) and radiation-induced ("rad", related to $\underline{G}$) dissipation – statistically decouple, i.e. $\underline{\mathcal{D}} = \underline{\mathcal{D}}_{\text{int}} + \underline{\mathcal{D}}_{\text{rad}}$. In leading order α_0, we can additionally write that

$$\underline{S}(\omega, v) \sim \alpha_0^2 \frac{\hbar}{\pi} \underline{\mathcal{D}}(\omega, v) \tag{3.79}$$

such that the friction force decouples similarly and we obtain

$$F_{\text{fric}} \sim F^{\text{int}} + F^{\text{rad}}, \tag{3.80}$$

where F^{int} is related to intrinsic and F^{rad} to radiation-induced damping. Comparing with Eq. (3.78), we note that only F^{rad} contains terms connected to rotational degrees of freedom F^r, while F^{int} is unaffected by them (see Sec. 3.4.2 for more details). Upon inserting Eqs. (3.79) and (3.16) into Eq. (3.77), F^{int} reads in leading order velocity [M2]

$$F^{\text{int}} \sim -\frac{\hbar \alpha_0 \epsilon_0}{\pi} v^3 \int_0^\infty \frac{\mathrm{d}h}{2\pi} \, \frac{h^4}{3} \mathrm{Tr} \left[\underline{\mu}_{\Re}^{\mathrm{T}}(0) \cdot \underline{G}_I^{\mathrm{s}\prime}(h, \mathbf{R}_a, 0) \right]. \tag{3.81}$$

Here, the prime denotes a derivative with respect frequency, we expanded for small velocities $v \ll \omega_r/|h|$ with ω_r the lowest resonance of the system and employed the θ-function appearing in Eq. (3.16) which effectively constraints the contributing frequencies to

$$\int \frac{\mathrm{d}h}{2\pi} \int_0^\infty \mathrm{d}\omega \; \theta(hv - \omega) = \int \frac{\mathrm{d}h}{2\pi} \theta(h) \int_0^{hv} \mathrm{d}\omega. \tag{3.82}$$

Further, in order to perform the expansion, we used that we can write $|h| \lesssim 1/\lambda$ with λ a length scale related to the geometry and material of the environment as well as the particle's distance from the surface $|\mathbf{R}_a|$ [188]. In the case of a rubidium atom in front of a planar metallic half-space, e.g., $\omega_r = \omega_a$ and $\lambda \sim z_a$ such that the expansion is valid for velocities $v \lesssim \omega_a z_a$. Lastly, we emphasize that the trace selects matrices with the same symmetry properties: Since $\underline{\mu}(0)$ is real, $\underline{\mu}_{\Re}(0)$ has to be symmetric, leaving only the symmetric part of $\underline{G}_{\Im} \to \underline{G}_I^{\mathrm{s}}$. As expected, the friction related to intrinsic dissipation is unaffected by skew-symmetric (rotational) degrees of freedom of the Green tensor.

For F^{rad}, the situation is technically more involved. Before we can perform the same low-velocity expansion, we need to solve the intertwined θ-functions appearing when inserting Eq. (3.14) into Eq. (3.77). To this end, we utilize the methods developed in Ref. [M4] and after some additional rearranging of terms we obtain [M2]

$$F^{\text{rad}} \sim -\frac{\hbar \alpha_0^2}{\pi} v^3 \int \frac{\mathrm{d}h}{2\pi} \int \frac{\mathrm{d}\tilde{h}}{2\pi} \, \frac{(h+\tilde{h})^4}{12} \mathrm{Tr} \left[\underline{G}_{\Im}^{\prime \mathrm{T}}(h, \mathbf{R}_a, 0) \cdot \underline{G}_{\Im}^{\prime}(\tilde{h}, \mathbf{R}_a, 0) \right]. \tag{3.83}$$

Hence, if the system behaves Ohmic, i.e. $\underline{\mu}, \underline{G}_I \sim \omega$ for low frequencies, the corresponding

frequency derivatives remain finite and the frictional force automatically scales cubed in the velocity. However, a different frequency scaling of the response functions yields a different velocity scaling and one might need to include higher order terms. For instance, in Ref. [236] it was shown that an effective description for multi-layer structures features a $\sqrt{\omega}$-scaling which translates into a quadratic scaling of the friction force, $F_{\mathrm{fric}} \propto v|v|$. Further, noting that $\underline{G}_{\Im}$ comprises of both translational and rotational degrees of freedom [see discussion below Eq. (3.35)] and enters quadratically in the evaluation of the friction force related to radiation-induced dissipation, Eq. (3.83) inherits that very properties and decomposes in translational and rotational components [Eq. (3.78)].

In principle, depending on the chosen velocity, quantum friction [Eq. (3.77)] can be divided in a non-resonant and a resonant regime [58], where we have focused on the former only in the preceding discussion. While the former covers the range of small velocities and thereby Eqs. (3.81) and (3.83), the resonant regime can theoretically be reached when the velocities are at the order of the atomic resonance frequency which drastically changes the qualitative as well as quantitative behavior of quantum friction [58]. However, recalling our estimates from Chap. 1, where we inserted some typical values for experimentally accessible regimes (see e.g. Sec. 1.3), the resonant regime appears usually difficult to access. Thus, we can frame quantum friction essentially as a low-frequency phenomenon that is dominantly given by the evanescent (non-resonant) sector [53, M1]. The relevance of resonant effects, which are connected to propagating waves and multiple interference, is strongly diminished and can be safely neglected. In other words, the leading-order contribution to quantum friction [Eqs. (3.81) and (3.83)] is not only corrected by long-time correlations, but they instead represent the dominant source of interaction. In the following, we will hence focus on the non-resonant regime and the low-velocity expansions in particular.

3.4.1 Impact of the material and spatial dispersion

We start our discussion on quantum friction by focusing on the dissipative properties of the environment's material. In Chapter 1, we have stressed how different materials (and their theoretical models) can be very different in the low-frequency regime which can usually be identified with some kind of dissipation in the material. Since quantum friction is essentially a low-frequency phenomenon, it might not be surprising that it reacts very sensitively to the specifics of dissipation in the materials surrounding the moving particle [M4, M5, 180, 236]. In the remainder of this Section we will concentrate on the low-velocity force experienced by neutral atoms, i.e. particles without intrinsic degrees of freedom ($\underline{\mu} \to 0$), since the effect is most prominent in this case [Eq. (3.83)]. Indeed, since the Green tensor contributes squared to the corresponding force and $\underline{G}'_{\Im}(h, \mathrm{R}_a, 0)$ can be related to dissipation in the material [see Sec. 1.2], F^{rad} can be expected to scale at least quadratically with respect to changes in the strength of dissipation in the material. For simplicity, we will further focus on the interaction with a single planar interface ($\mathrm{d}h/2\pi \to \mathrm{d}^2\mathbf{p}/(2\pi)^2$) and a symmetric correlation tensor for the atomic dipole. This means the we neglect rotational degrees of freedom and the frictional force is given by the symmetric part of the particle's power spectrum only [see discussion below Eq. (3.77)]. Mathematically, this symmetric simplification amounts to replacing the scalar vacuum polarizability with a dyadic that is fixing the dipole direction (artificially), i.e.

$\alpha_0 \to \underline{\alpha}_0 = 2\mathbf{dd}/(\hbar\omega_a)$ in Eq. (3.5) with $\mathrm{Tr}\underline{\alpha}_0 = 3\alpha_0$. This, instead of Eq. (3.19), leads to a strictly symmetric polarizability tensor $\underline{\alpha} = \underline{\alpha}^{\mathrm{T}}$ with $\underline{\Delta}(\omega, v) \to \mathrm{Tr}\int \frac{\mathrm{d}^2\mathbf{p}}{(2\pi)^2}\underline{G}(\mathbf{p}, z_a, \omega + p_x v)$. Equation (3.83) then substantially simplifies and we can write for the frictional force experienced by the atom [M4, M5]

$$F^{\mathrm{rad}} \sim -2\hbar\frac{v^3}{\pi}\frac{\alpha_0^2}{\epsilon_0^2}\left[\phi^{\mathrm{LTE}}\Phi_0(z_a)\Phi_2(z_a) + \phi^J\Phi_1^2(z_a)\right], \tag{3.84}$$

where we assumed Ohmic materials and employed the near-field expansion of the electric Green tensor [Eq. (1.51)]. The first term of Eq. (3.84) represents the assumption of LTE, while the second term is solely connected to full nonequilibrium corrections [$\sim \underline{J}$ in Eq. (3.46)]. We have averaged the dipole direction over the solid angle for the LTE and the J-contribution, separately [M5], obtaining

$$\phi^{\mathrm{LTE}} = \frac{21}{2^9 \times 5\pi^2}, \qquad \phi^J = \frac{87}{2^{10} \times 5\pi^2}. \tag{3.85}$$

The geometry as well as the dissipative properties of the bulk material are encoded in the functions

$$\Phi_n(z_a) = 2\epsilon_0\int_0^\infty \mathrm{d}p\; p^{2(n+1)}\rho(p)e^{-2pz_a} \tag{3.86}$$

with $p = |\mathbf{p}|$, i.e. the norm of the component of the electromagnetic wavevector parallel to the surface, and we expanded the transverse magnetic reflection coefficient by means of the nonlocal dissipation rate $\rho(p)$ [Eq. 1.35]. $\Phi_n(z_a)$ is related to the the n-th derivative with respect to frequency of the electromagnetic density of states, i.e. $\Phi_0(z_a)$ gives the atomic decay rate of the dressed atomic polarizability due to the interaction with the material-modified vacuum field [M4]. In this way, $\Phi_n(z_a)$ defines the functional dependence of the force with respect to distance and hence depends on the particular form of $\rho(p)$. Interestingly, for spatially local materials, where $\rho(p) = \rho_{\mathrm{lc}}$ is constant, the z_a-dependence is uniquely fixed by $\Phi_n(z_a)$: The integral over wavevectors can be solved exactly and we obtain

$$F_{\mathrm{lc}}^{\mathrm{rad}} \sim -\hbar\frac{864}{5}\frac{v^3}{\pi^3}\frac{\alpha_0^2\rho_{\mathrm{lc}}^2}{(2z_a)^{10}} \tag{3.87}$$

in accordance with[10] Refs. [53, M4]. As anticipated, the friction scales quadratically in the dissipative properties of the material. Also, the force is extraordinarily sensitive (in comparison to other fluctuation-induced forces [138]) to changes in the atom-surface separation scaling with z_a^{-10}. For instance, if an ^{87}Rb atom [142] travels in the close vicinity of a gold surface [140] at the speed of sound, the negative acceleration a experienced at extremely small separation of 1 nm evaluates to orders $|a| \sim \mathcal{O}(\mu\mathrm{m/s}^2)$. The same situation at 100 nm already is twenty orders of magnitude smaller. Of course, these numbers depend on the choice of the particle and the material (model) which we will discuss in the following and specifically in Chap. 5.

[10] We note that the difference in prefactors with respect to an additional factor of 9 to Ref. [M4] stems from a slightly different definition of the vacuum polarizability $\alpha_0 \to 3\alpha_0$.

Still, in order to obtain at least somewhat reasonably large values for the frictional force, we need to bring the atom as close as possible to the surface, preferably below one micron. On the one hand, this retroactively motivates our choice of focusing on the interaction in the near-field regime where retardation effects can be neglected. On the other hand, at such small separations, the corresponding wavelengths dominating the interaction $\lambda \sim z_a$ shrink to a size where they might be able to resolve some of the correlation lengths between the excitations in the bulk medium and the effective description with constant $\rho_{\rm lc}$ breaks down. We then need to include spatial dispersion (see Sec. 1.2.1 for further details). Fortunately, since spatial dispersion usually tends to increase the dissipation in the material (see e.g. Fig. 1.8), including the impact of that very mechanism into our description will turn out to be in favor of increasing the force [M4].

In the following we will focus on some models for metals, where spatial dispersion ($\rho_{\rm lc} \to \rho(p)$) can be analyzed comparably easy [191] by employing the relations obtained for conductors in Sec. 1.2.1. At the end of the present Section, we will further discuss more general materials featuring band-gaps.

Nonlocal conductors

We first employed the most simple situation of a spatially local Drude material [Eq. (1.31)] and take the corresponding force as a reference for the impact of spatial dispersion. Due to its simple structure, the permittivity of the Drude model at low frequencies asymptotically gives $\epsilon \sim \mathrm{i}[\epsilon_0 \rho_{\rm lc} \omega]^{-1}$ and the force is given exactly by Eq. (3.87). Aiming to increase the force inevitably calls for changing the parameters of the interaction. However, the Drude model ignores the impact of spatial dispersion; an effect that we get "for free" without the need to change parameters[11]. One possible choice of including spatial dispersion in the response of the conductor's electron plasma [191] is the semi-classical infinite barrier model (SCIB), leading to the form of the nonlocal dissipation $\rho(p)$ reported in Eq. 1.35, in combination with the semi-classical Boltzmann-Mermin permittivity [Eqs. (1.44)]. The SCIB model in combination with the Boltzmann-Mermin permittivity incorporates coherent damping of electromagnetic waves in the bulk in terms of the Landau damping and interweaves its features with collision-induced damping in the material leading to a reasonably reliable, but highly non-trivial expression for $\rho(p)$ in Eq. (1.43). The behavior and the impact of Landau damping on quantum friction derives from a complex interplay of a multitude of length scales and parameters (see Secs. 1.2.2, 2.2 and references therein), most notably the bulk electron's mean free path ℓ. For wavelengths $\lambda \lesssim \ell$, the Landau damping becomes important in the electric response of the material and we found that it can increase the damping $\rho(p)$ by roughly one order of magnitude (see Fig. 1.8). For quantum friction, in the planar geometry and from Eq. (3.87) we can roughly expect an increase of the force by at least *two* orders of magnitude, since $\rho(p)$ enters quadratically. The impact of the Boltzmann-Mermin model on atom-surface quantum friction and especially its connection to the underlying physical mechanisms were extensively studied in earlier work by the author and collaborators in Refs. [M4, 180] and we report the results here only for reasons of completeness. Indeed, a more careful investigation based on Eq. (3.86) confirms our

[11] In fact, "for free" is to be understood from the perspective of experimental physics. For the theory, including spatial dispersion comes for the price of a much more involved modeling (see Sec. 1.2.1).

prediction and in the region close to the surface, where $\lambda_{\mathrm{TF}} \ll z_a \lesssim \ell$ with $\lambda_{\mathrm{TF}} = v_{\mathrm{F}}/(\sqrt{3}\omega_{\mathrm{p}})$ the Thomas-Fermi wavelength, we obtain

$$\frac{F_{\mathrm{BM}}^{\mathrm{rad}}}{F_{\mathrm{lc}}^{\mathrm{rad}}} \sim \frac{\omega_{\mathrm{p}}^2}{\epsilon_0^2 \rho_{\mathrm{lc}}^2} \left(\frac{\lambda_{\mathrm{TF}}}{2z_a}\right)^2 \left\{ 7 \left[\ln \frac{B_0 z_a}{\lambda_{\mathrm{TF}}} + \frac{C_0 z_a}{\ell}\right] \left[\ln \frac{B_2 z_a}{\lambda_{\mathrm{TF}}} + \frac{C_2 z_a}{\ell}\right] + \frac{145}{7} \left[\ln \frac{B_1 z_a}{\lambda_{\mathrm{TF}}} + \frac{C_1 z_a}{\ell}\right]^2 \right\}. \tag{3.88}$$

Here, ρ_{lc} is the respective Drude resistivity, ω_{p} the Drude plasma frequency and the B_n and C_n some numerical constants of similar magitude (roughly between 1/3 and 1) that are defined in the appendix of Ref. [M4]. We note that the first term of the previous expression is related to the assumtion of LTE and the second term is a pure nonequilibrium correction not covered by the LTE approach which, notably, is equally important as the equilibrium-based term [53]. Spatial nonlocality leads to a non-algebraic change in the distance scaling of the force that implies a force that increases with $\omega_{\mathrm{p}}^2/\rho_{\mathrm{lc}}^2$ with respect to the local Drude result pointing towards the use of very clean materials with large plasma frequency. Moreover, as anticipated from the behavior of $\rho(p)$, spatial nonlocality increases the quantum friction force with respect to the local Drude model by roughly two orders of magnitude at distances in the range of the mean free path $z_a \sim \ell$ and even reaches a maximum of three orders of magnitude for distances that are at the order of ten times the Thomas-Fermi wavelength in the Boltzmann-Mermin description[12], i.e. $z_a \sim 10\lambda_{\mathrm{TF}}$ (see gray curve in Fig. 3.8). In summary, aiming to increase quantum friction forces, it is highly beneficial to get as close as possible due to the strong distance dependence of the force as well as its sensitivity towards dissipation in the material.

In the remainder of present Section, however, our interest is of a more practical nature. Keeping in mind that the effect of quantum friction, to this day, is a theoretical prediction and lacks the experimental evidence, it is certainly interesting to study more complicated scenarios that could potentially enhance the frictional force. While the Green tensor for our geometry is known analytically, more sophisticated geometries lack such a closed form in general and the available analytical methods for optimization are quickly exhausted. Here, one has to rely on advanced numerical methods to solve Maxwell's equations (see e.g. Ref. [235] for a method in time domain) and material properties are incorporated by assuming additional boundary conditions [497] and additional equations of motions governing the material's response [212].

Going beyond the local approximation and including spatial dispersion in the numerics is a formidable task [198, 212, 251]. As discussed in Chap. 1, the standard hydrodynamic model (see Sec. 1.2.2) has become quite popular [497, 498]. There, the advantage was that the standard hydrodynamic description allows to include some degree of spatial nonlocality into the material description while being numerically feasible at the same time. However, the range of applicability of the standard hydrodynamic model is limited as it ignores Landau damping. For our particular interest in low-frequency fluctuations, it hence brings close to no significant changes with respect to the local description (see Sec. 1.2.1). Extensions of the standard hydrodynamic model were developed in the literature [198, 208, 246] and we discussed one example, the extended hydrodnamic description, in Sec. 1.2.2. Such extensions are particularly

[12]Note that for distances $z_a \lesssim \lambda_{\mathrm{TF}}$ (typically at the order of angstroms), our description in terms of macroscopic electrodynamics is not valid anymore (see Chap. 1).

interesting since they can be implemented numerically in an efficient way. In contrast to the Boltzmann-Mermin model, where a numerical treatment in arbitrary geometries is highly non-trivial, the extended hydrodynamic description has the appeal of comparable simplicity but at the same time including important physical mechanisms (e.g. Landau damping) qualitatively. By revisiting the semi-infinite half-space and later considering the more complicated geometry of a finite sized slab (see Fig. 3.8), where the analysis can still be performed analytically, we aim to delineate the range of applicability of the extended hydrodynamic description in the case of quantum friction on atoms. The Boltzmann-Mermin model serves as a benchmark. Again, we want to emphasize that this is still a mere qualitative study since the complexities of describing the material-vacuum interface theoretically (see beginning of Sec. 1.2.1) become even more apparent for a finite-sized slab.

Starting with the semi-infinite half space, we have seen that the resistivity ρ in the extended hydrodynamic model decomposes into one term related to the standard hydrodynamic model *and* another term connected to Landau damping ρ_{La} [see Eq. (1.48) and appendix D.1]. As we discussed in Sec. 1.2.2, the standard hydrodynamic description deviates only marginally from the local Drude resistivity for atom-surface separations larger than the Thomas-Fermi wavelength such that we can write

$$\rho(p) \sim \rho_{\mathrm{lc}} + \rho_{\mathrm{La}}(p) \tag{3.89}$$

with $\rho_{\mathrm{lc}} = \Gamma/(\epsilon_0\omega_{\mathrm{p}}^2)$ and Γ the dissipation rate of the Drude plasma (Sec. 1.2.2). Upon inserting Eq. (3.89) into Eq. (3.86), the integral over the modulus of the parallel wavevetor can be solved analytically and we find for separations in the nonlocal regime, $z_a \sim \ell$, that the friction force obtained from the extended hydrodynamic model $F_{\mathrm{eH}}^{\mathrm{rad}}$ behaves with respect to the local asymptote $F_{\mathrm{lc}}^{\mathrm{rad}}$ as [M5]

$$\frac{F_{\mathrm{eH}}^{\mathrm{rad}}}{F_{\mathrm{lc}}^{\mathrm{rad}}} \sim \frac{\omega_{\mathrm{p}}^2}{\epsilon_0^2\rho_{\mathrm{lc}}^2}\left(2\frac{\lambda_{\mathrm{TF}}}{z_a} + \frac{73}{240}\frac{\ell^2}{z_a^2}\right). \tag{3.90}$$

In contrast to Eq. (3.88), the extended hydrodynamic (eH) description gives rise to an *algebraic* change in the distance-dependence of the force. In full analogy to the Boltzmann-Mermin model, $F_{\mathrm{eH}}^{\mathrm{rad}}/F_{\mathrm{lc}}^{\mathrm{rad}}$ features a distinct maximum at $z_a \sim 4\lambda_{\mathrm{TF}}$ and for separations

$$z_a \gg \bar{\ell} \sim 1.4\frac{\omega_{\mathrm{p}}}{\Gamma}\ell \tag{3.91}$$

the impact of Landau damping becomes negligible and the force transitions into a regime that is dominated by Drude physics. We refer for the details of the derivation to appendix D.1 and report a numerical evaluation of the friction using the extended hydrodynamic model in Fig. 3.8: As we expected from the behavior of the resistivity (see fig. 1.8), we observe that the eH model overestimates the friction force by several orders of magnitude when compared to the result using the Boltzmann-Mermin model. This frames the eH model quantitatively as an effective model which likely requires a careful adjustment of its effective parameters. However, for the semi-infinite half space, the eH model manages to reproduces the important qualitative features inherent in the spatially nonlocal description predicted by the Boltzmann-Mermin model: With

respect to the local Drude model, the friction force (i) is enhanced for atom-surface separations at the order of the bulk electron's mean free path, (ii) the enhancement shows a clear maximum monotonically approaching the Drude description for increasing separations $z_a \gg \ell$ and (iii) the deviation from the Drude model is the larger, the cleaner the material and the higher the plasma frequency due to the quadratic scaling in $\omega_\mathrm{p}^2/\rho_\mathrm{lc}^2$. Qualitatively, the eH model can indeed be used to make predictions for the friction force on atoms interacting with a semi-infinite half-space. We now explore how the nonlocal models behave in the context of quantum friction in a different geometry, namely a nonlocal thin film (or "slab", see Fig. 3.8). For transparency, we restrict our discussion to the eH model and contrast our findings with numerical results for the Boltzmann-Mermin model.

Due to the distinction between transverse and longitudinal fields (Sec. 1.2), the mathematical description of spatially nonlocal slabs (or more general layered structures) is non-trivial. One possible approach is based on the transfer-matrix technique [499] (see also Refs. [M5, 219, 236, 500, 501] for an application to quantum fluctuation-induced forces), where the different layers are connected by additional boundary conditions in order to account for longitudinal fields [202, 203]. Such composite materials feature a rich and complex resonance structure that substantially modifies the electromagnetic density of states. Fortunately, we are only concerned with the Ohmic[13] low-frequency behavior which simplifies the relevant parts of the slab's nonlocal reflection coefficients considerably. Following Refs. [M5, 219, 236], the finite width d of the bulk material generalizes the expression for the body's dissipative properties in Eq. (3.89) for wavevectors $p \ll \lambda_\mathrm{TF}^{-1}$ to the remarkably simple form

$$\rho_\mathrm{sb}(p) \sim \rho_\mathrm{lc} \coth[pd] + \rho_\mathrm{La}(p). \tag{3.92}$$

Focusing on the first term, we note that the only difference to the semi-infinite half space is the prefactor $\coth[pd]$ relating the wavelength dominating the interaction $\lambda \sim p^{-1}$ to the thickness of the plate d. Indeed, for wavelengths that are small compared to the size of the slab, $d/\lambda \gg 1$, $\coth[dp] \to 1$ and we recover the result of the semi-infinite bulk. In other words, the wavelengths are too small to resolve the finite width of the slab which then effectively acts as a bulk medium. In the opposite limit, $d/\lambda \ll 1$, the wave can probe the distant side of the slab and the finite width of the bulk tends to *increase* the dissipation ρ as $\coth[pd] \sim (pd)^{-1}$. Since the wavelength is connected to the atom-surface separation $z_a \sim \lambda$, the slab geometry can be expected to modify the friction for increasing atom-surface separations [236]. Physically, increase of the dissipation is related to the surface plasmon polaritons (SPP) appearing at the two interfaces: Due to the finite separation between the two interfaces, the SPPs are not independent anymore and can couple in either symmetric or anti-symmetric fashion with respect to the symmetries of the electric field [502]. Mathematically, it turns out that the appearance of the coth-function can be related to the symmetric field distribution [236, 503]. Hence, the coth-function in Eq. (3.92)

[13] Defining the Ohmic regime for spatially nonlocal materials requires some extra care due to the additional length scales involved in the description. While the Drude model as well as the standard hydrodynamic description are Ohmic for any frequency $\omega \ll \omega_\mathrm{sp}$, the Boltzmann-Mermin model and the extended hydrodynamic model behave Ohmic for frequencies $\omega \ll \max[\Gamma, v_\mathrm{F}]$ and $\omega \ll \Gamma$, respectively. Deviations from the Ohmic behavior would lead to a different velocity scaling and Eq. (3.84) would not hold anymore. However, since $\omega \lesssim v/z_a$, the Ohmic assumptions holds in very good approximation for the parameter regimes we are interested in (see main text). For further details, we refer to Chap. 1, appendix D and Ref. [M5].

indicates that the dissipation in the finite slab appears to be dominated by the *symmetrically* coupled SPP excitation. This can be understood by analyzing the spatial distribution of the electric field: The symmetric excitation is highly confined withing the metallic slab, while the field in the anti-symmetric configuration peaks at the edges of the slab [503]. Heuristically, it is hence no surprise that the symmetric mode is much more influenced by dissipation in the material, even though we note that a more careful treatment for particular applications requires advanced numerical methods to make reliable predictions [504, 505]. Due to its different sensitivity with respect to dissipation, the symmetric (anti-symmetric) excitations were coined short-range (long-range) SPP [506]. Quantum friction, deriving from the dissipative properties of the geometry, is therefore modified by short-range SPPs for large atom-surface separations.

For local materials, the consequences of the finite geometry were already studied in Ref. [236]: As soon as the wavelengths can resolve the dimensions of the slab, the increased resistivity of the material due to a confinement of symmetric, short-ranged SPPs in the material leads to an increase of the frictional force. Also, the distance-dependence with respect to the semi-infinite bulk is modified due to the additional wavevector dependence in $\rho_{\mathrm{lc}} \to \rho_{\mathrm{lc}} \coth[dp]$. In the nonlocal case using the eH model, it is quite interesting that the dissipative mechanisms decouple [Eq. (3.92)] which is inherited by the force: Upon inserting Eq. (3.92) into Eq. (3.84), the slab geometry ("sb") leads to ($d \ll z_a \ll \bar{\ell}$)

$$\frac{F_{\mathrm{sb}}^{\mathrm{rad}}}{F_{\mathrm{lc}}^{\mathrm{rad}}} \sim \frac{227}{768}\frac{z_a^2}{d^2} + \frac{73}{240}\frac{\omega_{\mathrm{p}}^2}{\epsilon_0^2\rho_{\mathrm{lc}}^2}\frac{\ell^2}{z_a^2}. \tag{3.93}$$

The first term of Eq. (3.93) gives the force expected from the interaction with a local Drude slab [236] and, as expected, increases the force for distances

$$z_a \gtrsim \ell_{\mathrm{sb}} = 2\left(73/3405\right)^{\frac{1}{4}} \ell\sqrt{d/\lambda_{\mathrm{TF}}} \approx 0.77\ell\sqrt{d/\lambda_{\mathrm{TF}}}. \tag{3.94}$$

The second term in Eqs. (3.92) and (3.93), however, is completely unaffected by the slab geometry for the considered parameters and corresponds to the response of a semi-infinite bulk dominated by Landau damping in the eH model. Below ℓ_{sb}, geometric nonlocality induced by the finite size of the slab plays a subordinate role with respect to spatial nonlocality related to the mean-free path of bulk electrons ℓ. Since $\ell \lesssim \ell_{\mathrm{sb}}$, the model automatically approaches its local Drude limit before the transition from bulk to slab geometry comes into play. For comparison, we report a numerical evaluation of the Boltzmann-Mermin model using a numerical tool developed in Ref. [355]. The Boltzmann-Mermin model shows similar characteristics and confirms our finding that the slab physics prevails with respect to physics related to spatial nonlocality for the chosen geometry (see dashed lines in Fig. 3.8).
In the light of the serious challenges connected to the numerical implementation of the Boltzmann-Mermin model and the relative simplicity of performing the same task for the hydrodynamic model, our results show that it can indeed be worthwhile to perform a first estimate for the frictional force based on the hydrodynamic model. In the case of a slab geometry, it gave the correct qualitative description and could have prevented us from employing the technically much more involved Boltzmann-Mermin model; thereby highlighting its potential relevance for numerical evaluations of quantum frictional forces in complex geometries.

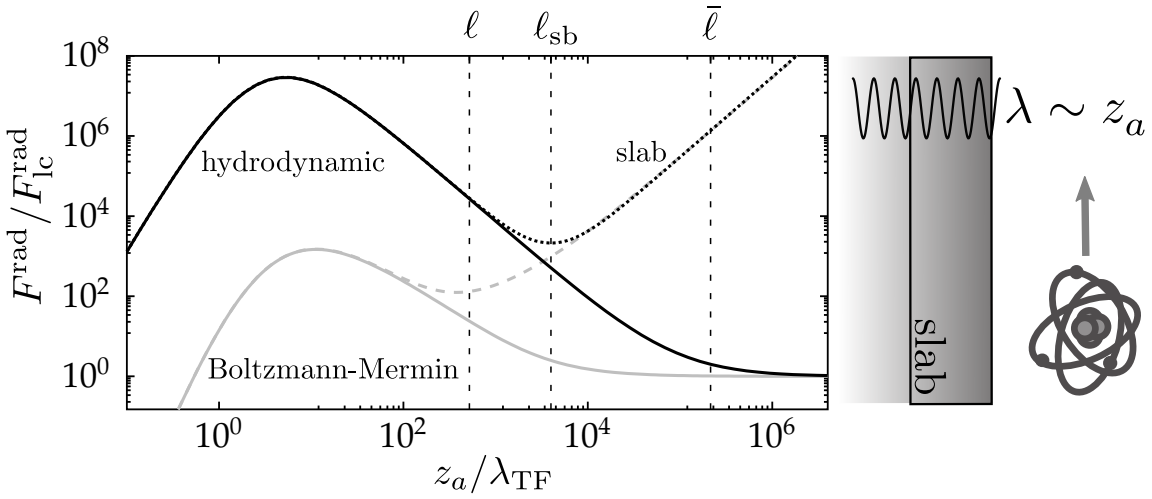

Figure 3.8: Left: Quantum frictional force experienced by an atom moving above a planar conducting surface as a function of separation z_a in multiples of the Thomas-Fermi wavelength $\lambda_{\rm TF}$ [Eq. (3.84)]. The surface separates vacuum from (i) an infinite half space (solid lines) and (ii) from a slab of finite thickness (dashed lines). We model the surface using the extended hydrodynamic description (black) and the Boltzmann-Mermin model (gray) and normalize to the respective result of the Drude model $F^{\rm rad}_{\rm lc}$ [Eq. (3.87)]. Parameters are chosen as in Fig. 1.8 and we further chose a slab thickness of $d = 10^2\lambda_{\rm TF}$. **Right**: Schematic visualization of the setup. The closer the atoms gets to the surface, the smaller the wavelengths λ dominating the interaction and hence the larger the impact of spatial dispersion on the frictional force (see also main text). Adapted from [M5].

Dielectrics and materials with band-gaps

From the observation that the frictional force at low velocities is determined by the dissipative properties of the material, we can comment on its behavior for other more generic substances/media. As long as it is possible to define a complex permittivity tensor with finite imaginary part in the limit $\omega \to 0$, the previous discussion applies and one will find finite frictional forces. For example, when the electromagnetic response of the environment is considered to be spatially local in good approximation and the material furthermore behaves Ohmic, we can directly refer to Eq. (3.83) and to its quadratic behavior in $\rho_{\rm lc}$. Remarkably, this estimate does not distinguish between the exact physical origin of dissipation in the material and the microscopic expressions for $\rho_{\rm lc}$ can be very different. This includes in particular any material described by a combination of Drude and Lorentz models (see Sec. 1.2.3). Hence, our discussion in the previous Section covers a wide range of conductors, semi-conductors (with band-gaps) and dielectrics (see e.g. [140, 261, 330]). However, for quantitatively more accurate descriptions or for describing more exotic materials, one also needs more sophisticated material models (in addition to an accurate estimate of their parameters) and we will briefly comment on intrinsic semi-conductors and graphene in the following.

We already established that friction forces arise as long as the reflection coefficients (which are connected to the material's permittivity) show a finite imaginary part [see Eq. (3.77)]. We

have seen that the frequencies relevant for the interaction are given by the velocity and the distance from the surface, i.e. $\omega \sim v/z_a$. Consequently, if $\epsilon_I(v/z_a) \approx 0$, the frictional forces vanish. Such a situation can, for example, appear theoretically for intrinsic semi-conductors which feature a sharp finite band-gap with energy E_g between valence and conduction band and show no dissipative behavior in the low-frequency regime. Here, a very simple theoretical description could be based on the Tauc-model (see Sec. 1.2.3) which gives $\epsilon_I \propto \theta(\hbar\omega - E_g)$. It allows for an excitation of the conduction band only for energies larger or equal than the band gap size E_g. For instance, typical semi-conductors such as germanium or silicon feature band-gap sizes of ~ 1 eV [194]. In combination with an atom-surface separation of 10 nm, this would already amount to velocities at the order of $v \sim 0.05c$ that are minimally needed to instigate friction forces.
Lastly, let us consider the case of graphene [507]: An (effectively) two-dimensional honeycomb lattice of monolayer carbon atoms whose band structure shows the typical shape of the two so-called Dirac cones facing each other [508]. For small excitation energies close to the Dirac point (at the order of some eV), graphene has a linear energy dispersion for the two Dirac cones of the conduction and the valence band, respectively, and hence theoretically no band gap. Graphene is spatially nonlocal and its band-structure highly symmetric with a fully filled valence band and an empty conduction band [509]. One possible theoretical approach to this is to model graphene in terms of a Dirac field describing the motion of fermions at velocities v_F in 2+1 space-time dimensions [507]. In many practical applications, however, graphene is suspended on a substrate for better handling. The interaction with the substrate might open a bandgap separating the two Dirac cones. Mathematically, the appearance of a band gap in graphene can be described in terms of a mass term occurring in Dirac model describing its electro-optical response [510, 511] (see also Refs. [264, 266, 512] for its use in the context of Casimir-Polder forces). Additionally, the conduction band can be partially filled due to a non-zero chemical potential induced, e.g., by finite temperatures or doping [513]. In the latter case, Landau damping becomes particularly interesting and the theoretical description is very similar to the Lindhard dielectric function [197] (a non-dissipative quantum version of the Boltzmann-Mermin model, see Sec. 1.2) for two-dimensional plasmas with linear energy dispersion [514, 515]. The low-frequency behavior of graphene can here vary between conducting properties (Ohmic behavior) in the local limit to insulating features for vanishing chemical potential [514]. In the present Chapter we focus on zero temperature. Then, based on the 2+1 Dirac field model with zero chemical potential but finite band-gap, the dissipative properties of graphene are connected to the excitation of conduction electrons from the valence band. The necessary excitation energy is essentially given by the ratio between the in-plane Fermi wavevector p_F and the band-gap $\aleph$: For the imaginary part of the transverse magnetic reflection coefficient, we obtain [512, 516]

$$\mathrm{Im} r^p_\mathrm{NF} \propto \theta(cp_\mathrm{F} - 2\aleph). \tag{3.95}$$

Equation (3.95) resembles the Tauc-model and, for large wavelengths, the oscillations between valence and conduction band are sometimes described using a simpler local description [513]. We report the exact expression of Eq. (3.95) and its derivation for completeness in appendix D.2. Qualitatively, however, we note that typical band-gap sizes are at the order of tens of meV [511] and already conclude that frictional forces in the 2+1 Dirac field model with vanishing

chemical potential can be expected to occur for a velocity higher than $v \sim 10^{-4}$c at 10 nm distance. Hence, for low velocities, a finite chemical potential can be beneficial for studying quantum friction forces since it promotes the conducting features of graphene similar to the discussion in the previous sections. This has already been done elsewhere and we refer to Refs. [133, 517] for details.

3.4.2 Quantum rolling friction

After having gained insights into quantum friction and its cubic velocity regime and the impact of different materials on its behavior, we now come back to more general observations based on the structure of quantum friction in our self-consistent description. To this end, we lift the constraint of a symmetric correlation tensor (Sec. 3.4.1) for the atom and explore the impact of rotational degrees of freedom (Sec. 3.2) on the low-velocity friction based on Eq. (3.83).

For an atom moving along an invariant axis in a general environment (see Fig. 3.1), the friction force derives from both the symmetric and the skew-symmetric parts of the Green tensor. Hence, the interplay between the atom and the material-modified vacuum field involves both translational and rotational degrees of freedom in the sense of Sec. 3.2. Choosing Cartesian coordinates and using that $\underline{G}_{\Im}$ is Hermitian as well as that any quadratic matrix can be decomposed into the sum of a symmetric and a skew-symmetric term, we can derive some general conclusions. Recalling the decomposition developed below Eq. (3.19), we can write [M2]

$$\underline{G}_{\Im}(h, \mathbf{R}_a, \omega) = \underline{\Sigma}(h, \mathbf{R}_a, \omega) + \mathbf{s}_\perp(h, \mathbf{R}_a, \omega) \cdot \underline{\mathbf{L}}, \tag{3.96}$$

where $\underline{L}_i = -\mathrm{i}\epsilon_{ijk}$ is the generator of rotations around the i-axis with ϵ_{ijk} the Levi-Civita symbol. Due to the passivity of the materials comprising the bodies in the sense of Eq. (3.11), the matrix $\underline{\Sigma}$ is real, symmetric, positive semi-definite for $\omega \geq 0$ and even in h. The real vector $\mathbf{s}_\perp$ is odd in h and, for symmetry reasons, orthogonal to the direction of invariance. For instance, for a planar interface in the near-field regime, Eq. (3.96) simply reduces to Eq. (3.60). Upon inserting into Eq. (3.83), the frictional force indeed decomposes into two contributions, $F^{\mathrm{rad}} = F^t + F^r$ [see Eq. (3.78)] with

$$F^t \sim -\frac{\hbar\alpha_0^2}{\pi} v^3 \int \frac{\mathrm{d}h}{2\pi} \int \frac{\mathrm{d}\tilde{h}}{2\pi} \left(\frac{h^4}{6} + \frac{h^2\tilde{h}^2}{2} \right) \mathrm{Tr}\left[\underline{\Sigma}'(h, \mathbf{R}_a, 0) \cdot \underline{\Sigma}'(\tilde{h}, \mathbf{R}_a, 0) \right], \tag{3.97a}$$

$$F^r \sim \frac{4}{3} \frac{\hbar\alpha_0^2}{\pi} v^3 \int \frac{\mathrm{d}h}{2\pi} \int \frac{\mathrm{d}\tilde{h}}{2\pi}\, h^3\tilde{h}\, \mathbf{s}'_\perp(h, \mathbf{R}_a, 0) \cdot \mathbf{s}'_\perp(\tilde{h}, \mathbf{R}_a, 0), \tag{3.97b}$$

where we used the symmetry properties with respect to h of the integral kernel. Most notably, the two contributions carry opposite signs which mathematically comes from $\mathrm{Tr}[\underline{L}_i^{\mathrm{T}} \cdot \underline{L}_j] = -2\delta_{ij}$ with δ_{ij} the Kronecker delta. Further, since $\underline{\Sigma}$ is a positive semi-definite matrix we have that $\mathrm{Tr}[\underline{\Sigma}'(h, \mathbf{R}_a, 0) \cdot \underline{\Sigma}'(\tilde{h}, \mathbf{R}_a, 0)] > 0$ such that the function under the integral is also positive. This frames F^t overall negative. For the contribution connected to rotational degrees of freedom, we note that the function

$$\int_0^\infty \frac{\mathrm{d}h}{2\pi}\, h^3 \mathbf{s}'_\perp(h, \mathbf{R}_a, 0) \cdot \int_0^\infty \frac{\mathrm{d}\tilde{h}}{2\pi}\, \tilde{h}\, \mathbf{s}'_\perp(\tilde{h}, \mathbf{R}_a, 0) > 0, \tag{3.98}$$

if the elements of $\mathbf{s}'_\perp(h, \mathbf{R}_a, 0) > 0$ are either completely positive or negative for all $h > 0$, i.e. when $\mathbf{s}'_\perp(h, \mathbf{R}_a, 0)$ is not changing its sign over the integration range. For quantum friction using common (passive) materials, which is most relevant in the evanescent regime of the surface response, this is typically the case[14]. Hence, the apparent subtraction between the terms in Eqs. (3.97) is indeed generally true. Including rotational degrees of freedom reduces the friction experienced by atoms, if the chosen geometry allows for the elements of $\mathbf{s}'_\perp(h, \mathbf{R}_a, 0)$ to be positive and larger than zero. Still, due to the passivity of our system, the overall friction will always remain negative and counteracts the motion [M1].

The difference in sign can be understood by linking the expression for the frictional forces to the peculiar behavior of the atom's average rotation discussed in Sec. 3.2 by means of the Doppler effect and the spin-momentum locking in the evanescent regime [Eqs. (3.97)]. Recalling the general expression for the frictional force in Eq. (3.77), the power spectrum is evaluated at negative, Doppler-shifted frequencies $\underline{S}(-[\omega - hv], v)$. From the perspective of the particle, the power spectrum at $\omega > 0$ is related to the probability to emit a photon after being excited due to the interaction with the electromagnetic field described by the Green tensor $\underline{G}_{\Im}$ [see discussion below Eq. (3.35)]. Even at zero temperature, instigated by the motion, there exists a non-zero probability for the particle to get excited for $-[\omega - hv] > 0$ which favors positive wavevectors $h > 0$ for a motion with $v > 0$. The friction force now depends on the sensitivity of the interaction to the spin (polarization) of the photon. The friction connected to translational degrees of freedom, F^t, is even in h and derives from linearly polarized excitations. Hence, F^t does not discriminate between different directions and evenly interacts with surface waves propagating in positive and negative x-direction. Indeed, linear polarizations are given by circularly polarized counter-propagating surface waves. This means that only for the emission process, the positive x direction is favored by the Doppler shift and induces a negative momentum recoil leading to the frictional force $F^t = -|F^t|$. The frictional force connected to rotational degrees of freedom F^r, on the other hand, can sense the polarization of the surface excitation due to the involvement of the skew-symmetric parts of the Green tensor. In this case, the absorption process prefers surface waves co-propagating with the atom due to the Doppler-shift of the radiation and leads to an imbalance in the absorbed angular momentum with emphasis on negative spin (rotating counter-clockwise) resulting in the counter-intuitive direction of rotation discussed in Sec. 3.2. From the perspective of dissipation in the atomic subsystem, we need to consider the emission of photons. In the steady-state, in order to keep the angular momentum $\boldsymbol{\mathcal{L}}$ constant, the particle prevalently emits photons with positive spin (rotating clockwise). In the interaction with the surface, this amounts to the excitation of surface waves traveling opposite to the atom's direction of motion due to spin-momentum locking leading to an effective acceleration of the particle and an overall reduction of the force [M1], $F^{\mathrm{rad}} = -|F^t| + |F^r| \leq 0$. For details we refer to Sec. 3.2 and Fig. 3.3.

[14] We recognize that the integral (3.98) can still be positive for oscillating functions changing sign which is less relevant for our purposes.

Back-action of the environment on the particle's dynamics is essential for observing the *quantum rolling friction*[15] $F^{\mathrm{rad}} = F^t + F^r$. To see this more clearly, we consider once again the example of the evanescent interaction between an atom and a semi-infinite half space made from a local Drude model described by the electric Green tensor in Eq. (3.60). We then obtain

$$F^t \sim -\hbar\frac{63}{\pi^3}\alpha_0^2\rho_{\mathrm{lc}}^2\frac{v^3}{(2z_a)^{10}}, \qquad F^r \sim \hbar\frac{45}{\pi^3}\alpha_0^2\rho_{\mathrm{lc}}^2\frac{v^3}{(2z_a)^{10}}. \tag{3.99}$$

We find that the force associated to rotations reduces the frictional force to roughly 29% of the originally proposed value ignoring the skew-symmetric components of the involved matrices [53]. Interestingly, by separating the force $F^{\mathrm{rad}} = F^{\mathrm{LTE}} + F^J$ in contributions associated with the assumption of LTE and the nonequilibrium (J) correction in the spirit of Eq. (3.46), we can show the LTE contributions vanish identically in the low-velocity regime due to the inclusion of rotational degrees of freedom, i.e.

$$F^{\mathrm{LTE}} = 0, \qquad F^J = F^t + F^r. \tag{3.100}$$

We find that frictional forces experienced by atoms in planar geometries are essentially a full nonequilibrium phenomenon. In such situations, it cannot be explained with equilibrium-based approaches such as the LTE assumption. Noting that $F^{\mathrm{LTE}} = 0$, our formalism not only corrects, but completely invalidates similar approaches aiming to describe low-velocity friction forces experienced by atoms in the vicinity of a local planar interface. The actual friction force in this simple geometry is in fact likely to be much smaller than expected earlier due to the impact of rotational degrees of freedom and the interplay of the Doppler-shift and spin-momentum locking of light at a material interface [M1]. Unfortunately, this also worsens the prospects of detecting the signatures of quantum friction forces in such simple geometries. Hence, it is not far to seek for different, more promising setups. In the following Section, we study the impact of changing the geometry on the friction force on atoms by considering planar as well as cylindrical cavities.

[15] We dub the phenomenon in resemblance of the effect in classical rolling friction.

3.4.3 Non-additive enhancement of atom-surface quantum friction

Quantum fluctuation-induced forces are known to behave in quite unintuitive ways. One interesting feature, their non-additivity, has been studied by the early experimental work of Derjaguin *et al.* [22]. Fluctuation-induced forces between tiny particles in the vicinity of macroscopic bodies do not result from the pairwise summation of the van der Waals forces between the particle and the atoms of the bodies. Instead, they are non-additive with respect to changes of the boundary conditions [518]. In short, two identical surfaces do not necessarily induce two times the force of the single interface.

The idea of the present Section is just simple enough that its pursuit can expose fundamental properties of the dynamics of particles in mechanical nonequilibrium. Aiming to tailor the strength of dispersion forces, we intend to increase the number of objects interacting with the particle. Then, one could make the approximation that the Green tensor of the N-body configuration is additive, i.e.

$$\underline{G} \approx \sum_{j=1}^{N} \underline{G}_j \tag{3.101}$$

with $\underline{G}_j$ the Green tensor of the jth body separately. Even though this clearly ignores the mutual interactions between separated bodies, Eq. (3.101) can usually be considered to be a good approximation in the evanescent regime of *equilibrium* fluctuation-induced interactions. We will see in the following that such an assumption can be prohibited in certain nonequilibrium situations. Now, if we stick with the additive approximation for the time being, the intuition might be tempted to extrapolate this observation to predict fluctuation-induced forces that are additive in leading order

$$F \overset{?}{\approx} F_{\mathrm{add}} = \sum_{j=1}^{N} F_j, \tag{3.102}$$

where F_j is the force induced by the jth body. When aiming to increase the friction force, this suggests to use a geometry consisting of an ensemble of identical bodies yielding

$$F_{\mathrm{add}} \sim N F_j \tag{3.103}$$

with respect to the force F_j caused by one body only. Such a situation could be realized, for instance, when N identical objects are placed around the particle. At some point, this is limited by the size and the proximity of the bodies. This includes non-additive contributions arising from quasi-electrostatics interactions between the bodies which lead to frequency shifts for the polaritonic excitations on their respective surfaces [251, 321, 519]. The closer the bodies, the stronger such effects become.

In mechanical nonequilibrium, intriguing extra non-additive features can appear which completely invalidate the additive approximation of Eq. (3.102). They are enhancing the friction force by orders of magnitudes: Consider the frictional force acting on a particle with *both* intrinsic and radiation-induced degrees of freedom given by Eqs. (3.81) and (3.83). The force related to intrinsic dissipative degrees of freedom, $F^{\mathrm{int}} \propto \underline{G}^{\mathrm{s}}_I$, describes e.g. the force on nano-

particles and scales *linearly* in the electric Green tensor. In contrast, the force related to the coupling of the particle to the electromagnetic field, $F^{\mathrm{rad}} \propto \underline{G}_{\Im} \cdot \underline{G}_{\Im}$, scales *quadratically* in the electric Green tensor and represents the dominant contribution to forces experienced by atoms. Hence, while the additive approximation of Eq. (3.102) can be expected to work well for the force related to intrinsic damping $F^{\mathrm{int}} \approx F^{\mathrm{int}}_{\mathrm{add}}$, the force on atoms (or particles without a macroscopic number of intrinsic dissipative degrees of freedom) can instead show significant non-additivities, $F^{\mathrm{rad}} \neq F^{\mathrm{rad}}_{\mathrm{add}}$, thereby indicating a huge potential for optimization. For one, choosing the geometry of the environment properly, the quadratic scaling in the Green tensor permits the possibility of enhancing the force by at least a factor $\sim N^2$. Remarkably, due to the involvement of material properties and rotational degrees of freedom, we will see in the following that more is possible. We closely follow Ref. [M2] in our discussion.

In equilibrium, the non-additivity of Casimir(-Polder) forces received recent attention [373, 520–524] and the naive additive approximation was shown to fail in accurately describing certain situations. Even when refined additive procedures are used, such as the proximity force approximation [22], both over- and under-estimations of up to 50% (depending on the geometry) from more accurate theoretical and experimental investigations are found [121, 224, 525, 526]. The proximity force approximation considers corrections of the Casimir force experienced by bodies with weakly curved interfaces in comparison to the planar case. It shows that the corrections are highly sensitive to the material properties [527, 528] and the number of interacting bodies [529] which has led to the development of advanced numerical methods for more accurate description in complicated geometries [146, 530, 531]. For the Casimir-Polder interaction, it is interesting to note that the leading order contribution to the force scales linearly in the Green tensor [encoding material and geometry, see Eq. (3.52)] which explains the corrections to the additive result which are less dramatic than what we expect in the quantum friction case, where the Green tensor can enter quadratically. Hence, at least qualitatively, the Casimir-Polder forces roughly follow the additive description of Eq. (3.102) and the proximity force approximation is often good enough in helping to understand the behavior of complicated geometries physically [532].

In nonequilibrium, however, completely new forms of non-additivity can occur. The scientific literature on quantum optics only sparsely covers the field of non-additivity in nonequilibrium fluctuation-induced phenomena. Focusing on the interaction between atoms and a material interface, to the best of our knowledge, non-additive behavior has been explored for temperature gradients [533], under the influence of external (Laser) fields [119] or in the context of multiple excited atoms [396, 455] only.

In the following, we show that *mechanical nonequilibrium* can feature strong non-additivities which can enhance friction forces experienced by atoms significantly [M2].

To make a first estimate based on our low-velocity formulas for the quantum friction experienced by particles with intrinsic [Eq. (3.81)] and external degrees of freedom [Eq. (3.97)], we can distinguish roughly three different sources of non-addditivity, two of which cannot be found without including long-time correlations between particle and material-modified vacuum into the description:

- Non-additivity due to changes in the geometry modifying the resonance structure of the single Green tensor (modifying the dispersion relation of the surface plasmon-polaritons for metals). This has been studied extensively in the context of Casimir(-Polder) forces (see above) and is usually neglected by the proximity force approximation which centers its expansion around the planar result.

- Non-additivity due to back-action of environment on the dynamics of the particle. This is particularly important for quantum friction on atoms and mathematically encoded in the quadratic scaling of frictional force with the Green tensor. It is closely related to long-time correlations between particle and environment.

- Non-additivity due to involvement of rotational degrees of freedom. They interlace with the dynamics in a complex way and can reduce friction forces. Again, as we have seen in the previous Section, rotational degrees of freedom are closely related to long-time correlations.

Hence, frictional forces experienced by atoms can be expected to potentially show complex non-additivities. In the spirit of the additive estimate [Eq. (3.103)], the involved non-additivites we expect for mechanical nonequilibrium lead us to an estimate for the possible enhancement (or reduction) of frictional forces on atoms interacting with an ensemble of similar bodies, i.e.

$$F^{\mathrm{rad}} \sim \phi N^2 F_j \tag{3.104}$$

with respect to the single body inducing the force F_j. We define ϕ as the factor connected to rotational degrees of freedom. For instance, in Eq. (3.99), we have seen that *ignoring* rotational degrees of freedom in the context of a single planar interface increases the estimate of the force by a factor of $\phi \sim 63/(63-45) = 3.5$. We can exploit this be choosing highly symmetric geometries: Taking the interaction with one surface at fixed distance as a reference, we expect the friction force in the center of a planar cavity to be enhanced by a factor of $\phi N^2 \sim 3.5(1+1)^2 = 14$, since the impact of exchanging angular momentum is effectively switched off due to the central position in the cavity. Following this line of thought, we expect a rectangular cavity to already lead to an enhancement by a factor of $\phi N^2 \sim 3.5(2+2)^2 = 56$. To sound a note of caution, a higher number of surfaces does not automatically mean a quadratic increase in the radiation-induced friction force. The above estimate is based on the assumption that geometric interference effects in the vicinity of two separated bodies can be neglected. We will illustrate this with the example of a cylindrical cavity which is particularly not to be confused with the geometric limit of an infinite number of surfaces. The cylindrical cavity rather resembles a rectangular cavity ($N = 4$) in its behavior, but shows quantitative deviations from the rectangular cavity since it does not distinguish between different surfaces due to its continuous curvature.

In order to quantitatively access such estimates, we discuss the two examples, the planar and the cylindrical cavity, explicitly in the following [M2].

Planar cavity

As a first example, we consider the case of a particle moving inside a planar cavity of width $2w$ parallel to the two interfaces. We choose the xy-plane of the coordinate system to coincide with the lower plane of the cavity ("1") and the z-axis pointing towards its inner in direction of the other plane ("2"). Without loss of generality, we further assume the motion of the atom to be along the x-axis such that its position is uniquely given by its distance from the lower surface $z_a \in (0, 2w)$. We once again write the component of the wavevector parallel to the planes of the cavity as $\mathbf{p} = (p_x, p_y)$ ($p = |\mathbf{p}|$), where the component along the invariance of motion is given by $h \equiv p_x$. Accordingly, the infinitesimal interval of parallel wavevectors is given by $\mathrm{d}h/2\pi \to \mathrm{d}^2\mathbf{p}/(2\pi)^2$. In the quasi-static regime ($\omega \to 0$), which is most relevant for quantum friction, we have that the cavity resonances are unimportant and the wavevectors are limited by $p \sim \max[z_a^{-1}, (2w - z_a)^{-1}]$. Further, we focus on the evanescent near-field regime for the interaction, where half the width of the cavity w is smaller than the plasma wavelength λ_p (usually hundreds of nanometers for metals [140] and some micrometer for doped semiconductors [534]) and the force can expected to be the strongest. We depict a sketch of the situation in Fig. 3.9. As we have seen for the single interface [Eq. (3.60)], the response of a planar setup in the near-field regime is dominated by transverse magnetic waves in terms of the corresponding TM-reflection coefficients $r_{1,2}$, where the subscript denotes the lower (1) or the upper (2) plate, respectively. The relevant contribution of the Green tensor is then given by (see Refs. [189, 494] and appendix A)

$$\underline{G}(p_x, z_a, \omega) \approx \int \frac{\mathrm{d}p_y}{2\pi} \left\{ \frac{p}{2\epsilon_0} \mathcal{P}_+(p, z_a, \omega) \underline{\Pi} - \frac{p}{2\epsilon_0} \mathcal{R}(p, \omega) \underline{\mathrm{M}} \cdot \underline{\Pi} - \frac{p_x}{2\epsilon_0} \mathcal{P}_-(p, z_a, \omega) \underline{L}_y \right\}, \quad (3.105)$$

where ϵ_0 is the vacuum permittivity and

$$\mathcal{R} = 2 \frac{r_1 r_2 e^{-4pw}}{1 - r_1 r_2 e^{-4pw}}, \qquad \mathcal{P}_\pm = \frac{r_1 e^{2p(w-z_a)} \pm r_2 e^{-2p(w-z_a)}}{1 - r_1 r_2 e^{-4pw}} e^{-2pw}. \quad (3.106)$$

Here, we defined $\underline{\Pi} = \mathrm{diag}[p_x^2/p^2, p_y^2/p^2, 1]$ and $\underline{\mathrm{M}} = \mathrm{diag}[1, 1, -1]$ describes the mirror reflections at the xy-plane. Roughly speaking, the functions $\mathcal{P}_\pm$ are associated with reflections at the planes of the cavity and $\mathcal{R}$ is associated with complete round way trips inside the cavity. We further remark the characteristic denominator which assigns to each of the previous terms an infinite number of Fabry-Perot reflections that are common for cavity systems. We restore the Green tensor for the single interface [Eq. (3.60)] by sending $\mathcal{R} \to 0$ and $\mathcal{P}_\pm \to \mathcal{P}_s = r_\mathrm{NF}^p e^{-2pz_a}$ with r_NF^p the TM-reflection coefficient of the single interface used earlier. In comparison with Eq. (3.96), we note that $\underline{\Sigma}$ is diagonal and $\mathbf{s}_\perp = (0, s_y, 0)$ allows for rotations of the atom around the y-axis only as we could expect from the symmetries of our system.

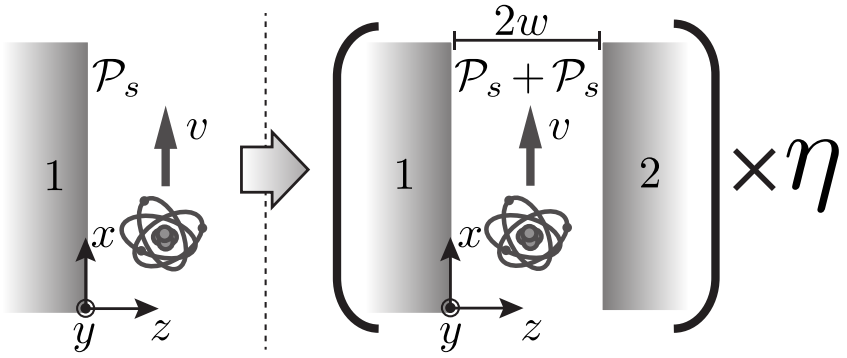

Figure 3.9: Left: The particle, depicted as an atom, moves at constant velocity v parallel to a planar semi-infinite bulk. The response of the single interface is encoded in $\mathcal{P}_s$ [Eq. (3.105)]. **Right**: The particle moves inside a planar cavity of width $2w$. The planes of the cavity can be made from differencent materials. With respect to the single interface, the particle experiences a non-additive friction force described by the factor η. The simple additive description corresponds to $\eta = 1$. Adapted from [M2].

Assuming an Ohmic response of the material, we obtain upon inserting into Eqs. (3.81) and (3.83) in leading order velocity that

$$F^{\mathrm{int}} = -\alpha_0 v^3 \frac{\hbar}{12\pi} \int \frac{\mathrm{d}^2\mathbf{p}}{(2\pi)^2}\, pp_x^4 \left(\mathcal{P}'_{+I} \mathrm{Tr}\left[\underline{\mu}\cdot\underline{\Pi}\right] - \mathcal{R}'_I \mathrm{Tr}\left[\underline{\mu}\cdot\underline{\mathrm{M}}\cdot\underline{\Pi}\right]\right), \tag{3.107a}$$

$$\begin{aligned} F^{\mathrm{rad}} = -\alpha_0^2 v^3 \frac{\hbar}{\pi} \int \frac{\mathrm{d}^2\mathbf{p}}{(2\pi)^2} \frac{\mathrm{d}^2\tilde{\mathbf{p}}}{(2\pi)^2} \frac{p\tilde{p}}{(2\epsilon_0)^2} \\ \times \left(\left[\frac{p_x^4}{6} + \frac{p_x^2\tilde{p}_x^2}{2}\right] \left\{ \left(\mathcal{P}'_{+I}\tilde{\mathcal{P}}'_{+I} + \mathcal{R}'_I\tilde{\mathcal{R}}'_I\right) \mathrm{Tr}\left[\underline{\Pi}\cdot\underline{\tilde{\Pi}}\right] - \left(\mathcal{P}'_{+I}\tilde{\mathcal{R}}'_I + \mathcal{R}'_I\tilde{\mathcal{P}}'_{+I}\right) \mathrm{Tr}\left[\underline{\Pi}\cdot\underline{\mathrm{M}}\cdot\underline{\tilde{\Pi}}\right] \right\} \right. \\ \left. + \frac{p_x\tilde{p}_x}{p\tilde{p}} \left[\frac{p_x^3\tilde{p}_x}{2} + \frac{p_x\tilde{p}_x^3}{6}\right] \mathcal{P}'_{-I}\tilde{\mathcal{P}}'_{-I} \mathrm{Tr}\left[\underline{L}_y^{\mathrm{T}}\underline{L}_y\right] \right). \end{aligned} \tag{3.107b}$$

For the sake of readability, we dropped the functional dependencies of the functions under the integral. Further, the prime again indicates the derivative with respect to frequency, all functions are evaluated at $\omega = 0$ and the tilde indicates a dependence on $\tilde{p}$ instead of p. For example, we have that

$$\tilde{\mathcal{P}}'_{\pm I} = \lim_{\omega\to 0} \mathrm{Im}[\partial_\omega \mathcal{P}_\pm(\tilde{p}, z_a, \omega)]. \tag{3.108}$$

Lastly, we assume local materials with both plates made from exactly the same material, i.e. $r \equiv r_1 = r_2 = r_{\mathrm{NF}}^p \sim 2\mathrm{i}\epsilon_0\rho_{\mathrm{lc}}\omega$ at small frequencies. We note that including spatial dispersion in the description is most likely to enhance the effect reported in the following (see Sec. 3.4.1).

We start with discussion the friction connected to intrinsic dissipative degrees of freedom of the particle, $F^{\rm int}$ [Eq. (3.107a)]. The tensor $\mu_{\Re}(\omega=0)$ is symmetric such that we have $\mathrm{Tr}[\underline{\mu}\cdot\underline{\mathrm{M}}\cdot\underline{\Pi}]=\mu_{xx}p_x^2/p^2+\mu_{yy}p_y^2/p^2-\mu_{zz}$. Writing further $(1-r^2e^{-4pw})^{-1}=\sum_{n=0}^{\infty}r^{2n}e^{-4npw}$, we can solve the appearing summations exactly and the force reads at the center of the cavity $z_a=w$ (see appendix E for the general formula valid for arbitrary position inside the cavity)

$$F^{\rm int}(z_a=w)=-\hbar v^3\frac{\alpha_0\epsilon_0\rho_{\rm lc}}{(2w)^7}\frac{\pi^4}{128}\left(\Big[5\mu_{xx}+\mu_{yy}+6\mu_{zz}\Big]-\frac{1}{64}\Big[5\mu_{xx}+\mu_{yy}-6\mu_{zz}\Big]\right) \tag{3.109}$$

which explicitly takes the infinite number of Fabry-Perot reflections into account. We recall that the dominant contribution to the total recoil momentum absorbed by the particle is given by wavevectors $p\lesssim\max(z_a^{-1},[2w-z_a]^{-1})$ and therefore the maximal deviation from the additive expression occurs for $z_a=w$. Further, we note that the first term in the brackets is related to $\mathcal{P}_+$ and the second to $\mathcal{R}$. For comparison, we define the additive approximation by neglecting $\mathcal{R}$ as well as the denominator describing Fabry-Perot reflections in Eqs. (3.105) such that we can write $\mathcal{P}_+(z_a)\approx\mathcal{P}_{\rm s}(z_a)+\mathcal{P}_{\rm s}(2w-z_a)$, where again $\mathcal{P}_{\rm s}$ gives the relation for the single interface defined below Eq. (3.106). The additive approximation of the force then takes the form

$$F^{\rm int}\approx F^{\rm int}_{\rm add}\equiv F^{\rm int}_{\rm s}(z_a)+F^{\rm int}_{\rm s}(2w-z_a),\quad\text{with } F^{\rm int}_{\rm s}(z_a)=-\frac{15\hbar}{4\pi^2}\frac{\alpha_0\epsilon_0[5\mu_{xx}+\mu_{yy}+6\mu_{zz}]\rho_{\rm lc}v^3}{(2z_a)^7} \tag{3.110}$$

the contribution of the single surface [58]. At the center of the cavity, this reduces to

$$F^{\rm int}_{\rm add}(z_a=w)=-\hbar v^3\frac{\alpha_0\epsilon_0\rho_{\rm lc}}{(2w)^7}\frac{15}{4\pi^2}[5\mu_{xx}+\mu_{yy}+6\mu_{zz}]\times 2, \tag{3.111}$$

where the factor of 2 explicitly takes the presence of the second surface into account. In order to quantify the impact of non-additivity on $F^{\rm int}$, we introduce the non-additivity factor $\eta^{\rm int}=F^{\rm int}/F^{\rm int}_{\rm add}$ and specify the components of the $\underline{\mu}$-tensor in the following. In the limit of an isotropic intrinsic bath[16], the tensor $\underline{\mu}\to\mu\mathbb{1}$ effectively becomes a scalar such that the term associated with $\mathcal{R}$ vanishes identically since $\mathrm{Tr}[\underline{\mathrm{M}}\cdot\underline{\Pi}]=0$. In this case, we obtain over the full range of the cavity that

$$1<\eta^{\rm int}(z_a)\leq\frac{1}{15}\left(\frac{\pi}{2}\right)^6\approx 1.0015. \tag{3.112}$$

The maximum value is reached at the center of the cavity $z_a=w$ and amounts to a non-additive correction of about 0.14%. It is interesting to note that the bounds of Eq. (3.112) are independent of the size of the cavity and do depend on the static value of the reflections coefficient only, saturating for $r(\omega=0)=1$. For comparison, over the range of the cavity and for the same setup, the Casimir-Polder forces would yield a non-additivity with similar magnitude, but show a strong dependence on the precise material properties. The reason is that

[16] Similarly, if we write the dissipation tensor in polar coordinates, $\mu_{xx}=\mu\cos^2\alpha\sin^2\beta$, $\mu_{yy}=\mu\sin^2\alpha\sin^2\beta$, $\mu_{zz}=\mu\cos^2\beta$ with $\alpha\in[0,2\pi)$ and $\beta\in[0,\pi]$ and average over the solid angle $\mathrm{d}\alpha\mathrm{d}\beta\sin\beta$, we also obtain a vanishing integral connected to roundway-trips ($\mathcal{R}_I'$).

the Casimir-Polder force derives from a comparably large frequency interval, while quantum friction originates from the atom-surface interaction around $\omega \approx 0$ only, where most common materials can be characterized by a limited number of constant parameters. Also, for symmetry reasons, the Casimir-Polder force vanishes at the center of the cavity when both sides of the cavity are exactly equal (see also discussion at the end of Sec. 3.3). If we break the condition of the internal bath to be isotropic, consider higher orders in the atomic polarizability α_0 or use the static atomic polarizability instead ($\alpha_0 \to \underline{\alpha}_0$), the result is slightly different since terms related to $\mathcal{R}'_I$ also contribute [second term in Eq. (3.109)]. We observe the largest deviation from the additive result again at the center of the cavity, but this time the approximation can both over- and underestimate the exact result of Eq. (3.109). Physically, for an anisotropic memory kernel, the term connected to $\mathcal{R}'_I$ introduces a distance-independent contribution connected to the constructive interference of excitations inside the cavity. Depending on the diagonal entries of $\underline{\mu}$, the qualitative impact of the correction can be different: If $\mu_{zz} > \mu_{xx}, \mu_{yy}$, this term tends to increase the force, while reducing it in the opposite case. For example, choosing $\mu_{zz} = 0 \neq \mu_{xx} = \mu_{yy}$ or $\mu_{zz} \neq 0 = \mu_{xx} = \mu_{yy}$, the correction due to non-additivity, respectively, evaluates to roughly $\mp 2\%$. Finally, we want to mention that we can exceed the bound of Eq. (3.112) when the two plates are made from different materials. The largest non-additivity can then be detected not in the center of the cavity, but at a position closer to the plate featuring lower dissipation. Indeed, if both plates can still be considered spatially local with the respective dissipation ρ_1 and ρ_2 (see Fig. 3.10) that are at the same order of magnitude, the position where maximal non-additivity can be encountered is shifted to

$$\frac{z_a}{w} \sim \frac{9 + 7\frac{\rho_2}{\rho_1}}{8\left(1 + \frac{\rho_2}{\rho_1}\right)} \to 1, \qquad \text{if } \rho_1 = \rho_2. \tag{3.113}$$

Remarkably, even when one plate of the cavity is made from a perfectly conducting material which by itself cannot generate friction forces [132], the total friction is still enhanced with respect to the interaction with the single surface: The reflection at the perfect conductor leads to an effectively larger number of image dipoles interacting with the dissipative surface[17]. In this way, as expected, the non-additivity of friction forces acting on particles with intrinsic dissipation mechanisms is mainly due to a modified resonance structure of the environment encoded in the precise form of the Green tensor.

In summary, if the particle possesses intrinsic dissipative degrees of freedom, the additive approximation holds to a very good approximation for frictional forces in the steady state. We refer to appendix E for an extensive derivation and discussion of the previous estimates.

The frictional force associated with radiation damping shows very different and intriguing characteristics which are mostly connected to the quadratic scaling in the electric Green tensor. In contrast to F^{int}, F^{rad} remains finite even in the limit $\underline{\mu} \to 0$. Again, we focus on local plates made from identical (dissipative) local materials with $r_{1,2} \sim r(\omega = 0) + 2\mathrm{i}\epsilon_0\rho_{\text{lc}}\omega$ and define, for

[17] Equivalently, this can also be understood by the fact that the boundary conditions at the interface of the perfect conductor lead to a shift of the surface plasmon-polariton frequency (compare Sec. 1.2).

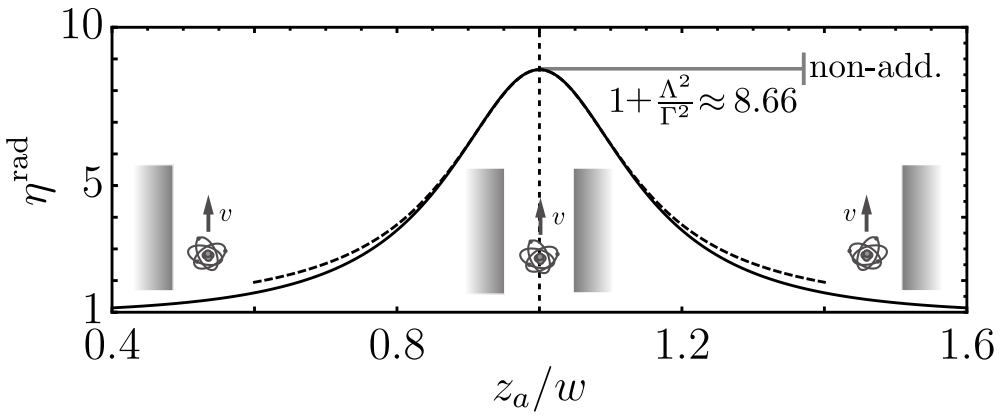

Figure 3.10: Non-additive enhancement [Eq. (3.115)] of the friction experienced by an atom ($\underline{\mu} \to 0$) moving inside a planar cavity [M2]. The two sides of the cavity are made of the same local material with $r(0) = 1$. At the center of the cavity, the non-additivity is the strongest and the shape of the curve can be approximated (dashed line) by the Lorentzian of Eq. (3.116). Adapted from [M2].

comparison, the additive approximation

$$F^{\rm rad}_{\rm add}(z_a) \equiv F^{\rm rad}_{\rm s}(z_a) + F^{\rm rad}_{\rm s}(2w - z_a) \qquad \text{with } F^{\rm rad}_{\rm s} = -\hbar v^3 \frac{18}{\pi^3} \frac{\alpha_0^2 \rho_{\rm lc}^2}{(2z_a)^{10}} \tag{3.114}$$

the force instigated by a single planar interface [M1]. Defining the non-additivity factor $\eta^{\rm rad}$ similar to Eq. (3.112), we now have for the full expression compared to its additive approximation that

$$1 < \eta^{\rm rad}(z_a) \leq \frac{13249}{56700} \left(\frac{\pi}{2}\right)^8 \approx 8.66, \tag{3.115}$$

which amounts to a non-additivity of about one order of magnitude. This is equivalent to a force that is 17 times larger than the single-plate result. Again, the non-additivity is the strongest at the center of the cavity and when $r(\omega = 0) = 1$. As in the case of $F^{\rm int}$, we can exceed the bound of Eq. (3.115) by using different materials for the plates of the cavity. Further, for local materials, the result is independent of the cavity's width and the shape of the curve $\eta(z_a)$ is robust against changes in the specifics of the materials. We report a numerical evaluation of $\eta(z_a)$ in Fig. 3.10 and the explicit form of $F^{\rm rad}$ as a function of the position inside the cavity leading to Eq. (3.115) can be found in appendix E. Around $z_a \sim w$, $\eta(z_a)$ shows a Lorentzian-like shape

$$\eta^{\rm rad}(z_a) \approx 1 + \frac{\Lambda^2}{(1 - z_a/w)^2 + \Gamma^2}, \tag{3.116}$$

where the parameters $\Lambda \approx 0.42$ and $\Gamma \approx 0.15$ are found by performing a numerical expansion of

η^{rad} around its maximum at $z_a = w$. The enhancement of the force at the center of the cavity clearly goes beyond a simple quadratic enhancement. The surprisingly strong enhancement can be dissected by having a closer look on the distinct terms in Eq. (3.107b): Starting with the second line which involves the diagonal part of the Green tensor, we note that the function $\mathcal{P}_{+I}$ is responsible for an enhancement of roughly a factor of two with respect to the naive addition. Hence it can most directly be associated with the squared non-additivity allowing for enhancements of $\sim N^2$. The other three terms containing contributions from $\mathcal{R}'_I$ arise from the anisotropy of the atomic damping induced by the material-modified vacuum and are non-existent in the intrinsic counterpart of the friction force. In particular, the second term of the second line, i.e. the one $\propto \mathcal{R}'_I\tilde{\mathcal{R}}'_I$, is independent of the particle's position inside the cavity and results from a constructive interference in the electromagnetic density of states of the cavity. Combined, these terms lead to a non-additivity of some percent. The other big contribution to the non-additivity of the force is related to the third line of Eq. (3.107b) which is connected to rotational degrees of freedom. While it tends to reduce the force in less symmetric configurations [see discussion around Eq. (3.104)], this term vanishes identically at the center of the cavity since $\mathcal{P}_- = 0$ for $z = w$. Physically, the symmetry of the system inhibits the exchange of net angular momentum between atom and field which starts to become important only if the particle assumes a position close to either one of the plates. Indeed, inserting the skew-symmetric part of the cavity Green tensor [Eq. (3.105)] into Eq. (3.35), we find that the spin local density of states vanishes at $z_a = w$, i.e. $\boldsymbol{\rho}_{\mathrm{s}}(h, z_a = w, \omega) = \mathbf{0}$. In combination, these effects cause the friction force on atoms to be highly non-additive leading to an actual enhancement of the force by a factor of $\phi N^2 \approx 17$ with respect to the interaction with a single planar interface. This is in excellent agreement with our first rough estimate of Eq. (3.104).

Cylindrical cavity

Encouraged by the previous findings, we now turn our attention to a more elaborate geometry. Instead of a rectangular cavity, which might be the next obvious choice, we rather consider a cylindrical cavity which is easier to treat analytically due to the absence of sharp edges. It will further provide the opportunity to discuss an additional mechanism enhancing friction forces connected to the surface plasmon-polaritons.

For simplicity, we focus on particles without intrinsic degrees of freedom ($\underline{\mu} \to 0$), e.g. atoms, and restrict our discussion to the center of the cavity where the non-additive features can be expected to be maximal (see previous Section). We consider the radius R of the cylinder smaller than the atomic resonance wavelength λ_a and any other resonances in the system such that retardation effects can safely be neglected (near-field regime discussed earlier), since this is where friction forces are most relevant. Further, we consider the cylindrical cavity to be made from a spatially local Drude material and the atom moves in coaxial direction in its center (see Fig. 3.11). We give the electric Green tensor for such a situation in appendix A.3. Choosing the xy-plane as the cross Section of the cylinder and the z-axis along its axis coinciding with vanishing radius ϱ in cylindrical coordinates, the scattered part of the Green tensor can be written as [357, 535, 536]

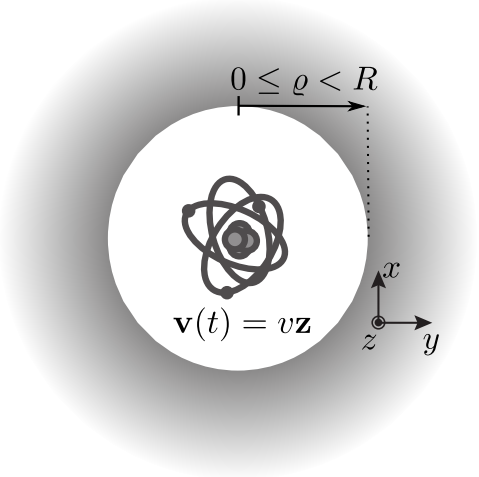

Figure 3.11: An atom moves with velocity v along the symmetry axis (z-direction) at the center of a cylindrical cavity.

$$\underline{g}(h, \varrho \to 0, \omega) \sim \frac{h^2}{8\epsilon_0} \left(r^{n=1}_{NN,\mathrm{NF}} \left[\boldsymbol{xx} + \boldsymbol{yy} \right] - 2 r^{n=0}_{NN,\mathrm{NF}} \boldsymbol{zz} \right), \tag{3.117}$$

where h is again the wavevector parallel to the cylinder axis. Interestingly, in comparison to the planar setup, the reflection coefficients are replaced by the discrete (Mie) scattering coefficients r^n_{NN}, where the substript "NN" denotes a certain type of cylindrical wavevector functions (see appendix A.3) and the additional subscript "NF" denotes that we need their near-field approximation only. In fact, for arbitrary position inside the cylinder with $\varrho > 0$, there is an infinite discrete number of such coefficients, but along the axis of the cylinder only the first two happen to remain in the near-field due to the high symmetry at this particular line. Comparing to the planar setup, the discrete number of resonances appears due to the finite perimeter of the cylinder which effectively changes the topology of the setup (compare also to the case of a sphere in Sec. 2.1.3): We have *one* continuous (h) and *one* discrete (n) coordinate in reciprocal space instead of two ($|\mathbf{p}| = \sqrt{p_x^2 + p_y^2}$). In particular, the coefficients in the near-field can be written as [537]

$$r^n_{NN,\mathrm{NF}} = (-1)^{n+1} \frac{2}{\pi} \frac{K_n(|h|R)}{I_n(|h|R)} \frac{\epsilon(\omega) - 1}{\epsilon(\omega) + f_n(|h|R)}, \quad f_n(|h|R) = -\frac{K_n(|h|R) I_n'(|h|R)}{I_n(|h|R) K_n'(|h|R)}, \tag{3.118a}$$

where $f_n(x)$ is a positive real function for all $x > 0$, the prime denotes a derivative with respect to the function's argument and $I_n(x)$ and $K_n(x)$ are the modified Bessel functions of first and second kind [538], respectively. Expanding further for small frequencies, the part of the Green tensor relevant for our purposes reads

$$\mathrm{Im} \lim_{\omega\to 0} \partial_\omega \underline{g}(h, \varrho \to 0, \omega) \sim \frac{h^2}{2} \left(\rho_1(|h|R) \left[\boldsymbol{xx} + \boldsymbol{yy} \right] + 2\rho_0(|h|R) \boldsymbol{zz} \right) e^{-2|h|R}. \tag{3.119}$$

Here, the exponential denotes that we are working in the evanescent regime and we note the formal resemblance to the planar case [see also Eq. (3.125) below]. However, its functional dependency is rather different due to the discrete orders of resonances (see right panel of Fig. 3.12) and the related functions

$$\rho_n(|h|R) = \frac{\rho_{\mathrm{lc}}}{2\pi} \frac{K_n(|h|R)[1 + f_n(|h|R)]}{I_n(|h|R)} e^{2|h|R} \to \rho_{\mathrm{lc}}, \qquad |h|R \to \infty, \tag{3.120}$$

indicating an asymmetric dissipation with respect to spatial directions. Further, Eq. (3.120) is spatially nonlocal and depends on the wavevector due to the impact of the geometry (see next paragraph). Upon inserting into the expression for the friction force experienced by atoms [Eq. (3.97)], we obtain

$$\frac{F^{\mathrm{rad}}}{F_{\mathrm{s}}^{\mathrm{rad}}(z_a = R)} \sim \mathcal{C} \approx 52, \tag{3.121}$$

where we define the positive constant

$$\mathcal{C} = \frac{256}{9} \int_0^\infty \mathrm{d}x\mathrm{d}y \; x^2 y^2 \left\{ \frac{x^4}{6} + \frac{x^2 y^2}{2} \right\} \frac{\rho_1(x)\rho_1(y) + 2\rho_0(x)\rho_0(y)}{\rho_{\mathrm{lc}}^2} e^{-2x} e^{-2y}. \tag{3.122}$$

Remarkably, we roughly obtain a 50-fold increase of the frictional force with respect to the force originating from the interaction with the single interface $F_{\mathrm{s}}^{\mathrm{rad}}$ at separation $z_a = R$ [Eq. (3.99)] which agrees well with our earlier rough estimate based on a simple local material and a rectangular cavity [see below Eq. (3.104)]. The difference between the rectangle and the cylinder of course originates from their different geometric symmetry (discrete vs. continuous). This clearly highlights the potential for geometric optimization and a broad study of different geometries.

Geometry-induced spatial nonlocality

Even though our rough estimate on the possible non-additive enhancements for frictional forces [Eq. (3.104)] could satisfyingly predict the correct orders of magnitude, the more accurate calculations of the previous two Sections still revealed a deviation of some percent. The physical reason lies in the spatial correlations present in the more complicated geometries. Indeed, in the case of a cylindrical cavity, the low frequency expansion of the electric Green tensor in Eq. (3.119) shows a dissipation $\rho_n(|h|R)$ that depends on the wavevector of the radiation. In contrast to Sec. 3.4.1, where spatial nonlocality was physically connected to material parameters,

we purposefully chose a local Drude model for deriving the results on the non-additivity of quantum friction. Hence, in the present case, the spatial nonlocality is *geometry-induced*. This can be seen more clearly by choosing metallic interfaces and once again investigating the surface plasmon-polariton (SPP) resonances (compare to Sec. 1.2.2). In the cylindrical geometry, the SPPs are given by the root of the denominator in Eq. (3.118) (see Refs. [539, 540] for early treatments of SPPs at cylindrical interfaces),

$$\epsilon(\omega_{\rm sp}^n) + f_n(|h|R) = 0 \to \omega_{\rm sp}^n(|h|R) \sim \frac{\omega_{\rm p}}{\sqrt{1+f_n(|h|R)}} - \mathrm{i}\frac{\Gamma}{2}, \qquad \omega_{\rm p} \gg \Gamma, \tag{3.123}$$

where we used the local Drude model for the bulk's permittivity $\epsilon(\omega) = 1 - \omega_{\rm p}^2/(\omega^2 + \mathrm{i}\Gamma\omega)$. Eq. (3.123) can bee seen as the generalization of the corresponding relation for the planar interface [Eq. (1.32)] and reduces to the planar result when the radius of the cylinder is much larger than the wavelength of the electromagnetic excitation, i.e. $\omega_{\rm sp}^n(|h|R) \to \omega_{\rm sp} = \omega_{\rm p}/\sqrt{2}$ for $|h|R \to \infty$. As one could have expected, for smaller and smaller wavelengths, the wave cannot resolve the curvature of the cylinder and effectively perceives the interface as planar. For finite values of $|h|R$, however, the curvature modifies the surface resonances and the corresponding frequency is larger than in the planar case, i.e. $\omega_{\rm sp}^n(|h|R) > \omega_{\rm sp}$ for all $|h|R$. We display a numerical evaluation of the dispersion relation for the SPP at the interface of a cylindrical cavity in the left panel of Fig. 3.12, where we compare the non-retarded solution of Eq. (3.123) to their retarded counterpart. We obtain the latter using a numerical root-finding routine applied to the retarded scattering coefficients for a cylindrical cavity listed in Eq. (A.34). Computing quantum friction, which is highly sensitive to long-time correlations between atom and environment, we are actually less interested in the real part of the SPPs resonance, but rather its dissipative low-frequency tail; see Fig. 1.6. For the cylindrical cavity, it becomes apparent from Eq. (3.120) that the geometry-induced nonlocality is passed on from the SPP resonance to the relation for the Green tensor by

$$\rho_n(|h|R) \sim \frac{\Gamma}{\epsilon_0[\omega_{\rm sp}^n(|h|R)]^2}\frac{K_n(|h|R)}{I_n(|h|R)}\frac{e^{2|h|R}}{2\pi} \tag{3.124}$$

and is hence also reflected in the low-frequency dissipation of the cylinder. Note that we take the limit $\Gamma/\omega_{\rm p} \ll 1$ for $\omega_{\rm sp}^n$ such that the previous expression is real.

Having identified the geometry-induced nonlocality as the deeper physical mechanism leading to some quite subtle non-additive features for quantum friction in a cylindrical cavity, it becomes opportune to revisit the planar cavity from this new perspective. To this end, we rewrite Eq. (3.105) as $\underline{G}(p_x, z_a, \omega) = \int \frac{\mathrm{d}p_y}{2\pi}\underline{g}(\mathbf{p}, z_a, \omega)$ and expand the result for small frequencies. At the center of the cavity ($z_a = w$), we obtain

$$\underline{g}_I'(\mathbf{p}, z_a = w, 0) \sim 2p\left\{\rho_{xy}(pw)\left[\frac{p_x^2}{p^2}\boldsymbol{xx} + \frac{p_y^2}{p^2}\boldsymbol{yy}\right] + \rho_z(pw)\boldsymbol{zz}\right\}e^{-2pw}. \tag{3.125}$$

The low-frequency dissipation in the Green tensor depends on the spatial direction and the resistivities,

$$\rho_{xy}(pw) = \rho_{\mathrm{lc}}(1+\tanh[pw])^2/4, \qquad \rho_z(pw) = \rho_{\mathrm{lc}}(1+\coth[pw])^2/4, \tag{3.126}$$

which are spatially nonlocal due to the geometry. They can be understood as the analog of the resistivity of the finite-sized Drude slab that we discussed earlier in Eq. (3.92): Both setups, the slab and the planar cavity, are included in the Green tensor description of a planar system consisting of three layers [189]. The difference is that in the slab geometry, the layers are chosen to be made of vacuum–metal–vacuum and field as well as source are placed in one of the vacuum layers, while in the case of a planar cavity one chooses the layers to be made of metal–vacuum–metal and places field and source in the middle layer. For large separations between the plates of the cavity, we recover the corresponding single-plate result since $\rho_{xy}(pw) = \rho_z(pw) \to \rho_{\mathrm{lc}}$ for $pw \to \infty$. Noting that $\tanh[x]$ and $\coth[x]$ are odd functions in their argument, we recall that such symmetry properties can be related to the symmetries of the electric field distribution of the SPPs in around the interface [502] [see also discussion after Eq. (3.92)]. Hence, $\rho_{xy/z}$ represent the combined dissipative properties of the coupled SPPs of the cavity's planar interfaces. The larger the distance between the plates, the weaker the coupling and the smaller the influence of geometry-induced nonlocality. We report a numerical evaluation for the dissipation in both the planar and the cylindrical cavity in the right panel of Fig. 3.12.

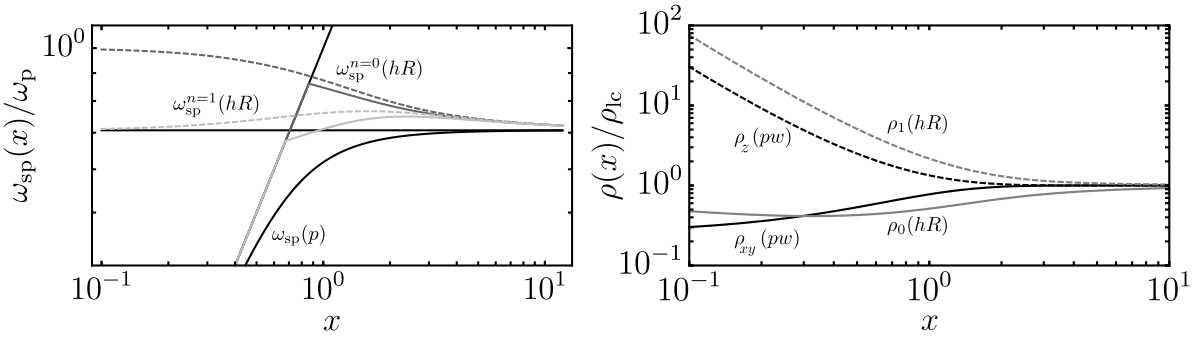

Figure 3.12: Left: Dispersion relation ($\rho_{\mathrm{lc}} = 0$) of the surface plasmon-polariton (SPP) resonance $\omega_{\mathrm{sp}}(x)$ for a planar interface with $x = p$ [Eq. (1.32)] (black, solid line) and the $n = 0$ (dark gray) as well as the $n = 1$ resonance (light gray) of a cylindrical cavity with $x = hR$ for $h > 0$. We report both the non-retarded near-field result of [Eq. (3.123)] (dashed) and the fully retarded version obtained numerically from the resonance structure of Eq. (A.34) (solid). Contrary to the visual impression in the plot, the retarded version of the SPP resonances are smooth functions that approximately align with the light cone for $x \to 0$. We display the SPP resonance of a single interface $\omega_{\mathrm{sp}} = \omega_{\mathrm{p}}/\sqrt{2}$ and the light-line $\omega = cp$ as black solid lines. **Right**: Corresponding dissipation ($\rho_{\mathrm{lc}} \neq 0$), i.e. the imaginary part of the Ohmic scattering coefficient. We report the results for the center of a planar cavity [Eq. (3.125)] with $x = pw$ (black) and a cylindrical cavity [Eq. (3.120)] with $x = hR$ for $h > 0$ (gray). For the planar cavity, we distinguish ρ_z (dashed) and ρ_{xy} (solid) and for the cylindrical cavity the $n = 0$ (solid) and the $n = 1$ (dashed) mode. We use the Drude model for the bulk permittivity and take parameters for gold from Ref. [140].

3.5 Summary and conclusion

We considered a particle moving along the symmetry axis of translational invariant ensemble of macroscopic bodies. Taking both intrinsic as well as external dissipative degrees of freedom for the particle into account, we solved the dynamics of the particle's dominant dipole transition exactly by means of a linear integro-differential quantum Langevin equation. In the static regime at constant velocity, where the system can reach a nonequilibrium steady-state, we obtained closed expressions for the particle's polarizability and the fluctuations of dipole and field. Our model is fully non-Markovian, does not rely on any equilibrium-based assumptions, fully takes the back-action of the environment on the particle into account and respects the potentially complex tensorial structure of the involved quantities which can be sensitive to the spin (polarization) of (virtual) photons. In all cases, we restricted our discussion to non-relativitstic velocities, assumed a linear response of the particle with respect to external perturbations and demanded that the particle's center of mass approximately obeys a classical uniform trajectory. In regard of the classical trajectory, it is important to emphasize that dispersion forces can actually lead to a decoherence of the particle's average center-of-mass position [541]. For our purposes, however, we assume that the Casimir-Polder interaction and friction forces only marginally affect the (approximate) uniform motion. Further we note that, in experiments, controlling the atomic motion could be achieved by lasers which are known to add linearly to the fluctuating fields [542] and lead to mixing terms between the fields and the vacuum- and laser-induced polarizability of the particle [119], respectively. This only quantitatively modifies the presented results.

Based on our model, we have studied velocity-corrections to the Casimir-Polder force [Eq. (3.50)] and the quantum friction force emerging due to the motion [Eqs. (3.81) and (3.83)]. We derived a low-frequency contribution (3.59) to the Casimir-Polder force which we could relate to long-time correlations that resemble the behavior of classical fluctuations [Eq. (3.74)]. Interestingly, due to the nonequilibrium interaction with the surface, the combination of confined light in the vicinity of the interface and the spin-momentum locking of surface waves leads to an asymmetric spin local density of states experienced by the particle particle. This can lead to mean rotations of the particle in counter-intuitive direction [Eq. (3.36)]. Capturing rotational degrees of freedom in the theoretical description also modifies the Casimir-Polder and quantum friction forces and enabled us to show that especially quantum friction is a pure nonequilibrium effect that cannot be explained by equilibrium-based approximations or assumptions [Eq. (3.99)]. Quantum friction, in particular, is very sensitive to the dissipative low-frequency tail of the interface's resonances and hence to all forms of dissipation in the materials. Here, we could show in the case of metals that including spatial dispersion in the description of the material can lead to enhancements of the frictional force by some orders of magnitude when the atom-surface separation becomes comparable to the bulk electron's mean free path [Eq. (3.84)]. Along these lines, we extensively discussed different theoretical approaches to model spatial dispersion and assessed their practicality when applied to increasingly complex geometries [Eqs. (3.88), (3.89) and (3.93)]. Further, we discovered that friction forces on atoms are highly non-additive with respect to changes in the geometry [Eq. (3.104)]. Considering the examples of a planar and a cylindrical cavity, we obtained a 17-fold (Eq. (3.115)) and a 52-fold [Eq. (3.121)] increase of friction at the center of the cavity when compared to the force resulting from the interac-

tion with a single interface, respectively. Physically, we explained this phenomenon from the complex interplay between geometry-induced spatial nonlocality [Eq. (3.123)], the effective transfer of angular momentum to the particle and the non-Markovian back-action of the environment on the dynamics of the atom in the nonequilibrium situation. Mathematically, the latter property is encoded in the fact that the friction force scales quadratically in the setup's Green tensor encoding geometry and material properties. In this respect, it is interesting to note that the friction on atoms scales quadratically also in the atom's vacuum polarizability $F^{\mathrm{rad}} \sim \alpha_0^2$. Hence, increasing the polarizability of the particle, or even using multiple atoms in close proximity might introduce additional correlations [543] in the system that add up to the friction force in a distinct non-additive way. In the prospect of recent success on controlling the motion and the interaction between a small number of single atoms separately [544], further studying the non-additivity connected to the atom's polarizability becomes a promising feature and is left for future work.

Finally, we want to emphasize again that most of the described effects can be seen as a direct consequence of including long-time correlations between particle and nonequilibrium environment in our description. In the following Chapter, we further elaborate on the fundamental meaning of long-time correlations for nonequilibrium dispersion forces.

CHAPTER 4

Steady-State Quantum Thermodynamics of Mechanical Nonequilibrium

We reconsider the case of mechanical nonequilibrium from the thermodynamic perspective. Focusing on the steady-state regime of an atom moving along the direction of invariance of a macroscopic ensemble, we discuss the internal energy as well as the power flux in and out of the atomic subsystem and establish a connection to the fluctuation-dissipation inequality which formalizes the increase of fluctuations in a driven system. We bring the arguments laid out in the first Chapter 1 full circle by providing a quantified and rigorous explanation why long-time correlations between separated subsystem constitute an unalienable feature of mechanical nonequilibrium. The present chapter contains work by the author that has been published in Ref. [M2, M6].

After providing a broad introduction to low-frequency fluctuations in the context of dispersion forces (see Chapter 1), we have dealt with several applications of the general formalism focusing on the impact of long-time correlations between different subsystems (Chapters 2-3). From the theoretical point of view, the general focus was set on the assumptions and approximations on the underlying statistics of the interaction between particle and material-modified vacuum. It is a characteristic of dispersion forces to derive from a broad range of frequencies and especially to be sensitive to small frequency (or long-time) correlations in the system. On that basis, we could already rule out the Markovian approach (in the case of a particle interacting with a thermodynamic bath sometimes extended to the so-called Born-Markov approximation [58, 113]) in certain equilibrium and nonequilibrium situations. The correct formulation for equilibrium dispersion forces turned out to be based on the fluctuation-dissipation relation (see Chapters 1 and 2). In nonequilibrium, the equilibrium-based approach of assuming local thermal equilibrium (LTE) seemed to appropriately describe the situation of Casimir-Polder forces in mechanical nonequilibrium (see Sec. 3.3), but failed completely in the context of quantum friction experienced by atoms without intrinsic dissipation mechanisms (see Sec. 3.4). In the latter case, we needed a fully self-consistent description that is exact within the realm of our assumptions in order to capture the relevant physics.

In this Chapter, we aim to raise the previous exemplary discussion to a more fundamental level by finding the common physical principles that determine the validity and accuracy of different statistical approaches to nonequilibrium situations. The goal is to narrow the problem down to a few important physical observables. We aim to deduce a set of guidelines that can contribute to the process of determining the actually needed level of complexity for describing dispersion forces in mechanical nonequilibrium situations. To this end, we change perspective and analyze the thermodynamics of the interaction between the particle and the material-modified vacuum. We concentrate on the situation of mechanical nonequilibrium in the steady-state, since we have derived an exact solution for the dynamics of the system. Further, if

not stated otherwise, we focus on the dynamics of an *atom* described by its dominant dipole transition for clarity of the drawn arguments. Finally, we again consider geometries featuring at least one invariant axis along the direction motion (see Fig. 3.1). For concrete numerical examples, however, we will adduce the simplest situation of an atom in front of a planar semi-infinite half space. We note, however, that our formalism can be readily applied to explore different geometries with arbitrary spatially homogeneous materials (see e.g. Section 3.4.3 and Ref. [M2]). We show that, even in cases where the discrepancy between the "approximate" and the more carefully derived results might seem to be quantitatively marginal on the level of forces, the errors become manifest and easily identifiable when one applies the thermodynamic principles. It turns out that the LTE approach is hardly justifiable and in fact leads to serious thermodynamic defects such as an unbounded increase of the particle's internal energy. This defect is artificial and not present in the actual physical system which can be resolved by a more careful calculation based on the approach introduced in Chapter 3. Our analysis shows how thermodynamic principles can provide strong constraints in the description of nonequilibrium atom-field interactions.

4.1 Quantum Langevin equation and equilibrium energy

From now on, we will proceed with one technical difference with respect to the previous Chapters: We employ the symmetric version of the fluctuation-dissipation relation [Eq. (1.23)] by using the symmetric quantum average instead, i.e. $\langle\hat{A}\hat{B}\rangle_{\mathrm{sym}} \equiv \langle\hat{A}\hat{B}+\hat{B}\hat{A}\rangle/2$ for two operators $\hat{A}$ and $\hat{B}$. For vector operators, this is to be understood component-wise, i.e. $\langle\hat{\mathbf{A}}\hat{\mathbf{B}}\rangle_{\mathrm{sym},ij} \equiv [\hat{A}_i\hat{B}_j+\hat{B}_j\hat{A}_i]/2$. Although the two approaches are mathematically equivalent, we chose the symmetric average since we intend to assign a physical meaning to every term in the dipole's equation of motion individually which is more intuitive by enforcing every taken average to be hermitian [156].

We start our discussion with revisiting the situation of an atom interacting with the material-modified vacuum in *equilibrium* at zero temperature. This situation has been discussed by many authors before and we refer, e.g., to Refs. [74, 136, 138, 353, 545–548] for further details. In our particular case, we start from the equation of motion for the atomic dipole moment operator $\hat{\mathbf{d}}$ coupled to the electric field $\hat{\mathbf{E}}$ we first introduced in Sec. 2.1.1 and later generalized in Eq. (3.3) for the situation of nonequilibrium. For now, we focus on the case evaluated at zero velocity $v=0$ and introduce a more convenient notation inspired by the works on the quantum Langevin equation (see e.g. [155]). In the (stationary) limit of large times, the system reaches its equilibrium state [136, 176, 288] and we can write for the quantum Langevin equation [53, M2, 155]

$$\frac{\ddot{\hat{\mathbf{d}}}(t)+\omega_a^2\hat{\mathbf{d}}(t)}{\alpha_0\omega_a^2}+2\int_0^\infty \mathrm{d}\tilde{t}\,\left[\frac{\partial}{\partial\tilde{t}}\,\underline{\gamma}(\tilde{t})\right]\hat{\mathbf{d}}(t-\tilde{t})=\hat{\boldsymbol{\xi}}(t), \tag{4.1}$$

where α_0 is the static polarizability of the atom, ω_a the bare resonance frequency of the dominant dipole transition and we chose the definition with the partial derivative for the integral kernel for convenience of notation. We can, in fact, add some physical intuition to this notation. By partial integration with respect to time, we obtain three terms

$$\lim_{-t_i,t\to\infty}\int_0^{t-t_i}\mathrm{d}\tilde{t}\,\left[\frac{\partial}{\partial\tilde{t}}\,\underline{\gamma}(\tilde{t})\right]\hat{\mathbf{d}}(t-\tilde{t})=\lim_{-t_i,t\to\infty}\underline{\gamma}(t-t_i)\hat{\mathbf{d}}(t_i)-\underline{\gamma}(0)\hat{\mathbf{d}}(t)+\int_0^\infty\mathrm{d}\tilde{t}\,\underline{\gamma}(\tilde{t})\dot{\hat{\mathbf{d}}}(t-\tilde{t}) \tag{4.2}$$

with t_i the initial time of the experiment. The first term implements the initial conditions and the coupling process between atom and field ("slip term") [432], the second term can be reabsorbed in the resonance frequency as a renormalization [136] and the last term relates the tensor $\underline{\gamma}$ to the memory function describing dispersion and dissipation in the dipole excitation [155]. However, in our particular case, we can use the causality properties of the involved response functions such that the boundary conditions of the integral vanish in the steady state. Our model in Eq. (4.1) then coincides formally with the so-called damping-kernel representation of the quantum Langevin equation, where only the last term of Eq. (4.2) remains [432]. The quantum Langevin force and the memory kernel, respectively, read [M1]

$$\hat{\boldsymbol{\xi}}(t)=\int\frac{\mathrm{d}\omega}{2\pi}\int\frac{\mathrm{d}h}{2\pi}\hat{\mathbf{E}}_{\mathrm{N}}(h,\mathbf{R}_a,\omega)e^{\mathrm{i}hx_a}e^{-\mathrm{i}\omega t}, \tag{4.3a}$$

$$\underline{\gamma}(t) = \int \frac{\mathrm{d}\omega}{2\pi} \int \frac{\mathrm{d}h}{2\pi} \frac{\underline{G}_{\Im}(h, \mathbf{R}_a, \omega)}{\omega} e^{-\mathrm{i}\omega t}. \tag{4.3b}$$

As a reminder, h is the component of the radiation's wavevector parallel to the direction of motion, and we split the atom's position as $\mathbf{r}_a = (x_a, \mathbf{R}_a)^{\mathrm{T}}$, where we chose the motion to be along the x-axis. We note that the previous three equations are equivalent to the relations introduced in Eq. (3.5) of Chap. 3, but using a different notation in order to identify the important quantities for our following arguments. Further, writing the quantum Langevin equation in the form of Eqs. (4.1) and (4.2) is quite common in the respective literature (see for example Refs. [107, 136, 155, 410, 422, 431, 432, 549, 550]) and allows us to compare our results directly.

The atomic internal degrees of freedom are driven by the integrated electric vacuum field fluctuations $\hat{\mathbf{E}}_{\mathrm{N}}$ and the dispersion as well as dissipation mechanisms are encoded in the Green tensor defined in Chapter 1 and appendix A. From Eqs. (4.3) it follows immediately that the power spectrum of the oscillator in equilibrium reads

$$\langle \hat{\mathbf{d}}(\omega) \hat{\mathbf{d}}(\omega') \rangle_{\mathrm{sym}} = 2\pi\delta(\omega + \omega')\, \underline{\alpha}(\omega) \cdot \underline{\nu}_{\mathrm{sym}}(\omega) \cdot \underline{\alpha}^{\dagger}(\omega), \tag{4.4}$$

where the polarizability tensor $\underline{\alpha}(\omega, v) = \alpha_B(\omega) \left[1 - \alpha_B(\omega)\underline{\Delta}(\omega, v)\right]^{-1}$ with $\alpha_B(\omega) = \alpha_0\omega_a^2/(\omega_a^2 - \omega^2)$ solves Eq. (4.1) in Fourier domain, i.e. $\hat{\mathbf{d}}(\omega) = \underline{\alpha}(\omega)\hat{\boldsymbol{\xi}}(\omega)$. Here, we defined the complex renormalization

$$\underline{\Delta}(\omega) = \mathcal{P} \int \frac{\mathrm{d}\bar{\omega}}{\pi} \frac{\bar{\omega}\underline{\gamma}(\bar{\omega})}{\bar{\omega} - \omega} + \mathrm{i}\omega\underline{\gamma}(\omega) \tag{4.5}$$

with $\mathcal{P}$ the Cauchy principal value which can be shown to be identical to Eq. (3.15) without intrinsic dissipative degrees of freedom for the particle and at zero velocity by means of the Kramers-Kronig relations for the Green tensor [147] [see Eq. (3.10)]. The symmetric correlation matrix of the Langevin force, i.e. the quantum fluctuations of the electric field, $\underline{\nu}_{\mathrm{sym}}(t, t') \equiv \langle \hat{\boldsymbol{\xi}}(t)\hat{\boldsymbol{\xi}}(t') \rangle_{\mathrm{sym}} \to \underline{\nu}_{\mathrm{sym}}(\tau)$, where $t - t' \equiv \tau$, is stationary and real in equilibrium. Moreover, the quantum noise is colored [50] and we can write

$$\underline{\nu}_{\mathrm{sym}}(\omega) = \hbar \int \frac{\mathrm{d}h}{2\pi}\, \mathrm{sgn}(\omega)\underline{G}_{\Im}(h, \mathbf{R}_a, \omega). \tag{4.6}$$

Here, the sign-function appears instead of the Heaviside theta due to our choice of the symmetric average [compare to Eq. (1.21)]. By combining Eqs. (4.3) and (4.6), the fluctuation-dissipation relation for the electric field reads

$$\underline{\nu}_{\mathrm{sym}}(\omega) = \hbar\omega\mathrm{sgn}(\omega)\underline{\gamma}(\omega) \tag{4.7}$$

which is probably the closest form showing that the field fluctuations are exactly equal to the hypothetical ground state fluctuations assigned to the given dissipation [M6, 422].

In equilibrium, it is not surprising, but rather a premise that the *average* energy of the atomic subsystem is constant [169]. To be precise, we multiply Eq. (4.1) with $\dot{\hat{\mathbf{d}}}$ first from the right, second from the left and then add the two resulting equations. The procedure is necessary in

order to fully symmetrize the Langevin equation with respect to the operator ordering such that we can employ the symmetric quantum average. As a result, we obtain that the average change in the atom's internal energy at late times E is given by the average power flux P through a closed surface around a volume enclosing the atom,

$$\frac{\mathrm{d}}{\mathrm{d}t}E \equiv \frac{1}{2\alpha_0\omega_a^2}\frac{\mathrm{d}}{\mathrm{d}t}\left[\langle\dot{\hat{\mathbf{d}}}^2(t)\rangle + \omega_a^2\langle\hat{\mathbf{d}}^2(t)\rangle\right] = P. \tag{4.8}$$

The total power flux $P = -P_{\mathrm{out}} + P_{\mathrm{in}}$ is the sum of the outgoing and the incoming power flux,

$$P_{\mathrm{out}} = 2\int_0^\infty \mathrm{d}\tau \left\langle \dot{\hat{\mathbf{d}}}(t)\cdot\underline{\gamma}(\tau)\cdot\dot{\hat{\mathbf{d}}}(t-\tau)\right\rangle_{\mathrm{sym}}, \qquad P_{\mathrm{in}} = \left\langle \hat{\boldsymbol{\xi}}(t)\cdot\dot{\hat{\mathbf{d}}}(t)\right\rangle_{\mathrm{sym}}, \tag{4.9}$$

respectively. Upon employing some algebraic modifications, we can show that they are equal in equilibrium, $P_{\mathrm{out}} = P_{\mathrm{in}}$, such that the internal energy of the atom is constant, $(\mathrm{d}/\mathrm{d}t)E = 0$, as expected (see appendix F). At this point, it is important to note that the distinction between incoming and outgoing power is somewhat artificial in equilibrium. It is particularly not supposed to imply that work is necessarily done [173]. Indeed, at zero temperature, the system cannot be excited in equilibrium and remains in its coupled common ground state. It can then be shown that the apparent cancellation (detailed balance) of the incoming and the outgoing power is of purely mathematical origin and a matter of representation [174]. This is in contrast to the nonequilibrium situation (see next Section 4.2) and we use the notation here only in order to coherently introduce the different concepts.

Integrating Eq. (4.8) over time, we find the constant energy in the nonequilibrium steady-state to be given by

$$E \sim \int_0^\infty \frac{\mathrm{d}\omega}{2\pi}\,\mathcal{E}(\omega), \tag{4.10}$$

where we defined the spectral energy density

$$\mathcal{E}(\omega) = \frac{\omega_a^2+\omega^2}{\alpha_0\omega_a^2}\mathrm{Tr}\left[\underline{\alpha}(\omega)\cdot\underline{\nu}_{\mathrm{sym}}(\omega)\cdot\underline{\alpha}^\dagger(\omega)\right]. \tag{4.11}$$

The energy per frequency contributing to the internal energy of the atom arises from the interaction between the atom's particular capacity of reacting to electromagnetic perturbations, namely its polarizability, and the material-modified vacuum fluctuations of the electromagnetic background. The prefactor measures the impact of this interaction energy to the corresponding potential ($\sim\omega_a^2$) as well as kinetic ($\sim\omega^2$) terms in the atom's Hamiltonian. Employing the fluctuation-dissipation relation of second type [32], $\underline{\alpha}_{\Im}(\omega) = \underline{\alpha}(\omega)\cdot\underline{\nu}_{\mathrm{sym}}(\omega)\cdot\underline{\alpha}^\dagger(\omega)$, and inserting the expression for the atomic polarizability defined below Eq. (4.4), it is straight-forward to show that we recover the expected ground-state energy of the oscillator in the limit of vanishing coupling between atom and material-modified vacuum[1],

$$E \sim \frac{3\hbar\omega_a}{2}, \qquad \alpha_0 \to 0. \tag{4.12}$$

[1] To this end, we use the relation $\lim_{\epsilon\to 0^+}\epsilon/(\epsilon^2+x^2) = \pi\delta(x)$.

Indeed, when we effectively decouple the atom from its fluctuating environment, the only contribution to the ground-state energy of the electric dipole at zero temperature can arise from the corresponding (virtual) zero-point fluctuations. The dispersive and dissipative properties of the environment become unimportant and the atom's potential is solely determined by frequencies $\omega \to \omega_a$. In the general case, however, it becomes clear from Eq. (4.11) that the energy of the atomic subsystem arises from the complex interplay between the atom's and the bath degrees of freedom which effectively modifies the atom's internal energy levels [111]. In other words, particle and material-modified vacuum are closely intertwined and the respective energy becomes a functional of the coupling as well as the specifics of the material distribution,

$$E = E(\alpha_0) \sim \mathcal{O}(\alpha_0). \tag{4.13}$$

We conclude the discussion on equilibrium with some comments. First, we note that, even if we would work at finite temperatures for the electromagnetic bath at the initial time of the experiment, the equilibrium state of the atom with constant energy is not necessarily a Gibbs state for the atomic internal degrees of freedom alone. In general, the coarse-grained density matrix (tracing over the environment degrees of freedom) depends on the coupling strength between atom and bath [106, 548]

Second, we are not necessarily dealing with the situation that is usually referred to as *thermodynamics* in textbooks which usually assumes an infinitely weak coupling between system and environment. In contrast, in our situation, the coupling is crucial and the bath dynamics is indeed also influenced by the interaction with the particle introducing some notion of *strong coupling*[2] in the thermodynamic sense [548]. It is properly capturing this connection between atomic and bath degrees of freedom in the nonequilibrium scenario that led to the surprising results of Chap. 3.

Third, in our particular setup of a planar interface, or even vacuum, the atom's internal energy $E(\alpha_0) \geq 3\hbar\omega_a/2$ can be show to exceed the ground-state fluctuations of the atomic oscillator [135] and, depending on the system's resonances, might call for the introduction of a high-frequency cut-off in order to regularize the integral (see Ref. [136] or appendix F). The internal energy of the atom hence depends on the coupling strength to the environment, the state of the environment itself and the frequency (cutoff) defining the highest physical energy scale in the system. Such a behavior is quite typical for a non-vanishing coupling between system and (quantum) bath and we refer to Refs. [50, 136, 289, 319, 412, 545] for further details.

Finally, we note that the previous discussion is in its essence nothing but the fluctuation-dissipation relation for both atom and field in equilibrium [Eq. (4.4)] which we extensively discussed in Chap. 1, but seen from the thermodynamical perspective: In equilibrium, in order to sustain a constant mean internal energy of the atom, fluctuations driving the atom and dissipation to its in environment have to balance.

Having reviewed the theory of the equilibrium state of an atom coupled to the material-modified vacuum, we now advance the discussion to the nonequilibrium scenarion, where the atom is moving with finite velocity v.

[2] This is not to be confused with other notions of strong coupling as e.g. in the case of strongly coupled light-matter interactions [340, 551].

4.2 Steady-state dynamics of mechanical nonequilibrium

We now turn our attention to the more complicated case of an atom moving with constant velocity v at late times. The system can reach a steady-state, when an external driving agent constantly infuses energy into the system in order to balance losses to the material-modified electromagnetic environment. For one, the agent needs to counterbalance frictional forces and fix the atom at constant altitude above the surface. In the (nonequilibrium) steady state (NESS), the actions of the external agent manifest themselves by a non-vanishing energy current in the total system; we refer to Sec. 3.1 for further details. For the atomic subsystem, however, we should expect a net zero relation between incoming P_{in} and outgoing power P_{out}. If otherwise, the atomic energy would be changing with time contradicting stationarity. A similar reasoning was used, e.g., in the context of heat transfer between oscillator systems by Refs. [288, 289] or particularly parallel plates by Ref. [552]. Atom-surface interactions in mechanical nonequilibrium were, e.g., investigated by Ref. [42, 553, 554]. Further, we refer to Ref. [57] for an extensive perturbative treatment of the frictional force and Ref. [44] for a study of different acceleration procedures leading to the constant motion. In any of these cases, under the idealizing assumption of a constant temperature difference in the system (for heat transfer) or a classical trajectory with constant velocity (for quantum friction), the system could indeed become stationary due to finite dissipation and the passivity of the system in combination with a constant driving. In the following, we provide an explicit late-time solution for our model [see Eq. (4.1)] and show that the anticipated power balance $P_{\mathrm{in}} = P_{\mathrm{out}}$ holds, but only under certain conditions. This provides a physical reasoning for its existence.

Formally, the generalization of the previous Section is straight forward. Based on the corresponding nonequilibrium fluctuations

$$\underline{\nu}_{\mathrm{sym}}(\omega, v) = \hbar \int \frac{\mathrm{d}h}{2\pi}\, \mathrm{sgn}(\omega_h^+)\underline{G}_{\Im}(h, \mathbf{R}_a, \omega_h^+) \tag{4.14}$$

with $\omega_h^+ = \omega + hv$ the Doppler-shifted frequency, we need to successively introduce the extra parameter into Eqs. (4.1), (4.4), (4.5) and (4.11) and regard the generalized Kramers-Kronig relations for the nonequilibrium case [see Eq. (3.11) and discussion below], i.e.

$$\underline{\gamma}(\omega) \to \underline{\gamma}(\omega, v) = \int \frac{\mathrm{d}h}{2\pi}\, \frac{\underline{G}_{\Im}(h, \mathbf{R}_a, \omega_h^+)}{\omega}, \tag{4.15a}$$

$$\underline{\Delta}(\omega) \to \underline{\Delta}(\omega, v), \quad \underline{\alpha}(\omega) \to \underline{\alpha}(\omega, v), \quad \mathcal{E}(\omega) \to \mathcal{E}(\omega, v). \tag{4.15b}$$

For instance, this leads to the nonequilibrium power spectrum of the atomic dipole

$$\langle \hat{\mathbf{d}}(\omega)\hat{\mathbf{d}}(\omega')\rangle_{\mathrm{sym}} = 2\pi\delta(\omega + \omega')\, \underline{\alpha}(\omega, v) \cdot \underline{\nu}_{\mathrm{sym}}(\omega, v) \cdot \underline{\alpha}^{\dagger}(\omega, v). \tag{4.16}$$

Despite the similarities to the equilibrium case, the finite velocity introduces low-frequency fluctuations ($\omega \sim v/\lambda$ with λ a typical length scale of the system) into the system (see Chap. 1) and leads to certain major conceptual differences, which we shall discuss piece by piece in the next Sections.

4.2.1 Fluctuation-dissipation inequality

The most immediate difference between the equilibrium ($v = 0$) and the nonequilibrium ($v \neq 0$) case can be seen from the field fluctuations

$$\underline{\nu}_{\mathrm{sym}}(\omega, 0) \neq \underline{\nu}_{\mathrm{sym}}(\omega, v). \tag{4.17}$$

While we can employ the fluctuation-dissipation relation in the equilibrium case, $\underline{\nu}_{\mathrm{sym}}(\omega, 0) = \hbar\omega\mathrm{sgn}(\omega)\underline{\gamma}(\omega, 0)$, this not true for finite velocities,

$$\underline{\nu}_{\mathrm{sym}}(\omega, v) \neq \hbar\omega\mathrm{sgn}(\omega)\underline{\gamma}(\omega, v). \tag{4.18}$$

Hence, we need to take a more careful look at the fluctuations in the NESS. Recalling that the Green tensor decomposes into a vacuum contribution $\underline{G}_0$ and a scattered contribution $\underline{g}$, we first note that – despite our non-relativistic treatment – we need to preserve the Lorentz invariance of the vacuum field. This means that, in general, the fluctuation's vacuum part $\underline{\nu}_{\mathrm{sym},0}$ needs to coincide with its equilibrium expression, $\underline{\nu}_{\mathrm{sym},0}(\omega, v) \to \underline{\nu}_{\mathrm{sym},0}(\omega, 0)$. Hence, the fluctuation-dissipation relation remains unaltered for the pure vacuum, i.e. $\underline{\nu}_{\mathrm{sym},0} = \hbar\omega\mathrm{sgn}(\omega)\underline{\gamma}_0(\omega)$ with the corresponding memory kernel of the vacuum $\underline{\gamma}_0$, irrespective of the mechanical nonequilibrium [132]. However, for the scattered contribution, this cannot be true since Lorentz invariance is broken by the presence of the material already due to the finite impact of dissipation in the open quantum system description. Due to the choice of the symmetric average, we further find that the memory kernel and the fluctuations are Hermitian tensors,

$$\underline{\gamma}(\omega, v) = \underline{\gamma}^\dagger(\omega, v), \qquad \underline{\nu}_{\mathrm{sym}}(\omega, v) = \underline{\nu}^\dagger_{\mathrm{sym}}(\omega, v). \tag{4.19}$$

Based on that, we can show that the matrix

$$\mathbf{a}^* \cdot \Big(\underline{\nu}_{\mathrm{sym}}(\omega, v) \pm \hbar\omega\underline{\gamma}(\omega, v)\Big) \cdot \mathbf{a} \geq 0 \tag{4.20}$$

is positive semi-definite for all $\mathbf{a} \in \mathbb{C}^3$. This is effectively due to the properties of the Green tensor, which is positive semi-definite for positive frequencies [M1, M6, 461], and the behavior of the bosonic occupation at zero temperature and Doppler-shifted frequencies since

$$n(\omega_h^+, T) + \frac{1}{2} \pm 1 \sim \mathrm{sgn}(\omega_h^+) \pm 1 \geq 0, \qquad h, v \geq 0. \tag{4.21}$$

We lay out the mathematical details in appendix F. In particular, we can conclude for the trace of the tensor that

$$\mathrm{Tr}\,\underline{\nu}_{\mathrm{sym}}(\omega, v) \geq |\hbar\omega\mathrm{Tr}\,\underline{\gamma}(\omega, v)|, \tag{4.22}$$

where we used that the tensor $\underline{G}_{\Im}$ is positive semi-definite (see appendix F). Naively, this can be understood by noting that $\underline{G}_{\Im}$ is connected to losses of an excited system by means of Fermi's golden rule [1]. For passive systems, this is bound to be positive [155]. Equation (4.22) is a central result of nonequilibrium physics and was first put forward for the nonequilibrium fluctuations of quantum fields in a somewhat different context by Ref. [422] who coined it the

fluctuation-dissipation inequality. The relation states that the field fluctuations ($\underline{\nu}$) in nonequilibrium are always equal or greater than the hypothetical ground-state fluctuations assigned to the dissipation in the system ($\hbar\omega\underline{\gamma}$) [M6, 422]. Disregarding this *inequality* and artificially enforcing the *equality* is what the assumption of local thermal equilibrium means. However, it follows from Eq. (4.22) that this is especially unjustified for low-frequency contributions. In fact, from Eqs. (F.3) and (4.15), we observe that the main difference between the fluctuations $\underline{\nu}$ and the memory kernel $\underline{\gamma}$ is given by the appearance of the sign function. For frequencies $\omega \gg |hv|$, we effectively can write $\mathrm{sgn}(\omega + hv) \sim \mathrm{sgn}(\omega)$ such that the equality holds asymptotically. In the opposite limit, the sign function most sensitively depends on the wavevector and the velocity as $\mathrm{sgn}(\omega + hv) \sim \mathrm{sgn}(hv)$ such that the deviation from the equilibrium relation (LTE) is maximal. In accordance with our extensive discussion in Chapter 1, we use that the relevant length scale of the setup λ is given by the distance to the closest surface such that, e.g., the wavevectors scale as the inverse distance of the atom from the closest surface, $h \sim z_a^{-1}$ for the planar case. The corresponding energy scale distinguishing between the regime where the LTE approach is still viable and the regime that calls for a full nonequilibrium calculation is then given by

$$\hbar\omega \sim \hbar\frac{v}{z_a}. \tag{4.23}$$

It is indeed the low-frequency/long-time correlations between subsystems that the approach of local thermal equilibrium disregards.

In order to obtain a concrete estimate, we once again consider the planar interface separating vacuum from the infinite material half-space in the near-field regime for simplicity ($\mathrm{d}h/(2\pi) \to \mathrm{d}^2\mathbf{p}/(2\pi)^2$ with $p = |\mathbf{p}| = \sqrt{p_x^2 + p_y^2}$ and $\mathbf{p}$ the wavevector parallel to the interface). Upon employing the respective Green tensor (see Eq. F.22 in appendix A), we can write for the regime of maximal deviation between the full nonequilibrium fluctuation-dissipation-relation (FDR) and the LTE approach ($\omega > 0$)

$$\frac{\mathrm{Tr}\,\underline{\nu}_{\mathrm{sym}}(\omega, v)}{\left|\hbar\omega\mathrm{Tr}\,\underline{\gamma}(\omega, v)\right|} \sim 1 + \Theta\left(\frac{\omega z_a}{v}\right) \sim \begin{cases} 1, & \omega \gg \frac{v}{z_a} \\ \frac{3}{\pi}\frac{|v|}{\omega z_a}, & \omega \ll \frac{v}{z_a}, \end{cases} \tag{4.24}$$

where we employed the spatially local Drude model for the material description and defined the positive, monotonic decreasing function $\Theta(x) \sim 3/(\pi x) - 1$ for $x \ll 1$. For large arguments $x \gg 1$, the function $\Theta(x)$ vanishes exponentially and we report its exact form in Eq. F.24 of appendix F. A numerical evaluation of the complete curve can be found in Fig. 4.1. From Eq. (4.24) we can clearly see the relevance of long-time correlations in our theoretical description. For $v = 0$, as expected, the ratio approaches unity and the equilibrium fluctuation-dissipation relation identically holds. At non-zero velocity, however, the previous relation always prescribes a finite frequency regime, where the nonequilibrium fluctuations not only deviate, but exceed the corresponding equilibrium relation. In statistical terms, the atom and the surrounding electromagnetic bath cannot be regarded as separated anymore and the long-time correlations

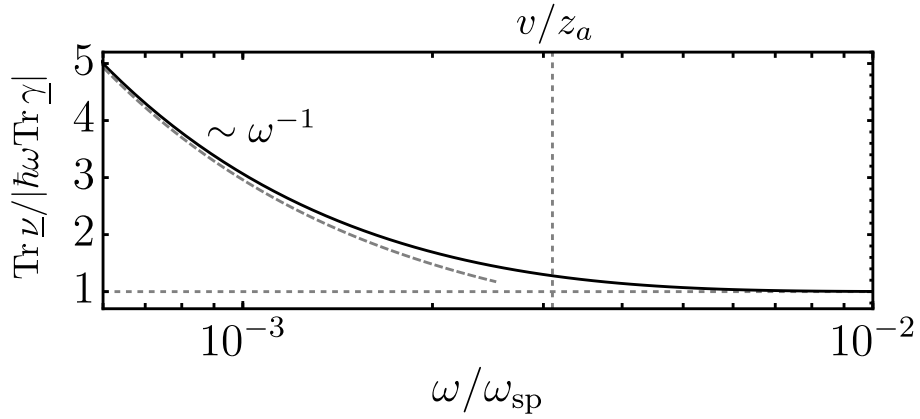

Figure 4.1: Ratio between fluctuations and the assigned ground-state fluctuations of the corresponding dissipation in the system [Eq. (4.22)] as a function of frequency (black, solid). We trace over the corresponding tensors and report the asymptotic result in Eq. (4.24) for small frequencies ($\propto 3|v|/(\pi z_a\omega)$) and large frequencies ($\mathcal{O}(1)$), respectively, in gray and dashed. We skip the subscript "sym" for better readability. We chose the planar interface to be made from gold described by the Drude model with dissipation rate $\Gamma = 30$ meV and plasma frequency $\omega_{\mathrm{p}} = 9\,\mathrm{eV}$ [140]. Further, we used a velocity of $v = 10^{-4}c$ and an atom-surface separation of $z_a = 1\,\mathrm{nm}$. The impact of nonequilibrium becomes clear below frequencies corresponding to the mechanical energy in the system $\omega \sim v/z_a$. Adapted from [M6].

between both subsystems begin to matter. More precisely, Eq. (4.24) introduces the time scale

$$t_{\mathrm{b}} \sim \frac{2\pi}{\omega} \gtrsim 2\pi\frac{z_a}{v} \tag{4.25}$$

into the system which is at the order of nanoseconds for hundred nanometer distance and the velocity at the order of the speed of sound. t_{b} can be interpreted as the time it takes for the Doppler-shifted frequency ($\sim v$) that dominates the interaction ($\sim z_a^{-1}$) to mediate the back-action of the environment on the atom. For larger times, the deviations from simple equilibrium statistics become inevitable in the interaction from the thermodynamic point of view. Of course, as we saw in the various examples throughout the thesis, the quantitative impact of this low-frequency regime still depends on the peculiarities of the system and the quantity of interest. In Sec. 4.3, we elaborate further on that topic.

4.2.2 Nonequilibrium power flux

In the previous Section, we discussed the fluctuations in the atom-surface system in mechanical nonequilibrium for given frequency. In realistic scenarios, on the other hand, we are mostly interested in observables describing the macroscopic state of the system. In principle, the macroscopic observables are given by a complex interplay of all the interaction channels present in the system and hence can derive from a large range of frequencies. It might therefore not be surprising that an improper representation of the relevant frequency regimes can have a problematic outcome for thermodynamic quantities in particular, since they usually rely on a careful *bookkeeping* of the system's states.

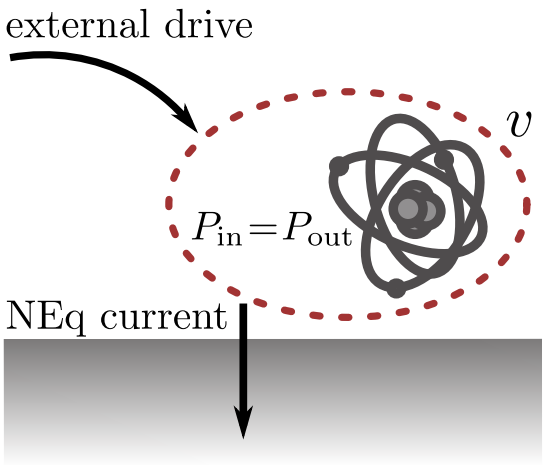

Figure 4.2: An atom moving with velocity v in front of a macroscopic body from the perspective of power fluxes. An external drive counterbalances eventual frictional forces and keeps the steady motion, thereby inserting energy to the system which is dissipated to the environment by a nonequilibrium current (NEq). In the steady-state, incoming and outgoing power of the atomic subsystem balance.

To see this more clearly, we now compute the nonequilibrium power flux *in* and *out* of the atomic subsystem. The *in* part represents the moving atom changing the configuration of the surrounding material-modified quantum field which in turn interacts with the atom's internal degrees of freedom. The *out* part, on the other hand, describes the atom loosing energy to the electromagnetic environment. We depict a sketch of the situation in figure 4.2. In analogy to our discussion on the equilibrium case [Eq. (4.11)], we multiply the equation of motion by the time derivative of the dipole moment, symmetrize the Langevin equation and obtain the velocity-dependent equation for the change in the internal energy of the atom,

$$\frac{\mathrm{d}}{\mathrm{d}t}E(v) = P(v), \tag{4.26}$$

with $P(v) = -P_{\mathrm{out}}(v) + P_{\mathrm{in}}(v)$, where we define in full analogy to the equilibrium case

$$P_{\mathrm{out}}(v) = 2\int_0^\infty \mathrm{d}\tau \left\langle \dot{\hat{\mathbf{d}}}(t)\cdot\underline{\gamma}(\tau,v)\cdot\dot{\hat{\mathbf{d}}}(t-\tau)\right\rangle, \qquad P_{\mathrm{in}}(v) = \left\langle \hat{\boldsymbol{\xi}}(t,v)\cdot\dot{\hat{\mathbf{d}}}(t)\right\rangle. \tag{4.27}$$

In order to present a clear line of arguments, we refer again to appendix F.3 for the mathematical details and discuss our main results in the following. In the NESS, the net energy flow entering or exiting the atomic subsystem can be written as

$$P(v) = \int \frac{\mathrm{d}\omega}{2\pi}\,\mathrm{Tr}\left[\underline{\mathcal{P}}(\omega,v) - \underline{\mathcal{P}}(-\omega,-v)\right]. \tag{4.28}$$

Here, we defined the spectral power tensors at finite velocity

$$\underline{\mathcal{P}}(\omega, v) = 2\omega^2 \underline{\alpha}(\omega, v) \cdot \underline{\gamma}(\omega, v) \cdot \underline{\alpha}^{\dagger}(\omega, v) \cdot \underline{\nu}_{\mathrm{sym}}(\omega, v). \tag{4.29}$$

Upon employing the symmetries of the atomic polarizability by noting that it decomposes into a diagonal tensor $\underline{\alpha}_{\mathrm{D}}(\omega, v)$ and an skew-symmetric part $\alpha_{\mathrm{R}}(\omega, v)\underline{L}_y$ with $\underline{L}_y$ the usual generator of rotations with respect to the axis perpendicular to the direction of motion [see Eq. (3.23)] [M1, P3, M6], we find that the detailed balance condition is indeed satisfied,

$$\mathcal{P}_{ii}(\omega, v) = \mathcal{P}_{ii}(-\omega, -v), \tag{4.30}$$

where we again sum over the identical indices that give the corresponding matrix components. Hence, the net energy flow vanishes $P = 0$. Consistently, a vanishing total power in the atomic subsystem is equivalent of saying that the mechanical work $-vF_{\mathrm{fric}}$, performed by the external agent per unit time (power) in order to counterbalance the friction force, balances the electromagnetic energy dissipated per unit time P^{rad} from the particle to the environment [44], i.e.

$$P^{\mathrm{rad}} = -vF_{\mathrm{fric}}. \tag{4.31}$$

To this end, we note that the condition $\langle \dot{\hat{\mathbf{d}}} \cdot \hat{\mathbf{E}} \rangle = 0$ implies that[3]

$$\lim_{-t_i, t \to \infty} \mathrm{Im} \int_0^{\infty} \mathrm{d}\omega \int_0^{t-t_i} \mathrm{d}\tau \int \frac{\mathrm{d}h}{2\pi} \mathrm{Tr} \left[\partial_t \underline{C}(t, t-\tau) \cdot \underline{G}^{\mathrm{T}}_{\Im}(h, \mathbf{R}_a, \omega) \right] e^{\mathrm{i}(h[x_a(t) - x_a(t-\tau)] - \omega\tau)} = 0, \tag{4.32}$$

where $\underline{C}(t, t') = \langle \hat{\mathbf{d}}(t) \hat{\mathbf{d}}(t') \rangle$ is the dipole's non-symmetric power spectrum. Using that $\partial_t \underline{C}(t, t-\tau) \to \partial_\tau \underline{C}(\tau) = \int \mathrm{d}\omega' \, (-\mathrm{i}\omega') \underline{S}(\omega', v) e^{-\mathrm{i}\omega'\tau}$ in the nonequilibrium steady-state, where $\underline{S}$ is the non-symmetric power spectrum defined earlier in Eq. (3.15), we find explicitly

$$P_{\mathrm{rad}} = 2 \int_0^{\infty} \mathrm{d}\omega \int \frac{\mathrm{d}h}{2\pi} \omega \mathrm{Tr} \left[\underline{S}^{\mathrm{T}}(-\omega_h^-, v) \underline{G}_{\Im}(h, \mathbf{R}_a, \omega) \right] \tag{4.33}$$

and F_{frac} is obtained by replacing $\omega \to -h$ in the previous integrand. We recover the result of Eq. (3.77) (see also Ref. [58]). We note that the result of Eq. (4.31) is slightly more general than Eqs. (4.28) and (4.29), since it does not require a particular model for the dynamics of the particle. We report further technical details in appendix F.

Equations (4.26)-(4.33) constitute one of the main results of the present thesis. Combining them, we can deduce that the internal energy of the atomic system in the (mechanical) nonequilibrium steady state is constant,

$$E(v) = \text{const.}, \qquad t - t_i \to \infty, \tag{4.34}$$

[3] Note that, when considering the full expression, it is more convenient to use the non-symmetric average $\langle \cdot \rangle$ instead of the symmetric one since the vacuum part of the field operator can be treated more elegantly. We refer to Sec. 3.1 for more details.

and that the incoming and outgoing power due to the interaction with the material-modified electromagnetic environment vanishes identically in the mean,

$$P(v) = 0, \qquad t - t_i \to \infty. \tag{4.35}$$

Within the realm of our assumptions (see e.g. above and Chapter 3), the result is general for every non-relativistic velocity, any linear dissipative material and arbitrary microscopic particles that are well-described by their linear polarizability. We do not rely on any assumptions on the underlying statistics of the interaction between particle and environment. In particular, our result is valid for a strong system-bath coupling[4], comprises a fully non-Markovian treatment of the bath degrees of freedom, self-consistently includes the back-action of the bath onto the particle and holds for any (physical) functional frequency behavior of the memory kernel. This means that $\omega\underline{\gamma}$ does not need to be Ohmic [353] or modeled by combination of a power law and an exponential cutoff [50, 337], but can rather contain any physical resonance of the system [411]. Moreover, even though we considered a particular setup in order to illustrate the derivation, the presented results are more general and depend on neither the chosen geometry nor the exact trajectory. It is the existence of a nonequilibrium steady-state in a dissipative open quantum system that implies the balance of energy flow in and out of the system. By implication, the condition on the energy flow imposes severe constraints on the behavior of the system's constituents and their dynamical observables. Otherwise, they could not meet the strict self-consistency requirements. From practical considerations, our formalism can be readily applied to explore different geometries with at least one direction of translational invariance (see Sec. 3 and for instance Refs. [M2, P2]).

Despite its direct appeal and the intuitive character of the statement, the detailed power balance in the nonequilibrium steady-state [Eq. (4.30)] is highly non-trivial to realize. In fact, any slight approximation can have massive consequences leading to, in principle, thermodynamic instabilities. For example, we introduce once again the LTE approximation and show that it contradicts the condition of stationarity [M6]. The assumption of local thermal equilibrium amounts to replacing

$$\underline{\nu}_{\mathrm{sym}}(\omega, v) \to \hbar\omega\mathrm{sgn}(\omega)\underline{\gamma}(\omega, v) \tag{4.36}$$

for the atomic dipole correlations in Eq. (4.16). It effectively neglects the Doppler-shift in the sign-function. The interpretation is clear: Within the LTE approach, the atom is considered as a separated subsystem which equilibrates locally with its immediate environment calling for an application of the equilibrium fluctuation-dissipation-relation (regular sign-function at zero temperature instead of Doppler-shifted one). In order to simplify our exact results to the LTE approximation, we note a technical subtlety: Since the atomic motion is driven by the nonequilibrium field at Doppler-shifted frequencies, where the fluctuation-dissipation relation in the steady state applies in Fourier domain, the LTE approach has no immediate consequence on the incoming power flux

$$P_{\mathrm{in}}^{\mathrm{LTE}}(v) = P_{\mathrm{in}}(v). \tag{4.37}$$

[4]Strong coupling is to be understood in the sense of Section 4.1 and, e.g., Refs. [136, 412].

However, since the replacement in Eq. (4.36) ignores the necessary self-consistency of the system (leading to the fluctuation-dissipation inequality discussed in the previous Section), we find fewer dissipation channels to the environment. In other words, the LTE approximation is usually employed from the perspective of the atom considering the interaction with the environment as a one-way-street: Both particle and field are correlated, but once the atom interacted with the field, the instigated modifications in the field will not back-act on the particle itself. Hence, for the LTE we obtain a reduced outgoing power

$$P_{\mathrm{out}}^{\mathrm{LTE}}(v) < P_{\mathrm{out}}(v). \tag{4.38}$$

Consequently, artificially assuming local thermal equilibrium to hold, we obtain for the total power in the steady state

$$P^{\mathrm{LTE}}(v) = -P_{\mathrm{out}}^{\mathrm{LTE}}(v) + P_{\mathrm{in}}(v) \neq 0 \tag{4.39}$$

contradicting the initial constraints of our system. To be more precise, let us consider again the case of an atom interacting with a planar interface made from a local material model and at separations within the near-field regime. In leading order of the atom's static polarizability α_0 and for velocities small enough that the corresponding Doppler-shifted frequency cannot coherently interact with any material or other system resonances[5], we obtain (see appendix F)

$$P^{\mathrm{LTE}} \sim \hbar \frac{45}{4} \frac{v^4}{(2\pi)^3} \frac{\alpha_0^2}{\epsilon_0^2} \frac{\left[\mathrm{Im}\left\{\lim_{\omega\to 0}\partial_\omega r^p\right\}\right]^2}{(2z_a)^{10}} > 0, \tag{4.40}$$

where r^p is the transverse magnetic reflection coefficient which we assumed to be Ohmic for simplicity and ϵ_0 gives the vacuum permittivity. Remarkably, equation (4.40) would imply a constant increase of the atom's internal energy and violates stationarity. Such a conclusion was, e.g., drawn by Refs. [43, 44, 55]. Note that the deviation from the detailed balance emerges earliest at second order order of the coupling between particle and material-modified vacuum, $\mathcal{O}(\alpha_0^2)$. This means that the LTE approach gives the correct result in first order of the coupling $\mathcal{O}(\alpha_0)$. We will discuss the leading order coupling regime in more detail in Sec. 4.3 in order to determine the regions of applicability of the LTE approach. In full generality, however, a consistent and reliable thermodynamic description needs to consider the complete series describing the interaction and cannot rely on a few perturbative expansion coefficients neglecting memory effects. One has to be careful and provide justification before assuming local or even global equilibrium [M6].

[5] We have referred to this regime earlier as *non-resonant* (see Chap. 3). For an extensive discussion of the resonant regime, see Ref. [M1].

4.2.3 Steady-state energy

The detailed balance between the incoming and the outgoing power flux implies a constant energy $E = \int_0^\infty \frac{\mathrm{d}\omega}{2\pi}\mathcal{E}(\omega, v)$ of the atomic subsystem in the nonequilibrium steady-state. For finite velocities, we can generalize Eq. (4.11) and obtain for the spectral energy density

$$\mathcal{E}(\omega, v) = \frac{\omega_a^2 + \omega^2}{\alpha_0 \omega_a^2} \mathrm{Tr}\left[\underline{\alpha}(\omega, v) \cdot \underline{\nu}_{\mathrm{sym}}(\omega, v) \cdot \underline{\alpha}^\dagger(\omega, v)\right]. \tag{4.41}$$

We note that equation (4.41) takes the possible complex tensor structure of the field fluctuations and the atomic polarizability into account: Due to the involved tracing operation, both the tensor's symmetric and skew-symmetric parts contribute to the total internal energy of the atom. Hence, the internal energy of particle explicitly considers rotational degrees of freedom for its mean dipole vector in the sense of Sec. 3.2. The orientation of the mean atomic dipole vector performs a stochastic motion and, as expected, the average torque changing the angular momentum $\boldsymbol{\mathcal{L}}$ vanishes in the steady state [M1, 468]

$$\frac{\mathrm{d}}{\mathrm{d}t}\boldsymbol{\mathcal{L}} = \frac{1}{\alpha_0 \omega_a^2}\frac{\mathrm{d}}{\mathrm{d}t}\left\langle \hat{\mathbf{d}}(t) \times \dot{\hat{\mathbf{d}}}(t) \right\rangle \to 0, \qquad t - t_i \to \infty, \tag{4.42}$$

where we used the definition of Sec. 3.2 and t_i is the initial time of the experiment. Recalling that the three-dimensional rotation vector $\boldsymbol{\Omega}$ describing the average rotation of the atomic dipole's directionality relates the torque and the particle's moment of inertia, $\underline{M} \cdot \boldsymbol{\Omega} = \boldsymbol{\mathcal{L}}$, one can compute the rotational energy stored in the atomic degrees of freedom in the steady-state using, e.g. for a planar interface, $E_{\mathrm{R}} = \frac{1}{2}\frac{\mathcal{L}_y^2}{M_{yy}}$. The full expressions for the torque and the moment of inertia can be found in Eqs. (3.24) - (3.26). In full resemblance of the classical analog of a rolling particle, the internal energy of the atom increases due to the rotational degrees of freedom. The frictional force, on the other hand, decreases due to the average rotation (see Chap. 3).

Next, we consider the behavior of the energy with respect to changes in the direction of motion. From Eq. (F.3), we deduce that $\underline{\nu}(\omega, -v) = \underline{\nu}^{\mathrm{T}}(\omega, v)$ as well as $\underline{\gamma}(\omega, -v) = \underline{\gamma}^{\mathrm{T}}(\omega, v)$. Combining with the decomposition of the polarizability into a diagonal and a skew-symmetric part [see discussion below Eq. (4.29)], we can indeed show that

$$E(-v) = E(v) \tag{4.43}$$

as we would expect from demanding consistency of the theory. In equilibrium, Eq. (4.41) reduces to the zero-velocity result, $E(v) \to E(0)$. In general, however, the internal atomic energy will be a functional of the velocity and the coupling between system and bath, $E = E(\alpha_0, v)$. The spectral energy correctly captures the long-time behavior of the correlations in the nonequilibrium atom-surface interaction: For frequencies much smaller than the systems's resonances, the spectral energy approaches a constant in leading order of α_0,

$$\lim_{\omega \to 0} \mathcal{E}(\omega, v) \sim \mathcal{O}(\alpha_0) \neq 0. \tag{4.44}$$

For comparison, we consider local thermal equilibirum for the underlying statistics of the in-

teraction. Further, we define the corresponding spectral density $\mathcal{E}^{\mathrm{LTE}}(\omega, v)$ in the sense of Eq. (4.36). In the limit of small frequencies, we obtain instead

$$\lim_{\omega\to 0} \mathcal{E}^{\mathrm{LTE}}(\omega, v) \to 0. \tag{4.45}$$

This can be understood by recalling that the LTE approach artificially forces subsystems of the full setup to equilibrate locally. Communication within the subsystems on large (non-exponentially decaying) timescales is thereby removed, cutting off the very low-frequency regime of the fluctuation spectrum $\underline{\nu}$ as well as the spectral energy $\mathcal{E}$. For comparison, Eq. (4.44) derives from a proper bookkeeping of all the possible interaction channels between separate subsystems. In particular, choosing again the example of a planar half-space filled with a local Drude metal in the near-field regime, the error amounts to (see appendix F)

$$\lim_{\omega\to 0} \mathcal{E}(\omega, v) \sim \hbar \frac{\alpha_0}{\epsilon_0} \frac{|v|}{\pi^2} \frac{6}{(2z_a)^4} \mathrm{Im}\left\{\lim_{\omega\to 0} \partial_\omega r^p\right\}, \tag{4.46}$$

where we considered the scattered part of the Green tensor only and for the Drude metal we usually have that $\mathrm{Im}\{\lim_{\omega\to\infty} \partial_\omega r^p\} = 2\epsilon_0 \rho_{\mathrm{lc}}$ with ρ_{lc} the local resistivity of the material [147]. We report a numerical evaluation of the situation in Fig. 4.3.

Finally, from the perspective of the atom's internal energy, we can grasp the deeper physical meaning of the fluctuation-dissipation-inequality that we discussed in Section 4.2.1. When contrasted with Eq. (4.41), the fluctuation-dissipation inequality quantifies the mismatch between the fluctuations of an equilibrated systems and the additional long-time correlations that occur between separated subsystems in nonequilibrium situations. Applying the LTE means neglecting the corresponding channels for exchanging energy. These are, however, an inevitable part of the nonequilibrium situation.

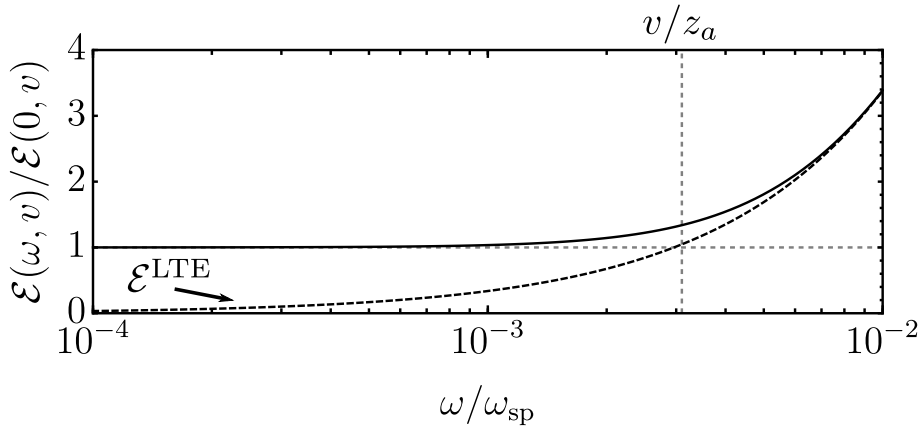

Figure 4.3: Spectral energy of an atom moving above a gold surface normalized to the zero-frequency result obtained in Eq. (4.46) (solid line). Parameters are chosen as in Fig. 4.1. For comparison, we report the LTE result $\mathcal{E}^{\mathrm{LTE}}$ with the dashed line. Clearly, the LTE underestimates the interaction energy at frequencies $\omega \ll v/z_a$. Adapted from [M6].

4.3 On the applicability of local thermal equilibrium and Markovianity

The results of the previous Section reveal that the assumption of local thermal equilibrium, as other statistically incomplete approaches, can lead to thermodynamic inconsistencies for atom-surface interactions in nonequilibrium. Strictly speaking, any assumption or approximation on the underlying statistics of the interaction might ignore fundamental parts of the interactions, most likely long-time correlations, and one might misinterpret important physical phenomena. In the previous Chapters we have discusses such examples in detail.

However, there is good evidence that in certain situations, the simplified equilibrium-based approaches (LTE, Markovianity, etc.) can lead to reliable predictions. For one thing, we already saw in a perturbative calculation in α_0 [see Eq. (4.40)] that the deviation from the detailed balance that is necessary to maintain the nonequilibrium steady-state emerges first in second order of the atomic dipole moment. Hence, any effect that is sufficiently well described in first order of the coupling is not obviously affected by the thermodynamic complexities. This means that a simpler, equilibrium-based approach might be sufficient, e.g. for calculating forces, when keeping in mind that one needs to exercise more care when interested in thermodynamic quantities. On these lines, there are already a number of experiments that seem to be sufficiently well explained by the assumption of LTE; e.g. see Refs. [49, 127] for two very recent examples considering the impact of temperature on atom-surface interactions and near-field heat transfer, respectively. In fact, keeping the complexities from the thermodynamic point of view in mind, it might even be desirable to identify the situations where simplifying assumptions are well-motivated in first approximation in order to reduce the technical complexity of the calculations.

In the context of fluctuation-induced phenomena, the main mathematical object needed for understanding the behavior of the system are the field fluctuations $\underline{\nu}$, or any related quantity such as the dipole fluctuations. In principle, a complete knowledge of the non-vanishing correlations in the system, $\underline{\nu}$ being the one in second order for the field, provides the full information on the dynamics of the system as a function of arbitrary time or frequency. However, depending on the quantity of interest and the desired accuracy of the prediction, one might not necessarily need the full information and can restrict the computation to a certain part of the frequency range. The validity of such an approach, as we will see in the following, is determined by the minimum order of perturbation in order to correctly describe the effect. We will hence now turn our attention to the coupling strength which allows us to relate different orders of perturbation to different channels of interaction.

To be precise, we consider a particle model that allows for N different dissipation channels $\underline{\mathcal{D}}_n$ originating from both internal and external degrees of freedom. If we assume that the corresponding fluctuations are uncorrelated, the dissipation channels add linearly

$$\underline{\mathcal{D}} = \sum_{n=1}^{N} \underline{\mathcal{D}}_n. \tag{4.47}$$

For instance, for a nano-particle that can loose energy either to its phononic (internal) bath or to the material-modified vacuum (external), we recover the model discussed in Eq. (3.16).

The corresponding field fluctuations

$$\underline{\tilde{\nu}}(\omega, v) = \hbar \sum_{n=1}^{N} \underline{\mathcal{D}}_n \tag{4.48}$$

for $N = 2$ are then given by the dissipation kernel of Eq. (3.16) and decompose into the internal $\underline{\mathcal{D}}_{\text{int}}$ and the external $\underline{\mathcal{D}}_{\text{rad}}$ dissipation kernels, respectively. In the frequency range where any of the system's constituents (particle and/or field) feature resonances, we have already seen in Chap. 1 that the correlation times scale exponentially [see discussion below Eq. (1.61)]. Hence, effects centered around the system's resonances are most likely well-described by strong assumptions on the statistics which justifies the basic formalism of cavity QED [113]. For smaller frequencies, the field fluctuations reveal a more subtle behavior. Separating the fluctuations $\underline{\nu}$ depending on their origin, we can write in the particular case of our model in Eq. (3.16)

$$\underline{\tilde{\nu}}(\omega, v) = \hbar \left[\underline{\mathcal{D}}_{\text{int}}(\omega, v) + \underline{\mathcal{D}}_{\text{rad}}(\omega, v)\right] \sim \hbar \left[\frac{\operatorname{sgn}(\omega)}{2} \frac{\epsilon_0}{\alpha_0} \underline{\mu}_{\Re}(0)\, \omega + \frac{\underline{\nu}(0, v)}{\hbar}\right], \tag{4.49}$$

where we, again, used the symmetric average. Using that the imaginary part of the Green tensor is an odd function in frequency (see appendix A), we note that for finite velocities $\underline{\nu}(0, v) \neq 0$ in general. The explicit expression for the planar half-space made from a local Drude metal can be found in Eq. (1.59). This means that the contribution to the field fluctuations stemming from radiation-induced coupling between particle and field does not vanish in the limit of small frequencies. Mathematically, the deviation from (local) equilibrium is encoded in the fluctuation-dissipation-inequality [Eq. (4.24)] and saves $\underline{\nu}(0, v)$ from vanishing identically.

Assuming LTE considerably changes the situation as $\underline{\nu}^{\text{LTE}}(0, v) = 0$. The low-frequency field fluctuations [Eq. (4.49)] are then determined by the constant $\underline{\mu}_{\Re}(0)$. As a reminder, in the context of quantum friction, we used the thermodynamic bath connected to $\underline{\mu}$ to describe the internal dissipative degrees of freedom of a nanoparticle. Even though we allowed for a quite general set of different materials (encoded in the functional and tensorial structure of $\underline{\mu}$), we assume that the coupling between the dissipative internal degrees of freedom is much stronger than cross-correlations to the external vacuum field leading us to assume local equilibration inside the nanoparticle. Further, from Eq. (4.49), our choice for the underlying statistics of the model becomes manifest in the linear frequency scaling which is characteristic for an Ohmic material model. Interestingly, the field fluctuations connected to the dissipative intrinsic bath of the particle scale as α_0^{-1}. In contrast, the contribution connected to $\underline{\nu}(0, v)$ is independent of α_0. This difference becomes important when $\tilde{\nu}$ is employed in describing the atom surface interaction such as the atom's power spectrum [see Eq. (4.4)] or its steady-state energy [see Eq. (4.41)]. Here, the contribution connected to $\underline{\mu}$ will enter in lower order α_0 than the contribution connected to $\underline{\nu}$ such that it can be quantitatively sufficient to neglect the latter and simply assume LTE. In other words, the dissipation channel(s) $\underline{\mathcal{D}}_{\text{int}}$ are dominating and the situation is well-described by the LTE approach. In this way, understanding the behavior of low-frequency fluctuations and their impact on the interaction is a powerful method to understand whether employing simplified techniques that modify or neglect parts of the

underlying statistics is justified or not. This covers for example explicitly the situation of heat transfer between macroscopic bodies, where large intrinsic dissipative baths are present and the LTE is commonly applied, and explains the good theory-experiment agreement that was, e.g., measured recently in Ref. [49]. However, one must always keep in mind that a concrete justification for assumptions on nonequilibrium systems varies from case to case.

By implication, if there is no internal dissipative material bath that is strongly correlated to the external environment, the common, equilibrium-based approaches are vulnerable. It is easy to construct some examples. One of them which we already discussed is the case when $\underline{\mu} = 0$. It has been our guiding example in the present and the previous Chapters for the case of an atom interaction with the vacuum electromagnetic field (see also Refs. [161, 275]). Another example arises from a possible violation of the statistical independence of the fluctuations of the heat baths or their respective dissipation channels $\underline{\mathcal{D}}_n$, i.e. when Eq. (4.47) is invalid. This can occur when the internal dissipative heat bath ($\propto \underline{\mathcal{D}}_{\text{int}}$) carries charge and its dynamics is hence intertwined with the dynamics of the electromagnetic field ($\propto \underline{\mathcal{D}}_{\text{rad}}$) [48]. Further, the internal bath itself might be influenced by the driving [484, 485, 555] or some of the internal excitations might resonate with certain electromagnetic wavelengths [446]. Especially the latter can occur when confined light modes (for instance in a cavity) strongly couple to organic molecules featuring phononic modes [300]. A proper and careful treatment of long-time correlations in the system can then become important.

4.4 Summary and conclusion

We revisited the situation of a microscopic particle interacting with the material-modified vacuum in nonequilibrium situations from the thermodynamic perspective. Focusing on the case of a relative motion between particle and surface, we where mainly interested in (i) the energy and (ii) the spectral power flux in the particle's subsystem. In the nonequilibrium steady-state, we found a detailed balance between incoming and the outgoing power. In line with the physical intuition, at late times and under the assumption of an exact balance of all the acting forces by an unspecified external agent, this means that the average energy of the particle's subsystem is constant. What appears to be a simple necessity – that the average energy of a system is constant in a steady state – has far-reaching consequences when compared to related state-of-the-art approaches aiming to describe the very same system. The constant energy, in our case, could be achieved only by finding a fully self-consistent description completely capturing the coupling and the back-action between particle and environment. Related approaches, however, usually rely on certain assumptions or approximation on the underlying statistics of the system and lead to thermodynamic inconsistency by contradicting the initially assumed steady-state.

We found the physical reason for the failure of approximate approaches to be rooted in insufficiently incorporating the so-called fluctuation-dissipation inequality. In short, it says that the fluctuations are always equal or larger than the assigned hypothetical ground-state fluctuations of the corresponding dissipation. In turns out that the *equality* approximately holds for sufficiently large interaction frequencies, or equivalently, short correlation times. But the fluctuations deviate substantially from the equality for very small frequency, or equivalently, long correlation times. It is exactly this frequency regime that is usually neglected or ill-represented by approaches such as the assumption of local thermal equilibrium, the Born-Markov approximation, the quantum regression hypothesis or standard time-dependent perturbation theory. Instead, in order to be thermodynamically consistent, one has to take all interaction time scales (inverse frequency) into account; in particular it is incorrect to simply ignore long-time correlations between far-separated subsystems of the complete physical setup.

We highlighted that the accuracy of the prediction derived using simplifying, sometimes equilibrium - based, approximations depends on the strength of the coupling between particle and bath. We describe the coupling in orders of the particles static polarizability α_0 in relation to the distance between particle and surface z_a, i.e. $\sim \mathcal{O}(\alpha_0/[\epsilon_0 z_a^3])$ with ϵ_0 the vacuum permittivity. Here, thermodynamics is relentless in the way that for finite coupling we always need to check the full perturbation series in coupling in order to be sure that we properly describe the statistics. However, depending on the specifics of the particle and the geometry, deviations from detailed balance necessary to sustain the nonequilibrium steady-state might not occur in lowest order perturbation theory already. Hence, for observables that are sufficiently well-described in first-order perturbation of the coupling between particle and material-modified field, one can use the formalism we developed in order to substantiate the simpler approach; always keeping the thermodynamics subtleties in mind [see Fig. 4.4 panel *a*)]. Based on the typical fluctuation spectrum of the material-modified electric field operator (see Chap. 1), we can roughly discern three different regimes that we depict in Fig. 4.4 and which require descending levels of accuracy for long-time correlations in their theoretical description:

First, in the most complicated case we considered, i.e. when there simply is no internal

dissipative heat bath or a strong coupling of the external driving to certain modes of the system, we must probably include low-frequency correlations of the interaction into our description. This is because the correlation length scales can in principle range over the full dimension of the complete system. One then needs to deal with power law dependencies of the interaction's correlation functions and might not be able to abstain from a full nonequilibrium calculation [see Fig. 4.4 panel *b*)]. Such a situation is, e.g., given for atom-surface quantum friction.

Second, in simpler situations, the interacting bodies can contain a macroscopic number of dissipative internal degrees of freedom. In addition to the coupling between spatially separated bodies, there is the coupling between the dissipative internal degrees of freedom. In first approximation, the latter is usually much stronger than the coupling between separated subsystems. Even though the typical correlation times of the interaction can still obey a power law dependency, we can safely assume local equilibration which simplifies the theoretical description as we can employ the standard fluctuation-dissipation relation. For instance, such a situation is given by the quantum friction force between a nanoparticle and a surface [M2] or near-field heat transfer [33] [see Fig. 4.4 panel *c*)].

Third, when the system is strongly confined in a cavity and the dominating interaction times are given by a limited number of strongly coupled resonant modes only (e.g. prescribed by an external laser frequency), it can be sufficient to assume the bath of the open system to be Markovian in first order [303]. The correlation times in such a system typically decrease exponentially such that time-dependent perturbation theory and the Born-Markov assumption are likely to be successful in describing the interaction. Long-time correlations can be safely neglected for most quantities [see Fig. 4.4 panel *d*)].

When trying to assess the statistical complexity needed for properly describing a quantum-optical setup, the task is to determine which of the frequency regimes [a)-d) in Fig. 4.4] is dominating the interaction at the leading order of coupling between system and bath.

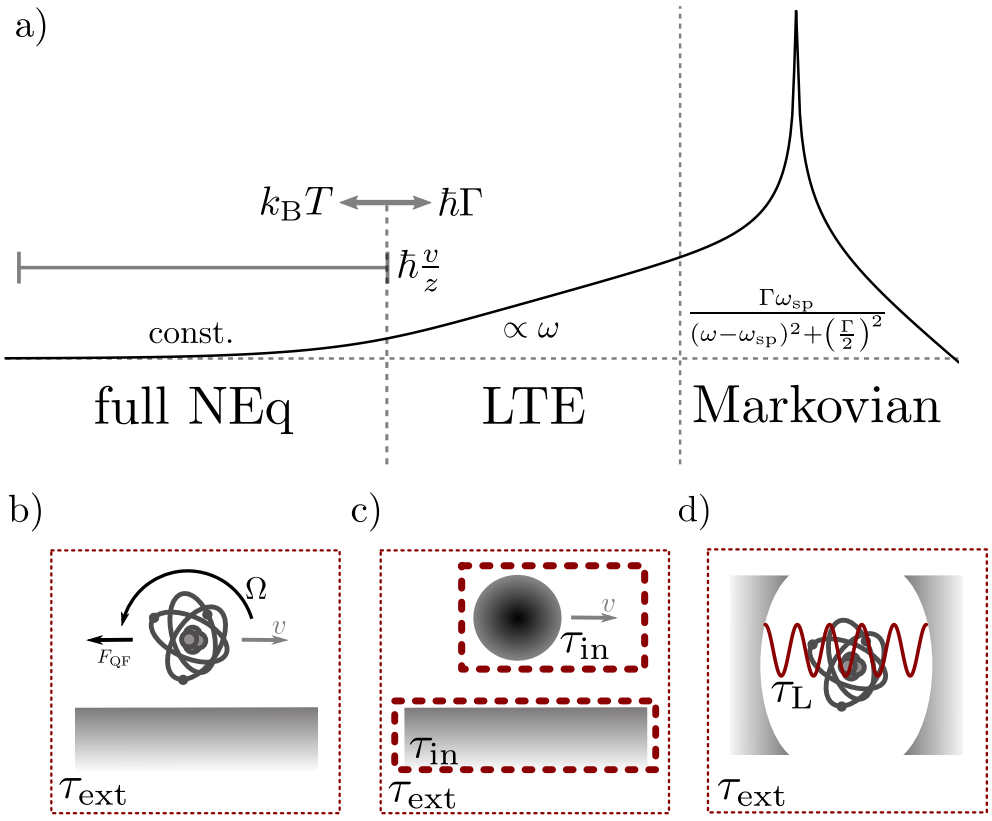

Figure 4.4: Panel a): Same curve reported in Fig. 1.13, where we mark the typical energy scales of different setups and denote typical functional dependencies for the frequency-dependence on the three distinct regimes, where a Makovian, an LTE approach or a full nonequilibrium calculation (NEq) are sufficient to describe the nonequilibrium fluctuations of the electric field, respectively. **Panel b):** An atom moving in front of a planar surface with velocity v will experience a frictional force F_{QF} and a rotation with frequency Ω. The dominant correlation time τ_{ext} is given by the long-time interaction between atom and material-modified vacuum. **Panel c):** Replacing the atom with a nano-particle, the intrinsic correlation times τ_{in} might be coupled more strongly than the external degrees of freedom such that one might be able to assume LTE in first order approximation (thick red dashed boxes). **Panel (d):** In strongly confined systems driven by a highly coherent laser mode, a situation typical for cavity QED, the relevant time τ_{L} of the interaction can be given by the laser frequency allowing for a Markovian treatment of the atom+bath interaction.

CHAPTER 5

Summary and Conclusions

We conclude the work by setting our main contributions into the context of the recent literature and provide an outlook for possible future investigations. To this end, we outline the fundamental and the experimental implications of our results by discussing the connections quantum optical master equations and the thermodynamic uncertainty relation as well as by estimating the chances of possible experimental confirmations of atom-surface interactions in mechanical nonequilibrium.

In the present thesis, we examined the role of long-time correlations in quantum-optical fluctuation-induced interactions in both equilibrium and nonequilibrium situations. In technical terms, long-time correlations are algebraic functions of time describing the importance of past events for the state of a current event, i.e. the memory of an interaction. These algebraic functions quantify the uncertainty, or auto-correlation, of a quantum observable that is relevant for the dynamics of the system of interest. In general, the existence of quantum mechanical ground-state fluctuations introduces finite correlation times to open systems. Hence, some degree of memory, even though possibly small, is appertain to quantum fluctuation-induced interactions and can sometimes even lead to power law dependencies of the correlation function on time delays. This contrasts many related approaches to (cavity) quantum electrodynamics where correlation times usually follow a simple exponential decrease, something which can be quite close to Markovianity, i.e. the complete lack of memory. The exponential behavior can justify simplifying assumptions on the underlying statistics of the interaction. However, such approximations might break down in the context of dispersion forces. Even though this difference is in principle well known and has been noted before, a systematic approach to long-time correlations is, to the best of our knowledge, underrepresented in the available literature describing quantum-optical systems, especially in nonequilibrium.

We focused on the interaction between a microscopic particle and the quantized electromagnetic field in the presence of macroscopic bodies. We developed a self-consistent, non-Markovian, dispersive and dissipative (internal as well as radiation-induced damping) model for the atom's internal degrees of freedom. We further included mechanical nonequilibrium in our description, where the atom moves with respect to an ensemble of macroscopic bodies. Our model allowed us to

- systematically quantify the impact of long-time correlations (see Chapters 1 and 3),
- conduct a careful thermodynamic scrutiny of the formalism in both equilibrium and nonequilibrium (see Chapters 2 and 4),
- and apply our results to the situations of Casimir-Polder interaction and atom-surface quantum friction (see Chapters 2 and 3).

Concerning the novelty of our description, within the context of nonequilibrium atom-surface interactions, we are the first to take both the particle's radiation-induced and intrinsic damping mechanisms simultaneously into account, while self-consistently solving the system's dynamics. Previous work either does not address the presence of internal dissipation within the microscopic object or it introduces dissipation in a rather phenomenological way without specifying its origin, thereby neglecting the impact of radiation-damping. In our description, internal and electromagnetic degrees of freedom interlace within the particle's dressed velocity-dependent polarizability and allow us to keep track of every correlation time scale explicitly. In terms which are very similar to the resolvent technique known from quantum field theory, the poles of the polarizability are related to the polaritonic states within the particle. Our formalism lead us to the prediction, description and quantification of fundamental effects that have been previously overlooked and can not be described with other state-of-the-art methods. Without self-consistently including the dressing of the particle, many of the effects described in the present thesis would not occur. In particular, we

- framed the auto-correlation tensor (power spectrum) of the electric field operator as a suitable quantity for studying long-time correlations in quantum dispersion interactions (see Chapter 1),
- related long-time correlations to the parameters temperature, coupling strength, dissipation (e.g. in materials) and the degree of thermal or mechanical nonequilibrium in the setup (see Chapter 1),
- confirmed long-time correlations to be responsible for thermal corrections to the Casimir-Polder force (Section 2.1) in both planar and curved geometries (Section 2.1.3),
- discovered long-time correlations induced by (spatially nonlocal) dissipation in materials to be the dominant effect determining the low-temperature entropy of the magnetic Casimir-Polder interaction (Section 2.2),
- predicted an average rotation of the atom's mean atomic dipole moment when moving parallel to a material-interface (Section 3.2),
- generalized equilibrium-based formulas for the Casimir-Polder interaction in mechanical nonequilibrium to the full nonequilibrium statistics and predicted corresponding corrections related to long-time correlations which we interpreted thermally (Section 3.3),
- predicted a significant enhancement of quantum friction forces by orders of magnitudes when the atom-surface separation is chosen at the order of the electron's mean free path in the material (Section 3.4.1),
- discussed a practical approach on how to estimate the impact of spatial dispersion on atom-surface quantum friction in geometries more complicated that a single planar interface (such as a finite-sized slab, Section 3.4.1),
- predicted a reduction of the quantum friction force (about 70% for a planar interface) due to the atomic dipole's mean rotation (Section 3.4.2),

- predicted a significant non-additive enhancement (roughly factor 14 for a planar and factor 56 for a rectangular or cylindrical cavity with respect to a single planar interface) of quantum friction forces with respect to changes in the geometry (Section 3.4.3),
- and connected our exact nonequilibrium fluctuation-dissipation theorem to the fluctuation-dissipation inequality quantifying nonequilibrium statistics (Section 4.2.1),
- which eventually enabled us to derive a general thermodynamic condition for quantum-optical nonequilibrium systems (Section 4.2.2) that can be used for assessing the physical consistency of analytical as well as numerical models (Sections 4.2.3 and 4.3).

Long-time correlations are an often overlooked, but inalienable part of interacting open quantum systems. We showed that studying their behavior bares great potential in understanding fundamental statistical relations and overcoming existent experimental challenges. We intend to conclude the present thesis by outlining two such possibilities which directly derive from the results we presented. Both are to be understood as an outline for future work.

5.1 Fundamental implications

Quantum fluctuation-induced phenomena are an interdisciplinary field in the sense that the theoretical formalism readily allows to include macroscopic geometries, material properties, the properties of the material-modified vacuum fields and quantized atomic level structures. Their flexibility and the predictive strength is further nurtured by the rich field of nonequilibrium statistical physics. Since concrete computations are often guided by experimental considerations, the underlying statistical architecture might not always be the main focus of the investigation. However, as we intended to show in the present work by focusing on long-time correlations, any assumption on the probabilistic nature of the interaction can have far-reaching consequences on the final result. To this end, we constructed an exactly solvable model for an atom moving along the symmetry axis of an ensemble of macroscopic bodies. For its methodological convenience, we chose the Langevin approach and modeled the dynamics of the atomic dipole operator $\hat{\mathbf{d}}$ as a three-dimensional stochastic integro-differential equation

$$\frac{\ddot{\hat{\mathbf{d}}}(t)+\omega_a^2\hat{\mathbf{d}}(t)}{\alpha_0\omega_a^2}+2\int_0^\infty \mathrm{d}\tau\ \underline{\gamma}(\tau,v)\cdot\dot{\hat{\mathbf{d}}}(t-\tau)=\hat{\boldsymbol{\xi}}, \tag{5.1}$$

where α_0 is the particle's static polarizability, ω_a its bare resonance frequency, $\hat{\boldsymbol{\xi}}$ the stochastic noise operator in the sense of Eq. (3.5) and $\underline{\gamma}$ the dissipation kernel of the environment interacting with the particle. Further, we allowed the particle to be moving at constant velocity v. Solving the previous equation by integral methods yields the operator in the Heisenberg picture $\hat{\mathbf{d}}=\hat{\mathbf{d}}(t)$ which depends on appropriate boundary conditions. In principle, for a given initial state, the system is now completely solved and we can generate any necessary statistical moment (see Chapters 3 and 4). From a practical perspective, the Langevin approach encapsulates the dynamics of the Schrödinger equation in the Heisenberg picture (given by the quantized Maxwell equations and by the equation of motion for $\hat{\mathbf{d}}$) and has the appeal of a direct physical interpretation. However, its strong resemblance to a deterministic equation of motion can be misleading. It might hence be interesting to consider the system from the statistical perspective and find the atom's reduced density matrix. Here, the notion *reduced* corresponds to a coarse-graining over the environment degrees of freedom [42]. For merely technical reasons we will work with the quasi-probability distribution W_r first, the Wigner function [430], and its corresponding equation of motion, the (quantum) Fokker-Planck equation[1] [106, 558], and derive the reduced density matrix in the second step.

To this end, we ignore rotational degrees of freedom for simplicity and consider a one-dimensional quantum degree of freedom for the oscillator, i.e. $\hat{\mathbf{d}}=\mathbf{d}\hat{q}$, for which we define the (quasi)-phase space coordinate $\mathbf{z}=(q,p)^{\mathrm{T}}=(q,\dot{q}/\alpha_0\omega_a^2)^{\mathrm{T}}$ that finds its rigorous interpretation by means of the Feynman-Vernon path integral [435, 559]. The moments of the system are given by $\langle\hat{q}^n(t)\hat{p}^m(t)\rangle=\int \mathrm{d}q\mathrm{d}p\ q^n p^m W_r(q,p,t)$. For the static atom with zero velocity $v=0$, we can then show that the reduced Wigner function for the one-dimensional atomic

[1] In fact, the formal connection between the Schrödinger equation and the (at this time classical) Fokker-Planck equation was first noted by Schrödinger himself (in German) [556]: "Außerdem [...] ergeben sich merkwürdige Analogien zur Quantenmechanik, die mir sehr des Hindenkens wert erscheinen.". Shortly after, the analogies and significant differences to the classical situation where systematically analyzed by Fürth [557].

degree of freedom coupled to a macroscopic number of field degrees of freedom acting as a thermal bath obeys the quantum Fokker-Planck equation

$$\frac{\mathrm{d}}{\mathrm{d}t}W_r(q,p,t)=\left\{-\alpha_0\omega_a^2 p\partial_q+2\Gamma(t)\partial_p p+\frac{\Omega^2(t)}{\alpha_0\omega_a^2}q\partial_p+2D_{qp}(t)\partial_q\partial_p+D_{pp}(t)\partial_p^2\right\}W_r(q,p,t), \tag{5.2}$$

where we followed the general procedure laid out in Refs. [432, 559, 560]. Equation (5.2) is the celebrated Hu-Paz-Zhang master equation [50] in its Fokker-Planck form [561] with the drift coefficients, $\Gamma(t)$ and $\Omega(t)$, given as a function of the covariance matrix in Refs. [431, 561] and the diffusion coefficients, $D_{qp}(t)$ and $D_{pp}(t)$ given in Refs. [50, 432], respectively. The three-dimensional case follows analogously. Remarkably, the Fokker-Planck equation is local in time and the coefficients are non-Markovian and depend on the quantum nature of the underlying interaction. In this way, we have shown that our atomic model at zero velocity is formally related to the problem of quantum Brownian motion [50, 353, 562] which might come to no surprise since both systems where modeled within a Langevin approach for linear oscillator systems [411]. One of the necessary requirements in order to arrive at Eq. (5.2) was that the involved memory kernel $\underline{\gamma}$ of the environment becomes stationary, i.e. it depends only on the difference between two times $\underline{\gamma}(t,t')=\underline{\gamma}(t-t')\equiv\underline{\gamma}(\tau)$ [see e.g. Eq. (4.3)]. The dissipative term of the Langevin equation in Eq. (5.1) can then be written in terms of a convolution and the formalism of Refs. [432, 559, 560] can be applied directly.

In nonequilibrium, when the particle is moving at finite velocity $v\neq 0$, the situation is considerably more complicated and at arbitrary time we cannot simply write the dissipative term of the Langevin equation in terms of a convolution [see, e.g., the corresponding relation for the material-modified vacuum field in Eq. (3.3)]. Hence, Eq. (5.2) does not generally apply to the situation of quantum friction. However, when we focus on late times and assume that the atomic trajectory prescribes linear motion with constant velocity, the system reaches a steady-state and all transition terms have vanished due to dissipation [44]. In this case, the correlation functions as well as the memory kernel of the environment become stationary. We arrive formally at Eq. (5.1), where the dissipation kernel additionally depends on the velocity (see e.g. Sec. 4.2). We can then derive a Fokker-Planck equation in full analogy to the Hu-Paz-Zhang equation, but with the difference that it is physically meaningful only when the Wigner function (or the density matrix) of the system is constant, i.e. $(\mathrm{d}/\mathrm{d}t)W_r\to 0$ for $t\to\infty$, and the coefficients in front of the differential operators in Eq. (5.2) are constant in time. In the steady-state, the velocity of the particle enters as an additional parameter into the derivation of the steady-state covariance matrix determining the coefficients of the master equation, e.g. $\Gamma(t)\to\Gamma_v$ for given velocity v. In other words, in the self-consistent model we introduced in the present thesis, the Wigner function of the atom's intrinsic degrees of freedom in the case of steady-state quantum friction is given by the steady-state solution of the Hu-Paz-Zhang master equation for given velocity-dependent covariance matrix of the particle's dipole. A few comments are in order.

Equation (5.2) prescribes solutions of a Gaussian form. This property is inherited by the reduced density matrix $\rho_r(q-q'/2,q+q'/2,t)=\int\mathrm{d}p\; e^{-\mathrm{i}pq'}W_r(q,p,t)$. Shifting coordinates $q\to(x+x')/2$ and $q'\to x-x'$, we obtain for the steady-state density matrix describing

quantum friction at constant velocity

$$\lim_{t\to\infty}\rho_r(x,x',t)=\frac{1}{\sqrt{2\pi\sigma_{v,qq}}}e^{-\frac{1}{2}(x'-x)\sigma_{v,pp}(x'-x)}e^{-\frac{1}{2}\frac{x+x'}{2}\sigma_{v,qq}^{-1}\frac{x+x'}{2}}, \tag{5.3}$$

where initial conditions as well as off-diagonal diffusion has vanished due to finite dissipation in the material. We furhter defined the steady-state covariance matrix $\lim_{t\to\infty}\underline{\sigma}_v(t)=\mathrm{diag}[\sigma_{v,qq},\sigma_{v,pp}]=\lim_{t\to\infty}\mathrm{diag}[\langle\hat{q}^2(t)\rangle,\langle\dot{\hat{q}}^2(t)\rangle/(\alpha_0\omega_a^2)^2]$, which depends on the constant velocity v of the atom. For the explicit expressions we refer to the results and methods in Chapter 4 and appendix F.

This seemingly simple result is in fact highly non-trivial to realize and could be achieved only by our fully self-consistent treatment of the coupled atom-field dynamics. It further allows us access to the van Neumann entropy of the reduced atomic system (see Refs. [563, 564] for explicit formulas). Somewhat more directly, we can establish a connection between the density matrix and the linear entropy of the atomic subsystem $\mathcal{S}_L=-\int\mathrm{d}x\mathrm{d}x'\ \rho_r(x,x',\infty)\rho_r(x',x,\infty)=-1/\sqrt{4\sigma_{v,qq}\sigma_{v,pp}}$ [564] by rewriting Eq. (5.3) in the canonical operator form, i.e. $\hat{\rho}_r\propto\exp[-(\frac{1}{2(\alpha_0\omega_a^2)^2\mathcal{B}}\dot{\hat{q}}^2+\frac{\mathcal{B}\omega_a^2}{2}\hat{q}^2)/\mathcal{A}]$ with $\mathcal{A},\mathcal{B}$ two parameters that are to be determined. Following Refs. [565, 566], we find $\mathcal{A}\equiv\frac{\hbar\omega_a}{2}\ln\frac{1-\mathcal{S}_L}{1+\mathcal{S}_L}$ and the parameter $\mathcal{B}$ follows similarly. Even though it would be a strictly formal resemblance so far, the previous reasoning could suggest to interpret the parameter $\mathcal{A}$ as an effective temperature determining the dynamics of the particle's internal degrees of freedom. In other words, the impression arises that the moving particle perceives its environment as acting as a thermal bath at an effective temperature that is given by the material-modified field fluctuations in the nonequilibrium steady state. In this way, steady-state quantum friction could be interpreted as the a non-relativistic analog of the Fulling-Davies-de Witt-Unruh effect [567–570] at constant velocity but in presence of macroscopic materials. In fact, using a very different approach based on the nonequilibrium fluctuation-dissipation relation, a similar conclusion was reported recently under the name of *vacuum incalescence* [132]. At this point, finding the rigorous justification of the thermal interpretation in quantum friction is left to future work.

Further, since the Hu-Paz-Zhang master equation [Eq. (5.2)] is quite general for oscillator systems, its structure is rather involved. In certain situations, where we do not need to be as general, it can be simplified to a perhaps more commonly used form by a series of approximations. Assuming Markovianity, the coefficients of the master equation become time-independent and the off-diagonal diffusion coefficient D_{qp} vanishes [571]. If we further work in the classical regime where $k_\mathrm{B}T\gg\hbar\omega_a$, the quantum properties can be neglected and we obtain the classical Klein-Kramers equation [558]. Finally, we might even want to consider overdamped dynamics, where the oscillating behavior is neglected by sending $\ddot{\hat{q}}(t)\to 0$. If we further average the continuous equation over m discretely measured time intervals, we arrive at the appealingly simple Pauli master equation [303]

$$\frac{\mathrm{d}}{\mathrm{d}t}\tilde{W}_n=\sum_m\Big[w_{nm}\tilde{W}_m-w_{mn}\tilde{W}_n\Big] \tag{5.4}$$

for the Markovian, one-dimensional, discrete and classical distribution function $\tilde{W}_n$ and the

transition probabilities w_{nm} from state m to state n. The Pauli master equation is a simple equation that can be used to study biomolecular processes and chemical reactions catalyzed by enzymes. A recent surge of interest in such setups has lead to the development of the thermodynamic uncertainty relation (TUR) by Barato and Seifert [572]. The TUR relates the mean fluctuations of a classical observable to the entropy production per unit time of a nonequilibrium process. It thereby introduces a notion of the thermodynamic cost for achieving a desired precision in an experiment. Since then, the TUR has been extended to underdamped classical systems [550, 573] as well as Markovian quantum systems [574, 575]. In this context, our work could provide some insights on the connection between the mentioned Markovian TUR and the fully non-Markovian uncertainty relations that were developed in the context of quantum Brownian motion [576, 577] by providing an exactly solvable example that can lead through the different simplifications. We briefly touched this topic already in Chapter 4 by considering the fluctuation-dissipation inequality [422] and finding possible connections to the TUR is left to future work.

5.2 Experimental implications

Atom-surface quantum friction is perhaps the most intriguing setup we considered in this thesis since there is, to the best of our knowledge, no experimental confirmation yet. One reason is the weakness of the effect: The quantum frictional force between a rubidium atom and a gold surface much thicker than their separation [Eq. (3.87)] yields a force that is many orders of magnitude smaller than the corresponding Casimir-Polder interaction. For example, the simplest estimate for a rubidium-87 atom moving at the speed v in front of a planar interface made from gold at the separation z_a yields the acceleration [see Eq. (3.87)]

$$a \approx -3\frac{\mu\mathrm{m}}{\mathrm{s}^2} \times \left(\frac{v}{v_s}\right)^3 \times \left(\frac{\mathrm{nm}}{z_a}\right)^{10} \tag{5.5}$$

experienced by the particle. We chose the speed of sound v_s and one nanometer distance as a reference scale. Note that placing the atom at 10 nm distance already results in a decrease of the acceleration by *ten orders of magnitude*.

From Eq. (5.5), we can deduce a simple principle leading to more friction: Minimize the atom-surface separation and simultaneously maximize the velocity and the interaction time. Further, we have shown that the friction force scales quadratically in both the material's resistivity (for conducting materials) and the polarizability of the particle. For example, choosing doped silicon instead of gold, a comparably well-controlled handle on the material's resistivity is achieved by the degree of doping. This can increase the resistivity by about four to six orders of magnitude (see e.g. Refs. [578, 579]). Simultaneously, it is worthwhile to consider working with another species of atoms such as lithium. It features roughly half the polarizability of rubidium, but only one tenth of its mass leading to an increase in the experienced acceleration by roughly a factor of three with respect to rubidium [580]. Clearly, an intelligent choice of atom and material represents a great potential for promoting the friction force to the measurable regime and we refer to Ref. [355] for a comprehensive overview of such possible choices. However, given that most experiments dealing with atom-surface forces operate in the regime of hundreds of nanometers and even micrometer [23, 25], we are confronted with an extra twenty to thirty orders of magnitude decrease with respect to the value at one nanometer given in Eq. (5.5). That is why estimates on the friction force based on Eq. (5.5) seem to suggest the conclusion that the quantum friction force on atoms is "far beyond experimental reach" [581].

In order to set such statements into context, it is necessary to have a look at the current experiments probing atom-surface interactions. We have identified three existing approaches which we think can be possibly used for detecting quantum friction: Atom interferometry using light-pulses, atomic diffraction at a material grating and the use of nitrogen-vacancy centers. We introduce them briefly in the following.

Atom interferometry exploits the de Broglie wave character of (ultra-)cold atoms or Bose-Einstein condensates in order separate and reconnect the evolution of atomic internal and external states[2] [582–584]. During the evolution, the wave function describing the two "paths" of the interferometer acquires a phase shift which can then be measured, e.g. in an interference

[2]Depending on whether the internal or external degrees of freedom of the atomic cloud are relevant for the interferometry, one distinguishes between Raman- and Bragg-type atom interferometry [582, 583], respectively.

pattern. One relevant realization of the necessary beam splitter and mirror operations for the atomic wave packet is by using a combination of laser pulses [584]. This technique is particularly suited for studying atom-surface interactions since the two arms of the interferometer can be spatially separated such that, in principle, one arm can be exposed to the interaction with a material and the other arm serves as a reference. Pioneered in the early nineties [93, 94, 585], atom light pulse interferometers have gained increasing complexity and accuracy. For one, while the first designs were macroscopic devices occupying the space of a small lab [94, 95], modern atom interferometers can be implemented on millimeter-scale devices [586, 587], so called atom chips [27]. This paved the way for high-precision experiments in microgravity environments on earth [588], planes or rockets [589, 590] and on the international space station [99, 315, 591, 592]. Atom interferometers have become a well-understood tool which is applied to high-precision measurements, often used for gravimetry, that has demonstrated acceleration sensitivities $\lesssim \mu\mathrm{m/s}^2$ [98, 590]. Especially on atom chips, it is further possible to achieve atom-surface separations at the order of micron and below [27]. Atomic wave gravimeters are usually optimized for long iteration times (up to milliseconds [98] or even seconds [592]) since the phase shift usually grows quadratically in time [94]. Unfortunately, long iteration times come at the price of speed. Commonly found velocities of the atomic wave packet are at the order of centimeter or meters per second or slower [98, 593] which probably represents the biggest downside when aiming to probe quantum friction [see Eq. (5.5)].

The second option, atomic diffraction, directly addresses the issue of achieving high velocities. Strictly speaking, atomic diffraction is another, much simpler type of atom interferometer [441]: A collimated beam of atoms is aimed at a material grid with periodically spaced slits and gets diffracted due to the interaction with the material during the transmission [594]. We note that the grid could in principle also be constructed using standing light waves [595], which we do not consider in the following since the interaction with the material is relevant for our purposes. The resulting interference pattern is, e.g., measured using laser-induced florescence microscopy at the screen [103, 596] or a number of gratings is combined to form a complete interferometer [597]. Interestingly, since the atomic beam is prepared first and then guided through the fixed grating, it is possible to obtain mean velocities of even $\sim$km/s by using a commercial ion gun in combination with a neutralization procedure subsequent to the acceleration process [598]. Atomic diffraction experiments can be conducted with large molecules [599] and the realized atom-surface interactions are in the realm of a few tens of nanometers [103]. Further, they have already been used to study the near-field van der Waals interaction between atom and surface [26, 102, 596]. However, in order to create a proper diffraction pattern, the gratings are usually designed to be comparably thin (hundred nanometer and thinner [103]) which, especially in combination with the high velocities, yields a comparably short interaction time between the atoms and the material.

The last class of experiments we want to introduce is rather different from the previous two approaches and makes use of so-called nitrogen-vacancy (NV) centers in nanodiamonds [600, 601]: An impurity in the diamond lattice, where one carbon atom is replaced with a nitrogen atom. The replacement leads to a neighboring vacancy in the lattice. The nitrogen-vacancy center is likely the best studied color-defect in the diamond lattice and has, e.g., been used as a single-photon emission source [602] or for magnetometry [603]. The NV center comes in two different charge configurations. There is the neutral configuration, which has

five unpaired electrons consisting of the four neighboring carbon atoms and the one extra from the intrinsic nitrogen atom. The most frequently used configuration due to its excellent coherence properties, however, is negatively charged and features one extra electron that is trapped at the NV site [602]. Mathematically, the interaction of the electromagnetic field with the single-electron spin of the negatively charged NV-center resembles a two-level system and thereby mimics the behavior of a simple atom [604]. Although it might seem quite abstract to connect the NV center in a diamond lattice to our original setup of an atom interacting with a surface, it involves many practical advantages: Among the robustness in fabrication and other experimental vantages such as a comparably simple optical spin-polarization and readout of the ground-state spin [601], NV centers allow for a precise position control. Due to their fixed place in the lattice of a larger bulk, it is possible to attach the system to the tip of an atomic force microscope and sustain position-control even at room temperatures [601]. Recently, this has lead to an experimental proposal aimed towards quantum friction. A NV center, glued to the tip of the cantilever of the atomic force microscope, is brought in the very close vicinity (3 to 8 nm) of a gold-coated disk rotating at the speed of up to 7000 cycles per second [30]. The aim is to measure the velocity-corrections to the geometric phase of the NV center. Thereby the probability of the two-level system to be in its excited state can be accessed.

In any of the mentioned cases, the detection of atom-surface quantum friction remains challenging. We point out, however, that using Eq. (5.5) as a reference is only half of the complete picture. In fact, nature seems to pose several intrinsic effects for enhancing the interaction which have been reported for the first time in the present thesis and the resulting publications: Aiming to increase the friction force, our results suggest that it is preferable to choose setups where (i) spatial dispersion in the material response is strong, (ii) the participation of rotational degrees of freedom in the interaction is diminished and (iii) the nonadditive properties of the interaction with respect to geometry are fully utilized, i.e. by preferring cavities over single interfaces. We have shown that quantum friction on atoms can be significantly modified by appropriately choosing the geometry and materials and we find for the actual acceleration

$$\tilde{a} \approx a \times \eta, \tag{5.6}$$

where η is an enhancement factor which can assume several orders of magnitude related to a suitable experimental design. For example, the results of the present thesis directly suggest a possible enhancement with respect to the simple planar Drude interface of (i) three orders of magnitude due to spatial dispersion, (ii) a factor of two when the particle is moving at the center of a cavity and (iii) more than one order of magnitude when the surrounding geometry is chosen to be a cylindrical cavity. This implies $\eta \gtrsim 2 \times 10^4$ and we emphasize that there is still room for optimization.

We combined these findings in one underlying principle: Nonequilibrium dispersion forces are highly sensitive to the low-frequency behavior of the material-modified spin-dependent electromagnetic local density of states or, in other words, long-time correlations in the system. Our comprehensive exploration and exploitation of long-time correlations has brought measurements of non-contact friction closer to reality. We have reached modest optimism for potential measurements of quantum friction not by improving an experimental design, but by understanding the deeper statistical mechanisms underlying the nonequilibrium interaction.

Metaphorically speaking, when we are looking for an object the size of a molecule and the only available tool is a meter stick, we are pretty ill-equipped. In this thesis, however, we have shown that the sought-after object might actually be much bigger than a molecule – maybe even in the realm of centimeters – promoting the meter stick as a suitable instrument.

APPENDIX A

Electromagnetic Green Tensor

We report the analytic expressions for the electric Green tensor in planar, spherical and cylindrical geometries which we use throughout the thesis. The source as well as the point of detection are placed outside the material body.

Solving electromagnetic boundary problems prescribed by Maxwell's equations, it is convenient to work in Fourier domain. We define the Fourier transform of a function $f(\mathbf{r},t)$ in time ($t \leftrightarrow \omega$) and spatial ($\mathbf{r} \leftrightarrow \mathbf{k}$) domain as

$$f(\mathbf{r},t) = \int \frac{\mathrm{d}\omega}{2\pi} \int \frac{\mathrm{d}^3\mathbf{k}}{(2\pi)^3}\, e^{\mathrm{i}(\mathbf{k}\cdot\mathbf{r}-\omega t)} f(\mathbf{k},\omega), \tag{A.1a}$$

$$f(\mathbf{k},\omega) = \int \mathrm{d}\omega \int \mathrm{d}^3\mathbf{r}\, e^{-\mathrm{i}(\mathbf{k}\cdot\mathbf{r}-\omega t)} f(\mathbf{r},t). \tag{A.1b}$$

Note that we distinguish between a function and its integral transform solely by its arguments. The one- and two- dimensional cases in space follow analogously.

The Green tensor is defined by Equation (1.11). In spatially local media, this reduces to

$$\left(\nabla\times\nabla\times -\underline{\epsilon}(\mathbf{r},\omega)\frac{\omega^2}{c^2}\right)\underline{G}(\mathbf{r},\mathbf{r}',\omega) = \frac{\omega^2}{\epsilon_0 c^2}\delta(\mathbf{r}-\mathbf{r}'), \tag{A.2}$$

with appropriate boundary conditions for the geometry under consideration. For instance, in pure vacuum where no materials are present ($\underline{\epsilon} = \mathbb{1}$), the vacuum Green tensor $\underline{G}_0$ can be found by taking the divergence on both sides of Eq. (A.2) and performing the spatial Fourier transform. The resulting Helmholtz equation allows for advanced and retarded propagators. Considering the Sommerfeld radiation condition, namely choosing $\underline{G}_0(\mathbf{r},\mathbf{r}',\omega)$ to be an outgoing wave for $|\mathbf{r}-\mathbf{r}'| \to \infty$, we obtain

$$\underline{G}_0(\mathbf{r},\mathbf{r}',\omega) = \underline{G}_0(\mathbf{r}-\mathbf{r}',\omega) = -\left[1+\frac{c^2}{\omega^2}\nabla\nabla\right]\left(-\frac{c^2 e^{\mathrm{i}\omega|\mathbf{r}-\mathbf{r}'|/c}}{4\pi\omega^2|\mathbf{r}-\mathbf{r}'|}\right). \tag{A.3}$$

The imaginary part of the Green tensor evaluated with both source and sink at the same position $\mathbf{r}_0$ yields the typical frequency-cubed behavior, i.e.

$$\lim_{\mathbf{r}'\to\mathbf{r}} \underline{G}_I(\mathbf{r}-\mathbf{r}',\omega) = \frac{\omega^3}{6\pi\epsilon_0 c^3}\mathbb{1}, \tag{A.4}$$

where $\mathbb{1}$ is the three-dimensional unity matrix and the subscript I gives the imaginary part of an expression.

In the presence of materials with $\underline{\epsilon} \neq 0$, the solution of Eq. (A.2) depends on the particular boundary condition of the material-vacuum interface. We will discuss some special cases in the following Sections. Still, some general remarks on the Green tensor's functional properties are possible [58, 188, 189]. Due to causality, we have that $\underline{G}(\mathbf{r}, \mathbf{r}', -|t|) = 0$ such that the Green tensor is an analytic function in the upper frequency plane. Its elements in time domain are real and we consider reciprocal materials only such that we, respectively, have that

$$\underline{G}(\mathbf{r}, \mathbf{r}', \omega) = \underline{G}^*(\mathbf{r}, \mathbf{r}', -\omega), \qquad \underline{G}(\mathbf{r}, \mathbf{r}', \omega) = \underline{G}^{\mathrm{T}}(\mathbf{r}', \mathbf{r}, \omega). \tag{A.5}$$

In spatial Fourier domain ($\mathbf{r}-\mathbf{r}' \to \mathbf{k}$), for homogeneous materials with $\underline{G}(\mathbf{r}, \mathbf{r}', \omega) = \underline{G}(\mathbf{r}-\mathbf{r}', \omega)$, the previous properties translate to

$$\underline{G}(\mathbf{k}, \omega) = \underline{G}^{\mathrm{T}}(-\mathbf{k}, \omega), \qquad \underline{G}(\mathbf{k}, \omega) = \underline{G}^*(-\mathbf{k}, -\omega). \tag{A.6}$$

Many general relations used in the thesis can be derived from the previous considerations. For example, combining Eqs. (A.6), we find $\underline{G}(\mathbf{k}, \omega) = \underline{G}^\dagger(\mathbf{k}, -\omega)$ which, in particular, means that

$$\underline{G}_R^{\mathrm{s}}(\mathbf{k}, \omega) = \underline{G}_R^{\mathrm{s}}(\mathbf{k}, -\omega), \qquad \underline{G}_R^{\mathrm{as}}(\mathbf{k}, \omega) = -\underline{G}_R^{\mathrm{as}}(\mathbf{k}, -\omega), \tag{A.7a}$$

$$\underline{G}_I^{\mathrm{s}}(\mathbf{k}, \omega) = -\underline{G}_I^{\mathrm{s}}(\mathbf{k}, -\omega), \qquad \underline{G}_I^{\mathrm{as}}(\mathbf{k}, \omega) = \underline{G}_I^{\mathrm{as}}(\mathbf{k}, -\omega). \tag{A.7b}$$

In the last line we used the subscripts "s" and "as" to denote the symmetric and the anti-symmetric part of a tensor, respectively. The subscript R (I) gives the real (imaginary) part of an expression. Further, defining $\underline{G}_\Im = (\underline{G} - \underline{G}^\dagger)/(2\mathrm{i})$ and using that $\underline{G}^{\mathrm{s}}$ ($\underline{G}^{\mathrm{as}}$) is even (odd) in $\mathbf{k}$, we find

$$\underline{G}_\Im(\mathbf{k}, \omega) = -\underline{G}_\Im^{\mathrm{T}}(-\mathbf{k}, -\omega). \tag{A.8}$$

Similar relations follow for $\underline{G}_\Re = (\underline{G} + \underline{G}^\dagger)/(2\mathrm{i})$. Again, in geometries with lower order symmetries, the three-dimensional wave vector is to be replaced with its two- or one-dimensional counterparts.

A.1 Planar geometry

In planar geometries it is convenient to perform a spatial Fourier transform along the directions parallel to the surface ($\mathbf{r}_\parallel - \mathbf{r}'_\parallel$ to $\mathbf{p}$) only, i.e.

$$\underline{G}(\mathbf{r},\mathbf{r}',\omega) = \underline{G}(\mathbf{r}_\parallel - \mathbf{r}'_\parallel, z, z', \omega) = \int \frac{\mathrm{d}\omega}{2\pi} \int \frac{\mathrm{d}^2\mathbf{p}}{(2\pi)^2}\, e^{\mathrm{i}(\mathbf{p}\mathbf{r}-\omega t)} \underline{G}(\mathbf{p}, z, z', \omega) \tag{A.9}$$

with $\mathbf{r}_\parallel = (x,y)^{\mathrm{T}}$. The analytic expression for the Green tensor in Fourier domain has been found by several authors before (see e.g. Ref. [189]). It decomposes into a sum of the vacuum contribution $\underline{G}_0$ and a scattered contribution $\underline{g}$.

Planar cavity

Suppose we have a planar cavity of width $2w$, where one side of the cavity coincides with the xy plane, the z direction pointing towards the inner of the cavity. The reflection of each of the radiation's polarization at the plates is described by the transverse electric $r^s_{-/+}$ and the transverse magnetic $r^p_{-/+}$ Fresnel reflection coefficients, where the subscript denotes the lower (-) and the upper (+) plate of the cavity. When the source $\mathbf{r}$ and the point of observation $\mathbf{r}'$ are both located outside of the material, the scattered part of the Green tensor is given by [189]

$$\begin{aligned}
\underline{g}(\mathbf{p}, z, z', \omega) = \frac{\kappa}{2\epsilon_0} \frac{e^{-2\kappa w}}{D_p} \Big(& r^p_- e^{-\kappa(z+z'-2w)} \tilde{\mathbf{P}}_+ \tilde{\mathbf{P}}_- + r^p_+ e^{-\kappa(2w-z-z')} \tilde{\mathbf{P}}_- \tilde{\mathbf{P}}_+ \\
& + r^p_+ r^p_- \left[e^{-\kappa(z-z'+2w)} \tilde{\mathbf{P}}_+ \tilde{\mathbf{P}}_+ + e^{-\kappa(2w-z+z')} \tilde{\mathbf{P}}_- \tilde{\mathbf{P}}_- \right] \Big) \\
& + \frac{1}{\kappa} \frac{\omega^2}{2\epsilon_0 c^2} \frac{e^{-\kappa d}}{D_s} \\
& \times \left(r^s_- e^{-\kappa(z+z'-2w)} + r^s_+ e^{-\kappa(2w-z-z')} + r^s_- r^s_+ \left[e^{-\kappa(2w+z-z')} + e^{-\kappa(2w-z+z')} \right] \right) \tilde{\mathbf{S}}\tilde{\mathbf{S}}
\end{aligned} \tag{A.10}$$

where we defined $\kappa = \sqrt{p^2 - \omega^2/c^2}$ with $\mathrm{Im}\kappa < 0$ and $p = |\mathbf{p}| = \sqrt{p_x^2 + p_y^2}$, the denominator $D_q = 1 - r^q_- r^q_+ e^{-4\kappa w}$ gives multiple Fabry-Perot reflections inside the cavity and we introduced the polarization vectors [58, 189]

$$\tilde{\mathbf{P}}_\pm = \frac{p}{\kappa}\mathbf{z} \mp \mathrm{i}\frac{\mathbf{p}}{p}, \qquad\qquad \tilde{\mathbf{S}} = \frac{\mathbf{p}}{p} \times \mathbf{z}. \tag{A.11}$$

For most of our applications it will be sufficient to know the scattered Green tensor at the position of the atom $z' \to z$.

The previous relation then reduces to

$$\underline{g}(\mathbf{p},z,\omega)=\frac{\kappa}{2\epsilon_0}\left(\frac{r_-^p e^{-2\kappa z}\tilde{\mathbf{P}}_+\tilde{\mathbf{P}}_- + r_+^p e^{-2\kappa(2w-z)}\tilde{\mathbf{P}}_-\tilde{\mathbf{P}}_+ + r_+^p r_-^p e^{-4\kappa w}\left[\tilde{\mathbf{P}}_+\tilde{\mathbf{P}}_+ + \tilde{\mathbf{P}}_-\tilde{\mathbf{P}}_-\right]}{1-r_+^p r_-^p e^{-4\kappa w}}\right. \tag{A.12}$$
$$\left. +\frac{\omega^2}{\kappa^2 c^2}\frac{r_-^s e^{-2\kappa z}+r_+^s e^{-2\kappa(2w-z)}+2r_-^s r_+^s e^{-4\kappa w}}{1-r_+^s r_-^s e^{-4\kappa w}}\tilde{\mathbf{S}}\tilde{\mathbf{S}}\right)$$

with the tensorial structure

$$\tilde{\mathbf{P}}_+\tilde{\mathbf{P}}_- = \begin{pmatrix} p_x^2/p^2 & p_xp_y/p^2 & -\mathrm{i}p_x/\kappa \\ p_xp_y/p^2 & p_y^2/p^2 & -\mathrm{i}p_y/\kappa \\ \mathrm{i}p_x/\kappa & \mathrm{i}p_y/\kappa & p^2/\kappa^2 \end{pmatrix} = \left(\tilde{\mathbf{P}}_-\tilde{\mathbf{P}}_+\right)^*,$$
$$\tilde{\mathbf{P}}_+\tilde{\mathbf{P}}_+ + \tilde{\mathbf{P}}_-\tilde{\mathbf{P}}_- = -2\begin{pmatrix} p_x^2/p^2 & p_xp_y/p^2 & 0 \\ p_xp_y/p^2 & p_y^2/p^2 & 0 \\ 0 & 0 & -p^2/\kappa^2 \end{pmatrix},$$
$$\tilde{\mathbf{S}}\tilde{\mathbf{S}} = \begin{pmatrix} p_y^2/p^2 & -p_xp_y/p^2 & 0 \\ -p_xp_y/p^2 & p_x^2/p^2 & 0 \\ 0 & 0 & 0 \end{pmatrix}. \tag{A.13}$$

At the center of the cavity at $z=w$, the above expression furthermore reduces to

$$\underline{g}(\mathbf{p},w,\omega)=\frac{\kappa}{2\epsilon_0}e^{-2\kappa w}\left(\frac{r_-^p\tilde{\mathbf{P}}_+\tilde{\mathbf{P}}_- + r_+^p\tilde{\mathbf{P}}_-\tilde{\mathbf{P}}_+ + r_+^p r_-^p e^{-2\kappa w}\left[\tilde{\mathbf{P}}_+\tilde{\mathbf{P}}_+ + \tilde{\mathbf{P}}_-\tilde{\mathbf{P}}_-\right]}{1-r_+^p r_-^p e^{-4\kappa w}}\right. \tag{A.14}$$
$$\left. +\frac{\omega^2}{\kappa^2 c^2}\frac{r_-^s + r_+^s + 2r_-^s r_+^s e^{-2\kappa w}}{1-r_+^s r_-^s e^{-4\kappa w}}\tilde{\mathbf{S}}\tilde{\mathbf{S}}\right)$$

In the near-field limit, the s-polarization vanishes and we can replace $\kappa\to p$. Focusing on the skew-symmetric part ("as"), we observe that

$$\underline{g}^{\mathrm{as}}(\mathbf{p},w,\omega)=\frac{\kappa}{2\epsilon_0}\frac{e^{-2\kappa w}}{1-r_+^p r_-^p e^{-4\kappa w}}(r_+^p-r_-^p)\begin{pmatrix} 0 & 0 & \frac{\mathrm{i}p_x}{\kappa} \\ 0 & 0 & \frac{\mathrm{i}p_y}{\kappa} \\ -\frac{\mathrm{i}p_x}{\kappa} & -\frac{\mathrm{i}p_y}{\kappa} & 0 \end{pmatrix} \tag{A.15}$$

which vanishes if both sides of the cavity are made from exactly the same material. Furthermore, choosing the reflection coefficients properly, this enables us to change the overall sign of the components. For further details we refer to the main text.

Flat surface

We obtain the scattered part of the Green tensor for a single planar interface from Eq. (A.12) by formally sending $2w \to \infty$. Denoting the Fresnel reflection coefficients of the remaining (lower) plate of the cavity with $r^{s/p}$, this gives

$$\underline{g}(\mathbf{p}, z, z', \omega) = \frac{\kappa}{2\epsilon_0} \left(r^p \tilde{\mathbf{P}}_+ \tilde{\mathbf{P}}_- + \frac{\omega^2}{\kappa^2 c^2} r^s \tilde{\mathbf{S}} \tilde{\mathbf{S}} \right) e^{-\kappa(z+z')}. \tag{A.16}$$

Performing the inverse spatial Fourier transform and sending $\mathbf{r}' \to \mathbf{r}$, the off-diagonal elements of the Green tensor vanish and we obtain

$$\begin{aligned} \lim_{\mathbf{r}' \to \mathbf{r}} \underline{g}(\mathbf{r}_\parallel - \mathbf{r}'_\parallel, z, z', \omega) &= \underline{g}(z, \omega) \\ &= \int \frac{\mathrm{d}^2\mathbf{p}}{(2\pi)^2} \frac{\kappa}{2\epsilon_0} \left[\left(r^p + \frac{\omega^2}{\kappa^2 c^2} r^s \right) \left(\frac{p_x^2}{p^2} \mathbf{xx} + \frac{p_y^2}{p^2} \mathbf{yy} \right) + r^p \frac{p^2}{\kappa^2} \mathbf{zz} \right] e^{-2\kappa z}, \end{aligned} \tag{A.17}$$

where the $\mathbf{x}, \mathbf{y}, \mathbf{z}$ denote the unit vectors in our Cartesian coordinate system.

A.2 Spherical geometry

We now report the electric Green tensor of a sphere. Again, source and sink of the electromagnetic field are placed outside of the material body. We ensure passitivity selecting $\mathrm{Im}\epsilon > 0$ for the material of the sphere. For simplicity, we assume the permittivity to be isotropic and spatially local inside the sphere, $\epsilon(\mathbf{r}, \omega) = \epsilon(\omega)$ for $\mathbf{r} \in V$ with V the volume of the sphere and vacuum anywhere else. Due to the high symmetry of the considered problem, solving Eq. (A.2) can be reduced to solving the scalar Helmholtz equation expanded in spherical coordinates $\mathbf{r} = (\rho, \phi, \theta)$ with $\rho \in [0, \infty)$, $\phi \in [0, 2\pi)$ and $\theta \in [0, \pi]$ (see e.g. Ref. [357] and references therein). Similar to the planar case, the Green tensor decomposes into a vacuum solution and a scattered contribution [357]. The former is given by Eq. (A.3) and a version adapted to cylindrical and spherical coordinate systems can be found in Refs. [535] and [605], respectively. The scattered contribution, on the other hand, can be found in Refs. [188, 605]. Focusing on the case of coinciding source and sink ($\mathbf{r}' \to \mathbf{r}$), we have

$$\underline{g}(\mathbf{r}, \mathbf{r}, \omega) = \frac{\omega^3}{16\pi^2 \epsilon_0 c^3} \sum_{n=1}^{\infty} \sum_{m=0}^{n} \left(2 - \delta_{m0}\right) \frac{2n+1}{n(n+1)} \frac{(n-m)!}{(n+m)!} \left[r_n^s \, \underline{S}_{nm}(\mathbf{r}, \mathbf{r}, \omega) + r_n^p \, \underline{T}_{nm}(\mathbf{r}, \mathbf{r}, \omega) \right] \tag{A.18}$$

where δ_{jk} is the Kronecker delta and the scattering coefficients are given by [292]

$$r_n^s(\omega) = -\mathrm{i} \frac{[x_\mathrm{s} j_n(x_\mathrm{s})]' j_n(x_\mathrm{v}) - [x_\mathrm{v} j_n(x_\mathrm{v})]' j_n(x_\mathrm{s})}{[x_\mathrm{s} j_n(x_\mathrm{s})]' h_n(x_\mathrm{v}) - [x_\mathrm{v} j_n(x_\mathrm{v})]' h_n(x_\mathrm{s})}, \tag{A.19a}$$

$$r_n^p(\omega) = -\mathrm{i} \frac{[x_\mathrm{s} j_n(x_\mathrm{s})]' j_n(x_\mathrm{v}) - \epsilon [x_\mathrm{v} j_n(x_\mathrm{v})]' j_n(x_\mathrm{s})}{[x_\mathrm{s} j_n(x_\mathrm{s})]' h_n(x_\mathrm{v}) - \epsilon [x_\mathrm{v} h_n(x_\mathrm{v})]' j_n(x_\mathrm{s})}. \tag{A.19b}$$

We defined the diffraction parameter $x_\mathrm{v} = k_\mathrm{v} R$ and $x_\mathrm{s} = k_\mathrm{s} R$ with $k_\mathrm{v} = \omega/c$, $k_\mathrm{s} = \omega\sqrt{\epsilon}/c$, $\epsilon = \epsilon(\omega)$ the permittivity and R the radius of the sphere. Further, the prime indicates a derivative with respect to $x_{\mathrm{s},v}$ and $j_n(x)$ and $h_n(x)$ are the spherical Bessel function and the spherical Hankel function of first kind. The tensorial structure reads in spherical coordinates

$$\underline{S}_{nm}(\mathbf{r},\mathbf{r},\omega) = [h_n(k_\mathrm{v}\rho)]^2 \left\{ \left[\frac{m}{\sin\theta} P_n^m(\cos\theta)\right]^2 \boldsymbol{\theta\theta} + \left[\frac{\mathrm{d}P_n^m(\cos\theta)}{\mathrm{d}\theta}\right]^2 \boldsymbol{\phi\phi} \right\} \tag{A.20}$$

and $\underline{T}_{nm} = \underline{T}_{nm}^\mathrm{diag} + \underline{T}_{nm}^\mathrm{off}$ decomposes into a diagonal

$$\begin{aligned} \underline{T}_{nm}^\mathrm{diag}(\mathbf{r},\mathbf{r},\omega) = &\left[\frac{n(n+1)}{k_\mathrm{v}\rho} h_n(k_\mathrm{v}\rho) P_n^m(\cos\theta)\right]^2 \boldsymbol{\rho\rho} \\ &+ \left[\frac{1}{k_\mathrm{v}\rho}\frac{\mathrm{d}[\rho h_n(k_\mathrm{v}\rho)]}{\mathrm{d}\rho}\right]^2 \left(\left[\frac{\mathrm{d}P_n^m(\cos\theta)}{\mathrm{d}\theta}\right]^2 \boldsymbol{\theta\theta} + \left[\frac{m}{\sin\theta} P_n^m(\cos\theta)\right]^2 \boldsymbol{\phi\phi} \right) \end{aligned} \tag{A.21}$$

and an off-diagonal, symmetric contribution

$$\underline{T}_{nm}^\mathrm{off}(\mathbf{r},\mathbf{r},\omega) = \frac{n(n+1)}{(k_\mathrm{v}\rho)^2} h_n(k_\mathrm{v}\rho) P_n^m(\cos\theta) \frac{\mathrm{d}[\rho h_n(k_\mathrm{v}\rho)]}{\mathrm{d}\rho} \frac{\mathrm{d}P_n^m(\cos\theta)}{\mathrm{d}\theta} \left(\boldsymbol{\rho\theta} + \boldsymbol{\theta\rho}\right). \tag{A.22}$$

Here, $P_n^m(x)$ denotes the associated Legendre polynomial of first kind and order (n,m) and the $\boldsymbol{\rho}, \boldsymbol{\theta}, \boldsymbol{\phi}$ denote the unit vectors in spherical coordinates. Noting that the scattering coefficients do not depend on the index m, we can simplify the previous relations using [292, 366]

$$\partial_\lambda^k P_n(\xi) = \sum_{m=0}^{n} (2-\delta_{m0}) \frac{(n-m)!}{(n+m)!} m^k \cos\left(m\lambda + \frac{k\pi}{2}\right) P_n^m(x) P_n^m(y) \tag{A.23}$$

with $\xi = xy + \sqrt{(1-x^2)(1-y^2)}\cos\lambda$ such that we obtain

$$\sin\theta\sin\bar{\theta} P_n'(\cos\theta\cos\bar{\theta} + \sin\theta\sin\bar{\theta}) = \sum_{m=0}^{n} (2-\delta_{m0}) \frac{(n-m)!}{(n+m)!}\, m^2 P_n^m(\cos\theta) P_n^m(\cos\bar{\theta}). \tag{A.24}$$

Further, we note that $P_n(1) = 1$, $P_n'(1) = n(n+1)/2$ and for $\xi = \xi(x,y,\lambda)$ with $x = \cos\theta$ and $y = \cos\bar{\theta}$, we have that

$$\lim_{\lambda\to 0} \partial_\theta P_n(\xi) = -\sin[\theta-\bar{\theta}] P_n'(\cos[\theta-\bar{\theta}])), \tag{A.25a}$$

$$\lim_{\lambda\to 0} \partial_\theta \partial_{\bar{\theta}} P_n(\xi) = \cos[\theta-\bar{\theta}] P_n'(\cos[\theta-\bar{\theta}]) - \sin^2[\theta-\bar{\theta}] P_n''(\cos[\theta-\bar{\theta}]). \tag{A.25b}$$

Combining Eqs. (A.18) - (A.25), the scattered part of the Green tensor reads

$$\underline{g}(\mathbf{r},\mathbf{r},\omega) = \frac{\omega}{32\pi^2\epsilon_0 c}\frac{1}{\rho^2}\sum_{n=1}^{\infty}(2n+1) \tag{A.26}$$
$$\times\left\{2n(n+1)\left[h_n(k_\mathrm{v}\rho)\right]^2 r_n^p\ \hat{\boldsymbol{\rho}}\hat{\boldsymbol{\rho}} + \left[\left(\frac{\mathrm{d}[\rho h_n(k_\mathrm{v}\rho)]}{\mathrm{d}\rho}\right)^2 r_n^p + \frac{\omega^2\rho^2}{c^2}\left[h_n(k_\mathrm{v}\rho)\right]^2 r_n^s\right]\left[\hat{\boldsymbol{\theta}}\hat{\boldsymbol{\theta}} + \hat{\boldsymbol{\phi}}\hat{\boldsymbol{\phi}}\right]\right\}.$$

Interestingly, due to symmetry reasons, the off-diagonal elements vanish identically and the scattered Green tensor evaluated outside of the sphere does not depend on the angular components of the coordinate system as $\underline{g}(\mathbf{r},\mathbf{r},\omega) = \underline{g}(\rho,\omega)$.

A.3 Cylindrical geometry

Lastly, we report the scattered part of the electric Green tensor valid inside a cylindrical cavity. We choose a cylindrical basis $(\boldsymbol{\varrho}, \boldsymbol{\varphi}, \mathbf{z})$ with $\boldsymbol{\varrho}$, $\boldsymbol{\varphi}$ and $\mathbf{z}$ the unit vectors along the diameter $0 \leq \varrho < R$, angular $0 \leq \varphi < 2\pi$ and coaxial $-\infty < z < \infty$ directions of the cylinder, respectively. Fortunately, the calculation of the Green tensor for layered cylindrical cavities consisting of a local material was already carried out by Lie *et al.* [535]. Following Ref. [535], the *scattered* Green tensor of a field source inside the cavity with a recipient also lying withing the cavity is given by (the inside of the cavity is supposed to be vacuum)

$$\underline{g}(\mathbf{r},\mathbf{r}',\omega) = \frac{\mathrm{i}}{4\pi}\frac{\omega^2}{\epsilon_0 c^2}\sum_{n=0}^{\infty\prime}\int\frac{\mathrm{d}h}{\kappa^2}\Big[r^n_{MM'}\mathbf{M}_{\binom{e}{o}n,\kappa}(h)\mathbf{M}'_{\binom{e}{o}n,\kappa}(-h) + r^n_{NN'}\mathbf{N}_{\binom{e}{o}n,\kappa}(h)\mathbf{N}'_{\binom{e}{o}n,\kappa}(-h) \\ \pm r^n_{NM'}\mathbf{N}_{\binom{o}{e}n,\kappa}(h)\mathbf{M}'_{\binom{e}{o}n,\kappa}(-h) \pm r^n_{MN'}\mathbf{M}_{\binom{o}{e}n,\kappa}(h)\mathbf{N}'_{\binom{e}{o}n,\kappa}(-h)\Big], \tag{A.27}$$

where the prime connected to the vector functions $\mathbf{M}'_{\binom{e}{o}n,\kappa}$ and $\mathbf{N}'_{\binom{e}{o}n,\kappa}$ indicates that the general expression is valid for two distinct positions $\mathbf{r}$ and $\mathbf{r}'$, the other prime connected to the summation symbol $\sum_{n=0}^{\prime\infty}$ indicates that the term $n = 0$ counts with an extra prefactor of $1/2$, $\kappa = \sqrt{\frac{\omega^2}{c^2} - h^2}$ ($\mathrm{Im}\kappa > 0$) with h the wavevector parallel to the central axis of the cavity, R the diameter of the cavity, the coefficients $r^n_{AB'} = r^n_{AB'}(h,\omega,R)$ with $A, B \in \{M, N\}$ are the Mie scattering coefficients inside of an infinitely extended cylinder and for symmetry reasons we have that $\pm r^n_{NM'} = \pm r^n_{MN'}$ [536]. We note that, following the notation of Lie *et al.* [535], κ carries an extra factor i with respect to the notation of Ref. [189] for a planar geometry (see Sec. A.1). For the wave vector functions, we use a particular notation for odd and even functions which is to be understood as a component-wise addition, i.e. $\pm\mathbf{A}_{\binom{k}{l}}\mathbf{B}_{\binom{m}{n}} = \mathbf{A}_k\mathbf{B}_m - \mathbf{A}_l\mathbf{B}_n$ for the even (e) and odd (o) components of the two vector functions $\mathbf{A}_{\binom{e}{o}}$ and $\mathbf{B}_{\binom{e}{o}}$. The cylindrical wavevector functions are given by [357]

$$\mathbf{M}_{\binom{e}{o}n,\kappa}(h) = \nabla\times\left[J_n(\kappa\varrho)\begin{pmatrix}\cos\\ \sin\end{pmatrix}(n\varphi)e^{\mathrm{i}hz}\mathbf{z}\right], \\ \mathbf{N}_{\binom{e}{o}n,\kappa}(h) = \frac{c^2}{\omega^2}\nabla\times\nabla\times\left[J_n(\kappa\varrho)\begin{pmatrix}\cos\\ \sin\end{pmatrix}(n\varphi)e^{\mathrm{i}hz}\mathbf{z}\right], \tag{A.28}$$

where J_n is the cylindrical Bessel function of first type [538]. The curl is to be performed in cylindrical coordinates. Using

$$\nabla\times\mathbf{A} = \left(\frac{1}{\varrho}\partial_\varphi A_z - \partial_z A_\varphi\right)\boldsymbol{\varrho} + \left(\partial_z A_\varrho - \partial_\varrho A_z\right)\boldsymbol{\varphi} + \frac{1}{\varrho}\left(\partial_\varrho(\varrho A_\varphi) - \partial_\varphi A_\varrho\right)\mathbf{z}, \tag{A.29}$$

we obtain [357]

$$\begin{aligned}
\mathbf{M}_{\binom{e}{o}n,\kappa}(h) &= \nabla \times \left[J_n(\kappa\varrho) \begin{pmatrix} \cos \\ \sin \end{pmatrix} (n\varphi) e^{\mathrm{i}hz} \mathbf{z} \right] \\
&= \mp \frac{n}{\varrho} J_n(\kappa\varrho) \begin{pmatrix} \sin \\ \cos \end{pmatrix} (n\varphi) e^{\mathrm{i}hz} \boldsymbol{\varrho} - \kappa J_n'(\kappa\varrho) \begin{pmatrix} \cos \\ \sin \end{pmatrix} (n\varphi) e^{\mathrm{i}hz} \boldsymbol{\varphi}, \\
\mathbf{N}_{\binom{e}{o}n,\kappa}(h) &= \frac{c}{\omega} \nabla \times \nabla \times \left[J_n(\kappa\varrho) \begin{pmatrix} \cos \\ \sin \end{pmatrix} (n\varphi) e^{\mathrm{i}hz} \mathbf{z} \right] \\
&= \frac{c}{\omega} e^{\mathrm{i}hz} \\
&\times \left(\mathrm{i}h\kappa J_n'(\kappa\varrho) \begin{pmatrix} \cos \\ \sin \end{pmatrix} (n\varphi) \boldsymbol{\varrho} \mp \frac{\mathrm{i}hn}{\varrho} J_n(\kappa\varrho) \begin{pmatrix} \sin \\ \cos \end{pmatrix} (n\varphi) \boldsymbol{\varphi} + \kappa^2 J_n(\kappa\varrho) \begin{pmatrix} \cos \\ \sin \end{pmatrix} (n\varphi) \mathbf{z} \right).
\end{aligned} \tag{A.30}$$

Evaluating source and recipient of the field at the same point $\mathbf{r}' \to \mathbf{r}$ and noting that

$$\underline{g}(\mathbf{r}, \mathbf{r}, \omega) = \int \frac{\mathrm{d}h}{2\pi} \, \underline{g}(h, \mathbf{R}, \omega) \tag{A.31}$$

with $\mathbf{R}$ the position in the $\varrho\varphi$-plane, we explicitly obtain

$$\begin{aligned}
\underline{g}(h, \mathbf{R}, \omega) &= \frac{\mathrm{i}}{2} \frac{\omega^2}{c^2 \epsilon_0} \sum_{n=0}^{\infty}{}' \frac{1}{\kappa^2} \\
&\times \left\{ r_{MM}^n \begin{bmatrix} \frac{n^2}{\varrho^2} [J_n(\kappa\varrho)]^2 & 0 & 0 \\ 0 & \kappa^2 [J_n'(\kappa\varrho)]^2 & 0 \\ 0 & 0 & 0 \end{bmatrix} \right. \\
&+ r_{NN}^n \begin{bmatrix} \frac{c^2}{\omega^2} h^2 \kappa^2 [J_n'(\kappa\varrho)]^2 & 0 & \mathrm{i}h\kappa^3 \frac{c^2}{\omega^2} J_n(\kappa\varrho) J_n'(\kappa\varrho) \\ 0 & \frac{c^2}{\omega^2} \frac{h^2 n^2}{\varrho^2} [J_n(\kappa\varrho)]^2 & 0 \\ -\mathrm{i}h\kappa^3 \frac{c^2}{\omega^2} J_n(\kappa\varrho) J_n'(\kappa\varrho) & 0 & \frac{c^2}{\omega^2} \kappa^4 [J_n(\kappa\varrho)]^2 \end{bmatrix} \\
&\left. + r_{MN}^n \begin{bmatrix} -2\mathrm{i}h \frac{c}{\omega} \frac{n}{\varrho} \kappa J_n(\kappa\varrho) J_n'(\kappa\varrho) & 0 & \frac{n}{\varrho} \frac{c}{\omega} \kappa^2 [J_n(\kappa\varrho)]^2 \\ 0 & -2\mathrm{i}h \frac{c}{\omega} \frac{n}{\varrho} \kappa J_n(\kappa\varrho) J_n'(\kappa\varrho) & 0 \\ -\frac{n}{\varrho} \frac{c}{\omega} \kappa^2 [J_n(\kappa\varrho)]^2 & 0 & 0 \end{bmatrix} \right\},
\end{aligned} \tag{A.32, A.33}$$

where we have adapted the cylindrical basis for the matrices and the prime in connection to the Hankel and Bessel functions denotes a derivative with respect to a function's argument. It can be seen that, in the center of the cavity, the Green tensor is diagonal in cylindrical coordinates.

The scattering coefficients are given by

$$r_\alpha^n = -\frac{H_n^{(1)}[x]}{J_n[x]}\frac{A+B_\alpha}{A+B_D}, \tag{A.34a}$$

$$A = -n^2\frac{R^4\omega^2h^2}{c^2}(\varepsilon-1)^2, \tag{A.34b}$$

$$B_{\mathrm{D}} = x_1^2x^2\left(\varepsilon\tilde{h}_n^2[x_1]x^2 - (\varepsilon+1)\tilde{h}_n[x_1]\tilde{j}_n[x]x_1x + \tilde{j}_n^2[x]x_1^2\right), \tag{A.34c}$$

$$B_{\mathrm{MM}} = x_1^2x^2\left(\varepsilon\tilde{h}_n^2[x_1]x^2 - \left(\tilde{h}_n[x_1]\tilde{j}_n[x] + \varepsilon\tilde{h}_n[x_1]\tilde{h}_n[x]\right)x_1x + \tilde{h}_n[x]\tilde{j}_n[x]x_1^2\right), \tag{A.34d}$$

$$B_{\mathrm{NN}} = x_1^2x^2\left(\varepsilon\tilde{h}_n^2[x_1]x^2 - \left(\varepsilon\tilde{h}_n[x_1]\tilde{j}_n[x] + \tilde{h}_n[x_1]\tilde{h}_n[x]\right)x_1x + \tilde{h}_n[x]\tilde{j}_n[x]x_1^2\right), \tag{A.34e}$$

$$B_{\mathrm{MN}} = -A + \mathrm{i}nx_1^2x(R\omega/c)(hR)(1-\epsilon)\left(\tilde{h}_n[x] - \tilde{j}_n[x]\right), \tag{A.34f}$$

where $\alpha \in (MM, NN, MN)$ and we introduced the short-hand notation

$$x = \kappa R = R\sqrt{\omega^2/c^2 - h^2}, \qquad x_1 = \eta R = R\sqrt{\varepsilon(\omega)\omega^2/c^2 - h^2}, \tag{A.35a}$$

$$\tilde{h}_n[x] = \frac{H_n^{\prime(1)}[x]}{H_n^{(1)}[x]} = \frac{d}{dx}\ln H_n^{(1)}[x], \qquad \tilde{j}_n[x] = \frac{J_n'[x]}{J_n[x]} = \frac{d}{dx}\ln J_n[x]. \tag{A.35b}$$

Here, $H_n^{(1)}(x)$ is the cylindrical Hankel function of first kind. We further note that r_{MM}^n and r_{NN} are even in h and r_{MN}^n is odd in h.

Coaxial position and small cylinder radius

Aiming to study the non-additivity of quantum friction (see Sec. 3.4.3), it is sufficient to consider the position at the center of the cavity, $\varrho = 0$, and focus on a small cylinder radius where the force becomes the strongest, retardation is neglected and the above relations can be reduced to their evanescent (near-field) counterpart (formally $c \to \infty$). To this end, we use that at $\varrho \to 0$, we have that [536]

$$\frac{n^2}{\kappa^2\varrho^2}[J_n(\kappa\varrho)]^2 \overset{n=1}{\to} \frac{1}{4}, \quad [J_n'(\kappa\varrho)]^2 \overset{n=1}{\to} \frac{1}{4}, \quad [J_n(\kappa\varrho)]^2 \overset{n=0}{\to} 1, \quad \frac{n}{\kappa\varrho}J_n(\kappa\varrho)J_n'(\kappa\varrho) \overset{n=1}{\to} \frac{1}{4} \tag{A.36}$$

and zero if n takes any other value as well as $J_n(\kappa\varrho)J_n'(\kappa\varrho)$, $\frac{n}{\varrho}[J_n(\kappa\varrho)]^2 \to 0$ for all n. This means we only need to consider the terms $n = 0, 1$ and the Green tensor becomes diagonal, as expected due to symmetry. Using that $\kappa \sim \mathrm{i}h$ with $h > 0$, the Green tensor can be written as

$$\underline{g}(h, \varrho \to 0, \omega) \sim \frac{\mathrm{i}}{8\epsilon_0}h^2\left(r_{NN,\mathrm{NF}}^{n=1}\left[\boldsymbol{\varrho}\boldsymbol{\varrho} + \boldsymbol{\varphi}\boldsymbol{\varphi}\right] - 2r_{NN,\mathrm{NF}}^{n=0}\boldsymbol{z}\boldsymbol{z}\right), \tag{A.37}$$

where we obtain for the near-field expressions for the scattering coefficients

$$r_{NN,\mathrm{NF}}^n = (-1)^n\frac{2\mathrm{i}}{\pi}\frac{K_n(y)}{I_n(y)}\frac{\epsilon-1}{\epsilon+f_n(y)}, \qquad f_n(y) = -\frac{K_n(y)I_n'(y)}{I_n(y)K_n'(y)}. \tag{A.38a}$$

Here, we defined $y = hR$ and used the relations $J_n(\mathrm{i}y) = \mathrm{i}^n I_n(y)$ and $K_n(y) = \frac{\pi}{2}\mathrm{i}^{n+1} H_n^{(1)}(\mathrm{i}y)$ with $I_n(y)$ and $K_n(y)$ the modified Bessel function of first and second kind [538], respectively. We thereby restore the result of Ref. [537]. Using the Drude model for the materials permittivity, the relevant scattering coefficients are Ohmic for small frequencies, i.e.

$$\mathrm{i}r^n_{NN,\mathrm{NF}} = (-1)^{n+1}\frac{2}{\pi}\frac{K_n(y)}{I_n(y)} + (-1)^{n+1}2\mathrm{i}\epsilon_0 \underbrace{\frac{\rho_{\mathrm{lc}}}{\pi}\frac{K_n(y)[1+f_n(y)]}{I_n(y)}e^{2y}}_{\equiv\rho_n(y)} e^{-2y}\omega + \mathcal{O}(\omega^2). \tag{A.39}$$

Combining the previous relations, the imaginary part of the scattered Green tensor at small frequencies behaves as

$$\mathrm{Im}\lim_{\omega\to 0}\partial_\omega \underline{g}(h, \varrho \to 0, \omega) \sim \frac{h^2}{4}\left(\rho_1(hR)\left[\boldsymbol{\varrho}\boldsymbol{\varrho} + \boldsymbol{\varphi}\boldsymbol{\varphi}\right] + 2\rho_0(hR)\boldsymbol{z}\boldsymbol{z}\right)e^{-2hR}. \tag{A.40}$$

Finally, due to the high symmetry of the system, we have that the basis vectors are equivalent in the cylindrical as well as the Cartesian coordinate system, i.e. $\boldsymbol{\varrho}\boldsymbol{\varrho} + \boldsymbol{\varphi}\boldsymbol{\varphi} = \boldsymbol{x}\boldsymbol{x} + \boldsymbol{y}\boldsymbol{y}$, where the xy-plane is perpendicular to the cylinder axis. This gives the expression reported in Eq. (3.119).

APPENDIX B

Low-frequency Behavior of the Power Spectrum of the Electric Field

In this appendix we provide the background information and calculations supporting the results and discussions provided in Chap. 1. We derive the low-frequency behavior of the electric field flcutuations [Eq. (1.17)] in both equilibrium [Eqs. (1.20), (1.21) and (1.24), (1.52)] and mechanical nonequilibrium [Eqs. (1.23),(1.56), (1.57) and (1.59)].

In planar geometries, the material-modified quantum noise of the electric field obeys the fluctuation-dissipatoin relation of Eq. (1.23). We define the corresponding power spectrum:

$$2\pi\delta(\omega+\omega')\underline{\nu}(\omega,v) \equiv \lim_{\mathbf{r}'\to\mathbf{r}} \left\langle \hat{\mathbf{E}}_{\mathrm{N}}(\mathbf{r},\omega)\hat{\mathbf{E}}_{\mathrm{N}}(\mathbf{r},\omega') \right\rangle, \tag{B.1}$$

where we incorporated a possible nonequilibrium situation due to the velocity v. Upon performing a Fourier transform in the wavevector, we obtain for the electric field's power spectrum using the approach outlined in Chap. 3

$$\underline{\nu}(\omega,v) = 2\hbar \int \frac{\mathrm{d}^2\mathbf{p}}{(2\pi)^2} \left[n(\omega^+_{\mathbf{p}},T)+1 \right] \underline{G}_{\Im}(\mathbf{p},z,\omega^+_{\mathbf{p}}) \tag{B.2}$$

which is valid in mechanical nonequilibrium at temperature T and we defined $\omega^+_{\mathbf{p}} = \omega + p_x v$.

Vacuum

The vacuum Green tenor reads [Eq. (A.3)]

$$\underline{G}_0(\mathbf{r}-\mathbf{r}',\omega) = -\left[1+\frac{c^2}{\omega^2}\nabla\nabla\right]\left(-\frac{c^2 e^{\mathrm{i}\omega|\mathbf{r}-\mathbf{r}'|/c}}{4\pi\omega^2|\mathbf{r}-\mathbf{r}'|}\right)$$

whose imaginary part is given by $\lim_{\mathbf{r}'\to\mathbf{r}} \underline{G}_{\Im}(\mathbf{r}-\mathbf{r}',\omega) = \frac{\omega^3}{6\pi\epsilon_0 c^3}\mathbb{1}$, where $\mathbb{1}$ is the three-dimensional unity matrix. In Fourier space, on the other hand, we obtain [189, 355, 606]

$$\underline{G}_{\Im}(\mathbf{p},z,\omega) = \frac{\theta\left(\frac{\omega^2}{c^2}-p^2\right)}{2\epsilon_0\sqrt{\frac{\omega^2}{c^2}-p^2}} \left(\mathbb{1}\frac{\omega^2}{c^2} - \mathrm{diag}\left[p_x^2, p_y^2, \frac{\omega^2}{c^2}-p^2\right]\right). \tag{B.3}$$

We are interested in the trace of $\underline{\nu} \equiv \nu_{ii}$ so that we obtain

$$\nu_{ii}(\omega, v) = 2\frac{\hbar}{\epsilon_0} \int \frac{\mathrm{d}^2\mathbf{p}}{(2\pi)^2} \left[n(\omega_{\mathbf{p}}^+, T) + 1\right] \frac{\theta\left(\frac{(\omega_{\mathbf{p}}^+)^2}{c^2} - p^2\right)}{\sqrt{\frac{(\omega_{\mathbf{p}}^+)^2}{c^2} - p^2}} \frac{(\omega_{\mathbf{p}}^+)^2}{c^2}. \tag{B.4}$$

The Heaviside θ-function prescribes

$$(\omega_{\mathbf{p}}^+)^2 - p_x^2 \geq p_y^2. \tag{B.5}$$

Since the integral is symmetric in p_y, we can write

$$\nu_{ii}(\omega, v) = 2\frac{\hbar}{\epsilon_0} \int \frac{\mathrm{d}p_x}{2\pi} \left[n(\omega_{\mathbf{p}}^+, T) + 1\right] \frac{(\omega_{\mathbf{p}}^+)^2}{c^2} \theta\left(\frac{(\omega_{\mathbf{p}}^+)^2}{c^2} - p_x^2\right) \int_0^y \frac{\mathrm{d}p_y}{\pi} \frac{1}{\sqrt{y^2 - p_y^2}} \tag{B.6}$$

with $y = \sqrt{(\omega_{\mathbf{p}}^+)^2 - p_x^2}$. Using that $\int_0^y \mathrm{d}x \ \sqrt{y^2 - x^2}^{-1} = \pi/2$, we obtain

$$\nu_{ii}(\omega, v) = \frac{\hbar}{\epsilon_0} \int \frac{\mathrm{d}p_x}{2\pi} \left[n(\omega_{\mathbf{p}}^+, T) + 1\right] \frac{(\omega_{\mathbf{p}}^+)^2}{c^2} \theta\left(\frac{(\omega_{\mathbf{p}}^+)^2}{c^2} - p_x^2\right). \tag{B.7}$$

The integral boundaries need to obey the relation

$$\frac{(\omega + p_x v)^2}{c^2} \geq p_x^2 \Leftrightarrow \begin{cases} \frac{\omega}{c-v} \leq p_x \leq -\frac{\omega}{c+v}, & \omega < 0 \\ -\frac{\omega}{c+v} \leq p_x \leq \frac{\omega}{c-v}, & \omega > 0 \end{cases}. \tag{B.8}$$

This yields for the field's power spectrum

$$\nu_{ii}(\omega, v) = \frac{\hbar}{\epsilon_0 c^2} \int_{-\frac{|\omega|}{c+\mathrm{sgn}[\omega]v}}^{\frac{|\omega|}{c-\mathrm{sgn}[\omega]v}} \frac{\mathrm{d}p_x}{2\pi} \left[n(\omega_{\mathbf{p}}^+, T) + 1\right] (\omega + p_x v)^2. \tag{B.9}$$

Zero velocity.–

In equilibrium at temperature T we have that

$$\int_{-\frac{|\omega|}{c}}^{\frac{|\omega|}{c}} \frac{\mathrm{d}p_x}{2\pi} = \frac{|\omega|}{\pi c} \tag{B.10}$$

and obtain for the equilibrium vacuum fluctuations

$$\nu_{ii}(\omega, 0) = \frac{\hbar}{\epsilon_0 c^3} \frac{\omega^3}{\pi} \left[n(\omega, T) + 1\right] = \frac{\hbar}{\pi} \left[n(\omega, T) + 1\right] \frac{\omega^3}{\epsilon_0 c^3}, \qquad \omega > 0. \tag{B.11}$$

For negative frequencies we obtain an extra sign function. With respect to zero or finite

temperature, we obtain the following limits for small frequencies

$$\nu_{ii}(\omega,0) = \operatorname{sgn}[\omega]\frac{\hbar}{\pi}\left[n(\omega,T)+1\right]\frac{\omega^3}{\epsilon_0 c^3} \tag{B.12}$$
$$\sim \frac{\operatorname{sgn}[\omega]}{\pi}\begin{cases}\theta(\omega)\frac{\hbar\omega^3}{\epsilon_0 c^3}, & \hbar\omega \gg k_\mathrm{B}T\\ \frac{k_\mathrm{B}T\omega^2}{\epsilon_0 c^3}+\frac{1}{2}\frac{\omega^3}{\epsilon_0 c^3}, & \hbar\omega \ll k_\mathrm{B}T\end{cases}.$$

Finite velocity.–
Starting with

$$\nu_{ii}(\omega,v) = \frac{\hbar}{\epsilon_0 c^2}\int_{-\frac{|\omega|}{c+\operatorname{sgn}[\omega]v}}^{\frac{|\omega|}{c-\operatorname{sgn}[\omega]v}}\frac{\mathrm{d}p_x}{2\pi}\left[n(\omega^+_{\mathbf{p}},T)+1\right](\omega+p_x v)^2 \tag{B.13}$$
$$= \operatorname{sgn}[\omega]\frac{\hbar}{\epsilon_0 c^2}\int_{-\frac{\omega}{c+v}}^{\frac{\omega}{c-v}}\frac{\mathrm{d}p_x}{2\pi}\left[n(\omega^+_{\mathbf{p}},T)+1\right](\omega+p_x v)^2,$$

we substitute

$$x = \omega + p_x v \leftrightarrow p_x = \frac{x-\omega}{v} \leftrightarrow \mathrm{d}p_x = \frac{\mathrm{d}x}{v}, \qquad x \in \left[\frac{c\omega}{c+v},\frac{c\omega}{c-v}\right]. \tag{B.14}$$

This gives

$$\nu_{ii}(\omega,v) = \operatorname{sgn}[\omega]\frac{\hbar}{\epsilon_0 c^2 v}\int_{\frac{c\omega}{c+v}}^{\frac{c\omega}{c-v}}\frac{\mathrm{d}x}{2\pi}\left[n(x,T)+1\right]x^2 \tag{B.15}$$
$$\sim \operatorname{sgn}[\omega]\frac{\hbar}{\pi\epsilon_0 c^3}$$
$$\times\left(\omega^3\left[n(\omega,T)+1\right]+\frac{1}{3}\left[10\omega^3\left[n(\omega,T)+1\right]+5\omega^4 n'(\omega,T)+\frac{1}{2}\omega^5 n''(\omega,T)\right]\frac{v^2}{c^2}\right),$$

where the prime denotes a derivative with respect to frequency and we used that $v \ll c$. The previous result reduces to

$$\nu_{ii}(\omega,0) \to \operatorname{sgn}[\omega]\frac{\hbar\omega^3}{\pi\epsilon_0 c^3}\left[n(\omega,T)+1\right] \tag{B.16}$$

which is consistent with the zero velocity result. For zero temperature, on the other hand, we utilize the relation by Estrada *et al.* [185, 186]: Using that $2n(\omega,T) = \operatorname{sgn}(\omega)\coth[\hbar\omega/(2k_\mathrm{B}T)]-1$ and regarding the expression $\coth\left[\hbar\omega/(2k_\mathrm{B}T)\right]$ as a distribution, we have for $\tau\to\infty$ that

$$\coth\left[\tau\omega\right] \sim \operatorname{sgn}[\omega] - \frac{\pi^2}{6}\frac{\delta^{(1)}(\omega)}{\tau^2} - \frac{\pi^4}{360}\frac{\delta^{(3)}(\omega)}{\tau^4}, \tag{B.17}$$

which gives for the Bose distribution

$$n(\omega,T)+1=\frac{1}{2}\mathrm{sgn}(\omega)\coth\left[\frac{\hbar\omega}{2k_\mathrm{B}T}\right]+\frac{1}{2}\sim\frac{1}{2}\mathrm{sgn}(\omega)+\frac{1}{2}=\theta(\omega). \tag{B.18}$$

Hence, at zero temperature

$$\nu_{ii}(\omega,v,0)\sim\theta(\omega)\frac{\hbar\omega^3}{\pi\epsilon_0c^3}\left(1+\frac{10}{3}\frac{v^2}{c^2}\right). \tag{B.19}$$

For small frequencies, however, we are always automatically in the large temperature regime ($\hbar\omega\ll k_\mathrm{B}T$), where we have that

$$n(\omega,T)\sim\frac{k_\mathrm{B}T}{\hbar\omega}-\frac{1}{2}. \tag{B.20}$$

Hence, in the small frequency regime it is the classical nature of fluctuations that dominates. We obtain

$$\nu_{ii}(0,v)\sim\mathrm{sgn}[\omega]\frac{k_\mathrm{B}T}{\pi\epsilon_0c^3}\left(1+2\frac{v^2}{c^2}\right)\omega^2+\frac{1}{2}\mathrm{sgn}[\omega]\frac{\hbar\omega^3}{\pi\epsilon_0c^3}\left(1+\frac{10}{3}\frac{v^2}{c^2}\right). \tag{B.21}$$

Finite temperatures lead to a different frequency scaling $\omega^3\to\omega^2$. Hence, the higher the temperature or the higher the degree of nonequilibrium, the more fluctuations we have. This is in accordance with the fluctuation-dissipation inequality [422]. We note, however, that the velocity corrections for the motion in vacuum are physically a mere artifact of our non-relativistic treatment (see main text).

Finite velocity and LTE.–
Applying the equilibrium fluctuation-dissipation relation in the spirit of the local thermal equilibrium approximation (LTE) amounts to replacing

$$\underline{\nu}(\omega,v)=2\hbar\int\frac{\mathrm{d}^2\mathbf{p}}{(2\pi)^2}\left[n(\omega^+_\mathbf{p},T)+1\right]\underline{G}_\Im(\mathbf{p},z,\omega^+_\mathbf{p})\to2\hbar\left[n(\omega,T)+1\right]\int\frac{\mathrm{d}^2\mathbf{p}}{(2\pi)^2}\underline{G}_\Im(\mathbf{p},z,\omega^+_\mathbf{p}). \tag{B.22}$$

This gives for the planar geometry

$$\begin{aligned}\nu^\mathrm{LTE}_{ii}(\omega,v)&=\mathrm{sgn}(\omega)\left[n(\omega,T)+1\right]\frac{\hbar}{\epsilon_0c^2v}\int_{\frac{c\omega}{c+v}}^{\frac{c\omega}{c-v}}\frac{\mathrm{d}x}{2\pi}x^2\\&=\mathrm{sgn}(\omega)\left[n(\omega,T)+1\right]\frac{\hbar}{\pi\epsilon_0c^3}\frac{\omega^3}{3}\frac{3+\frac{v^2}{c^2}}{\left(1+\frac{v^2}{c^2}\right)^3}\\&\sim\mathrm{sgn}(\omega)\left[n(\omega,T)+1\right]\frac{\hbar\omega^3}{\pi\epsilon_0c^3}\left(1+\frac{10}{3}\frac{v^2}{c^2}\right).\end{aligned} \tag{B.23}$$

Material-modified vacuum

Starting from

$$\underline{\nu}(\omega, v) = 2\hbar \int \frac{\mathrm{d}^2\mathbf{p}}{(2\pi)^2} \left[n(\omega_{\mathbf{p}}^+, T) + 1 \right] \underline{G}_{\Im}(\mathbf{p}, z, \omega_{\mathbf{p}}^+), \tag{B.24}$$

we insert the Green tensor of the infinite half space

$$\underline{g}(\mathbf{p}, z, \omega) = \frac{\kappa}{2\epsilon_0} \left(r^p(\omega, p) \tilde{\mathbf{P}}_+ \tilde{\mathbf{P}}_- + \frac{\omega^2}{\kappa^2 c^2} r^s(\omega, p) \tilde{\mathbf{S}} \tilde{\mathbf{S}} \right) e^{-2\kappa z}. \tag{B.25}$$

Upon tracing over spatial coordinates and focusing on small frequencies, we obtain

$$\nu_{ii}(\omega, v) \sim \frac{2\hbar}{\epsilon_0} \int \frac{\mathrm{d}^2\mathbf{p}}{(2\pi)^2} \left[n(\omega_{\mathbf{p}}^+, T) + 1 \right] p \; e^{-2pz} r_I^p(\omega + p_x v), \tag{B.26}$$

where we assumed that the imaginary part of the reflection coefficient is Ohmic, i.e. $r_I^p \sim 2\epsilon_0 \rho(p)\omega$. From now on, we focus on the $T = 0$ case. Consequently, the problem reduces to

$$\nu_{ii}(\omega, v) \sim \frac{2\hbar}{\pi^2} \int \mathrm{d}p_x \int_0^\infty \mathrm{d}p_y \; \theta(\omega + p_x v) p \; \rho(p) e^{-2pz} (\omega + p_x v). \tag{B.27}$$

The θ-function prescribes that

$$\omega + p_x v \geq 0 \Leftrightarrow p_x \geq -\frac{\omega}{v} \tag{B.28}$$

such that we obtain

$$\nu_{ii}(\omega, v, 0) \sim \frac{2\hbar}{\pi^2} \frac{\omega}{z^3} \int_{-\frac{\omega}{v} z}^\infty \mathrm{d}x \int_0^\infty \mathrm{d}y \; \sqrt{x^2 + y^2} \; \rho \left(\frac{\sqrt{x^2 + y^2}}{z} \right) e^{-2\sqrt{x^2+y^2}} \left(1 + x \frac{v}{z} \frac{1}{\omega} \right), \tag{B.29}$$

where we set $x = p_x z$ and $y = p_y z$. At exactly zero velocity, the integral boundaries approach infinity and the integral can be solved exactly, i.e.

$$\begin{aligned} \nu_{ii}(\omega, 0) &\sim \frac{2\hbar}{\pi^2} \frac{\omega}{z^3} \int_{-\infty}^\infty \mathrm{d}x \int_0^\infty \mathrm{d}y \; \sqrt{x^2 + y^2} \; \rho \left(\frac{\sqrt{x^2 + y^2}}{z} \right) e^{-2\sqrt{x^2+y^2}} \\ &\to \frac{2\hbar\rho}{\pi^2} \frac{\omega}{z^3} \frac{\pi}{4}, \end{aligned} \tag{B.30}$$

where we assumed local materials in the last line. The fluctuations scale linearly in frequency.

For finite velocities, on the other hand, there will always be a regime where $\omega \ll \frac{v}{z}$. We eventually obtain

$$\nu_{ii}(\omega \to 0, v, 0) \sim \frac{2\hbar}{\pi^2}\frac{\omega}{z^3}\int_0^\infty \mathrm{d}x \int_0^\infty \mathrm{d}y\ \sqrt{x^2+y^2}\ \rho\left(\frac{\sqrt{x^2+y^2}}{z}\right) e^{-2\sqrt{x^2+y^2}}\left(1+x\frac{v}{z}\frac{1}{\omega}\right) \tag{B.31}$$
$$\to \frac{2\hbar\rho}{\pi^2}\frac{\omega}{z^3}\frac{\pi}{4}\left(\frac{1}{2}+\frac{3}{2\pi}\frac{v}{z}\frac{1}{\omega}\right),$$

where we again employed the local approximation in the last lines. For comparison, the LTE calculation gives

$$\nu_{ii}(\omega, v) = \frac{2\hbar}{\pi^2}\theta(\omega)\frac{\omega}{z^3}\int \mathrm{d}x \int_0^\infty \mathrm{d}y\ \sqrt{x^2+y^2}\ \rho\left(\frac{\sqrt{x^2+y^2}}{z}\right) e^{-2\sqrt{x^2+y^2}}\left(1+x\frac{v}{z}\frac{1}{\omega}\right) \tag{B.32}$$
$$\to \frac{2\hbar\rho}{\pi^2}\theta(\omega)\frac{\omega}{z^3}\frac{\pi}{4}$$

identically vanishing at zero frequency and thereby neglecting parts of the low-frequency fluctuations. Hence, we find that the LTE approximation underestimates the impact of low frequency fluctuations.

Non-Markovianity

We recall the general expression for the power spectrum of the electric field fluctuations

$$\underline{\nu}(\omega, v) = 2\hbar\int \frac{\mathrm{d}^2\mathbf{p}}{(2\pi)^2}\left[n(\omega_{\mathbf{p}}^+, T)+1\right]\underline{G}_{\Im}(\mathbf{p}, z, \omega_{\mathbf{p}}^+). \tag{B.33}$$

For simplicity, we are first interested in the equilibrium case with $v = 0$ and zero temperature,

$$\underline{\nu}(\omega, 0) = 2\hbar\int \frac{\mathrm{d}^2\mathbf{p}}{(2\pi)^2}\theta(\omega)\underline{G}_{\Im}(\mathbf{p}, z, \omega). \tag{B.34}$$

Further, we trace over the spatial degrees of freedom and consider the scattered Green tensor in the local limit only. Focusing on the near-field limit and following Ref. [58], the field fluctuations yield

$$\nu_{ii}(\tau, 0) = 2\hbar\mathrm{Tr}\int\frac{\mathrm{d}\omega}{2\pi}e^{-\mathrm{i}\omega\tau}\int\frac{\mathrm{d}^2\mathbf{p}}{(2\pi)^2}\theta(\omega)\underline{G}_I(\mathbf{p}, z, \omega) \tag{B.35}$$
$$= 2\hbar\lim_{\mathbf{r}'\to\mathbf{r}}\mathrm{Tr}\int_0^\infty\frac{\mathrm{d}\omega}{2\pi}e^{-\mathrm{i}\omega\tau}\frac{\underline{G}(\mathbf{r}, \mathbf{r}', \omega)-\underline{G}^*(\mathbf{r}, \mathbf{r}', \omega)}{2\mathrm{i}}$$
$$= \frac{\hbar}{\pi}\lim_{\mathbf{r}'\to\mathbf{r}}\left(-\pi\sum_\mu e^{-\mathrm{i}\Omega_\mu\tau}\mathrm{Res}\left[G_{ii}(\mathbf{r}, \mathbf{r}', \Omega_\mu)\right]+\mathrm{Tr}\int_0^\infty \mathrm{d}\xi\ e^{-\xi\tau}\underline{G}_I(\mathbf{r}, \mathbf{r}', -\mathrm{i}\xi)\right),$$

where $\Omega_\mu \in \mathbb{C}$ are the complex resonances of the fourth quadrant and we used that only certain poles can contribute to the residues since $G_{ii}(\mathbf{r},\mathbf{r}',\omega) = G_{ii}^*(\mathbf{r},\mathbf{r}',-\omega^*)$ fulfills the crossing relation. In the particular case of the infinite half space filled by a Drude metal, the previous relation reduces to

$$\nu_{ii}(\omega,0) \sim \frac{2\hbar}{\epsilon_0}\theta(\omega)\int \frac{\mathrm{d}^2\mathbf{p}}{(2\pi)^2}\; p\;\mathrm{Im}\left[\frac{\epsilon(\omega)-1}{\epsilon(\omega)+1}\right] e^{-2pz}. \tag{B.36}$$

The near-field limit ensures that there are no propagating modes and we have a simple set of resonances in the complex frequency plane without branch cuts. The previous relation is stationary in time and the corresponding time correlation function reads ($\tau = t - t_i > 0$)

$$\begin{aligned}\nu_{ii}(\tau,0) &\sim \int \frac{\mathrm{d}\omega}{2\pi}\; e^{-\mathrm{i}\omega\tau}\frac{2\hbar}{\epsilon_0}\theta(\omega)\int \frac{\mathrm{d}^2\mathbf{p}}{(2\pi)^2}\; p\;\mathrm{Im}\left[\frac{\epsilon(\omega)-1}{\epsilon(\omega)+1}\right] e^{-2pz} \\ &= \frac{\hbar}{\pi\epsilon_0}\frac{1}{8\pi z^3}\int_0^\infty \mathrm{d}\omega\;\mathrm{Im}\left[\frac{\epsilon(\omega)-1}{\epsilon(\omega)+1}\right] e^{-\mathrm{i}\omega\tau},\end{aligned} \tag{B.37}$$

where we have for the Drude model that

$$\mathrm{Im}\left[\frac{\epsilon(\omega)-1}{\epsilon(\omega)+1}\right] = \frac{\Gamma\omega\omega_{\mathrm{sp}}}{(\omega_{\mathrm{sp}}^2-\omega^2)^2+(\Gamma\omega)^2}. \tag{B.38}$$

The frequency integral can be solved by contour integration following Ref. [58]. For positive $\tau > 0$, we close the contour in mathematical negative orientation (responsible for extra minus sign for the residues) circling the fourth quadrant,

$$\nu_{ii}(\tau,0) \sim \frac{\hbar}{\pi\epsilon_0}\frac{1}{8\pi z^3}\left[-2\pi\mathrm{i}\sum_\mu \mathrm{Res}\left\{\frac{r^p(\Omega_\mu)-r^{p*}(\Omega_\mu)}{2\mathrm{i}}\right\} e^{-\mathrm{i}\Omega_\mu\tau} + \mathrm{i}\int_0^\infty \mathrm{d}\xi\; r_I^p(-\mathrm{i}\xi)e^{-\xi\tau}\right], \tag{B.39}$$

where the limit $\omega \to -\mathrm{i}\xi + 0^+$ is to be understood as approaching the negative imaginary axis from the right side of the complex frequency plane (positive real part). Since the susceptibility fulfills the crossing relation

$$r^*(-\omega^*) = r(\omega), \tag{B.40}$$

we note that the complex poles are symmetric with respect to the negative complex frequency axis. Choosing the poles on the positive axis only, the second term in the evaluation of the residues ($\propto r^{p*}(\Omega_\mu)$) cannot contribute and the field fluctuations reduce to

$$\nu_{ii}(\tau,0) \sim \frac{\hbar}{\pi\epsilon_0}\frac{1}{8\pi z^3}\left[-\pi\sum_\mu \mathrm{Res}\left\{r^p(\Omega_\mu)\right\} e^{-\mathrm{i}\Omega_\mu\tau} + \mathrm{i}\int_0^\infty \mathrm{d}\xi\; r_I^p(-\mathrm{i}\xi)e^{-\xi\tau}\right]. \tag{B.41}$$

Using that

$$r^p(\omega) = \frac{\omega_{\rm sp}^2}{\omega_{\rm sp}^2 - \omega^2 - {\rm i}\Gamma\omega} \to \infty \Leftrightarrow \omega \to \pm\sqrt{\omega_{\rm sp}^2 - \frac{\Gamma^2}{4}} - {\rm i}\frac{\Gamma}{2} \sim \pm\omega_{\rm sp} - {\rm i}\frac{\Gamma}{2}, \quad \Gamma \ll \omega_{\rm sp}, \tag{B.42}$$

we need to take one residue into account which is given by

$${\rm Res}\left\{r^p(\Omega_\mu)\right\} = -\frac{\omega_{\rm sp}^2}{2}\frac{1}{\sqrt{\omega_{\rm sp}^2 - \frac{\Gamma^2}{4}}} \sim -\frac{\omega_{\rm sp}}{2}, \qquad \Gamma \ll \omega_{\rm sp}. \tag{B.43}$$

This gives for the correlation tensor

$$\nu_{ii}(\tau,0) \sim \frac{\hbar}{\pi\epsilon_0}\frac{1}{8\pi z^3}\left[\frac{\pi}{2}\omega_{\rm sp}e^{-{\rm i}\omega_{\rm sp}\tau}e^{-\frac{\Gamma}{2}\tau} + {\rm i}\int_0^\infty {\rm d}\xi\ r_I^p(-{\rm i}\xi)e^{-\xi\tau}\right]. \tag{B.44}$$

The integral reads

$$\begin{aligned}
{\rm i}\int_0^\infty {\rm d}\xi\ r_I^p(-{\rm i}\xi)e^{-\xi\tau} &= -\frac{\rm i}{\tau^2}\int_0^\infty {\rm d}y\ \frac{{\rm i}\Gamma\omega_{\rm sp}^2 y}{\tau^{-4}(y^2+\tau^2\omega_{\rm sp}^2)^2 - \tau^{-2}\Gamma^2 y^2}e^{-y} \\
&\sim -\frac{\rm i}{\tau^2}\int_0^\infty {\rm d}y\ \frac{{\rm i}\Gamma\omega_{\rm sp}^2 y}{\tau^{-4}(\tau^2\omega_{\rm sp}^2)^2}e^{-y} \\
&= \frac{\Gamma}{\tau^2\omega_{\rm sp}^2},
\end{aligned} \tag{B.45}$$

where we considered the limit of large time delays $\tau^{-1} \ll \Gamma \ll \omega_{\rm sp}$. Hence, the correlation function reads for long times

$$\nu_{ii}(\tau,0) \sim \frac{\hbar}{\pi\epsilon_0}\frac{1}{8\pi z^3}\left[\frac{\pi}{2}\omega_{\rm sp}e^{-{\rm i}\omega_{\rm sp}\tau}e^{-\frac{\Gamma}{2}\tau} + \frac{\Gamma}{\tau^2\omega_{\rm sp}^2}\right]. \tag{B.46}$$

For delay times $\tau \gg \Gamma^{-1}$, we actually have a power law decrease of the correlations instead of an exponential decay. The exponential decay can be identified with quasi-Markovian behavior, the power law with the non-Markovian relation. For negative $\tau \to -\tau$, we need to replace $e^{-\frac{\Gamma}{2}\tau} \to e^{-\frac{\Gamma}{2}|\tau|}$. Upon performing a Fourier transform, we obtain for the power spectrum in the quasi-Markovian approximation

$$\begin{aligned}
\nu_{ii}^{\rm M}(\omega,0) &\sim \frac{\hbar}{\pi\epsilon_0}\frac{1}{8\pi z^3}\frac{\pi}{2}\omega_{\rm sp}\int {\rm d}\tau\ e^{{\rm i}\omega\tau}e^{-{\rm i}\omega_{\rm sp}\tau}e^{-\frac{\Gamma}{2}|\tau|} \\
&= \frac{\hbar}{\pi\epsilon_0}\frac{1}{8\pi z^3}\frac{\pi}{2}\omega_{\rm sp}\frac{\Gamma}{(\omega-\omega_{\rm sp})^2 + \left(\frac{\Gamma}{2}\right)^2}.
\end{aligned} \tag{B.47}$$

The long-time correlations connected to the power law behavior in time domain, on the other hand, read in frequency space

$$\begin{aligned}\nu_{ii}^{\mathrm{nM}}(\omega,0) &\sim \frac{\hbar}{\pi\epsilon_0}\frac{\mathrm{i}}{8\pi z^3}\int \mathrm{d}\tau\; e^{\mathrm{i}\omega\tau}\int_0^\infty \mathrm{d}\xi\; \frac{\mathrm{i}\Gamma\omega_{\mathrm{sp}}^2\xi}{(\xi^2+\omega_{\mathrm{sp}}^2)^2-\Gamma^2\xi^2}e^{-\xi|\tau|} \\ &= -\frac{\hbar}{\pi\epsilon_0}\frac{1}{8\pi z^3}\int_0^\infty \mathrm{d}\xi\; \frac{\Gamma\omega_{\mathrm{sp}}^2\xi}{(\xi^2+\omega_{\mathrm{sp}}^2)^2-\Gamma^2\xi^2}\frac{2\xi}{\omega^2+\xi^2} \\ &\sim -\frac{\hbar}{\epsilon_0}\frac{1}{16\pi z^3}\frac{\Gamma\omega_{\mathrm{sp}}}{(\omega+\omega_{\mathrm{sp}})^2},\end{aligned} \tag{B.48}$$

where we again took the limit of small dissipation $\Gamma \ll \omega_{\mathrm{sp}}$. The sum of the previous two equations reproduces the full correct result of Eqs. (B.36) and (1.61).

APPENDIX C

Auxiliary Calculations for Magnetic Casimir-Polder Interaction

We provide the background information and calculations supporting the results and discussions provided in Sec. 2.2 of Chap. 2. In particular, we compute Eqs. (2.48) and (2.49) and their connection to the formula obtained in Refs. [143, 398]. Further, we discuss the limiting behavior of the function $\varpi^T(\mathbf{r},\omega)$ in Eq. (2.46).

C.1 Limiting behavior of magnetic Casimir-Polder free energy

We provide the details of the derivation of Eqs. (2.48) and (2.49). We assume a constant collision-induced dissipation rate Γ in the following considerations. The free energy in terms of Matsubara frequencies reads [see Eqs. (2.10) and (2.46)]

$$\begin{aligned}\mathcal{F}_{\mathrm{B}} &= -k_{\mathrm{B}}T\sum_{n=0}^{\infty}{}' \operatorname{Tr}\left[\underline{\beta}^T(\mathrm{i}n\nu)\cdot\underline{G}_{\mathrm{B}}(\mathrm{i}n\nu,z_a)\right] \\ &\approx -k_{\mathrm{B}}T\sum_{n=0}^{\infty}{}' \left[\beta_{ii}^T(\mathrm{i}n\nu)+\beta_{zz}^T(\mathrm{i}n\nu)\right]\frac{\mu_0}{8\pi}\int_0^\infty \mathrm{d}p\; p^2 e^{-2pz_a} r^s(\mathrm{i}n\nu,p),\end{aligned} \tag{C.1}$$

where we sum over same indices, implicitly assume the near-field limit of the transverse electric reflection coefficient r^s, employed the magnetic counterpart of the Green tensor in Eq. (A.17) and focused on the near-field regime of a planar interface where $\omega/(cp)\ll 1$ with $p\sim 1/z_a$ and $\omega\sim\nu\sim T$. In order to proceed, we need to insert an expression for the transverse electric reflection coefficient.

Local Drude model

The near-field limit of the transverse electric reflection coefficient in the Drude model reads

$$r^s \sim \left[\epsilon_{\mathrm{Dr}}(\omega)-1\right]\frac{\omega^2}{4c^2p^2}. \tag{C.2}$$

The remaining integrals can be solved trivially and we obtain

$$\mathcal{F}_{\mathrm{B}} \sim k_{\mathrm{B}}T\frac{\mu_0}{8\pi}\frac{\omega_{\mathrm{p}}^2}{4c^2}\frac{1}{2z_a}\sum_{n=0}^{\infty}{}' \left[\beta_{ii}^T(\mathrm{i}n\nu)+\beta_{zz}^T(\mathrm{i}n\nu)\right]\frac{n\nu}{n\nu+\Gamma}. \tag{C.3}$$

Since $\beta(\mathrm{i}n\nu) \propto 1/(\omega_a^2 + n^2\nu^2)$, the sum converges and the free energy increases as the inverse separation. This is in contrast with the results of Refs. [143, 398]. They observe a logarithmic correction $\mathcal{F} \propto \frac{1}{\pi\delta_m^2 z_a} \ln[\delta_m/z_a]$ with $\delta_m = \lambda\!\!\!^{-}_{\mathrm{p}}\sqrt{2\Gamma/\omega_a}$, in the limit of zero temperatures. To this end, the authors of Refs. [143, 398] approximate the permittivity as $\epsilon_{\mathrm{Dr}} - 1 = -\frac{\omega_{\mathrm{p}}^2}{\omega(\omega+\mathrm{i}\Gamma)} \sim -\frac{\omega_{\mathrm{p}}^2}{\mathrm{i}\omega\Gamma}$ for low frequencies. They further introduce the upper bound $\Lambda \sim 2\Gamma\lambda\!\!\!^{-}_{\mathrm{p}}/z_a^2$ for the integration (summation), because the integral (sum) in Eq. (C.1) would otherwise be diverging. For $T \to 0$, following their trail, this modifies our calculation to

$$\begin{aligned}
\mathcal{F}_{\mathrm{B}} &\approx k_{\mathrm{B}}T\frac{\mu_0}{8\pi}\frac{\omega_{\mathrm{p}}^2}{4c^2}\frac{1}{2z_a}\sum_{n=0}^{\infty}{}'\left[\beta_{ii}^T(\mathrm{i}n\nu) + \beta_{zz}^T(\mathrm{i}n\nu)\right]\frac{n\nu}{n\nu+\Gamma} \\
&\overset{T\to 0}{\sim} \frac{\mu_0}{8\pi}\frac{\omega_{\mathrm{p}}^2}{4c^2}\frac{1}{2z_a}\left[\mu_{ii} + \mu_{zz}\right]\frac{\hbar}{2\pi}\int_0^{2\Gamma\lambda\!\!\!^{-2}_{\mathrm{p}}/z_a^2}\mathrm{d}\nu\ \frac{\omega_a}{\omega_a^2+\nu^2}\frac{\nu}{\Gamma} \\
&= \frac{\mu_0}{8\pi}\frac{\omega_{\mathrm{p}}^2}{4c^2}\frac{1}{2z_a}\left[\mu_{ii} + \mu_{zz}\right]\frac{\hbar}{2\pi}\frac{\omega}{\Gamma}\ln[2\Gamma\lambda\!\!\!^{-2}_{\mathrm{p}}/(\omega_a z_a^2)]
\end{aligned} \tag{C.4}$$

which is the result of Refs. [143, 398] modulo a factor of 2π since we chose a slightly different definition of the upper bound. The previous result seems to work sufficiently in the regime of interest for Refs. [143, 398]. However, we note that approximating the permittivity $\epsilon_{\mathrm{Dr}} - 1 \sim -\frac{\omega_{\mathrm{p}}^2}{\mathrm{i}\omega\Gamma}$ implicitly also prescribes the relation $\omega \ll \Gamma$. For $z_a \ll \lambda\!\!\!^{-}_{\mathrm{p}}$ we have that $\Lambda \sim \Gamma \ll 2\Gamma\lambda\!\!\!^{-2}_{\mathrm{p}}/z_a^2$ such that the actual integral should be corrected to

$$\begin{aligned}
\mathcal{F}_{\mathrm{B}} &\sim \frac{\mu_0}{8\pi}\frac{\omega_{\mathrm{p}}^2}{4c^2}\frac{1}{2z_a}\left[\mu_{ii} + \mu_{zz}\right]\frac{\hbar}{2\pi}\int_0^{\Gamma}\mathrm{d}\nu\ \frac{\omega_a}{\omega_a^2+\nu^2}\frac{\nu}{\Gamma} \\
&= \frac{\mu_0}{8\pi}\frac{\omega_{\mathrm{p}}^2}{4c^2}\frac{1}{2z_a}\left[\mu_{ii} + \mu_{zz}\right]\frac{\hbar}{2\pi}\frac{\omega_a}{2\Gamma}\ln\left[1 + \left(\frac{\Gamma}{\omega_a}\right)^2\right]
\end{aligned} \tag{C.5}$$

For comparison, we consider our result from Eq. (C.3) in the limit of $T \to 0$:

$$\begin{aligned}
\mathcal{F}_{\mathrm{B}} &\overset{T\to 0}{\sim} \frac{\mu_0}{8\pi}\frac{\omega_{\mathrm{p}}^2}{4c^2}\frac{1}{2z_a}\left[\mu_{ii} + \mu_{zz}\right]\frac{\hbar}{2\pi}\int_0^{\infty}\mathrm{d}\nu\frac{\omega_a}{\omega_a^2+\nu^2}\frac{\nu}{\nu+\Gamma} \\
&= \frac{\mu_0}{8\pi}\frac{\omega_{\mathrm{p}}^2}{4c^2}\frac{1}{2z_a}\left[\mu_{ii} + \mu_{zz}\right]\frac{\hbar}{2\pi}\frac{\omega_a\left(\pi\omega_a + 2\Gamma\ln\left[\frac{\Gamma}{\omega_a}\right]\right)}{2(\omega_a^2+\Gamma^2)}.
\end{aligned} \tag{C.6}$$

Both results, Eqs. (C.5) and (C.6), coincide for $\omega_a \ll \Gamma$ which is true for typical magnetic resonances.

Nonlocal Boltzmann-Mermin model

The transverse electric reflection coefficient reads [see Eqs. (1.26) and (1.28) and below]

$$r^s = \frac{\frac{Z^s}{Z_0^s} - 1}{\frac{Z^s}{Z_0^s} + 1}, \qquad \frac{Z^s}{Z_0^s} - 1 = -\frac{2}{\pi}\int_0^1 \frac{\mathrm{d}x}{\sqrt{1-x^2}} \frac{\epsilon_t(\omega, p/x)\frac{\omega^2 x^2}{c^2}}{\epsilon_t(\omega, p/x)\frac{\omega^2 x^2}{c^2} - p^2}, \tag{C.7a}$$

$$\epsilon_t(\omega, p/x) \overset{u\to 0^+}{\sim} 1 - \frac{3}{\lambda_{\mathrm{TF}}^2 p^2}x^2 + \mathrm{i}\frac{\omega_\mathrm{p}^2}{\omega\Gamma_t^\mathrm{L}(p/x)}, \tag{C.7b}$$

with $\Gamma_t^\mathrm{L}(k) = 4v_\mathrm{F}k/(3\pi)$. We assumed that $|\omega + \mathrm{i}\Gamma| \ll v_\mathrm{F}p/x$. Using $p \sim 1/(2z_a)$, this constrains the validity of the approximation to frequencies $\omega \ll v_\mathrm{F}/(2z_a)$ and wave vectors $p \gg 1/\ell = \Gamma/v_\mathrm{F}$. For small frequencies compared to the magnetic transition frequency $\omega \ll \omega_a \ll \Gamma$ ω_sp, we can write

$$r^s \sim \frac{1}{2}\left[\frac{Z^s}{Z_0^s} - 1\right]. \tag{C.8}$$

Inserting into the near-field expansion of the magnetic Green tensor, we can write

$$\begin{aligned}
\underline{G}_\mathrm{B} &\propto \frac{1}{2}\int_{\ell^{-1}}^\infty \mathrm{d}p\; p^2 e^{-2pz_a}\left(-\frac{2}{\pi}\int_0^1 \frac{\mathrm{d}x}{\sqrt{1-x^2}}\frac{\epsilon_t(\omega, p/x)\frac{\omega^2x^2}{c^2}}{\epsilon_t(\omega, p/x)\frac{\omega^2x^2}{c^2} - p^2}\right) \\
&\sim \frac{1}{2}\int_{\ell^{-1}}^\infty \mathrm{d}p\; p^2 e^{-2pz_a}\left(-\frac{2}{\pi}\int_0^1 \frac{\mathrm{d}x}{\sqrt{1-x^2}}\left[-\frac{3\pi}{4}\mathrm{i}x^3\frac{\omega\omega_\mathrm{p}^2}{v_\mathrm{F}c^2p^3}\right]\right) \\
&= \frac{\mathrm{i}}{2}\frac{\omega\omega_\mathrm{p}^2}{v_\mathrm{F}c^2}\int_{\ell^{-1}}^\infty \mathrm{d}p\; \frac{e^{-2pz_a}}{p} \overset{2z_a\ll\ell}{\sim} -\frac{\mathrm{i}}{2}\frac{\omega\omega_\mathrm{p}^2}{v_\mathrm{F}c^2}(\gamma_\mathrm{E} + \ln[2z_a/\ell]).
\end{aligned} \tag{C.9}$$

This is consistent with the result of Ref. [184]. Noting that $\omega \lesssim \Gamma$ or, expressed in Matsubara frequencies, $n \leq \Gamma/\nu$, we eventually obtain

$$\mathcal{F}_\mathrm{B} \sim -k_\mathrm{B}T\frac{\mu_0}{8\pi}\frac{\omega_\mathrm{p}^2}{2v_\mathrm{F}c^2}\ln\left[\frac{2z_a}{\ell}e^{\gamma_\mathrm{E}}\right]{\sum_{n=0}^{[\Gamma/\nu]}}'\left[\beta_{ii}^T(\mathrm{i}n\nu) + \beta_{zz}^T(\mathrm{i}n\nu)\right]n\nu, \tag{C.10}$$

where the brackets $[\cdot]$ on top of the sum denote the largest integer smaller than Γ/ν.

C.2 Limiting behavior of the mode number

We now consider the limiting behavior of the mode number [Eq. (2.46)]

$$\varpi^T(\mathbf{r}_a,\omega) = -\frac{1}{\pi}\mathrm{Tr}\left[\underline{\beta}^T(\omega)\cdot\underline{G}_\mathrm{B}(\mathbf{r}_a,\mathbf{r}_a,\omega)\right]. \tag{C.11}$$

We consider the local Drude as well as the spatially dispersive Boltzmann-Mermin model for the metal's permittivity such that the reflection coefficient of the interface is wavevector-dependent even in the near-field, e.g. $r^s = r^s(\omega,p)$. Further, we focus on the non-retarded region $z_a \ll \lambda_a$. With the function Φ^T defined below Eq. (2.48) and the magnetic Green tensor for the planar interface (Eq. (A.17) with interchanged reflection coefficients), we can write in the near-field

$$\varpi^T(\mathbf{r}_a,\omega) \sim -\frac{\Phi^T(\omega)}{z_a^3}\int_0^\infty \mathrm{d}y\; y^2 e^{-y} r^s\left(\omega,\frac{y}{2z_a}\right), \tag{C.12}$$

where we substitute $y = 2z_a p$ for the integral measure. Inserting the local Drude permittivity of the metal, we obtain

$$\varpi^T(\mathbf{r}_a,\omega) \sim -\frac{\Phi^T(\omega)}{z_a}\frac{\omega^2}{c^2}[\epsilon_\mathrm{Dr}(\omega)-1]. \tag{C.13}$$

In the nonlocal case, the situation becomes considerably more complicated. Using Eqs. (1.26) and (1.28), the reflection coefficient can be written as

$$\begin{aligned} r^s(\omega,p) &\sim \frac{1}{2}\left[\frac{Z^s(\omega,p)}{Z_0^s(\omega,p)}-1\right] \sim \frac{1}{2}\left[\int_0^1 \mathrm{d}x\;\frac{\frac{2}{\pi}}{\sqrt{1-x^2}}\frac{1}{1-\epsilon_t\left(\omega,\frac{p}{x}\right)\frac{\omega^2x^2}{p^2c^2}}-1\right] \\ &= \frac{1}{2}\int_0^1 \mathrm{d}x\;\frac{\frac{2}{\pi}}{\sqrt{1-x^2}}\frac{\epsilon_t\left(\omega,\frac{p}{x}\right)\frac{\omega^2x^2}{p^2c^2}}{1-\epsilon_t\left(\omega,\frac{p}{x}\right)\frac{\omega^2x^2}{p^2c^2}}, \end{aligned} \tag{C.14}$$

where we have used that $\int_0^1 \mathrm{d}x\;\frac{2/\pi}{\sqrt{1-x^2}} = 1$. In the limit $|\omega| \ll \Gamma$, the transverse permittivity [Eq. (1.41)] behaves as

$$\epsilon_t\left(\omega,\frac{y}{2z_a x}\right) \sim \mathrm{i}\frac{\omega_\mathrm{p}^2}{\omega\Gamma}g_t\left(\mathrm{i}\frac{z_a}{\ell}\frac{2x}{y}\right). \tag{C.15}$$

The largest contributions to the integrals in Eqs. (C.12) and (C.14) arise from $x, y \sim 1$, such that the ratio z_a/ℓ is determines the limiting behavior of the function $g_t(u)$. For $z_a \gg \ell$, $g_t \sim 1$ and we recover the local Drude result. In the opposite case, where $z_a \lesssim \ell$ ($|u| \to 0$), we have

$$\epsilon_t\left(\omega,\frac{y}{2z_a x}\right) \sim \mathrm{i}\frac{\omega_\mathrm{p}^2}{\omega}\frac{3\pi}{2}\frac{z_a}{v_\mathrm{F}}\frac{x}{y}. \tag{C.16}$$

We note that the previous result is valid only if

$$\frac{z_a}{\ell}\frac{2x}{y} < 1 \Rightarrow y > \frac{2z_a}{\ell} \quad (0 \leq x \leq 1). \tag{C.17}$$

Even though this prescribes a minimal value for y and our approximation might hence not be applicable to the integral in Eq. (C.12) around $y \sim 0$. However, since $z_a \ll \ell$, the range $0 < y < 2z_a/\ell$ gives a subleading contribution to the integral and can safely be neglected. Inserting Eq. (C.16) into Eq. (C.14) yields

$$\begin{aligned} r^s\left(\omega, \frac{y}{2z_a}\right) &\sim \frac{1}{2}\int_0^1 \mathrm{d}x \; \frac{\frac{2}{\pi}}{\sqrt{1-x^2}} \frac{\mathrm{i}\omega\frac{3\pi}{4}\frac{\lambda\!\!\!^{-}_{\mathrm{p}}}{v_{\mathrm{F}}}\frac{x^3}{y^3}\left(\frac{2z_a}{\lambda\!\!\!^{-}_{\mathrm{p}}}\right)^3}{1-\mathrm{i}\omega\frac{3\pi}{4}\frac{\lambda\!\!\!^{-}_{\mathrm{p}}}{v_{\mathrm{F}}}\frac{x^3}{y^3}\left(\frac{2z_a}{\lambda\!\!\!^{-}_{\mathrm{p}}}\right)^3} \\ &\sim \mathrm{i}\frac{3\pi}{4}\omega\frac{z_a}{v_{\mathrm{F}}}\left(\frac{2z_a}{\lambda\!\!\!^{-}_{\mathrm{p}}}\right)^2 \int_0^1 \mathrm{d}x \; \frac{\frac{2}{\pi}}{\sqrt{1-x^2}}\frac{x^3}{y^3} \\ &= \mathrm{i}\frac{\omega}{y^3}\frac{z_a}{v_{\mathrm{F}}}\left(\frac{2z_a}{\lambda\!\!\!^{-}_{\mathrm{p}}}\right)^2. \end{aligned} \tag{C.18}$$

From Eq. (C.16) we can see that the dielectric function stays finite as long as $y > 2z_a/\ell$. The dominant values in the integral stem from $y \sim 1$. This enabled us to approximate the denominantor in the second line of the previous equation. However, neglecting the functional dependence of the denominator in our approximation, $z_a \ll \ell$ must be replaced with

$$z_a \ll \ell\left[\frac{2}{3\pi}\frac{\lambda\!\!\!^{-2}_{\mathrm{p}}}{\ell^2}\right]^{1/3}. \tag{C.19}$$

Combining the previous results and inserting in Eq. (C.12), we obtain

$$\varpi^T(\mathbf{r}_a, \omega) \sim -4\mathrm{i}\omega\frac{\Phi^T(\omega)}{v_{\mathrm{F}}\lambda\!\!\!^{-2}_{\mathrm{p}}}\int_{\frac{2z_a}{\ell}}^{\infty}\mathrm{d}y \; \frac{e^{-y}}{y} \sim 4\mathrm{i}\omega\frac{\Phi^T(\omega)}{v_{\mathrm{F}}\lambda\!\!\!^{-2}_{\mathrm{p}}}\ln\left[\frac{2z_a}{\gamma'_{\mathrm{E}}\ell}\right], \tag{C.20}$$

where $\gamma'_{\mathrm{E}} = e^{-\gamma_{\mathrm{E}}}$ with γ_{E} the Euler-Mascheroni constant.

Solving the integral in Eq. (C.20) is no longer possible in the limit $\Gamma \to 0$. The latter limit becomes particularly relevant for the evaluation of the magnetic Casimir-Polder entropy at small temperature and is usually accompanied by the limit $|\omega| \to 0$ (see Sec. 2.2). In this situation, we have that $\ell \to \infty$ and it is simply no longer possible to neglect the denominator in Eq. (C.18). We can circumvent that problem by imposing that

$$y \gg \left[\frac{3\pi}{4}\frac{|\omega|\lambda\!\!\!^{-}_{\mathrm{p}}}{v_{\mathrm{F}}}\right]^{1/3}\frac{2z_a}{\lambda\!\!\!^{-}_{\mathrm{p}}} = 2\left[\frac{\hbar|\omega|}{E^{\mathrm{nl}}}\right]^{1/3}, \tag{C.21}$$

where E^{nl} gives the characteristic energy of the eddy currents for the nonlocal description of

the metal [Eq. (2.62)]. We then obtain

$$\varpi^T(\mathbf{r}_a,\omega) \sim \frac{4}{3}\mathrm{i}\omega\frac{\Phi^T(0)}{v_\mathrm{F}\lambda\!\!\!^{-2}_\mathrm{p}}\ln\left[\left(\frac{2}{\gamma'_\mathrm{E}}\right)^3\frac{\hbar|\omega|}{E^\mathrm{nl}}\right]. \tag{C.22}$$

Equations (C.20) and (C.22) can be used to derive the free energy as well as the entropy in the limit of interest [see e.g. Eq. (2.51)].

APPENDIX D

Supplemental Material for Spatial Dispersion in Metals and Graphene

We provide additional information on the impact of spatially nonlocal material models on atom-surface quantum friction (Section 3.4.1). In particular, we discuss the reflection coefficients of a planar interface modeled by the extended hydrodynamic description (complementing also Section 1.2) and put a particular focus on their low-frequency behavior as well as the connection to quantum friction. We further review the (2+1)-Dirac model commonly used for describing the optical properties of graphene which is used in the main text to provide an estimate on the corresponding quantum frictional force.

D.1 Extended hydrodynamic model and low-velocity quantum friction

Reflection coefficients and resistivity of spatially dispersive metals at planar interface

Assuming specular reflection of electrons at the metal/vacuum interface, the transverse electric and transverse magnetic reflection coefficients read

$$r^s = \frac{Z^s - Z_0^s}{Z^s + Z_0^s} = 1 - 2\frac{1}{1 + Z^s/Z_0^s} \qquad r^p = \frac{Z_0^p - Z^p}{Z_0^p + Z^p} = -1 + 2\frac{1}{1 + Z^p/Z_0^p}, \tag{D.1}$$

where the surface impedance can be written as [Eq. (1.28)]

$$Z^s/Z_0^s = -\frac{2}{\pi}\sqrt{p^2 - \omega^2/c^2}\int_0^\infty \mathrm{d}q\ \frac{1}{\epsilon_t(\omega,k)\omega^2/c^2 - k^2 + \mathrm{i}0^+}, \tag{D.2a}$$

$$Z^p/Z_0^p = \frac{2}{\pi c^2}\frac{\omega^2}{\sqrt{p^2 - \omega^2/c^2}}\int_0^\infty \mathrm{d}q\ \frac{1}{k^2}\left(\frac{q^2}{\epsilon_t(\omega,k)\omega^2/c^2 - k^2 + \mathrm{i}0^+} + \frac{p^2}{\epsilon_l(\omega,\mathbf{k})\omega^2/c^2}\right). \tag{D.2b}$$

Employing the extended hydrodynamic model, the longitudinal and transverse permittivities of the metal read

$$\epsilon_t(\omega,k) = \epsilon_{\mathrm{Dr}}(\omega) = 1 - \frac{\omega_\mathrm{p}^2}{\omega(\omega + \mathrm{i}\Gamma)}, \qquad \epsilon_l(\omega,k) = 1 - \frac{\omega_\mathrm{p}^2}{\omega(\omega + \mathrm{i}\Gamma) - \beta^2 k^2}, \tag{D.3}$$

where the impact of non-locality is determined by the parameter [246, 247]

$$\beta^2 = \beta^2(\omega) = f\left(\frac{\gamma}{\omega}\right) v_{\mathrm{F}}^2 = \frac{\frac{3}{5}\omega + \frac{1}{3}\mathrm{i}\Gamma}{\omega + \mathrm{i}\Gamma} v_{\mathrm{F}}^2 = \begin{cases} \frac{1}{3}v_{\mathrm{F}}^2 & \omega \ll \Gamma \\ \frac{3}{5}v_{\mathrm{F}}^2 & \omega \gg \Gamma \end{cases}. \tag{D.4}$$

Inserting the expression for β into the longitudinal permittivity, we can write

$$\epsilon_l(\omega, k) = 1 - \frac{1}{\omega(\omega + \mathrm{i}\Gamma)/\omega_{\mathrm{p}}^2 - (\lambda_{\mathrm{D}}(\frac{\Gamma}{\omega})p)^2(1 + q^2/p^2)} \to \begin{cases} \epsilon_{\mathrm{Dr}}(\omega) & p\lambda_{\mathrm{D}} \ll 1 \\ 1 + \frac{1}{1+q^2/p^2} \frac{1}{(p\lambda_{\mathrm{D}}(\frac{\Gamma}{\omega}))^2} & p\lambda_{\mathrm{D}} \gg 1 \end{cases}, \tag{D.5}$$

where

$$\lambda_{\mathrm{D}}\left(\frac{\Gamma}{\omega}\right) = \frac{v_{\mathrm{F}}}{\omega_{\mathrm{p}}} \sqrt{f\left(\frac{\Gamma}{\omega}\right)} \overset{\omega \ll \Gamma}{\sim} \lambda_{\mathrm{TF}}\left(1 - \frac{2}{5}\mathrm{i}\frac{\omega}{\Gamma}\right) \tag{D.6}$$

approaches the Thomas-Fermi wavelength $\lambda_{\mathrm{TF}} = v_{\mathrm{F}}/(\sqrt{3}\omega_{\mathrm{p}})$ for small frequencies and can be considered as a quantized version of the Debeye length. Further, the functional dependence of β introduces another length-scale into the system, i.e. the bulk electron's mean free path $\ell = v_{\mathrm{F}}/\Gamma$ that is connected to dissipative Landau damping in the material. The extended hydrodynamic model is valid in the limit

$$\frac{q v_{\mathrm{F}}}{\omega} \ll 1. \tag{D.7}$$

It is to be understood as a small deviation from the local Drude model [246]. Since there is no wave-vector dependency in the transverse permittivity, the transverse electric reflection coefficient reduces to the corresponding (Drude) Fresnel coefficient

$$r^s(\omega, p) = \frac{\sqrt{p^2 - \omega^2/c^2} - \sqrt{p^2 - \epsilon_{\mathrm{Dr}}(\omega)\omega^2/c^2}}{\sqrt{p^2 - \omega^2/c^2} + \sqrt{p^2 - \epsilon_{\mathrm{Dr}}(\omega)\omega^2/c^2}}. \tag{D.8}$$

For the transverse magnetic case, in contrast, we obtain

$$Z^p/Z_0^p \quad = \frac{2}{\pi c^2} \frac{\omega^2}{\sqrt{p^2 - \omega^2/c^2}} \left(-\frac{\pi}{2} \frac{1}{p + \sqrt{p^2 - \epsilon_{\mathrm{Dr}}(\omega)\omega^2/c^2}} + \int_0^\infty \mathrm{d}q \; \frac{1}{k^2} \frac{p^2}{\epsilon_l(\omega, k)\omega^2/c^2} \right). \tag{D.9}$$

We can write the integral in the second term of the previous line as

$$\mathcal{I} := \int_0^\infty \mathrm{d}q \; \frac{1}{k^2} \frac{p^2}{\epsilon_l(\omega, k)\omega^2/c^2} = \frac{c^2 p}{\omega^2} \int_0^\infty \mathrm{d}x \; \frac{1}{1 + x^2} \frac{1}{1 - \frac{1}{\omega(\omega + \mathrm{i}\Gamma)/\omega_{\mathrm{p}} - (\lambda_D(\frac{\Gamma}{\omega})p)^2(1+x^2)}}. \tag{D.10}$$

In the local limit ($p\lambda_\mathrm{D} \ll 1$), we obtain

$$\mathcal{I}(p\lambda_\mathrm{D} \ll 1) = -\frac{pc^2\pi}{2\omega^2}\frac{1}{\epsilon_\mathrm{Dr}(\omega)} \tag{D.11}$$

and restore the transverse magnetic Fresnel reflection coefficient

$$r^p(\omega,p) = \frac{\epsilon_\mathrm{Dr}(\omega)\sqrt{p^2-\omega^2/c^2} - \sqrt{p^2-\epsilon_\mathrm{Dr}(\omega)\omega^2/c^2}}{\epsilon_\mathrm{Dr}(\omega)\sqrt{p^2-\omega^2/c^2} + \sqrt{p^2-\epsilon_\mathrm{Dr}(\omega)\omega^2/c^2}}. \tag{D.12}$$

In the nonlocal case, however, the integral can still be solved without making further approximations and we obtain

$$Z^p/Z_0^p = \frac{1}{\epsilon_\mathrm{Dr}(\omega)\sqrt{p^2-\omega^2/c^2}}\left(\sqrt{p^2-\epsilon_\mathrm{Dr}(\omega)\omega^2/c^2} + \frac{p(\epsilon_\mathrm{Dr}(\omega)-1)}{\sqrt{1+\frac{1}{(\lambda_\mathrm{D}(\frac{\gamma}{\omega})p)^2}\left(\frac{\epsilon_\mathrm{Dr}(\omega)}{\epsilon_\mathrm{Dr}(\omega)-1}\right)}}\right). \tag{D.13}$$

This coincides with the expression obtained by Refs. [204, 205]. It gives for the transverse magnetic reflection coefficient in the extended hydrodynamic description

$$r^p(\omega,p) = \frac{\epsilon_\mathrm{Dr}(\omega)\sqrt{p^2-\omega^2/c^2} - \sqrt{p^2-\epsilon_\mathrm{Dr}(\omega)\omega^2/c^2} - \frac{p(\epsilon_\mathrm{Dr}(\omega)-1)}{\sqrt{1+\frac{1}{(\lambda_\mathrm{D}(\frac{\Gamma}{\omega})p)^2}\left(1-\frac{\omega(\omega+\mathrm{i}\Gamma)}{\omega_\mathrm{p}^2}\right)}}}{\epsilon_\mathrm{Dr}(\omega)\sqrt{p^2-\omega^2/c^2} + \sqrt{p^2-\epsilon_\mathrm{Dr}(\omega)\omega^2/c^2} + \frac{p(\epsilon_\mathrm{Dr}(\omega)-1)}{\sqrt{1+\frac{1}{(\lambda_\mathrm{D}(\frac{\Gamma}{\omega})p)^2}\left(1-\frac{\omega(\omega+\mathrm{i}\Gamma)}{\omega_\mathrm{p}^2}\right)}}}. \tag{D.14}$$

In the near-field (formally $c \to \infty$) we have

$$r^p(\omega,p) = \frac{\epsilon_\mathrm{Dr}-1}{\epsilon_\mathrm{Dr}+1+2(\epsilon_\mathrm{Dr}-1)(\lambda_D p)^2\left(1+\sqrt{1+\frac{1}{(\lambda_\mathrm{D}p)^2}\frac{\epsilon_\mathrm{Dr}}{\epsilon_\mathrm{Dr}-1}}\right)}, \tag{D.15}$$

where we skipped the functional dependencies for the sake of readability. We note that the reflection coefficient features surface plasmon-polaritons. They obey the relation for constant (large frequency) β [233]

$$\omega_\mathrm{sp}^2 = \frac{1}{2}\left[\omega_\mathrm{p}^2 + \beta^2k^2 + \beta k\sqrt{2\omega_\mathrm{p}^2+\beta^2k^2}\right]. \tag{D.16}$$

For small frequencies, meaning frequencies $\omega \ll \Gamma$, the reflection coefficient behaves Ohmic and can be expanded as

$$r^p(\omega,p) \sim R(\lambda_\mathrm{TF}p) + 2\mathrm{i}\omega\epsilon_0\rho\left(\lambda_\mathrm{TF}p, \frac{\lambda_D'(\infty)}{\lambda_\mathrm{TF}}\right), \tag{D.17}$$

where

$$R(x) = 1 + 2x\left(x - \sqrt{1+x^2}\right) \to \begin{cases} 1, & x \ll 1 \\ (2x)^{-2}, & x \gg 1 \end{cases} \tag{D.18a}$$

$$\rho(x,y) = \rho_{\mathrm{lc}}(x) + \rho_{\mathrm{La}}(x,y) \tag{D.18b}$$

$$\rho_{\mathrm{lc}}(x) = \frac{\Gamma}{\epsilon_0\omega_{\mathrm{p}}^2} \frac{\left(\frac{x}{2}\left(\sqrt{x^2+1}+2x\right)+1\right)}{\left(x^2+1\right)\left(2x\left(\sqrt{x^2+1}+x\right)+1\right)^2} \to \frac{\Gamma}{\epsilon_0\omega_{\mathrm{p}}^2} \begin{cases} 1, & x \ll 1 \\ \frac{3}{32x^2}\frac{1}{2+x^2}, & x \gg 1 \end{cases} \tag{D.18c}$$

$$\rho_{\mathrm{La}}(x,y) = \mathrm{i}\frac{y}{\epsilon_0} \frac{x\left(2x^2\left(\sqrt{x^2+1}+x\right)+\sqrt{x^2+1}+2x\right)}{\left(x^2+1\right)\left(2x\left(\sqrt{x^2+1}+x\right)+1\right)^2} \to \mathrm{i}\frac{y}{\epsilon_0} \begin{cases} x, & x \ll 1 \\ \frac{1}{4}\frac{1}{1+x^2}, & x \gg 1 \end{cases} \tag{D.18d}$$

and we used that $\lambda_D(0) = \lambda_{\mathrm{TF}}$. $R(x)$ and $\rho_{\mathrm{lc}}(x)$ are monotonously decreasing functions, whilst $\rho_{\mathrm{La}}(x)$ monotonously increases, features a maximum at $x = \sqrt{\frac{1}{\sqrt{2}} - \frac{1}{2}} \approx 0.46 \sim 1$ and then monotonously decreases to zero. $\rho_{\mathrm{lc}}(x)$ is connected to the Drude collision-induced damping in the material and we can approximate $\rho_{\mathrm{lc}}(x) \approx$ const. for all realistic parameters of the Thomas Fermi wavelength (usually in the range of angstrom). $\rho_{\mathrm{La}}(x)$ is connected to coherent Landau damping. Being a function of the wavevector ($\sim$ inverse distance), Landau damping features a maximum that is connected to

$$y = \frac{\lambda_D'(\infty)}{\lambda_{\mathrm{TF}}} = -\mathrm{i}\frac{2}{5}\frac{1}{\Gamma}. \tag{D.19}$$

In the simplest case, one might neglect the frequency-dependence of β and – for small frequencies – just assume that

$$\beta = \frac{v_{\mathrm{F}}}{\sqrt{3}} \to \lambda_D = \lambda_{\mathrm{TF}}. \tag{D.20}$$

In this case, we have completely neglected the Landau damping and its corresponding length scale and resistivity reduces to

$$\rho(x) \sim \rho_{\mathrm{lc}}. \tag{D.21}$$

The inclusion of the frequency dependence in the compressibility factor β incorporates Landau damping into the description and hence introduces extra damping channels. In figure D.1, we report the imaginary part of the transverse magnetic reflection coefficient using the extended hydrodynamic model as a function of frequency with both constant and frequency dependent compressibility factor β. We compare the behavior to the more general Boltzmann-Mermin model (see main text).

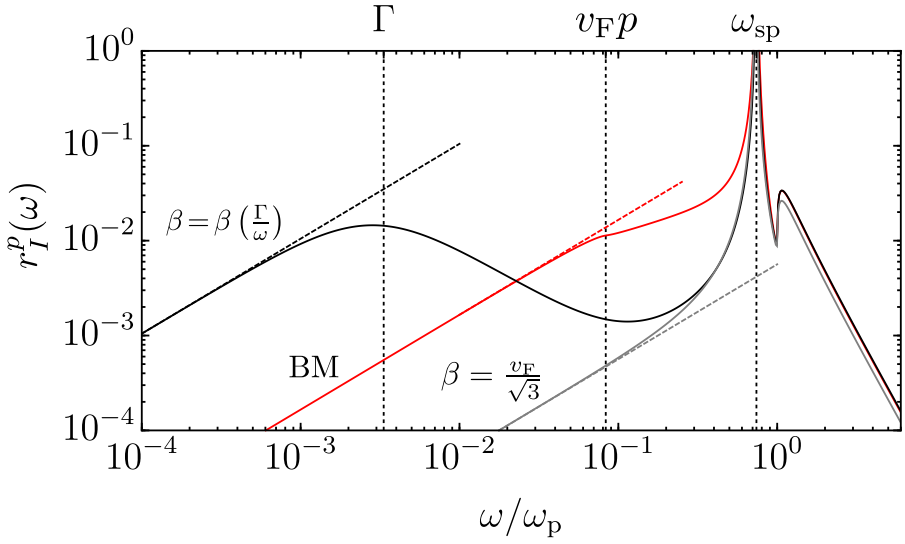

Figure D.1: Imaginary part of the transverse magnetic reflection coefficient in the extended hydrodynamic description [246] for fixed $\beta = v_F/(\omega_p\sqrt{3})$ (gray) and the frequency-dependent $\beta = \beta(\Gamma/\omega)$ (black) in the near-field limit. We choose the wavevector $k = 50/(2\ell)$ in relation to the bulk electron's mean free path $\ell = v_F/\Gamma$. The asymptotes (dashed) are given in Eqs. (D.17) and (D.18). We compare our results to the Boltzmann-Mermin description ("BM", red) [M4]. We refer to Section 1.2 for details of the respective models. Adapted from [M3].

Low-velocity quantum friction

In order to compute the quantum frictional force based on the resistivity of the extended hydrodynamic description [Eqs. (D.18)], we need to find the function $\Phi_n(z_a)$ in Eq. (3.86). Since the resistivity decomposes into the sum of two functions, $\rho = \rho_{lc} + \rho_{La}$, Φ also decomposes into

$$\begin{aligned}\Phi_n(z_a) &= \Phi_n^{lc}(z_a) + \Phi_n^{La}(z_a) \\ &= \frac{2\epsilon_0}{\lambda_{TF}^{2n+3}} \int_0^\infty \mathrm{d}x\, x^{2(n+1)} e^{-2\frac{z_a}{\lambda_{TF}}x} \left[\rho_{lc}\left(\frac{x}{\lambda_{TF}}\right) + \rho_{La}\left(\frac{x}{\lambda_{TF}}, \frac{\lambda_D'(0)}{\lambda_{TF}}\right)\right]. \end{aligned} \tag{D.22}$$

With help of Eqs. (D.18), we obtain

$$\Phi_{\{0,1,2\}}^{lc}(z_a) \to 2\epsilon_0 \frac{\Gamma}{\epsilon_0\omega_p^2} \begin{cases} \left\{\frac{3\pi}{64\sqrt{2}\lambda_{TF}^3}, \frac{1}{z_a}\frac{3}{64\lambda_{TF}^4}, \frac{1}{z_a^3}\frac{3}{128\lambda_{TF}^4}\right\}, & z_a \ll \lambda_{TF}, \\ \left\{\frac{1}{4z_a^3}, \frac{3}{4z_a^5}, \frac{45}{8z_a^7}\right\}, & z_a \gg \lambda_{TF}, \end{cases} \tag{D.23a}$$

$$\mathcal{D}^{\mathrm{La}}_{\{0,1,2\}}(z_a) \to 2\epsilon_0 \frac{2}{5\epsilon_0\Gamma} \begin{cases} \left\{ \frac{1}{z_a}\frac{1}{8\lambda_{\mathrm{TF}}^2}, \frac{1}{z_a^3}\frac{1}{16\lambda_{\mathrm{TF}}^2}, \frac{1}{z_a^5}\frac{3}{16\lambda_{\mathrm{TF}}^2} \right\}, & z_a \ll \lambda_{\mathrm{TF}}, \\ \left\{ \frac{1}{z_a^4}\frac{3\lambda_{\mathrm{TF}}}{8}, \frac{1}{z_a^6}\frac{15\lambda_{\mathrm{TF}}}{8}, \frac{1}{z_a^8}\frac{315\lambda_{\mathrm{TF}}}{16} \right\}, & z_a \gg \lambda_{\mathrm{TF}}. \end{cases} \tag{D.23b}$$

Combining the previous results and comparing to the local Drude model yields the results reported in Eq. (3.90) and the discussion below.

D.2 Reflection coefficients for graphene

Important ingredient of the atom-surface interaction is the electromagnetic response of the surface' material encoded in its transverse electric and magnetic reflection coefficients. For the (2+1)-Dirac model, which assumes a linear dispersion relation at the Dirac point and allows for a band-gap Δ, they read[1] [264–266, 512]

$$r^p = \frac{\alpha_{\mathrm{fs}}\kappa\Phi}{\alpha_{\mathrm{fs}}\kappa\Phi + 2\kappa_{\mathrm{F}}^2}, \quad r^s = -\frac{\alpha_{\mathrm{fs}}\Phi}{\alpha_{\mathrm{fs}}\Phi + 2\kappa}, \tag{D.24}$$

where α_{fs} is the fine-structure constant, $\kappa = \sqrt{p^2 - \omega^2/c^2}$, $\kappa_{\mathrm{F}} = \sqrt{v_{\mathrm{F}}^2 p^2/c^2 - \omega^2/c^2} \equiv -\mathrm{i}p_{\mathrm{F}}$ with v_{F} the Fermi velocity and p the modulus of the wavevector parallel to the interface. We further defined the function

$$\begin{aligned} \Phi &= 2\Omega_\Delta \left(1 + \left[1 - \left(\frac{\Omega_\Delta}{\kappa_{\mathrm{F}}} \right)^2 \right] \frac{\kappa_{\mathrm{F}}}{\Omega_\Delta} \arctan[\frac{\kappa_{\mathrm{F}}}{\Omega_\Delta}] \right) \\ &= 2\Omega_\Delta \left(1 - \left[1 + \left(\frac{\Omega_\Delta}{p_{\mathrm{F}}} \right)^2 \right] \frac{p_{\mathrm{F}}}{\Omega_\Delta} \mathrm{arctanh}[\frac{p_{\mathrm{F}}}{\Omega_\Delta}] \right) = -2\Omega_\Delta \Psi\left(\frac{p_{\mathrm{F}}}{\Omega_\Delta} \right), \quad \Omega_\Delta = \frac{2\Delta}{\hbar c}. \end{aligned} \tag{D.25}$$

Here, Ω_Δ is the band-gap's energy converted into a wavevector. Upon scaling ($\sim \Omega_\Delta$), Φ relates the energy of the electron in the Fermi liquid, $E \sim \pm v_{\mathrm{F}} p$, to the energy of the band-gap, i.e. $E \sim \Delta$. Depending on the ratio and the domain (real or complex), we can distinguish between different physical mechanisms in the electromagnetic response of the material (see Fig. D.2). First, we note that apart from the usual light cone at

$$\omega = cp \tag{D.26}$$

that distinguishes propagating from evanescent waves (with respect to the direction perpendicular to the surface), we also need to consider the material cone

$$\omega = v_{\mathrm{F}} p. \tag{D.27}$$

[1] A similar dispersion relation can be realized for photonic metamaterials [267].

Above the light-cone, the reflection coefficients acquire a non-vanishing imaginary part, introducing dissipation channels. This kind of dissipation is not connected to the material properties in particular, but to the velocity of particles in their respective environment. The material does not feature any other dissipation channels for incoming waves as long as the energy imposed on the fermions is smaller to the size of the band gap energy, i.e. $p_\mathrm{F} < \Omega_\Delta$. This corresponds to a situation where no electrons can enter the conduction band. We note that the transverse electric reflection coefficient does feature evanescent modes, the surface plasmon-polaritons [264]: Since $\kappa > 0$ in the evanescent region, a real solution $\omega(k)$ for the root of the denominator of r^s is possible and can be written as

$$k[p_\mathrm{F}] = k_\Delta \sqrt{\frac{p_\mathrm{F}^2}{\Omega_\Delta^2} + \alpha_\mathrm{fs}^2 \left(\left[1 + \left(\frac{\Omega_\Delta}{p_\mathrm{F}} \right)^2 \right] \frac{p_\mathrm{F}}{\Omega_\Delta} \mathrm{arctanh}[\frac{p_\mathrm{F}}{\Omega_\Delta}] - 1 \right)^2}, \tag{D.28}$$

$$\omega[p_\mathrm{F}] = c k_\Delta \sqrt{\frac{p_\mathrm{F}^2}{\Omega_\Delta^2} + \alpha_\mathrm{fs}^2 v_\mathrm{F}^2 \left(\left[1 + \left(\frac{\Omega_\Delta}{p_\mathrm{F}} \right)^2 \right] \frac{p_\mathrm{F}}{\Omega_\Delta} \mathrm{arctanh}[\frac{p_\mathrm{F}}{\Omega_\Delta}] - 1 \right)^2} \tag{D.29}$$

with $k_\Delta = \Omega_\Delta / \sqrt{1 - v_\mathrm{F}^2/c^2}$. A further simplification can be obtained by setting $p_\mathrm{F}/\Omega_\Delta = \tanh[q]$ [512], i.e.

$$k[q] = k_\Delta \sqrt{\tanh^2[q] + \alpha_\mathrm{fs}^2 \left(q \frac{\tanh^2[q] + 1}{\tanh[q]} - 1 \right)^2}, \tag{D.30}$$

$$\omega[q] = c k_\Delta \sqrt{\tanh^2[q] + \alpha_\mathrm{fs}^2 v_F^2 \left(q \frac{\tanh^2[q] + 1}{\tanh[q]} - 1 \right)^2}. \tag{D.31}$$

From the previous expression, since $v_\mathrm{F} < 1$, we have that $k[q] > \omega[q]$ confirming that the mode lies in the evanescent sector. However, these modes are purely real and scattering of waves on the material is hence completely elastic. As soon as $p_\mathrm{F} > \Omega_\Delta$, the imposed radiation carries enough energy to promote electrons to the conduction band and the scattering becomes inelastic opening a dissipation channel. Mathematically, this can be seen from

$$\mathrm{arctanh}[x] \overset{x>1}{\in} \mathbb{C} \tag{D.32}$$

giving the reflection coefficients a non-vanishing imaginary part. The corresponding threshold energy for electron-hole pair-creating is given by

$$p_\mathrm{F} \overset{!}{=} \Omega_\Delta \Leftrightarrow \omega_\mathrm{pc} = \sqrt{c^2 \Omega_\Delta^2 + v_\mathrm{F}^2 p^2}. \tag{D.33}$$

Pair-creation is possible in both the propagating and the evanescent region of the dispersion relation.

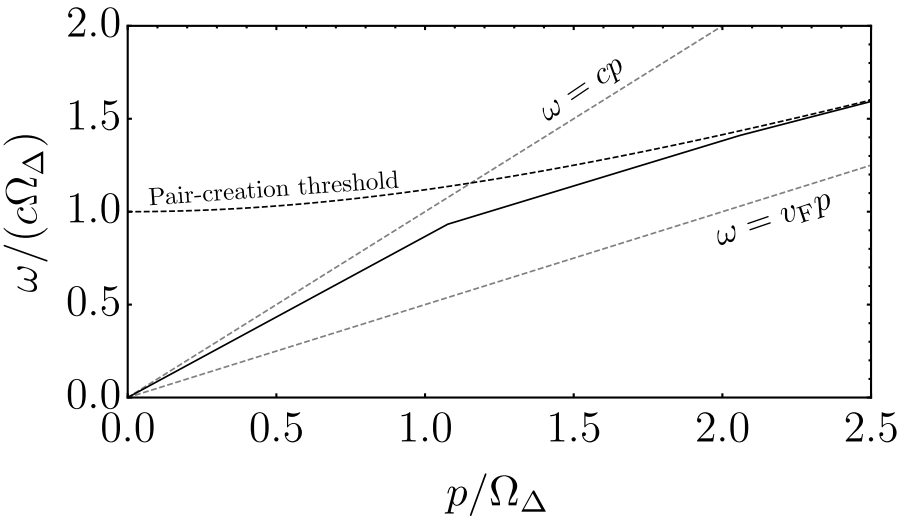

Figure D.2: Dispersion relation for Graphene in the (2+1)-Dirac model. We display the surface plasmon-polariton dipersion relation [Eq. (D.30)] (black, solid line), the pair-creation threshold (black, dashed), and the light and material cone (gray, dashed). For better visibility we artificially chose $\alpha_{\rm fs} = 0.5$ and $v_F = 0.5c$.

For low-velocity quantum friction, the relevant frequency regime is usually smaller than any of the system resonances, where the interaction with the material-modified vacuum is usually dominated by the transverse magnetic reflection coefficient. Also, we are particularly interested in dissipation in the system, i.e. $\mathrm{Im}[r]$, since this gives the necessary coupling for frictional forces. As can be seen from Figs. D.2 and D.3, for realistic values of $\alpha_{\rm fs}, v_{\rm F}$, we have that $p_{\rm F} \geq 0$ so that $\kappa_{\rm F}$ is purely imaginary. We almost exclusively work above the material cone. Also, in the non-retarded limit, we have that $\kappa \approx p$ and hence operate below the light-cone. This means that dissipation, i.e. when the transverse magnetic reflection coefficient becomes imaginary, can only occur above the Pair-creation threshold (see shaded area in Fig. D.3). Explicitly, we have $p_{\rm F}/\Omega_\Delta = \hbar\sqrt{\omega^2 - v_{\rm F}^2 p^2}/(2\Delta)$ such that

$$\begin{aligned}\mathrm{Im}r^p &= \mathrm{Im}\frac{\alpha_{\rm fs}\kappa\Phi}{\alpha_{\rm fs}\kappa\Phi + 2\kappa_{\rm F}^2} = \mathrm{Im}\frac{-2\alpha_{\rm fs}\kappa\Omega_\Delta\Psi\left(\frac{p_{\rm F}}{\Omega_\Delta}\right)}{-2\alpha_{\rm fs}\kappa\Omega_\Delta\Psi\left(\frac{p_{\rm F}}{\Omega_\Delta}\right) + 2\kappa_{\rm F}^2} = \mathrm{Im}\frac{\alpha_{\rm fs}\kappa\Psi\left(\frac{p_{\rm F}}{\Omega_\Delta}\right)}{\alpha_{\rm fs}\kappa\Psi\left(\frac{p_{\rm F}}{\Omega_\Delta}\right) + \left(\frac{p_{\rm F}}{\Omega_\Delta}\right)^2} \\ &\overset{c\to\infty}{\sim} \mathrm{Im}\frac{\alpha_{\rm fs}p\Psi\left(\frac{p_{\rm F}}{\Omega_\Delta}\right)}{\alpha_{\rm fs}p\Psi\left(\frac{p_{\rm F}}{\Omega_\Delta}\right) + \left(\frac{p_{\rm F}}{\Omega_\Delta}\right)^2} \overset{\frac{p_{\rm F}}{\Omega_\Delta}=x}{=} \frac{\alpha_{\rm fs}px^2\mathrm{Im}\Psi(x)}{[\alpha_{\rm fs}p\mathrm{Im}\Psi(x)]^2 + [x^2 + \alpha_{\rm fs}p\mathrm{Re}\Psi(x)]^2}. \end{aligned} \tag{D.34}$$

The Ψ function becomes imaginary for real $p_{\rm F}$ (above material cone) and frequencies above the

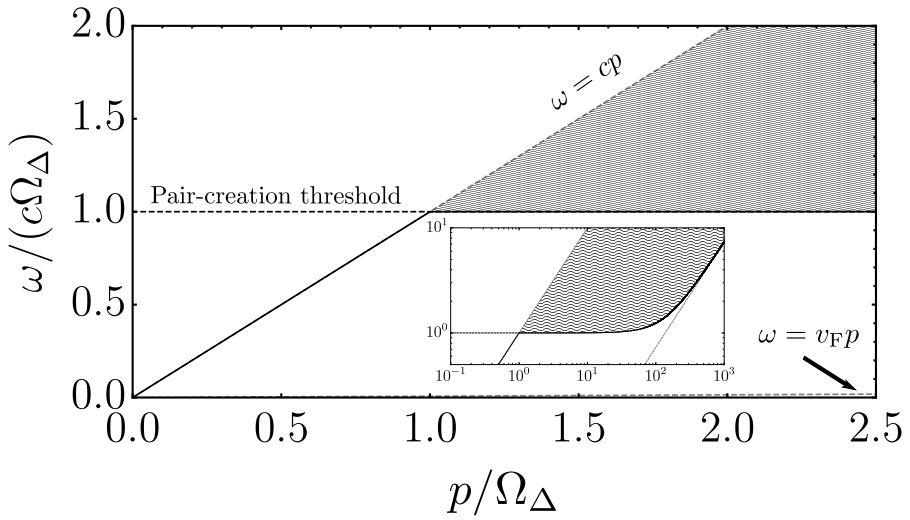

Figure D.3: Same as in Fig. D.2, but with realistic parameters $\alpha_{\rm fs} = 137^{-1}$ and $v_F = \alpha_{\rm fs} c$. The shaded area displays the relevant domain for atom-surface quantum friction. For a better overview, we report the same plot over a wide range of wavevectors in the inset.

pair-creation threshold only. Hence, we have

$$\mathrm{Im}\Psi(x) = \mathrm{Im}\left[\left(x+\frac{1}{x}\right)\mathrm{arctanh}[x] - 1\right] = -\pi\left(x+\frac{1}{x}\right)\theta(x-1) \tag{D.35}$$

as well as for the real part for $x > 1$

$$\begin{aligned}\mathrm{Re}\Psi(x)\theta(x-1) &= \mathrm{Re}\left[\left(x+\frac{1}{x}\right)\mathrm{arctanh}[x] - 1\right]\theta(x-1) \\ &= \left(\left(x+\frac{1}{x}\right)\frac{1}{2}\ln\left[\frac{x+1}{x-1}\right] - 1\right)\theta(x-1).\end{aligned} \tag{D.36}$$

Equations (D.35) and (D.36) give the exact expressions corresponding to our qualitative discussion in Eq. (3.95).

APPENDIX E

Auxiliary Calculations for the Non-additivity of Quantum Friction

In this appendix we provide additional information on the details of the calculations presented in discussion on the non-additive properties of quantum friction in Sec. 3.4.3. In particular, we display the derivations of Eqs. (3.111)-(3.116).

Starting from Eqs. (3.107) and writing $(1-r^2e^{-4pw})^{-1} = \sum_{n=0}^{\infty} r^{2n}e^{-4npw}$, the general expression for the friction force related to intrinsic dissipative degrees of freedom reads

$$
\begin{aligned}
F^{\mathrm{int}} &= -\alpha_0 v^3 \frac{\hbar}{12\pi}\frac{1}{(2\pi)^2}(2\epsilon_0\rho)\sum_{n=0}^{\infty}\int_0^{\infty}\mathrm{d}p\ \int_0^{2\pi}\mathrm{d}\phi\ p^6\cos^4\phi \qquad \text{(E.1)}\\
&\times\left(e^{-2pw}e^{-4npw}[1+2n]\left[e^{-2p(w-z_a)}+e^{2p(w-z_a)}\right]\left[\frac{p_x^2}{p^2}\mu_{xx}+\frac{p_y^2}{p^2}\mu_{yy}+\mu_{zz}\right]\right.\\
&\quad\left.-4e^{-4pw(1+n)}(1+n)\left[\frac{p_x^2}{p^2}\mu_{xx}+\frac{p_y^2}{p^2}\mu_{yy}-\mu_{zz}\right]\right)\\
&= -\alpha_0 v^3 \frac{\hbar}{12\pi}\frac{1}{(2\pi)^2}(2\epsilon_0\rho)\frac{\pi}{8}\sum_{n=0}^{\infty}\\
&\times\left(\frac{45}{8}\left[\frac{1+2n}{(z_a+2nw)^7}+\frac{1+2n}{(2[1+n]w-z_a)^7}\right]\left[5\mu_{xx}+\mu_{yy}+6\mu_{zz}\right]\right.\\
&\quad\left.-\frac{45}{256(1+n)^6w^7}\left[5\mu_{xx}+\mu_{yy}-6\mu_{zz}\right]\right).
\end{aligned}
$$

The leading order term ($n=0$) gives the naive addition of two surfaces including one roundway trip and reads

$$
\begin{aligned}
F_{\mathrm{add}}^{\mathrm{int}} &= -\alpha_0 v^3\epsilon_0\rho\hbar\frac{15}{4\pi^2} \qquad \text{(E.2)}\\
&\times\left(\left[\frac{1}{(2z_a)^7}+\frac{1}{(2[2w-z_a])^7}\right]\left[5\mu_{xx}+\mu_{yy}+6\mu_{zz}\right]-\frac{1}{32(2w)^7}\left[5\mu_{xx}+\mu_{yy}-6\mu_{zz}\right]\right).
\end{aligned}
$$

For isotropic $\underline{\mu}$, the last term vanishes and this reduces to the known result [58]. However, for anisotropic $\underline{\mu}$, the correction to the naive addition even in zeroth order of Fabry-Perot reflections

is maximal at the center of the cavity $z_a = w$ due to the strong power law dependence. Here, the correction due to roundway-trips depends on the exact values for μ_{xx}, μ_{yy} and μ_{zz}, but is at the order of $1/32 \approx 3\%$. The actual error can be expected to be much smaller due to the different sign in front of μ_{zz} so that we can safely write

$$F^{\rm int} \approx F^{\rm int}_{\rm add} = F^{\rm int}_s(z_a) + F^{\rm int}_s(2w - z_a) \tag{E.3}$$

with $F^{\rm int}_s(z_a) = -\frac{15\hbar}{4\pi^2}\frac{\alpha_0\epsilon_0[5\mu_{xx}+\mu_{yy}+6\mu_{zz}]\rho v^3}{(2z_a)^7}$. Due to the strong power law dependence of the force and since the denominator $(1 - r^2 e^{-4pw})^{-1}$ can only be different from unity for small $p \ll 1/w$, the overall correction to the above result for arbitrary order of Fabry-Perot resonances is maximal in the center of the cavity and evaluates to the result reported in Eq. (3.109). To this end, if we define the nonadditivity coefficient $\eta = F/F_{\rm add}$, we obtain for the force connected to intrinsic damping in the isotropic case $\mu_{xx} = \mu_{yy} = \mu_{zz}$ that

$$0 < \eta^{\rm int} \leq \frac{\pi^6}{960} = \frac{(\pi/2)^6}{15}. \tag{E.4}$$

The previous expression is independent of the cavity size and only depends on $r(\omega = 0) \equiv R(p)$, which can be seen from the derivative we used in order to obtain the low-frequency expansion,

$$\mathrm{Im}\lim_{\omega\to 0}\partial_\omega \frac{\mathcal{R}\left(p,\omega\right)}{(1 - r^2 e^{-4pw})^{-1}} = 8\epsilon_0\rho(p)\sum_{n=0}^{\infty}(n+1)R^{2n+1}(p)e^{-4pw(n+1)}. \tag{E.5}$$

For comparison, in the case $\mu_{zz} = 0 \neq \mu_{xx} = \mu_{yy}$, the frictional force gives

$$\frac{F^{\rm int}(z_a = w)}{F^{\rm int}_{\rm add}(z_a = w)} = \frac{\pi^6}{960}\left(1 - \frac{1}{64}\right) \approx 0.986 \tag{E.6}$$

and for $\mu_{zz} \neq 0 = \mu_{xx} = \mu_{yy}$,

$$\frac{F^{\rm int}(z_a = w)}{F^{\rm int}_{\rm add}(z_a = w)} = \frac{\pi^6}{960}\left(1 + \frac{1}{64}\right) \approx 1.017. \tag{E.7}$$

For cavity plates made from different spatially local materials (denoted by "1" and "2"), the frictional force for a isotropic intrinsic dissipation ($\mu_{xx} = \mu_{yy} = \mu_{zz} \equiv \mu$) reads

$$\begin{aligned} F^{\rm int} = &-\alpha_0 v^3 \mu\epsilon_0\hbar\frac{45}{\pi^2}\frac{1}{(2w)^7}\sum_{n=0}^{\infty}\left[r_1(0)r_2(0)\right]^n \\ &\times\left[\frac{1}{(\frac{z_a}{w}+2n)^7}\left([1+n]\rho_1 + n\frac{r_1(0)}{r_2(0)}\rho_2\right) + \frac{1}{(2[1+n]-\frac{z_a}{w})^7}\left([1+n]\rho_2 + n\frac{r_2(0)}{r_1(0)}\rho_1\right)\right]. \end{aligned} \tag{E.8}$$

The previous expression shows that the contribution of one side of the cavity to the force corresponding to the other side of the cavity (last terms in brackets) depends on the reflection properties given by the ratio $r_2(0)/r_1(0)$. For slightly different materials with $\rho_2/\rho_1 \sim 1$, the

minimum of the force is found at $(n = 0)$

$$\frac{z_a}{w} \sim \frac{9 + 7\frac{\rho_2}{\rho_1}}{8\left(1 + \frac{\rho_2}{\rho_1}\right)} \tag{E.9}$$

and hence is shifted towards the plate with smaller dissipation. Further, we note that the maximum value of the above expression is obtained for

$$r_1(0) = r_2(0) \to 1. \tag{E.10}$$

For the radiation-induced force [Eq. (3.107b)], on the other hand, we obtain

$$\begin{aligned} F^{\mathrm{rad}} = -\alpha_0^2 v^3 \hbar \frac{3}{256\epsilon_0^2\pi^3} \int_0^\infty \mathrm{d}p\mathrm{d}\tilde{p}\ \ p^2\tilde{p}^2 \\ \times \left(\left[\frac{p^4}{2} + \frac{13}{12} p^2\tilde{p}^2 \right] \left(\mathcal{P}'_{+I}\tilde{\mathcal{P}}'_{+I} + \mathcal{R}'_I\tilde{\mathcal{R}}'_I \right) \right. \\ \left. + \left[\frac{p^4}{6} + \frac{p^2\tilde{p}^2}{4} \right] \left(\mathcal{P}'_{+I}\tilde{\mathcal{R}}'_I + \mathcal{R}'_I\tilde{\mathcal{P}}'_{+I} \right) - \left[p^3\tilde{p} + \frac{p\tilde{p}^3}{3} \right] \mathcal{P}'_{-I}\tilde{\mathcal{P}}'_{-I} \right), \end{aligned} \tag{E.11}$$

where $\mathrm{Tr}\left[\underline{L}_y^{\mathrm{T}}\underline{L}_y\right] = -2$ and we transformed the integral to polar coordinates and performed the angular integration. The corresponding derivatives are given by

$$\begin{aligned} \mathrm{Im}\lim_{\omega\to 0}\partial_\omega\mathcal{P}_\pm &= 2\epsilon_0 \sum_{n=0}^\infty e^{-2pw(1+2n)} \left[r_1(0)r_2(0)\right]^n \\ &\times \left[e^{2p(w-z_a)} \left([1+n]\rho_1 + n\frac{r_1(0)}{r_2(0)}\rho_2 \right) \pm e^{-2p(w-z_a)} \left([1+n]\rho_2 + n\frac{r_2(0)}{r_1(0)}\rho_1 \right) \right] \\ &\equiv 2\epsilon_0 \sum_{n=0}^\infty \left[r_1(0)r_2(0)\right]^n \left[e^{-2p(2nw+z_a)} A_{12}(n) \pm e^{-2p(2[1+n]w-z_a)} A_{21}(n) \right] \end{aligned} \tag{E.12a}$$

$$\begin{aligned} \mathrm{Im}\lim_{\omega\to 0}\partial_\omega\mathcal{R} &= 4\epsilon_0 \sum_{n=0}^\infty (1+n) \left[r_1(0)r_2(0)\right]^n \left[r_2(0)\rho_1 + r_1(0)\rho_2\right] e^{-4pw(1+n)} \\ &\equiv 2\epsilon_0 \sum_{n=0}^\infty \left[r_1(0)r_2(0)\right]^n B(n) e^{-4pw(1+n)} \end{aligned}$$

for spatially local materials.

This yields for the radiation-induced force experienced by the atom inside the cavity

$$
\begin{aligned}
F^{\mathrm{rad}} = -\alpha_0^2 v^3 \hbar \frac{3}{64\pi^3}\frac{1}{w^{10}} \sum_{n,m=0}^{\infty} \left[r_1(0) r_2(0)\right]^{n+m} \qquad \text{(E.13)}\\
\times \Bigg(\frac{45}{64}\left[\frac{A_{12}(n)}{(2n+\frac{z_a}{w})^7} + \frac{A_{21}(n)}{(2[1+n]-\frac{z_a}{w})^7}\right]\left[\frac{A_{12}(m)}{(2m+\frac{z_a}{w})^3} + \frac{A_{21}(m)}{(2[1+m]-\frac{z_a}{w})^3}\right]\\
+ \frac{39}{64}\left[\frac{A_{12}(n)}{(2n+\frac{z_a}{w})^5} + \frac{A_{21}(n)}{(2[1+n]-\frac{z_a}{w})^5}\right]\left[\frac{A_{12}(m)}{(2m+\frac{z_a}{w})^5} + \frac{A_{21}(m)}{(2[1+m]-\frac{z_a}{w})^5}\right]\\
+ \frac{45}{1024}\frac{1}{64}\frac{B(n)}{(1+n)^7}\frac{B(m)}{(1+m)^3}\\
+ \frac{13}{12}\frac{1}{128}\frac{9}{128}\frac{B(n)}{(1+n)^5}\frac{B(m)}{(1+m)^5}\\
+ \frac{15}{512}\frac{B(m)}{(1+m)^3}\left[\frac{A_{12}(n)}{(2n+\frac{z_a}{w})^7} + \frac{A_{21}(n)}{(2[1+n]-\frac{z_a}{w})^7}\right]\\
+ \frac{45}{1024}\frac{1}{24}\frac{B(n)}{(1+n)^7}\left[\frac{A_{12}(m)}{(2m+\frac{z_a}{w})^3} + \frac{A_{21}(m)}{(2[1+m]-\frac{z_a}{w})^3}\right]\\
+ \frac{1}{64}\frac{9}{16}\frac{B(m)}{(1+m)^5}\left[\frac{A_{12}(n)}{(2n+\frac{z_a}{w})^5} + \frac{A_{21}(n)}{(2[1+n]-\frac{z_a}{w})^5}\right]\\
- \frac{15}{16}\left[\frac{A_{12}(n)}{(2n+\frac{z_a}{w})^6} - \frac{A_{21}(n)}{(2[1+n]-\frac{z_a}{w})^6}\right]\left[\frac{A_{12}(m)}{(2m+\frac{z_a}{w})^4} - \frac{A_{21}(m)}{(2[1+m]-\frac{z_a}{w})^4}\right]
\end{aligned}
$$

after radial integration. For identical plates, $r_i(0) = 1$ and at the center of the cavity, we obtain a non-additivity correction of $\eta^{\mathrm{rad}} \approx 8.66$. We obtain Eq. (3.116) from a numerical interpolation of Eq. (E.13).

APPENDIX F

Auxiliary Calculations for the Thermodynamics of Quantum Friction

We provide auxiliary calculations and proofs for the statements made in Chapter 4. This appendix relies on the explicit expressions for the electric Green tensor given in appendix A and the definition of the dynamical quantities for the particle's internal degrees of freedom given in Chapters 3 and 4.

As described in the main text, the reported results are valid for all geometries that share at least one invariant direction. Without loss of generality, we assume this direction to be along the x-axis with h being the corresponding wavevector. However, since we will focus on planar geometries with $h \equiv p_x$ and $p = |\mathbf{p}| = \sqrt{p_x^2 + p_y^2}$ for our numerical examples, we already adapt the corresponding choice of coordinates in the following derivations in order to shorten notation. This does not limit the generality of our results and can by done be performing the following transformations

$$\frac{\mathrm{d}h}{2\pi} \leftrightarrow \frac{\mathrm{d}^2\mathbf{p}}{(2\pi)^2}, \tag{F.1a}$$

$$\underline{G}(h, \mathbf{R}_a, \omega) \leftrightarrow \underline{G}(\mathbf{p}, z_a, \omega), \tag{F.1b}$$

$$\underline{G}(h \equiv p_x, \mathbf{R}_a = z_a\mathbf{z}, \omega) = \int \frac{\mathrm{d}p_y}{2\pi} \underline{G}(\mathbf{p}, z_a, \omega). \tag{F.1c}$$

Further, as explained in the main text, we use the symmetric quantum average $\langle\cdot\rangle_{\mathrm{sym}}$. However, in this appendix, in order to shorten notation, we skip the extra subscript, i.e.

$$\langle\rangle_{\mathrm{sym}} \to \langle\rangle, \qquad\qquad \underline{\nu}_{\mathrm{sym}} \to \underline{\nu}. \tag{F.2}$$

F.1 On the positive semi-definiteness of the field spectra

We intend to provide a proof of Eq. (4.20) which establishes a tensor relation between the fluctuation and the dissipation spectrum. They read

$$\underline{\nu}(\omega, v) = \hbar \int \frac{\mathrm{d}^2\mathbf{p}}{(2\pi)^2}\, \mathrm{sgn}(\omega_{\mathbf{p}}^+)\underline{G}_{\Im}(\mathbf{p}, z_a, \omega_{\mathbf{p}}^+), \qquad \underline{\gamma}(\omega, v) = \int \frac{\mathrm{d}^2\mathbf{p}}{(2\pi)^2}\, \frac{\underline{G}_{\Im}(\mathbf{p}, z_a, \omega_{\mathbf{p}}^+)}{\omega}. \tag{F.3}$$

Note that both expressions are hermitian since $\underline{G}_{\Im} = \underline{G}_{\Im}^\dagger$. Following the discussion around Eq. (3.96), we recall that a hermitian matrix can be decomposed as [M2]

$$\underline{G}_{\Im}(\mathbf{p}, z_a, \omega) = \underline{\Sigma}(\mathbf{p}, z_a, \omega) + s_y(\mathbf{p}, z_a, \omega)\underline{L}_y, \tag{F.4}$$

where we, without loss of generality, assumed the direction of motion to be along the x axis in the vicinity of a planar interface and $\underline{L}_y = -\mathrm{i}\epsilon_{yjk}$ is the generator of rotations around the y-axis and ϵ_{ijk} the Levi-Civita symbol. Due to the passivity of the materials comprising the bodies, the matrix $\underline{\Sigma}$ is real, symmetric, positive semi-definite for $\omega \geq 0$ and even in $\mathbf{p}$. The real function $\mathbf{s}_y$ is odd in $\mathbf{p}$ and, for symmetry reasons, orthogonal to the direction of motion. Hence, we can write

$$f(\mathbf{p}, z_a, \omega, v) \equiv \mathbf{a}^* \cdot \underline{G}_{\Im}(\mathbf{p}, z_a, \omega_{\mathbf{p}}^+) \cdot \mathbf{a} = \mathbf{a}^* \cdot \underline{\Sigma}(\mathbf{p}, z_a, \omega_{\mathbf{p}}^+) \cdot \mathbf{a} + 2s_y(\mathbf{p}, z_a, \omega_{\mathbf{p}}^+)\mathrm{Im}(a_x a_z^*), \quad \text{(F.5)}$$

where $\mathbf{a}$ is an arbitrary three-dimensional complex vector. At zero velocity, the asymmetric part of $\underline{\nu}$ and $\underline{\gamma}$ vanishes identically because $s_y(\mathbf{p}, z_a, \omega)$ is an odd function in $\mathbf{p}$. Since the matrix $\underline{\Sigma}$ is positive semi-definite for positive frequencies, it follows that $f(\mathbf{p}, z_a, \omega, 0) \geq 0$ for $\omega > 0$. For finite velocities, the sign of f can, in principle, depend on the particular choice of materials and the geometry of the setup and the chosen velocity. However, working in the evanescent region and focusing on non-relativistic velocities much smaller than the corresponding resonances of the system, the finite-velocity correction will not alter the qualitative behavior of the Green tensor such that we can write

$$f(\mathbf{p}, z_a, \omega, v) \geq 0 \quad \text{(F.6)}$$

for our purposes. We will explicitly show this relation for the case of a single planar interface below. For the full relation we hence obtain

$$\mathbf{a}^* \cdot \Big(\underline{\nu}(\omega, v) \pm \hbar\omega\underline{\gamma}(\omega, v)\Big) \cdot \mathbf{a} = \hbar \int \frac{\mathrm{d}^2\mathbf{p}}{(2\pi)^2} \Big[\mathrm{sgn}(\omega_{\mathbf{p}}^+) \pm 1\Big] f(\mathbf{p}, z_a, \omega, v). \quad \text{(F.7)}$$

The range of contributing wavevectors $p \lesssim 1/\lambda$ is usually constrained by the Green tensor incorporating the typical length scales λ of the system. For instance, in the evanescent region, as we will see below explicitly, the dominating length scale is given by the atom-surface separation $\lambda \sim z_a$. Consequently, for large frequencies $\omega \gtrsim v/\lambda$, the (fluctuation-dissipation) equality holds asymptotically since

$$\mathrm{sgn}(\omega + p_x v) \sim 1. \quad \text{(F.8)}$$

In the opposite limit, $\omega \ll v/\lambda$, we can expect the largest deviation from the equality. We can then approximate

$$\begin{aligned}
\int \frac{\mathrm{d}^2\mathbf{p}}{(2\pi)^2} \Big[\mathrm{sgn}(\omega_{\mathbf{p}}^+) \pm 1\Big] f(\mathbf{p}, z_a, \omega, v) &\sim \int \frac{\mathrm{d}^2\mathbf{p}}{(2\pi)^2} \Big[\mathrm{sgn}[p_x v] \pm 1\Big] f(\mathbf{p}, z_a, \omega, v) \quad \text{(F.9)} \\
&\sim \int_0^\infty \frac{\mathrm{d}^2\mathbf{p}}{(2\pi)^2} \Big[\mathrm{sgn}[p_x v] \pm 1\Big] \Big(f(\mathbf{p}, z_a, 0, v) - f(-\mathbf{p}, z_a, 0, v)\Big) \\
&= \frac{v}{|v|} \int_0^\infty \frac{\mathrm{d}^2\mathbf{p}}{(2\pi)^2} \Big[\mathrm{sgn}[p_x v] \pm 1\Big] \mathbf{a}^* \cdot \underline{\Sigma}(\mathbf{p}, z_a, 0, p_x|v|) \cdot \mathbf{a} \geq 0.
\end{aligned}$$

We note that the previous conclusion holds not only in the limiting scenarios, but is also true for arbitrary ratios between frequency ω and the Doppler-shift $p_x v$. This can be seen by simply

separating the parts of the wavevector integral with $\omega \leq p_x v$ from those with $\omega \geq p_x v$. In other words, Eq. (4.20) is a smooth function with constant sign for positive or negative velocities, respectively. Hence, for sufficiently well-behaving $f(\mathbf{p}, z_a, \omega, v)$ (positive for positive frequency and velocity), we indeed find that

$$\mathbf{a}^* \cdot \Big(\underline{\nu}(\omega, v) \pm \hbar\omega \underline{\gamma}(\omega, v) \Big) \cdot \mathbf{a} \geq 0. \tag{F.10}$$

We now consider the explicit example of a planar interface in the near-field regime. We first note that the corresponding Green tensor decomposes into a vacuum contribution $\underline{G}_0$ describing the pure vacuum in absence of the bulk and a scattered contribution $\underline{g}$ describing the interaction with the macroscopic material. Even though we work in a non-relativistic description, we need to respect Lorentz invariance, which we need to do explicitly (see also Chap. 1) by setting

$$\underline{\nu}^0(\omega, v) = \hbar \int \frac{\mathrm{d}^2\mathbf{p}}{(2\pi)^2}\, \mathrm{sgn}(\omega^+_{\mathbf{p}}) \underline{G}_{0,\Im}(\mathbf{p}, z_a, \omega^+_{\mathbf{p}}) \to \hbar \mathrm{sgn}(\omega) \int \frac{\mathrm{d}^2\mathbf{p}}{(2\pi)^2}\, \underline{G}_{0,\Im}(\mathbf{p}, z_a, \omega) \tag{F.11}$$

and similarly for $\underline{\gamma}$. This means that the regular fluctuation-dissipation relation remains unchanged for the pure vacuum contribution to the interaction, i.e.

$$\mathbf{a}^* \cdot \Big(\underline{\nu}^0(\omega, v) - \hbar\omega \underline{\gamma}^0(\omega, v) \Big) \cdot \mathbf{a} = 0. \tag{F.12}$$

As one could expect, the vacuum contribution of the fluctuations for constant velocity is not affected by the motion and we have

$$\underline{\nu}^0(\omega, v) = \hbar\omega \mathrm{sgn}(\omega) \underline{\gamma}^0(\omega, v) \tag{F.13}$$

in accordance with Ref. [422]. For the scattered ("sc") part of the Green tensor, the situation is sightly more complicated. In the near-field regime and assuming spatially local materials, the electric Green tensor can be written as (see appendix A)

$$\underline{g}(\mathbf{p}, z_a, \omega) \sim \frac{p}{2\epsilon_0} r^p_{\mathrm{NF}}(\omega) e^{-2pz_a} \tilde{\mathbf{P}}_+ \tilde{\mathbf{P}}_- \tag{F.14}$$

with r^p_{NF} the transverse magnetic reflection coefficient in the near-field regime and $\tilde{\mathbf{P}}_\pm$ the polarization vectors [189]. Following our notation of Eq. (3.96), we can identify

$$\underline{\Sigma}^{\mathrm{sc}}(\mathbf{p}, z_a, \omega) = \frac{p}{2\epsilon_0} r^p_{\mathrm{NF}}(\omega) e^{-2pz_a} \mathrm{diag}\left[p_x^2/p^2, p_y^2/p^2, 1 \right], \quad s^{\mathrm{sc}}_y(\mathbf{p}, z_a, \omega) = \frac{p_x}{2\epsilon_0} r^p_{\mathrm{NF}}(\omega) e^{-2pz_a}, \tag{F.15}$$

where $\mathrm{diag}[\cdot,\cdot,\cdot]$ gives a diagonal matrix. As anticipated above, the relevant length scale is determined by the exponential constraining the contributing wavevectors to

$$p \lesssim \frac{1}{z_a} \tag{F.16}$$

such that for frequencies $\omega_{\mathrm{sp}} \geq \omega \gtrsim \frac{v}{z_a}$, with ω_{sp} the typical resonance of the material (e.g. given by the surface plasmon-polariton excitation for the simple Drude model), the sgn-function effectively gives

$$\mathrm{sgn}(\omega + p_x v) \sim 1 \tag{F.17}$$

and we can write

$$\lim_{\omega/(v/z_a)\to\infty} \underline{\nu}^{\mathrm{sc}}(\omega, v) \sim \hbar\omega \mathrm{sgn}(\omega) \underline{\gamma}^{\mathrm{sc}}(\omega, v). \tag{F.18}$$

Consequently, in the opposite limit $\omega/(v/z_a) \to 0$, we obtain for the low-frequency fluctuations

$$\begin{aligned} \underline{\nu}^{\mathrm{sc}}(\omega \to 0, v) &\sim \hbar \int \frac{\mathrm{d}^2\mathbf{p}}{(2\pi)^2}\, \mathrm{sgn}(p_x v) \underline{g}_{\Im}(\mathbf{p}, z_a, p_x v) \\ &= \hbar \int_0^\infty \frac{\mathrm{d}^2\mathbf{p}}{(2\pi)^2} \begin{cases} \underline{g}_{\Im}(\mathbf{p}, z_a, p_x v) + \underline{g}^T_{\Im}(\mathbf{p}, z_a, p_x v), & v > 0 \\ \underline{g}_{\Im}(\mathbf{p}, z_a, p_x |v|) + \underline{g}^T_{\Im}(\mathbf{p}, z_a, p_x |v|), & v < 0 \end{cases} \\ &= 2\hbar\, \mathrm{Re} \int_0^\infty \frac{\mathrm{d}^2\mathbf{p}}{(2\pi)^2} \underline{g}_{\Im}(\mathbf{p}, z_a, p_x |v|). \end{aligned} \tag{F.19}$$

which is a symmetric matrix. For the associated low-frequency dissipation, on the other hand, we find that

$$\underline{\gamma}^{\mathrm{sc}}(\omega \to 0, v) = 2\frac{v}{|v|}\frac{\mathrm{i}}{\omega}\, \mathrm{Im} \int_0^\infty \frac{\mathrm{d}^2\mathbf{p}}{(2\pi)^2} \underline{g}_{\Im}(\mathbf{p}, z_a, p_x |v|) + 2\mathrm{Re} \int_0^\infty \frac{\mathrm{d}^2\mathbf{p}}{(2\pi)^2}\, \underline{g}'_{\Im}(\mathbf{p}, z_a, p_x |v|) \tag{F.20}$$

which is a purely anti-symmetric, hermitian and imaginary matrix in leading order of frequency. The next-to-leading order is constant with respect to frequency and a purely real and symmetric matrix. As usual, the prime indicates a derivative with respect to frequency. Upon performing the trace and inserting the explicit form of the Green tensor in the near-field using a local Drude permittivity for the near-field reflection coefficients, we directly obtain Eq. (4.24) in the main text. Further, we can identify the function

$$f(\mathbf{p}, z_a, \omega, v) = \mathbf{a}^* \cdot \underline{g}_{\Im}(\mathbf{p}, z_a, \omega^+_{\mathbf{p}}) \cdot \mathbf{a} = \frac{p}{2\epsilon_0} r^p_{\mathrm{NF},I}(\omega^+_{\mathbf{p}}) e^{-2pz_a} \frac{|a_y|^2 p_y^2 + |a_x p_x - \mathrm{i} a_z p|^2}{p^2} \geq 0 \tag{F.21}$$

for positive frequency and velocity. Hence, we explicitly found that $\underline{\nu} \pm \underline{\gamma}$ is a positive semi-definite matrix for the evanescent regime of a planar interface. From this, we can directly infer Eq. (4.22).

Lastly, we derive the particular relation for a semi-infinite planar half space reported in Eq. (4.24). Using the scattered part of the Green tensor, we obtain for the ratio between the fluctuations and the dissipation at small frequencies

$$\begin{aligned}\frac{\mathrm{Tr}\underline{\nu}^{\mathrm{sc}}}{\hbar\omega\mathrm{Tr}\underline{\gamma}^{\mathrm{sc}}}-1&=\frac{\mathrm{Tr}\underline{\nu}^{\mathrm{sc}}-\hbar\omega\mathrm{Tr}\underline{\gamma}^{\mathrm{sc}}}{\hbar\omega\mathrm{Tr}\underline{\gamma}^{\mathrm{sc}}}\\&=\frac{\int\frac{\mathrm{d}^2\mathbf{p}}{(2\pi)^2}\ \left[\mathrm{sgn}(\omega+p_xv)-1\right]\mathrm{Tr}\underline{g}_{\Im}(\mathbf{p},z_a,\omega+p_xv)}{\int\frac{\mathrm{d}^2\mathbf{p}}{(2\pi)^2}\ \mathrm{Tr}\underline{g}_{\Im}(\mathbf{p},z_a,\omega+p_xv)}\\&=\frac{2\int\frac{\mathrm{d}^2\mathbf{p}}{(2\pi)^2}\ \left[\theta(\omega+p_xv)-1\right]\mathrm{Tr}\underline{g}_{\Im}(\mathbf{p},z_a,\omega+p_xv)}{\int\frac{\mathrm{d}^2\mathbf{p}}{(2\pi)^2}\ \mathrm{Tr}\underline{g}_{\Im}(\mathbf{p},z_a,\omega+p_xv)}\\&=-\frac{2\int\mathrm{d}p_y\int_{\frac{\omega}{v}}^{\infty}\mathrm{d}p_x\ \mathrm{Tr}\underline{g}_{\Im}(\mathbf{p},z_a,\omega-p_xv)}{\int\mathrm{d}p_y\mathrm{d}p_x\ \mathrm{Tr}\underline{g}_{\Im}(\mathbf{p},z_a,\omega+p_xv)}.\end{aligned}\tag{F.22}$$

Employing the relation for the Green tensor in Eq. (F.14), we obtain

$$\begin{aligned}\frac{\mathrm{Tr}\underline{\nu}^{\mathrm{sc}}}{\hbar\omega\mathrm{Tr}\underline{\gamma}^{\mathrm{sc}}}&\sim 1-2\frac{\int\mathrm{d}p_y\int_{\frac{\omega}{v}}^{\infty}\mathrm{d}p_x\ p(\omega-p_xv)e^{-2pz_a}}{\int\mathrm{d}p_y\mathrm{d}p_x\ p(\omega+p_xv)e^{-2pz_a}}\\&=1-\frac{8z_a^3}{\pi\omega}\int_0^{\infty}\mathrm{d}p_y\int_{\frac{\omega}{v}}^{\infty}\mathrm{d}p_x\ p(\omega-p_xv)e^{-2pz_a}\\&=1+\Theta\left(\frac{\omega z_a}{v}\right)\sim\begin{cases}1, & \omega\gg\frac{v}{z_a}\\ \frac{3v}{\pi\omega z_a}, & \omega\ll\frac{v}{z_a}\end{cases},\end{aligned}\tag{F.23}$$

where we assumed $\omega+v/z$ to be in the Ohmic regime of the transverse magnetic reflection coefficient, considered ω, v to be positive and defined the positive, monotonically decreasing function

$$\Theta(\delta)\equiv\frac{4}{\pi}\int_{\delta}^{\infty}\mathrm{d}x\ \frac{x-\delta}{\delta}x^2\left[K_0(2|x|)+K_2(2|x|)\right]\tag{F.24}$$

with $K_n(x)$ the n-order modified Bessel function of second kind [607]. In the limit $\delta\ll 1$, we have $\Theta(\delta)\sim 3/(\pi\delta)-1$. For large arguments, Θ vanishes exponentially due to the involvement of the modified Bessel function [607]. Performing the analogous calculation for $v=-|v|$ leads to Eq. (4.24).

F.2 On the nonequilibrium power flux

Based on the (quantum Langevin) equation of motion describing the atom's internal degrees of freedom in Eq. (4.1), we can compute the power coming into the atomic subsystem due to fluctuations as

$$\begin{aligned} P_{\text{in}} &= \left\langle \hat{\xi}_i(t,v)\dot{\hat{d}}_i(t) \right\rangle = \int \frac{\mathrm{d}\omega}{2\pi} \int \frac{\mathrm{d}\omega'}{2\pi}\ (-\mathrm{i}\omega') e^{-\mathrm{i}(\omega+\omega')t} \alpha_{ji}(\omega',v) \left\langle \hat{\xi}_i(\omega,v)\hat{\xi}_j(\omega',v) \right\rangle \\ &= -2\mathrm{i}\hbar \int \frac{\mathrm{d}^2\mathbf{p}}{(2\pi)^2}\ \int_0^\infty \frac{\mathrm{d}\omega}{2\pi}\ \mathrm{sgn}(\omega+p_x v)(\mathrm{i}\omega)\mathrm{Tr}\left[\underline{\alpha}_{\Im}(\omega,v)\cdot\underline{G}_{\Im}(\mathbf{p},z_a,\omega+p_x v)\right] \\ &= 2\hbar \int \frac{\mathrm{d}^2\mathbf{p}}{(2\pi)^2} \int \frac{\mathrm{d}^2\mathbf{p}'}{(2\pi)^2} \int_0^\infty \frac{\mathrm{d}\omega}{2\pi}\ \omega\ \mathrm{sgn}(\omega+p_x v) \\ &\times \left[\alpha_{ik}(\omega,v) G_{\Im,km}(\mathbf{p}',z_a,\omega+p_x' v)\alpha^\dagger_{mj}(\omega,v)\right] G_{\Im,ji}(\mathbf{p},z_a,\omega+p_x v), \end{aligned} \tag{F.25}$$

where the indices denote the vector or tensor components, we sum over identical indices and used the fluctuation-dissipation-relation of second kind $\underline{\alpha}_{\Im}(\omega,v) = \underline{\alpha}(\omega,v)\cdot\int \frac{\mathrm{d}^2\mathbf{p}}{(2\pi)^2}\underline{G}_{\Im}(\mathbf{p},z_a,\omega+p_x v)\cdot\underline{\alpha}^\dagger(\omega,v)$ as well as $\underline{G}_{\Im}(-\mathbf{p},z_a,-\omega) = -\underline{G}^{\mathrm{T}}_{\Im}(\mathbf{p},z_a,\omega)$. Further, we emplyoed the stationarity of the system, i.e. $\underline{\nu}(t,t') \equiv \langle\hat{\boldsymbol{\xi}}(t)\hat{\boldsymbol{\xi}}(t')\rangle_{\text{sym}} \to \underline{\nu}(\tau)$ by means of Eq. (4.6) and used that $\underline{\nu}(-\omega,v) = \underline{\nu}^{\mathrm{T}}(\omega,v)$. The power leaving the atomic subsystem due to dissipation, on the other hand, reads

$$\begin{aligned} P_{\text{out}} &= 2\int_0^\infty \mathrm{d}\tau\ \left[\frac{\partial}{\partial\tau}\ \gamma_{ij}(\tau)\right] \left\langle \hat{d}_j(t-\tau)\dot{\hat{d}}_i(t) \right\rangle \\ &= -\int \frac{\mathrm{d}\omega'}{2\pi}\int\frac{\mathrm{d}\omega''}{2\pi}\ \int \frac{\mathrm{d}^2\mathbf{p}}{(2\pi)^2} G_{ij}(\mathbf{p},z_a,\omega'+p_x v) e^{-\mathrm{i}\omega' t} e^{-\mathrm{i}\omega'' t}(-\mathrm{i}\omega'') \left\langle \hat{d}_j(\omega')\hat{d}_i(\omega'') \right\rangle \\ &= 2\hbar \int \frac{\mathrm{d}^2\mathbf{p}}{(2\pi)^2} \int \frac{\mathrm{d}^2\mathbf{p}'}{(2\pi)^2} \int_0^\infty \frac{\mathrm{d}\omega}{2\pi}\ \omega\ \mathrm{sgn}(\omega+p_x v) \\ &\times \left[\alpha^\dagger_{kj}(\omega,v) G_{\Im,ji}(\mathbf{p}',z_a,\omega+p_x' v)\alpha_{im}(\omega,v)\right] G_{\Im,mk}(\mathbf{p},z_a,\omega+p_x v), \end{aligned} \tag{F.26}$$

where we used that $\langle\hat{\mathbf{d}}(\omega)\hat{\mathbf{d}}(\omega')\rangle = \underline{\alpha}(\omega,v)\cdot\langle\hat{\boldsymbol{\xi}}(\omega,v)\hat{\boldsymbol{\xi}}(\omega',v)\rangle\cdot\underline{\alpha}^\dagger(\omega,v)$. Summarizing, we find that

$$P_{\text{in}} = \int_0^\infty \frac{\mathrm{d}\omega}{2\pi}\ \mathrm{Tr}\left[\underline{\mathcal{P}}(\omega,v)\right], \qquad P_{\text{out}} = \int_0^\infty \frac{\mathrm{d}\omega}{2\pi}\ \mathrm{Tr}\left[\underline{\mathcal{P}}(-\omega,-v)\right]. \tag{F.27}$$

Here, we defined the function

$$\begin{aligned} \underline{\mathcal{P}}(\omega,v) &= 2\ \omega \int \frac{\mathrm{d}^2\mathbf{p}}{(2\pi)^2} \int \frac{\mathrm{d}^2\mathbf{p}'}{(2\pi)^2}\ \mathrm{sgn}(\omega+p_x v) \\ &\qquad \times \underline{\alpha}(\omega,v)\cdot\underline{G}_{\Im}(\mathbf{p}',z_a,\omega+p_x' v)\cdot\underline{\alpha}^\dagger(\omega,v)\cdot\underline{G}_{\Im}(\mathbf{p},z_a,\omega+p_x v) \\ &= 2\omega^2\ \underline{\alpha}(\omega,v)\cdot\underline{\gamma}(\omega,v)\cdot\underline{\alpha}^\dagger(\omega,v)\cdot\underline{\nu}(\omega,v), \end{aligned} \tag{F.28}$$

where we used that $\underline{\alpha}(\omega,-v)=\underline{\alpha}^{\mathrm{T}}(\omega,v)$. In our choice of signs, the full power passing the system reads

$$P=-P_{\mathrm{out}}+P_{\mathrm{in}}. \tag{F.29}$$

This comes down to computing

$$P=\int_0^\infty \frac{\mathrm{d}\omega}{2\pi}\,\mathrm{Tr}\left[\underline{\mathcal{P}}(\omega,v)-\underline{\mathcal{P}}(-\omega,-v)\right]. \tag{F.30}$$

Note that we consistently have that

$$\underline{\mathcal{P}}(\omega,0)=2\mathrm{sgn}(\omega)|\alpha(\omega,0)|^2\int\frac{\mathrm{d}^2\mathbf{p}'}{(2\pi)^2}\,\underline{G}_{\Im}(\mathbf{p}',z_a,\omega)\cdot\int\frac{\mathrm{d}^2\mathbf{p}}{(2\pi)^2}\,\underline{G}_{\Im}(\mathbf{p},z_a,\omega)=-\underline{\mathcal{P}}(-\omega,0) \tag{F.31}$$

such that the full power goes to zero in accordance with the zero-velocity fluctuation-dissipation theorem. For finite velocities, however, the main difference in the terms is in the role of the atomic polarizability. For the given setup, we can generally write [Eq. (3.23)]

$$\underline{\alpha}(\omega,v)=\underline{\alpha}_D(\omega,v)-\alpha_R(\omega,v)\underline{L}_y, \tag{F.32}$$

where $\underline{L}_y$ is the hermitian generator of rotations along the y-axis and $\underline{\alpha}_D(\omega,v)$ is a diagonal matrix. Further, we have that

$$\underline{\alpha}_D(-\omega,-v)=\underline{\alpha}_D^*(\omega,v)\qquad\qquad \alpha_R(-\omega,-v)=-\alpha_R^*(\omega,v) \tag{F.33}$$

such that under the trace we can write

$$\mathrm{Tr}\left[\underline{\mathcal{P}}(\omega,v)\right]=\mathrm{Tr}\left[\underline{\mathcal{P}}(-\omega,-v)\right] \tag{F.34}$$

and the total power of the system evaluates to zero

$$P=0,\qquad\qquad P_{\mathrm{in}}=P_{\mathrm{out}}. \tag{F.35}$$

In order to get a quantitative insight, let us consider the case for small velocities. For the incoming power we can write

$$\begin{aligned}P_{\mathrm{in}}=2\hbar\int\frac{\mathrm{d}^2\mathbf{p}}{(2\pi)^2}\int\frac{\mathrm{d}^2\mathbf{p}'}{(2\pi)^2}\int_0^\infty\frac{\mathrm{d}\omega}{2\pi}\,\omega\,\mathrm{sgn}(\omega+p_xv)\\ \times\left[\alpha_{ik}(\omega,v)G_{\Im,km}(\mathbf{p}',z_a,\omega+p_x'v)\alpha_{mj}^\dagger(\omega,v)\right]G_{\Im,ji}(\mathbf{p},z_a,\omega+p_xv).\end{aligned} \tag{F.36}$$

Assuming $v > 0$, the sign function decomposes the integral into

$$\int \frac{\mathrm{d}^2\mathbf{p}}{(2\pi)^2} \int \frac{\mathrm{d}^2\mathbf{p}'}{(2\pi)^2} \int_0^\infty \frac{\mathrm{d}\omega}{2\pi} \mathrm{sgn}(\omega + p_x v) = \tag{F.37}$$
$$\int \frac{\mathrm{d}^2\mathbf{p}'}{(2\pi)^2} \left[\int_0^\infty \frac{\mathrm{d}^2\mathbf{p}}{(2\pi)^2} \int_0^\infty \frac{\mathrm{d}\omega}{2\pi} + \int_{-\infty}^0 \frac{\mathrm{d}^2\mathbf{p}}{(2\pi)^2} \int_{-p_x v}^\infty \frac{\mathrm{d}\omega}{2\pi} - \int_{-\infty}^0 \frac{\mathrm{d}^2\mathbf{p}}{(2\pi)^2} \int_0^{-p_x v} \frac{\mathrm{d}\omega}{2\pi} \right].$$

For the last two terms, this means

$$\begin{aligned} &\int \frac{\mathrm{d}^2\mathbf{p}'}{(2\pi)^2} \left[\int_{-\infty}^0 \frac{\mathrm{d}^2\mathbf{p}}{(2\pi)^2} \int_{-p_x v}^\infty \frac{\mathrm{d}\omega}{2\pi} - \int_{-\infty}^0 \frac{\mathrm{d}^2\mathbf{p}}{(2\pi)^2} \int_0^{-p_x v} \frac{\mathrm{d}\omega}{2\pi} \right] \omega \\ &\qquad \times \left[\alpha_{ik}(\omega, v) G_{\Im,km}(\mathbf{p}', z_a, \omega + p_x' v) \alpha_{mj}^\dagger(\omega, v) \right] G_{\Im,ji}(\mathbf{p}, z_a, \omega + p_x v) \\ &= \int \frac{\mathrm{d}^2\mathbf{p}'}{(2\pi)^2} \int_0^\infty \frac{\mathrm{d}^2\mathbf{p}}{(2\pi)^2} \left[\int_{-\infty}^{-p_x v} \frac{\mathrm{d}\omega}{2\pi} + \int_0^{-p_x v} \frac{\mathrm{d}\omega}{2\pi} \right] (-\omega) \\ &\qquad \times \left[\alpha_{ik}(\omega, v) G_{\Im,km}(\mathbf{p}', z_a, \omega + p_x' v) \alpha_{mj}^\dagger(\omega, v) \right] G_{\Im,ji}(\mathbf{p}, z_a, \omega + p_x v) \end{aligned} \tag{F.38}$$

such that we obtain for the power

$$\begin{aligned} P_{\mathrm{in}} &= 2\hbar \int \frac{\mathrm{d}^2\mathbf{p}'}{(2\pi)^2} \int_0^\infty \frac{\mathrm{d}^2\mathbf{p}}{(2\pi)^2} \left[\int_{-p_x v}^\infty \frac{\mathrm{d}\omega}{2\pi} - \int_{-\infty}^{-p_x v} \frac{\mathrm{d}\omega}{2\pi} \right] \\ &\quad \times \omega \left[\alpha_{ik}(\omega, v) G_{\Im,km}(\mathbf{p}', z_a, \omega + p_x' v) \alpha_{mj}^\dagger(\omega, v) \right] G_{\Im,ji}(\mathbf{p}, z_a, \omega + p_x v) \\ &= 2\hbar \int \frac{\mathrm{d}^2\mathbf{p}'}{(2\pi)^2} \left[\int_0^\infty \frac{\mathrm{d}^2\mathbf{p}}{(2\pi)^2} \int_{-p_x v}^\infty \frac{\mathrm{d}\omega}{2\pi} + \int_{-\infty}^0 \frac{\mathrm{d}^2\mathbf{p}}{(2\pi)^2} \int_{-p_x v}^\infty \frac{\mathrm{d}\omega}{2\pi} \right] \\ &\quad \times \omega \left[\alpha_{ik}(\omega, v) G_{\Im,km}(\mathbf{p}', z_a, \omega + p_x' v) \alpha_{mj}^\dagger(\omega, v) \right] G_{\Im,ji}(\mathbf{p}, z_a, \omega + p_x v) \\ &= 2\hbar \int \frac{\mathrm{d}^2\mathbf{p}'}{(2\pi)^2} \int \frac{\mathrm{d}^2\mathbf{p}}{(2\pi)^2} \int_{-p_x v}^\infty \frac{\mathrm{d}\omega}{2\pi} \, \omega \\ &\qquad \times \left[\alpha_{ik}(\omega, v) G_{\Im,km}(\mathbf{p}', z_a, \omega + p_x' v) \alpha_{mj}^\dagger(\omega, v) \right] G_{\Im,ji}(\mathbf{p}, z_a, \omega + p_x v). \end{aligned} \tag{F.39}$$

Since the previous result considers the full range of frequencies, the finite-velicity corrections to the $v = 0$ result for the incoming power are considerably small; very much resembling the case of the dynamical Casimir-Polder force (see Sec. 3.3). However, since the small correction is accumulating over time, the consequences of making artificial assumptions on the underlying statistics of the interaction can be dramatic. In the following, we discuss the concrete example of assuming local thermal equilibrium (LTE) for an atom moving in the vicinity of a planar interface.

We can write the input power alternatively as

$$P_{\mathrm{in}} = 2 \int_0^\infty \frac{\mathrm{d}\omega}{2\pi} \, \omega \, \mathrm{Tr} \left[\underline{\alpha}_\Im(\omega, v) \cdot \underline{\nu}(\omega, v) \right]. \tag{F.40}$$

In order to find an estimate on the impact of the LTE approximation, we need to emphasize a technical subtlety here. Even though ν describes the field fluctuations in the nonequilibirum situation and is larger than the dissipation in the system, it is derived in Fourier space from the regular equilibrium fluctuation-dissipation relation. Hence, a LTE calculation would not modify the corresponding term, i.e.

$$P_{\mathrm{in}} = P_{\mathrm{in}}^{\mathrm{LTE}}. \tag{F.41}$$

However, the nonequilibrium fluctuation theorem is intimately related to the exact fluctuations of the atomic dipole by the relation $\langle \hat{\mathbf{d}}(\omega)\hat{\mathbf{d}}(\omega')\rangle = 2\pi\delta(\omega+\omega')\underline{\alpha}(\omega,v)\cdot\underline{\nu}(\omega,v)\cdot\underline{\alpha}^{\dagger}(\omega,v)$. That is exactly where the LTE would differ [43]: The LTE would also assume the dipole correlations to fulfill the equilibrium FDR leading to

$$\langle \hat{\mathbf{d}}(\omega)\hat{\mathbf{d}}(\omega')\rangle_{\mathrm{LTE}} \overset{!}{=} 2\pi\delta(\omega+\omega')\underline{\alpha}(\omega,v)\cdot\hbar\omega\mathrm{sgn}(\omega)\underline{\gamma}(\omega,v)\cdot\underline{\alpha}^{\dagger}(\omega,v). \tag{F.42}$$

This means that the LTE assumption would instead change the outgoing power,

$$\begin{aligned} P_{\mathrm{out}} \neq P_{\mathrm{out}}^{\mathrm{LTE}} = 2\hbar\int_0^\infty \frac{\mathrm{d}\omega}{2\pi}\,\omega \int \frac{\mathrm{d}^2\mathbf{p}}{(2\pi)^2}\int\frac{\mathrm{d}^2\mathbf{p}'}{(2\pi)^2} \\ \times \alpha_{jk}(\omega,v)G_{\Im,km}(\mathbf{p},z_a,\omega+p_xv)\alpha^{\dagger}_{mi}(\omega,v)G_{\Im,ij}(\mathbf{p}',z_a,\omega+p_x'v). \end{aligned} \tag{F.43}$$

Eventually, this leads to a disbalance of the total power, i.e.

$$\begin{aligned} P^{\mathrm{LTE}} = 2\hbar\int\frac{\mathrm{d}^2\mathbf{p}'}{(2\pi)^2}\int\frac{\mathrm{d}^2\mathbf{p}}{(2\pi)^2}\left[\int_{-p_xv}^{\infty}\frac{\mathrm{d}\omega}{2\pi}-\int_0^\infty\frac{d\omega}{2\pi}\right]\,\omega \\ \times\left[\alpha_{ik}(\omega,v)G_{\Im,km}(\mathbf{p}',z_a,\omega+p_x'v)\alpha^{\dagger}_{mj}(\omega,v)\right]G_{\Im,ji}(\mathbf{p},z_a,\omega+p_xv), \end{aligned} \tag{F.44}$$

that is non-zero in general and ignores important contributions of the power leaving the atom. Eventually, it could lead to falsely conclude a heating of the atom [43].

For the planar interface and in leading order α_0, the first velocity correction reads in the near-field

$$P^{\mathrm{LTE}} \sim \frac{\hbar}{\pi}\frac{\alpha_0^2v^4}{12}\int\frac{\mathrm{d}^2\mathbf{p}}{(2\pi)^2}\int\frac{\mathrm{d}^2\mathbf{p}'}{(2\pi)^2}\,p_x^2\left(p_x^2-2p_xp_x'\right)\mathrm{Tr}\left[\underline{G}'_{\Im}(\mathbf{p},z_a,0)\cdot\underline{G}'_{\Im}(\mathbf{p}',z_a,0)\right], \tag{F.45}$$

where the prime indicates a derivative with respect to frequency. Upon inserting the near-field expression of the Green tensor [see Eq. (F.14)] and choosing the locally spatial Drude model with $r^p_{\mathrm{NF},I}\sim 2\epsilon_0\rho_{\mathrm{lc}}\omega$, the power evaluates to

$$P^{\mathrm{LTE}} \sim \hbar\frac{v^4}{(2\pi)^3}\frac{\alpha_0^2\rho_{\mathrm{lc}}^2}{(2z_a)^{10}}\,(135-90) = 45\hbar\frac{v^4}{(2\pi)^3}\frac{\alpha_0^2\rho_{\mathrm{lc}}^2}{(2z_a)^{10}}. \tag{F.46}$$

The second contribution in the previous line stems from rotational degrees of freedom and is usually also neglected within the LTE approach.

F.3 Atomic steady-state energy

In our self-consistent description, we found that $P = 0$. The total energy of the atomic subsystem is hence constant and given by

$$E(\infty, v) = \frac{1}{2\alpha_0\omega_a^2} \lim_{t\to\infty} \left[\langle \dot{\hat{\mathbf{d}}}^2(t) \rangle + \omega_a^2 \langle \hat{\mathbf{d}}^2(t) \rangle \right]. \tag{F.47}$$

At late times, we already found that

$$\hat{\mathbf{d}}(t) \sim \int \frac{\mathrm{d}\omega}{2\pi} e^{-\mathrm{i}\omega t} \int \frac{\mathrm{d}^2\mathbf{p}}{(2\pi)^2} \underline{\alpha}(\omega, v) \hat{\mathbf{E}}_{\mathrm{N}}(\mathbf{p}, z_a, \omega + p_x v) e^{\mathrm{i}\mathbf{p}\mathbf{R}_a}, \tag{F.48a}$$

$$\dot{\hat{\mathbf{d}}}(t) \sim \int \frac{\mathrm{d}\omega}{2\pi} \, (-\mathrm{i}\omega) e^{-\mathrm{i}\omega t} \int \frac{\mathrm{d}^2\mathbf{p}}{(2\pi)^2} \underline{\alpha}(\omega, v) \hat{\mathbf{E}}_{\mathrm{N}}(\mathbf{p}, z_a, \omega + p_x v) e^{\mathrm{i}\mathbf{p}\mathbf{R}_a}, \tag{F.48b}$$

such that the energy can be written as

$$E(\infty, v) = \frac{\hbar}{2\alpha_0\omega_a^2} \mathrm{Tr} \int \frac{\mathrm{d}\omega}{2\pi} \int \frac{\mathrm{d}^2\mathbf{p}}{(2\pi)^2} \left[\omega_a^2 + \omega^2 \right] \mathrm{sgn}(\omega_{\mathbf{p}}^+) \underline{\alpha}(\omega, v) \cdot \underline{G}_{\Im}(\mathbf{p}, \omega_{\mathbf{p}}^+) \cdot \underline{\alpha}^\dagger(\omega). \tag{F.49}$$

At zero velocity, we can employ the FDR and obtain the equilibrium energy of the atom

$$E(\infty, 0) = \frac{\hbar}{2\alpha_0\omega_a^2} \mathrm{Tr} \int \frac{\mathrm{d}\omega}{2\pi} \, \mathrm{sgn}(\omega) \left[\omega_a^2 + \omega^2 \right] \underline{\alpha}_{\Im}(\omega). \tag{F.50}$$

The imaginary part of the polarizability is determined by the spontaneous vacuum decay rate and the interaction with the dissipative properties of the surface which means that the imaginary part of the polarizability scales at least as $\alpha_I \propto \omega^{-3}$, when no surface resonances are taken into account. This can make the integral divergent and calls for regularization (see main text and e.g. Ref. [136]) or the inclusion of surface resonances [347] or the saturation of the atomic energy using nonlinear (e.g. two-level) models [85, 456]. We are, however, more interested in the velocity corrections to the given equilibrium energy $E(\infty, 0)$ of the atom. In order to study the role of finite velocities, we rewrite the energy of the atomic subsystem in the nonequilibrium steady-state as

$$\begin{aligned} E(\infty, v) = {} & \frac{\hbar}{\alpha_0\omega_a^2} \mathrm{Tr} \int_0^\infty \frac{\mathrm{d}\omega}{2\pi} \left[\omega_a^2 + \omega^2 \right] \underline{\alpha}_{\Im}(\omega, v) \\ & - \frac{\hbar}{\alpha_0\omega_a^2} \mathrm{Tr} \int \frac{\mathrm{d}^2\mathbf{p}}{(2\pi)^2} \int_0^{p_x v} \frac{\mathrm{d}\omega}{2\pi} \left[\omega_a^2 + \omega^2 \right] \underline{\alpha}(\omega, v) \cdot \underline{G}_{\Im}^T(\mathbf{p}, \omega - p_x v) \cdot \underline{\alpha}^\dagger(\omega). \end{aligned} \tag{F.51}$$

The first term is almost identical to the equilibrium energy, but takes the velocity-dependent dressing of the atom's polarizability into account. The second term, for comparison, identically vanishes at $v = 0$. Its functional dependence for finite velocities further depends on the particularly chosen velocity in combination with the dominating length scale in the system. For planar surfaces, we have already established that $p \sim 1/z_a$. If the corresponding frequency $\omega \sim v/z_a$ is smaller than any resonance (ω_r) of the system (for planar Drude metals this would, e.g., be the surface plasmon-polariton resonance), the second term of the previous equation

shows a *power law* dependence for sufficiently small velocities. In contrary, if the frequency $v/z_a \sim \omega_r$, system and bath interact resonantly and the corresponding velocity-scaling changes to an *exponential* that vanishes for decreasing v. This can be understood by the fact that, in the resonant regime, the finite coupling between atom and bath becomes less relevant showing some resemblance to usual quantum thermodynamics [136].

Bibliography

1. P. A. M. Dirac, The Quantum Theory of the Emission and Absorption of Radiation, Proceedings of the Royal Society of London A: Mathematical, Physical and Engineering Sciences **114,** 243 (1927).
2. F. London, Zur Theorie und Systematik der Molekularkräfte, Zeitschrift für Physik **63,** 245 (1930).
3. A. Einstein, Über die von der molekularkinetischen Theorie der Wärme gefordert Bewegung von in ruhenden Flüßigkeiten suspendierten Teilchen. (German) [On the molecular-kinetic theory of the movement by heat of particles suspended in liquids at rest], **322,** 549 (1905).
4. C. Lozano, B. ten Hagen, H. Löwen and C. Bechinger, Phototaxis of synthetic microswimmers in optical landscapes, Nature Communications **7,** 12828 EP (2016).
5. H. Hähl *et al.,* Subsurface Influence on the Structure of Protein Adsorbates as Revealed by in Situ X-ray Reflectivity, Langmuir **28,** 7747 (2012).
6. The Nobel Prize in Physics 2019, press release, https://www.nobelprize.org (2019).
7. P. J. E. Peebles, Large-scale background temperature and mass fluctuations due to scale-invariant primeval perturbations, Astrophys. J. **263,** L1 (1982).
8. V. Mukhanov, H. Feldman and R. Brandenberger, Theory of cosmological perturbations, Physics Reports **215,** 203 (1992).
9. E. Calzetta and B. L. Hu, Quantum fluctuations, decoherence of the mean field, and structure formation in the early Universe, Phys. Rev. D **52,** 6770 (1995).
10. B. P. Abbott *et al.,* Observation of Gravitational Waves from a Binary Black Hole Merger, Phys. Rev. Lett. **116,** 061102 (2016).
11. W. H. Zurek, Decoherence and the transition from quantum to classical, Phys. Today **44N10,** 36 (1991).
12. B. Duplantier, J.-M. Raimond and V. Rivasseau, *Quantum Decoherence: Poincaré Seminar 2005* (Birkhäuser, Basel, 2007).
13. M. Lessel *et al.,* Impact of van der Waals Interactions on Single Asperity Friction, Phys. Rev. Lett. **111,** 035502 (2013).
14. M. Lämmel *et al.,* Aeolian sand sorting and megaripple formation, Nature Physics **14,** 759 (2018).
15. W. Heisenberg, Bemerkungen zur Diracschen Theorie des Positrons, Zeitschrift für Physik **90,** 209 (1934).
16. W. Heisenberg and H. Euler, Folgerungen aus der Diracschen Theorie des Positrons, Zeitschrift für Physik **98,** 714 (1936).

17. A. Gonoskov *et al.,* Probing Nonperturbative QED with Optimally Focused Laser Pulses, Phys. Rev. Lett. **111,** 060404 (2013).

18. F. Karbstein, A. Blinne, H. Gies and M. Zepf, Boosting Quantum Vacuum Signatures by Coherent Harmonic Focusing, Phys. Rev. Lett. **123,** 091802 (2019).

19. H. B. G. Casimir, On the Attraction Between Two Perfectly Conducting Plates, Indag. Math. **10,** 261 (1948).

20. H. B. G. Casimir and D. Polder, The Influence of Retardation on the London-van der Waals Forces, Phys. Rev. **73,** 360 (1948).

21. O. Kenneth and I. Klich, Opposites Attract: A Theorem about the Casimir Force, Phys. Rev. Lett. **97,** 160401 (2006).

22. B. V. Derjaguin, I. I. Abrikosova and E. M. Lifshitz, Direct measurement of molecular attraction between solids separated by a narrow gap, Q. Rev. Chem. Soc. **10,** 295 (1956).

23. C. I. Sukenik, M. G. Boshier, D. Cho, V. Sandoghdar and E. A. Hinds, Measurement of the Casimir-Polder force, Phys. Rev. Lett. **70,** 560 (1993).

24. G. Sagué, E. Vetsch, W. Alt, D. Meschede and A. Rauschenbeutel, Cold-Atom Physics Using Ultrathin Optical Fibers: Light-Induced Dipole Forces and Surface Interactions, Phys. Rev. Lett. **99,** 163602 (2007).

25. H. Bender, P. W. Courteille, C. Marzok, C. Zimmermann and S. Slama, Direct Measurement of Intermediate-Range Casimir-Polder Potentials, Phys. Rev. Lett. **104,** 083201 (2010).

26. S. Lepoutre *et al.,* Atom interferometry measurement of the atom-surface van der Waals interaction, The European Physical Journal D **62,** 309 (2011).

27. M. Keil *et al.,* Fifteen years of cold matter on the atom chip: promise, realizations, and prospects, J Mod Opt **63,** 1840 (2016).

28. D. A. T. Somers, J. L. Garrett, K. J. Palm and J. N. Munday, Measurement of the Casimir torque, Nature **564,** 386 (2018).

29. E. A. Chan *et al.,* Tailoring optical metamaterials to tune the atom-surface Casimir-Polder interaction, Science Advances **4** (2018).

30. M. B. Farías, F. C. Lombardo, A. Soba, P. I. Villar and R. S. Decca, Towards detecting traces of non-contact quantum friction in the corrections of the accumulated geometric phase, npj Quantum Information **6,** 25 (2020).

31. J. B. Pendry, Shearing the vacuum - quantum friction, Journal of Physics: Condensed Matter **9,** 10301 (1997).

32. R. Kubo, The fluctuation-dissipation theorem, Reports on Progress in Physics **29,** 255 (1966).

33. D. Polder and M. Van Hove, Theory of Radiative Heat Transfer between Closely Spaced Bodies, Phys. Rev. B **4,** 3303 (1971).

34. M. Antezza, L. P. Pitaevskii and S. Stringari, New Asymptotic Behavior of the Surface-Atom Force out of Thermal Equilibrium, Phys. Rev. Lett. **95,** 113202 (2005).

35. P. Ben-Abdallah, S.-A. Biehs and K. Joulain, Many-Body Radiative Heat Transfer Theory, Phys. Rev. Lett. **107,** 114301 (2011).

36. M. Krüger, T. Emig and M. Kardar, Nonequilibrium Electromagnetic Fluctuations: Heat Transfer and Interactions, Phys. Rev. Lett. **106,** 210404 (2011).

37. R. Messina, S.-A. Biehs and P. Ben-Abdallah, Surface-mode-assisted amplification of radiative heat transfer between nanoparticles, Phys. Rev. B **97,** 165437 (2018).

38. Y. Zhang, H.-L. Yi, H.-P. Tan and M. Antezza, Giant resonant radiative heat transfer between nanoparticles, Phys. Rev. B **100,** 134305 (2019).

39. C. Henkel and P. P. Schmidt, On anomalously large nano-scale heat transfer between metals, J. Opt. Soc. Am. B **36,** C10 (2019).

40. G. L. Klimchitskaya, V. M. Mostepanenko and R. I. P. Sedmik, Casimir pressure between metallic plates out of thermal equilibrium: Proposed test for the relaxation properties of free electrons, Phys. Rev. A **100,** 022511 (2019).

41. M. F. Maghrebi, A. V. Gorshkov and J. D. Sau, Fluctuation-Induced Torque on a Topological Insulator out of Thermal Equilibrium, Phys. Rev. Lett. **123,** 055901 (2019).

42. R. O. Behunin and B.-L. Hu, Nonequilibrium forces between atoms and dielectrics mediated by a quantum field, Phys. Rev. A **84,** 012902 (2011).

43. G. V. Dedkov and A. A. Kyasov, Fluctuation-electromagnetic interaction under dynamic and thermal nonequilibrium conditions, Physics-Uspekhi **60,** 559 (2017).

44. F. Intravaia *et al.,* Friction forces on atoms after acceleration, Journal of Physics: Condensed Matter **27,** 214020 (2015).

45. A. Manjavacas, F. J. Rodríguez-Fortuño, F. J. García de Abajo and A. V. Zayats, Lateral Casimir Force on a Rotating Particle near a Planar Surface, Phys. Rev. Lett. **118,** 133605 (2017).

46. D. A. R. D. P. Rodriguez-Lopez W. J. M. Kort-Kamp and L. M. Woods, Casimir force phase transitions in the graphene family, Nature Communications **8,** 14699 (2017).

47. S. Sanders, W. J. M. Kort-Kamp, D. A. R. Dalvit and A. Manjavacas, Nanoscale transfer of angular momentum mediated by the Casimir torque, Communications Physics **2,** 71 (2019).

48. N. Rivera, L. J. Wong, J. D. Joannopoulos, M. Soljacic and I. Kaminer, Light emission based on nanophotonic vacuum forces, Nature Physics (2019).

49. J. DeSutter, L. Tang and M. Francoeur, A near-field radiative heat transfer device, Nature Nanotechnology **14,** 751 (2019).

50. B. L. Hu, J. P. Paz and Y. Zhang, Quantum Brownian motion in a general environment: Exact master equation with nonlocal dissipation and colored noise, Phys. Rev. D **45,** 2843 (1992).

51. G. Ford, J. Lewis and R. O'Connell, Master Equation for an Oscillator Coupled to the Electromagnetic Field, Annals of Physics **252,** 362 (1996).

52. G. W. Ford and R. F. O'Connell, The rotating wave approximation (RWA) of quantum optics: serious defect, Physica A **243,** 377 (1997).

53. F. Intravaia, R. O. Behunin, C. Henkel, K. Busch and D. A. R. Dalvit, Failure of Local Thermal Equilibrium in Quantum Friction, Phys. Rev. Lett. **117,** 100402 (2016).

54. S. Scheel and S. Y. Buhmann, Casimir-Polder forces on moving atoms, Phys. Rev. A **80,** 042902 (2009).

55. A. A. Svidzinsky, Excitation of a uniformly moving atom through vacuum fluctuations, Phys. Rev. Research **1,** 033027 (2019).

56. J. M. Wylie and J. E. Sipe, Quantum electrodynamics near an interface. II, Phys. Rev. A **32,** 2030 (1985).

57. J. Klatt, M. B. Farías, D. A. R. Dalvit and S. Y. Buhmann, Quantum friction in arbitrarily directed motion, Phys. Rev. A **95,** 052510 (2017).

58. F. Intravaia, R. O. Behunin, C. Henkel, K. Busch and D. A. R. Dalvit, Non-Markovianity in atom-surface dispersion forces, Phys. Rev. A **94,** 042114 (2016).

59. M. Smoluchowski, Essai d'une théorie cinétique du mouvement Brownien et des milieux troubles, Bulletin International de l'Académie des Sciences de Cracovie (1906).

60. P. Langevin, Sur la théorie du mouvement brownien, C. R. Acad. Sci. (Paris) **146,** 530 (1908).

61. M. Planck, Ueber das Gesetz der Energieverteilung im Normalspectrum, Annalen der Physik **309,** 553 (1901).

62. A. Einstein, Über einen die Erzeugung und Verwandlung des Lichtes betreffenden heuristischen Gesichtspunkt, Annalen der Physik **322,** 132 (1905).

63. E. Schrödinger, Quantisierung als Eigenwertproblem, Annalen der Physik **385,** 437 (1926).

64. W. Heisenberg, Über den anschaulichen Inhalt der quantentheoretischen Kinematik und Mechanik, Zeitschrift für Physik **43,** 172 (1927).

65. H. P. Robertson, The Uncertainty Principle, Phys. Rev. **34,** 163 (1929).

66. D. Dalvit, P. Milloni, D. Roberts and F. da Rosa, *Lecture Notes in Physics 834: Casimir Physics* (Springer, Berlin, 2011).

67. P. W. Milonni, *The Quantum Vacuum* (ed P. W. Milonni) (Academic Press, San Diego, 1994).

68. S. K. Lamoreaux, The Casimir force: background, experiments, and applications, Reports on Progress in Physics **68,** 201 (2004).

69. S. K. Lamoreaux, Casimir forces: Still surprising after 60 years, Physics Today, 40 (2007).

70. J. N. Munday, A new twist on the quantum vacuum, Physics Today **72,** 74 (2019).

71. C. H. Henry and R. F. Kazarinov, Quantum noise in photonics, Rev. Mod. Phys. **68,** 801 (1996).

72. K. A. Milton, *The Casimir Effect* (World Scientific, 2001).

73. G. L. Klimchitskaya, U. Mohideen and V. M. Mostepanenko, The Casimir force between real materials: Experiment and theory, Rev. Mod. Phys. **81,** 1827 (2009).

74. S. Y. Buhmann, *Dispersion Forces I: Macroscopic Quantum Electrodynamics and Ground-State Casimir, Casimir-Polder and van der Waals Forces* (Springer, Berlin Heidelberg, 2012).

75. L. M. Woods *et al.,* Materials perspective on Casimir and van der Waals interactions, Rev. Mod. Phys. **88,** 045003 (2016).

76. A. I. Volokitin and B. Persson, *Electromagnetic Fluctuations at the Nanoscale* (Springer, Berlin, 2017).

77. B. E. Sernelius, *Fundamentals of van der Waals and Casimir Interactions* (Springer, Cham Switzerland, 2018).

78. E. M. Lifshitz, The theory of molecular attractive forces between solids, Sov. Phys. JETP **2,** 73 (1956).

79. I. E. Dzyaloshinskii, E. M. Lifshitz and L. P. Pitaevskii, General Theory of van der Waals′ Forces, Soviet Physics Uspekhi **4,** 153 (1961).

80. E. S. Sabisky and C. H. Anderson, Verification of the Lifshitz Theory of the van der Waals Potential Using Liquid-Helium Films, Phys. Rev. A **7,** 790 (1973).

81. A. Shih and V. A. Parsegian, Van der Waals forces between heavy alkali atoms and gold surfaces: Comparison of measured and predicted values, Phys. Rev. A **12,** 835 (1975).

82. V. Sandoghdar, C. I. Sukenik, E. A. Hinds and S. Haroche, Direct measurement of the van der Waals interaction between an atom and its images in a micron-sized cavity, Phys. Rev. Lett. **68,** 3432 (1992).

83. J. M. Obrecht *et al.,* Measurement of the Temperature Dependence of the Casimir-Polder Force, Phys. Rev. Lett. **98,** 063201 (2007).

84. S. Chu, L. Hollberg, J. E. Bjorkholm, A. Cable and A. Ashkin, Three-dimensional viscous confinement and cooling of atoms by resonance radiation pressure, Phys. Rev. Lett. **55,** 48 (1985).

85. C. Adams, M. Sigel and J. Mlynek, Atom optics, Physics Reports **240,** 143 (1994).

86. R. Decca *et al.,* Precise comparison of theory and new experiment for the Casimir force leads to stronger constraints on thermal quantum effects and long-range interactions, Annals of Physics **318,** 37 (2005).

87. R. S. Decca *et al.,* Tests of new physics from precise measurements of the Casimir pressure between two gold-coated plates, Phys. Rev. D **75,** 077101 (2007).

88. G. Bimonte, D. López and R. S. Decca, Isoelectronic determination of the thermal Casimir force, Phys. Rev. B **93,** 184434 (2016).

89. U. Delić *et al.,* Cavity Cooling of a Levitated Nanosphere by Coherent Scattering, Phys. Rev. Lett. **122,** 123602 (2019).

90. D. Windey *et al.,* Cavity-Based 3D Cooling of a Levitated Nanoparticle via Coherent Scattering, Phys. Rev. Lett. **122,** 123601 (2019).

91. U. Delić *et al.,* Cooling of a levitated nanoparticle to the motional quantum ground state, Science **367,** 892 (2020).

92. R. J. Cook and R. K. Hill, An electromagnetic mirror for neutral atoms, Optics Communications **43,** 258 (1982).

93. M. Kasevich and S. Chu, Atomic interferometry using stimulated Raman transitions, Phys. Rev. Lett. **67,** 181 (1991).

94. M. Kasevich and S. Chu, Measurement of the gravitational acceleration of an atom with a light-pulse atom interferometer, Applied Physics B **54,** 321 (1992).

95. A. Peters, K. Y. Chung and S. Chu, Measurement of gravitational acceleration by dropping atoms, Nature **119,** 849 (1999).

96. A. D. Cronin, J. Schmiedmayer and D. E. Pritchard, Optics and interferometry with atoms and molecules, Rev. Mod. Phys. **81,** 1051 (2009).

97. E. Vetsch *et al.,* Optical Interface Created by Laser-Cooled Atoms Trapped in the Evanescent Field Surrounding an Optical Nanofiber, Phys. Rev. Lett. **104,** 203603 (2010).

98. M. Jaffe *et al.,* Testing sub-gravitational forces on atoms from a miniature in-vacuum source mass, Nature Physics **13,** 938 EP (2017).

99. D. Becker *et al.,* Space-borne Bose-Einstein condensation for precision interferometry, Nature **562,** 391 (2018).

100. A. Landragin *et al.,* Measurement of the van der Waals Force in an Atomic Mirror, Phys. Rev. Lett. **77,** 1464 (1996).

101. F. Shimizu, Specular Reflection of Very Slow Metastable Neon Atoms from a Solid Surface, Phys. Rev. Lett. **86,** 987 (2001).

102. J. D. Perreault and A. D. Cronin, Observation of Atom Wave Phase Shifts Induced by Van Der Waals Atom-Surface Interactions, Phys. Rev. Lett. **95,** 133201 (2005).

103. C. Brand *et al.,* An atomically thin matter-wave beamsplitter, Nature Nanotechnology **10,** 845 EP (2015).

104. C. Jarzynski, Nonequilibrium Equality for Free Energy Differences, Phys. Rev. Lett. **78,** 2690 (1997).

105. A. I. Volokitin and B. N. J. Persson, Near-field radiative heat transfer and noncontact friction, Rev. Mod. Phys. **79,** 1291 (2007).

106. E. A. Calzetta and B. L. Hu, *Nonequilibrium Quantum Field Theory* (Cambridge University Press, Cambridge, 2008).

107. U. Seifert, Stochastic thermodynamics, fluctuation theorems and molecular machines, Reports on Progress in Physics **75,** 126001 (2012).

108. S. Deffner and S. Campbell, *Quantum Thermodynamics* (Morgan & Claypool Publishers, 2019).

109. G. Compagno, R. Passante and F. Persico, *Atom-Field Interactions and Dressed Atoms* (Cambridge University Press, Cambridge, 1995).

110. G. S. Agarwal, Quantum electrodynamics in the presence of dielectrics and conductors. IV. General theory for spontaneous emission in finite geometries, Phys. Rev. A **12,** 1475 (1975).

111. E. Purcell, Proceedings of the American Physical Society, Phys. Rev. **69,** 674 (1946).

112. J. M. Wylie and J. E. Sipe, Quantum electrodynamics near an interface, Phys. Rev. A **30,** 1185 (1984).

113. H. Carmichael, *An Open Systems Approach to Quantum Optics* (Springer-Verlag, Berlin, 1993).

114. C. Gerry and P. Knight, *Introductory Quantum Optics* (Cambridge University Press, 2004).

115. A. Reiserer and G. Rempe, Cavity-based quantum networks with single atoms and optical photons, Rev. Mod. Phys. **87,** 1379 (2015).

116. D. E. Chang, K. Sinha, J. M. Taylor and H. J. Kimble, Trapping atoms using nanoscale quantum vacuum forces, Nature Communications **5,** 4343 (2014).

117. J. Gallego *et al.,* Strong Purcell Effect on a Neutral Atom Trapped in an Open Fiber Cavity, Phys. Rev. Lett. **121,** 173603 (2018).

118. P. Lalanne, W. Yan, K. Vynck, C. Sauvan and J.-P. Hugonin, Light Interaction with Photonic and Plasmonic Resonances, Laser & Photonics Reviews **12,** 1700113 (2018).

119. S. Fuchs, R. Bennett, R. V. Krems and S. Y. Buhmann, Nonadditivity of Optical and Casimir-Polder Potentials, Phys. Rev. Lett. **121,** 083603 (2018).

120. S. Y. Buhmann and S. Scheel, Thermal Casimir versus Casimir-Polder Forces: Equilibrium and Nonequilibrium Forces, Phys. Rev. Lett. **100,** 253201 (2008).

121. F. Intravaia *et al.,* Strong Casimir force reduction through metallic surface nanostructuring, Nature Communications **4,** 2515 EP (2013).

122. E. Rousseau *et al.,* Radiative heat transfer at the nanoscale, Nature Photonics **3,** 514 (2009).

123. K. Y. Fong *et al.,* Phonon heat transfer across a vacuum through quantum fluctuations, Nature **576,** 243 (2019).

124. J.-J. Greffet *et al.,* Coherent emission of light by thermal sources, Nature **416,** 61 (2002).

125. C. Henkel, K. Joulain, J.-P. Mulet and J.-J. Greffet, Radiation forces on small particles in thermal near fields, Journal of Optics A: Pure and Applied Optics **4,** S109 (2002).

126. M. Sonnleitner, M. Ritsch-Marte and H. Ritsch, Attractive Optical Forces from Blackbody Radiation, Phys. Rev. Lett. **111,** 023601 (2013).

127. P. Haslinger *et al.,* Attractive force on atoms due to blackbody radiation, Nature Physics **14,** 257 (2018).

128. G. T. Moore, Quantum Theory of the Electromagnetic Field in a Variable-Length One-Dimensional Cavity, Journal of Mathematical Physics **11,** 2679 (1970).

129. V. V. Dodonov, Current status of the dynamical Casimir effect, Physica Scripta **82,** 038105 (2010).

130. R. d. M. e. Souza, F. Impens and P. A. M. Neto, Microscopic dynamical Casimir effect, Phys. Rev. A **97,** 032514 (2018).

131. B. L. Hu, A. Roura and S. Shresta, Vacuum fluctuations and moving atoms/detectors: from the Casimir–Polder to the Unruh–Davies–DeWitt–Fulling effect, Journal of Optics B: Quantum and Semiclassical Optics **6,** S698 (2004).

132. F. Intravaia, Vacuum Incalescence, arXiv:1604.02990, online preprint (2016).

133. A. I. Volokitin, Casimir friction force between a SiO2 probe and a graphene-coated SiO2 substrate, JETP Letters **104,** 504 (2016).

134. D. W. Hook, S. J. Porter and C. Herzog, Dimensions: Building Context for Search and Evaluation, Frontiers in Research Metrics and Analytics **3,** 23 (2018).

135. G. W. Ford and R. F. O'Connell, A Quantum Violation of the Second Law?, Phys. Rev. Lett. **96,** 020402 (2006).

136. J.-T. Hsiang, C. H. Chou, Y. Subaşı and B. L. Hu, Quantum thermodynamics from the nonequilibrium dynamics of open systems: Energy, heat capacity, and the third law, Phys. Rev. E **97,** 012135 (2018).

137. K. Joulain, R. Carminati, J.-P. Mulet and J.-J. Greffet, Definition and measurement of the local density of electromagnetic states close to an interface, Phys. Rev. B **68,** 245405 (2003).

138. F. Intravaia, C. Henkel and M. Antezza. *Casimir Physics* (eds D. Dalvit, P. Milonni, D. Roberts and F. da Rosa) 345 (Springer, Berlin / Heidelberg, 2011).

139. A. García-Etxarri *et al.,* Strong magnetic response of submicron Silicon particles in the infrared, Opt. Express **19,** 4815 (2011).

140. D. Barchiesi and T. Grosges, Fitting the optical constants of gold, silver, chromium, titanium, and aluminum in the visible bandwidth, Journal of Nanophotonics **8,** 083097 (2014).

141. C. Tserkezis *et al.,* Mie excitons: Understanding strong coupling in dielectric nanoparticles, Phys. Rev. B **98,** 155439 (2018).

142. D. A. Steck, Technical Report, Rubidium 87 D Line Data, Oregon Center for Optics and Department of Physics, available online at http://steck.us/alkalidata, 2010.

143. H. Haakh *et al.,* Temperature dependence of the magnetic Casimir-Polder interaction, Phys. Rev. A **80,** 062905 (2009).

144. J. A. Crosse and S. Scheel, Atomic multipole relaxation rates near surfaces, Phys. Rev. A **79,** 062902 (2009).

145. I. Fernandez-Corbaton, X. Zambrana-Puyalto, N. Bonod and C. Rockstuhl, Transverse multipolar light-matter couplings in evanescent waves, Phys. Rev. A **94,** 053822 (2016).

146. M. Hartmann, G.-L. Ingold and P. A. M. Neto, Advancing numerics for the Casimir effect to experimentally relevant aspect ratios, Physica Scripta **93,** 114003 (2018).

147. J. D. Jackson, *Classical Electrodynamics* (John Wiley & Sons, New York, 1999).

148. R. Raab and O. De Lange, *Multipole Theory in Electromagnetism: Classical, Quantum, and Symmetry Aspects, with Applications* (OUP Oxford, 2005).

149. R. Feynman, R. Leighton and M. Sands, *The Feynman Lectures on Physics, Vol. II: Mainly Electromagnetism and Matter* (Addison-Wesley, Reading, Massachusetts, 1977).

150. V. Berestetskii, E. Lifshitz and L. Pitaevskii, *Quantum Electrodynamics (Second Edition)* , Second Edition (Butterworth-Heinemann, Oxford, 1982).

151. L. Klaczynski, Haag's theorem in renormalised quantum field theories, arXiv:1602.00662, online preprint (2016).

152. R. Haag, On quantum field theories, Kong. Dan. Vid. Sel. Mat. Fys. Med. **29N12,** 1 (1955).

153. F. J. Dyson, *Why is Maxwell's Theory so hard to understand? The Second European Conference on Antennas and Propagation, EuCAP 2007* (2007), 1.

154. S. M. Rytov, *Teorija ėlektričeskich fluktuacij i teplovogo izlučenija / S. M. Rytov. Akad. Nauk SSSR, Fizičeskij Inst. im. P. M. Lebedeva*. rus (Moskva : Izdat. Akad. Nauk SSSR, Moskva, 1953).

155. G. W. Ford, J. T. Lewis and R. F. O'Connell, Quantum Langevin equation, Phys. Rev. A **37,** 4419 (1988).

156. Dalibard, J., Dupont-Roc, J. and Cohen-Tannoudji, C., Vacuum fluctuations and radiation reaction: identification of their respective contributions, J. Phys. France **43,** 1617 (1982).

157. G. Ford and R. O'Connell, Radiation reaction in electrodynamics and the elimination of runaway solutions, Physics Letters A **157,** 217 (1991).

158. P. R. Johnson and B. L. Hu, Stochastic theory of relativistic particles moving in a quantum field: Scalar Abraham-Lorentz-Dirac-Langevin equation, radiation reaction, and vacuum fluctuations, Phys. Rev. D **65,** 065015 (2002).

159. F. Intravaia, R. Behunin, P. W. Milonni, G. W. Ford and R. F. O'Connell, Consistency of a causal theory of radiative reaction with the optical theorem, Phys. Rev. A **84,** 035801 (2011).

160. C. H. Fleming, P. R. Johnson and B. L. Hu, Nonequilibrium dynamics of charged particles in a quantized electromagnetic field: causal, stable and self-consistent dynamics from 1/c expansion, Journal of Physics A: Mathematical and Theoretical **45,** 255002 (2012).

161. A. E. Rubio López and O. Romero-Isart, Radiation Reaction of a Jiggling Dipole in a Quantum Electromagnetic Field, Phys. Rev. Lett. **123,** 243603 (2019).

162. F. Intravaia and R. Behunin, Casimir effect as a sum over modes in dissipative systems, Phys. Rev. A **86,** 062517 (2012).

163. S. Y. Buhmann, D. T. Butcher and S. Scheel, Macroscopic quantum electrodynamics in nonlocal and nonreciprocal media, New Journal of Physics **14,** 083034 (2012).

164. S. Fuchs, J. A. Crosse and S. Y. Buhmann, Casimir-Polder shift and decay rate in the presence of nonreciprocal media, Phys. Rev. A **95,** 023805 (2017).

165. S. Y. Buhmann, V. N. Marachevsky and S. Scheel, Charge-parity-violating effects in Casimir-Polder potentials, Phys. Rev. A **98,** 022510 (2018).

166. A. Hanke and W. Zwerger, Density of states of a damped quantum oscillator, Phys. Rev. E **52,** 6875 (1995).

167. L. D. Landau, On the vibrations of the electronic plasma, J. Phys.(USSR) **10,** 25 (1946).

168. S.-i. Sasa and H. Tasaki, Steady State Thermodynamics, Journal of Statistical Physics **125,** 125 (2006).

169. L. Landau and E. Lifshitz, *Statistical Physics (Third Edition)*, Third Edition (Pergamon International, Oxford, 1980).

170. T. Matsubara, A New Approach to Quantum-Statistical Mechanics, Progress of Theoretical Physics **14,** 351 (1955).

171. R. Kubo, Statistical-Mechanical Theory of Irreversible Processes. I. General Theory and Simple Applications to Magnetic and Conduction Problems, Journal of the Physical Society of Japan **12,** 570 (1957).

172. R. Haag, N. M. Hugenholtz and M. Winnink, On the equilibrium states in quantum statistical mechanics, Communications in Mathematical Physics **5,** 215 (1967).

173. X. L. Li, G. W. Ford and R. F. O'Connell, Energy balance for a dissipative system, Phys. Rev. E **48,** 1547 (1993).

174. I. R. Senitzky, Comment on "Energy balance for a dissipative system", Phys. Rev. E **51,** 5166 (1995).

175. H. Nyquist, Thermal Agitation of Electric Charge in Conductors, Phys. Rev. **32,** 110 (1928).

176. H. B. Callen and T. A. Welton, Irreversibility and Generalized Noise, Phys. Rev. **83,** 34 (1951).

177. L. P. Pitaevskii, Thermal Lifshitz Force between an Atom and a Conductor with a Small Density of Carriers, Phys. Rev. Lett. **101,** 163202 (2008).

178. B. Geyer, G. L. Klimchitskaya, U. Mohideen and V. M. Mostepanenko, Comment on "Thermal Lifshitz Force between an Atom and a Conductor with a Small Density of Carriers", Phys. Rev. Lett. **102,** 189301 (2009).

179. S. Scheel, S. Y. Buhmann, C. Clausen and P. Schneeweiss, Directional spontaneous emission and lateral Casimir-Polder force on an atom close to a nanofiber, Phys. Rev. A **92,** 043819 (2015).

180. D. Reiche, *Equilibrium and non-equilibrium atom-surface interaction and the influence of spatial dispersion*, MA thesis (Department of Physics, Humboldt-Universität zu Berlin, 2016).

181. W. Eckhardt, Macroscopic theory of electromagnetic fluctuations and stationary radiative heat transfer, Phys. Rev. A **29,** 1991 (1984).

182. J.-P. Mulet, K. Joulain, R. Carminati and J.-J. Greffet, Enhanced Radiative Heat Transfer at Nanometric Distances, Microscale Thermophysical Engineering **6,** 209 (2002).

183. M. Arndt and K. Hornberger, Testing the limits of quantum mechanical superpositions, Nature Physics **10,** 271 (2014).

184. H. Haakh and C. Henkel, Magnetic near fields as a probe of charge transport in spatially dispersive conductors, The European Physical Journal B **85** (2012).

185. R. Estrada and R. Kanwal, A distributional theory for asymptotic expansions, Proceedings of the Royal Society of London A: Mathematical, Physical and Engineering Sciences **38,** 399 (1990).

186. R. Estrada and S. A. Fulling, How singular functions define distributions, Journal of Physics A: Mathematical and General **35,** 3079 (2002).

187. C. Henkel, P. Krüger, R. Folman and J. Schmiedmayer, Fundamental limits for coherent manipulation on atom chips, Applied Physics B **76,** 173 (2003).

188. C. Tai, I. Antennas, P. Society, I. M. Theory and T. Society, *Dyadic Green Functions in Electromagnetic Theory* (IEEE Press, New York, 1994).

189. M. S. Tomaš, Green function for multilayers: Light scattering in planar cavities, Phys. Rev. A **51,** 2545 (1995).

190. R. Carminati *et al.,* Electromagnetic density of states in complex plasmonic systems, Surface Science Reports **70,** 1 (2015).

191. D. Pines and P. Nozieres, *The theory of quantum liquids Volume I: Normal Fermi Liquids* (W.A. Benjamin, Inc, New York, 1966).

192. P. Anderson, *Basic Notions of Condensed Matter Physics* (Addison-Wesley, Reading, 1984).

193. J. Ziman, *Prinzipien der Festkörpertheorie* (Harri Deutsch Verlag, Frankfurt am Main, 1992).

194. C. Kittel, *Introduction to Solid State Physics* (Wiley, 1996).

195. M. Dressel and G. Grüner, *Electrodynamics of Solids: Optical Properties of Electrons in Matter* (Cambridge University Press, 2002).

196. G. Giuliani and G. Vignale, *Quantum Theory of the Electron Liquid* (Cambridge University Press, 2005).

197. J. Lindhard, On the Properties of a Gas of Charged Particles, Kgl. Danske Videnskab. Selskab Mat.-fys. Medd. **28** (1954).

198. N. A. Mortensen, S. Raza, M. Wubs, T. Søndergaard and S. I. Bozhevolnyi, A generalized non-local optical response theory for plasmonic nanostructures, Nature Communications **5,** 3809 EP (2014).

199. F. Bloch, Inkohärente Röntgenstreuung und Dichteschwankungen eines entarteten Fermigases, Helv. Phys. Acta **7,** 385 (1934).

200. K. L. Kliewer and R. Fuchs, Anomalous Skin Effect for Specular Electron Scattering and Optical Experiments at Non-Normal Angles of Incidence, Phys. Rev. **172,** 607 (1968).

201. W. E. Jones, K. L. Kliewer and R. uchs, Nonlocal Theory of the Optical Properties of Thin Metallic Films, Phys. Rev. **178,** 1201 (1969).

202. P. J. Feibelman, Surface electromagnetic fields, Progress in Surface Science **12,** 287 (1982).

203. W. L. Mochán, R. Fuchs and R. G. Barrera, Surface contribution to the optical properties of nonlocal systems, Phys. Rev. B **27,** 771 (1983).

204. R. Esquivel, C. Villarreal and W. L. Mochán, Exact surface impedance formulation of the Casimir force: Application to spatially dispersive metals, Phys. Rev. A **68,** 52103 (2003).

205. R. Esquivel-Sirvent, C. Villarreal, W. L. Mochán, A. M. Contreras-Reyes and V. B. Svetovoy, Spatial dispersion in Casimir forces: a brief review, Journal of Physics A: Mathematical and General **39,** 6323 (2006).

206. B. Horovitz and C. Henkel, Surface plasmons at composite surfaces with diffusive charges, EPL (Europhysics Letters) **97,** 57010 (2012).

207. T. V. Teperik, P. Nordlander, J. Aizpurua and A. G. Borisov, Robust Subnanometric Plasmon Ruler by Rescaling of the Nonlocal Optical Response, Phys. Rev. Lett. **110,** 263901 (2013).

208. S. Raza, S. I. Bozhevolnyi, M. Wubs and N. A. Mortensen, Nonlocal optical response in metallic nanostructures, Journal of Physics: Condensed Matter **27,** 183204 (2015).

209. R. Schmidt and S. Scheel, Local density of states near spatially dispersive nanospheres, Phys. Rev. A **93,** 033804 (2016).

210. R. Schmidt and S. Scheel, Radiative heat transfer between spatially nonlocally responding dielectric objects, Journal of Physics B: Atomic, Molecular and Optical Physics **51,** 044003 (2018).

211. G. Ford and W. Weber, Electromagnetic interactions of molecules with metal surfaces, Physics Reports **113,** 195 (1984).

212. D.-N. Huynh, *Nonlinear optical phenomena within the discontinuous Galerkin time-domain method*, PhD thesis (Humboldt-Universität zu Berlin, Mathematisch - Naturwissenschaftliche Fakultät, 2018).

213. A. B. Pippard and W. L. Bragg, The surface impedance of superconductors and normal metals at high frequencies II. The anomalous skin effect in normal metals, Proceedings of the Royal Society of London A: Mathematical, Physical and Engineering Sciences **191,** 385 (1947).

214. G. E. H. Reuter and E. H. Sondheimer, The theory of the anomalous skin effect in metals, Proceedings of the Royal Society of London A: Mathematical, Physical and Engineering Sciences **195,** 336 (1948).

215. R. G. Chambers, The anomalous skin effect, Proceedings of the Royal Society of London A: Mathematical, Physical and Engineering Sciences **215,** 481 (1952).

216. I. M. Kaganova and M. I. Kaganov, Effective surface impedance of polycrystals under anomalous skin effect conditions, Phys. Rev. B **63,** 054202 (2001).

217. G. Toscano *et al.,* Resonance shifts and spill-out effects in self-consistent hydrodynamic nanoplasmonics, Nature Communications **6,** 7132 (2015).

218. K. L. Kliewer and R. Fuchs, Collective Electronic Motion in a Metallic Slab, Phys. Rev. **153,** 498 (1967).

219. F. Intravaia and K. Busch, Fluorescence in nonlocal dissipative periodic structures, Phys. Rev. A **91,** 053836 (2015).

220. K. L. Kliewer and R. Fuchs, *s*-Polarized Optical Properties of Metals, Phys. Rev. B **2,** 2923 (1970).

221. R. Esquivel and V. B. Svetovoy, Correction to the Casimir force due to the anomalous skin effect, Phys. Rev. A **69,** 062102 (2004).

222. G. L. Klimchitskaya and V. M. Mostepanenko, Comment on "Effects of spatial dispersion on electromagnetic surface modes and on modes associated with a gap between two half spaces", Phys. Rev. B **75,** 036101 (2007).

223. B. E. Sernelius, Reply to "Comment on 'Effects of spatial dispersion on electromagnetic surface modes and on modes associated with a gap between two half spaces' ", Phys. Rev. B **75,** 036102 (2007).

224. M. Hartmann, G.-L. Ingold and P. A. M. Neto, Plasma versus Drude Modeling of the Casimir Force: Beyond the Proximity Force Approximation, Phys. Rev. Lett. **119,** 043901 (2017).

225. A. Reyes-Coronado, C. G. Ortíz-Solano, N. Zabala, A. Rivacoba and R. Esquivel-Sirvent, Analysis of electromagnetic forces and causality in electron microscopy, Ultramicroscopy **192,** 80 (2018).

226. P. Drude, Zur Elektronentheorie der Metalle, Annalen der Physik **306,** 566 (1900).

227. F. Intravaia, S. Å. Ellingsen and C. Henkel, Casimir-Foucault interaction: Free energy and entropy at low temperature, Phys. Rev. A **82,** 032504 (2010).

228. J. C. M. Garnett, Colours in Metal Glasses and in Metallic Films, Philosophical Transactions of the Royal Society of London. Series A, Containing Papers of a Mathematical or Physical Character **203,** 385 (1904).

229. J. C. M. Garnett, Colours in Metal Glasses, in Metallic Films, and in Metallic Solutions. II, Philosophical Transactions of the Royal Society of London. Series A, Containing Papers of a Mathematical or Physical Character **205,** 237 (1906).

230. G. Mie, Beiträge zur Optik trüber Medien, speziell kolloidaler Metallösungen, Annalen der Physik **330,** 377 (1908).

231. R. H. Ritchie, Plasma Losses by Fast Electrons in Thin Films, Phys. Rev. **106,** 874 (1957).

232. R. Ritchie, Surface plasmons in solids, Surface Science **34,** 1 (1973).

233. J. M. Pitarke, V. M. Silkin, E. V. Chulkov and P. M. Echenique, Theory of surface plasmons and surface-plasmon polaritons, Reports on Progress in Physics **70,** 1 (2007).

234. K. Y. Bliokh, Y. P. Bliokh, V. Freilikher, S. Savel'ev and F. Nori, Colloquium: Unusual resonators: Plasmonics, metamaterials, and random media, Rev. Mod. Phys. **80,** 1201 (2008).

235. K. Busch, M. König and J. Niegemann, Discontinuous Galerkin methods in nanophotonics, Laser & Photonics Reviews **5,** 773 (2011).

236. M. Oelschläger, K. Busch and F. Intravaia, Nonequilibrium atom-surface interaction with lossy multilayer structures, Phys. Rev. A **97,** 062507 (2018).

237. J. C. Maxwell, I. On the induction of electric currents in an infinite plane sheet of uniform conductivity, Proceedings of the Royal Society of London **20,** 159 (1872).

238. C. Henkel and F. Intravaia, On the Casimir entropy between 'perfect crystals', Int. J. Mod. Phys. **A25,** 2328 (2010).

239. C. Henkel, Thermally excited quasiparticles in metals, dispersion forces, and the thermal anomaly, Modern Physics Letters A **35,** 2040009 (2020).

240. L. D. Landau, The theory of a Fermi Liquid, Sov. Phys. JETP (USSR) **3,** 920 (1957).

241. L. D. Landau, On the Theory of the Fermi Liquid, Sov. Phys. JETP (USSR) **8,** 70 (1958).

242. G. Manfredi, How to model quantum plasma, Fields Institute Communications **46** (2005).

243. J. Heinrichs, Response of Metal Surfaces to Static and Moving Point Charges and to Polarizable Charge Distributions, Phys. Rev. B **8,** 1346 (1973).

244. G. Baym and C. Pethick, *Landau Fermi-Liquid Theory: Concepts and Applications* (Wiley, 2008).

245. G. Barton, Some surface effects in the hydrodynamic model of metals, Reports on Progress in Physics **42,** 963 (1979).

246. P. Halevi, Hydrodynamic model for the degenerate free-electron gas: Generalization to arbitrary frequencies, Phys. Rev. B **51,** 7497 (1995).

247. G. S. Atwal and N. W. Ashcroft, Relaxation of an electron system: Conserving approximation, Phys. Rev. B **65,** 115109 (2002).

248. D. A. R. Dalvit and S. K. Lamoreaux, Contribution of Drifting Carriers to the Casimir-Lifshitz and Casimir-Polder Interactions With Semiconductor Materials, Phys. Rev. Lett. **101,** 163203 (2008).

249. R. H. Ritchie, On Surface Plasma Oscillations in Metal Foils, Progress of Theoretical Physics **29,** 607 (1963).

250. D. P. Fromm, A. Sundaramurthy, P. J. Schuck, G. Kino and W. E. Moerner, Gap-Dependent Optical Coupling of Single "Bowtie" Nanoantennas Resonant in the Visible, Nano Letters **4,** 957 (2004).

251. M. Moeferdt, T. Kiel, T. Sproll, F. Intravaia and K. Busch, Plasmonic modes in nanowire dimers: A study based on the hydrodynamic Drude model including nonlocal and nonlinear effects, Phys. Rev. B **97,** 075431 (2018).

252. S. Franke *et al.,* Quantization of Quasinormal Modes for Open Cavities and Plasmonic Cavity Quantum Electrodynamics, Phys. Rev. Lett. **122,** 213901 (2019).

253. N. D. Mermin, Lindhard Dielectric Function in the Relaxation-Time Approximation, Phys. Rev. B **1,** 2362 (1970).

254. P.-O. Chapuis, S. Volz, C. Henkel, K. Joulain and J.-J. Greffet, Effects of spatial dispersion in near-field radiative heat transfer between two parallel metallic surfaces, Phys. Rev. B **77,** 035431 (2008).

255. P. L. Bhatnagar, E. P. Gross and M. Krook, A Model for Collision Processes in Gases. I. Small Amplitude Processes in Charged and Neutral One-Component Systems, Phys. Rev. **94,** 511 (1954).

256. F. Haas, A magnetohydrodynamic model for quantum plasmas, Physics of Plasmas **12,** 062117 (2005).

257. A. K. Das, The relaxation-time approximation in the RPA dielectric formulation, Journal of Physics F: Metal Physics **5,** 2035 (1975).

258. N. V. Kampen, The dispersion equation for plasma waves, Physica **23,** 641 (1957).

259. V. B. Svetovoy, Application of the Lifshitz Theory to Poor Conductors, Phys. Rev. Lett. **101,** 163603 (2008).

260. I. Hamberg and C. G. Granqvist, Transparent and infrared-reflecting indium-tin-oxide films: quantitative modeling of the optical properties, Appl. Opt. **24,** 1815 (1985).

261. I. Pirozhenko and A. Lambrecht, Influence of slab thickness on the Casimir force, Phys. Rev. A **77,** 013811 (2008).

262. G. E. Jellison and F. A. Modine, Parameterization of the optical functions of amorphous materials in the interband region, Applied Physics Letters **69,** 371 (1996).

263. H. Fujiwara and M. Kondo, Effects of carrier concentration on the dielectric function of ZnO:Ga and In_2O_3 : Sn studied by spectroscopic ellipsometry: Analysis of free-carrier and band-edge absorption, Phys. Rev. B **71,** 075109 (2005).

264. M. Bordag and I. G. Pirozhenko, Transverse-electric surface plasmon for graphene in the Dirac equation model, Phys. Rev. B **89,** 035421 (2014).

265. J. F. M. Werra, F. Intravaia and K. Busch, TE resonances in graphene-dielectric structures, Journal of Optics **18,** 034001 (2016).

266. J. F. M. Werra, P. Krüger, K. Busch and F. Intravaia, Determining graphene's induced band gap with magnetic and electric emitters, Phys. Rev. B **93,** 081404 (2016).

267. S. Yves, T. Berthelot, M. Fink, G. Lerosey and F. Lemoult, Measuring Dirac Cones in a Subwavelength Metamaterial, Phys. Rev. Lett. **121,** 267601 (2018).

268. P. Giannozzi, S. de Gironcoli, P. Pavone and S. Baroni, Ab initio calculation of phonon dispersions in semiconductors, Phys. Rev. B **43,** 7231 (1991).

269. R. O. Jones, Density functional theory: Its origins, rise to prominence, and future, Rev. Mod. Phys. **87,** 897 (2015).

270. F. Intravaia and C. Henkel, *Mode contributions to the Casimir effect Quantum Field Theory Under the Influence of External Conditions (QFEXT09)* **1** (2010), 199.

271. Y. De Wilde *et al.,* Thermal radiation scanning tunnelling microscopy, Nature **444,** 740 (2006).

272. L. van Hove, Quantum-mechanical perturbations giving rise to a statistical transport equation, Physica **21,** 517 (1954).

273. V. A. Golyk, M. Krüger and M. Kardar, Heat radiation from long cylindrical objects, Phys. Rev. E **85,** 046603 (2012).

274. V. A. Golyk, M. Krüger, M. T. H. Reid and M. Kardar, Casimir forces between cylinders at different temperatures, Phys. Rev. D **85,** 065011 (2012).

275. A. E. Rubio López, P. M. Poggi, F. C. Lombardo and V. Giannini, Landauer's formula breakdown for radiative heat transfer and nonequilibrium Casimir forces, Phys. Rev. A **97,** 042508 (2018).

276. L. Zhu, Y. Guo and S. Fan, Theory of many-body radiative heat transfer without the constraint of reciprocity, Phys. Rev. B **97,** 094302 (2018).

277. C. Guo, Y. Guo and S. Fan, Relation between photon thermal Hall effect and persistent heat current in nonreciprocal radiative heat transfer, Phys. Rev. B **100,** 205416 (2019).

278. L. Fan *et al.,* Nonreciprocal radiative heat transfer between two planar bodies, Phys. Rev. B **101,** 085407 (2020).

279. L. Zhu and S. Fan, Near-complete violation of detailed balance in thermal radiation, Phys. Rev. B **90,** 220301 (2014).

280. P. Ben-Abdallah, Photon Thermal Hall Effect, Phys. Rev. Lett. **116,** 084301 (2016).

281. B. V. Budaev and D. B. Bogy, On the role of acoustic waves (phonons) in equilibrium heat exchange across a vacuum gap, Applied Physics Letters **99,** 053109 (2011).

282. J. B. Pendry, K. Sasihithlu and R. V. Craster, Phonon-assisted heat transfer between vacuum-separated surfaces, Phys. Rev. B **94,** 075414 (2016).

283. M. Antezza, Surface-atom force out of thermal equilibrium and its effect on ultra-cold atoms, Journal of Physics A: Mathematical and General **39,** 6117 (2006).

284. R. Carminati and J.-J. Greffet, Near-Field Effects in Spatial Coherence of Thermal Sources, Phys. Rev. Lett. **82,** 1660 (1999).

285. C. Henkel, K. Joulain, R. Carminati and J.-J. Greffet, Spatial coherence of thermal near fields, Optics Communications **186,** 57 (2000).

286. W. Zhou and H. Yu, Energy shift and Casimir-Polder force for an atom out of thermal equilibrium near a dielectric substrate, Phys. Rev. A **90,** 032501 (2014).

287. M. Luo, J. Dong, J. Zhao, L. Liu and M. Antezza, Radiative heat transfer between metallic nanoparticle clusters in both near field and far field, Phys. Rev. B **99,** 134207 (2019).

288. J.-T. Hsiang and B. L. Hu, Nonequilibrium steady state in open quantum systems: Influence action, stochastic equation and power balance, Annals of Physics **362,** 139 (2015).

289. G. Barton, Near-Field Heat Flow Between Two Quantum Oscillators, Journal of Statistical Physics **165,** 1153 (2016).

290. S. Å. Ellingsen, S. Y. Buhmann and S. Scheel, Temperature-independent Casimir-Polder forces in arbitrary geometries, Phys. Rev. A **84,** 060501 (2011).

291. S. Å. Ellingsen, S. Y. Buhmann and S. Scheel, Casimir-Polder energy-level shifts of an out-of-equilibrium particle near a microsphere, Phys. Rev. A **85,** 022503 (2012).

292. S. Y. Buhmann, H. T. Dung and D.-G. Welsch, The van der Waals energy of atomic systems near absorbing and dispersing bodies, Journal of Optics B: Quantum and Semiclassical Optics **6,** S127 (2004).

293. L. P. Pitaevskii, Long-distance behaviour of the surface–atom Casimir–Polder forces out of thermal equilibrium, Journal of Physics A: Mathematical and General **39,** 6665 (2006).

294. P. T. Kristensen, K. Herrmann, F. Intravaia and K. Busch, Modeling electromagnetic resonators using quasinormal modes, Adv. Opt. Photon. **12,** 612 (2020).

295. M. B. Doost, W. Langbein and E. A. Muljarov, Resonant state expansion applied to two-dimensional open optical systems, Phys. Rev. A **87,** 043827 (2013).

296. E. Travkin *et al.,* Anomalous resonances of an optical microcavity with a hyperbolic metamaterial core, Phys. Rev. B **97,** 195133 (2018).

297. C. C. Gerry and P. L. Knight, Quantum superpositions and Schrödinger cat states in quantum optics, American Journal of Physics **65,** 964 (1997).

298. M. Aspelmeyer, T. J. Kippenberg and F. Marquardt, Cavity optomechanics, Rev. Mod. Phys. **86,** 1391 (2014).

299. W. H. Renninger, P. Kharel, R. O. Behunin and P. T. Rakich, Bulk crystalline optomechanics, Nature Physics **14,** 601 (2018).

300. J. Feist, J. Galego and F. J. Garcia-Vidal, Polaritonic Chemistry with Organic Molecules, ACS Photonics **5,** 205 (2018).

301. J. Galego, C. Climent, F. J. Garcia-Vidal and J. Feist, Cavity Casimir-Polder Forces and Their Effects in Ground-State Chemical Reactivity, Phys. Rev. X **9,** 021057 (2019).

302. G. S. Agarwal, *Quantum Optics* (Cambridge University Press, 2012).

303. L. Mandel and E. Wolf, *Optical coherence and quantum optics* (Cambridge University Press, Cambridge, 1995).

304. P. L. Knight and V. Bužek. *Quantum Squeezing* (eds P. D. Drummond and Z. Ficek) 3 (Springer, Berlin, 2004).

305. S. Bose, K. Jacobs and P. L. Knight, Preparation of nonclassical states in cavities with a moving mirror, Phys. Rev. A **56,** 4175 (1997).

306. R. O. Behunin, N. T. Otterstrom, P. T. Rakich, S. Gundavarapu and D. J. Blumenthal, Fundamental noise dynamics in cascaded-order Brillouin lasers, Phys. Rev. A **98,** 023832 (2018).

307. M. Reitz, C. Sommer and C. Genes, Langevin Approach to Quantum Optics with Molecules, Phys. Rev. Lett. **122,** 203602 (2019).

308. A. Puglisi, A. Sarracino and A. Vulpiani, Temperature in and out of equilibrium: A review of concepts, tools and attempts, Physics Reports **709-710,** 1 (2017).

309. D. Zhang, X. Zheng and M. D. Ventra, Local temperatures out of equilibrium, Physics Reports **830,** 1 (2019).

310. W. Nolting, *Grundkurs Theoretische Physik 6: Statistische Physik* (Springer, 2007).

311. A. Einstein, Strahlungs-Emission und Absorption nach der Quantentheorie, Deutsche Physikalische Gesellschaft **18,** 318 (1916).

312. V. Weisskopf and E. Wigner, Berechnung der natürlichen Linienbreite auf Grund der Diracschen Lichttheorie, Zeitschrift für Physik **63,** 54 (1930).

313. D. Braak, Q.-H. Chen, M. T. Batchelor and E. Solano, Semi-classical and quantum Rabi models: in celebration of 80 years, Journal of Physics A: Mathematical and Theoretical **49,** 300301 (2016).

314. L. Amico, G. Birkl, M. Boshier and L.-C. Kwek, Focus on atomtronics-enabled quantum technologies, New Journal of Physics **19,** 020201 (2017).

315. E. R. Elliott, M. C. Krutzik, J. R. Williams, R. J. Thompson and D. C. Aveline, NASA's Cold Atom Lab (CAL): system development and ground test status, npj Microgravity **4,** 16 (2018).

316. H. B. Chan, V. A. Aksyuk, R. N. Kleiman, D. J. Bishop and F. Capasso, Nonlinear Micromechanical Casimir Oscillator, Phys. Rev. Lett. **87,** 211801 (2001).

317. Y. Meng, A. Dareau, P. Schneeweiss and A. Rauschenbeutel, Near-Ground-State Cooling of Atoms Optically Trapped 300 nm Away from a Hot Surface, Phys. Rev. X **8,** 031054 (2018).

318. P. Glick *et al.,* A Soft Robotic Gripper With Gecko-Inspired Adhesive, IEEE Robotics and Automation Letters **3,** 903 (2018).

319. G. W. Ford, J. T. Lewis and R. F. O'Connell, Quantum Oscillator in a Blackbody Radiation Field, Phys. Rev. Lett. **55,** 2273 (1985).

320. W. E. Lamb and R. C. Retherford, Fine Structure of the Hydrogen Atom by a Microwave Method, Phys. Rev. **72,** 241 (1947).

321. F. Intravaia and A. Lambrecht, Surface Plasmon Modes and the Casimir Energy, Phys. Rev. Lett. **94,** 110404 (2005).

322. A. O. Sushkov, W. J. Kim, D. A. R. Dalvit and S. K. Lamoreaux, Observation of the thermal Casimir force, Nature Physics **7,** 230 (2011).

323. G. Ford, J. Lewis and R. O'Connell, Quantum oscillator in a blackbody radiation field II. Direct calculation of the energy using the fluctuation-dissipation theorem, Annals of Physics **185,** 270 (1988).

324. F. Intravaia and C. Henkel, Casimir Interaction from Magnetically Coupled Eddy Currents, Phys. Rev. Lett. **103,** 130405 (2009).

325. V. B. Bezerra, G. L. Klimchitskaya, V. M. Mostepanenko and C. Romero, Violation of the Nernst heat theorem in the theory of the thermal Casimir force between Drude metals, Phys. Rev. A **69,** 022119 (2004).

326. F. Intravaia and C. Henkel, Casimir energy and entropy between dissipative mirrors, Journal of Physics A: Mathematical and Theoretical **41,** 164018 (2008).

327. K. A. Milton *et al.,* Negative entropies in Casimir and Casimir-Polder interactions, Fortschr. Phys. **65,** 1600047 (2017).

328. G.-L. Ingold *et al.,* Geometric origin of negative Casimir entropies: A scattering-channel analysis, Phys. Rev. E **91,** 033203 (2015).

329. A. A. Banishev, G. L. Klimchitskaya, V. M. Mostepanenko and U. Mohideen, Demonstration of the Casimir Force between Ferromagnetic Surfaces of a Ni-Coated Sphere and a Ni-Coated Plate, Phys. Rev. Lett. **110,** 137401 (2013).

330. V. M. Mostepanenko, How to confirm and exclude different models of material properties in the Casimir effect, Journal of Physics: Condensed Matter **27,** 214013 (2015).

331. M. Liu, J. Xu, G. L. Klimchitskaya, V. M. Mostepanenko and U. Mohideen, Precision measurements of the gradient of the Casimir force between ultraclean metallic surfaces at larger separations, Phys. Rev. A **100,** 052511 (2019).

332. G. L. Klimchitskaya, U. Mohideen and V. M. Mostepanenko, Thermal Casimir–Polder force between an atom and a dielectric plate: thermodynamics and experiment, Journal of Physics A: Mathematical and Theoretical **41,** 432001 (2008).

333. L. P. Pitaevskii, Pitaevskii Replies:, Phys. Rev. Lett. **102,** 189302 (2009).

334. V. B. Bezerra, G. L. Klimchitskaya, V. M. Mostepanenko and C. Romero, Nernst heat theorem for the thermal Casimir interaction between two graphene sheets, Phys. Rev. A **94,** 042501 (2016).

335. C. C. Korikov and V. M. Mostepanenko, Nernst heat theorem for the Casimir-Polder interaction between a magnetizable atom and ferromagnetic dielectric plate, Modern Physics Letters A **0,** 2040010 (2020).

336. R. H. Dicke, Coherence in Spontaneous Radiation Processes, Phys. Rev. **93,** 99 (1954).

337. A. J. Leggett *et al.,* Dynamics of the dissipative two-state system, Rev. Mod. Phys. **59,** 1 (1987).

338. T. E. Chupp, P. Fierlinger, M. J. Ramsey-Musolf and J. T. Singh, Electric dipole moments of atoms, molecules, nuclei, and particles, Rev. Mod. Phys. **91,** 015001 (2019).

339. R. J. Cook, Atomic motion in resonant radiation: An application of Ehrenfest's theorem, Phys. Rev. A **20,** 224 (1979).

340. D. Braak, Integrability of the Rabi Model, Phys. Rev. Lett. **107,** 100401 (2011).

341. N. J. Schilder *et al.,* Polaritonic modes in a dense cloud of cold atoms, Phys. Rev. A **93,** 063835 (2016).

342. N. J. Schilder, C. Sauvan, Y. R. P. Sortais, A. Browaeys and J.-J. Greffet, Near-Resonant Light Scattering by a Subwavelength Ensemble of Identical Atoms, Phys. Rev. Lett. **124,** 073403 (2020).

343. W. L. Bade, Drude-Model Calculation of Dispersion Forces. I. General Theory, The Journal of Chemical Physics **27,** 1280 (1957).

344. R. A. DiStasio, O. A. von Lilienfeld and A. Tkatchenko, Collective many-body van der Waals interactions in molecular systems, Proceedings of the National Academy of Sciences **109,** 14791 (2012).

345. G. W. Ford and M. Kac, On the quantum Langevin equation, Journal of Statistical Physics **46,** 803 (1987).

346. H. Kleinert and S. Shabanov, Quantum Langevin equation from forward-backward path integral, Physics Letters A **200,** 224 (1995).

347. M. G. Silveirinha, Optical Instabilities and Spontaneous Light Emission by Polarizable Moving Matter, Phys. Rev. X **4,** 031013 (2014).

348. M. Lax, Formal Theory of Quantum Fluctuations from a Driven State, Phys. Rev. **129,** 2342 (1963).

349. L. Onsager, Reciprocal Relations in Irreversible Processes. I., Phys. Rev. **37,** 405 (1931).

350. L. Onsager, Reciprocal Relations in Irreversible Processes. II., Phys. Rev. **38,** 2265 (1931).

351. G. W. Ford and R. F. O'Connell, There is No Quantum Regression Theorem, Phys. Rev. Lett. **77,** 798 (1996).

352. C. Fleming and B. L. Hu, Non-Markovian dynamics of open quantum systems: Stochastic equations and their perturbative solutions, Annals of Physics **327,** 1238 (2012).

353. H. Grabert, P. Schramm and G.-L. Ingold, Quantum Brownian motion: The functional integral approach, Physics Reports **168,** 115 (1988).

354. L. B. Valdes, Resistivity Measurements on Germanium for Transistors, Proceedings of the IRE **42,** 420 (1954).

355. M. Oelschläger, *Fluctuation-induced phenomena in nanophotonic systems*, PhD thesis (Humboldt-Universität zu Berlin, Mathematisch-Naturwissenschaftliche Fakultät, 2020).

356. G. L. Klimchitskaya and V. M. Mostepanenko, Conductivity of dielectric and thermal atom–wall interaction, Journal of Physics A: Mathematical and Theoretical **41,** 312002 (2008).

357. S. Scheel and S. Y. Buhmann, Macroscopic Quantum Electrodynamics - Concepts and Applications, Acta Physica Slovaca **58,** 675 (2008).

358. H. van de Hulst, *Light Scattering by Small Particles* (Dover Publishing, New York, 1981).

359. X. Fan, W. Zheng and D. J. Singh, Light scattering and surface plasmons on small spherical particles, Light: Science & Applications **3,** e179 (2014).

360. L. Landau, E. Lifshitz and L. Pitaevskii, *Electrodynamics of Continuous Media - 2nd ed.* (Elsevier BH, Oxford, 2009).

361. I. Romero, J. Aizpurua, G. W. Bryant and F. J. G. de Abajo, Plasmons in nearly touching metallic nanoparticles: singular response in the limit of touching dimers, romero06 **14,** 9988 (2006).

362. F. J. García de Abajo, Colloquium: Light scattering by particle and hole arrays, Rev. Mod. Phys. **79,** 1267 (2007).

363. R. Ruppin, Optical Properties of a Plasma Sphere, Phys. Rev. Lett. **31,** 1434 (1973).

364. M. Houtput, N. Van den Broeck, F. Brosens, M. Morshed Behbahani and J. Tempere, Alternative derivation of Mie theory with electromagnetic potentials for diffuse particles, Phys. Rev. B **100,** 235409 (2019).

365. B. E. Sernelius, Effects of spatial dispersion on electromagnetic surface modes and on modes associated with a gap between two half spaces, Phys. Rev. B **71,** 235114 (2005).

366. M. Abramowitz and I. Stegun, *Handbook of Mathematical Functions* (Dover Books, New York, 1971).

367. C. M. Bender and S. A. Orszag, *Advanced Mathematical Methods for Scientists and Engineers I Asymptotic Methods and Perturbation Theory* (Springer, New York, NY, 1999).

368. D. C. Tzarouchis, P. Ylä-Oijala and A. Sihvola, Unveiling the scattering behavior of small spheres, Phys. Rev. B **94,** 140301 (2016).

369. D. Tzarouchis and A. Sihvola, Light Scattering by a Dielectric Sphere: Perspectives on the Mie Resonances, Applied Sciences **8** (2018).

370. A. Wokaun, J. P. Gordon and P. F. Liao, Radiation Damping in Surface-Enhanced Raman Scattering, Phys. Rev. Lett. **48,** 957 (1982).

371. M. Meier and A. Wokaun, Enhanced fields on large metal particles: dynamic depolarization, Opt. Lett. **8,** 581 (1983).

372. L. Bergström, Hamaker constants of inorganic materials, Advances in Colloid and Interface Science **70,** 125 (1997).

373. K. A. Milton, The Casimir effect: recent controversies and progress, Journal of Physics A: Mathematical and General **37,** R209 (2004).

374. G. L. Klimchitskaya and V. M. Mostepanenko, Comment on "Lifshitz-Matsubara sum formula for the Casimir pressure between magnetic metallic mirrors", Phys. Rev. E **94,** 026101 (2016).

375. R. Guérout, A. Lambrecht, K. A. Milton and S. Reynaud, Reply to "Comment on 'Lifshitz-Matsubara sum formula for the Casimir pressure between magnetic metallic mirrors' ", Phys. Rev. E **94,** 026102 (2016).

376. G. L. Klimchitskaya, V. M. Mostepanenko, R. I. Sedmik and H. Abele, Prospects for Searching Thermal Effects, Non-Newtonian Gravity and Axion-Like Particles: Cannex Test of the Quantum Vacuum, Symmetry **11,** 407 (2019).

377. G.-L. Ingold, G. L. Klimchitskaya and V. M. Mostepanenko, Nonequilibrium effects in the Casimir force between two similar metallic plates kept at different temperatures, Phys. Rev. A **101,** 032506 (2020).

378. F. Belgiorno, Notes on the third law of thermodynamics: I, Journal of Physics A: Mathematical and General **36,** 8165 (2003).

379. L. Masanes and J. Oppenheim, A general derivation and quantification of the third law of thermodynamics, Nature Communications **8,** 14538 (2017).

380. E. Fermi, *Thermodynamics* (Dover Nova Iorque, New York, 1956).

381. A. Kox, Confusion and clarification: Albert Einstein and Walther Nernst's Heat Theorem, 1911–1916, Studies in History and Philosophy of Science Part B: Studies in History and Philosophy of Modern Physics **37,** 101 (2006).

382. H. B. G. Casimir, Über die statistische Begründung des Nernstschen Wärmetheorems, Zeitschrift für Physik **171,** 246 (1963).

383. M. E. Fisher, The free energy of a macroscopic system, Archive for Rational Mechanics and Analysis **17,** 377 (1964).

384. R. B. Griffiths, Microcanonical Ensemble in Quantum Statistical Mechanics, Journal of Mathematical Physics **6,** 1447 (1965).

385. M. Aizenman and E. H. Lieb, The third law of thermodynamics and the degeneracy of the ground state for lattice systems, Journal of Statistical Physics **24,** 279 (1981).

386. H. S. Leff, Proof of the Third Law of Thermodynamics for Ising Ferromagnets, Phys. Rev. A **2,** 2368 (1970).

387. V. B. Svetovoy and R. Esquivel, Nonlocal impedances and the Casimir entropy at low temperatures, Phys. Rev. E **72,** 036113 (2005).

388. M.-P. Gorza, S. Saltiel, H. Failache and M. Ducloy, Quantum theory of van der Waals interactions between excited atoms and birefringent dielectric surfaces, The European Physical Journal D - Atomic, Molecular, Optical and Plasma Physics **15,** 113 (2001).

389. M. Levin, A. P. McCauley, A. W. Rodriguez, M. T. H. Reid and S. G. Johnson, Casimir Repulsion between Metallic Objects in Vacuum, Phys. Rev. Lett. **105,** 090403 (2010).

390. K. A. Milton, P. Parashar, N. Pourtolami and I. Brevik, Casimir-Polder repulsion: Polarizable atoms, cylinders, spheres, and ellipsoids, Phys. Rev. D **85,** 025008 (2012).

391. P. P. Abrantes, Y. Fran ça, F. S. S. da Rosa, C. Farina and R. de Melo e Souza, Repulsive van der Waals interaction between a quantum particle and a conducting toroid, Phys. Rev. A **98,** 012511 (2018).

392. I. Fialkovsky, N. Khusnutdinov and D. Vassilevich, Quest for Casimir repulsion between Chern-Simons surfaces, Phys. Rev. B **97,** 165432 (2018).

393. J. S. Høye and I. Brevik, Repulsive Casimir force, Phys. Rev. A **98,** 022503 (2018).

394. Y. Ye, Q. Hu, Q. Zhao and Y. Meng, Casimir repulsive-attractive transition between liquid-separated dielectric metamaterial and metal, Phys. Rev. B **98,** 035410 (2018).

395. G. Song *et al.,* Repulsive Casimir force between hyperbolic metamaterials, Opt. Express **26,** 34461 (2018).

396. K. Sinha, Repulsive vacuum-induced forces on a magnetic particle, Phys. Rev. A **97,** 032513 (2018).

397. Q.-D. Jiang and F. Wilczek, Chiral Casimir forces: Repulsive, enhanced, tunable, Phys. Rev. B **99,** 125403 (2019).

398. C. Henkel, B. Power and F. Sols, New light on cavity QED with ultracold atoms, Journal of Physics: Conference Series **19,** 34 (2005).

399. F. Bloch, Zum elektrischen Widerstandsgesetz bei tiefen Temperaturen, Zeitschrift für Physik **59,** 208 (1930).

400. E. Grüneisen, Die Abhängigkeit des elektrischen Widerstandes reiner Metalle von der Temperatur, Annalen der Physik **408,** 530 (1933).

401. F. Bloch, Über die Quantenmechanik der Elektronen in Kristallgittern, Zeitschrift für Physik **52,** 555 (1929).

402. J. Bass, W. P. Pratt and P. A. Schroeder, The temperature-dependent electrical resistivities of the alkali metals, Rev. Mod. Phys. **62,** 645 (1990).

403. M. Bordag and I. G. Pirozhenko, Casimir entropy for a ball in front of a plane, Phys. Rev. D **82,** 125016 (2010).

404. J. C. Bonner and M. E. Fisher, The Entropy of an Antiferromagnet in a Magnetic Field, Proceedings of the Physical Society **80,** 508 (1962).

405. N. V. Kampen, On the theory of stationary waves in plasmas, Physica **21,** 949 (1955).

406. M. A. Kristensen *et al.,* Observation of Atom Number Fluctuations in a Bose-Einstein Condensate, Phys. Rev. Lett. **122,** 163601 (2019).

407. J. R. Torgerson and S. K. Lamoreaux, Low-frequency character of the Casimir force between metallic films, Phys. Rev. E **70,** 047102 (2004).

408. G. Bimonte, Johnson noise and the thermal Casimir effect, New Journal of Physics **9,** 281 (2007).

409. V. B. Svetovoy, Evanescent character of the repulsive thermal Casimir force, Phys. Rev. A **76,** 062102 (2007).

410. P. Hänggi, G.-L. Ingold and P. Talkner, Finite quantum dissipation: the challenge of obtaining specific heat, New Journal of Physics **10,** 115008 (2008).

411. G.-L. Ingold, A. Lambrecht and S. Reynaud, Quantum dissipative Brownian motion and the Casimir effect, Phys. Rev. E **80,** 041113 (2009).

412. K. E. Nagaev and M. Büttiker, Ground-state energy fluctuations of a system coupled to a bath, EPL (Europhysics Letters) **58,** 475 (2002).

413. G. L. Klimchitskaya and V. M. Mostepanenko, Casimir free energy of metallic films: Discriminating between Drude and plasma model approaches, Phys. Rev. A **92,** 042109 (2015).

414. M. Esposito, U. Harbola and S. Mukamel, Nonequilibrium fluctuations, fluctuation theorems, and counting statistics in quantum systems, Rev. Mod. Phys. **81,** 1665 (2009).

415. M. Campisi, P. Hänggi and P. Talkner, Colloquium: Quantum fluctuation relations: Foundations and applications, Rev. Mod. Phys. **83,** 771 (2011).

416. C. Jarzynski, Equalities and Inequalities: Irreversibility and the Second Law of Thermodynamics at the Nanoscale, Annual Review of Condensed Matter Physics **2,** 329 (2011).

417. P. Hänggi and P. Talkner, The other QFT, Nature Physics **11,** 108 (2015).

418. G. E. Crooks, Entropy production fluctuation theorem and the nonequilibrium work relation for free energy differences, Phys. Rev. E **60,** 2721 (1999).

419. T. Hatano and S.-i. Sasa, Steady-State Thermodynamics of Langevin Systems, Phys. Rev. Lett. **86,** 3463 (2001).

420. K. Saito, Energy dissipation and fluctuation response in driven quantum Langevin dynamics, EPL (Europhysics Letters) **83,** 50006 (2008).

421. S. Deffner and E. Lutz, Nonequilibrium Entropy Production for Open Quantum Systems, Phys. Rev. Lett. **107,** 140404 (2011).

422. C. H. Fleming, B. L. Hu and A. Roura, Nonequilibrium fluctuation-dissipation inequality and nonequilibrium uncertainty principle, Phys. Rev. E **88,** 012102 (2013).

423. A. Bartolotta and S. Deffner, Jarzynski Equality for Driven Quantum Field Theories, Phys. Rev. X **8,** 011033 (2018).

424. J. Åberg, Fully Quantum Fluctuation Theorems, Phys. Rev. X **8,** 011019 (2018).

425. J.-T. Hsiang, B. L. Hu and S.-Y. Lin, Fluctuation-dissipation and correlation-propagation relations from the nonequilibrium dynamics of detector-quantum field systems, Phys. Rev. D **100,** 025019 (2019).

426. T. Ohta and T. Ohkuma, Fluctuations and Response in Nonequilibrium Steady State, Journal of the Physical Society of Japan **77,** 074004 (2008).

427. T. Speck, Thermodynamic formalism and linear response theory for nonequilibrium steady states, Phys. Rev. E **94,** 022131 (2016).

428. U. Seifert and T. Speck, Fluctuation-dissipation theorem in nonequilibrium steady states, EPL (Europhysics Letters) **89,** 10007 (2010).

429. H. Ness, Nonequilibrium Thermodynamics and Steady State Density Matrix for Quantum Open Systems, Entropy **19,** 158 (2017).

430. M. Hillery, R. O'Connell, M. Scully and E. Wigner, Distribution functions in physics: Fundamentals, Physics Reports **106,** 121 (1984).

431. G. W. Ford and R. F. O'Connell, Exact solution of the Hu-Paz-Zhang master equation, Phys. Rev. D **64,** 105020 (2001).

432. C. Fleming, A. Roura and B. Hu, Exact analytical solutions to the master equation of quantum Brownian motion for a general environment, Annals of Physics **326,** 1207 (2011).

433. S. Deffner, Quantum entropy production in phase space, EPL (Europhysics Letters) **103,** 30001 (2013).

434. S. Y. Buhmann, L. Knöll, D.-G. Welsch and H. T. Dung, Casimir-Polder forces: A nonperturbative approach, Phys. Rev. A **70,** 052117 (2004).

435. R. Feynman and F. Vernon, The Theory of a General Quantum System Interacting with a Linear Dissipative System, Annals of Physics **24** (1963).

436. R. O. Behunin and B. L. Hu, Nonequilibrium Casimir–Polder force in non-stationary systems, Journal of Physics A: Mathematical and Theoretical **43,** 012001 (2010).

437. R. O. Behunin and B.-L. Hu, Nonequilibrium forces between neutral atoms mediated by a quantum field, Phys. Rev. A **82,** 022507 (2010).

438. J. del Pino, F. A. Y. N. Schröder, A. W. Chin, J. Feist and F. J. Garcia-Vidal, Tensor Network Simulation of Non-Markovian Dynamics in Organic Polaritons, Phys. Rev. Lett. **121,** 227401 (2018).

439. S. Gröblacher *et al.,* Observation of non-Markovian micromechanical Brownian motion, Nature Communications **6,** 7606 (2015).

440. R. Zhao, A. Manjavacas, F. J. García de Abajo and J. B. Pendry, Rotational Quantum Friction, Phys. Rev. Lett. **109,** 123604 (2012).

441. K. Hornberger, S. Gerlich, P. Haslinger, S. Nimmrichter and M. Arndt, Colloquium: Quantum interference of clusters and molecules, Rev. Mod. Phys. **84,** 157 (2012).

442. J. Tisler *et al.,* Single Defect Center Scanning Near-Field Optical Microscopy on Graphene, Nano Letters **13,** 3152 (2013).

443. A. W. Schell *et al.,* Scanning Single Quantum Emitter Fluorescence Lifetime Imaging: Quantitative Analysis of the Local Density of Photonic States, Nano Letters **14,** 2623 (2014).

444. D. S. Bykov, O. A. Schmidt, T. G. Euser and P. S. J. Russell, Flying particle sensors in hollow-core photonic crystal fibre, Nature Photonics **9,** 461 EP (2015).

445. R. O. Behunin, F. Intravaia and P. T. Rakich, Dimensional transformation of defect-induced noise, dissipation, and nonlinearity, Phys. Rev. B **93,** 224110 (2016).

446. A. E. Rubio López, C. Gonzalez-Ballestero and O. Romero-Isart, Internal quantum dynamics of a nanoparticle in a thermal electromagnetic field: A minimal model, Phys. Rev. B **98,** 155405 (2018).

447. D. Sanvitto and S. Kéna-Cohen, The road towards polaritonic devices, Nature Materials **15,** 1061 (2016).

448. V. G. Polevoi and S. M. Rytov, Some remarks on the application of the fluctuation-dissipation theorem to nonlinear systems, Theoretical and Mathematical Physics **25,** 1096 (1975).

449. F. Intravaia, S. Maniscalco and A. Messina, Comparison between the rotating wave and Feynman-Vernon system-reservoir couplings in the non-Markovian regime, The European Physical Journal B - Condensed Matter and Complex Systems **32,** 97 (2003).

450. C. Fleming, N. I. Cummings, C. Anastopoulos and B. L. Hu, The rotating-wave approximation: consistency and applicability from an open quantum system analysis, Journal of Physics A: Mathematical and Theoretical **43,** 405304 (2010).

451. H. Mäkelä and M. Möttönen, Effects of the rotating-wave and secular approximations on non-Markovianity, Phys. Rev. A **88,** 052111 (2013).

452. T. M. Stace, A. C. Doherty and D. J. Reilly, Dynamical Steady States in Driven Quantum Systems, Phys. Rev. Lett. **111,** 180602 (2013).

453. K. Sinha, B. P. Venkatesh and P. Meystre, Collective Effects in Casimir-Polder Forces, Phys. Rev. Lett. **121,** 183605 (2018).

454. S. Fuchs and S. Y. Buhmann, Purcell-Dicke enhancement of the Casimir-Polder potential, EPL (Europhysics Letters) **124,** 34003 (2018).

455. K. Sinha *et al.,* Non-Markovian Collective Emission from Macroscopically Separated Emitters, Phys. Rev. Lett. **124,** 043603 (2020).

456. A. Cerjan and A. D. Stone, Why the laser linewidth is so narrow: a modern perspective, Physica Scripta **91,** 013003 (2015).

457. D. P. Craig and E. A. Power, The asymptotic Casimir–Polder potential from second-order perturbation theory and its generalization for anisotropic polarizabilities, International Journal of Quantum Chemistry **3,** 903 (1969).

458. B. Labani, M. Boustimi and J. Baudon, van der Waals interaction between a molecule and a spherical cavity in a metal:Nonlocality and anisotropy effects, Phys. Rev. B **55,** 4745 (1997).

459. P. Barcellona, R. Passante, L. Rizzuto and S. Y. Buhmann, Dynamical Casimir-Polder interaction between a chiral molecule and a surface, Phys. Rev. A **93,** 032508 (2016).

460. J. C. Hopkins, R. Podgornik, W.-Y. Ching, R. H. French and V. A. Parsegian, Disentangling the Effects of Shape and Dielectric Response in van der Waals Interactions between Anisotropic Bodies, The Journal of Physical Chemistry C **119,** 19083 (2015).

461. M. R. Dennis, Geometric interpretation of the three-dimensional coherence matrix for nonparaxial polarization, Journal of Optics A: Pure and Applied Optics **6,** S26 (2004).

462. M. Berry and M. Dennis, Polarization singularities in isotropic random vector waves, Proceedings of the Royal Society of London. Series A: Mathematical, Physical and Engineering Sciences **457,** 141 (2001).

463. K. Y. Bliokh, F. J. Rodríguez-Fortuño, F. Nori and A. V. Zayats, Spin-orbit interactions of light, Nature Photonics **9,** 796 EP (2015).

464. P. Lodahl *et al.,* Chiral quantum optics, Nature **541,** 473 EP (2017).

465. D. O'Shea, C. Junge, J. Volz and A. Rauschenbeutel, Fiber-Optical Switch Controlled by a Single Atom, Phys. Rev. Lett. **111,** 193601 (2013).

466. C. Sayrin *et al.,* Nanophotonic Optical Isolator Controlled by the Internal State of Cold Atoms, Phys. Rev. X **5,** 041036 (2015).

467. S.-H. Gong, F. Alpeggiani, B. Sciacca, E. C. Garnett and L. Kuipers, Nanoscale chiral valley-photon interface through optical spin-orbit coupling, Science **359,** 443 (2018).

468. B. A. Stickler, B. Schrinski and K. Hornberger, Rotational Friction and Diffusion of Quantum Rotors, Phys. Rev. Lett. **121,** 040401 (2018).

469. S. M. Barnett *et al.,* On the natures of the spin and orbital parts of optical angular momentum, Journal of Optics **18,** 064004 (2016).

470. L. Allen, M. W. Beijersbergen, R. J. C. Spreeuw and J. P. Woerdman, Orbital angular momentum of light and the transformation of Laguerre-Gaussian laser modes, Phys. Rev. A **45,** 8185 (1992).

471. A. Aiello, P. Banzer, M. Neugebauer and G. Leuchs, From transverse angular momentum to photonic wheels, Nature Photonics **9,** 789 (2015).

472. G. Pieplow, H. R. Haakh and C. Henkel, A note on longitudinal fields in the Weyl expansion of the electromagnetic Green tensor, International Journal of Modern Physics: Conference Series **14,** 460 (2012).

473. T. V. Mechelen and Z. Jacob, Universal spin-momentum locking of evanescent waves, Optica **3,** 118 (2016).

474. A. Manjavacas and F. J. García de Abajo, Vacuum Friction in Rotating Particles, Phys. Rev. Lett. **105,** 113601 (2010).

475. B. A. Stickler, F. T. Ghahramani and K. Hornberger, Rotational Alignment Decay and Decoherence of Molecular Superrotors, Phys. Rev. Lett. **121,** 243402 (2018).

476. Y. Arita, M. Mazilu and K. Dholakia, Laser-induced rotation and cooling of a trapped microgyroscope in vacuum, Nature Communications **4,** 2374 (2013).

477. T. M. Hoang *et al.,* Torsional Optomechanics of a Levitated Nonspherical Nanoparticle, Phys. Rev. Lett. **117,** 123604 (2016).

478. S. Kuhn *et al.,* Optically driven ultra-stable nanomechanical rotor, Nature Communications **8,** 1670 (2017).

479. A. Kyasov and G. Dedkov, Electromagnetic fluctuation forces on a particle moving near a surface, Surface Science **463,** 11 (2000).

480. G. Dedkov and A. Kyasov, Dynamical van der Waals atom-surface interaction, Surface Science **605,** 1077 (2011).

481. G. Dedkov and A. Kyasov, Dynamical Casimir-Polder atom-surface interaction, Surface Science **606,** 46 (2012).

482. M. T. H. Reid *et al.,* Photon Torpedoes and Rytov Pinwheels: Integral-Equation Modeling of Non-Equilibrium Fluctuation-Induced Forces and Torques on Nanoparticles, online preprint, arXiv:1708.01985 (2017).

483. M. Hartmann and G.-L. Ingold, CaPS: Casimir Effect in the Plane-Sphere Geometry, Journal of Open Source Software **5,** 2011 (2020).

484. H. Grabert, P. Nalbach, J. Reichert and M. Thorwart, Nonequilibrium Response of Nanosystems Coupled to Driven Quantum Baths, The Journal of Physical Chemistry Letters **7,** 2015 (2016).

485. H. Grabert and M. Thorwart, Quantum mechanical response to a driven Caldeira-Leggett bath, Phys. Rev. E **98,** 012122 (2018).

486. K. Milton, The Casimir Force: Feeling the heat, Nat. Phys. **7,** 190 (2011).

487. F. Intravaia, R. O. Behunin and D. A. R. Dalvit, Quantum friction and fluctuation theorems, Phys. Rev. A **89,** 050101 (2014).

488. G. S. Agarwal, Fluctuation-dissipation theorems for systems in non-thermal equilibrium and applications, Zeitschrift für Physik A Hadrons and nuclei **252,** 25 (1972).

489. P. Talkner, M. Campisi and P. Hänggi, Fluctuation theorems in driven open quantum systems, Journal of Statistical Mechanics: Theory and Experiment **2009,** P02025 (2009).

490. R. R. Q. P. T. Oude Weernink, P. Barcellona and S. Y. Buhmann, Lateral Casimir-Polder forces by breaking time-reversal symmetry, Phys. Rev. A **97,** 032507 (2018).

491. R. de Melo e Souza, W. J. M. Kort-Kamp, C. Sigaud and C. Farina, Image method in the calculation of the van der Waals force between an atom and a conducting surface, American Journal of Physics **81,** 366 (2013).

492. É. V. Teodorovich, Contribution of macroscopic van der Waals interactions to friction forces, Soviet Physics Journal **19,** 1471 (1976).

493. J. Mahanty, Velocity dependence of the van der Waals force between molecules, Journal of Physics B: Atomic and Molecular Physics **13,** 4391 (1980).

494. G. V. Dedkov and A. A. Kyasov, The relativistic theory of fluctuation electromagnetic interactions of moving neutral particles with a flat surface, Physics of the Solid State **45,** 1815 (2003).

495. T. G. Philbin and U. Leonhardt, No quantum friction between uniformly moving plates, New Journal of Physics **11,** 033035 (2009).

496. G. Barton, On van der Waals friction: I. Between two atoms, New Journal of Physics **12,** 113044 (2010).

497. S. Raza, T. Christensen, M. Wubs, S. I. Bozhevolnyi and N. A. Mortensen, Nonlocal response in thin-film waveguides: Loss versus nonlocality and breaking of complementarity, Phys. Rev. B **88,** 115401 (2013).

498. C. Ciracì, J. B. Pendry and D. R. Smith, Hydrodynamic Model for Plasmonics: A Macroscopic Approach to a Microscopic Problem, ChemPhysChem **14,** 1109 (2013).

499. P. Yeh, A. Yariv and C.-S. Hong, Electromagnetic propagation in periodic stratified media. I. General theory∗, J. Opt. Soc. Am. **67,** 423 (1977).

500. J. Fiedler *et al.,* Dispersion forces in inhomogeneous planarly layered media: A one-dimensional model for effective polarizabilities, Phys. Rev. A **99,** 062512 (2019).

501. V. Esteso, S. Carretero-Palacios and H. Míguez, Optical interference effects on the Casimir-Lifshitz force in multilayer structures, Phys. Rev. A **101,** 033815 (2020).

502. P. Berini, Plasmon-polariton waves guided by thin lossy metal films of finite width: Bound modes of symmetric structures, Phys. Rev. B **61,** 10484 (2000).

503. J. A. Dionne, L. A. Sweatlock, H. A. Atwater and A. Polman, Planar metal plasmon waveguides: frequency-dependent dispersion, propagation, localization, and loss beyond the free electron model, Phys. Rev. B **72,** 075405 (2005).

504. R. Charbonneau *et al.,* Passive integrated optics elements based on long-range surface plasmon polaritons, Journal of Lightwave Technology **24,** 477 (2006).

505. P. Berini, Long-range surface plasmon polaritons, Adv. Opt. Photon. **1,** 484 (2009).

506. B. Frank *et al.,* Short-range surface plasmonics: Localized electron emission dynamics from a 60-nm spot on an atomically flat single-crystalline gold surface, Science Advances **3** (2017).

507. E. McCann, Electronic properties of monolayer and bilayer graphene, (2012).

508. J. Wang, S. Deng, Z. Liu and Z. Liu, The rare two-dimensional materials with Dirac cones, National Science Review **2,** 22 (2015).

509. J. González, F. Guinea and M. Vozmediano, Non-Fermi liquid behavior of electrons in the half-filled honeycomb lattice (A renormalization group approach), Nuclear Physics B **424,** 595 (1994).

510. G. Giovannetti, P. A. Khomyakov, G. Brocks, P. J. Kelly and J. van den Brink, Substrate-induced band gap in graphene on hexagonal boron nitride: Ab initio density functional calculations, Phys. Rev. B **76,** 073103 (2007).

511. S. Y. Zhou *et al.,* Substrate-induced bandgap opening in epitaxial graphene, Nature Materials **6,** 770 (2007).

512. C. H. Egerland, K. Busch and F. Intravaia, Polaritonic contribution to the Casimir energy between two graphene layers, Phys. Rev. B **100,** 235418 (2019).

513. G. L. Klimchitskaya, V. M. Mostepanenko and V. M. Petrov, Impact of chemical potential on the reflectance of graphene in the infrared and microwave domains, Phys. Rev. A **98,** 023809 (2018).

514. B. Wunsch, T. Stauber, F. Sols and F. Guinea, Dynamical polarization of graphene at finite doping, New Journal of Physics **8,** 318 (2006).

515. E. H. Hwang and S. Das Sarma, Dielectric function, screening, and plasmons in two-dimensional graphene, Phys. Rev. B **75,** 205418 (2007).

516. I. V. Fialkovsky, V. N. Marachevsky and D. V. Vassilevich, Finite-temperature Casimir effect for graphene, Phys. Rev. B **84,** 035446 (2011).

517. A. I. Volokitin and B. N. J. Persson, Quantum Friction, Phys. Rev. Lett. **106,** 094502 (2011).

518. P. W. Milonni and M.-L. Shih, Casimir forces, Contemporary Physics **33,** 313 (1992).

519. F. Intravaia, C. Henkel and A. Lambrecht, Role of surface plasmons in the Casimir effect, Phys. Rev. A **76,** 033820 (2007).

520. H. Gies and K. Klingmüller, Casimir Effect for Curved Geometries: Proximity-Force-Approximation Validity Limits, Phys. Rev. Lett. **96,** 220401 (2006).

521. D. E. Krause, R. S. Decca, D. López and E. Fischbach, Experimental Investigation of the Casimir Force beyond the Proximity-Force Approximation, Phys. Rev. Lett. **98,** 050403 (2007).

522. M. Bordag, Generalized Lifshitz formula for a cylindrical plasma sheet in front of a plane beyond proximity force approximation, Phys. Rev. D **75,** 065003 (2007).

523. H.-C. Chiu, G. L. Klimchitskaya, V. N. Marachevsky, V. M. Mostepanenko and U. Mohideen, Lateral Casimir force between sinusoidally corrugated surfaces: Asymmetric profiles, deviations from the proximity force approximation, and comparison with exact theory, Phys. Rev. B **81,** 115417 (2010).

524. G. Bimonte, Beyond-proximity-force-approximation Casimir force between two spheres at finite temperature, Phys. Rev. D **97,** 085011 (2018).

525. H. B. Chan *et al.,* Measurement of the Casimir Force between a Gold Sphere and a Silicon Surface with Nanoscale Trench Arrays, Phys. Rev. Lett. **101,** 030401 (2008).

526. J. L. Garrett, D. A. T. Somers and J. N. Munday, Measurement of the Casimir Force between Two Spheres, Phys. Rev. Lett. **120,** 040401 (2018).

527. L. P. Teo, Material dependence of Casimir interaction between a sphere and a plate: First analytic correction beyond proximity force approximation, Phys. Rev. D **88,** 045019 (2013).

528. G. Bimonte, T. Emig and M. Kardar, Material dependence of Casimir forces: Gradient expansion beyond proximity, Applied Physics Letters **100,** 074110 (2012).

529. J. Zou *et al.,* Casimir forces on a silicon micromechanical chip, Nature Communications **4,** 1845 EP (2013).

530. A. Rodriguez *et al.,* Computation and Visualization of Casimir Forces in Arbitrary Geometries: Nonmonotonic Lateral-Wall Forces and the Failure of Proximity-Force Approximations, Phys. Rev. Lett. **99,** 080401 (2007).

531. B. Beverungen, *Optimierung nanophotonischer Strukturen mit Fokus auf Casimir-Polder-Wechselwirkungen*, MA thesis (Department of Physics, Humboldt-Universität zu Berlin, 2020).

532. L. Tang *et al.,* Measurement of non-monotonic Casimir forces between silicon nanostructures, Nature Photonics **11,** 97 EP (2017).

533. M. Antezza, L. P. Pitaevskii, S. Stringari and V. B. Svetovoy, Casimir-Lifshitz Force Out of Thermal Equilibrium and Asymptotic Nonadditivity, Phys. Rev. Lett. **97,** 223203 (2006).

534. S. Kalusniak, S. Sadofev and F. Henneberger, ZnO as a Tunable Metal: New Types of Surface Plasmon Polaritons, Phys. Rev. Lett. **112,** 137401 (2014).

535. L.-W. Li, M.-S. Leong, T.-S. Yeo and P.-S. Kooi, Electromagnetic Dyadic Green's Functions in Spectral Domain for Multilayered Cylinders, Journal of Electromagnetic Waves and Applications **14,** 961 (2000).

536. S. Å. Ellingsen, S. Y. Buhmann and S. Scheel, Casimir-Polder potential and transition rate in resonating cylindrical cavities, Phys. Rev. A **82,** 032516 (2010).

537. N. R. Arista and M. A. Fuentes, Interaction of charged particles with surface plasmons in cylindrical channels in solids, Phys. Rev. B **63,** 165401 (2001).

538. *NIST* Digital Library of Mathematical Functions, http://dlmf.nist.gov/, Release 1.0.25 of 2019-12-15,

539. J. Ashley and L. Emerson, Dispersion relations for non-radiative surface plasmons on cylinders, Surface Science **41,** 615 (1974).

540. C. A. Pfeiffer, E. N. Economou and K. L. Ngai, Surface polaritons in a circularly cylindrical interface: Surface plasmons, Phys. Rev. B **10,** 3038 (1974).

541. K. Sinha and Y. Subaşı, Quantum Brownian motion of a particle from Casimir-Polder interactions, Phys. Rev. A **101,** 032507 (2020).

542. N. Bartolo, R. Messina, D. A. R. Dalvit and F. Intravaia, Nonequilibrium Casimir-Polder plasmonic interactions, Phys. Rev. A **93,** 042111 (2016).

543. L. Viotti, F. C. Lombardo and P. I. Villar, Boundary-induced effect encoded in the corrections to the geometric phase acquired by a bipartite two-level system, Phys. Rev. A **101,** 032337 (2020).

544. L. A. Reynolds *et al.,* Direct Measurements of Collisional Dynamics in Cold Atom Triads, Phys. Rev. Lett. **124,** 073401 (2020).

545. G. W. Ford, M. Kac and P. Mazur, Statistical Mechanics of Assemblies of Coupled Oscillators, Journal of Mathematical Physics **6,** 504 (1965).

546. K. Hepp and E. H. Lieb, Equilibrium Statistical Mechanics of Matter Interacting with the Quantized Radiation Field, Phys. Rev. A **8,** 2517 (1973).

547. A. Caldeira and A. Leggett, Path integral approach to quantum Brownian motion, Physica A: Statistical Mechanics and its Applications **121,** 587 (1983).

548. Y. Subaşı, C. H. Fleming, J. M. Taylor and B. L. Hu, Equilibrium states of open quantum systems in the strong coupling regime, Phys. Rev. E **86,** 061132 (2012).

549. G.-L. Ingold, Thermodynamic anomaly of the free damped quantum particle: the bath perspective, The European Physical Journal B **85,** 30 (2012).

550. T. Van Vu and Y. Hasegawa, Uncertainty relations for underdamped Langevin dynamics, Phys. Rev. E **100,** 032130 (2019).

551. P. Forn-Díaz, L. Lamata, E. Rico, J. Kono and E. Solano, Ultrastrong coupling regimes of light-matter interaction, Rev. Mod. Phys. **91,** 025005 (2019).

552. F. C. Lombardo, F. D. Mazzitelli, A. E. R. López and G. J. Turiaci, Nonequilibrium Lifshitz theory as a steady state of a full dynamical quantum system, Phys. Rev. D **94,** 025029 (2016).

553. M. B. Farías, C. D. Fosco, F. C. Lombardo and F. D. Mazzitelli, Motion induced radiation and quantum friction for a moving atom, Phys. Rev. D **100,** 036013 (2019).

554. L. Viotti, M. Belén Farías, P. I. Villar and F. C. Lombardo, Thermal corrections to quantum friction and decoherence: A closed-time-path approach to atom-surface interaction, Phys. Rev. D **99,** 105005 (2019).

555. J. Reichert, P. Nalbach and M. Thorwart, Dynamics of a quantum two-state system in a linearly driven quantum bath, Phys. Rev. A **94,** 032127 (2016).

556. E. Schrödinger, Über die Umkehrung der Naturgesetze, S.B. Preuss. Akad. Wiss., Physik.-math. Klasse **IX,** 412 (1931).

557. R. Fürth, Über einige Beziehungen zwischen klassischer Statistik und Quantenmechanik, Zeitschrift für Physik **81,** 143 (1933).

558. H. Risken, *The Fokker-Planck Equation* (Springer-Verlag, Berlin, 1989).

559. E. Calzetta, A. Roura and E. Verdaguer, Master Equation for Quantum Brownian Motion Derived by Stochastic Methods, International Journal of Theoretical Physics **40,** 2317 (2001).

560. E. Calzetta, A. Roura and E. Verdaguer, Stochastic description for open quantum systems, Physica A: Statistical Mechanics and its Applications **319,** 188 (2003).

561. J. J. Halliwell and T. Yu, Alternative derivation of the Hu-Paz-Zhang master equation of quantum Brownian motion, Phys. Rev. D **53,** 2012 (1996).

562. F. Intravaia, S. Maniscalco and A. Messina, Density-matrix operatorial solution of the non-Markovian master equation for quantum Brownian motion, Phys. Rev. A **67,** 042108 (2003).

563. E. Joos and H. D. Zeh, The emergence of classical properties through interaction with the environment, Zeitschrift für Physik B Condensed Matter **59,** 223 (1985).

564. D. Koks, A. Matacz and B. L. Hu, Entropy and uncertainty of squeezed quantum open systems, Phys. Rev. D **55,** 5917 (1997).

565. H. Grabert, U. Weiss and P. Talkner, Quantum theory of the damped harmonic oscillator, Zeitschrift für Physik B Condensed Matter **55,** 87 (1984).

566. Ratchov, A., Faure, F. and Hekking, F. W.J., Loss of quantum coherence in a system coupled to a zero-temperature environment, Eur. Phys. J. B **46,** 519 (2005).

567. S. A. Fulling, Nonuniqueness of Canonical Field Quantization in Riemannian Space-Time, Phys. Rev. D **7,** 2850 (1973).

568. P. C. W. Davies, Scalar production in Schwarzschild and Rindler metrics, Journal of Physics A: Mathematical and General **8,** 609 (1975).

569. B. S. DeWitt, Quantum field theory in curved spacetime, Physics Reports **19,** 295 (1975).

570. W. G. Unruh, Notes on black-hole evaporation, Phys. Rev. D **14,** 870 (1976).

571. R. Dillenschneider and E. Lutz, Quantum Smoluchowski equation for driven systems, Phys. Rev. E **80,** 042101 (2009).

572. A. C. Barato and U. Seifert, Thermodynamic Uncertainty Relation for Biomolecular Processes, Phys. Rev. Lett. **114,** 158101 (2015).

573. J. S. Lee, J.-M. Park and H. Park, Thermodynamic uncertainty relation for underdamped Langevin systems driven by a velocity-dependent force, Phys. Rev. E **100,** 062132 (2019).

574. F. Carollo, R. L. Jack and J. P. Garrahan, Unraveling the Large Deviation Statistics of Markovian Open Quantum Systems, Phys. Rev. Lett. **122,** 130605 (2019).

575. Y. Hasegawa, Quantum Thermodynamic Uncertainty Relation for Continuous Measurement, Phys. Rev. Lett. **125,** 050601 (2020).

576. B. L. Hu and Y. Zhang, Squeezed States and uncertainty relation at finite temperature, Modern Physics Letters A **08,** 3575 (1993).

577. B. L. Hu and Y. Zhang, Uncertainty relation for a quantum open system, International Journal of Modern Physics A **10,** 4537 (1995).

578. F. Chen, G. L. Klimchitskaya, V. M. Mostepanenko and U. Mohideen, Demonstration of the Difference in the Casimir Force for Samples with Different Charge-Carrier Densities, Phys. Rev. Lett. **97,** 170402 (2006).

579. P. Sonnentag and F. Hasselbach, Measurement of Decoherence of Electron Waves and Visualization of the Quantum-Classical Transition, Phys. Rev. Lett. **98,** 200402 (2007).

580. D. Das and V. Natarajan, Absolute frequency measurement of the lithium D lines: Precise determination of isotope shifts and fine-structure intervals, Phys. Rev. A **75,** 052508 (2007).

581. K. A. Milton, J. S. Høye and I. Brevik, The Reality of Casimir Friction, Symmetry **8,** 29 (2016).

582. S. Abend *et al.,* Atom interferometry and its applications, arXiv:2001.10976 (2020).

583. S. Hartmann *et al.,* Regimes of atomic diffraction: Raman versus Bragg diffraction in retroreflective geometries, Phys. Rev. A **101,** 053610 (2020).

584. J.-F. Schaff, T. Langen and J. Schmiedmayer. *Atom Interferometry* (eds G. Tino and M. Kasevich) (IOS Press, Bologna, Italy, 2014).

585. F. Riehle, T. Kisters, A. Witte, J. Helmcke and C. J. Bordé, Optical Ramsey spectroscopy in a rotating frame: Sagnac effect in a matter-wave interferometer, Phys. Rev. Lett. **67,** 177 (1991).

586. Y.-J. Wang *et al.,* Atom Michelson Interferometer on a Chip Using a Bose-Einstein Condensate, Phys. Rev. Lett. **94,** 090405 (2005).

587. T. Schumm *et al.,* Matter-wave interferometry in a double well on an atom chip, Nature Physics **1,** 57 (2005).

588. H. Müntinga *et al.,* Interferometry with Bose-Einstein Condensates in Microgravity, Phys. Rev. Lett. **110,** 093602 (2013).

589. V. Schkolnik *et al.,* A compact and robust diode laser system for atom interferometry on a sounding rocket, Applied Physics B **122,** 217 (2016).

590. B. Barrett *et al.,* Dual matter-wave inertial sensors in weightlessness, Nature Communications **7,** 13786 EP (2016).

591. K. Frye *et al.,* The Bose-Einstein Condensate and Cold Atom Laboratory, arXiv:1912.04849 (2019).

592. D. C. Aveline *et al.,* Observation of Bose–Einstein condensates in an Earth-orbiting research lab, Nature **582,** 193 (2020).

593. M. Carey, J. Saywell, D. Elcock, M. Belal and T. Freegarde, Velocimetry of cold atoms by matter-wave interferometry, Phys. Rev. A **99,** 023631 (2019).

594. D. W. Keith, M. L. Schattenburg, H. I. Smith and D. E. Pritchard, Diffraction of Atoms by a Transmission Grating, Phys. Rev. Lett. **61,** 1580 (1988).

595. E. M. Rasel, M. K. Oberthaler, H. Batelaan, J. Schmiedmayer and A. Zeilinger, Atom Wave Interferometry with Diffraction Gratings of Light, Phys. Rev. Lett. **75,** 2633 (1995).

596. J. D. Perreault, A. D. Cronin and T. A. Savas, Using atomic diffraction of Na from material gratings to measure atom-surface interactions, Phys. Rev. A **71,** 053612 (2005).

597. D. W. Keith, C. R. Ekstrom, Q. A. Turchette and D. E. Pritchard, An interferometer for atoms, Phys. Rev. Lett. **66,** 2693 (1991).

598. C. Brand *et al.,* Coherent diffraction of hydrogen through the 246 pm lattice of graphene, New Journal of Physics **21,** 033004 (2019).

599. Y. Y. Fein *et al.,* Quantum superposition of molecules beyond 25 kDa, Nature Physics **15,** 1242 (2019).

600. A. Gruber *et al.,* Scanning Confocal Optical Microscopy and Magnetic Resonance on Single Defect Centers, Science **276,** 2012 (1997).

601. M. W. Doherty *et al.,* The nitrogen-vacancy colour centre in diamond, Physics Reports **528,** 1 (2013).

602. I. Aharonovich *et al.,* Diamond-based single-photon emitters, Reports on Progress in Physics **74,** 076501 (2011).

603. J. F. Barry *et al.,* Sensitivity optimization for NV-diamond magnetometry, Rev. Mod. Phys. **92,** 015004 (2020).

604. R. Schirhagl, K. Chang, M. Loretz and C. L. Degen, Nitrogen-Vacancy Centers in Diamond: Nanoscale Sensors for Physics and Biology, Annual Review of Physical Chemistry **65,** 83 (2014).

605. L.-W. Li, P.-S. Kooi, M.-S. Leong and T.-S. Yee, Electromagnetic dyadic Green's function in spherically multilayered media, IEEE Transactions on Microwave Theory and Techniques **42,** 2302 (1994).

606. B. Amorim, P. A. D. Gonçalves, M. I. Vasilevskiy and N. M. R. Peres, Impact of Graphene on the Polarizability of a Neighbour Nanoparticle: A Dyadic Green's Function Study, Applied Sciences **7** (2017).

607. I. S. Gradshteyn and I. M. Ryzhik, *Table of integrals, series, and products* , Seventh Edition (Elsevier/Academic Press, Amsterdam, 2007).

Publication List

M1. F. Intravaia, M. Oelschläger, D. Reiche, D. A. R. Dalvit and K. Busch, Quantum Rolling Friction, Phys. Rev. Lett. **123,** 120401 (2019).

M2. D. Reiche, K. Busch and F. Intravaia, Nonadditive Enhancement of Nonequilibrium Atom-Surface Interactions, Phys. Rev. Lett. **124,** 193603 (2020).

M3. D. Reiche, K. Busch and F. Intravaia, Quantum thermodynamics of overdamped modes in local and spatially dispersive materials, Phys. Rev. A **101,** 012506 (2020).

M4. D. Reiche, D. A. R. Dalvit, K. Busch and F. Intravaia, Spatial dispersion in atom-surface quantum friction, Phys. Rev. B **95,** 155448 (2017).

M5. D. Reiche, M. Oelschläger, K. Busch and F. Intravaia, Extended hydrodynamic description for nonequilibrium atom-surface interactions, J. Opt. Soc. Am. B **36,** C52 (2019).

M6. D. Reiche, F. Intravaia, J.-T. Hsiang, K. Busch and B. L. Hu, Nonequilibrium thermodynamics of quantum friction, Phys. Rev. A **102,** 050203 (2020).

In Preparation

P1. M. Oelschläger, D. Reiche, S. Hermann, C. Egerland, K. Busch and F. Intravaia, (working title) Non-Conservative Dispersion Forces in the Quantum-Thermal Crossover Regime, in preparation (2020).

P2. D. Reiche, C. Egerland, K. Busch and F. Intravaia, (working title) Enhancing atom-surface quantum friction: The interplay of confined light, dissipation and geometrically induced spatial nonlocality, in preparation (2020).

P3. D. Reiche, K. Busch and F. Intravaia, (working title) Non-perturbative Treatment of Casimir-Polder Force in Mechanical Nonequilibrium, in preparation (2020).

Presentations

- D. Reiche, Oral presentation, Quantum Thermodynamics of Atom-Surface Interactions in Nonequilibrium Steady-States, 713. WE-Heraeus Seminar: Quantum Thermodynamics for Young Scientists, Bad Honnef, Germany (2020).

- D. Reiche, M. Oelschläger, K. Busch, and F. Intravaia, Poster session, Modeling Landau Damping in Atom-Surface Quantum Friction, Workshop on Theoretical and Numerical Tools for Nanophotonics, Berlin, Germany (2020).

- D. Reiche, K. Busch, R.O. Behunin, Oral presentation, Quantum States of Acoustic Modes in Optomechanical Systems, DPG Spring Meeting, Hannover, Germany (2020), cancelled due to COVID-19.

- D. Reiche, K. Busch, and F. Intravaia, Oral presentation, Spatial Dispersion in Atom-Surface Interactions, Workshop/Summer School 2018 NTNU: Casimir effect: Theory and Applications, Trondheim, Norway (2018).
- D. Reiche, F. Intravaia, and K. Busch, Poster session, Statistical and Geometrical Aspects of Atom-Surface Interactions in Dynamical Nonequilibrium, DPG Spring Meeting, Erlangen, Germany (2018).
- D. Reiche, K. Busch, and F. Intravaia, Poster session, Dissipation in Fluctuation-induced Atom-Surface Interactions, 671. WE-Heraeus Seminar: Fluctuation-induced Phenomena in Complex Systems, Bad Honnef, Germany (2018).
- D. Reiche, F. Intravaia, and K. Busch, Poster session, Magnetic Casimir-Polder Interaction and the Influence of Foucault Currents, DPG Spring Meeting, Hannover, Germany (2016).

Public Outreach and Science Communication

- D. Reiche, Oral presentation, Try to picture vacuum, Lindau Nobel Laureate Meetings – Online Science Days 2020, Next Generation Science Session 5 (available online at the Lindau Nobel Mediatheque, accessed July 30, 2020), digital conference (2020).
- D. Reiche, Oral presentation, German reunification and its impact on German-American relations, Fulbright “Meet-a-German”, High School in Sykesville, MD, USA (2019).
- D. Reiche, Oral presentation, Research on nothing, Fulbright Berlin Seminar, Berlin, Germany (2019).
- D. Reiche, K. Busch, and F. Intravaia, Poster session, Forces from nothing, N2 Event “From Research to Application”, Berlin, Germany (2020).

Acknowledgments

The complexities are overwhelming. Luckily, I am not alone.

First and foremost I would like to thank Kurt Busch and Francesco Intravaia who not only provided the basic conditions enabling the present thesis, but most importantly were excellent mentors. *Everything you see I owe to* their support.

Special gratitude belongs to Bei-Lok Hu and Ryan Behunin who hosted and mentored me, thereby becoming *main characters in the drama*.

It is further my great pleasure to thank Prof. Greffet, Prof. Ingold, Prof. Sokolov and Prof. Rauschenbeutel for forming the committee and reviewing the present dissertation.

My thesis greatly benefited from the mutual work with Marty Oelschläger, Dan-Nha Huynh, Christoph Egerland and Bettina Beverungen as well as the TO&Ps at the Humboldt University and the Max Born Institute in Berlin-Adlershof. Further, a special thanks goes to Mrs. Götsch at the HU as well as Mrs. Rapelius and Mrs. Hüneburg at the MBI for administrative support.

I immensely value the countless helpful and inspiring discussions with Paul Balduf, Cordula Schwappach, Philip Kristensen, Simon Hermann, Kanupriya Sinha, Jen-Tsung Hsiang, Diego Dalvit, John Dallyn, Reinaldo de Melo e Souza, Markus Krutzik, Sascha Vowe, Bastian Leykauf, Salvatore Butera, the anonymous referees and last, but not least, the students of the classes I was lucky to teach.

I am indebted to Francesco Intravaia, Cordula Schwappach, Paul Balduf, Dan-Nha Huynh, Bettina Beverungen, Marty Oelschläger, Christoph Egerland, Alexander Ruf and Tom Schumann for proofreading the manuscript.

Particular credit goes to Cordula Schwappach for designing the cover and binding of the thesis and Dan-Nha Huynh for providing the LaTeX-template. Printed by Druckwerkstatt Regel, Samariterstraße 7, 10247 Berlin.

I am very grateful for support from the German-American Fulbright Commission (Doktorandenprogramm) and particularly thank the Joint Quantum Institute and the Maryland Center for Fundamental Physics at the University of Maryland as well as the Northern Arizona University for their hospitality. I appreciate the financial support from the Wilhelm-and-Else Heraeus foundation for organizing a scientific retreat as well as for participating at the spring meetings of the German Physical Society and the Heraeus seminars. Further, I thank the Norwegian University of Science and Technology in Trondheim for sponsoring my participation at the Casimir workshop, the Optical Society of America for inviting me to the OSA Light the Future Plenary 2019 and the Council for the Lindau Nobel Laureate Meetings for inviting me to their 70th congress.